Università degli Studi di Torino

Doctoral School of Sciences and Innovative Technologies

Earth Sciences
XXX Cycle

Metamorphism and CO_2-production in collisional orogens: case studies from the Himalayas

Candidate: Giulia Rapa

Tutors
Dr. Chiara Groppo – Università di Torino
Prof. Franco Rolfo – Università di Torino
Dr. Pietro Mosca – IGG-CNR, Torino

Members of the Committee
Dr. Gisella Rebay – Università di Pavia
Dr. Silvio Ferrero – Universität Potsdam
Prof. Daniele Castelli – Università di Torino

Extended abstract

The aim of this work is to achieve a deeper understanding of the role exerted by the Himalayan orogeny on the long-term global carbon cycle, clarifying the abundance, distribution and types of CO_2-source rocks in selected sectors of the Himalayan orogen, the nature of the metamorphic CO_2-producing reactions, the amounts of CO_2 produced through these reactions and the chronology of the CO_2-producing reactions. To achieve these results, a detailed knowledge of the structural and metamorphic architecture of the selected sector of the Himalayan chain is mandatory.

The study area is located in central Nepal, north of Kathmandu, in the Gatlang–Langtang and Gosainkund–Helambu regions. All the main tectono-metamorphic units of the Himalayan chain are exposed. From lower to upper structural level these are: Lesser Himalayan Sequence (LHS) and Ramgarh Thrust Sheet (LHS-RST), mainly consisting of phyllites and slates with intercalations of orthogneiss upsection, the Lower Greater Himalayan Sequence (L-GHS), consisting of highly deformed garnetiferous schists and kyanite/sillimanite -bearing gneisses; the Upper-Greater Himalayan Sequence (U-GHS) consisting of migmatites and granitic orthogneisses with bodies of leucogranites.
In order to understand the structural and metamorphic architecture of both LHS and GHS in the study area, detailed fieldwork and petrological studies were performed along the Gosainkund–Helambu and Gatlang-Langtang transects.
Peak *P–T* conditions were estimated for selected metapelite samples using the pseudosection approach and the Average PT method. The structurally lowest LHS samples have a metamorphic evolution characterized by a narrow hairpin *P–T* path with peak *P–T* conditions of 595 ± 25 °C, 7.5 ± 0.8 kbar, corresponding to a *T/*depth ratio of 24 ± 3 °C/km (using both the phase diagram approach and the Average PT approach). The structurally upper LHS samples belong to the LHS-RTS, which is characterized by a P-T evolution at higher P-T conditions (635 ± 15 °C, 9.6 ± 1 kbar) and defines a lower *T/*depth ratio of 20 ± 2 °C/km (21 ± 3 °C/km using Average PT). Based on the difference in peak metamorphic conditions and *T/*depth ratios, the occurrence of a tectono-metamorphic discontinuity separating these two sets of samples is confirmed (i.e. the Ramgarh Thrust). Along the Gatlang-Langtang section, two tectono-metamorphic units have been distinguished within the GHS: L–GHS, characterized by peak *P–T* conditions at 725 ± 4 °C, 10 ± 0.1 kbar (corresponding to a *T/*depth ratio of 22 ± 0.5 °C/km; 23 ± 2 °C/km using the Average PT approach), and the structurally higher U–GHS, with peak metamorphic conditions at 780 ± 20 °C, 7.8 ± 0.8 kbar (corresponding to a *T/*depth ratio of 30 ± 4 °C/km; 40 ± 12 °C/km using the Average PT method). These data show the existence of a main tectono-metamorphic discontinuity within the GHS, as previously suggested by other authors. The LHS and GHS are in turn separated by the Main Central Thrust.

The Gosainkund–Helambu region occupies a key area for the development of Himalayan kinematic models, connecting the well-investigated Gatlang-Langtang area to the north with the Kathmandu Nappe, whose interpretation is still debated, to the south.
The results of petrological modelling of the metapelites from the Gosainkund–Helambu section show that this region is entirely comprised within the L–GHS unit: the estimated peak metamorphic conditions of 737 ± 8 °C, 10 ± 0.4 kbar correspond to a uniform *T/*depth ratio of 23 ± 1 °C/km (22 ± 3 °C/km using the Average PT approach). The metamorphic discontinuity identified along the Langtang transect and dividing the GHS in two tectono-metamorphic units is located at a structural level too high to be intersected along the Gosainkund–Helambu section. These results have significant implications for the tectonic interpretation of the Kathmandu Nappe (KN) and provide a contribution to the more general discussion of the Himalayan kinematic models. The structurally lower unit of the KN (known as Sheopuri Gneiss) can be correlated to the L–GHS unit; this result strongly supports those models that correlate the KN to the Tethyan Sedimentary Sequence and that suggest the merging of the South Tibetan Detachment System and the Main Central Thrust on the northern side of the KN. In this sector of the Himalayan chain, the most appropriate kinematic model able to explain the observed tectono-metamorphic architecture of the GHS is the duplexing model, or hybrid models which combine the duplexing model with another end-member model.

Fieldwork performed in the study area and in eastern Nepal highlighted that CO_2-source rocks are widespread at different structural levels and occur as: dm- to m- thick layers or boudins in both the LHS and the L-GHS, *vs*. tens to hundreds of meter thick layers within anatectic gneisses in the structurally upper U-GHS. Three different chemical groups have been recognized, and they can be described in terms of relatively complex chemical systems: (1) CFMAST-HC (CaO-FeO-MgO-Al_2O_3-SiO_2-TiO_2-H_2O-CO_2) group, significantly more abundant in the U-GHS; (2) NCFMAST-HC (Na_2O-CaO-FeO-MgO-Al_2O_3-SiO_2-TiO_2-H_2O-CO_2) and (3) NKCFMAST-HC (Na_2O-K_2O-CaO-FeO-MgO-Al_2O_3-SiO_2- TiO_2-H_2O-CO_2) groups, widespread in both the GHS (L-GHS and U-GHS) and LHS. In all groups, mineral assemblages vary with increasing metamorphic grade from lower to upper structural levels. Different petrographic types have been distinguished for each chemical group, based on the mineral assemblages (i.e. Types 1A to D; Types 2A-2B; Types 3A to F). Most of these assemblages, especially those equilibrated at lower temperatures and still containing abundant phyllosilicates, are not easy to recognize in the field and have been probably considerably overlooked by previous studies.

Major and trace element patterns suggest that CO_2-source rocks belonging to the NKCFMAST-HC group derive from a marly protolith, with variable modal amounts of biogenic (carbonatic) and pelitic components. On the contrary, CO_2-source rocks belonging to the CFMAST-HC and NCFMAST-HC groups show a significantly different trend, suggesting that their protoliths were smectite-rich bentonites, possibly deriving

from the alteration of volcanic ash layers. Minor impure marble layers also occur in both the CFMAST-HC and NKCFMAST-HC groups, and they derive either from impure limestones or from impure dolostones.

The phase petrology approach was used to investigate the most relevant CO_2-producing reactions in different types of CO_2-source rocks (Type 1C, 3C and 3F) and to quantify the amounts of CO_2 that were released through these reactions. This approach allowed an indirect estimate of the amount of CO_2 released during prograde metamorphism. The thermodynamic modelling of metacarbonate rocks is challenging: the main difficulties are related to the presence of a H_2O-CO_2 fluid, whose composition is an additional variable, and to the common occurrence of complex Mg-Fe-Ca (garnet, clinopyroxene, amphibole) and Ca-Na (plagioclase, scapolite) solid solutions, as well as of K-bearing phases (white mica, biotite, K-feldspar) and Ti-bearing phases (biotite, titanite).
Decarbonation reactions were modelled in the CFMAST-HC system and in the more complex MnNKCFMAST-HC and NKCFMAST-HC systems using different types of phase diagrams: P/T-XCO_2 pseudosections, P/T-XCO_2 sections and mixed-volatile P-T phase diagrams. P-T data (i.e. P/T gradient) obtained from the metapelites hosting the CO_2-source rocks were used.

In Type 1C sample (likely deriving from bentonite), the CO_2-producing process was a continuous process, and mostly occurred at relatively high T conditions. The final CO_2 production was lower than 1 wt% of CO_2, and more likely almost negligible because at least some of the CO_2-rich fluid internally produced during the prograde evolution of this sample remained confined within the system, allowing carbonation reactions to proceed at decreasing P-T conditions.

In Type 3C sample (derived from calcite-rich pelite) the majority of CO_2 (~2.5 wt%) is released through continuous reactions occurring at relatively low P-T conditions (T< 500 °C; P< 6 kbar), during the early prograde evolution. A small amount of CO2 (<0.5 wt%) was additionally produced at ~500 °C through a garnet-forming, calcite-consuming, discontinuity reaction. Overall, the CO_2 productivity of this sample is therefore < 3.5 wt%.

In Type 3F lithologies (derived from marly protoliths) CO_2 was produced through distinct, short-lived events, which occurred at specific P-T conditions along the whole prograde metamorphic evolution, and especially at relatively high temperature. The predicted amounts of produced CO_2 are quite high (from a minimum of 2 wt% to > 8 wt% of CO_2) and vary as a function of the bulk composition. Most of the CO_2-producing reactions modelled in the Type 3F CO_2-source rocks also produced titanite. Taking advantage of the possibility of simultaneously applying U-Pb geochronology and Zr-in-titanite thermometry, sample 14-53 was selected as a case study for constraining the timing of CO_2 production in the most abundant type of CO_2-source rocks within the GHS. Titanite grains grew during two nearly consecutive episodes of titanite formation: a near-peak

event at 730–740 °C, 10 kbar, 30–26 Ma, and a peak event at 740–765 °C, 10.5 kbar, 25–20 Ma.

In order to extrapolate the amount of produced CO_2 to the orogen scale, an estimate of the total volume of this type of CO_2-source rocks in the whole Himalayan belt is needed, as well as the total volume of the GHS itself. Type 3F are by far the easiest to be recognized in the field, therefore they have been used as a starting point for the calculation. Considering the uncertainties associated with all the input values (volume of the whole GHS unit; vol% of the CO_2-source rocks; CO_2 productivity; duration of CO_2-producing process), the metamorphic CO_2 flux resulting from the studied CO_2-source rocks ranges between a minimum value of 1.4 Mt/yr and a maximum value of 19.4 Mt/yr. This estimated metamorphic CO_2 flux is of the same order of magnitude as present-day degassing from hot springs, thus suggesting that CO_2-producing processes similar to those described in this Project still occur along the active Himalayan orogen, and should be considered in any future attempts of estimating the global budget of non-volcanic carbon fluxes from the lithosphere.

Table of contents

Chapter 1

Introduction

1.1 Problem statement

Understanding the processes controlling the nature and magnitude of CO_2 global cycle is fundamental for the comprehension of the past-to-present global climate changes (Evans, 2011). Considerable attention has been given so far to the short-time scale (< 1000 yr) fluctuations in atmospheric CO_2 levels that result from cycling of carbon between biological, atmospheric and oceanic reservoirs ("short-term carbon cycle"). However, "long-term carbon cycle" (Berner, 1999) that operates over millions of years and that involves the slow exchange of carbon between rocks and the surficial systems (oceans, atmosphere, biota and soils) is also worth of attention for the huge volume of CO_2 possibly involved (Kerrick & Caldeira, 1993; Bickle, 1996; Evans, 2011; Gaillardet & Galy, 2008; Skelton, 2011, 2013). Modelling of the global carbon cycle shows that on time scales > 1 Ma, global temperatures are largely controlled by the relative fluxes of CO_2 degassed through metamorphic and magmatic processes *vs*. CO_2 consumed by chemical weathering (e.g. Menzies et al., 2018).

So far, the CO_2 degassing flux was mainly estimated based on the CO_2 emitted by volcanoes in different geodynamic contexts, magmatic CO_2 derived from the mantle and metamorphic CO_2 degassed from subduction zones (Berner, 1991). This estimated flux does not take into account CO_2 derived from orogenic zones, where CO_2 is formed through metamorphic reactions between carbonates and silicates. Primary geologic settings for the production of significant amounts of metamorphic CO_2 include collisional contexts where decarbonation reactions occur at relatively high temperatures within metacarbonate rocks (e.g. calc-silicate rocks and impure marbles, derived from carbonate-rich pelites, marls, impure limestones and/or dolostones). The nature and magnitude of metamorphic CO_2 cycle, however, is still poorly understood and remains difficult to be defined (Evans, 2001; Gaillardet & Galy, 2008; Ague, 2000; Galy & France-Lanord, 1999; Skelton, 2011, 2013; Groppo et al., 2013b, 2017; Rolfo et al., 2015b).

The Himalayan belt is the largest ''large-hot'' collisional orogen on Earth (Beaumont et al., 2010), where tectonic processes are still active. The medium to high geothermal gradients experienced (at least in the central and eastern sectors of the orogen: Goscombe et al., 2006) during the Himalayan continental collision, may have allowed the release of metamorphic CO_2 through prograde devolatilization reactions. Moreover, CO_2-source rocks are widespread at different structural levels (Rolfo et al., 2017): the Himalayan belt is therefore the ideal natural laboratory in which to study metamorphic CO_2-producing processes. However, the CO_2-producing lithologies in Himalaya have been largely ignored

in previous petrological studies, being mainly mentioned as intercalations within the prevailing metapelitic sequences of the Lesser Himalayan Sequence and Greater Himalayan Sequence (e.g. Goscombe et al., 2006).

Major uncertainties in the fully quantitative modelling of the CO_2 fluxes from the Himalaya in the past are:

(i) limited information on the volumes of potential CO_2-source rocks in the Himalayan belt, on their distribution and on their relevant mineral assemblages;

(ii) poor knowledge of the nature of metamorphic CO_2-producing reactions and of the magnitude and rate of metamorphic CO_2 release;

(iii) uncertainties in the estimates of the timing and duration of prograde metamorphism, which is essential for the determination of the amount of CO_2 released per time units.

Appealing indicators for a contemporary metamorphic CO_2 production in Himalaya are represented by the widespread occurrence of high CO_2-bearing hot springs located along the major tectonic discontinuities of the Himalayan belt (Becker et al., 2008; Evans et al., 2008; Perrier et al., 2009), and by the recent discovery of gaseous CO_2 discharges from the ground associated or not to the hot springs (Perrier et al., 2009; Girault et al., 2014a,b). Peak values of the measured CO_2 flux at these gas discharges are exceptionally high (Perrier et al., 2009); geochemical and isotopic studies confirm that CO_2 is released at mid-crustal depth by metamorphic reactions within the Indian basement, transported along pre-existing faults by meteoric hot water circulation, and degassed before reaching surface, suggesting that further studies should be undertaken to better constrain the carbon budget of the Himalaya, and, more generally, the contribution of collisional belts building to the global carbon balance.

1.2 Aim of the Thesis

The **final goal** of this PhD project is **to achieve a deeper understanding of the role exerted by the Himalayan orogeny on the long-term global carbon cycle.** In particular, it **aims to clarify:** (i) the abundance, distribution and types of CO_2-source rocks in selected sectors of the Himalayan orogen, (ii) the nature of the metamorphic CO_2-producing reactions, the P-T conditions at which they have occurred, as well as the composition of the produced fluid; (iii) the amounts of CO_2 produced through these reactions, and the metamorphic CO_2 fluxes along the Himalayan chain, and (iv) chronology of the CO_2-producing reactions which occurred during the Himalayan collision.

To answer these questions, a detail knowledge of the structural and metamorphic architecture of the selected sector of the Himalayan chain is required, in order to understand the P-T evolution experienced by samples at different structural levels and to recognize in the field the evidence of those structural discontinuities that may have acted as conduits for the channelized fluid flow toward the Earth's surface.

1.3 Dissertation format

The Thesis has been organized in 6 chapters: most of them include data and results that have been already published in a number of papers in peer-reviewed, international journals or are at various stages of preparation for publication.

Chapter 1. This chapter is an introduction to the Thesis. The main open questions related to the production of metamorphic CO_2 in orogenic settings are outlined, and the specific objectives of the PhD project are presented.

Chapter 2. In this chapter, the large-scale geological architecture of the Himalayan chain is briefly discussed. More details are given for central Nepal Himalaya, where the study area is located (Rasuwa District); the main litho-stratigraphic and tectonic features are described and summarized. At the end of the chapter, a general overview of the present-day metamorphic CO_2-degassing occurring along the Himalayan chain is given. This last point is important in order to connect decarbonation reactions which took place at depth to the release of metamorphic CO_2 at surface, and to attest that the production of metamorphic CO_2 is still occurring along the chain.

Chapter 3. A detail litho-stratigraphic, structural and petrological reconstruction of the study area is presented in this chapter. Field-based investigations, meso- and micro-structural data are integrated with a detailed petrologic study of several metapelite samples from different structural levels and tectono-metamorphic units. The P-T evolution of the studied samples is constrained using both the pseudosection approach and optimal thermobarometry; the integration of structural and petrologic data allows the identification of three tectono-metamorphic discontinuities. In addition, the main results outlined in this chapter are discussed in the framework of the main current Himalayan tectonic and kinematic models, in order to understand which is the most appropriate to explain the observed tectono-metamorphic architecture.

Data and results presented in this Chapter have been published in two papers (Rapa et al., 2016, *Journal of metamorphic Geology*; Rapa et al., in press, *Journal of Asian Earth Sciences*).

Chapter 4. This chapter focuses on the types, distribution and protolith's nature of different types of CO_2-source rocks in the Himalayan orogen (central-eastern Nepal and Sikkim). Fieldwork data, combined with petrographic observations and minero-chemical characterization of the different lithologies allow to identify three main types of CO_2-source rocks (i.e. Types 1, 2 and 3), which correspond to different protoliths (i.e. bentonitic layers: Types 1 and 2; marls and carbonate-rich pelites: Type 3). The nature of these protoliths is investigated using major and trace element bulk-rock compositions.

A paper presenting data and results discussed in this Chapter is currently in preparation for submission to *Chemical Geology*.

Chapter 5. The aim of this chapter is to constrain the P-T-t conditions at which CO_2 was produced during the Himalayan orogeny, focusing on different types of CO_2-source rocks, in order to point out similarities and/or differences in the CO_2-producing processes. Different types of phase diagrams are used to constrain the prograde P-T-X(CO_2) evolution of the studied samples. The different metamorphic CO_2-producing reactions are petrologically investigated and the amounts of CO_2 produced per volume unit of reacting rock are estimated. For one sample, the correlation of T-t data from different titanite generations with specific CO_2-producing reactions, allows constraining the timing, duration and P-T conditions of the main CO_2-producing events, as well as the amounts of CO_2 produced.

Results presented in this Chapter are summarized in a paper published on *Lithos* (Rapa et al., 2017), and in a paper currently in preparation for submission to *Journal of metamorphic Geology*.

Chapter 6. This is the concluding chapter of the Thesis. A first order extrapolation of the CO_2 amounts constrained in Chapter 5 to the orogen scale is proposed (see also Rapa et al., 2017). The results are compared to literature estimates of both past CO_2 fluxes and present-day degassing, leading to interesting considerations for the global carbon cycle.

Chapter 2

Geological outline

2.1 Introduction to the geology of Himalaya

The Himalaya is the highest and the youngest mountain range on Earth and is commonly considered as the archetype of collisional orogens (e.g. Le Fort, 1975; Kohn, 2014). It describes a 2500 km-long, 100-150 km wide, arcuate belt, with sharp bends at the western (Nanga Parbat) and eastern (Namche Barwa) syntaxes (Wadia, 1933). Politically, the Himalayan range is located between Pakistan, India, Nepal, China and Bhutan. Geographically, the Himalaya is bounded by the Indus and Brahamaputra (Tsangpo) rivers to the west and east, respectively, and by the Indo-Gangetic plain and the Tibetan Plateau to the south and north, respectively .

As a whole, the Himalayan-Tibetan orogen consists of several terranes, rifted from the eastern margin of Gondwana during the Late Paleozoic, drifted northward across the Tethyan Ocean basins and then progressively accreted to the southern margin of Asia during the Mesozoic (e.g. Allégre et al., 1984; Sengör, 1987; Yin and Harrison, 2000). The Himalaya s.s. is the result of the last of these collisional events, deriving from the collision between the India terrane and the southern margin of Asia (Lhasa terrane). The evolution of the Himalaya *s.s.* started during the Early-Middle Cretaceous (e.g. Zhu et al., 2013) with the northward subduction of the Neo-Tethys ocean, originally interposed between the India and Lhasa terranes, below the Asian Plate. The final closure of the Neo-Tethys ocean led to the India-Asia continental collision, which has been constrained at ca. 60 to 50 Ma (e.g. Tapponier et al., 1982; Patriat and Achache, 1984; Tapponier et al., 1986; Dewey et al., 1989; LePichon et al., 1992; Zhu et al., 2005; Leech et al., 2005; Hu et al. 2016 and references therein). The average convergence rate between India and Asia was ~20 mm/yr during most of the Neogene, decreasing to 13-20 mm/yr during Pliocene to recent time (Powers et al., 1998; DeCelles et al., 1998a, 2001; Lavé and Avouac, 2000), with a present day mean value of 17 mm/yr in the central part of the belt (Bilham et al., 1997; Larson et al., 1999). Most of the deformation is nowadays accommodated along the Main Himalayan Thrust (MHT), where most of the major earthquakes occur (Cattin and Avouac, 2000; Lavé and Avouac, 2000). The MHT is a low-angle fault where Main Frontal Thrust, Main Boundary Thrust and Main Central Thrust merge together, proposed on structural and seismic profiles (Shelling and Arita, 1991; Zhao et al., 1993; Nelson et al., 1996).

The 2000 km long Indus-Tsangpo Suture Zone (ITS), running approximately parallel to the Indus and Tsangpo rivers in the E-W direction, marks the present boundary between the Indian and the Asian plates, and records the closure of the Neo-Tethys ocean (Yin and

Harrison, 2000). The ITS thus represents the northern boundary of the Himalayan orogen. The ITS consists of Triassic-Cretaceous turbidites deposited on the Indian Plate (Frank et al., 1977; Burg and Chen, 1984; Robertson and Degnan, 1994), ophiolitic mélanges interpreted as relics of paleo-accretionary prisms (e.g. Corfield et al., 1999; Robertson, 2000; Mahéo et al., 2006; Guillot et al., 2008) and minor well-preserved ophiolites like Xigaze-Kiogar in Xigang (near Lhasa and Xigaze, Tibet) and Spongtang in Ladakh (Hodges, 2000 and references therein). Ophiolitic rocks in the ITS were metamorphosed at various conditions ranging from very low- and low- metamorphic grade to blueschist and, rarely, eclogite-facies conditions (e.g. Ghose and Singh, 1980; Honegger et al., 1989; Chatterjee and Ghose, 2010; Ao and Bhowmik, 2014; Bhowmik and Ao, 2016; Groppo et al., 2016). Along the suture the Kohistan-Ladack arc terrane represents a remarkable cross-section through an island sequence developing as a result of the subduction (Treolar et al., 1996; Rolfo et al., 1997).

South of the ITS, the Himalayan orogen exposes the deformed and variably metamorphosed sedimentary sequences originally deposited on the India's leading northern edge, ranging in age from Paleoproterozoic to Eocene (Upreti and Yoshida, 2005). The tectono-stratigraphic architecture of the Himalayan belt is relatively uniform at the regional scale; one of the most striking aspects of the orogen is, in fact, the lateral continuity of its main tectonic features. Four main tectono-stratigraphic units are usually distinguished along strike, separated by major north-dipping tectonic discontinuities (e.g. Heim and Gansser, 1939; Gansser, 1964; LeFort, 1975; Lombardo et al., 1993; Upreti, 1999; Hodges, 2000; Yin, 2006). From south to north, and from lower to upper structural levels, these units are (Fig. 2.1): the Sub-Himalayan Zone (or Siwalik Group), the Lesser Himalayan Sequence, the Greater Himalayan Sequence and the Tethyan Sedimentary Sequence, bounded by the Main Frontal Thrust (MFT), the Main Boundary Thrust (MBT), the Main Central Thrust (MCT) and the South Tibetan Detachment System (STDS), respectively. Age of activation of thrusting is progressively older from S to N. In Central Nepal, age of activation of MBT is constrained at <12 Ma, of MCT at 23-20 Ma and of STDS at 23-13 Ma (Yin et al., 2006 and references therein).

Local perturbations of this general east-west attitude occur around major tectonic windows (e.g. Arun, Tamur and Tista windows in eastern Nepal and Sikkim: e.g. Goscombe et al., 2006 and references therein) and klippens (e.g. the Kathmandu Nappe in central Nepal; e.g. Upreti and Le Fort, 1999; Johnson et al., 2001).

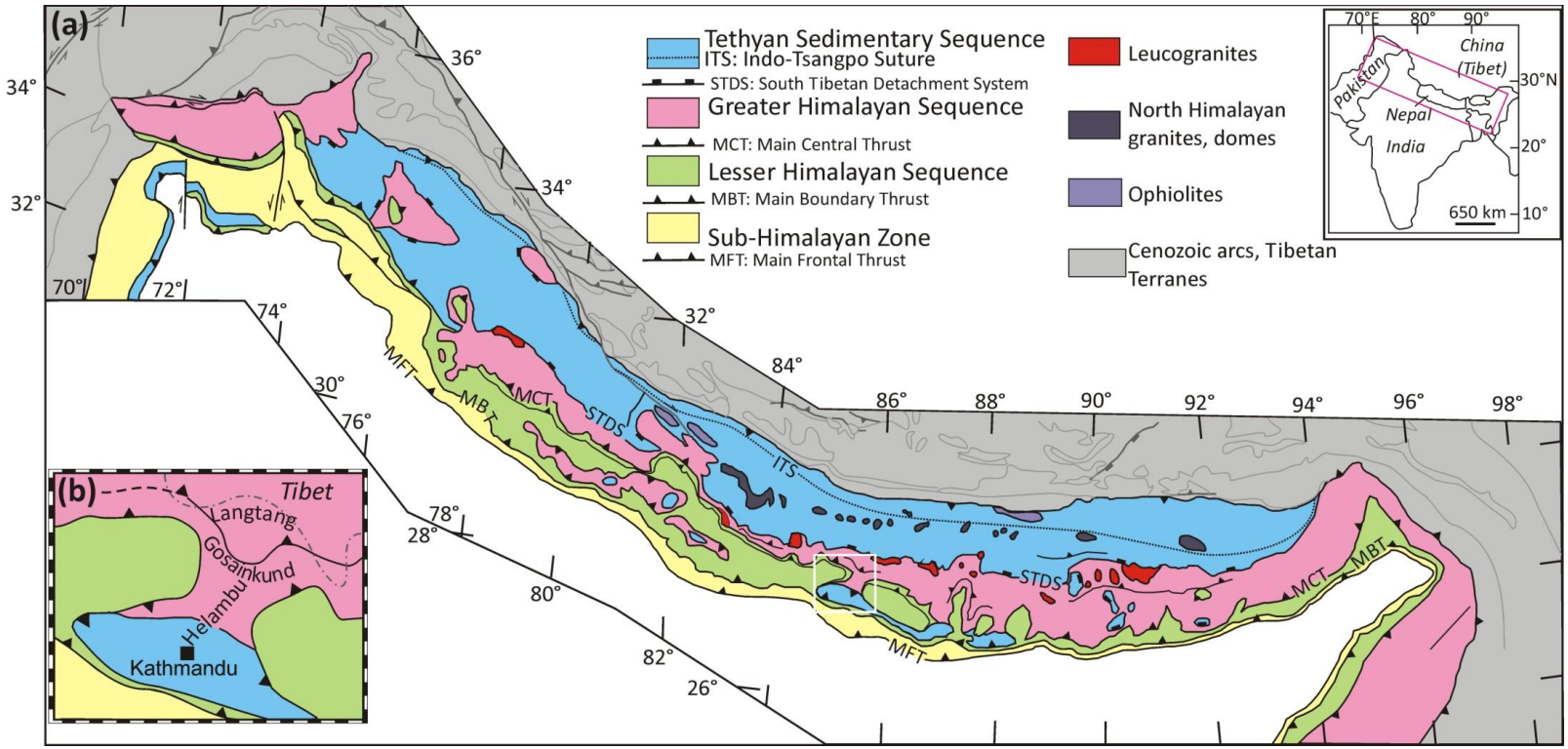

Fig. 2.1 – (a) Simplified tectonic map of the Himalaya, showing the major tectono-metamorphic units and tectonic discontinuities. Modified from: Yin (2006), He et al. (2015), Wang et al. (2016). The white rectangle locates the study area, which is enlarged in (b). **(b)** Simplified tectonic sketch of the study area, with the indication of the studied transects (Gatlang-Langtang, Gosainkund-Helambu). The dotted-dashed grey line is the political boundary between Nepal and China (Tibet).

The **Sub-Himalaya** consists of middle Miocene to Pleistocene molasse-type unmetamorphosed sediments deposited in the foreland basin (Hodges, 2000). The best exposure of this unit is in western Himalaya, where Miocene-Pleistocene conglomerates, sandstones and mudstones of the Siwalik Group are geometrically followed by Eocene-Miocene siltstones and sandstones of the Rawalpindi Group (Burbank et al., 1997; Hodges, 2000). The Sub-Himalayan Zone is bounded to the south by the **Main Frontal Thrust** (**MFT)**, which separates the Sub-Himalayan Zone from the Quaternary active foreland basin of the belt, and to the north by the **Main Boundary Thrust (MBT)** along which the Lesser Himalayan Zone is thrusted over the Sub-Himalayan Zone.

The **Lesser Himalayan Sequence** (**LHS**) consists of unmetamorphosed to greenschist/lower amphibolite facies metasediments, tectonically defining a duplex structure (e.g. De Celles et al., 1998a; Pearson and DeCelles 2005; Webb et al. 2011). Bodies of augen orthogneisses and minor metavolcanics intrude the sequence at different structural levels (e.g. Frank et al., 1995; DeCelles et al., 1998a; Upreti, 1999; Kohn et al., 2010). The LHS has been interpreted as a thick Paleo- to Mesoproterozoic sedimentary sequence deposited on the northern margin of the Indian Plate (e.g. Gansser, 1964; Upreti, 1999; Hodges, 2000; Pearson and DeCelles, 2005), in a more proximal position with respect to the Tethyan Sedimentary Sequence (Hodges, 2000). Age constraints for the lower section of the sequence (i.e. known as Nawakot Group in central Nepal Himalaya; Stöcklin, 1980) gave a depositional age between 1870 and 1600 Ma (Parrish and Hodges, 1996; Upreti, 1999; Hodges, 2000; DeCelles et al., 2000; Miller et al., 2000; Robinson et al., 2001). The Nawakot Group is unconformably overlain by Permian to Paleocene (Sakai, 1985; Valdiya, 1998) limestones and calcareous sandstones. Eocene-Miocene syn-orogenic sediments (Critelli and Garzanti, 1994; DeCelles et al., 1998b, 2004) and continental strata constitute the uppermost deposits of LHS.

The LHS is tectonically overlaid by the Greater Himalayan Sequence along the **Main Central Thrust (MCT,** as originally defined by Gansser, 1964), a large ductile shear zone ranging in thickness from several hundreds of meters to several kilometres and showing a top-to-the-SW sense of movement. Despite the intensive studies over the last decades, the MCT remains one of the most debated tectonic features of the Himalaya and there is still not a unique interpretation about the position of its lower and upper boundaries, as well as on its discrete *vs*. "tectonic melange" nature (see Hodges et al., 2000, Searle et al., 2008 and Martin, 2017 for reviews).

The **Greater Himalayan Sequence** (**GHS**) mainly consists of metamorphic rocks derived from Neoproterozoic to Cambrian protoliths and represents the exhumed metamorphic core of the Himalaya (Le Fort, 1975, Parrish and Hodges, 1996; Upreti, 1999; Hodges, 2000; DeCelles et al., 2000; Robinson et al., 2001). From the lower to the upper structural levels, the GHS is characterized by medium- to high-grade metasedimentary rocks and granitic orthogneisses (e.g. Pecher, 1989; Goscombe et al., 2006; Kohn, 2008, 2014; Searle et al., 2008; Groppo et al., 2009, 2010; Mosca et al., 2012) and by migmatitic para-

and ortho- gneisses (also known as Higher Himalayan Crystallines: e.g. Lombardo et al., 1993; Pognante and Benna, 1993). The paleogeographic provenance of the GHS metasedimentary rocks is either from eastern Africa or from eastern Antarctica (DeCelles et al., 2000; Upreti and Yoshida, 2005). In eastern Nepal, the GHS has been subdivided in different tectono-stratigraphic units (Le Fort, 1975), whose stratigraphic and geometric relationships are complex and still largely unknown (Goscombe et al., 2006). The upper portion of the sequence is intruded by Miocenic two-mica and tourmaline leucogranites (Hodges, 2000; Visonà and Lombardo, 2002). The GHS has long been considered as a coherent tectonic unit. However, since the discoveries of the first tectono-metamorphic discontinuities in some sectors of the GHS (e.g. Langtang: Inger and Harris, 1992; Reddy et al., 1993; Fraser et al., 2000; Kohn et al., 2004, 2005; Eastern Nepal: Goscombe et al., 2006; Groppo et al., 2009; Imayama et al., 2010, 2012), it is becoming more and more evident that the structural architecture of the GHS is much more complex than previously supposed (see Montomoli et al., 2015 and Larson et al., 2015 and references therein). It is now widely accepted that at least one, first-order, regional-scale tectono-metamorphic discontinuity (e.g. High Himalayan Discontinuity as defined by Montomoli et al., 2013 in western Nepal) characterizes the GHS, which is thus divided in two portions with different metamorphic evolutions (e.g. Carosi et al., 2010; Larson et al., 2010; Yakymchuk and Godin, 2012; Montomoli et al., 2013; Rapa et al, in press; see § 3.5.1).

The contact between the GHS and the overlying **Tethyan Sedimentary Sequence (TSS)** is represented by a brittle-ductile normal fault system, the **South Tibetan Detachment System (STDS)**, with top-to-the-NE sense of movement (e.g. Burg and Chen, 1984; Burchfield et al., 1992; Carosi et al., 1998; Kellet et al., 2010). The TSS was deposited on the northern edge of the Indian passive margin from Cambrian to Eocene (Gaetani and Garzanti, 1991; Garzanti, 1999). The sequence consists of both siliciclastic and carbonatic sedimentary rocks interbedded with Paleozoic and Mesozoic volcanic rocks (Yin, 2006 and references therein); it is unmetamorphosed, except at its lower structural levels near the contact with the GHS, where it shows a low- to medium-grade metamorphic overprint (Lombardo et al., 1993; Upreti, 1999).

2.2 Geological setting of central Nepal Himalaya

The study area is located in central Nepal, north of Kathmandu, in the Gatlang–Langtang and Gosainkund–Helambu regions (Fig. 2.1b). The Gatlang–Langtang transect represents an ideal E–W cross-section through the metamorphic core of the Himalayan belt, passing through both the STDS to the east and the MCT to the west. The Gosainkund–Helambu region is located between the Langtang to the north and the Kathmandu Nappe to the south; it represents a link connecting lithological and structural features recognized in the Gatlang–Langtang region with those of the Kathmandu Nappe.

In the following paragraphs, the main litho-stratigraphic and tectonic features of central Nepal Himalaya are briefly summarized. A more detailed discussion of the geological setting of the study area, integrated with field observations and petrographic data, is presented in Chapter 3.

2.2.1 Lesser Himalayan Sequence

In central Nepal, the LHS is characterized by a complex tectono-stratigraphic architecture variably interpreted by different Authors, as summarized in Tab. 2.1. At the lower structural levels of the LHS, Pearson and DeCelles (2005) (following Stöckling, 1980) described the Kuncha Formation, consisting of greenish-grey phyllites and phyllitic quartzites. The Kuncha Formation could be the central Nepal equivalent of the Kushma and Ranimata Formations of western and eastern Nepal, respectively (Upreti, 1999; DeCelles et al., 2001). At the top of the Kuncha Formation, Pearson (2002) and Pearson and DeCelles (2005) documented the presence of the Ramgarh Thrust (RT), which emplaces older augen gneisses (Ulleri gneiss) and quartzites on younger calcschists and marbles (Schelling, 1992; DeCelles et al., 2001; Robinson et al., 2001; Pearson, 2002). Pearson and DeCelles (2005) traced the RT and the MCT in the Langtang region near the village of Syabrubensi, combining stratigraphic relationships and Nd isotopic analysis (Robinson et al., 2001; Pearson, 2002). The same Authors interpreted both the MCT and the RT as discrete structures rather than broad shear zones incorporating elements of both LHS and GHS, i.e. according to their interpretation, the RT is totally included within the LHS (Tab. 2.1). Kohn et al. (2004) confirmed the presence of the RT by means of geochronology on monazites.

The interpretation of MacFarlane et al. (1992) is completely different. According to these Authors, the LHS and the GHS are juxtaposed through a thick shear zone, the Main Central Thrust Zone (MCTZ), consisting of several thrust sheets derived from the LHS and, to a lesser extent, from the GHS (Tab. 2.1). Within the MCTZ, the different thrust sheets are separated by brittle faults with an inverse sense of movement.

Tab. 2.1 - Tectono-stratigraphic architecture of LHS in central Nepal

<table>
<tr><th colspan="2">Pearson and DeCelles, 2005 (after Stöcklin, 1980)</th><th colspan="2">MacFarlane et al. (1992) (and Takagi et al., 2003)</th><th colspan="2">Kohn et al., 2004</th><th colspan="2">This study</th></tr>
<tr><td>GHS</td><td>Formation I
MCT</td><td>GHS</td><td>Gosainkund gneiss</td><td>GHS</td><td>ZG1
MCT</td><td>GHS</td><td>L-GHS
MCT</td></tr>
<tr><td rowspan="10">Lower Nawakot Unit - LHS</td><td rowspan="2">Robang Fm
(+ Ulleri gneiss)</td><td rowspan="2">MCTZ - GHS</td><td>Syabru gneiss</td><td rowspan="10">LHS</td><td rowspan="2">ZL4</td><td rowspan="2">LHS- RTS</td><td rowspan="2">Two-mica augen gneiss, quartzites and phyllites</td></tr>
<tr><td>MCT</td></tr>
<tr><td>RT</td><td rowspan="9">MCTZ (affinity) - LHS</td><td>Syabru Bensi gneiss</td><td>RT</td></tr>
<tr><td rowspan="9">Kuncha Fm</td><td>Barabal schist</td><td rowspan="9">ZL3

ZL2

ZL1</td><td rowspan="9">LHS</td><td rowspan="9">Calcareous phyllite and calcschist
Graphitic schist
Quartzite

Kuncha Fm (phyllitic schist)</td></tr>
<tr><td>Bothe calc-schist</td></tr>
<tr><td>Trisuli schist</td></tr>
<tr><td>Chilime calc-schist</td></tr>
<tr><td>Goljhong schist</td></tr>
<tr><td>Thanjet schist
MCT-I</td></tr>
<tr><td>LHS</td><td>Dunche schist</td></tr>
</table>

Vertical axis is not to scale

These brittle faults are interpreted as relatively late structures related to the motion of the MBT at ca. 9-7 Ma and post-date the mylonitic fabric associated to the ductile movements along the MCT, which occurred at 20-15 Ma (MacFarlane et al., 1992). Takagi et al. (2003) followed the MacFarlane et al. (1992) tectono-stratigraphic nomenclature with minor modifications. They interpreted the fault boundary separating the Dunche schists from the overlying Thanjet schists (MCTZ lower unit) as MCT I (already defined by Arita et al. 1973), whereas the MCT, dividing the LHS from the GHS is placed higher in the sequence, but still within the MCTZ. Moreover, Takagi et al. (2003) described for the first time the evidence of north-eastward brittle extensional movements in the MCTZ, overprinting the southward ductile thrust movements. Pearson and DeCelles (2005)

rejected the stratigraphic nomenclature proposed by MacFarlane et al. (1992), as well as their large-scale duplex geometric architecture of the MCTZ, assigning to the brittle faults a minor relevance and interpreting them as local-scale faults, ubiquitous along the belt (see also Hodges et al., 2004).

2.2.2 Greater Himalayan Sequence

In central Nepal, the GHS consists of highly deformed garnetiferous schists and kyanite/sillimanite -bearing gneisses, passing to migmatites and granitic orthogneisses toward the upper structural levels. Leucogranite dykes cross-cut the main foliation upward in the section (e.g. Inger and Harris, 1992; Reddy et al., 1993).

Reddy et al. (1993) identified four different lithotectonic units (Tab. 2.2) within the GHS of central Nepal. The lowermost unit (Syabru Unit) is exposed immediately above the MCT and consists of a metapelitic sequence characterized by an inverted metamorphism reaching sillimanite-grade at the top, with local evidences of anatexis. The Kyanjjin Unit consists of a 1-km thick migmatitic augen gneiss body, similar to the orthogneisses exposed westward in the Annapurna and Manaslu regions. The uppermost units (Langshisa Unit and Langtang Lirung Unit) are lithologically similar, consisting of metasedimentary rocks intruded by a variable percentage of leucogranites. Layers of marbles and metre-scale calc-silicate layers also occur in these units.

Focusing on the Langtang region, which is by far the most studied area in central Nepal, several Authors have recognised a major metamorphic discontinuity within the GHS (Tab. 2.2), which separates a lower GHS unit, characterized by higher pressure at peak–*T* conditions, from an upper GHS unit, which experienced lower pressure at peak–*T* conditions (Inger and Harris, 1992; Macfarlane, 1995; Fraser et al., 2000; Kohn et al., 2004, 2005; Kohn, 2008). Dating monazites, Kohn et al. (2004,2005) further demonstrated that the age of peak metamorphism is progressively younger from upper to lower structural levels. In the upper GHS unit they defined an early prograde metamorphism occurred at 32-30 Ma, a late prograde event at 24-21 Ma, and melting and final melt crystallization at 20 and 19-17 Ma, respectively. In the lower GHS unit the early prograde, late prograde, melting and crystallization events occurred at 37-24, 24-17, 18 and 16-13 Ma, respectively. These monazite ages are in agreement with Rb-Sr mica ages (Inger and Harris, 1992), which constrained prograde metamorphism at 34 Ma, with possible re-crystallization due to MCT activity at 23 Ma. The upper portion of the Langtang transect cooled below 350 °C at 17 Ma, while the lower one has younger cooling ages (5 Ma) associated with recent uplift (Inger and Harris, 1992). MacFarlane (1993) gave similar results using ^{40}Ar-^{39}Ar geochronometry on biotite. She estimated an age of 19-22 Ma for the metamorphic peak, with cooling at 19 Ma in the upper and at 5-10 Ma in the lower portion.

Tab. 2.2 - Tectono-stratigraphic architecture of GHS in central Nepal

Inger and Harris, 1992		Reddy et al., 1993		Fraser et al., 2000		Kohn, 2004		This study	
TSS	Tethyan Sedimentary Sequence	GHS	Langtang Lirung Unit	GHS	Langtang Lirung Unit	GHS	ZG4	GHS	U-GHS
	LNF		Langshisha Unit		Kyangjing augengneiss				
GHS	High Himalayan		Kyangjin Unit		Syabru		LT		LT
			Syabru				ZG3		
					Unit		ZG2		L-GHS
	Cristalline Sequence						ZG1		
			Unit						
	MCT		MCT		MCT		MCT		MCT
LHS+GHS	MCT Zone	?	MCT Zone	?	MCT Zone	LHS	ZL4	LHS-RTS	Augen gneiss

Vertical axis is not to scale. LNF: Langtang Normal Fault.

2.2.3 Tethyan Sedimentary Sequence

In central Nepal, the TSS is exposed in very limited areas, generally confined in the proximity of the boundary with China (Tibet). Concerning the study area, Inger and Harris (1992) placed the contact between the GHS and the TSS at the very top of the Langtang Valley, still on the Nepalese side (Tab. 2.2). The contact is marked by a low-angle N-dipping normal fault, with biotite-grade metasedimentary rocks of the TSS in the hanging wall, and migmatites of the GHS in the footwall. A 1-km thick leucogranite body is

intruded in the TSS (Inger and Harris, 1992).

2.2.4 Kathmandu Nappe

The Kathmandu Nappe (KN) represents a local perturbation of the general west-east trend of the main Himalayan tectonic features (Fig. 2.1a). The KN has a synformal shape elongated parallel to the chain (Fig. 2.1b), with the city of Kathmandu in the middle. The tectonic interpretation of this half-klippen is still largely debated (e.g. He et al., 2015 and references therein; Rapa et al., 2016).

The southern tectonic margin of the KN, the Mahabharat thrust, is commonly interpreted as the southward propagation of the MCT (Stöcklin, 1980; Johnson et al., 2001), which emplaces the KN over the Nawakot Complex of the LHS. From top to bottom, the KN is conventionally divided in the Phulchauki Group, Bhimphedi Group and Sheopuri Gneiss (Stöcklin and Bhattarai, 1977; Stöcklin, 1980). The Phulchauki Group, ~6 km thick, consists of Neoproterozoic or Early Cambrian to Devonian limestones and minor shales and sandstones, unmetamorphosed or anchimetamorphic. Since it shows remarkably similarities to the TSS, it has been generally correlated with the TSS units of similar ages (Stöcklin, 1980; Johnson et al., 2001; Gehrels et al., 2006). A detailed stratigraphy of the Phulchauki Group is presented by Dithal (2015), following Stockiln (1980). The Bhimphedi Group consists of a ~8 km thick, medium- to high-grade metasedimentary sequence with a Proterozoic age, intruded by two different types of Cambro-Ordovician granites: porphyritic biotite-rich granites and pegmatitic tourmaline-rich granites intruding the first ones (Dithal, 2015). The contact between the Phulchauki Group and the Bhimphedi Group has been interpreted either as an angular unconformity (Pradhan et al., 1980; He et al., 2015) or as a transitional contact (Stöcklin, 1980). The interpretation of the Bhimphedi Group is still debated having been correlated to different tectono-metamorphic units (see discussion in Chapter 3).

Altogether, the Bhimpedi–Phulchauki succession is characterized by a right- way-up thermal gradient ranging from the kyanite zone (~650 °C) at its base to anchimetamorphic or unmetamorphosed rocks at its top (Johnson et al., 2001; Webb et al., 2011). This metamorphic field gradient is opposite compared to the renowned inverted metamorphic pattern that characterized most of the GHS. The Bhimpedi–Phulchauki succession occurs in the hangingwall of the Galchi Shear Zone (Webb et al., 2011), which separates the Bhimpedi and Phulchauki Groups from the Sheopuri Gneiss in the footwall. Sheopuri Gneiss consists of micaschists and gneisses mostly exposed along the Sheopuri Range.

Several chronological constraints have been obtained for the timing of emplacement and deformation of the KN. Early Paleozoic deformation was experienced by the frontal part of the klippen (Gehrels et al. 2003, 2006), but the age of emplacement of the KN on the

LHS is significantly younger. A 18 Ma age of emplacement was obtained by Johnson et al. (2001) from a syn-kinematic leucogranite close to the Sheopuri-Bhimphedi contact. Webb et al. (2011) obtained a similar age (20 Ma) from a leucogranite in the same structural position. ^{40}Ar-^{39}Ar and Rb-Sr muscovite cooling ages span from 22 Ma at the southern margin of the nappe to 12 Ma on its northern margin (Arita et al. 1997; Johnson and Rogers, 1997; Bollinger et al., 2006; Herman et al., 2010). Finally He et al. (2015) constrained the emplacement of the KN between 23 and 19 Ma.

Tab. 2.3 - Tectono-stratigraphic architecture of KN

Stöckiln, 1980	
Phulchauki Group	Devonian limestones
	Chitlan Fm
	Chandragiri limestone
	Sopyang Fm
	Tistung Fm
Bimphedi Group	Markhu Fm and marbles
	Kulikhani Fm
	Kalitar Fm
	Bhainsedobhan marble
	Raduwa Fm

Vertical axis is not to scale

2.3 Present-day metamorphic CO_2-degassing in the Himalaya

Numerous hot springs are located along the entire length of the Himalayan chain, from the Nanga Parbat syntaxis in Pakistan (Chamberlain et al., 2002), to NW India (Giggenbach et al., 1983; Tiwari et al., 2016), Nepal (Bhattarai, 1980; Bogacz and Kotarba, 1981; Kotarba et al., 1981; Colchen et al., 1986; Evans et al., 2004; Becker et al., 2008; Evans et al., 2008; Perrier et al., 2009; Girault et al., 2014a), NE India (Evans et al., 2008 and references therein) and Bhutan (Singh et al., 2004). Most of them are located in the proximity of the main structural discontinuities like the MCT.

Evidence for massive metamorphic CO_2 release from these hot springs is their high alkalinity (up to 56×10^{-3} $molL^{-1}$) which, for example, contributes to the total dissolved inorganic carbon (DIC) of the Narayani river (Evans et al., 2004). Moreover, high values of

$\delta^{13}C$ suggest a metamorphic origin for CO_2 at depth (Becker et al., 2008; Evans et al., 2008; Tiwari et al., 2016). In western and central Nepal, Girault et al. (2014a) made a systematic measurement of gaseous CO_2 and radon-222 emissions in the proximity of 13 hot springs, spanning from from lower Dolpo to the west to Kodari, east of Kathmandu (Fig. 2.2). They found a remarkably uniform isotopic CO_2 metamorphic signature; CO_2 and radon-222 emissions are concentrated along a 110 km long segment of the Himalayan chain, with a total CO_2 discharge of ~11 $t \times d^{-1}$.

The study area is characterized by numerous hot springs which have been studied in quite detail. Perrier et al. (2009) exhaustively characterized the Syabru Bensi hot springs (after LeFort, 1975; Kotarba, 1986), as well as the Chilime, Timure and Langtang Khola hot springs, all located in the studied area (Fig. 2.2), and the Kodari hot springs, located ~50 km eastward. In the Syabru Bensi area, CO_2 directly degassed from the ground was additionally discovered, with peak values of 19000 $g \times m^2 \times d^{-1}$, comparable to values reported for some volcanoes (e.g Granieri et al., 2010; Carapezza et al., 2011); an extremely high radon-222 signature is associated to these CO_2 fluxes (Perrier et al., 2009). Later on, Girault et al. (2014b) made a comprehensive study of the Syabru Bensi hydrothermal system (SBHS), studying five gas emission zones (mofette-like degassing) located along the Trisuli river. These Authors found a positive correlation between CO_2 and radon: total CO_2 emission of ~6 $t \times d^{-1}$ and a minimum radon discharge of ~140 MBq $\times d^{-1}$ have been estimated, respectively (note that CO_2 value is six time the value obtained by Perrier et al., 2009, which was based on a smaller area). The extremely high radon flux measured in the Syabru Bensi area makes the SBHS unique compared to other natural sites: this flux is, in fact, higher than those measured in volcanic, hydrothermal and mofette sites, and comparable to uranium mining sites (Girault et al., 2014b and references therein). The CO_2 fluxes measured at SBHS are similar to those observed at some volcanic, geothermal and hydrothermal sites and higher compared to those measured in fault-related sites (Girault et al., 2014b and references therein).

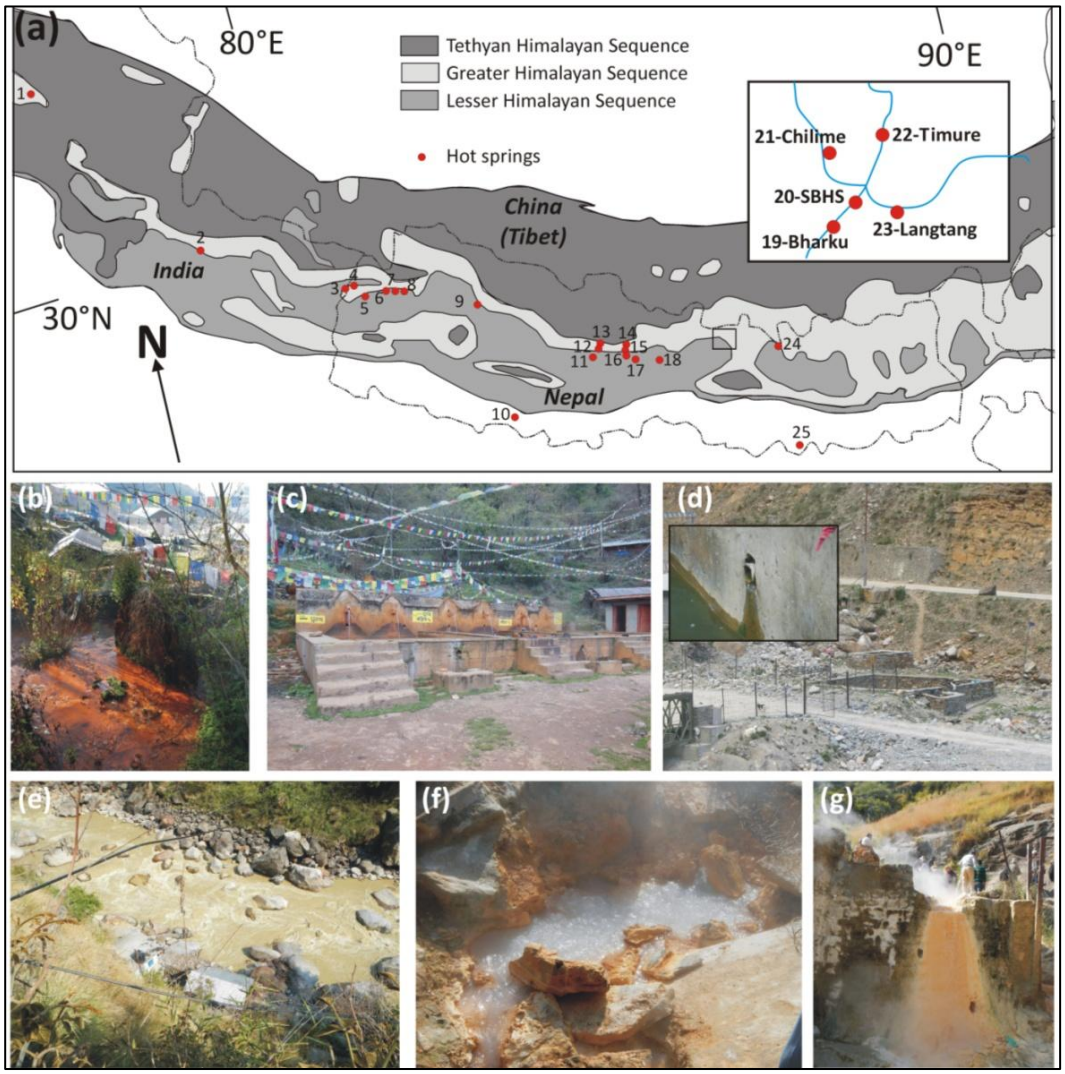

Fig. 2.2 – (a) Location of the main hot springs in the Himalayas (modified after Joshi et al., 2003; Girault et ., 2014a; He et al. (2015); Tiwari et al., 2016 and Wang et al. (2016). 1: Thopan, 2:Tapovan, 3:Sirbani, 4: SIna, 5: Barpata, 6: Joeligad, 7: Bauligad, 8: Chainpur, 9: Jumla, 10: Rear, 11: Mayangdi, 12: Sekeaurku, 13: Kali Gandaki, 14: Seti Khola, 15: Nayagaon, 16: Chlepani-1, 17: Chlepani-2, 18: Marsyangdi, 19: Bharku, 20: SBHS (Syabru Bensi Hydrothermal System according to Girault et al., 2014a), 21: Chilime, 22: Timure, 23: Langtang, 24: Kodari, 25: Janakpur. The top right inset shows the location of hot springs in the studied area. **(b,c)**: Chilime hot spring; **(d)** Timure hot spring; **(e)** SBHS; **(f,g)**: Tapovan.

Chapter 3

Tectono-stratigraphic architecture and metamorphic evolution of the Gatlang-Langtang and Gosainkund-Helambu regions, Central Nepal Himalaya

3.1 Introduction

Being the archetype of collisional orogens, the Himalayan chain is considered as an exceptional natural laboratory for studying the tectono-metamorphic processes that occur during continental collision. The GHS, which represents the exhumed metamorphic core of the Himalaya, is especially important for our understanding of orogenic processes. The GHS has long been considered as a coherent tectonic unit. However, since the discoveries of the first tectono-metamorphic discontinuities in some sectors of the GHS (e.g. Langtang: Inger and Harris, 1992; Reddy et al., 1993; Fraser et al., 2000; Kohn et al., 2004, 2005; Eastern Nepal: Goscombe et al., 2006; Groppo et al., 2009; Imayama et al., 2010, 2012), it is becoming more and more evident that the structural architecture of the GHS is much more complex than previously supposed (see Montomoli et al., 2015 and Larson et al., 2015 and references therein). It is now widely accepted that at least one, first-order, regional-scale tectono-metamorphic discontinuity (e.g. High Himalayan Discontinuity as defined by Montomoli et al., 2013 in western Nepal) characterizes the GHS, which is thus divided in two portions with different P–T–t evolution (e.g. Carosi et al., 2010; Larson et al., 2010; Yakymchuk and Godin, 2012; Montomoli et al., 2013). The scenario seems to be locally even more complex, with the possible existence of several tectono-metamorphic discontinuities (e.g. Larson and Cottle, 2014; Ambrose et al., 2015; Larson et al., 2015) within the GHS, which would therefore consist of multiple juxtaposed slices. The discovery of these discontinuities, often interpreted as in-sequence thrusts that were active prior to the MCT (Montomoli et al., 2015), has progressively weakened some of the most popular tectonic models used so far to explain the metamorphic and structural architecture of the Himalayan chain, such as the Channel flow model (Beaumont et al., 2001, 2004; Jamieson et al., 2004; Godin et al., 2006), and has led to the formulation of new “hybrid” models that combine elements of different end-member models (e.g. Cottle et al., 2015; He et al., 2015 and references therein).

Although the tectono-metamorphic architecture of the Langtang area is relatively well-known, a combined structural and petrological study of both the LHS and GHS is lacking. Moreover, most of the petrological studies published so far on the Langtang transect, constrained the peak P-T conditions experienced by the different LHS and GHS units, but did not provide information about their P-T path or evolution. This Chapter aims to fill this this knowledge gap: it focuses on the Gatlang-Langtang and Gosainkund–Helambu

regions in the central Nepal Himalaya with new detailed structural, lithological and petrological data. The **main goal** of this Chapter is the reconstruction of the stratigraphic, structural and tectono-metamorphic architecture of this sector of the orogen, with emphasis on the identification of tectono-metamorphic discontinuities within both the LHS and GHS. Field-based investigations, meso- and micro-structural data are integrated with detailed petrologic study of several metapelite samples. The P-T evolution of the studied samples is constrained using both the pseudosection approach and optimal thermobarometry and is compared with the P–T estimates published by previous authors.

3.2 Geological outline

The study area is located north of the Kathmandu Nappe (KN), in the Gatlang-Langtang and Gosainkund–Helambu regions (Fig. 3.1).

The **Gatlang-Langtang transect** represents an ideal E-W cross section through the entire GHS, passing through both the STDS to the east and the MCT (in the proximity of the junction between the Langtang and the Trisuli rivers) to the west. For this reason, and for its easy accessibility, the Gatlang-Langtang region has been investigated in detail since the ’90, and its structural and lithological architecture is quite well known (e.g. Inger and Harris, 1992; Macfarlane et al., 1992; Macfarlane, 1993, 1995; Upreti, 1999; Fraser et al., 2000; Takagi et al., 2003; Kohn et al., 2004, 2005; Pearson and DeCelles, 2005; Kohn, 2008). Inger and Harris (1992) first identified a metamorphic discontinuity in the Langtang region, based on detailed thermobarometric study. This discontinuity separates a lower GHS unit, characterized by higher pressure at peak–T conditions (680–740 °C, 8–10 kbar), from an upper GHS unit, which experienced lower pressure at peak–T conditions (730–790 °C, 5.4–6.2 kbar) (Fig. 3.1b). These authors also confirmed that the metamorphic grade is inverted along the Langtang section, with the highest temperature samples clustered at the top of the section. In contrast, Macfarlane (1995) did not observe significant variations in peak–T upsection, but confirmed the decrease of peak–P towards structurally higher levels. Fraser et al. (2000) recognised two metamorphic discontinuities along the Langtang transect, thanks to the presence of pressure breaks detected using multi-equilibrium thermobarometry; the uppermost discontinuity recognised by Fraser et al. (2000) roughly coincides with that described by Inger and Harris (1992) (Fig. 3.1b). Kohn et al. (2004, 2005) and Kohn (2008) further refined the tectono-metamorphic architecture of the Gatlang-Langtang region combining detailed thermobarometric data (conventional thermobarometry and Zr–in–rutile thermometry) with geochronological data (Th–Pb on monazites) and indicated the existence of a main discontinuity (Langtang Thrust) separating an upper unit that experienced earlier melting at lower P conditions (20–18 Ma, 8.0–8.5 kbar) from a lower unit that experienced later melting at higher P conditions (c. 16–13 Ma, 10–12 kbar). The Langtang Thrust, as defined by Kohn et al. (2004, 2005) and Kohn (2008), is located few km structurally higher than the Inger and

Harris (1992) discontinuity (Fig. 3.1b). Moreover, Kohn et al. (2004), Pearson and DeCelles (2005) and Kohn (2008) provided evidence for the existence of a tectono-metamorphic discontinuity in the uppermost structural levels of the LHS; this discontinuity corresponds to the Ramgarh Thrust (RT) originally defined in western Nepal (DeCelles et al., 2001) (also called Munsiari Thrust; e.g. Kohn, 2008). The RT is a discrete tectonostratigraphic boundary located within the LHS (i.e. below the MCT), and places older augen gneisses (Ulleri gneiss) and quartzites (Robang Formation; ~1940 Ma according to Pearson and DeCelles, 2005) above the younger Kuncha Formation (~1860 Ma; e.g. Schelling, 1992; DeCelles et al., 2001; Robinson et al., 2001; Pearson, 2002; Pearson and DeCelles, 2005).

Compared to the Gatlang-Langtang region, which has been investigated in detail, the **Gosainkund–Helambu region**, extending for ~40 km to the south of Langtang toward the Kathmandu valley (Fig. 3.1b), has been sparsely investigated remaining a "blank in the map" (see for example Fig. 3b in Kohn, 2014). A notable exception is that of Rai et al. (1998); these authors combined conventional and multi-equilibrium thermobarometric methods and constrained peak P–T conditions for this region at 600–750 °C, 6–9 kbar. Although little studied, the Gosainkund–Helambu transect occupies a crucial position in the geological framework of the central Nepal Himalaya, connecting the Gatlang-Langtang region to the north with the **Kathmandu Nappe** (KN) to the south, whose tectonic interpretation is still largely debated in literature (e.g. He et al., 2015 and references therein). Studied since the '70–80s (Hagen, 1969; Stöcklin, 1980; Arita, 1983), the KN has been variously considered as part either of the LHS (e.g. Rai et al., 1998; Upreti and Le Fort, 1999; Hodges, 2000) or of the GHS (e.g. Johnson et al., 2001; Gehrels et al., 2003; Robinson et al., 2003). More recently, the KN has been partially (e.g. Yin, 2006; Khanal et al., 2015) or completely (e.g. Webb et al., 2011) correlated to the TSS. Specifically, the interpretation of Khanal et al. (2015) implies that an intra–GHS thrust merges with the MCT on the northern side of the KN, whereas according to Webb et al. (2011) it is the STDS that merges with the MCT.

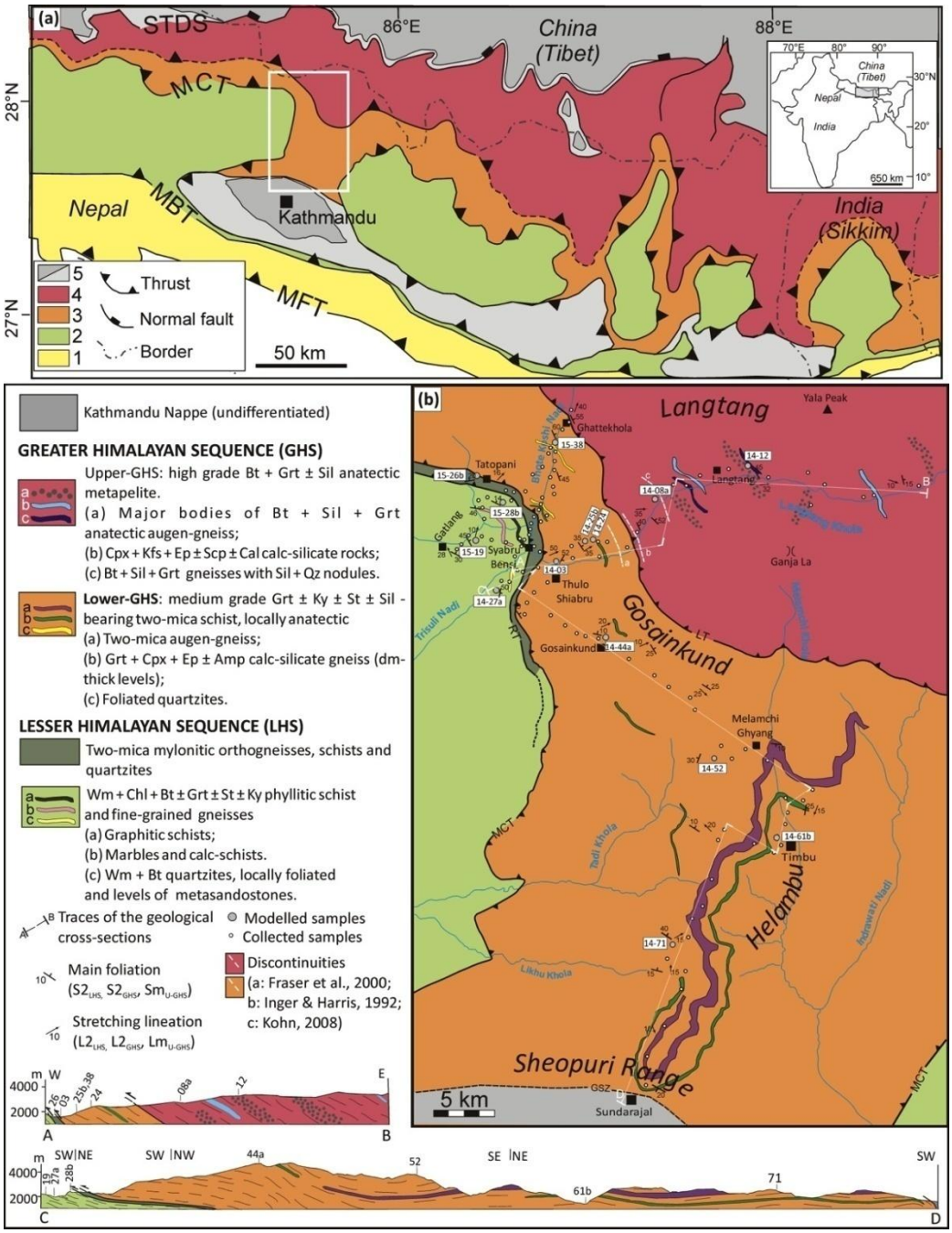

Fig. 3.1 - (a) Geological sketch map of the central–eastern Nepal Himalaya, with major tectono-metamorphic units (modified from Goscombe and Hand, 2000, He et al., 2015,Wang et al., 2016 and based on our own data). The white rectangle indicates the study area, reported in (b). 1: Siwalik deposits; 2: Lesser Himalayan Sequence; 3: Lower Greater Himalayan Sequence; 4: Upper Greater Himalayan Sequence; 5: Tethyan Sedimentary Sequence. MFT: Main Frontal Thrust; MBT: Main Boundary Thrust; MCT: Main Central Thrust; STDS: South Tibetan Detachment System. The inset locates the study area in the framework of the Himalayan chain. **(b)** Geological map and representative cross sections of the Gatlang-Langtangand Gosainkund–Helambu regions (central Nepal Himalaya). GSZ: Galchi Shear Zone (from He et al., 2015); RT: Ramgarh Thrust; MCT: Main Central Thrust; LT: Langtang Thrust.

3.3 Methods

3.3.1 Fieldwork

In order to document the metamorphic and structural features of the different rock packages cropping out in the studied areas, detailed geological mapping was performed along three transects crossing both the LHS and the GHS. From west to east these are the Gatlang, Langtang and Gosainkund-Helambu transects (Fig. 3.2). (i) The Gatlang transect is about 20 km in length: it consists of a N-S portion which runs along the Bothe Koshi River, from the village of Gattekhola (N28°16'10'' E85°22'40'', 1755 m a.s.l.) to the north, at the border with China (Tibet), to the small town of Syabru Bensi (N28°09'42'' E85°20'11'', 1468 m a.s.l.) to the south, and of a circular loop connecting Syabru Bensi to the Tamang villages of Gatlang (N28°09'45'' E85°16'05'', 2300 m a.s.l.) and Tatopani (N28°13'14'' E85°17'51'', 3155 m a.s.l.). (ii) The Langtang transect runs E-W for more than 30 km along the Langtang River, from Syabru Bensi to the west up to the edge of Shalbachum Glacier to the east (N28°12'12'' E85°39'25'', 4016 m a.s.l.). (iii) The Gosainkund-Helambu transect consists of a NW-SE portion connecting Syabru Bensi with the village of Melamchi Ghyang (N28°00'53.5'' E85°30'52.5'', 2710 m a.s.l.) in the Melamchi Khola, and of a N-S portion from Melamchi Ghyang to the village of Sundarajal (N27°45'41'' E85°25'16'', 1397 m a.s.l.), in the suburbs of Kathmandu, to the south. The maximum height along this transect is encountered at the pass of Laurebina La (N28°04'34'' E85°25'43'', 4670 m a.s.l.). Fieldwork was performed in November-December 2014 (Langtang and Gosainkund-Helambu transects) and April 2015 (Gatlang transect), just before the devastating earthquake, which occurred on April 25th, 2015, causing thousands of casualties and impressive landslides especially in the Langtang region. Outcrop conditions are highly variable: outcrops are abundant and in good conditions in the upper Langtang Valley and in the high-altitude region around the Gosainkund lakes, whereas they are scarce in the lower Langtang valley, and highly weathered in the Helambu region. Along the Gatlang transect, outcrops are especially abundant along the Bhote Khosi due to the road cuttings.

A total number of 77, 69 and 38 samples were collected along the Gatlang, Gosainkund-Helambu and Langtang transects, respectively (Fig. 3.2); the majority of the samples are metapelites with minor orthogneisses, and 35 samples are CO_2-source rocks (i.e. different types of calc-silicate rocks). A total of 184 thin sections were studied and petrographically characterized. A compilation of the collected samples is given in Fig. 3.2 and Appendix 1. Representative photos of lithologies and meso-structures are given in Fig. 3.3-Fig. 3.11. Stereographic plots are given in Fig. 3.12.

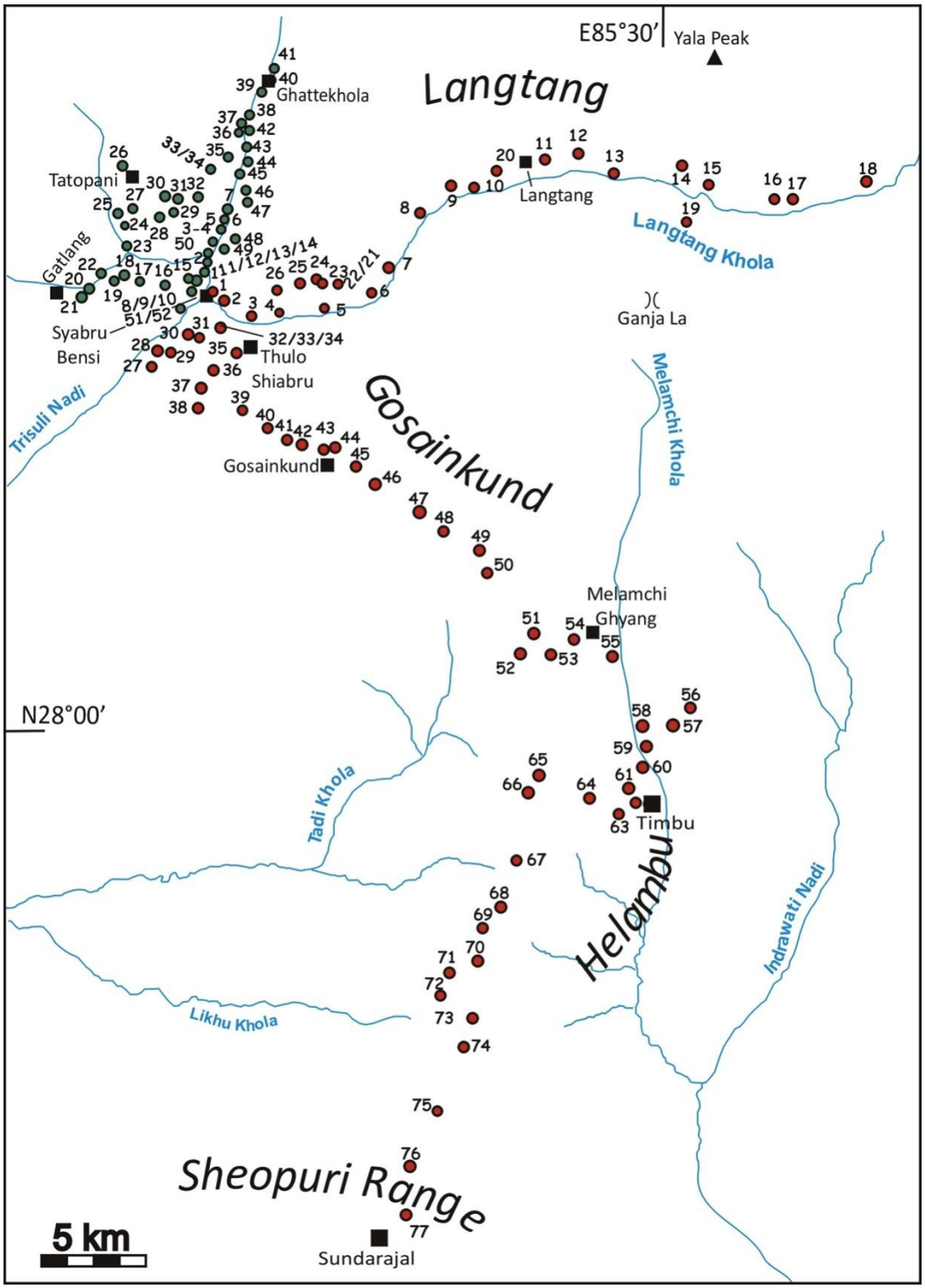

Fig. 3.2 – Simplified map of the studied area with locations of samples collected in 2014 (red) and 2015 (green).

3.3.2 Mineral chemistry

Detailed petrologic study was performed on five (samples 15-19, 14-27a, 15-28b, 15-26b and 15-38), five (samples 14-03, 14-25b, 14-24, 14-08a and 14-12) and four (samples 14-44a, 14-61b, 14-71 and 14-52) metapelite samples selected from the Gatlang, Langtang and Gosainkund-Helambu transects, respectively, as representative of different structural levels.

The rock-forming minerals were analysed with a SEM-EDS system. Most analyses were performed using a Cambridge Stereoscan 360 Scanning Electron Microscopeat the Department of Earth Sciences, University of Torino; the instrument was renewed in 2016 and the most recent analyses have been performed using a Jeol JSM-IT300LV Scanning Electron Microscope. Both the instruments were equipped with an energy dispersive spectrometry (EDS) Energy 200 system and an SDD X-Act3 detector (Oxford Inca Energy). The operating conditions were 50 s counting time and 15 kV accelerating voltage. SEM-EDS quantitative data (spot size 2 μm) were acquired and processed using the Microanalysis Suite Issue 12, INCA Suite version 4.01; natural mineral standards were used to calibrate the raw data; the $\phi\rho Z$ correction (Pouchou and Pichoir, 1988) was applied. The different phases occurring in nanogranites have been analysed using the same instrument and the same operating conditions. Due to the small size of nanogranites (20–50 μm) and to the relatively large size of the spot (2 μm), the obtained analyses are generally mixed analyses; however, they can be qualitatively interpreted based on the relative intensity of each peak.

The most representative microstructures are reported in Fig. 3.13-Fig. 3.15,-Fig. 3.23; mineral chemical data are reported in Fig. 3.16, Fig. 3.24, Fig. 3.26. Abbreviations are following Whitney and Evans (2010) [Wm: white mica].

3.3.3 Micro-X-ray fluorescence (μ-XRF) maps of the thin sections

Qualitative major element X–ray maps of the whole thin sections of nine representative samples (15-26b, 14-03, 14-25b, 14-24, 14-44a, 14-61b, 14-71, 14-52 and 14-08a) were acquired using a μ-XRF Eagle III–XPL spectrometer equipped with an EDS Si(Li) detector and with an EdaxVision32 microanalytical system, located at the Department of Earth Sciences, University of Torino. The operating conditions were 100ms counting time, 40 kV accelerating voltage and a probe current of 900 mA. The spatial resolution is about 65 μm in both x and y directions. Quantitative modal amounts of each mineral phase were obtained by processing the μ-XRF maps with the software program Petromod (Cossio et al., 2002). Fig. 3.13 gives μ-XRF of the samples.

3.3.4 Estimate of the bulk compositions for pseudosection modelling

The bulk-rock compositions of nine representative samples (five for the Gatlang-Langtang section and four for the Gosainkund-Helambu section) were calculated by combining the mineral proportions obtained from the modal estimates of the μ-XRF maps with the mineral chemistry acquired by SEM-EDS. The grain-size of sample 14–27a is too small to allow a precise estimate of the modal amount of each phase. Therefore, its bulk composition was calculated as an average of 15 SEM–EDS analyses of 4.70 mm x 3.20 mm areas. The micro-XRF map of this sample was nevertheless useful to obtain the modal amount of garnet cores (< 0.5 vol%), needed for estimating the fractionation effects on the bulk composition due to the growth of garnet porphyroblasts (see below).

For those samples lacking microstructural evidence of partial melting except for the presence of nanogranites included in garnet rim (i.e. samples: 14–03, 14–24, 14–25b, 14–44a, 14–71), the amount of H_2O used for the calculation of the supra-solidus topologies corresponds to the amount of H_2O sufficient to saturate the system at P-T conditions immediately below the solidus (i.e. H_2O -saturated conditions).

For those samples with microstructures indicative of partial melting (i.e. samples 14–08a, 14–61b), the amount of H_2O used for the calculation was derived from the modal proportion of biotite (± white mica) and using the biotite Ti–H substitution scheme of White et al. (2007) (for further details see Indares et al., 2008). To avoid possible biotite overestimation owing to its preferred orientation, the relevant thin sections were made by cutting the samples perpendicular to the main foliation and lineation.

The possible effects of chemical fractionation of the bulk composition due to the growth of the zoned garnet porphyroblasts were considered for samples 14–27a, 15-26b, 14–03 and 14–25b. The bulk compositions effectively in equilibrium during the growth of garnet rim were therefore calculated by subtracting the garnet core compositions from the whole rock compositions. Bulk compositions used for the thermodynamic modelling are reported in Tab. 3.3.

3.3.5 Pseudosection modelling

Ten samples were modelled in the system MnNCKFMASTH; Fe^{3+} was neglected because Fe^{3+}-rich oxides are absent and the amount of Fe^{3+} in the analysed minerals is very low. Pseudosections were calculated using Perplex 6.7.1 / 6.7.2 (versions December 2014/June 2015; Connolly, 1990, 2009) and the internally consistent thermodynamic dataset and equation of state for H_2O of Holland and Powell (1998, revised 2004). The minerals considered in the calculation were: garnet, biotite, chlorite, kyanite, andalusite, sillimanite, staurolite, zoisite/clinozoisite, plagioclase, white mica, K-feldspar, cordierite, quartz, titanite, rutile, ilmenite and melt. The following solid solution models were used: garnet, chloritoid, cordierite and staurolite (Holland and Powell, 1998), biotite

(Tajčmanová et al., 2009), chlorite (Holland et al., 1998), plagioclase (Newton et al., 1980), white mica (Coggon and Holland 2002; Auzanneau et al., 2010), K-feldspar (Thompson and Hovis, 1979), and melt (Holland and Powell, 2001; White et al., 2001, 2007). The fluid was considered as pure H_2O (aH_2O=1). Most of the studied samples are two-mica schists lacking microstructural evidence of partial melting, except for the presence of ''nanogranites'' included in garnet rim (i.e. samples: 14-03, 14-24, 14-25b, 14-44a, 14-71). Nanogranites are poliphase cryptocrystalline aggregates resulting from melt crystallization (Cesare et al., 2009), typically containing a granitic assemblage made of crystals with micrometric grain-size. Nanogranites similar to those described in this work have been found in metapelites from both L-GHS (Carosi et al., 2015) and U-GHS (Ferrero et al., 2012).

These rocks were therefore modelled at both sub-solidus and supra-solidus conditions. H_2O was considered as an excess fluid phase at sub-solidus conditions. The position of the solidus and the supra-solidus topologies were calculated at H_2O-saturated conditions, i.e. using an amount of H_2O sufficient to saturate the system at P–T conditions immediately below the solidus.

For those samples with microstructures indicative of partial melting (i.e. samples 14-08a, 14-61b) a different approach was used. The P–T pseudosection modelling of migmatitic rocks, in fact, is complicated by the possibility that the system had experienced one or more episodes of melt loss and that the actually measured bulk rock composition is somewhat different from that of the protolith. Since in migmatitic rocks the observed mineral assemblages and modes are those corresponding to the final crystallization of the melt (i.e. at the P–T conditions where the P–T trajectory intersects the solidus of the system), the measured bulk composition (and H_2O content) can be used to model the P–T conditions of melt crystallization. Furthermore, because it is unlikely that melt loss occurred during crystallization (i.e. at decreasing temperature), the measured bulk composition can be also used to model the retrograde portion of the metamorphic evolution, from peak temperature to the final melt crystallization (e.g. Clarke et al., 2007; Indares et al., 2008; Groppo et al., 2012 for further details). In this case, the pseudosections were therefore calculated using the measured bulk compositions and a H_2O content derived from the modal proportion of biotite ± white mica.

3.3.6 Optimal thermobarometry

The Thermocalc "Average PT" (AvPT) method was applied to 14 samples. Thermocalc v3.33 (Powell and Holland, 1994) and the Holland and Powell (1998, revised in 2004) dataset were used. Activity-composition relationships were calculated using the software AX. The internal constincency of the method was examined with the samples already investigated using the pseudosection approach. To mantein the consistency between the thermodynamic datasetsused for pseudosections and Average PT, respectively, we have

preferred not to choose the updated version of the dataset (version 6.02) based on Holland and Powell (2011).

The AvPT method evaluates P-T conditions through the calculation of a set of independent reactions, which represent all the equilibria between the end-members of the equilibrium assemblage; if the number of reactions between end-members is too low, the method does not converge to a result. Mineral compositions used for thermobarometric calculations are given in Appendix 3. For samples with zoned garnets, calculations were done considering garnet core and garnet rim compositions, combined with the mineral assemblages in equilibrium with each of them. The presence of melt in equilibrium with the peakmineral assemblage in some samples was simulated by reducing the activity of H_2O ($0.7<aH_2O<1$) (see Mosca et al., 2012), because it is not possible to includethe melt solution model in AvPT calculations.

3.4 Results

3.4.1 Tectono-statigraphic setting of the study area

Lithologies outcropping in the Gatlang, Langtang and Gosainkund-Helambu transects are ascribed to two tectono-stratigraphic domains, which are, from lower to upper structural levels, the LHS and the GHS. The latter is subdivided into the Lower-GHS (L-GHS) and the Upper-GHS (U-GHS): gneiss and micaschists of L-GHS are characterized by a pervasive mylonitization and by an increase in the metamorphic grade towards upper structural levels, while the U-GHS is dominated by migmatitic paragneisses.

Structural terms annotation: S (schistosity), L (mineral lineation), A (axe), F (fold), D (deformation event).

3.4.1.1 Lesser Himalayan Sequence

❖ ***LHS lithologies***

The LHS is exposed in the westernmost part of the study area, south of the village of Syabru Bensi, and it extends northward up to Tatopani (Fig. 3.1b). The LHS is mainly composed of grey to pale-green fine-grained phyllites, slates and phyllitic schists (Fig. 3.3a-e), with ubiquitous dm-thick intercalations of metasandstones (Fig. 3.3c), characterized by the presence of detrital grains of quartz, feldspar and tourmaline. The gradual increase of metamorphic grade upsection (i.e. from SW to NE) is already evident at the outcrop scale and is evidenced by the occurrence of low-grade chlorite + white mica assemblages at the lowest structural levels, passing to medium-grade two-mica (± garnet ± staurolite ± kyanite) assemblages close to the MCT (Fig. 3.3d).

In its uppermost structural levels, the LHS is more eterogeneous, with different lithologies intercalated within the phyllites. The most common lithologies include:

(i) dm-thick layers of graphitic schists (Fig. 3.3g).

(ii) laminated impure marbles (Fig. 3.3h), calcareous phyllites and calchscists. The bedding in the marbles is mm- to pluri-cm thick, and the foliationis defined by the preferred orientation of white mica ± phologopite ± chlorite ± amphibole. Calcareous phyllites and calcschists occur as dm–thick layers and contain white mica ± biotite ± phlogopite ± chlorite ± graphite in varying proportions.

(iii) biotitic schists with porphyroblastic garnet, green amphibole and carbonate, in which the foliation is defined by the prefferd orientation of biotite + amphibole.

Upsection, the dominantly calcic and graphitic lithologies give way to strongly foliated phyllitic schists with abundant intercalations of:

(iv) dm- to m-thick banded quartzites (Fig. 3.3f): the bands are mm- to cm-thick and show a rough foliation defined by white mica ± biotite ± chlorite ± staurolite;

(v) two mica augen-gneisses: this lenticular body of othogneiss crops out close to Syabru Bensi and along the road running parallel to the Bhote Khosi (Fig. 3.3i,l). It is usually coarse-grained, with a well-developed mylonitic fabric with top-to-S sense of shear. It contains large porphyroclasts of orthoclase and plagioclase, stretched and flattened quartz, and abundant biotite and white mica oriented parallel to the main foliation. Within this lithology, dm-thick intercalations of fine-grained aplitic gneiss are observed. Quartz veins, stretched parallel to the main foliation, are quite abundant.

Pearson and DeCelles (2005) ascribed the quartzites and phyllitic schists to the Kushma and Robang Formations, respectively, which represent the lowermost Paleoproterozoic layers of the LHS. The mylonitic augen-gneiss may be correlated to the Ulleri gneiss (e.g. Le Fort and Rai, 1999), stratigraphically intercalated within the lowermost portion of the Kuncha-Ranimata Formations in the Lower-LHS. This indicates that, in the study area, Lower-LHS lithologies (i.e. quartzites: Robang-Kushma Fm.; augen-gneisses: Ulleri gneiss) are tectonically emplaced over Upper-LHS lithologies (i.e. calcschists and marbles). The thrust fault responsible for this emplacement, the Ramgarh Thrust has been documented by a number of authors (e.g. Schelling, 1992; DeCelles et al., 2001; Robinson et al., 2001; Pearson, 2002; Kohn et al., 2004) based on stratigraphic, geochemical (Nd isotopic analysis) and geochronological data. In the following, the relatively thin package of Lower-LHS lithologies bounded by the Ramgarh Thrust at its bottom and by the MCT at its top, will be referred to as Ramgarh Thrust Sheet (LHS-Ramgarh Thrust Sheet).

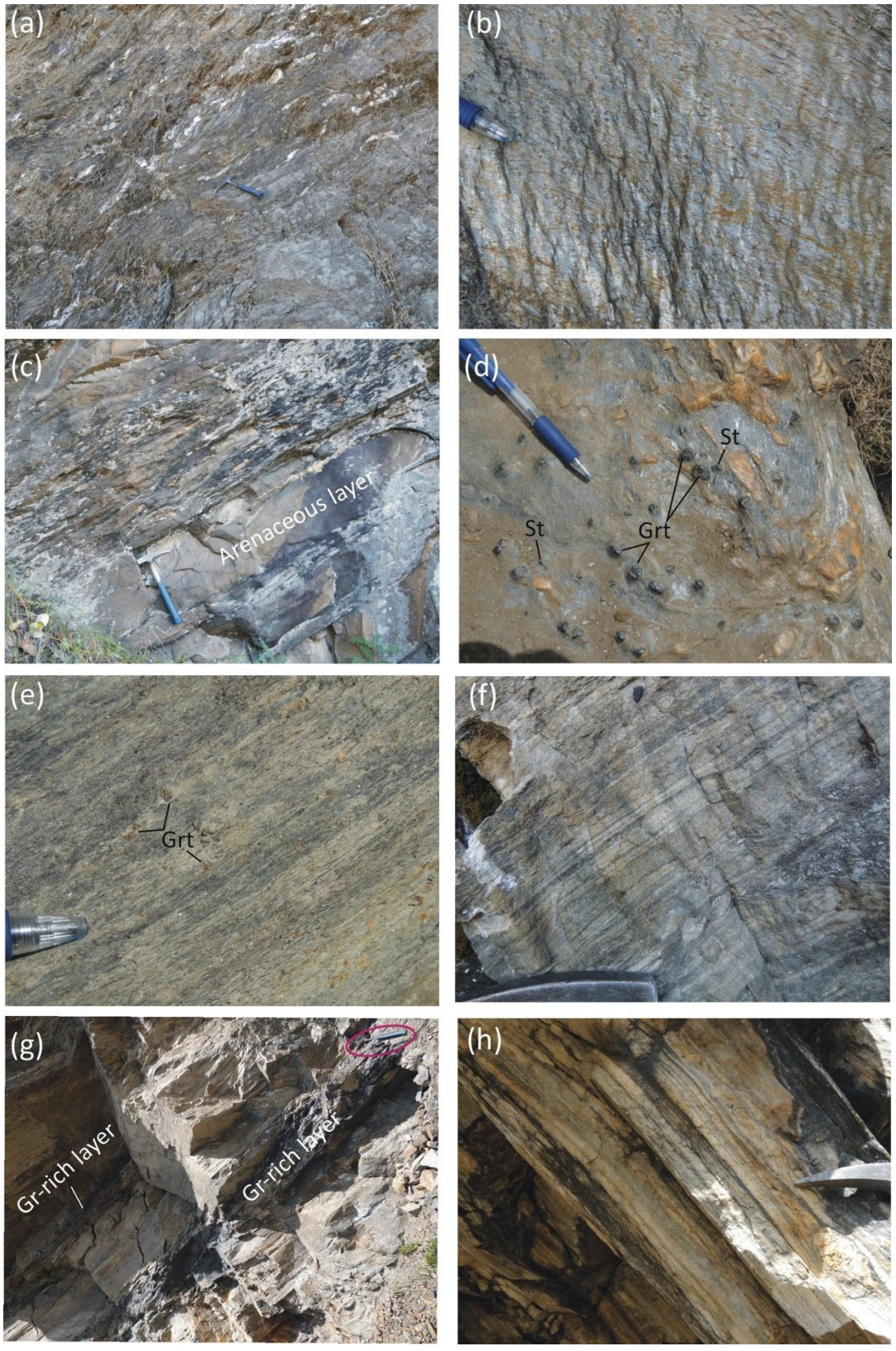
(a)
(b)
(c)
Arenaceous layer
(d)
St
St
Grt
(e)
Grt
(f)
(g)
Gr-rich layer
Gr-rich layer
(h)

Fig. 3.3

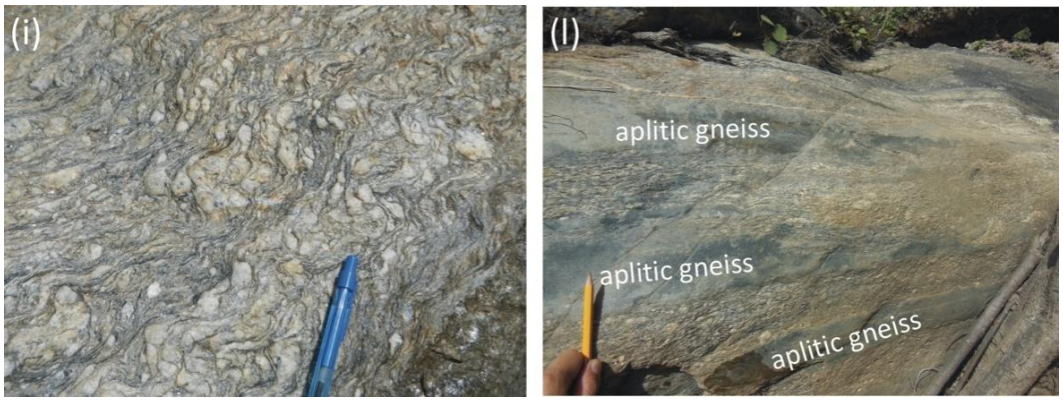

Fig. 3.3 – Representative LHS lithologies. (a) Fine-grained grey slates with quartz veins stretched along the main foliation. **(b)** Intensively crenulated phyllites. **(c)** Pluri-decimetric thick layers of metasandstone interbedded in the slates. **(d, e)** Micaschists from the uppermost structural levels of LHS, with porphyroblastic garnet ± staurolite. **(f)** Banded quartzite. **(g)** Graphite-rich layers intercalated in the metapelites. Hammer for scale (pink circle). **(h)** M-thick layers of banded marble; nodules with coarse-grained calcite are present. **(i)** Two-mica mylonitic augen-gneiss with large porphyroclasts of k-feldspar elongated parallel to the main foliation. **(l)** Pluri-cm thick layers of fine-grained aplitic gneisses within the augen-gneiss, stretched along the main foliation.

❖ *LHS meso-structures*

The most pervasive foliation recognizable at the mesoscale is a pervasive schistosity **$S2_{LHS}$** (Fig. 3.4a), defined by quartz + white mica ± chlorite ± biotite depending from the structural position. $S2_{LHS}$ is a transpositive foliation, which deforms an earlier $S1_{LHS}$ foliation preserved in microlithons, as intrafolial folds and/or isolated folds (Fig. 3.4b-d). **$S1_{LHS}$** is defined by quartz ± white mica ± chlorite ± biotite. The $S2_{LHS}$ dips on average to the NNE in the northern sectors of the study area and progressively rotates toward NE-ENE moving to the east (Fig. 3.1b and Fig. 3.12). $F2_{LHS}$ folds (whose axial plane is approximated by the $S2_{LHS}$) have stretched limbs and slightly thickened hinges, and often have an asymmetric shape, synthetic with top-to-the-south shearing. Syntectonic quartz veins are often stretched and boudinated along the $S2_{LHS}$ (Fig. 3.4a). A pervasive dip-slip mineral/stretching lineation ($L2_{LHS}$) is associated with $S2_{LHS}$ (Fig. 3.4e). The **$L2_{LHS}$** is marked by white mica, biotite and quartz alignment and by stretching of orthoclase and plagioclase porphyroclasts in the two mica augen-gneisses. $L2_{LHS}$ plunges mainly to the N-NE (Fig. 3.12). It is often parallel to the $A2_{LHS}$ of mesocale folds, identifiable also by intersection lineations between $S1_{LHS}$ and $S2_{LHS}$ (Fig. 3.12). These relationships between $L2_{LHS}$ mineral/stretching lineation and $A2_{LHS}$ axes indicates non-cylindrical folding for the related $D2_{LHS}$ event. In the upper structural levels of the LHS, the $D2_{LHS}$ event results increasingly transpositive. Mesoscopic shear zones (from cm to m-thick) related to the D2 event are widely present, resulting either parallel with or at very low angle to the $S2_{LHS}$. Usually, these shear zones are marked by the pervasive occurrence of stretched folds and stretched veins of quartz. Kinematic indicator as S-C fabrics, asymmetric folds, rotated porphyroclasts and mica-fish indicate a top-to-SW sense of shear (Fig. 3.5a-c). Field

observations indicate that these shear zones pervasively increase their abundance around Syabru Bensi, namely in the upper part of the LHS and in the LHS-Ramgarh Thrust Sheet.

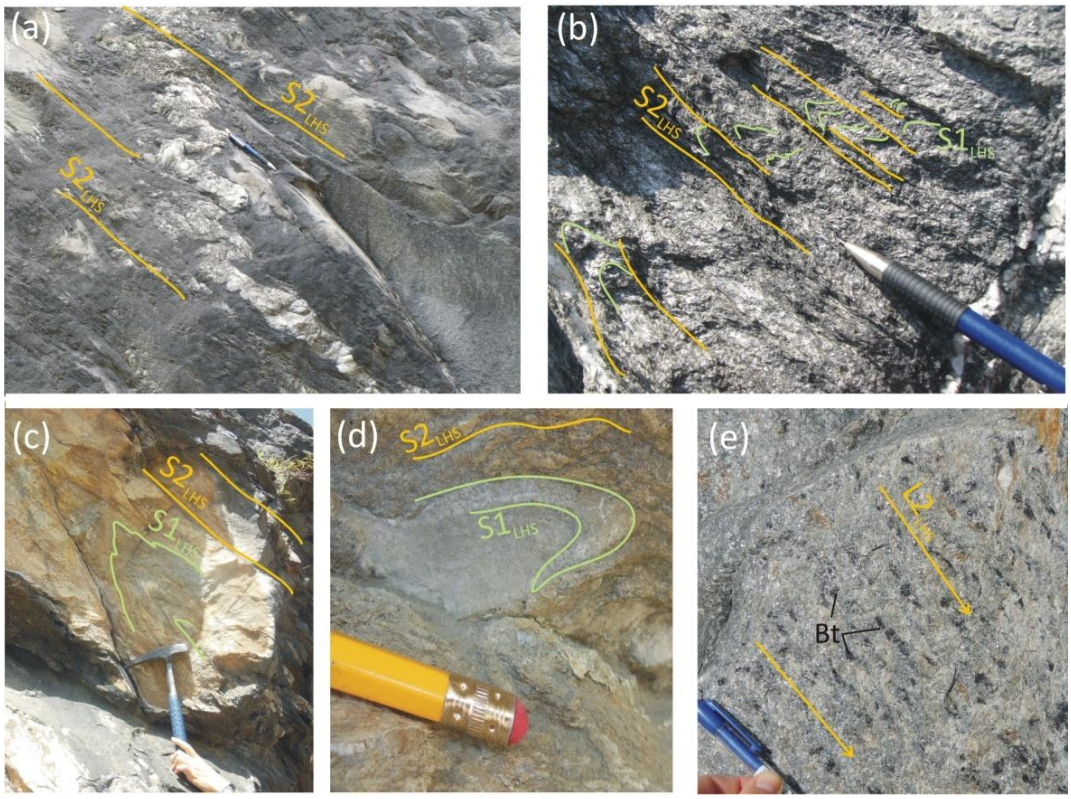

Fig. 3.4 – Representative LHS mesostructures (schistosities and lineations). (a) Quartz ribbons stretched along $S2_{LHS}$. **(b)** Cm-thick microlithons in which the earlier $S1_{LHS}$ is preserved. **(c,d)** $F2_{LHS}$ folds in a banded marble (c), and in a slate (d). **(e)** Biotite-aggregates in mylonitic orthogneiss defining a stretching lineation $L2_{LHS}$.

Fig. 3.5 - Representative LHS mesostructures. (a-c) Decimetric- to metric thick shear zones with top-to-S sense of shear, as indicted by kinematic indicators such as asymmetric foliations (a, c), Z-like drag folds in a metaslate (b), rotated porphyroclasts (c) and quartz ribbons (a). Hammer for scale in (a) is encircled. **(d)** Relationship between $S2_{LHS}$ and $S3_{LHS}$. $S3_{LHS}$ foliation is only developed in the micaceous layers, while it lacks in the more competent lithologies such metasandstones and quartz veins. **(e)** $L2_{LHS}$ defined by biotite is evident, which is deformed by a later crenulation event (see the lineation $A3_{LHS}$). **(f,g)** Extensional shear sense indicators such as brittle shear bands and asymmetric foliations, defining a top-to-NE sense of shear. **(h)** $S2_{LHS}$ is folded and crenulated by a $D3_{LHS}$ phase.

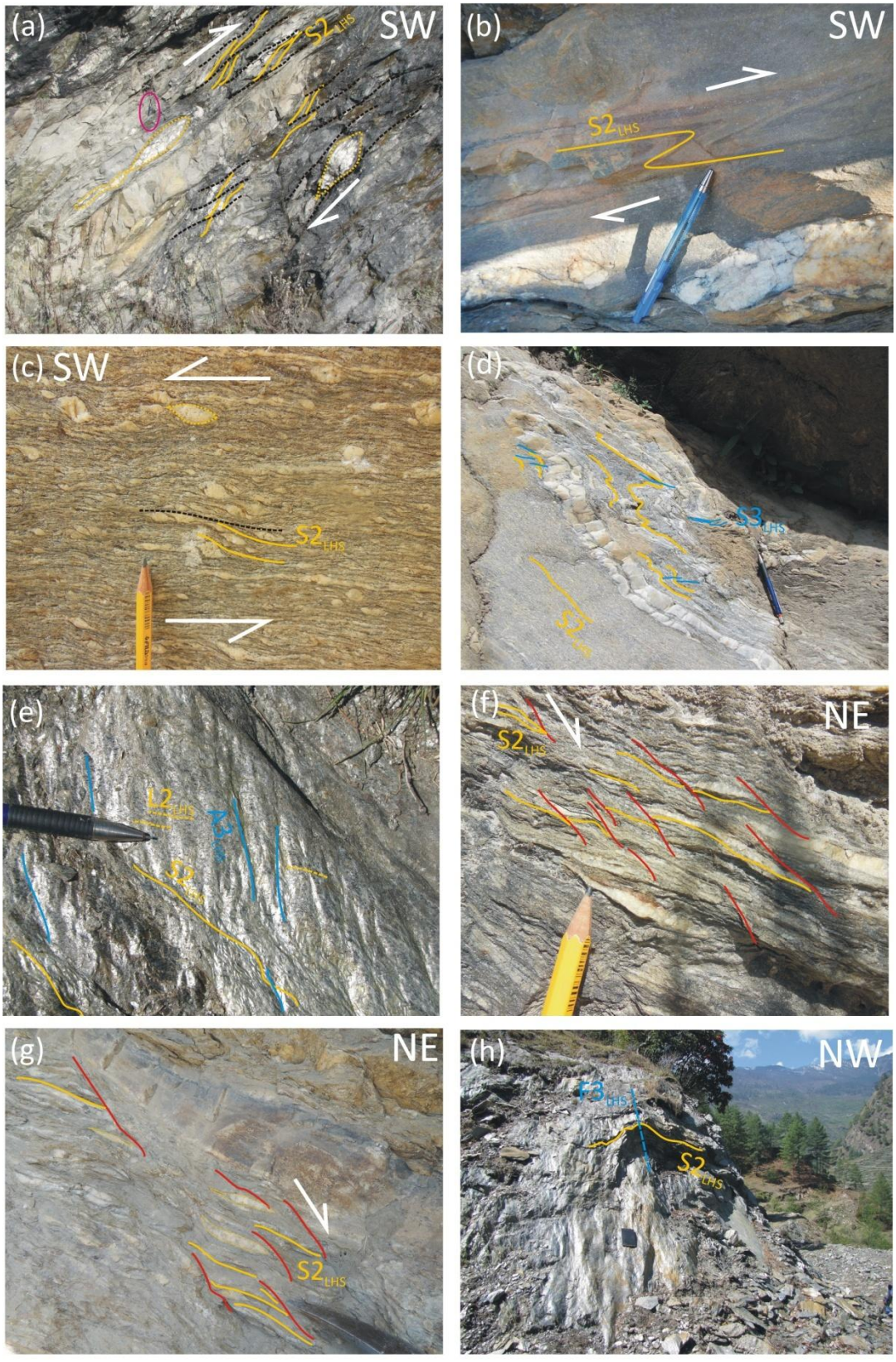
(a)
SW
$S2_{LHS}$
(b)
SW
$S2_{LHS}$
(c) SW
$S2_{LHS}$
(d)
$S3_{LHS}$
$S2_{LHS}$
(e)
$L2_{LHS}$
$A3_{LHS}$
$S2_{LHS}$
(f)
NE
$S2_{LHS}$
(g)
NE
$S2_{LHS}$
(h)
NW
$F3_{LHS}$
$S2_{LHS}$

Fig. 3.5

Structural features related to the $D2_{LHS}$ are overprinted by a $D3_{LHS}$ phase represented by a crenulation cleavage (Fig. 3.5d) and local development of open folds (Fig. 3.5h). A $S3_{LHS}$ is locally developed in the more micaceous lithologies and is defined by white mica + biotite. The fold axis $A3_{LHS}$, coincinding with the crenulation lineation, plunges towards NE and E (Fig. 3.12) at a certain angle with respect to the $L2_{LHS}$ (Fig. 3.5e). Locally, oriented white mica + biotite ± chlorite lepidoblasts statically overgrow the $S2_{LHS}$, without a clear $S3_{LHS}$ development. A later $D4_{LHS}$ phase is marked by N-S to NW-SE trending folds, with axes plunging at low/moderate angle to the N and NW and sub-vertical axial planes.

Late extensional shear band dipping to the N also occur at upper structural levels, with local development of extension gashes (Fig. 3.5f,g). Extensional shear planes have a mean trend of 70/70 (Fig. 3.12).

3.4.1.2 Lower Greater Himalayan Sequence

❖ ***L-GHS lithologies***

Lower GHS lithologies are characterized by highly variable grain size, which is generally coarser with respect to that of the LHS.The most frequent lithology is a medium-grained two-mica gneissic micaschist with porphyroblastic dark-red garnet (Fig. 3.6a-c). These rocks exhibit a compositional layering defined by white mica + biotite continuous domains alternating with discontinuous quartz + plagioclase domains; the main planar foliation is defined by isoriented biotite and white mica flakes (usually up to 5 mm in length). Locally, a later generation of white mica statically overgrows the planar fabric. Kyanite occurs as large idioblasts mainly oriented parallel to the main foliation or overgrowing it (Fig. 3.6a,b). Staurolite is rarely observed at the outcrop scale. Fibrolitic sillimanite appears in the uppermost structural levels of the lower GHS, especially in the Gosainkund-Helambu transect; it is concentrated in mm-thick domains togheter with biotite.

Layers of fine-grained two-mica/biotite ± garnet –bearing gneisses are often intercalated with this two-mica gneissic micaschists; their proportion is highly variable, and they range in thickness between few centimetres to several metres (Fig. 3.6c,f). Calc-silicate rocks occur as dm-thick deformed layers or m-sized massive boudins enveloped by the main schistosity (Fig. 3.6g,h). The more common calc-silicate type consists of garnet + clinopyroxene + plagioclase + quartz (± zoisite ± amphibole ± calcite), and have a granofelsic structure; locally, a banded structure is observed. Calc-silicate rocks of this type occur as thin layers (dm-thick) within the host metapelites (Fig. 3.6g) and are widespread in the Langtang and Gosainkund-Helambu regions, while in the Gatlang transect they have been rarely observed. Although thin, these calc-silicate layers are probably quite continuous: in the Gosainkund-Helambu transect such layerscan be followed for more than 10 Km, from Chisopani to N of Timbu (Fig. 3.1b). A second, less

common, type of calc-silicate rocks has been recognised in the lower GHS. It is a clinopyroxene + k-feldspar + scapolite + plagioclase + quartz (± garnet ± epidote ± calcite) banded gneiss occurring as metre thick layers within the host paragneiss (Fig. 3.6h). Layers of quartzites occur at the lowermost part of the L-GHS (Fig. 3.7a,b). These rocks are especially abundant in the Gatlang region, where they constitute pluri-dm to pluri-m thick layers intercalated in the metapelites, along the Bothe Khosi River. Quartzites are pale-green to greyish and locally banded, with white mica and phlogopite defining the main foliation.

In the Gosainkund-Helambu region, a pluri-km body of a two-mica orthogneiss is hosted within the metapelites. The orthogneiss shows a well-developed schistosity and cm- to pluri-cm quartz + feldspar eyes, stretched parallel to the main foliation (Fig. 3.7c). Where deformation was less pervasive, the primary granitic porphyric structure is still preserved (Fig. 3.7d).

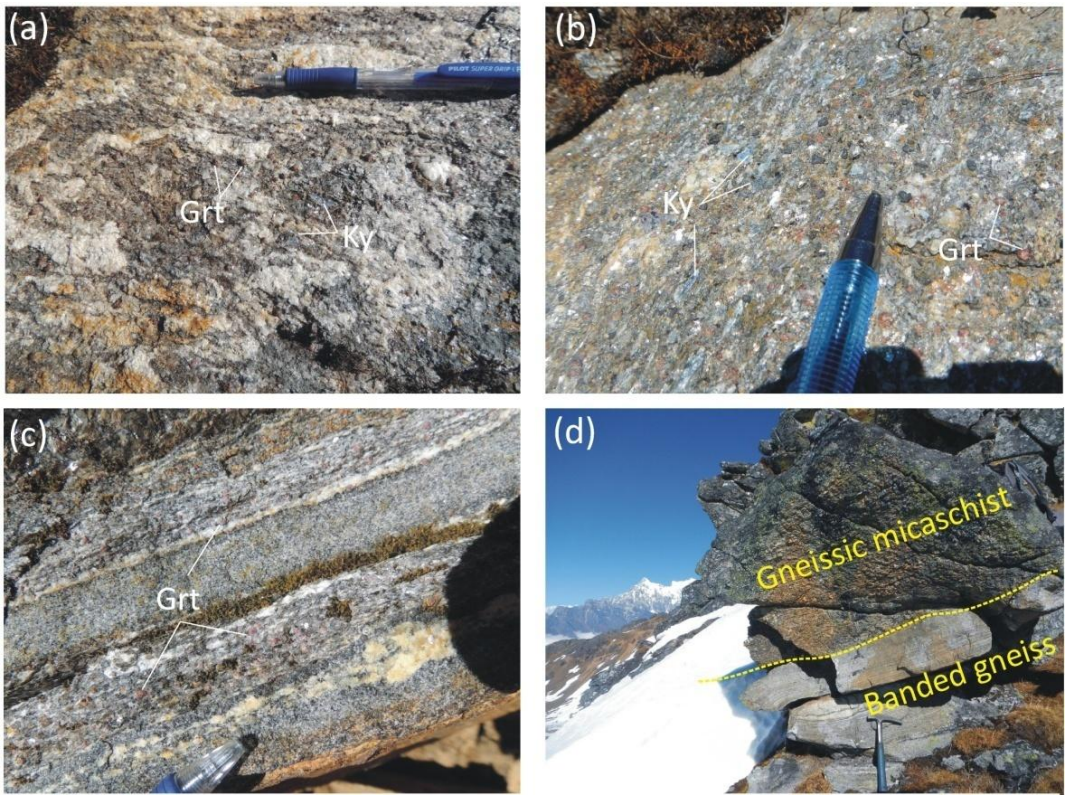

Fig. 3.6 - Representative L-GHS lithologies (micaschists, gneisses and calc-silicate rocks). (a) Typical appearance of a two-mica gneissic micaschist with porphyroblastic garnet and minor kyanite. **(b)** Kyanite porphyroblasts are elongated parallel to the $S2_{L\text{-}GHS}$ and define a stretching lineation. **(c)** Alternating cm-scale compositional bands of micaschists and fine-graind gneisses. The picture side is about 10 cm. **(d)** Compositional layering defined by alternating m-thick gneissic micaschists and pluri-dm thick fine-grained banded gneisses, which constitutes boudins enveloped by the main foliation.

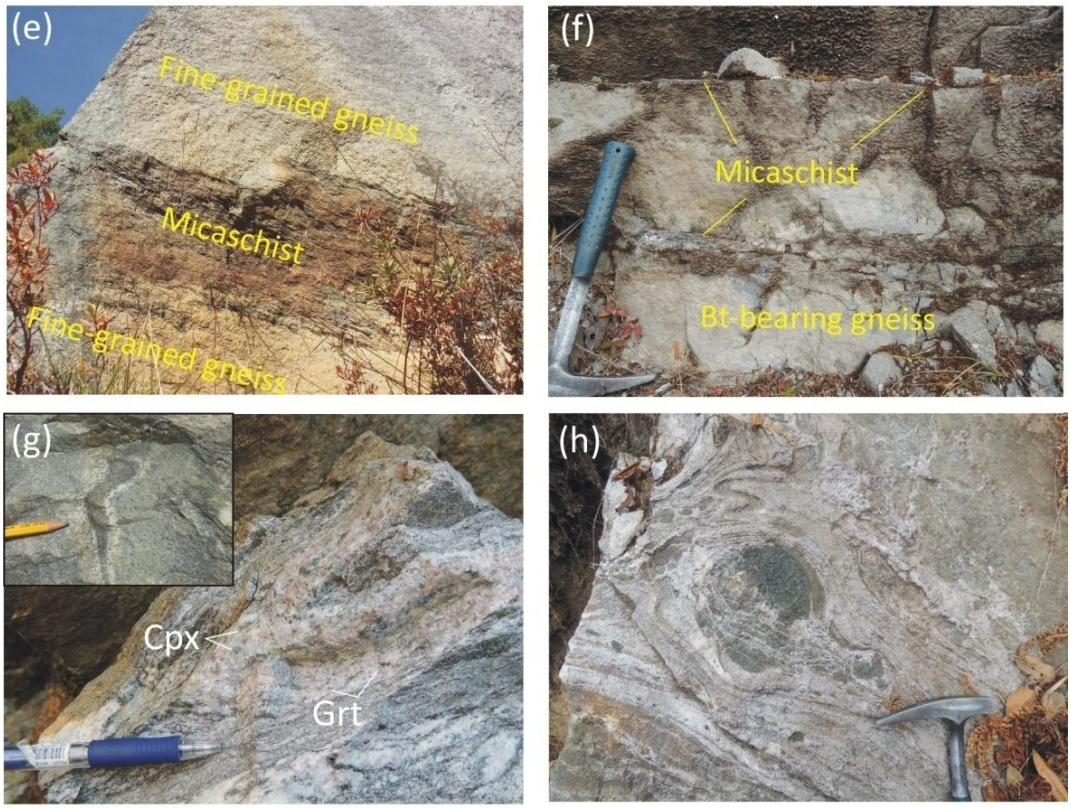

Fig. 3.6 (continued) - Representative L-GHS lithologies (micaschists, gneisses and calc-silicate rocks). (e,f) Layers of micaschists with variable thickness intercalated in fine-grained gneisses. **(g,h)** Layers and boudins of different types of calc-silicate rocks. The inset in (g) shows a garnet + epidote calc-silicate layer surrounded by a reaction rim at the contact with the host rock.

❖ *L-GHS meso-structures*

The two-mica + garnet ± kyanite ± staurolite –bearing gneisses and schists exposed at the lowermost structural levels of the L-GHS are intensively deformed and show a pervasive foliation **S2$_{L\text{-}GHS}$** defined by biotite ± white mica ± kyanite ± staurolite (Fig. 3.8a,b). The S2$_{L\text{-}GHS}$ derives from a D2$_{L\text{-}GHS}$ event leading the transposition of an earlier metamorphic foliation, S1$_{L\text{-}GHS}$. The **S1$_{L\text{-}GHS}$** is preserved in microlithons, intrafolial folds and isolated fold hinges. The S2$_{L\text{-}GHS}$ foliation corresponds to the axial plane foliation of **F2$_{L\text{-}GHS}$** asymmetric, south-verging, tight folds. D2$_{L\text{-}GHS}$ is also responsible for the development of a pervasive stretching lineation **L2$_{L\text{-}GHS}$** defined K-feldspar porphyroclasts in the orthogneisses and and mineral lineation defined by biotite ± white mica ± kyanite in the metapelites (Fig. 3.6b). The S2$_{L\text{-}GHS}$ mainly dips toward NE to E in the Gatlang-Langtang transects (Fig. 3.12), with a moderate angle, resulting then parallel to the S2$_{LHS}$. In the Gosainkund-Helambu transect, the S2$_{L\text{-}GHS}$ strikes E-W and dips gently (Fig. 3.12), being affected by later folds with WNW-ESE trending axes. Kinematic indicators (σ-type porphyroclasts, asymmetric foliations and fold asimmetry) indicate a consistent top-to-S sense of shear for F2.

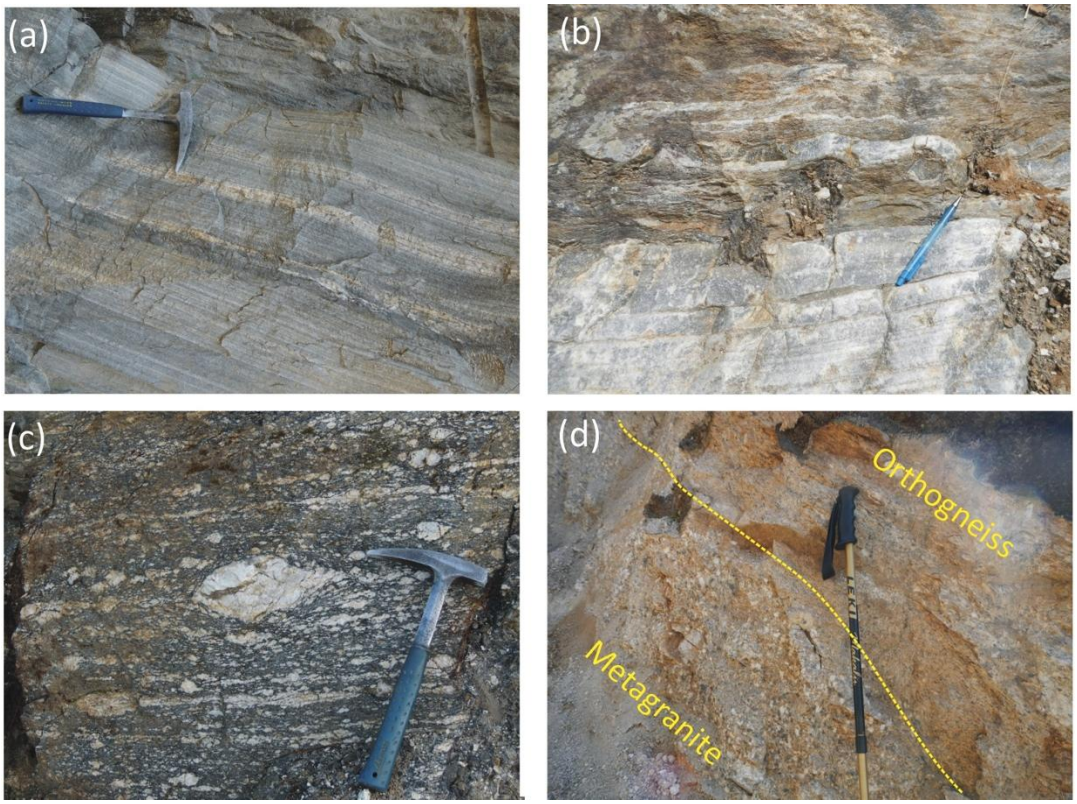

Fig. 3.7 - Representative L-GHS lithologies (quartzite and orthogneisses). (a,b) Banded quartz-rich fine-grained gneiss (a), and banded white mica + biotite + chlorite quartzite. **(c)** Strongly foliated augen-gneiss with top-to-S sense of shear. **(d)** Typical, highly alterated, appearance of the orthogneiss in the Gosainkund-Helambu region: note the preserved granitic structure in the lower portion of the photo.

The $S2_{L\text{-}GHS}$ is deformed by a $D3_{L\text{-}GHS}$ folding event, associated with the development of a locally pervasive $S3_{L\text{-}GHS}$ crenulation cleavage defined by biotite + white mica (Fig. 3.8c,d). The **$L3_{L\text{-}GHS}$** crenulation lineation and the $F3_{L\text{-}GHS}$ fold axes (also identified by $S3\text{-}S2_{L\text{-}GHS}$ intersection lineation) plunge moderately to steeply (up to 60°) to NE and E (Fig. 3.12). In highly deformed areas, the meso-scale $F3_{L\text{-}GHS}$ folds are isoclinal to tight and the $S3_{L\text{-}GHS}$ is highly penetrative, transposing and parallelizing the $S2_{L\text{-}GHS}$ (Fig. 3.8e,f). There, localized shear bands and shear zones are approximately parallel to the $S3_{L\text{-}GHS}$, and the $F3_{L\text{-}GHS}$ folds show stretched limbs. Biotite and locally kyanite crystals define a dip-slip stretching lineation on the $S3\text{-}S2_{L\text{-}GHS}$ composite foliation. Pinch and swell structure of syntectonic quartz layers and foliations related to $D2_{L\text{-}GHS}$ and $D3_{L\text{-}GHSH}$ events are present in several outcrops (Fig. 3.8f). Kinematic indicators (e.g. S-C cleavage relationships, mica fish, clast rotated) indicate top-to-south sense of shear during both $D2_{L\text{-}GHS}$ and $D3_{L\text{-}GHS}$ deformation events.

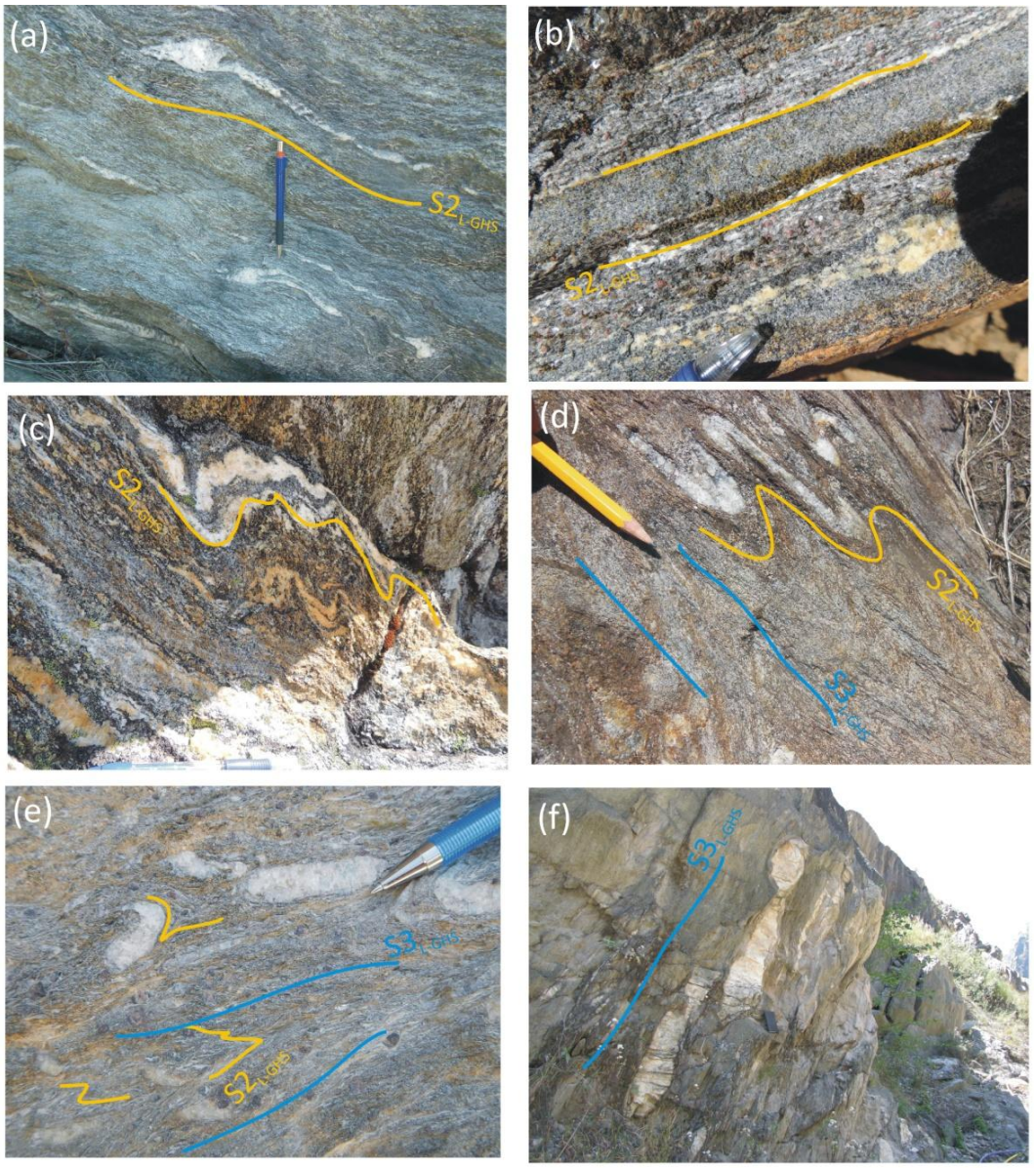

Fig. 3.8–Representative L-GHS mesostructures. (a) Two-mica micaschist with pervasive $S2_{L\text{-}GHS}$ foliation. **(b)** Compositional layering in two-mica + garnet metapelites, with bands parallel to the $S2_{L\text{-}GHS}$ schistosity. **(c)** Crenulated $S2_{L\text{-}GHS}$ surface. **(d,e)** Micaschist with relationships between the $S2_{L\text{-}GHS}$ regional foliation and the later $S3_{L\text{-}GHS}$ (parallel to the pencil). **(f)** Buodinated quartz layers are stretched along $S3_{L\text{-}GHS}$.

3.4.1.3 Upper Greater Himalayan Sequence

❖ ***U-GHS lithologies***

The most common lithology in the **upper GHS** is garnet + k-feldspar + sillimanite migmatitic paragneiss. At the outcrop scale, these rocks typically consist of mm-to cm-thick leucocratic quartzo-feldspathic domains alternating with mm-thick dark biotite +

plagioclase + sillimanite ± garnet layers, which generally define a more or less continuousplanar foliation (Fig. 3.9a-c).

The amount of garnet is variable; it occurs as mm- to cm-sized porphyroblasts often surrounded by a plagioclase corona (Fig. 3.9b). Late white mica generation locally occurs as large flakes overgrowing the main foliation.

Calc-silicate granofels and gneisses occur as tens of metre thick layers within the host metapelites (Fig. 3.9d-f). They are easily recognized in the field because of their characteristic deformation styles, due to their relatively stiff rheological behavior compared to the host quartz-feldspar rich rocks. The main mineral assemblage consists of clinopyroxene + k-feldspar + scapolite ± plagioclase ± quartz ± calcite, with late green amphibole. A banded structure is observed locally, defined by the different modal proportion of the rock-forming minerals in adjacent layers.

Large bodies of migmatitic biotite + sillimanite ± garnet –bearing orthogneisses are present at different structural levels in the sequence (Fig. 3.9g), concordant with the regional schistosity. Metre- to tens of metre thick layers of fine-grained biotitic gneisses with sillimanite-rich nodules ("Black Gneisses" according to Lombardo et al., 1993) are sometimes associated with these orthogneisses (Fig. 3.9h); the nodules, up to several cm in length, mainly consist of sillimanite + quartz and are elongated parallel to the foliation. Pegmatitic dykes and two-mica + garnet + tourmaline leucogranite bodies and dykes (Fig. 3.10a-c) occur at the higher structural levels of U-GHS, variably oriented with respect to the main foliation. They are the dominant lithology in the highest peaks of the Langtang Valley (e.g. Langtang Lirung, Langtang II, Kimshung).

❖ ***U-GHS meso-structures***

In the high-grade, often migmatitic, U-GHS lithologies, it is difficult to have a unique interpretation of all the penetrative structures occurringat the mesoscale, due to the interplay between tectonic, melt-producing and melt-crystallizing processes. A pervasive planar structure is always present at the outcrop scale, which is parallel to the compositional layering (Fig. 3.11a,b). An earlier foliation has not been observed; it is therefore not possible to unequivocally ascribe this main regional schistosity to a precise deformational phase, and to correlate it with the planar fabrics observed in the LHS and in L-GHS units. In other words, it is not possible to clearly understand if the main foliation is a $S1_{U\text{-}GHS}$ or a $S2_{U\text{-}GHS}$, therefore the neutral term $\mathbf{Sm_{U\text{-}GHS}}$ is preferred.

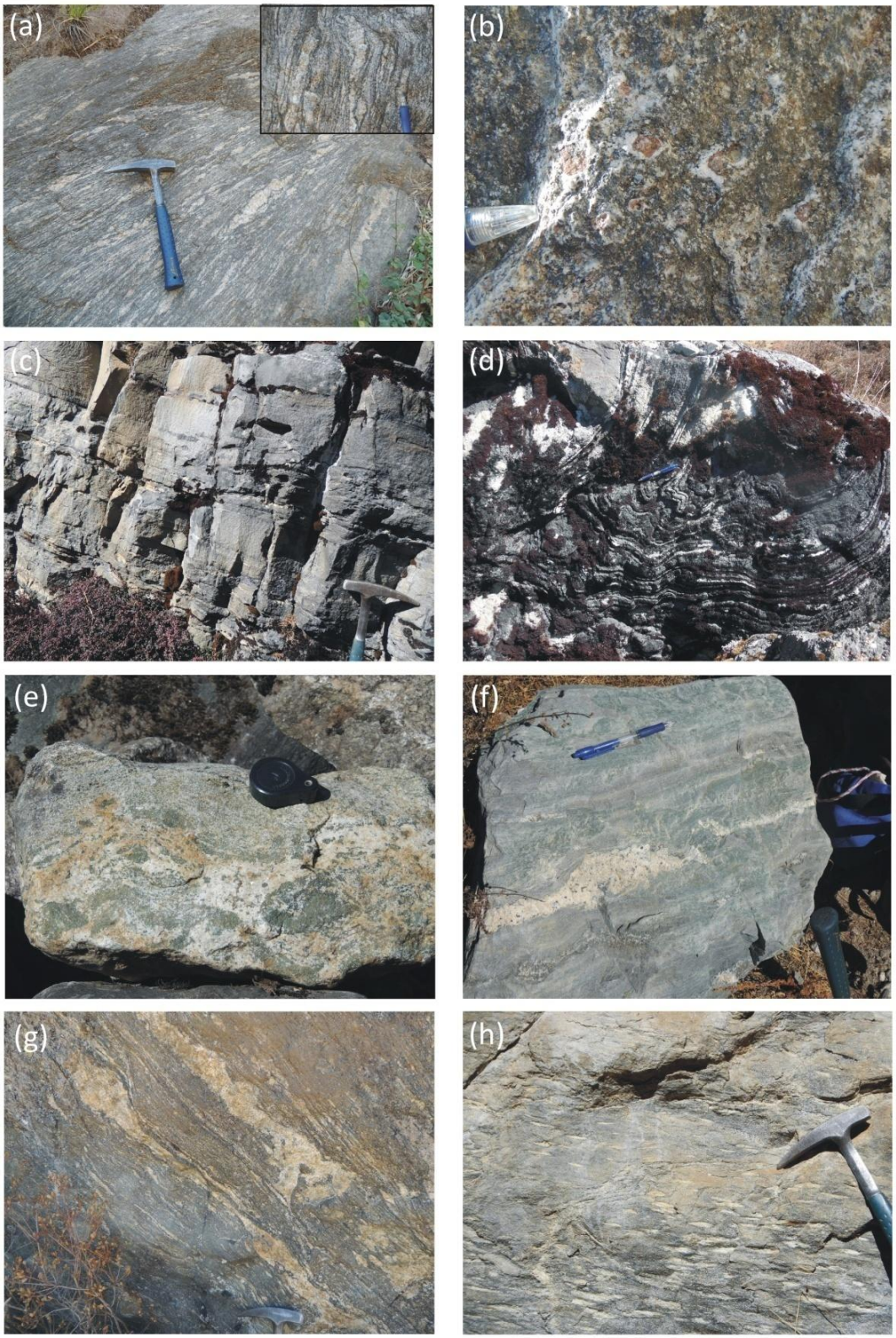

Fig. 3.9

Fig. 3.9 – Representative U-GHS lithologies. (a) Strongly mylonitic migmatitic paragneiss in the Gatlang region, with leucosomes elongated parallel to the main foliation. The inset shows a later generation of melt cross-cutting the main schistosity. **(b)** Detail of garnet + sillimanite –bearing gneiss, with garnet surrounded by a plagioclase corona. (**c)** Detail of the sillimanite + quartz nodules in a biotite –bearing paragneiss, elongated parallel to the main foliation. **(d-f)** Layers of calc-silicate rocks (clinopyroxene + k-feldspar + scapolite ± plagioclase ± quartz ± calcite), variably deformed. In (f) a tourmaline-leucogranite intrudes the rocks. **(g)** Migmatitic orthogneiss. **(h)** Metre thick layers of fine-grained biotite –bearing gneisses with sillimanite nodules intercalated with migmatitic orthogneisses.

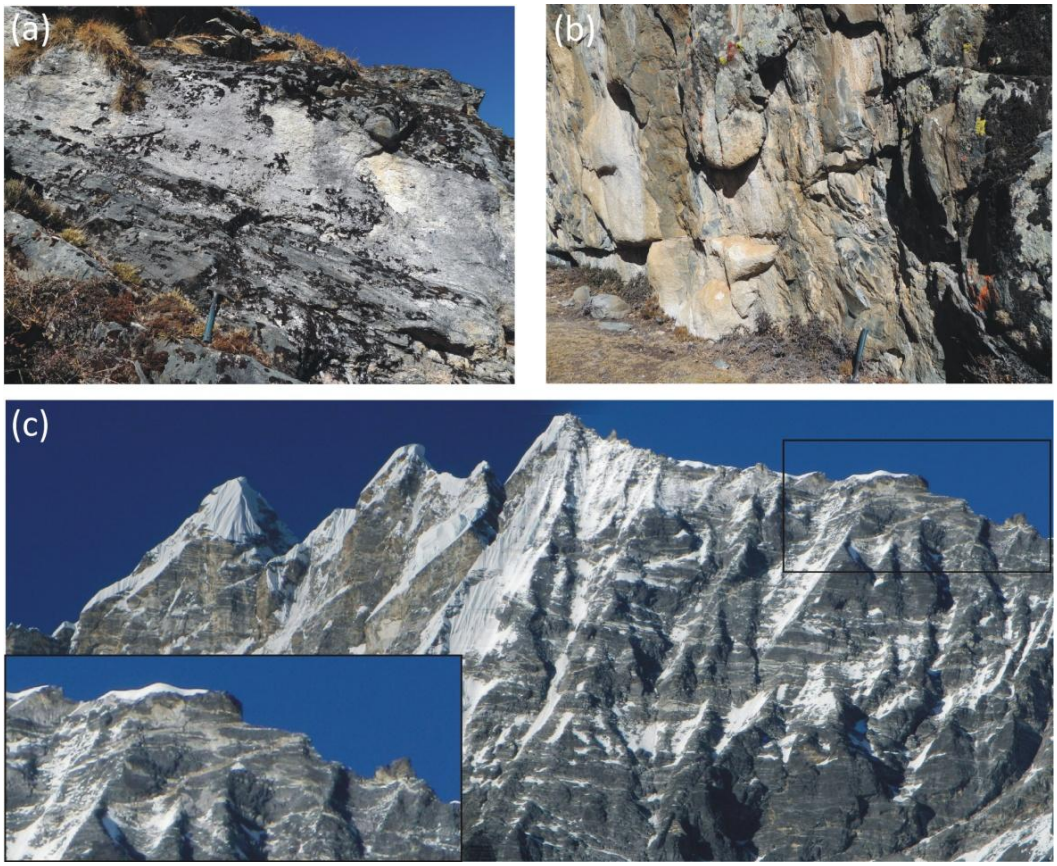

Fig. 3.10 -Representative U-GHS lithologies (leucogranites). (a,b) Leucogranite dykes variably oriented with respect to the main foliation (a: concordant; b: discordant). **(c)** Several leucogranite dykes (light colour) intrude the U-GHS of the Kimshung and Langtang Lirung peaks. The inset shows a detail of this network of dykes, characterized by different orientations.

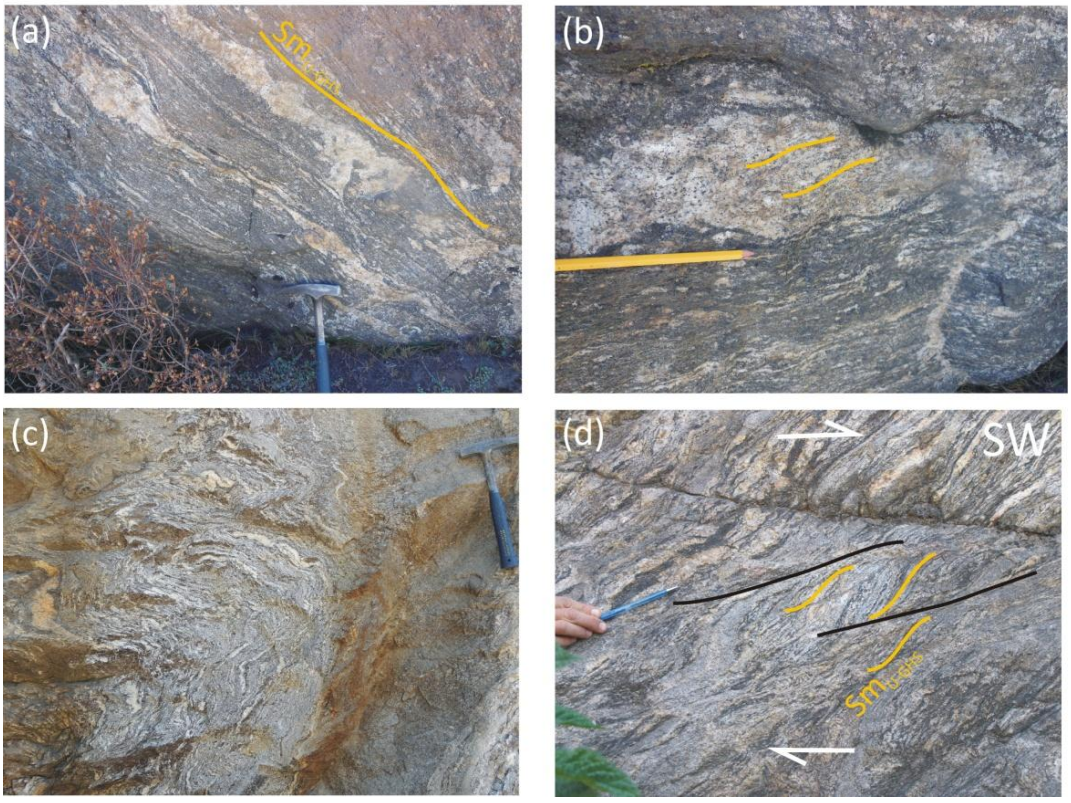

Fig. 3.11 – Representative U-GHS mesostructures. (a) Migmatitic paragneiss with leucosomes parallel to the Sm_{U-GHS}. **(b)** Detail of a leucosome, in which is visible the schistosity parallel to Sm_{U-GHS}. **(c)** Highly deformed migmatitic paragneiss. **(d)** Shear zone with top-to-SW movement in the mylonitic migmatitic gneisses.

In the migmatitic metapelites and orthogneisses, Sm_{U-GHS} is defined by mm- to pluri-cm leucocratic quartz + plagioclase + k-feldspar domains alternating to mm-thick mesocratic domains, rich in biotite, sillimanite and plagioclase (Fig. 3.11a,b). Leucosomes are almost parallel to the $Sm_{U-GHS,}$ and contain a planar fabric defined by biotite (Fig. 3.11c), thus indicating that melting was contemporary to the Sm_{U-GHS} development. In the fine-grained biotitic gneiss with sillimanite nodules, the Sm_{U-GH} is defined by biotite alignment in millimetric domains. Calc-silicate rocks are stretched and deformed along the main schistosity, sometimes forming boudins enveloped by the $Sm_{U-GHS.}$

The Sm_{U-GHS} generally dips toward NE to E with an angle between 10° and 40° (Fig. 3.12); this foliation contains a down-dip stretching mineral lineation $\mathbf{L_{U-GHS}}$ (Fig. 3.12) locally defined by biotite, sillimanite or feldspar. The migmatitic orthogneisses often show a mylonitic fabric, with clasts of K-feldspar stretched and rotated. In these rocks, S-C fabrics indicate top-the S/SW sense of shear. The Sm_{U-GHS} is highly deformed and folded (Fig. 3.11c,d) by open to tight folds, with fold axes often striking NE-SW and axial planes plunging moderately to the north.

Ductile shear zones occur at different structural levels in the U-GHS, with S-C fabrics and/or rotated porphyroclasts indicating top-to-SW sense of shear (Fig. 3.11d). The lowermost shear zone is visible in the Gatlang transect at Ghattekhola, at the very beginning of the migmatitic U-GHS sequence (Fig. 3.11d).

The occurrence of undeformed leucogranites occurring both parallel and crosscutting all the previously mentioned meso-structures testifies that melting was protracted after the development of the regional schistosity (Fig. 3.10c).

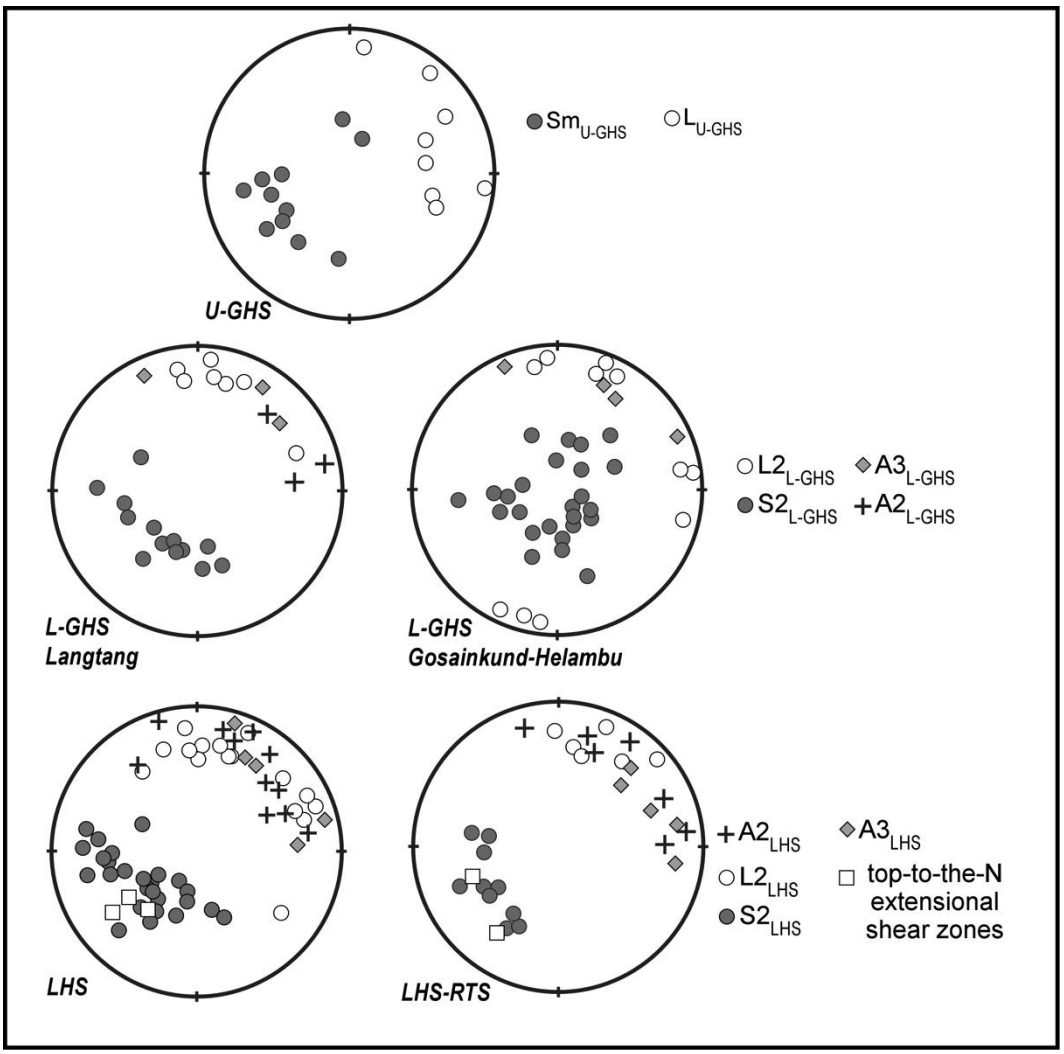

Fig. 3.12 – Equal area stereo plots of representative structural data from LHS, L-GHS and U-GHS.

3.4.2 Petrography and mineral chemistry

This section presents detailed petrographic description of most lithologies from both the LHS and GHS, excluding the CO_2-source rocks that are discussed in detail in Section 4.3.2.

The studied samples are described from lower to higher structural levels (Fig. 3.1b) and are reported in the same order in all relevant figures and tables.

The most representative microstructures are reported in Fig. 3.13-Fig. 3.15,Fig. 3.23; mineral chemical data are reported in Fig. 3.16, Fig. 3.24, Fig. 3.26. Cristallization-deformation relations for the modelled samples are given in Fig. 3.17 and Fig. 3.25.

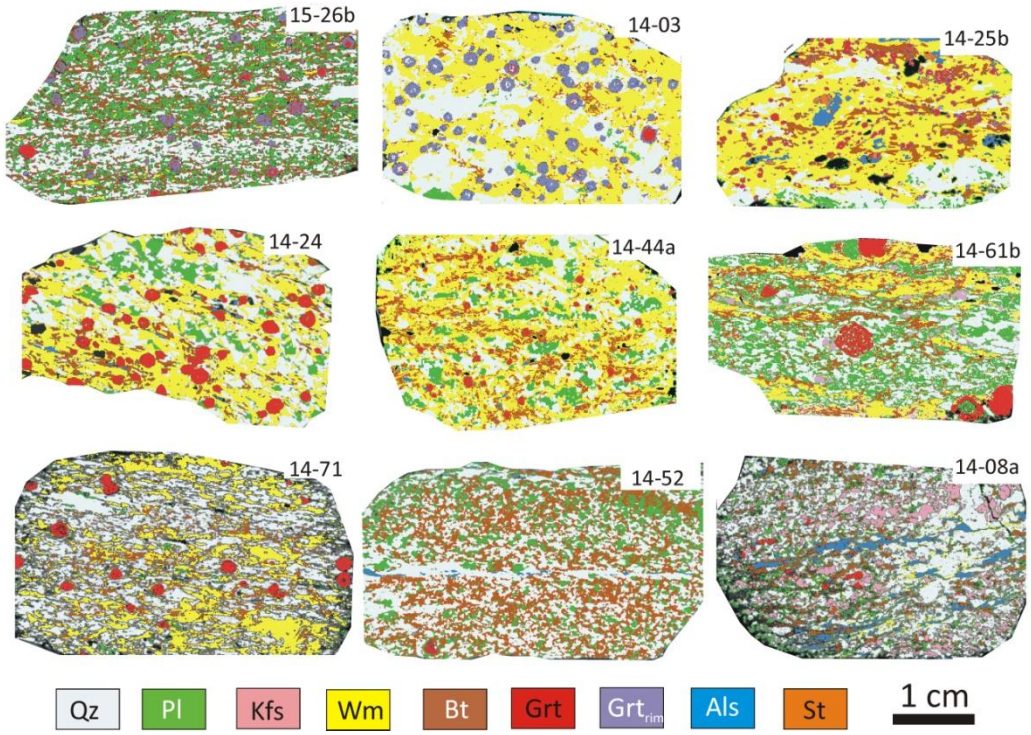

Fig. 3.13 - μ-XRF maps of the modelled metapelites using the pseudosection approach. Sample 14–27a is not reported because its grain-size is too fine to allow a precise interpretation of the mineral distribution and to estimate the modal amount of each phase. Samples are reported from lower to upper structural level.

3.4.2.1 Lesser Himalayan Sequence – Petrography

❖ ***Phyllites, phyllitic micaschists and fine-grained gneisses***

Phyllites and **phytic micaschists** are fine-grained rocks consisting of white mica + biotite + quartz ± chlorite ± garnet ± plagioclase ± staurolite ± kyanite ± minor epidote and accessory graphite, ilmenite and tourmaline. They are characterized by a well-developed foliation ($S2_{LHS}$; Fig. 3.14a-d and Fig. 3.13), which is derived from the transposition of an older schistosity ($S1_{LHS}$), sometimes still preserved in microlithons. The $S1_{LHS}$ schistosity is defined by the preferred orientation of biotite + white mica ± chlorite (+ plagioclase and ilmenite) (Fig. 3.14b,c). Similarly, the $S2_{LHS}$ schistosity is defined by white mica + biotite ±

chlorite, which are concentrated in mm-thick domains, alternated to discontinuous quartz ± plagioclase lenses, few mm-thick, parallel to the main foliation. Few mm-thick quartz aggregates with a granoblastic structure are locally enveloped by the $S2_{LHS}$ foliation. At the lowermost structural levels, chlorite is in equilibrium with white mica and biotite in the $S2_{LHS}$ schistosity, while up in the section only white mica and biotite are present. The $S2_{LHS}$ schistosity is often crenulated, with the local development of a later $S3_{LHS}$ foliation (Fig. 3.14d,g) defined by biotite + white mica + ilmenite alignment in pluri-mm thick domains that cross-cut at low angle the $S2_{LHS.}$

Garnet is is nearly ubiquitous and dispersed in the rock matrix; it occurs either as coarse-grained porphyroblasts, sometimes with a skeletal habit, up to 2 mm in diameter, or as fine-grained idioblasts. Typically, garnet is partly wrapped by the $S2_{LHS}$, except for the outer rim which appears in equilibrium with the main foliation: it often includes a rotated internal foliation (i.e. snow-ball microstructure, Fig. 3.14a,e,f) defined by the alignment of quartz + chlorite + ilmenite and graphite inclusions.

Staurolite and kyanite only occur in the phyllitic micaschists exposed in the LHS uppermost structural levels. Staurolite porphyroblasts occur both as inclusions in the garnet rims and in the matrix (Fig. 3.14g), where they include an internal foliation defined by graphite $\pm$ quartz $\pm$ white mica and ilmenite, which is continuous with the external $S2_{LHS}$ matrix foliation. Kyanite is rare and occurs both as inclusion in the garnet rims (Fig. 3.14e) and in the matrix (Fig. 3.14g); it can include quartz and ilmenite. Small plagioclase granoblasts occur both in the microlithons and in the S2LHS schistosity. In some samples, plagioclase has a poikiloblastic habit and overgrows the $S2_{LHS}$ schistosity. Late biotite, white mica and chlorite locally occur as small flakes statically overgrowing $S2_{LHS}$ (Fig. 3.14b). Sub-millimetric idioblastic crystals of epidote are locally dispersed in the matrix. Fine-grained graphite is locally abundant in the micaceous domains (Fig. 3.14a).

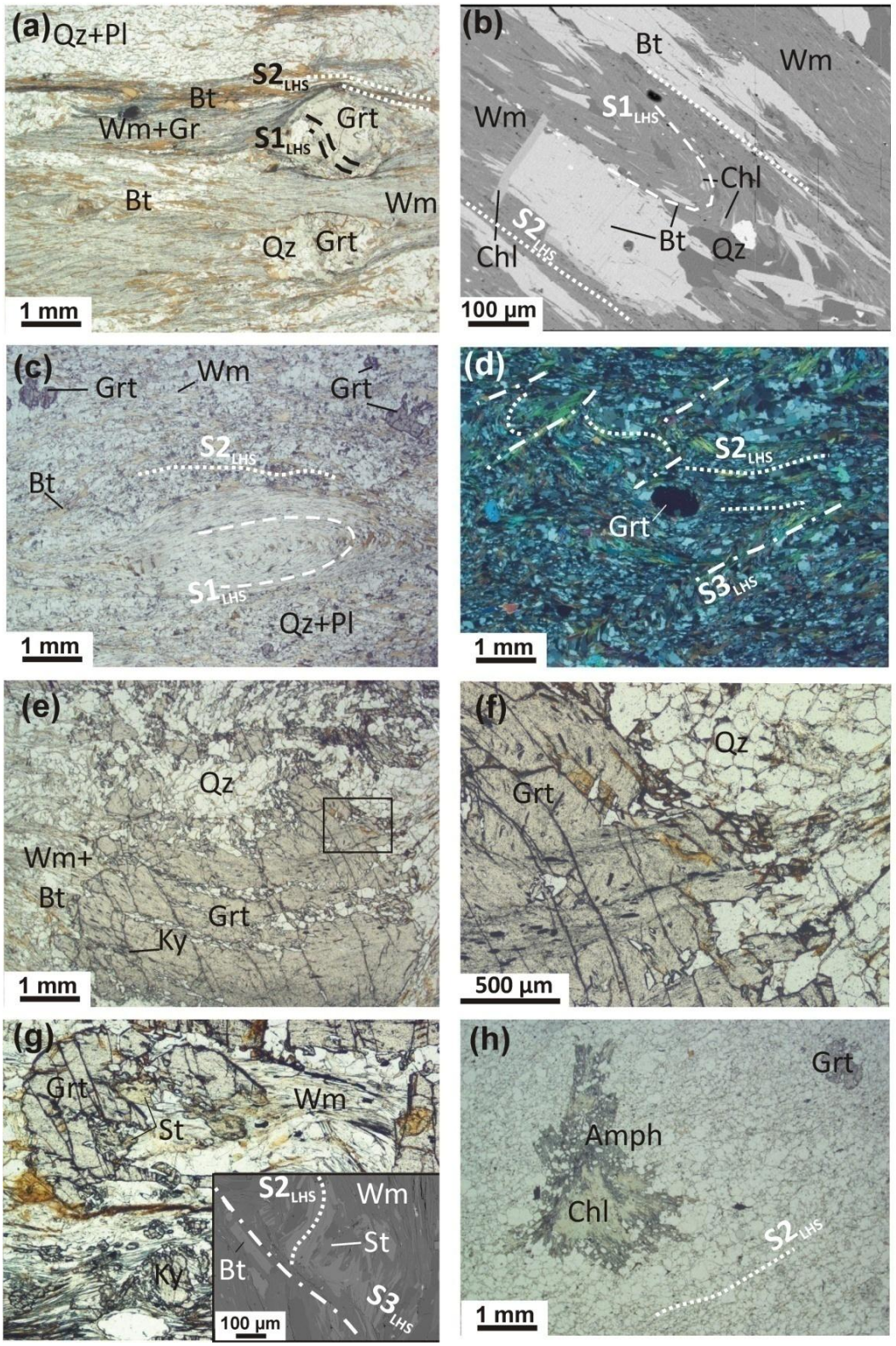
(a)
Qz+Pl
S2LHS
Bt
Wm+Gr
Grt
S1LHS
Bt
Wm
Qz
Grt
1 mm
(b)
Bt
Wm
Wm
S1LHS
Chl
S2LHS
Chl
Bt
Qz
100 µm
(c)
Grt
Wm
Grt
S2LHS
Bt
S1LHS
Qz+Pl
1 mm
(d)
S2LHS
Grt
S3LHS
1 mm
(e)
Qz
Wm+
Bt
Grt
Ky
1 mm
(f)
Qz
Grt
500 µm
(g)
Grt
Wm
St
S2LHS
Wm
St
Ky
Bt
S3LHS
100 µm
(h)
Grt
Amph
Chl
S2LHS
1 mm

Fig. 3.14

Fig. 3.14 - Representative microstructures of LHS lithologies (phyllitic micaschists and fine-grained gneisses). Sample 14-27a. **(a)** Garnet porphyroblasts are wrapped around by the $S2_{L\text{-}GHS}$ foliation defined by the alignment of biotite + white mica + graphite. Note the rotated internal schistosity in garnet (Plane Polarized Light: PPL). **(b)** Detail of a microlithon, preserving an older foliation $S1_{L\text{-}GHS}$ defined by white mica + biotite + chlorite + ilmenite ± plagioclase. Note the static growth of a large biotite flake on $S2_{L\text{-}GHS}$, and chlorite replacing it at its rims (Back Scattered Electron image: BSE). Sample 15-12. **(c)** The $S2_{L\text{-}GHS}$ foliation is defined by white mica + biotite; $S1_{L\text{-}GHS}$ is preserved in pluri-mm thick microlithons, and is defined by white mica + biotite (PPL). **(d)** The $S2_{L\text{-}GHS}$ foliation is crenulated, with the development of a $S3_{L\text{-}GHS}$ fabric, defined by white mica + biotite (Crossed Polarized Light: XPL). Sample 15-28b. **(e)** Cm-sized garnet porphyroblast with kyanite included in the rim. The rotated internal foliation is continutous with the external $S2_{L\text{-}GHS}$ schistosity, defined by white mica + biotite (PPL). **(f**) Detail of the rotated internal foliation in the same garnet porphyroblast as in (e) (PPL). **(g)** Detail of staurolite included in garnet rim and kyanite in the matrix (PPL). The inset show a detail of the $S3_{L\text{-}GHS}$ foliation derived from the crenulation of the main $S2_{L\text{-}GHS}$ foliation. Staurolite is in equilibrium with $S2_{L\text{-}GHS}$. (BSE). Sample 15-19b. **(h)** Amphibole + chlorite aggregates statically overgrowing the $S2_{L\text{-}GHS}$ foliation, defined by biotite alignment (PPL).

The **fine-grained gneisses** are characterized by a discontinuous planar fabric defined by biotite and minor white mica concentrated in mm-thick domains, alternated to pluri-mm thick quartz + plagioclase layers. The $S2_{LHS}$ gneissic structure is parallel to the compositional layering. Garnet has a typical skeletal habit, and is either dispersed in the matrix or concentrated in few cm-thick domains, togheter with coarse-grained randomly oriented biotite, chlorite and plagioclase. It is worth noting that garnet growth is oriented parallel to the $S2_{LHS}$ structure. Plagioclase occurs either as fine-grained granoblasts in equilibrium with the $S2_{LHS}$ or less commonly overgrowing it, or as coarse-grained porphyroclasts enveloped by the main foliation. Peculiar aggregates of coarse-grained green amphibole and chlorite are often observed in these gneisses (Fig. 3.14h).

❖ ***Quartzites and metasandstones***

Pure **quartzites** have grain size variable from fine to medium. The structure is granoblastic, often with triple joints. Very fine-grained white mica and minor biotite are present, roughly iso-oriented in discontinuous mm-thick domains, defining the $S2_{LHS}$ foliation (Fig. 3.15a). In the impure, **foliated quartzites**, white mica and biotite are more abundant; these rocks are characterized by a marked schistosity defined by phyllosilicates ± staurolite ± chlorite concentrated in continuous millimetric domains, alternated to pluri-mm quartz domains (Fig. 3.15b). The grain size is generally coarser with respect to that of pure quartzites. White mica dominates over biotite. Opaque minerals and tourmaline are present as accessory phases in both pure and impure quartzites. Tourmaline is sharply zoned, with a bluish core and a green-yellow rim.

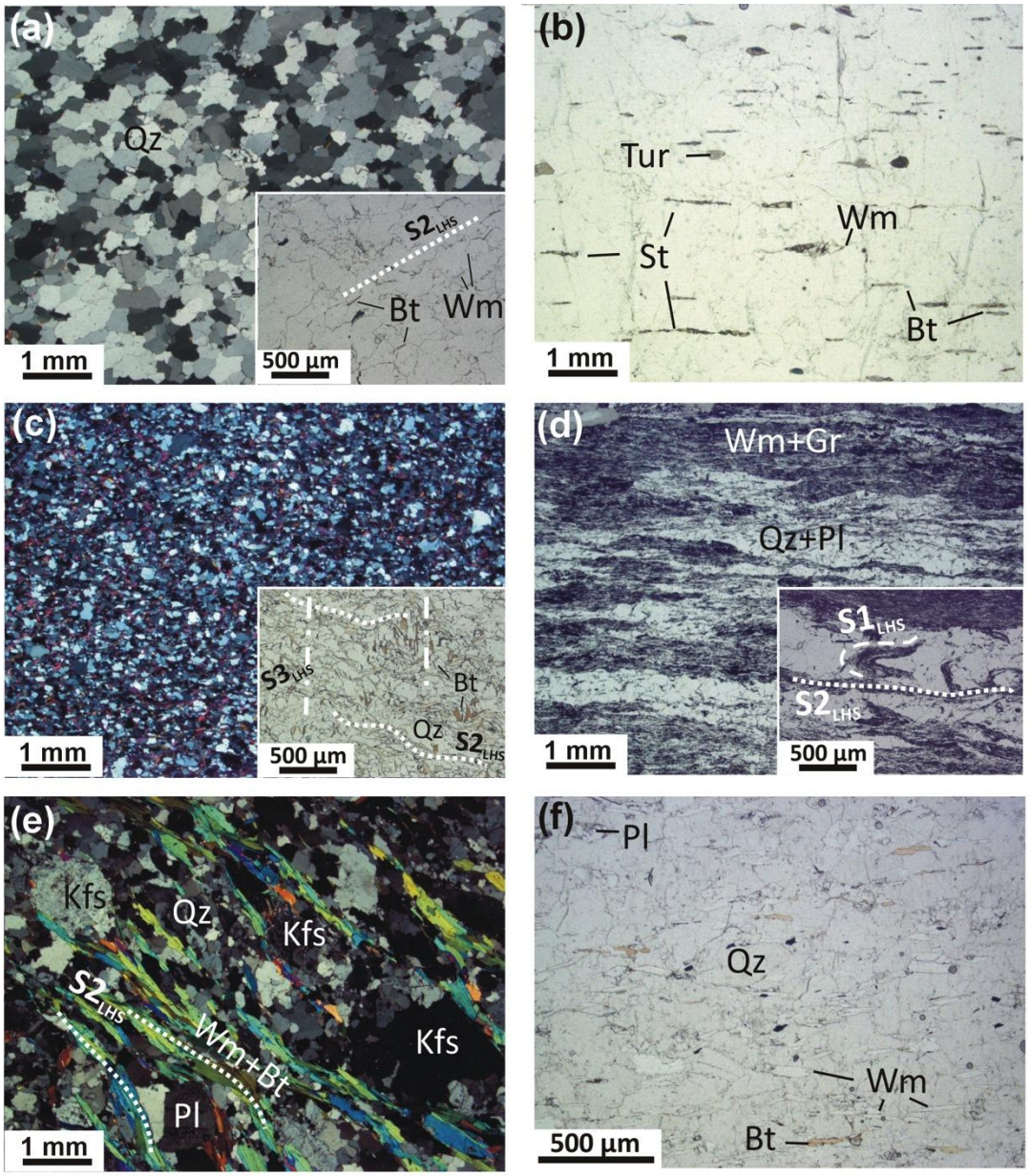

Fig. 3.15 – Representative microstructures of LHS lithologies (quartzites, metasandstones, graphitic schists and orthogneisses). Sample 14-29b. **(a)** Pure quartzite in which the $S2_{LHS}$ foliation is defined by fine-grained biotite + white mica, as shown in the inset (XPL; inset: PPL). Sample 14-26d. **(b)** Foliated quartzite, with a more developed planar fabric defined by white mica ± biotite ± staurolite ± tourmaline (PPL). Sample 14-27b. **(c)** Fine-grained biotite-bearing metasandstone, with quartz and plagioclase clasts. The inset shows the main $S2_{LHS}$ schistosity defined by biotite ± white mica, and the development of biotite ± white mica $S3_{LHS}$ fabric, at high angle to $S2_{LHS}$ (XPL; inset: PPL). Sample 15-25b**. (d)** Graphitic schist: graphite + white mica define the main $S2_{L\text{-}GHS}$ schistosity, which is parallel to the compositional layering. The inset shows $S1_{LHS}$ still preserved in microlithons, defined by white mica + Gr (PPL). Sample 14-01**. (e)** Two-mica augen gneiss, with a well-developed mylonit fabric defined by white mica + biotite. (XPL). Sample 14-02. **(f)** Aplitic gneiss, with white mica + biotite defining the main $S2_{L\text{-}GHS}$ foliation (PPL).

Metasandstones are fine-grained and show a well-developed $S2_{LHS}$ schistosity, defined by biotite ± white mica mm-thick domains alternating with pluri-mm thick quartzo-feldspathic domains (Fig. 3.15c). A discontinuous $S3_{LHS}$ foliation defined by biotite ± white mica cross-cuts at high angle the $S2_{LHS}$ foliation. The granoblastic quartzo-feldspathic domains are generally fine-grained, although pluri-mm quartz and plagioclase crystals are locally dispersed in the matrix and enveloped by the main $S2_{LHS}$foliation. Graphite and tourmaline are accessory mineral phases.

❖ ***Graphitic schists***

Graphitic schists are fine-grained rocks with a well-developed schistosity defined by pluri-mm thick continuous graphite + white mica ± quartz domains, alternated to mm-to pluri-mm thick domains consisting of quartz and minor white mica + graphite. The $S2_{LHS}$ foliation, parallel to the compositional layering, is defined by white mica alignment; the $S1_{LHS}$ foliation is locally preserved in microlithons and isolated fold hinges, and it is defined by white mica + graphite (Fig. 3.15d).

❖ **Two-mica orthogneiss**

The **two-mica orthogneisses** are characterized by a more or less developed mylonitic fabric (Fig. 3.15e). The $S2_{LHS}$ mylonitic foliation is defined by the preferred orientation of white mica and minor biotite, associated with quartz and plagioclase in mm-thick domains alternating with coarse-grained quartzo-feldspathic domains. K-feldspar ± plagioclase ± quartz porhyroclasts are enveloped by the main $S2_{LHS}$foliation (Fig. 3.15e); the porphyroclasts size is extremely variable, varying from few millimetres up to 1 cm. K-feldspar is often partially replaced by albite; it can include quartz and biotite. A late generation of biotite and white mica locally overgrows the $S2_{LHS}$ foliation. Accessory apatite is ubiquitous, whereas rutile and epidote aggregates are only locally observed. Layers of **aplitic gneisses** are widespread in the orthogneiss sequence. These rocks are typically fine-grained. White mica and minor biotite, which define the main $S2_{LHS}$ foliation (Fig. 3.15f), are concentrated in sub-mm thick discontinuous domains, alternated to quartzo-feldspathic layers. Opaque minerals and apatite are present as accessory minerals.

3.4.2.2 Lesser Himalayan Sequence – Mineral chemistry

Mineral chemistry data for samples 15-19, 14-27a, 15-28b and 15-26b are summarized in Tab. 3.1 and Fig. 3.16.

Garnet porphyroblasts are rich in almandine with variable amounts of the other components. Garnet is strongly zoned in samples 14-27a, 15-26b and 15-19 and slightly

zoned in sample 15-28b: in all samples, XMn and XCa decrease towards the garnet rim, while both XMg and XFe increase, reflecting a prograde compositional zoning. Biotite is homogeneous in composition in samples 14-27a and 15-28b, where it defines both $S1_{LHS}$ and$S2_{LHS,}$ while in sample 14-19 and 15-26b biotite included in garnet has lower Ti content and/or higher XMg compared to biotite defining $S2_{LHS}$. In sample 14-27a, 15-26b and 15-19 the different white mica generations have different compositions, with Si content increasing in lepidoblasts defining the $S2_{LHS}$; in sample 15-28b white mica is homogeneous in composition. Plagioclase in the matrix is an oligoclase-andesine; it is homogeneous or slightly zoned, with anorthite content decreasing toward the rim. In sample 15-19, rare plagioclase inclusions in garnet are more sodic in composition than plagioclase in the matrix. Chlorite in sample 14-27a shows slight differences in composition in different microstructural sites: chlorite included in garnet has lower XMg than chlorite defining $S1_{LHS}$ and replacing biotite and garnet. Most chlorite is ripidolite (with minor pycnochlorite) according to Hey (1954). Staurolite in sample 15-28b is slightly zoned, with XMg decreasing toward the rim. Epidote in sample 14-27a varies in composition from XZo=0.40 to XZo=0.55 [XZo component defined as: Al/ (Al + Fe^{3+})].

Table 3.1 - Mineral composition for the LHS metapelites

	Grt	Bt	Wm	Pl	Chl	Ep	St
15-19	→ XMg=0.03-0.07 XCa=0.19-0.09 XMn=0.16-0.02 XFe=0.63-0.81	XMg^{i}=0.39 Ti^{i}=0.03 XMg$^{\#}$=0.39-0.41 Ti$^{\#}$=0.10-0.11 XMg=0.40-0.42 Ti=0.06-0.11	→ Si$^{\#}$=3.09-3.10 Na$^{\#}$=0.12-0.20 Si=3.09-3.18 Na=0.14-0.20 Si*=3.10-3.11 Na*=0.10-0.13	XAn=0.21-0.23 XAn^{i}=0.18-0.22	XMg*=0.39-0.40		
14-27a	→ XMg=0.030-0.055 XCa=0.25-0.19 XMn=0.15-0.05 XFe=0.57-0.72	XMg=0.38-0.43 Ti=0.09-0.13	Si$^{\#}$=3.05-3.13 Na$^{\#}$=0.08-0.14 Si=3.05-3.17 Na=0.08-0.14 Si*=3.13-3.15 Na*=0.08-0.14	→ XAn=0.34-0.28	XMg^{i}=0.39 XMg$^{\#}$=0.41-0.44 XMg*=0.41-0.44	XZo=0.40-0.55	
14-28b	→ XMg=0.08-0.13 XCa=0.17-0.14 XMn=0.02-0.00 XFe=0.72-0.75	XMg=0.51-0.56 Ti=0.06-0.10	Si=3.08-3.20 Na=0.1-0.14				→ XMg=0.18-0.13
15-26b	→ XMg=0.09-0.14 XCa=0.2-0.14 XMn=0.09-0.03 XFe=0.64-0.70	XMg^{i}=0.57-0.59 Ti^{i}=0.09-0.10 XMg=0.50-0.52 Ti=0.10-0.13	Si=3.07-3.18 Na=0.15-0.19	→ XAn=0.30-0.24	XMg*=0.16		

^{i} included in garnet $^{\#}$ defining S_{m-1} * overgrowing S_m ^{r} relict
The arrows indicate a zonation from core to rim; Ti, Si,Na are expressed as a.p.f.u.

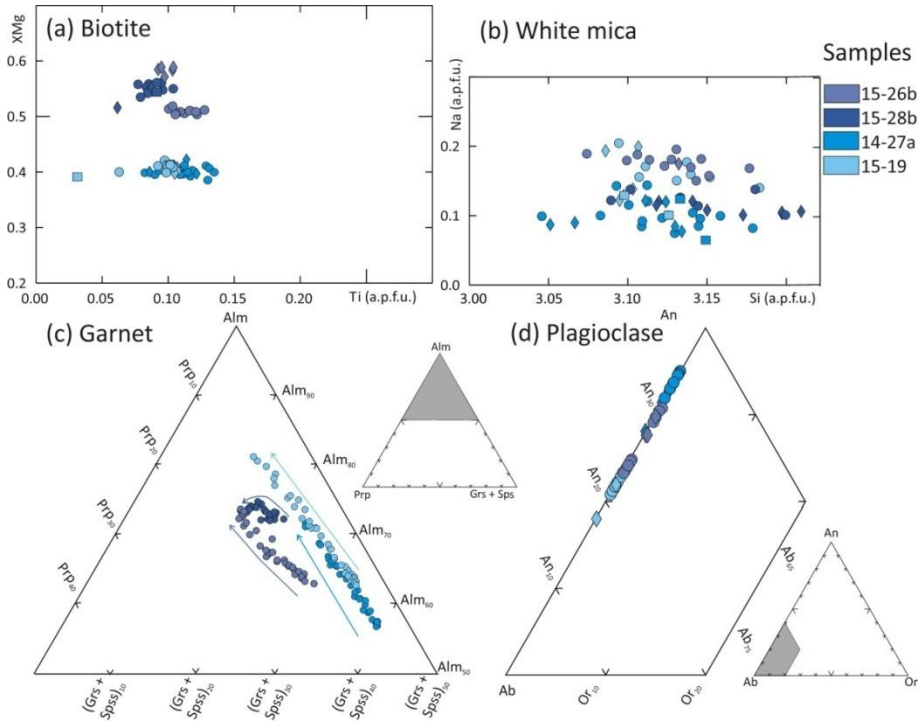

Fig. 3.16- Compositional diagrams for LHS metapelites. (a) Biotite, **(b)** white mica, **(c)** garnet, and **(d)** plagioclase. For each sample, biotite, white mica and plagioclase have been distinguished according to their microstructural position (diamond: in equilibrium with $S1_{LHS}$; circle: in equilibrium with $S2_{LHS}$; square: post-$S2_{LHS}$). Garnet zoning from core to rim is pointed out with coloured arrows.

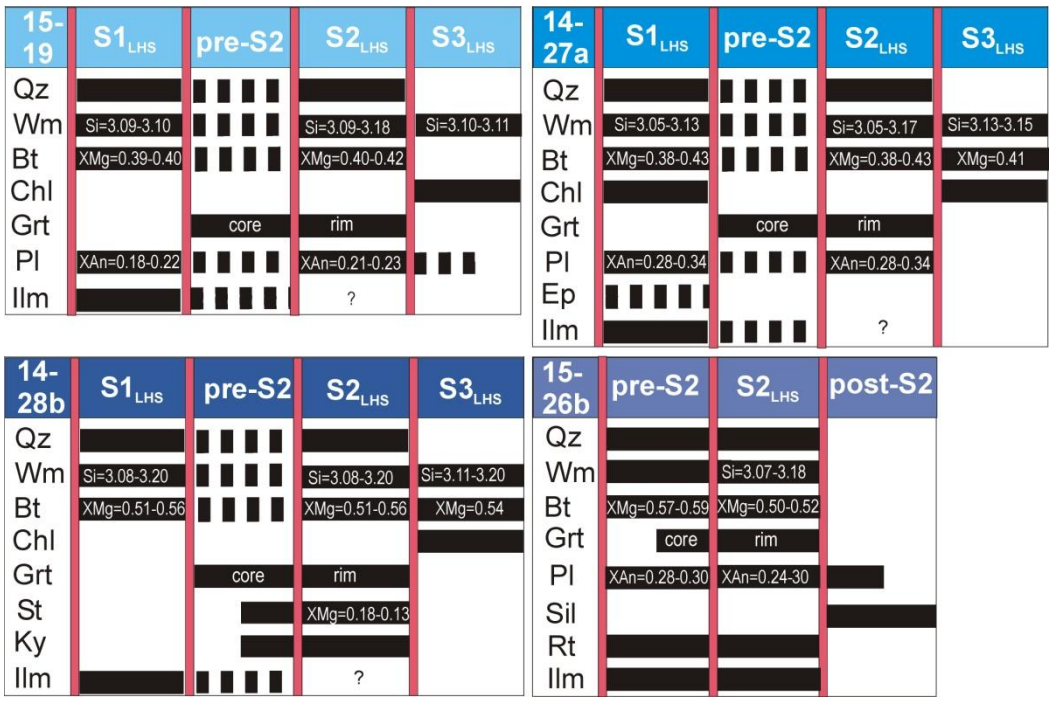

Fig. 3.17 – Crystallization–deformation relations of the studied LHS samples, with mineral compositions.

3.4.2.3 Lower Greater Himalayan Sequence – Petrography

❖ ***Two-mica + garnet ± staurolite ± kyanite –bearing gneissic micaschists and associated fine-grained gneisses***

The **two-mica + garnet ± staurolite ± kyanite –bearing gneissic micaschists** are the dominant lithology at the L-GHS lowermost structural levels. These are medium- to coarse-grained rocks (Fig. 3.13) consisting of white mica, biotite, garnet, plagioclase, quartz ± kyanite ± staurolite and accessory rutile, ilmenite and tourmaline. The main planar foliation ($S2_{L\text{-}GHS}$) is defined by mm-thick white mica + biotite layers alternated with pluri-mm thick discontinuous quartz domains (Fig. 3.18a,c,e). White mica and biotite occur as large flakes (up to 5 mm in length) oriented to define the main foliation; locally, a later generation of white mica statically overgrows the $S2_{L\text{-}GHS}$ fabric. The $S2_{L\text{-}GHS}$ foliation is locally crenulated and folded, and an axial plane foliation ($S3_{L\text{-}GHS}$) is sometimes observed, defined by biotite + white mica alignment in pluri-mm discontinuous domains (Fig. 3.18g,h).

Garnet porphyroblasts (up to 2 mm in diameter) are mostly in equilibrium with white mica and biotite and are mainly concentrated in the micaceous layers. Larger garnet porphyroblasts are microstructurally zoned (b,d), with the core and mantle crowded with inclusions (quartz, biotite, rutile, ilmenite ± plagioclase), and the rim almost free of inclusions. The transition between garnet core and rim is marked by the presence of small polymineralic inclusions (Fig. 3.18d,e and Fig. 3.19), up to 50 μm in width, interpreted as "nanogranites"; these inclusions mainly consist of quartz ± albite ± k-feldspar ± biotite ± epidote ± rutile ± zircon ± apatite ± ilmenite. The occurrence of nanogranites at the transition core-rim indicates that garnet rim is peritectic. Kyanite generally occurs at medium structural levels of the L-GHS, and forms large idioblasts mainly oriented parallel to $S2_{L\text{-}GHS}$ or overgrowing it (Fig. 3.18c,e). In few cases, kyanite occurs as inclusions in garnet rims. Staurolite generally overgrows the $S2_{L\text{-}GHS}$ and replaces kyanite at its rim (Fig. 3.18f); it occurs at the same structural levels of kyanite and it is rarely found included in garnet rims. Plagioclase is locally abundant, although it is not always present. It occurs either as subhedral crystals in equilibrium with the main foliation and locally including quartz, or as porphyroblasts overgrowing the $S2_{L\text{-}GHS}$ fabric and including biotite and quartz. Small and rare fibrolitic sillimanite locally replaces garnet, kyanite and white mica rims. Rutile and ilmenite occur both as inclusions in garnet and in the matrix; ilmenite often replaces rutile at its rim. Graphite is often present as accessory phase.

Dm- thick layers of **biotite-rich fine-grained gneisses** are intercalated in the two-mica + garnet ± staurolite ± kyanite –bearing gneissic micaschists. They show a typical banded structure, with biotite ± white mica ± garnet pluri-mm domains alternating with cm-thick quartz + plagioclase ± garnet domains. Compositional layering is parallel to the $S2_{L\text{-}GHS}$ foliation, defined by biotite ± white mica. White mica often occurs as large flakes overgrowing the planar fabric. Ilmenite and minor rutile, apatite and graphite occur as

accessory phases. Unusual concentrations of apatite are locally observed in these fine-grained gneisses.

❖ ***Two-mica + garnet ± sillimanite (± relict kyanite) -bearing gneissic micaschists and associated fine-grained gneisses***

In the structurally higher levels of the L-GHS, the metapelitic sequence mainly consists of **two-mica + garnet ± sillimanite (± relict kyanite) –bearing micaschists and gneissic micaschists**. These are medium-grained rocks (Fig. 3.13) consisting of plagioclase, quartz, biotite, white mica, garnet ± k-feldspar ± sillimanite (± relict kyanite) and accessory rutile and/or ilmenite, tourmaline and apatite. The well-developed $S2_{L\text{-}GHS}$ foliation is defined by the preferred orientation of biotite, minor white mica ± sillimanite, concentrated in continuous mm-thick layers, alternated with pluri-mm quartz + plagioclase ± k-feldspar ± biotite leucocratic domains (Fig. 3.20a,c,e). Locally, late white mica flakes overgrow the foliation. The modal amount of white mica in equilibrium with the $S2_{L\text{-}GHS}$ foliation decreases upsection, counterbalanced by an increase in the amount of late white mica flakes growing on the planar fabric. Toward the top of the sequence, microstructures indicating the presence of former melt appear. These include: leucosomic pods with coarse-grained k-feldspar + plagioclase + quartz (Fig. 3.20g); white mica + quartz ± plagioclase symplectites (back-reaction microstructure: e.g. Waters, 2001; Cenki et al., 2002; Kriegsman and Alvarez-Valero, 2010) thin films of quartz and/or feldspar (Fig. 3.20h), occupying interstitial positions, interpreted as "pseudomorphs after melt" (according to the definition of Holness and Clemens, 1999; Holness and Sawyer, 2008).

Garnet is generally porphyroblastic and wrapped around by the $S2_{L\text{-}GHS}$ foliation (Fig. 3.20b,c,e); its microstructural features differ from sample to sample. In most cases, garnet hosts abundant inclusions of quartz, biotite, plagioclase, white mica, minor kyanite and ilmenite, equally distributed from core to rim (except for kyanite, observed only in garnet rims); locally, garnet has the typical appearance of a peritectic phase, growing around large polymineralic inclusions consisting of rounded and corroded white mica, plagioclase and quartz (Fig. 3.20b). In contrast, in few samples garnet is microstructurally zoned, with the core crowded with monomineralic inclusions (quartz, plagioclase, biotite, ilmenite), and the rim almost inclusion-free (Fig. 3.20c). In these cases, the transition from core to rim is marked by the presence of few quartz + plagioclase + white mica + zircon + rutile + chlorite nanogranites (Fig. 3.20c and Fig. 3.19), up to 30 μm in width (i.e. garnet rim has a peritectic nature). Finally, some samples at higher structural levels are characterized by garnet porpryroblasts crowded with very small inclusions (except for the very outermost rim), which locally define concentric growth rings (Fig. 3.20d).

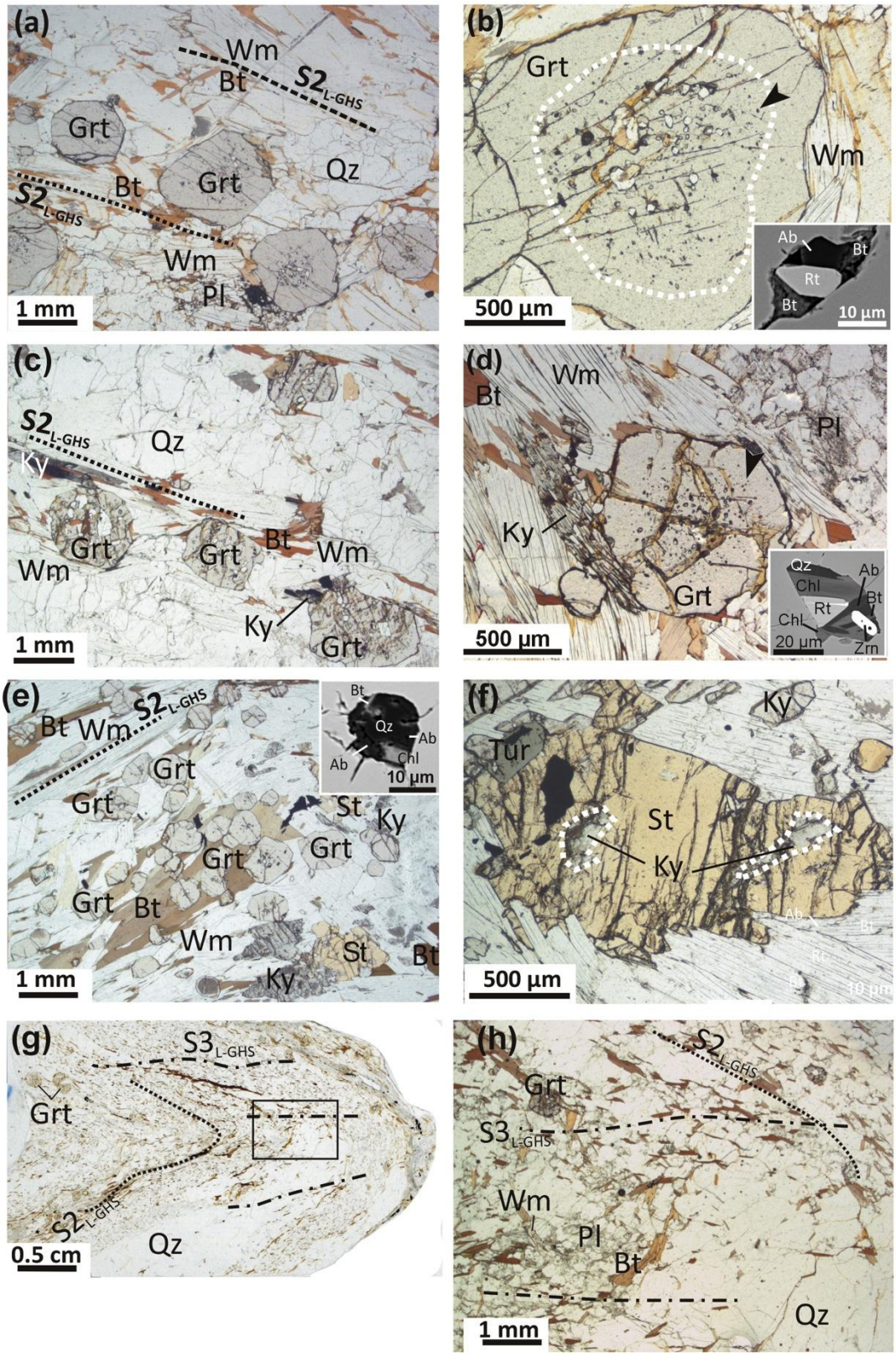
(a)
Wm
Bt
S2 L-GHS
Grt
Qz
Bt
Grt
S2 L-GHS
Wm
Pl
1 mm
(b)
Grt
Wm
Ab
Bt
Rt
Bt
10 µm
500 µm
(c)
S2 L-GHS
Qz
Ky
Grt
Grt
Bt
Wm
Wm
Ky
Grt
1 mm
(d)
Wm
Bt
Pl
Ky
Grt
Qz
Ab
Chl
Bt
Rt
Chl
Zrn
20 µm
500 µm
(e)
Bt
Qz
Ab
Ab
Chl
10 µm
Bt Wm
S2 L-GHS
Grt
Grt
St
Ky
Grt
Grt
Grt
Bt
Wm
St
Bt
Ky
1 mm
(f)
Ky
Tur
St
Ky
500 µm
(g)
S3 L-GHS
Grt
S2 L-GHS
Qz
0.5 cm
(h)
S2 L-GHS
Grt
S3 L-GHS
Wm
Pl
Bt
Qz
1 mm

Fig. 3.18

Fig. 3.18 - Representative microstructures of L-GHS lithologies (two-mica + garnet ± staurolite ± kyanite – bearing gneissic micaschist). Sample 14–03. **(a)** The main $S2_{L\text{-}GHS}$ foliation is defined by the alignment of white mica and biotite; garnet porphyroblasts are in equilibrium contact with both micas (PPL). **(b)** Detail of a garnet porphyroblast; garnet core includes coarse-grained rounded quartz, ilmenite and rutile, whereas garnet rim is almost free of inclusions. The transition from core to rim is underlined by the presence of nanogranites (black arrow). The inset shows a detail of a nanogranite (BSE). Sample 14-24. **(c)** The gneissic $S2_{L\text{-}GHS}$ fabric is defined by micaceous layers alternating to quartz–rich domains. The main foliation is defined by the alignment of white mica, biotite and kyanite (PPL). Sample 14-44a. **(d)** The $S2_{L\text{-}GHS}$ schistosity is defined by the alignment of biotite + white mica; garnet porphyroblasts are in equilibrium with $S2_{L\text{-}GHS}$ (PPL).The inset shows a detail of a nanogranite (BSE). Sample 14–25b. **(e)** The $S2_{L\text{-}GHS}$ foliation is marked by the alignment of white mica and biotite; garnet rim shows equilibrium relationship with micas. Note the kyanite porphyroblasts, either aligned parallel to the main foliation or overgrowing it (PPL). The inset shows a detail of a nanogranite included in Garnet (BSE). **(f)** Detail of a staurolite porphyroblast including kyanite (PPL). Sample 15-34b. **(g)** The main $S2_{L\text{-}GHS}$ schistosity, defined by white mica + biotite, derives from the transposition of an older $S1_{L\text{-}GHS}$, marked by coarse-grained quartz veins, now parallel to $S2_{L\text{-}GHS}$. The $S2_{L\text{-}GHS}$ foliation is folded, and in the hinges a $S3_{L\text{-}GHS}$ fabric develops, defined by biotite ± white mica (PPL). **(h)** Detail of (g) (PPL).

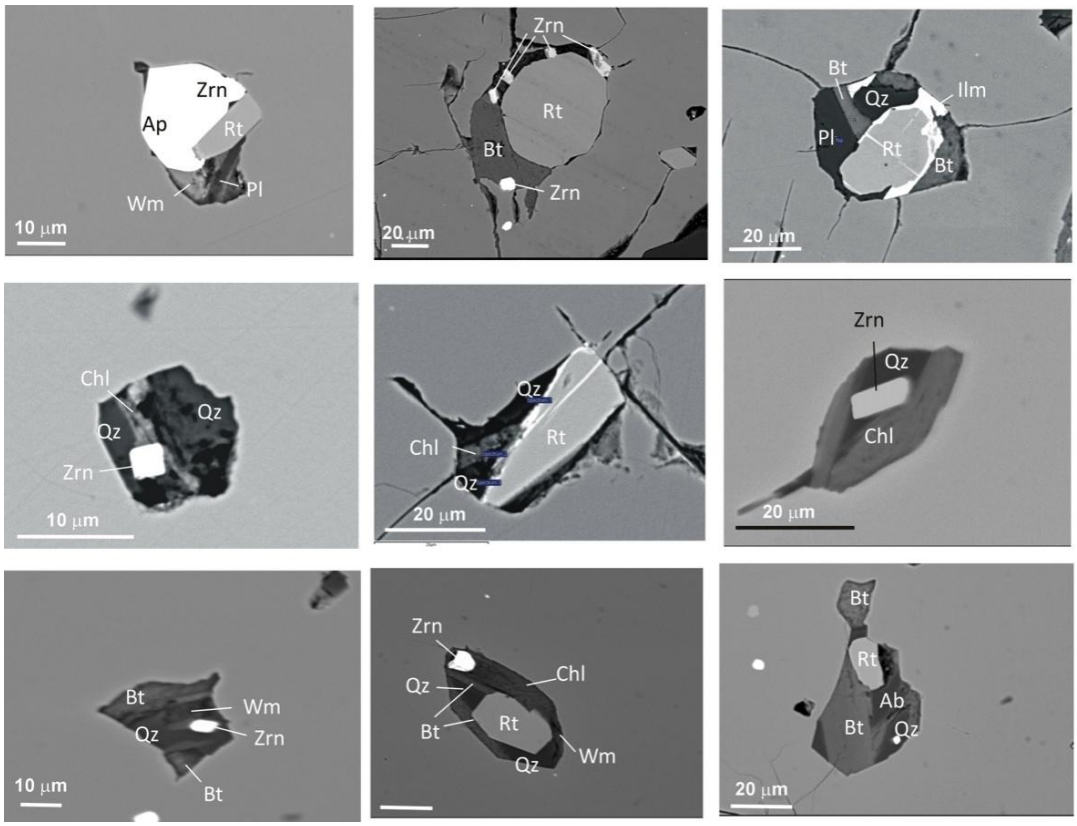

Fig. 3.19 - Representative images (BSE) of nanogranites included in garnets from the L–GHS two-mica schists exposed along the Langtang and Gosainkund–Helambu transects. Note the euhedral shape of zircon, indicating that it crystallized in situ from the melt.

Sillimanite is the aluminosilicate stable in the equilibrium mineral assemblage. It increases in modal amounts upsection; in the lower structural levels sillimanite is randomnly oriented and mostly replaced by white mica, whereas in the higher structural levels

sillimanite is oriented parallel to $S2_{L\text{-}GHS}$ foliation (Fig. 3.20e,f). Kyanite is rare, and is always a relic phase; it occurs both as inclusion in garnet rims and in the matrix, where it is generally rimmed by a plagioclase corona. If present, k-feldspar is widespread in the matrix and is partially replaced by plagioclase at its rims. Plagioclase is ubiquitous in these lithologies and occurs as large granoblastic crystals, up to 5 mm in length, locally with anti-perthitic structures. Accessory rutile is rare and is replaced by ilmenite; ilmenite occurs both as inclusions in garnet and in the matrix.

Fine-grained biotite ± white mica ± garnet ± sillimanite -bearing gneisses are often intercalated in these micaschists. Their mineral assemblages and microstructures are similar to those described for the associated micaschists, but they are finer-grained and the modal amount of micas is lower. Some samples are enriched in quartz.

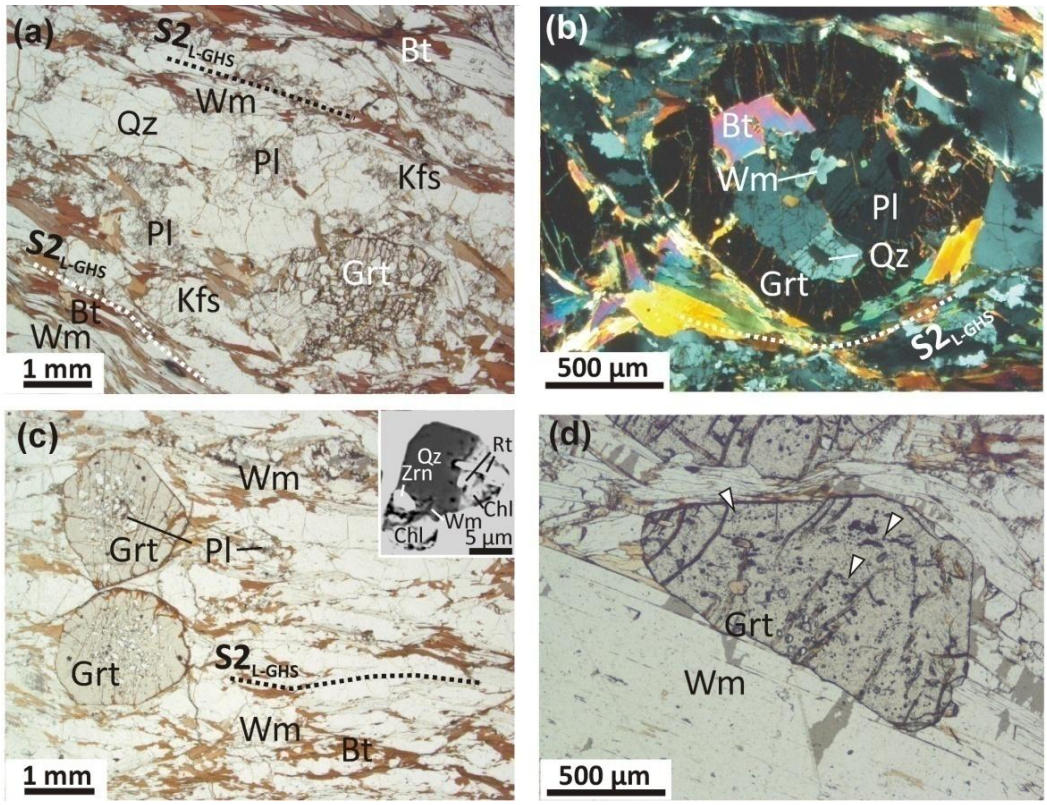

Fig. 3.20 - Representative microstructures of L-GHS lithologies (two-mica + garnet ± sillimanite (± relict kyanite) -bearing gneissic micaschist). Sample14–61b. **(a)** The main $S2_{L\text{-}GHS}$ foliation, marked by the alignment of biotite + white mica, wraps around a garnet porphyroblast with numerous rounded inclusions (PPL). **(b)** Detail of a peritectic garnet hosting rounded inclusions of white mica + plagioclase + quartz + ilmenite (XPL). Sample 14–71. **(c)** Garnet porphyroblasts are partially wrapped by the $S2_{L\text{-}GHS}$, but the rims show equilibrium contacts with biotite + white mica defining the $S2_{L\text{-}GHS}$ (PPL). Sample 14-06a. **(d)** Detail of a garnet porphyroblast crowded of small inclusions concentrated in growth rings. Some of the inclusions are possibly nanogranites.

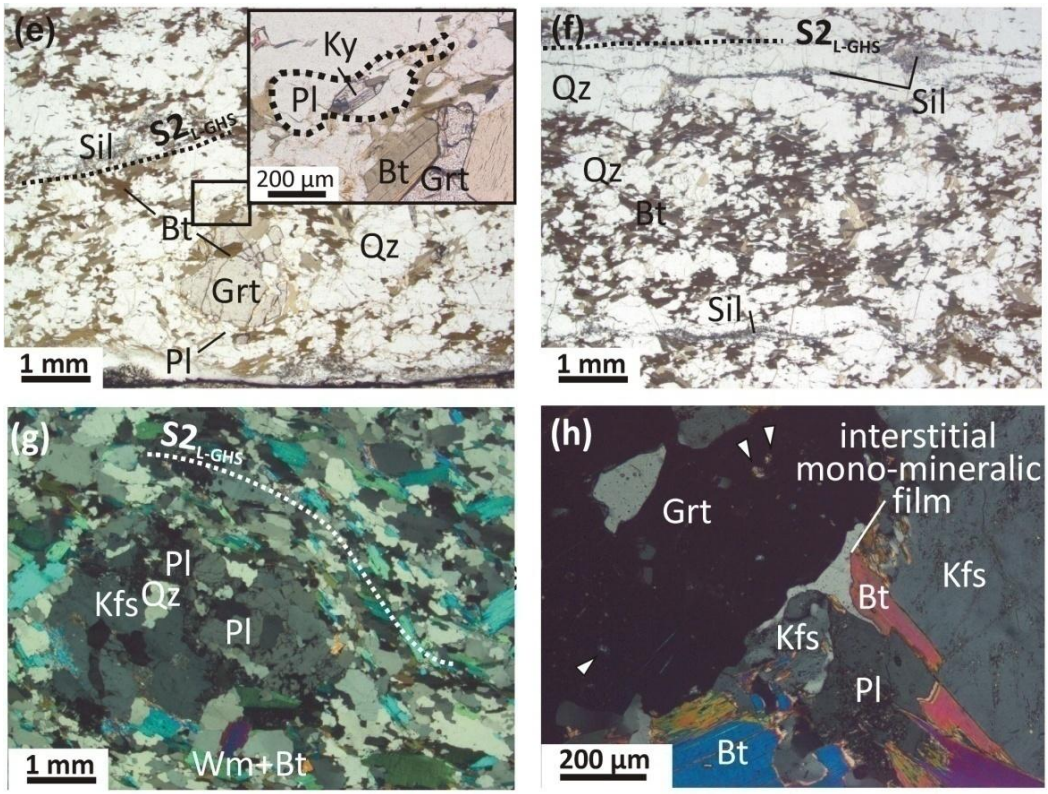

Fig. 3.20 (continued) - Representative microstructures of L-GHS lithologies (two-mica + garnet ± sillimanite (± relict kyanite) -bearing gneissic micaschist). Sample 14–52. **(e)** Detail of a garnet porphyroblast wrapped by the main foliation, defined by the alignment of biotite + sillimanite. The inset shows a relict kyanite replaced by plagioclase (PPL). **(f)** Detail of the banded structure characterized by cm-thick mesocratic layers consisting of biotite + sillimanite + quartz + plagioclase and mm-thick leucocratic quartz + sillimanite + plagioclase domains (PPL). Sample 14-49. **(g)** Leucosomic k-feldspar + plagioclase + quartz pod enveloped by the main foliation (XPL). **(h)** Detail of melt-related microstructures. White arrows indicate nanogranites in garnet rim (PPL).

❖ ***Quartzites***

Quartzites are exposed at lower structural levels; they always exhibit a foliated structure defined by the preferred alignment of biotite ± white mica concentrated in sub-mm to mm-thick domains (Fig. 3.21a). Garnet porphyroblasts are often skeletal. The quartz grain-size is extremely variable, from millimetric to pluri-millimetric; it is sometimes slightly stretched along the main $S2_{L\text{-}GHS}$ foliation. All the other mineral phases are fine-grained and mostly oriented to define $S2_{L\text{-}GHS}$. Chlorite flakes locally overgrow the $S2_{L\text{-}GHS}$ fabric. Among the accessory minerals, tourmaline is quite abundant, and stretched along the $S2_{L\text{-}GHS}$ foliation.

❖ ***Two-mica orthogneisses***

The **two-mica ± mylonitic augen gneisses** consist of biotite + white mica + quartz + k-feldspar + plagioclase. The gneissic structure is defined by pluri-mm thick biotite + white mica + quartz ± plagioclase continuous domains which envelope mm- to pluri-cm thick

lenticular/discontinuous leucocratic domains, consisting of k-feldspar + quartz + plagioclase (± biotite ± white mica). The main $S2_{L\text{-}GHS}$ foliation is parallel to the compositional layering and is defined by biotite + white mica alignment (Fig. 3.21b). K-feldspar includes plagioclase, biotite, quartz and minor white mica; myrmekites are common at its rim. Late white mica flakes locally overgrow the $S2_{L\text{-}GHS}$ foliation. Orthogneisses are usually coarse-grained, especially the leucocratic domains, with k-feldspar reaching several mm in length. However, in the more deformed orthogneisses, the grain size is extremely reduced and the structure becomes mylonitic (Fig. 3.21b).

Aplitic white mica -bearing gneisses are associated with the augen gneisses; they consist of white mica + quartz + k-feldspar + plagioclase ± garnet. The $S2_{L\text{-}GHS}$ foliation is defined by large iso-oriented white mica flakes (Fig. 3.21c).

Cm-thick **white mica-bearing granitic dykes** are locally associated with the orthogneisses (Fig. 3.21d). These rocks show a typical hypidiomorphic texture and consist of coarse-grained quartz + plagioclase + k-feldspar + white mica.

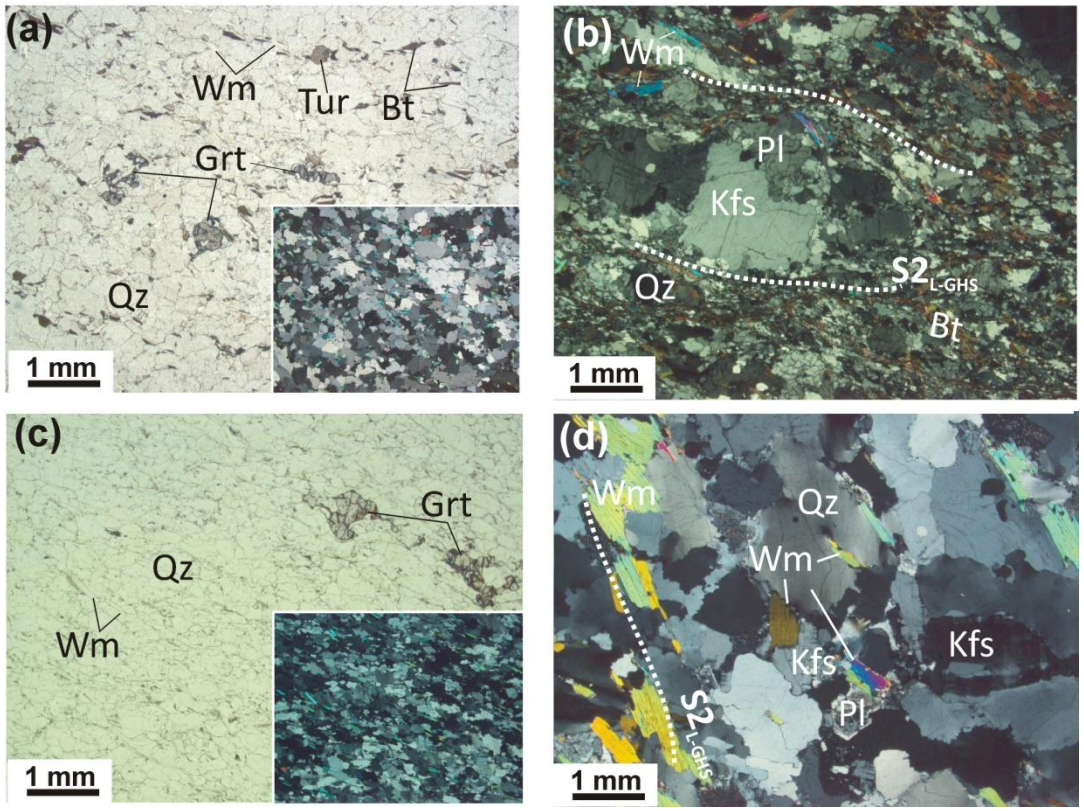

Fig. 3.21 - Representative microstructures of L-GHS lithologies (quartzites and orthogneisses). Sample 15-06b. **(a)** Quartzite in which the $S2_{L\text{-}GHS}$ foliation is defined by biotite + white mica + tourmaline alignment (PPL). Sample 14-69. **(b)** K-feldspar + plagioclase porphyroclast enveloped by the main $S2_{L\text{-}GHS}$ mylonitic foliation, defined by biotite and minor white mica; note the significant grain size reduction of quartz and biotite in the $S2_{L\text{-}GHS}$ (XPL). Sample 14-73. **(c)** Garnet-bearing aplitic gneiss, with white mica poikiloblasts defining the $S2_{L\text{-}GHS}$ planar fabric (PPL). Sample 14-76. **(d)** Granitic dyke at the contact with the host gneiss, with the main $S2_{L\text{-}GHS}$ foliation defined by white mica lepidoblasts (XPL).

3.4.2.4 Upper Greater Himalayan Sequence – Petrography

❖ ***Biotite + sillimanite + k-feldspar + garnet migmatites***

The **biotite + sillimanite + k-feldspar + garnet migmatites** are the dominant lithology at the lower structural levels of U-GHS. These are medium-grained rocks (Fig. 3.13), consisting of quartz, plagioclase, k-feldspar, biotite, sillimanite and garnet, late white mica, and accessory ilmenite and graphite. The modal proportion of the mineral phases is quite variable: some lithologies are enriched in quartz and have minor modal amounts of biotite, garnet, sillimanite and k-feldspar, while other samples have minor quartz and higher modal amounts of biotite, sillimanite, garnet and k-feldspar.

The migmatites are characterized by a banded structure (Fig. 3.22a), defined by biotite + sillimanite + quartz ± garnet mm-thick mesocratic domains alternating with quartz + plagioclase + k-feldspar ± sillimanite ± garnet pluri-mm leucocratic layers. The main foliation ($Sm_{U\text{-}GHS}$) is parallel to the compositional layering and is defined by the preferred orientation of biotite lepidoblasts and fibrolitic sillimanite. Garnet porphyroblasts are usually scarce but, where present, they contain large polymineralic inclusions of biotite + quartz ± plagioclase in addition to biotite + quartz ± zircon ± apatite ± plagioclase ± feldpsar ± white mica nanogranites, up to 100 µm in diameter (Fig. 3.22a,c), indicating that it has a peritectic nature. Garnet is locally rimmed by a plagioclase corona (Fig. 3.22b), especially in the migmatites exposed upsection. Biotite in the matrix mainly defines the $Sm_{U\text{-}GHS}$, which is locally overgrown by large flakes of white mica (Fig. 3.22f). K-feldspar and plagioclase are mainly concentrated in the leucocratic domains; large crystals of plagioclase (up to 5 mm) contain vermicular inclusions of quartz. Myrmekitic structures often occur at the interface between k-feldspar and plagioclase.

The mesocratic domains are characterized by the occurrence of biotite + quartz + sillimanite + plagioclase symplectites developed at the expense of k-feldspar and garnet (Fig. 3.22d) and of white mica + quartz + plagioclase symplectites developed at the expense of k-feldspar. These symplectitic microstructures are generally interpreted, in migmatites, as related to the late interactions between solids and melt (i.e. back-reactions) during final melt crystallization (e.g. Waters, 2001; Cenki et al., 2002; Kriegsman and Alvarez-Valero, 2010). Further evidence for the presence of former melt is the occurrence of thin films of quartz and/or feldspar, occupying interstitial positions, and interpreted as “pseudomorphs after melt” (Fig. 3.22d).

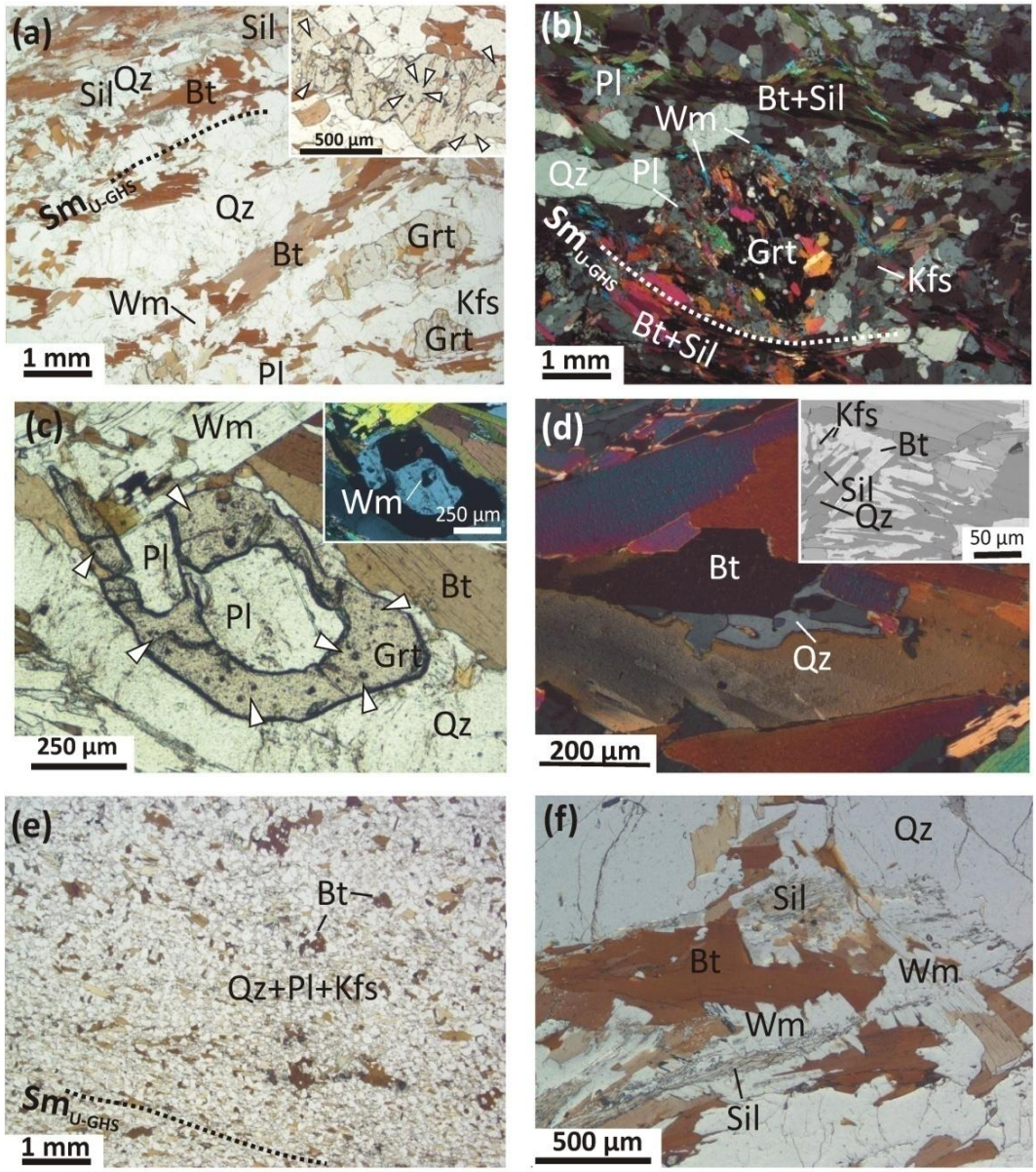

Fig. 3.22– Representative microstructure of U-GHS lithologies (biotite + sillimanite + k-feldspar + garnet migmatites and fine-grained biotite –bearing gneisses). Sample 14-08a. **(a)** The gneissic fabric is defined by biotite + sillimanite ± garnet domains alternating with quartz-feldspathic leucocratic layers. The inset shows a detail of garnet with location of nanogranites (white arrows) (PPL). Sample 14-12. **(b)** Peritectic garnet porphyroblast rimmed by a plagioclase corona. The main $Sm_{U\text{-}GHS}$ foliation is defined by biotite + sillimanite alignment (XPL). Sample 14-07. **(c)** Small peritectic garnet growing around plagioclase and lobate white mica. Garnet is full of nanogranites (white arrows) (PPL). **(d)** Detail of a pseudomorph after melt (Holness and Clemens, 1999; Holness and Sawyer, 2008), defined by a thin film of quartz with a cuspate shape (XPL). The inset shows a biotite + sillimanite + quartz symplectite replacing rounded k-feldspar (BSE). Sample 14-13b. **(e)** Fine-grained biotite -bearing gneiss, with biotite roughly defining the $Sm_{U\text{-}GHS}$ foliation (PPL). Sample 14-08a. (**f)** Late white mica flakes develop on biotite (PPL).

❖ **Fine-grained biotitic gneisses**

Fine-grained biotite-bearing gneisses are common at higher structural levels with respect to migmatites. These rocks typically show a banded structure (Fig. 3.22e), with pluri-mm thick domains consisting offine-grained biotite + quartz + plagioclase + k-feldspar alternated to pluri-mm thick coarser-grained biotite + quartz + plagioclase ± k-feldspar domains. The $Sm_{U\text{-}GHS}$ is less pervasive in the coarser-grained domains. Microstructures related to the presence of former melt are lacking in this lithology (or difficult to be identified).

❖ ***Migmatitic orthogneisses***

The **migmatitic orthogneisses** consist of quartz, plagioclase, k-feldspar, biotite, sillimanite, ± garnet, minor white mica and accessory ilmenite. They are characterized by irregular pluri-mm biotite + sillimanite + quartz + plagioclase mesocratic domains, alternating to discontinuous leucocratic domains consisting of k-feldspar + plagioclase + quartz ± biotite ± sillimanite, from few millimetres up to 1 cm in thickness. The main $Sm_{U\text{-}GHS}$ foliation is parallel to the compositional layering, and is defined by biotite ± sillimanite alignment (Fig. 3.23a,b). Leucocratic domains are coarser-grained than the mesocratic domains. K-feldspar porphyroclasts often includes plagioclase, quartz and biotite (Fig. 3.23a) and is replaced by plagioclase; myrmekites are abundant. Plagioclase is anti-perthitic and frequently includes vermicular quartz; it is highly zoned, with a sub-mm thick rim more birefringent than the core.

Garnet (from few mm up to 1 cm in diameter) is scarce and occurs in both the leucocratic and mesocratic domains as a peritectic phase, including rounded quartz, plagioclase and biotite. It is partially replaced by plagioclase + biotite + white mica ± chlorite at its rim (Fig. 3.23b). Evidences for the presence of former melt are frequent, and include: white mica + quartz ± feldspar symplectites formed at the expense of k-feldspar; biotite + sillimanite + quartz + feldspar symplectites formed at the expense of k-feldspar and garnet (Fig. 3.23b) and melt pseudomorphs (Fig. 3.23c). White mica is scarce and it is a late phase; it grows either in the biotite ± sillimanite layers, overgrowing the sillimanite, or in the leucosomes.

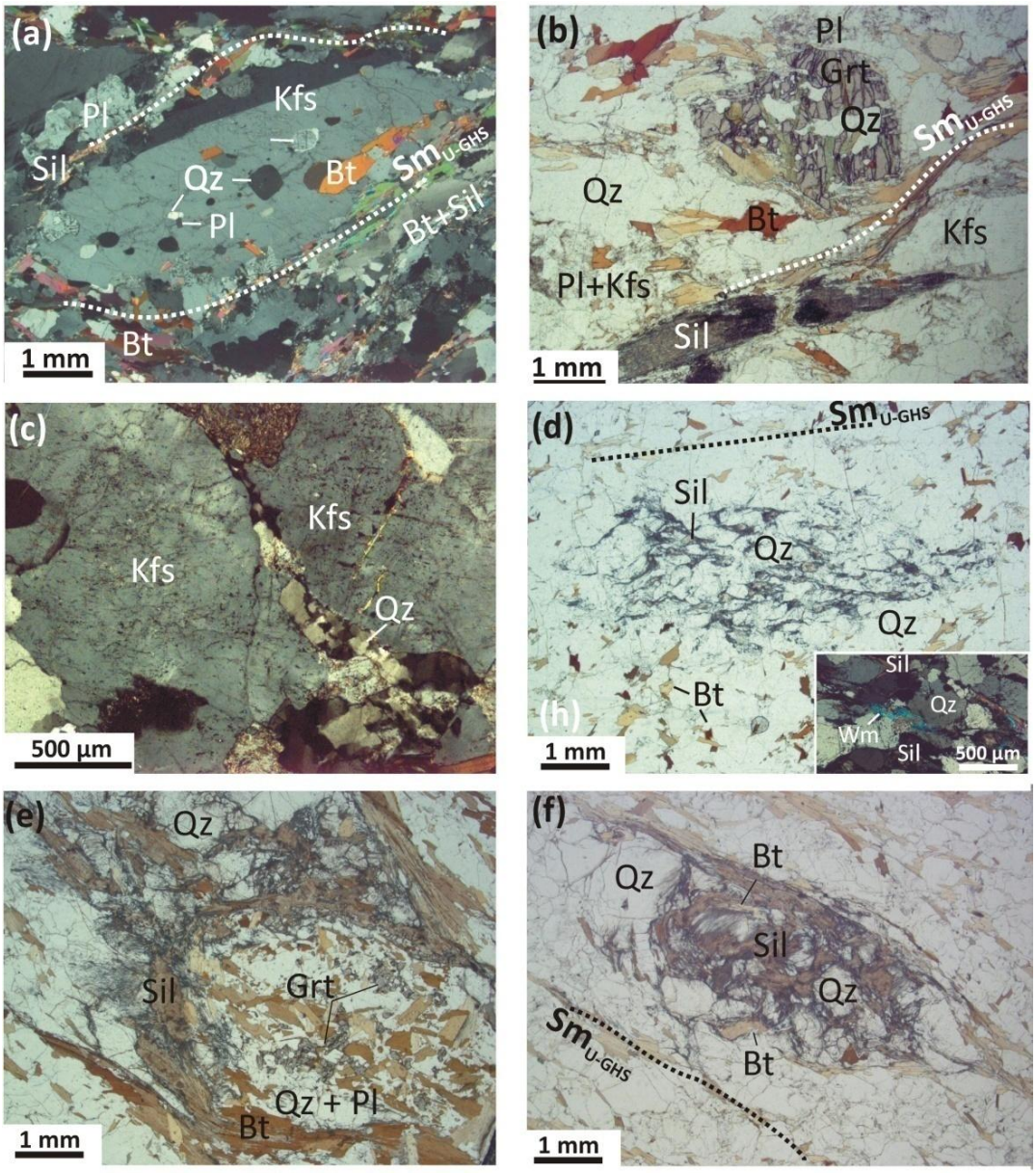

Fig. 3.23 - Representative microstructure of U-GHS lithologies (migmatitic orthogneisses and biotite -bearing gneisses with sillimanite nodules). Sample 14-13. **(a)** K-feldspar porphyroclast enveloped by the main $Sm_{U\text{-}GHS}$ foliation, defined by biotite + sillimanite (XPL). Sample 14-19. **(b)** Migmatitic orthogneiss with mesocratic biotite + sillimanite domains alternating to leucocratic quartz + plagioclase + k-feldspar + garnet domains. Garnet rim is replaced by biotite + sillimanite + quartz + feldspar symplectites (PPL). **(c)** Detail of a ''pseudomorph after melt'', represented by a monomineralic quartz film with a cuspate shape at the contact with k-feldspar crystals. Sample 14-12d. **(d)** Quartz + sillimanite pluri-mm nodule concordant with $Sm_{U\text{-}GHS}$. Quartz is predominant over sillimanite (PPL). The inset shows late white mica flakes growing on sillimanite (XPL). **(e)** Garnet is almost replaced by plagioclase and biotite (PPL). **(f)** Sillimanite + quartz + biotite ± garnet nodule, with predominant sillimanite (PPL).

❖ ***Biotite ± sillimanite + garnet –bearing gneisses with sillimanite + quartz nodules***

The **biotite ± sillimanite + garnet –bearing gneisses with sillimanite + quartz nodules** are typically associated with the anatectic orthogneisses. The gneissic fabric is defined by oriented biotite lepidoblasts concentrated in sub-mm thick domains (Fig. 3.23d), alternated to quartzo-feldsphatic layers; in the biotite-rich varieties the $Sm_{U\text{-}GHS}$ is more pervasive (Fig. 3.23e) and the mesocratic biotite + sillimanite domains are mm- to pluri-mm in thickness.

Garnet is usually rare and fine-grained, with few inclusions. Garnet is more abundant and have a larger size (up to several mm in diameters) in the biotite-rich varieties. The largest garnet porphyroblasts have a peritectic habit, hosting large polimineralc quartz + plagioclase ± biotite ± white mica inclusions and numerous nanogranites. Garnet is locally replaced by biotite + plagioclase ± sillimanite.

Nodules consist of fibrolitic sillimanite + quartz and are elongated parallel to the $Sm_{U\text{-}GHS}$; their size ranges from few mm up to 1 cm. sillimanite grows preferably at quartz joints; the relative proportion of quartz and sillimanite is variable, with quartz > sillimanite (Fig. 3.23d) varieties and viceversa (3.23f). Biotite locally occurs in the nodules, replaced by sillimanite (3.23f). Fine-grained white mica flakes often overgrow sillimanite.

3.4.2.5 Greater Himalayan Sequence – Mineral chemistry

Mineral chemistry data for samples 14-03, 14-25b, 14-24, 15-38, 14-44a, 14-61b, 14-71, 14-52 (L-GHS) and 14-08, 14-12 (U-GHS) are summarized in Tab. 3.2 and Fig. 3.24.

Garnet porphyroblasts from the L-GHS are either strongly or slightly zoned: XMn and XCa systematically decrease from core to rim, whereas both XMg and XFe increase. The outermost rim of garnet is locally characterized by a decrease in XMg, balanced by a slight increase in both XFe and XMn, likely reflecting diffusional re-homogenization at high temperatures. Garnet porphyroblasts from the U-GHS are instead homogeneous in composition. In samples from the L-GHS, biotite inclusions in garnet generally have higher XMg and/or lower Ti content compared to lepidoblasts defining the main foliation, although some exceptions are also present (e.g. in sample 14-61b, biotite inclusions in Garnet have lower XMg than the biotite in the matrix). White mica is internally homogeneous in composition in almost all the samples. In samples 14-44a and 14-61b, white mica included in garnet and the cores of white mica defining the $S2_{L\text{-}GHS}$ have higher Si content compared to the rims of white mica in the matrix, while Na content is homogeneous. Only in sample 15-38, white mica included in garnet has lower Si compared to white mica defining $S2_{L\text{-}GHS}$. Late white mica flakes overgrowining $S2_{L\text{-}GHS}$ have a similar composition with respect to those defining the $S2_{L\text{-}GHS}$. Plagioclase included in garnet core has usually higher anorthite content than that included in garnet rim and present in the matrix (except in sample 14-25b). Plagioclase in the matrix is locally zoned,

with XAn increasing towards the rim. Staurolite is slightly zoned, with XMg decreasing towards the rim; it contains a little Zn (ZnO up to 4 wt%). Kyanite contains a little amount of Fe^{+2} (up to 0.03 a.p.f.u.). Chlorite replacing garnet and/orbiotite is ripidolite (plus minor pycnochlorite) according to Hey (1954).

In samples from the U-GHS, plagioclase is strongly zoned, with anorthite content decreasing towards the albitic rim. Where present, K-feldspar is slightly zoned, with orthoclase content locally increasing towards the rim (e.g. sample 14-61b).

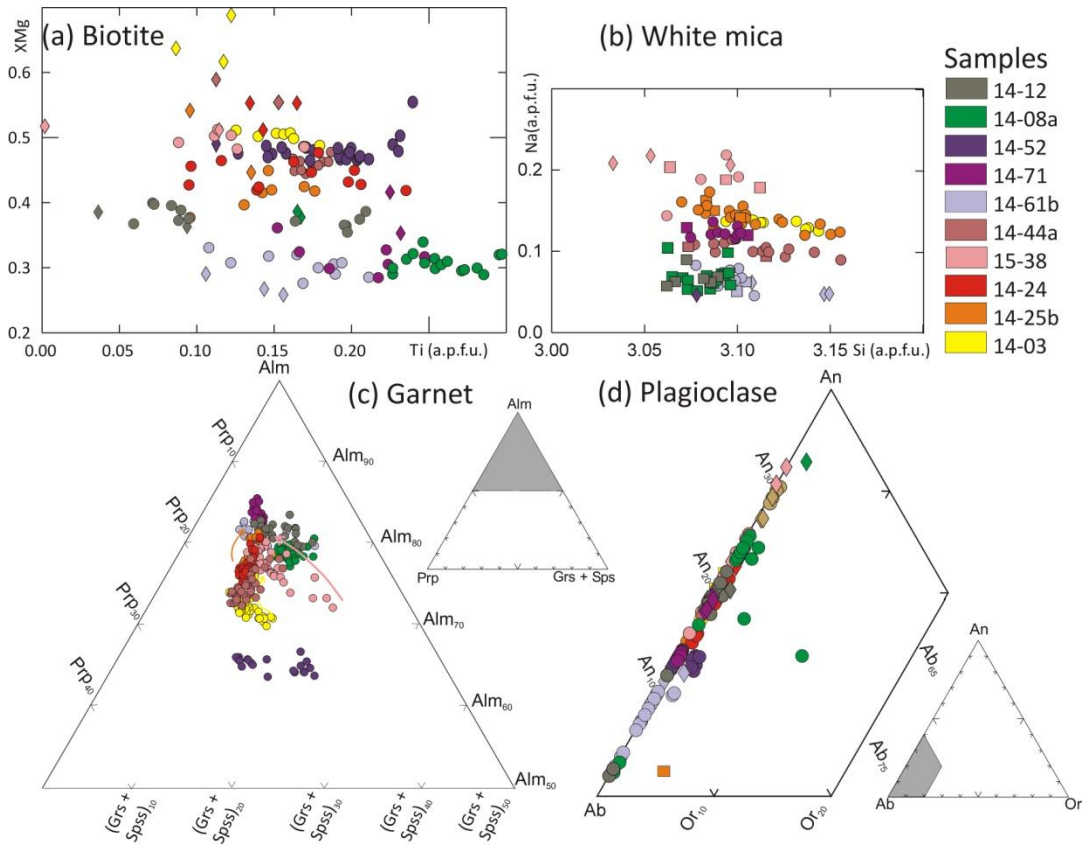

Fig. 3.24 - Compositional diagrams for GHS metapelites. (a) Biotite**, (b)** white mica, **(c)** garnet, and **(d)** plagioclase. For each sample, biotite, white mica and plagioclase have been distinguished according to their microstructural position (diamond: in equilibrium with $S1_{L\text{-}GHS}$/pre-$Sm_{U\text{-}GHS}$; circle: in equilibrium with $S2_{L\text{-}GHS}$/$Sm_{U\text{-}GHS}$; square: post-$S2_{L\text{-}GHS}$/$Sm_{U\text{-}GHS}$). Garnet zoning from core to rim is pointed out with coloured arrows.

Table 3.2 - Mineral composition for the metapelite samples

		Grt	Bt	Wm	Pl	St	Kfs	Chl
L-GHS	14-03	→ XMg=0.14-0.18 XCa=0.075-0.05 XMn=0.07-0.035 XFe=0.71-0.74	XMg^{i}=0.61-0.68 Ti^{i}=0.09-0.12 XMg=0.44-0.51 Ti=0.10-0.18	Si=3.09-3.14 Na=0.13-0.14	→ XAn=0.17-0.22			XMg*=0.24-0.51
	14-25b	→ XMg=0.13-0.15 XCa=0.04-0.03 XMn=0.05-0.035 XFe=0.78-0.81	XMg^{i}=0.44-0.54 Ti^{i}=0.10-0.14 XMg=0.38-0.46 Ti=0.09-0.17	Si=3.07-3.10 Na=0.15-0.17	XAn^{i}=0.12 XAn=0.15-0.16	→ XMg=0.16-0.12		
	14-24	→ XMg=0.14-0.16 XCa=0.05-0.04 XMn=0.05-0.04 XFe=0.75-0.79	XMg^{i}=0.50-0.55 Ti^{i}=0.13-0.16 XMg=0.41-0.47 Ti=0.10-0.24	Si=3.08-3.15 Na=0.13-0.14	→ XAn^{i}=0.23 XAn=0.15-0.22	→ XMg=0.16-0.14		
	15-38	→ XMg=0.09-0.14 XCa=0.08-0.04 XMn=0.11-0.03 XFe=0.72-0.80	XMg^{i}=0.51 Ti^{i}=0-0.11 XMg=0.48-0.50 Ti=0.09-0.17	Si*=3.03-3.09 Na*=0.15-0.22 Si=3.08-3.16 Na=0.15-0.22	XAn^{i}=0.30-0.32 XAn=0.16-0.24	→ XMg=0.20-0.16		XMg*=0.26-0.36
	14-44a	XMg=0.16-0.18 XCa=0.04-0.05 XMn=0.05-0.06 XFe=0.72-0.75	XMg^{i}=0.57-0.60 Ti^{i}=0.11-0.15 XMg=0.45-0.49 Ti=0.16-0.19	→ Si=3.16-3.07 Na=0.09-0.12 Si*=3.07-3.12 Na*=0.10	→ XAn=0.18-0.26			XMg*=0.48
	14-61b	XMg=0.12-0.13 XCa=0.02-0.03 XMn=0.03-0.04 XFe=0.80-0.84	XMg^{i}=0.26-0.29 Ti^{i}=0.11-0.16 XMg=0.28-0.34 Ti=0.11-0.21	Si^{i}=3.11-3.15 Na^{i}=0.05-0.06 Si=3.07-3.11 Na=0.05-0.09	→ XAn^{i}=0.11-0.12 XAn=0.02-0.10		→ XOr=0.87-0.93	
	14-71	XMg=0.10-0.11 XCa=0.04-0.03 XMn=0.035-0.04 XFe=0.84-0.87	XMg^{i}=0.35-0.42 Ti^{i}=0.22-0.23 XMg=0.28-0.36 Ti=0.15-0.25	Si=3.06-3.10 Na=0.12-0.14	→ XAn^{i}=0.18-0.20 XAn=0.14			
	14-52	XMg=0.20-0.21 XCa=0.025-0.03 XMn=0.11-0.12 XFe=0.64-0.67	XMg^{i}=0.50 Ti^{i}=0.12 XMg=0.47-0.55 Ti=0.14-0.23	Si^{i}=3.08 Na^{i}=0.045	→ XAn=0.12-0.15			
U-GHS	14-08a	XMg=0.10-0.12 XCa=0.035-0.045 XMn=0.07-0.08 XFe=0.78-0.81	XMg^{i}=0.37-0.38 Ti^{i}=0.17 XMg=0.29-0.33 Ti=0.23-0.30	Si*=3.07-3.10 Na*=0.05-0.10	→ XAn^{i}=0.33 XAn=0.26-0.03		XOr=0.90	XMg*=0.19
	14-12	XMg=0.10-0.11 XCa=0.02 XMn=0.04-0.07 XFe=0.80-0.84	XMg^{i}=0.35-0.40 Ti^{i}=0.04-0.09 XMg=0.35-0.40 Ti=0.06-0.20	Si*=3.07-3.09 Na*=0.06-0.09	→ XAn^{i}=0.20-0.21 XAn=0.22-0.02		XOr=0.90	

^{i} included in garnet * overgrowing S_m ^{f} fibrolitic, replacing Grt and Wm at the rims

The arrows indicate a zonation from core to rim; Ti, Si,Na are expressed as a.p.f.u.

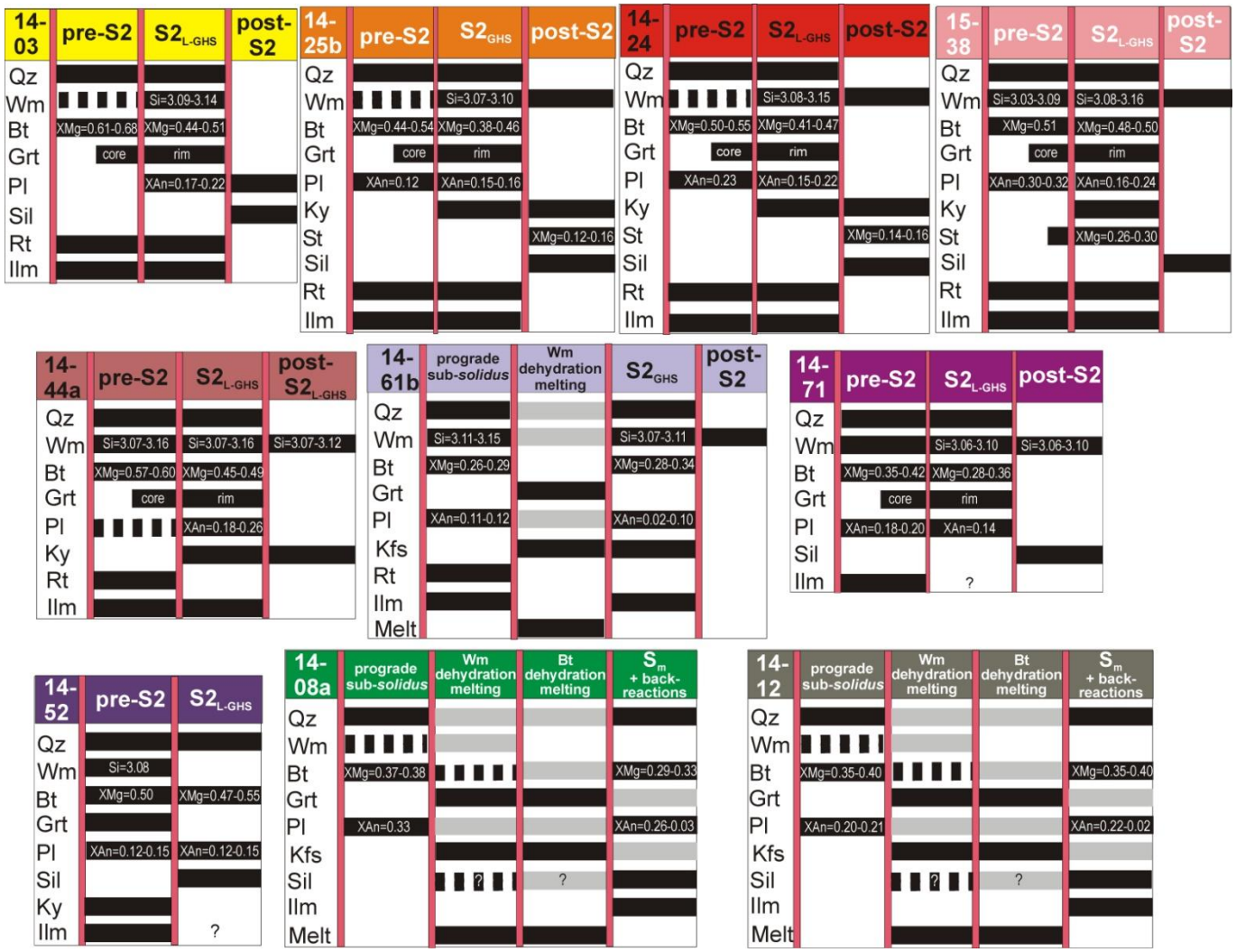

Fig. 3.25 – Crystallization–deformation relations of the studied GHS samples, with mineral compositions. For those samples that clearly show migmatitic microstructures (i.e. samples 14–61b, 14–08a and 14-12), the melting *vs.* crystallization relations are also shown (i.e. prograde sub-solidus crystallization, white mica ± biotite dehydration melting, melt crystallization, retrograde sub-solidus crystallization): in the melt–bearing domain (muscovite ± biotite dehydration melting) grey *vs.* black bars discriminate between reactants and products of the melting reactions, respectively.

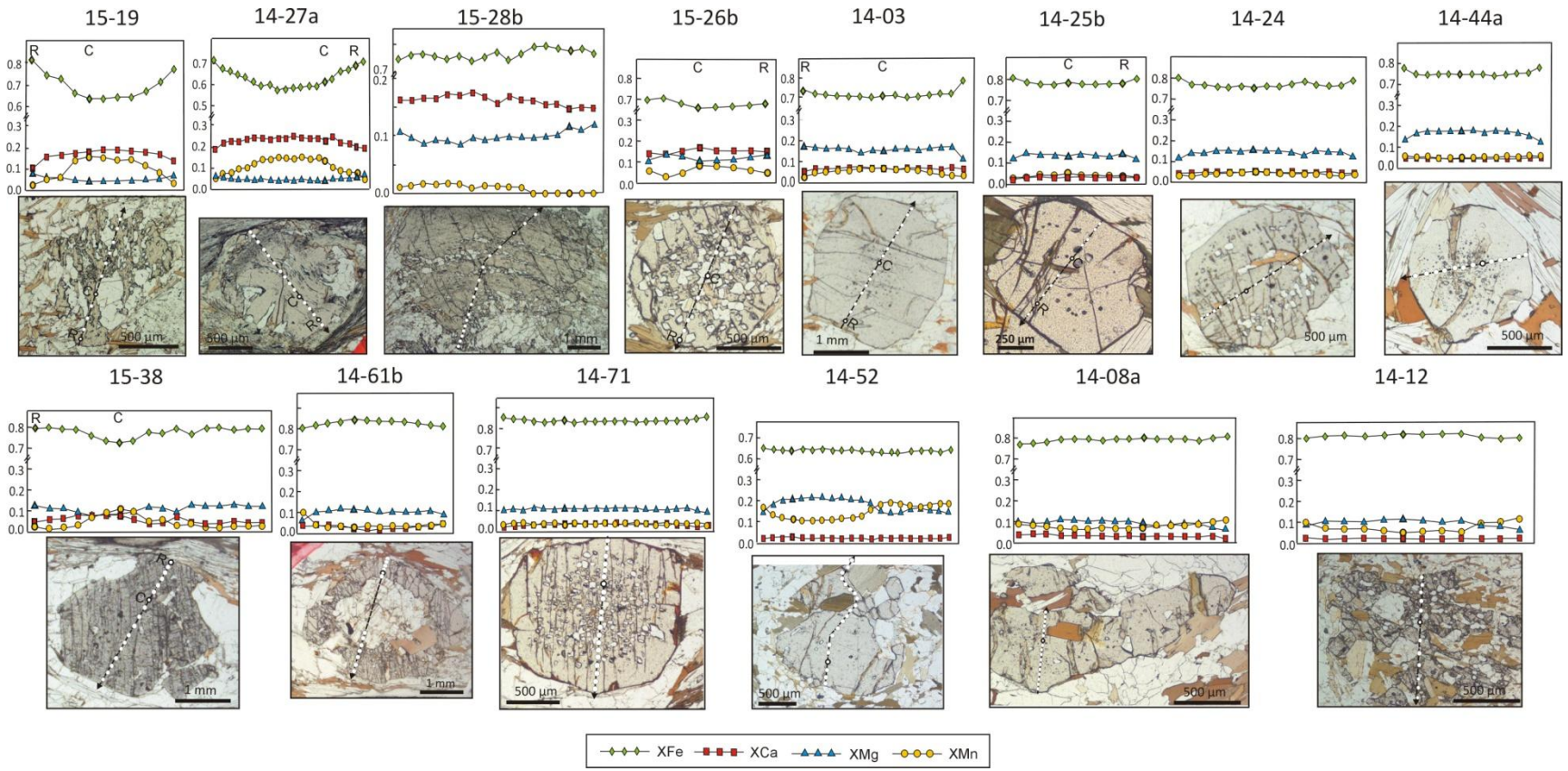

Fig. 3.26 - Zoning profiles of garnet from the LHS and GHS. Relative distance between point analyses is not to scale. The analysed garnet crystals are reported. The dotted circles indicate the analysis used for optimal thermobarometry. XCa, XMg, XFe and XMn defined as: XCa=Ca/(Mg+Fe+Ca+Mn); XMg=Mg/(Mg+Fe+Ca+Mn); XFe=Fe/(Mg+Fe+Ca+Mn); XMn=Mn/(Mg+Fe+Ca+Mn).

3.4.3 Thermodynamic modelling

10 metapelite samples from both the LHS and GHS have been modelled using the P-T pseudosection approach; for some of them, more than one pseudosection has been calculated, considering the effects of bulk-rock fractionation due to the presence of strongly zoned garnet porphyroblasts. A total of 14 P–T pseudosections have been therefore calculated. Details on the calculation (i.e. model system, solution models) are given in the Methods section (§3.3.5).

For all the samples, prograde and peak P–T conditions have been constrained based on the stability fields of the observed prograde and peak mineral assemblages, combined with garnet compositional isopleths. Biotite compositional isopleths have been additionally used for the migmatitic sample 14-08a, because garnet composition has been likely modified by diffusion. The retrograde portion of the P–T trajectories is generally less tightly constrained than the prograde one; P–T constraints are given by the inferred stability fields of the retrograde assemblages. For the migmatitic sample 14-08a further constraints are given by the intersection between the minerals iso- modes and the solidus. Bulk compositions used for pseudosection calculations are reported in Tab. 3.3.

Table 3.3. Bulk compositions of the modelled metapelites (mol%)

	14-27a	14-27a*	15-26b	15-26b*	14-03	14-03*	14-25b	14-25b*	14-24	14-44a	14-61b	14-71	14-52	14-08a
SiO_2	67.45	67.47	72.26	73.02	71.27	71.86	63.81	65.24	70.7	68.05	69.36	75.57	71.01	73.94
TiO_2	0.62	0.62	0.68	0.69	0.69	0.7	0.61	0.62	0.61	0.53	0.52	0.6	0.95	0.5
Al_2O_3	16.42	16.39	9.17	9.04	13.82	13.81	17.77	18.02	14.01	16.24	10.81	11.63	8.91	10.71
FeO	6.6	6.52	5.82	5.25	6.1	5.6	7.68	5.89	6.12	4.75	6.23	5.49	7.25	3.97
MgO	1.96	1.96	4.71	4.72	2.85	2.76	3.05	2.91	2.59	3.18	2.16	1.74	6.63	1.47
MnO	0.15	0.13	0.17	0.07	0.2	0.16	0.24	0.07	0.21	0.12	0.1	0.12	0.07	0.09
CaO	0.88	0.86	2.49	2.36	0.45	0.4	0.56	0.49	3.28	0.84	0.64	0.32	0.61	1.02
Na_2O	0.8	0.8	2.99	3.07	0.72	0.73	1.77	1.9	0.72	1.76	3.41	1	1.83	2.02
K_2O	5.24	5.25	1.74	1.79	3.91	3.99	3.54	4.86	3.65	4.63	3.1	3.53	2.75	2.55
H_2O											3.68			3.73

The asterisk (*) refers to the fractionated bulk compositions (i.e. whole-rock composition minus garnet core composition) used to model the growth of garnet rim.

3.4.3.1 Lesser Himalayan Sequence

Prograde and peak P–T conditions

- **Sample 14-27a**. The pseudosection calculated for the unfractionated bulk composition (Fig. 3.27a) gives information about the mineral assemblage stable during the prograde growth of garnet core, represented by the relatively large biotite + quartz + plagioclase + muscovite + garnet + ilmenite + H_2O field, which occurs at >500 °C and <12 kbar; the fractionated pseudosection (Fig. 3.27c) predicts the growth of garnet rim in the same quini-variant field. The earlier $S1_{LHS}$ mineral assemblage is modelled by the tri-variant biotite + chlorite + quartz + plagioclase + muscovite + garnet + zoisite + ilmenite + H_2O field, at <510 °C, 4.0 < P < 7.5 kbar. Garnet core compositional isopleths (XMg = 0.03–0.04; XCa = 0.23–0.25; XMn = 0.12–0.15) give 510–540 °C and 5.3–5.7 kbar (Fig. 3.27b), whereas garnet rim composition (XMg

=0.05–0.06; XCa = 0.19–0.22; XMn = 0.05–0.07) constrains peak P–T conditions at 570–620 °C, 6.7– 8.2 kbar (Fig. 3.27c; Tab. 3.5a).

❖

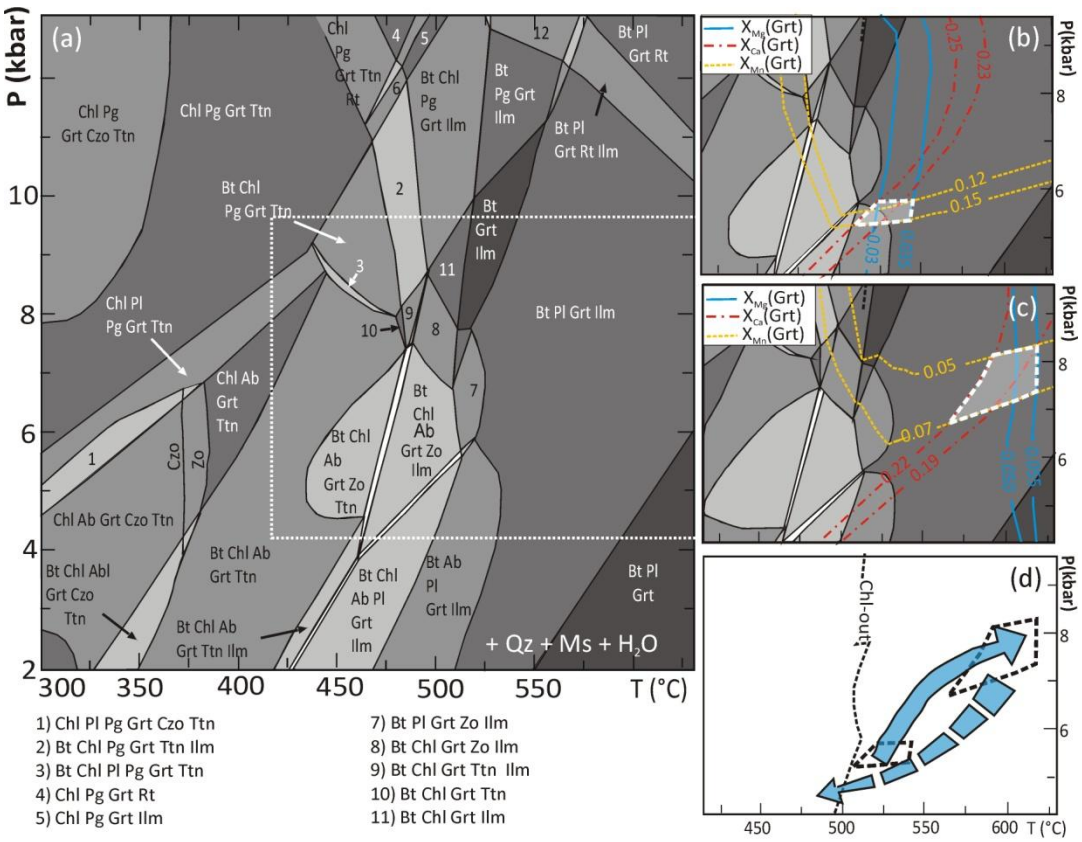

Fig. 3.27 - P–T pseudosection for sample 14–27a (LHS) calculated in the MnNKCFMASTH system at a(H_2O)=1. **(a)** P–T pseudosection calculated using the whole–rock bulk composition, used to model the P–T conditions for the growth of garnet core. **(b)** Detail of (a) with compositional isopleths of garnet core. **(c)** P–T pseudosection calculated using the fractionated bulk composition, used to model the P–T conditions for the growth of garnet rim, contoured for garnet rim composition. In (a–c), white, light–, medium–, dark– and very dark– grey fields are di– tri, quadri–, quini– and esa–variant fields, respectively. Ms and Pg refer to K–rich and Na–rich white mica, respectively. White dashed rectangle in (a) refers to the P–T interval shown in (b), (c) and (d). White dashed polygons in (b) and (c) constrain the P–T conditions of garnet core and rim growth, respectively. **(d)** P–T path inferred for sample 14–27a on the basis of mineral assemblages and compositions (light blue arrow). Dashed–line arrow represents the inferred retrograde P–T path.

❖ **Sample 15–26b –** Pseudosection calculated for the unfractionated bulk composition (Fig. 3.28a) gives information about the mineral assemblage stable during the prograde growthof garnet core, which includes biotite, white mica, plagioclase, rutile ± ilmenite. This assemblage is stable in the biotite ± chlorite + plagioclase + muscovite ± paragonite + garnet + quartz + rutile + H_2O fields, at T>450°C. Garnet core compositional isopleths (XMg=0.09-0.11, XCa=0.17-0.20, XMn=0.09-0.07) further constrain the P-T conditions of the prograde garnet growth at T=550-575 °C

and P=7.5-8.5 kbar, in the biotite + chlorite + plagioclase + muscovite + garnet + quartz + rutile ± paragonite + H_2O field. Chlorite and paragonite have never been observed included in garnet, perhaps reflecting complete consuming during prograde metamorphism. The fractionated pseudosection (Fig. 3.28c) predicts the growth of garnet rim in the quini-variant biotite + plagioclase + muscovite + garnet + rutile field, since garnet rim is in equilibrium with biotite, muscovite, plagioclase and rutile (± ilmenite). Compositional isopleths (XMg=0.13–0.14; XCa=0.16–0.14; XMn=0.03–0.04) constrain the growth of garnet rim at peak metamorphic P-T conditions of T=620–650 °C and P=8.7–10.4 kbar (Fig. 3.28c and Tab. 3.5a). Both garnet core and garnet rim are predicted to grow at sub-solidus conditions (Fig. 3.28d), in agreement with microstructural observations.

❖

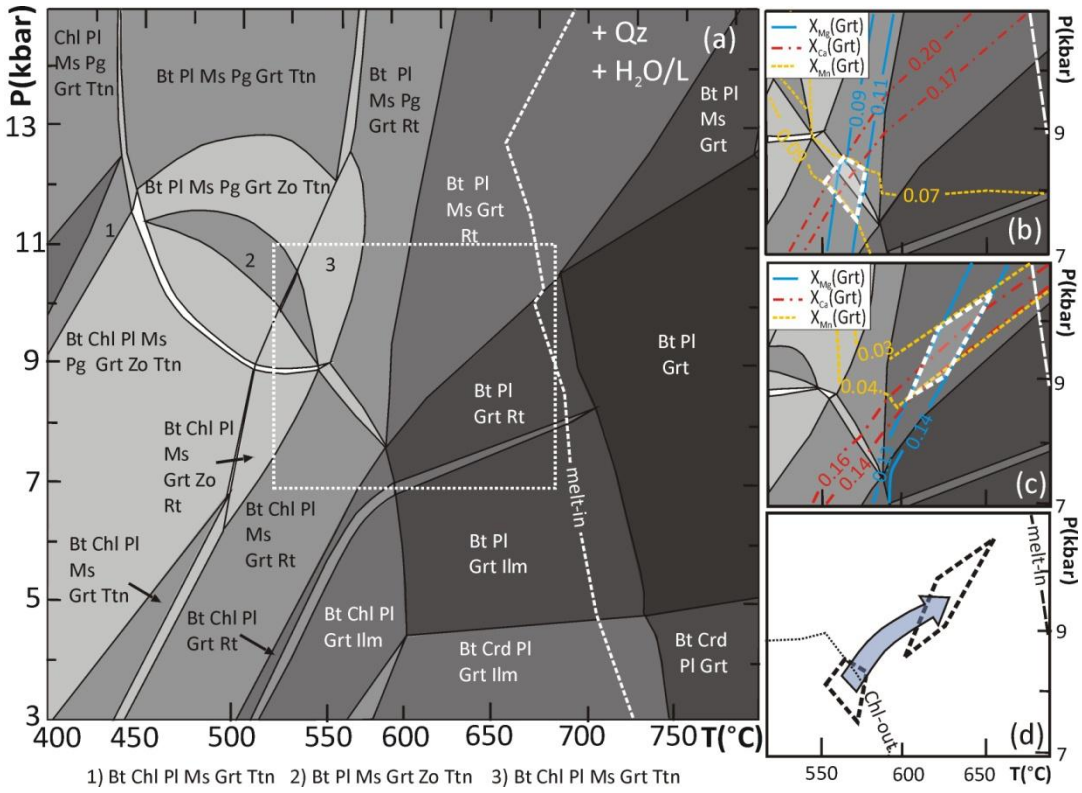

Fig. 3.28- P–T pseudosection for sample 15-26b (LHS, Gatlang section) calculated in the MnNCKFMASTH system at a(H_2O)=1. **(a)** P–T pseudosection calculated using the whole-rock bulk composition, used to model the P–T conditions for the growth of Garnet core. Variance of the fields as in Fig. 3.27. **(b)** Detail of (a) with compositional isopleths of garnet core. **(c)** P–T pseudosection calculated using the fractionated bulk composition, used to model the P-T conditions for the growth of garnet rim, contoured for garnet rim composition. Ms and Pg refer to K–rich and Na–rich white mica, respectively. White dotted rectangle in (a) refers to the P–T interval shown in (b), (c) and (d). White dashed polygon in (b) and (c) constrain the P–T conditions of Garnet core and rim growth, respectively. **(d)** P–T path inferred for sample 15-26b on the basis of mineral assemblages and compositions (gold arrow). Dashed lines (melt-in) in (a) to (d) are the H_2O-saturated solidus.

Retrograde evolution

- **Sample 14-27a**. The retrograde portion of the P–T path is less tightly constrained than the prograde one. Local occurrence of biotite, white mica and chlorite statically overgrowing $S2_{LHS}$ indicates a retrograde path dominated by cooling and decompression toward the chlorite stability field (Fig. 3.27d). These observations are in agreement with the calculated isomodes for biotite and chlorite (not reported in the figures), showing that both these minerals can grow during cooling and decompression.
- **Sample 15-26b.** Retrograde evolution of the P–T path is not constrained.

3.4.3.2 Lower Greater Himalayan Sequence

Prograde and peak P–T conditions

- **Sample 14–03** – Pseudosection calculated for the unfractionated bulk-composition (Fig. 3.29a) gives information about the mineral assemblage stable during the growth of garnet core, which includes biotite, quartz, rutile, ilmenite and white mica. This assemblage is represented by the quini-variant biotite + quartz + plagioclase + muscovite + garnet + rutile + H_2O (± ilmenite) fields at T>600 °C and P>7 kbar; plagioclase has not been observed as inclusions in garnet, perhaps because it was totally consumed during prograde metamorphic reactions. Further constraints on the P–T conditions at which garnet core grew are given by its compositional isopleths (XMg=0.14–0.15; XCa=0.070–0.075; XMn=0.06–0.07), which give T=650–670 °C and P=7.4–8.8 kbar (Fig. 3.29b). The topology of the fractionated pseudosection (Fig. 3.29c) is almost identical to the previous one, indicating that fractionation effects were minimal. Garnet rim is in equilibrium with biotite, white mica, plagioclase, quartz and rutile: this assemblage is modelled by the quini-variant fields biotite + quartz + plagioclase + muscovite + garnet + rutile + H_2O/L (± kyanite), at P>7 kbar and T>600 °C. Compositional isopleths (XMg=0.17–0.18; XCa=0.05–0.06; XMn=0.035–0.045) constrain the growth of garnet rim at T=710–730 °C and P=9.6–11.0 kbar (Fig. 3.29c and Tab. 3.5a). Garnet core grew at sub-solidus conditions, whereas the first melt appears in the T range 670–700 °C, i.e. during the growth of garnet rim (Fig. 3.29d), coherently with its peritectic nature indicated by the presence of nanogranites (Fig. 3.18b). The amount of melt produced at peak P–T conditions is very low, i.e. < 1 vol%. Even if peak P-T conditions are partly predicted in the kyanite-stability field, its modal amount is negligibile.

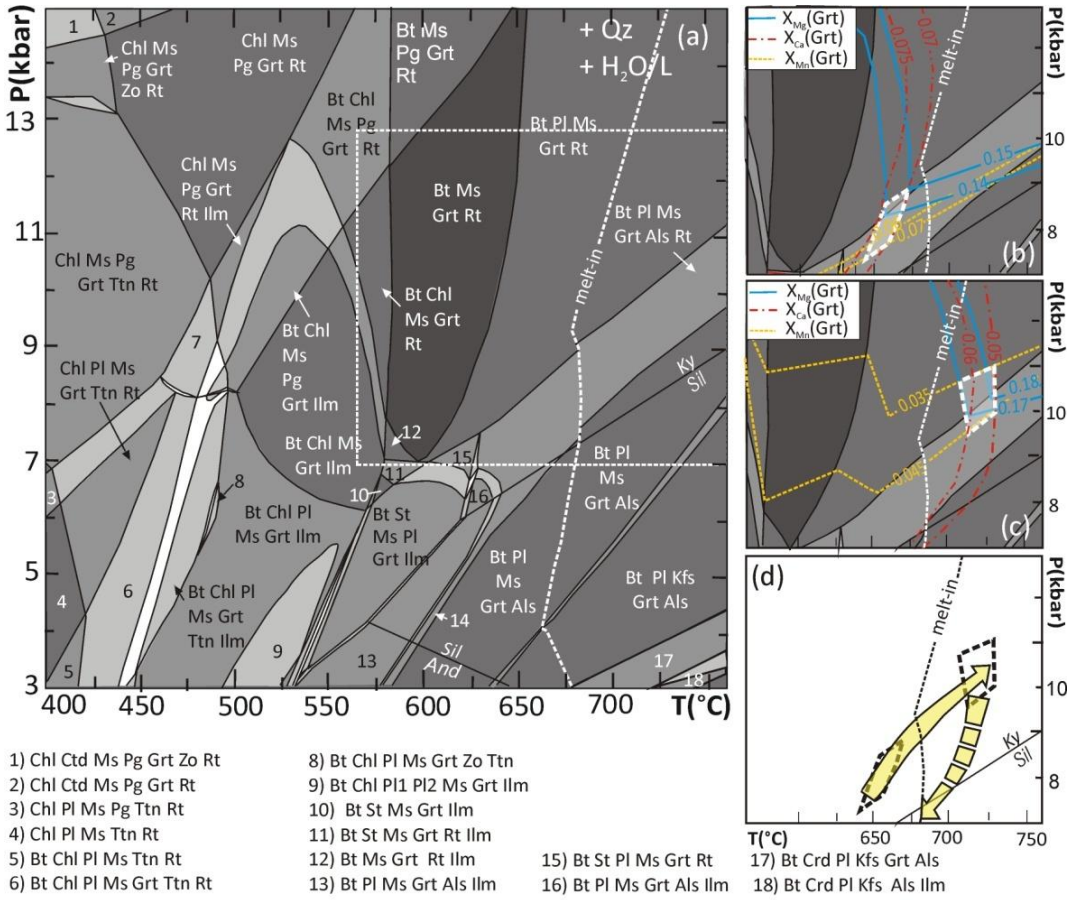

Fig. 3.29 - P–T pseudosections for sample 14-03 (GHS, Langtang section) calculated in the MnNCKFMASTH system at a(H_2O)=1. **(a)** P–T pseudosection calculated using the whole-rock bulk composition, used to model the P–T conditions for the growth of Garnet core. Variance of the fields as in Fig. 3.27. **(b)** Detail of (a) with compositional isopleths of garnet core. **(c)** P–T pseudosection calculated using the fractionated bulk composition, used to model the P-T conditions for the growth of garnet rim, contoured for garnet rim composition. Ms and Pg refer to K–rich and Na–rich white mica, respectively. White dotted rectangle in (a) refers to the P–T interval shown in (b), (c) and (d). White dashed polygon in (b) and (c) constrain the P–T conditions of Garnet core and rim growth, respectively. **(d)** P–T path inferred for sample 14–03 on the basis of mineral assemblages and compositions (red arrow). Dashed lines (melt-in) in (a) to (c) are the H_2O-saturated solidus. Note that garnet core grew in the sub-solidus domain, whereas garnet rim grew at P–T conditions that lie immediately above the solidus.

❖ **Samples 14–25b and 14–24** – Although the pseudosections calculated for these samples are very similar (Fig. 3.30a, Fig. 3.31a), the preserved growth zoning of garnet in sample 14–25b allows to constrain its prograde evolution, whereas only peak P–T conditions can be inferred from sample 14–24. In sample 14–25b the prograde mineral assemblage stable during the growth of garnet core is represented by white mica, biotite, quartz, plagioclase, rutile and ilmenite. This assemblage is modelled by the quadri- and quini-variant biotite + quartz + plagioclase + muscovite + garnet + rutile + H_2O ± ilmenite fields at T>600 °C and P>7.8 kbar. Compositional isopleths for garnet core (XMg=0.13; XCa=0.04; XMn=0.05) further constrain its

growth at 630<T<640°C and 8.0<P<8.2 kbar, very close to the kyanite-in curve (Fig. 3.30b). Garnet rim is in equilibrium with biotite, white mica, kyanite, plagioclase, quartz and rutile; this assemblage is modelled by the relatively narrow quadri-variant biotite + quartz + plagioclase + muscovite + garnet + kyanite + rutile + H_2O/L fields, at T>640°C and P>7.8 kbar. Compositional isopleths of garnet rim (XMg=0.15; XCa=0.03; XMn=0.035) intersect perfectly in this field and constrain the growth of the peak assemblage at 715–725 °C, 9.7–10.0 kbar (Fig. 3.30b and Tab. 3.5a). As concerning sample 14–24, the equilibrium assemblage, consisting of quartz, garnet, biotite, white mica, kyanite, plagioclase and rutile, is modelled by a quadri-variant field at T>640 °C and P>7 kbar. Compositional isopleths of garnet (XMg=0.14–0.16; XCa=0.04–0.05; XMn=0.04–0.05) constrain peak P–T conditions at 725<T<760 °C and 9.7<P<10.8 kbar (Fig. 3.31b and Tab. 3.5a). For both the samples, the peak P-T conditions lie just above the H_2O-saturated solidus (Fig. 3.30c, Fig. 3.31c), thus explaining the peritectic nature of garnet rim evidenced by the occurrence of nanogranites (Fig. 3.30d,e). The amount of melt produced at peak P-T conditions is very low (< 2 vol% and < 1 vol%, respectively).

- **Sample 14–44a** – The equilibrium assemblage, consisting of garnet, biotite, white mica, kyanite, quartz, plagioclase ± rutile ± ilmenite, is modelled by the quini-variant biotite + quartz + plagioclase + muscovite + garnet + kyanite + H_2O/L fields at T>640 °C, P>6.4 kbar (Fig. 3.32a). Further constraints are given by garnet compositional isopleths (XMg=0.16–0.18; XCa=0.04–0.05; XMn=0.05–0.06) that indicate peak P–T conditions of 700–750 °C, 8.6–10.0 kbar (Fig. 3.32b and Tab. 3.5a). H_2O-saturated solidus is located at 670–700 °C (Fig. 3.32c), implying that the peak assemblage was stable in the presence of very low amounts of melt (< 2 vol%); this is in agreement with the observed peritectic nature of garnet (nanogranites at core-rim transition).

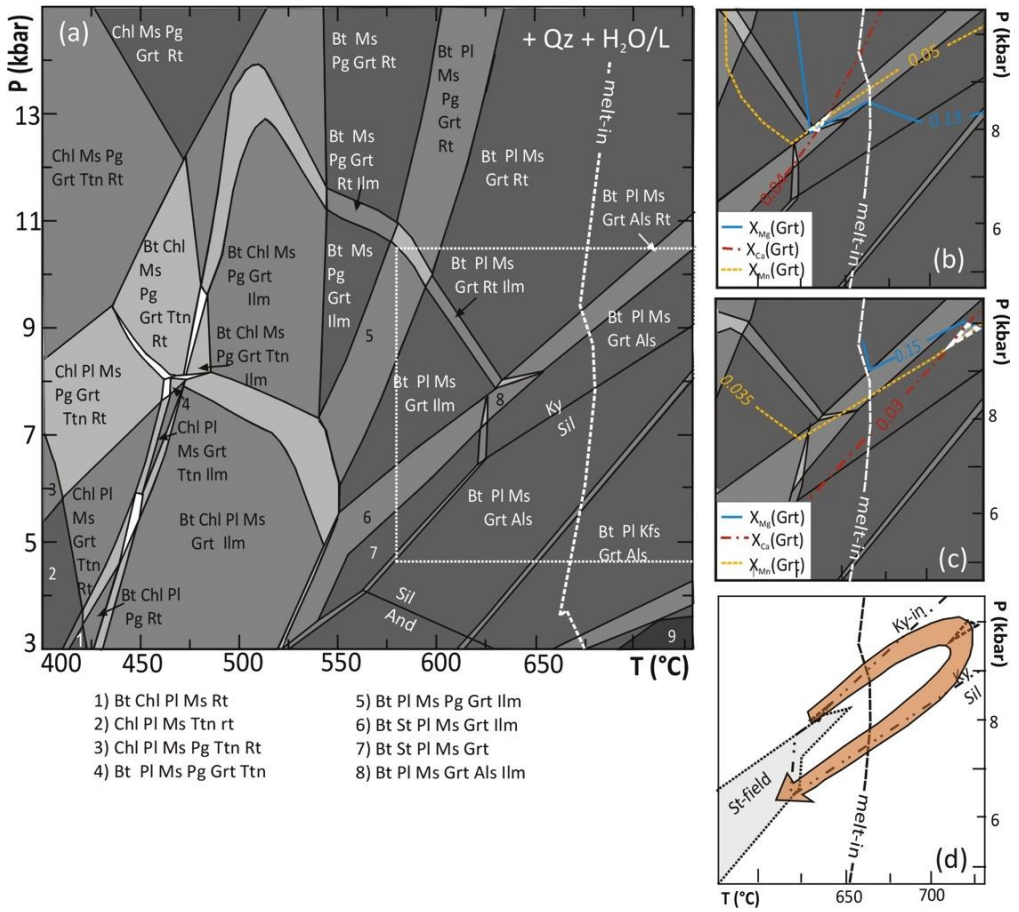

Fig. 3.30- (a) P–T pseudosection for sample 14–25b (GHS, Langtang section) calculated in the MnNKCFMASTH system at a(H_2O)=1 using the unfractionated bulk composition. Variance of the fields as in Fig. 3.27. Ms and Pg refer to K-rich and Na-rich white mica, respectively. White dotted rectangle refers to the P-T interval shown in (b) and (c). **(b,c)** Detail of (a) contoured for garnet core (b) and rim (c) compositions. The small white dashed polygons constrain the P–T conditions for the growth of garnet core (b) and rim (c). **(d)** P–T path inferred for sample 14–25b (orange arrow); the staurolite stability field (in grey) constrains the retrograde evolution of sample 14–25b. Dashed lines (melt–in) in (a) to (d) represent the H_2O-saturated solidus.

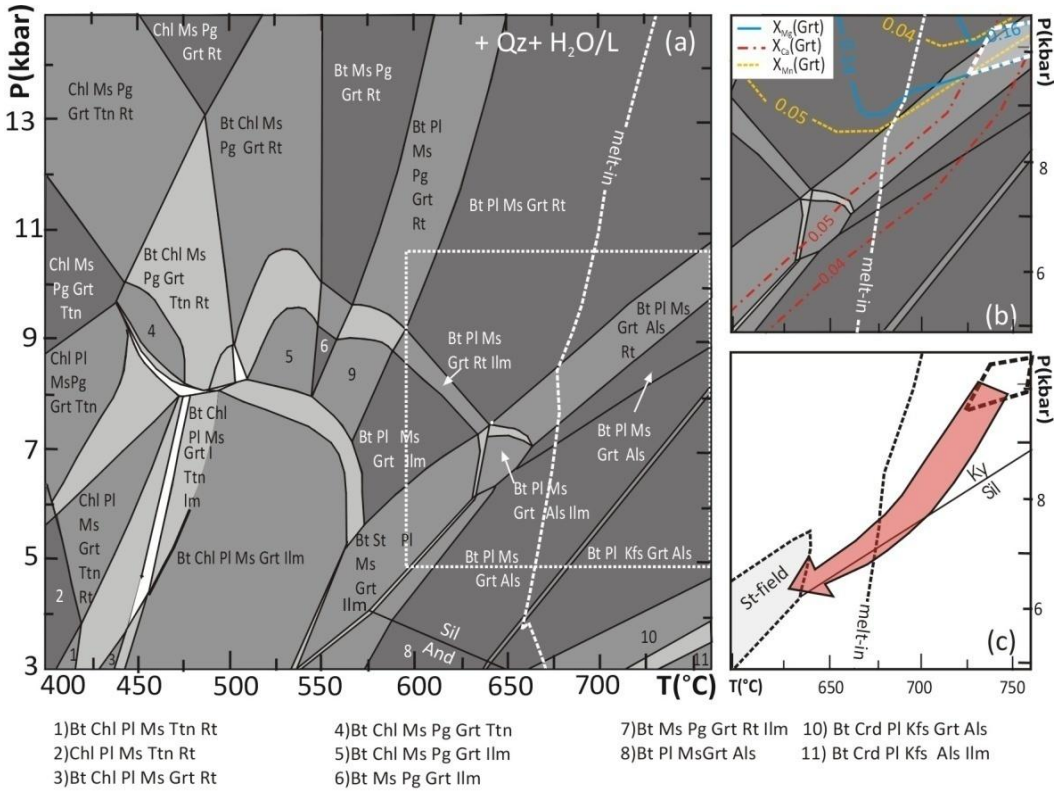

Fig. 3.31 - (a) P–T pseudosection for sample 14–24 (GHS, Langtang section) calculated in the MnNKCFMASTH system at a(H_2O)=1. Variance of the fields as in Fig. 3.27. Ms and Pg refer to K–rich and Na–rich white mica, respectively. White dotted rectangle refers to the P–T interval shown in (b) and (c). **(b)** Detail of (a) contoured for garnet (XMn, XMg and XCa) composition. White dashed polygon constrains the P–T conditions of the growth of peak mineral assemblage. **(c)** P–T path inferred for sample 14–24 (grey arrow) and stability field of staurolite (in grey). The two black dashed polygons constrain the P–T conditions of the growth of peak- and retrograde- mineral assemblages, respectively. Dashed lines (melt–in) in (a) to (c) represent the H_2O-saturated solidus.

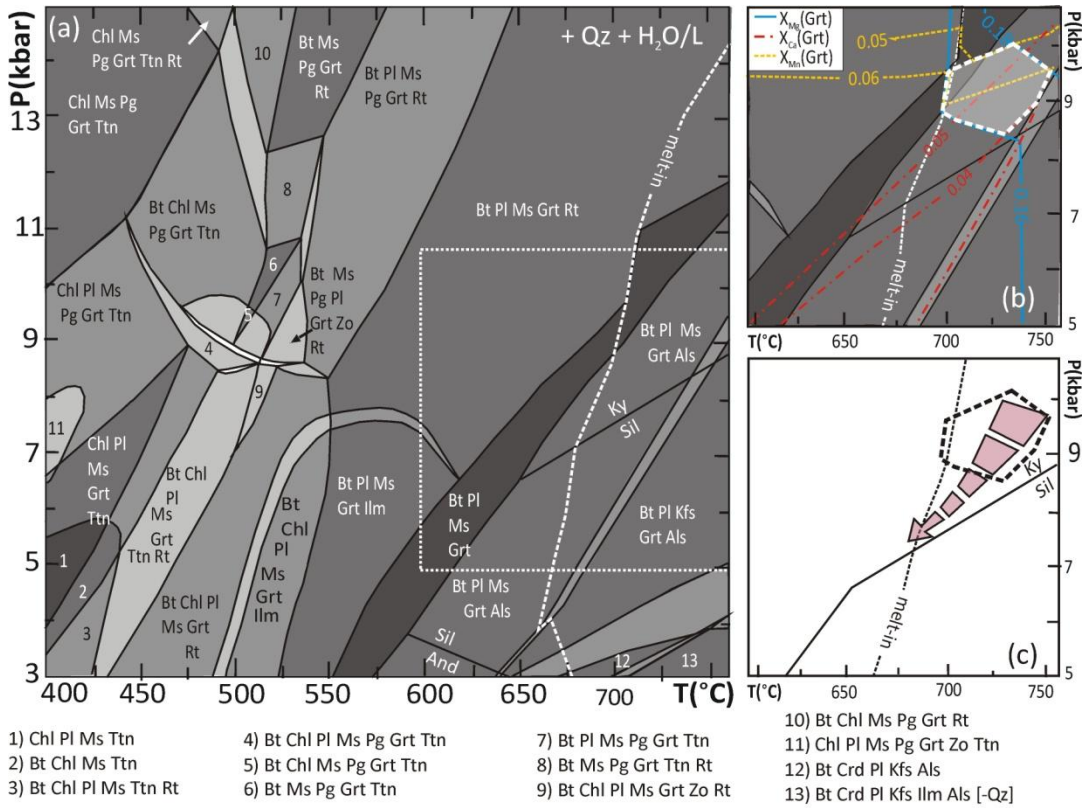

Fig. 3.32 - (a) P–T pseudosection for sample 14–44a (GHS, Gosainkund–Helambu section) calculated in the MnNKCFMASTH system at a(H_2O)=1. Variance of the fields as in Fig. 3.27. Ms and Pg refer to K–rich and Na–rich white mica, respectively. White dashed rectangle refers to the P–T interval shown in (b) and (c). **(b)** Detail of (a) contoured for garnet composition. White dashed polygon constrains the P–T conditions for the growth of the peak mineral assemblage. **(c)** P–T trajectory inferred for sample 14–44a on the basis of mineral assemblages and compositions (yellow arrow). Dotted line (melt–in) in (a) to (c) represents the H_2O-saturated solidus.

❖ **Sample 14–61b –** The modelled pseudosection shows that the first melt production occurs at 720–750 °C, > 8 kbar (Fig. 3.33a). A low amount of melt (< 2.4 vol%) is predicted in the biotite + quartz + plagioclase + k-feldspar + muscovite + garnet + L field, located in between the solidus and the white mica-out reaction curve, whereas up to 8.0 vol% of melt is produced through the complete white mica dehydration melting. The equilibrium assemblage, consisting of garnet, biotite, white mica, k-feldspar and plagioclase ± melt, is modelled by the large quini-variant biotite + plagioclase + quartz + garnet + k-feldspar + muscovite, melt-absent, field and by the narrow quadri-variant biotite + quartz + plagioclase + garnet + k-feldspar + muscovite + L, melt-bearing, field (Fig. 3.33a). Further constraints are given by garnet compositional isopleths (XMg=0.12–0.13; XCa=0.02–0.03; XMn=0.03–0.04), which indicate equilibration temperatures of 730–750 °C and pressures of 9.4–11.3 kbar (Fig. 3.33b and Tab. 3.5a). The stability field of peak mineral assemblage is thus located

across the solidus, but still inside the white mica stability field, in agreement with microstructural observations that indicate that partial melting was incipient (Fig. 3.33b) and that white mica is still stable (Fig. 3.33a).

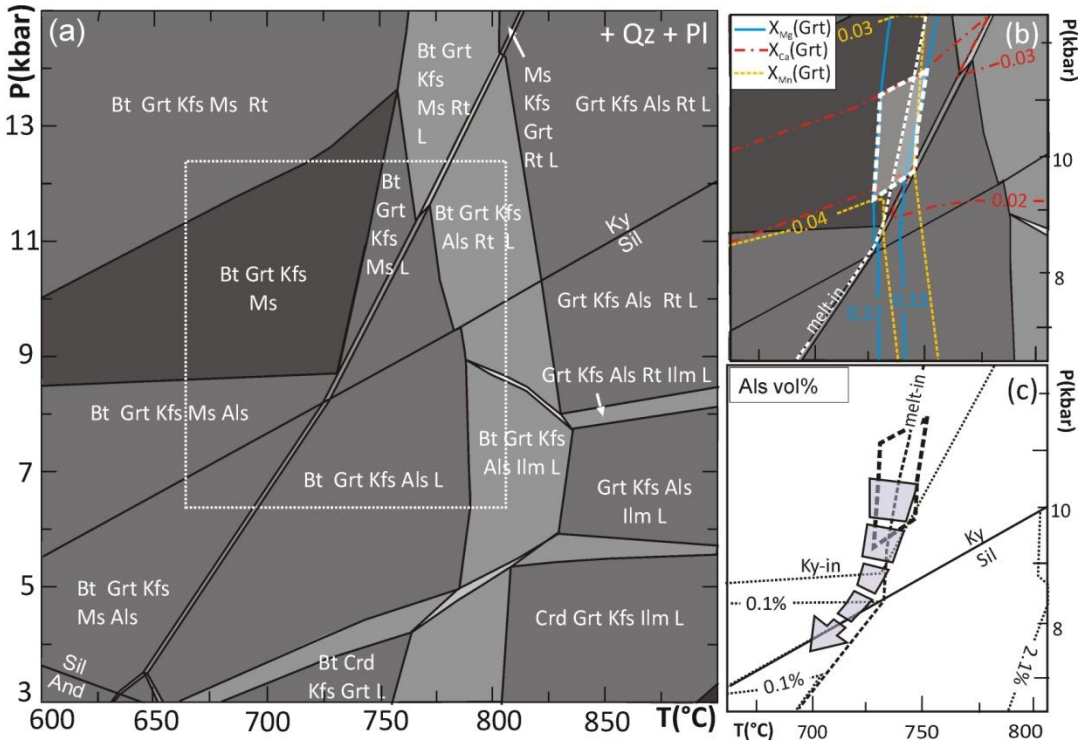

Fig. 3.33 - (a) P–T pseudosection for sample 14–61b (GHS, Gosainkund–Helambu section) calculated in the MnNKCFMASTH system. Variance of the fields as in Fig. 3.27. White dashed rectangle refers to the P–T interval shown in (b) and (c). **(b)** Detail of (a) contoured for garnet composition. White dashed polygon constrains the P–T conditions for the growth of peritectic garnet. **(c)** P–T path inferred for sample 14–61b (pink arrow). Dotted line (melt–in) in (b) and (c) represent the solidus of the system.

❖ **Sample 14–71** – The equilibrium assemblage, consisting of garnet, biotite, white mica, plagioclase, quartz, ilmenite ± rutile, is modelled by the biotite + quartz + plagioclase + muscovite + garnet + H_2O/L ± ilmenite ± rutile (± kyanite) fields, located at T=500–760 °C and P=3–15 kbar (Fig. 3.34a). Garnet compositional isopleths (XMg=0.10–0.11; XCa=0.03–0.04; XMn=0.035–0.040) constrain the growth of the equilibrium assemblage at 710<T<750 °C and 8.5<P<10.8 kbar (Fig. 3.34b and Tab. 3.5a). Peak P–T conditions lie just above the H_2O-saturated solidus (Fig. 3.34c); the predicted amount of melt at peak P–T conditions is nevertheless very low (< 1.5 vol%), as well as for kyanite.

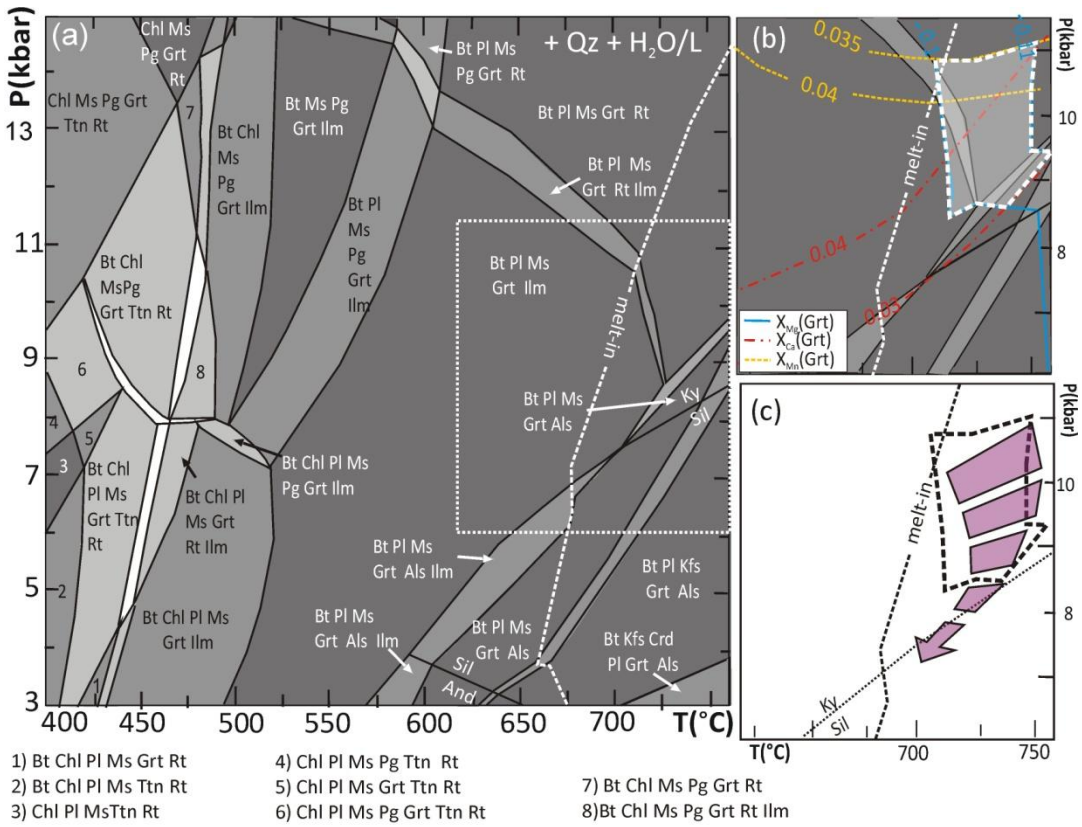

Fig. 3.34 - (a) P–T pseudosection for sample 14–71 (GHS, Gosainkund–Helambu section) calculated in the MnNKCFMASTH system at a(H_2O)=1. Variance of the fields as in Fig. 3.27. Ms and Pg refer to K–rich and Na–rich white mica, respectively. White dashed rectangle refers to the P–T interval shown in (b) and (c). **(b)** Detail of (a) contoured for garnet composition. White dashed polygon constrains the P–T conditions for the growth of the peak mineral assemblage. **(c)** P–T path inferred for sample 14–71 (purple arrow); note that the occurrence of rare late sillimanite implies that the retrograde P–T trajectory enters the sillimanite stability field. Dotted line (melt–in) in (a) to (c) represents the H_2O-saturated solidus.

❖ **Sample 14–52** – Maximum values of XMg measured in garnet core have been considered to constrain peak P–T conditions. Garnet includes biotite, quartz, minor kyanite and very minor white mica; this assemblage is modelled by the quini-variant field biotite + plagioclase + muscovite + garnet + kyanite + quartz + H_2O at T>650 °C and 8.7<P<11.7 kbar (Fig. 3.35a). Further constrains are given by garnet core compositional isopleths (XMg=0.20–0.21; XCa=0.025–0.030; XMn=0.11–0.12) that point to peak conditions of 720<T<760 °C and 9.0<P<10.0 kbar (Fig. 3.35b and Tab. 3.5a). Modelled XMn isopleths predict lower XMn at these P–T conditions (XMn=0.06–0.07), further supporting that garnet composition may have been modified by diffusional homogenization (see the Mineral chemistry section §3.4.2.5).

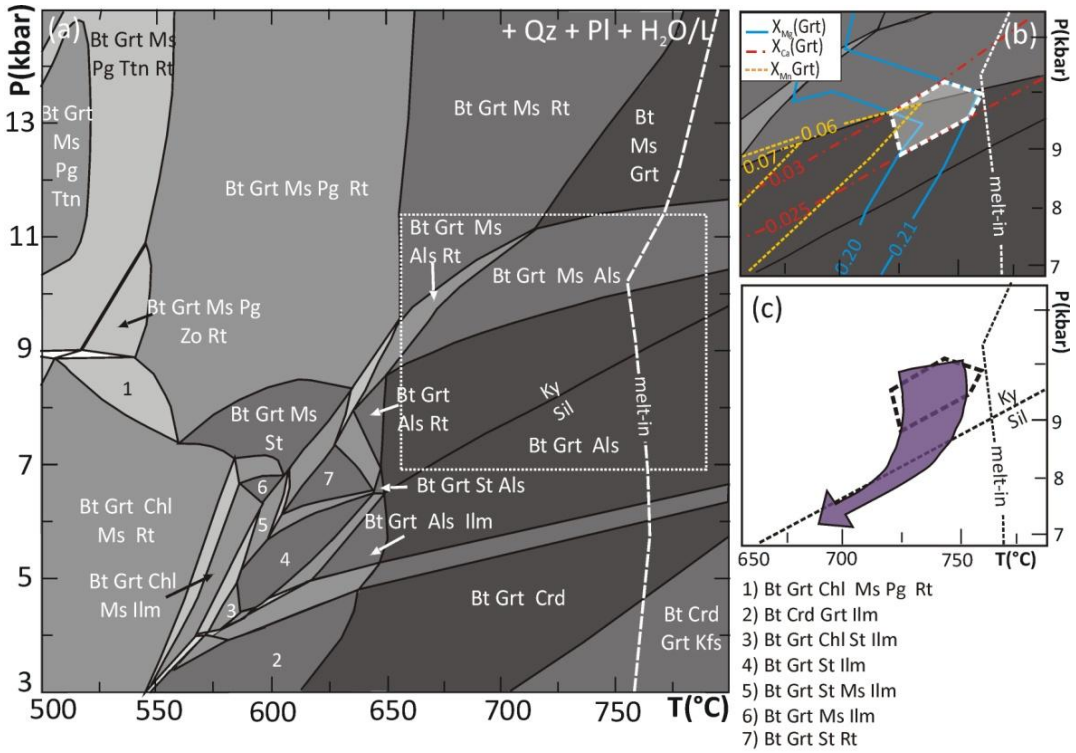

Fig. 3.35 - (a) P–T pseudosection for sample 14–52 (GHS, Gosainkund–Helambu section) calculated in the MnNKCFMASTH system at a(H_2O)=1. Variance of the fields as in Fig. 3.27. Ms and Pg refer to K–rich and Na–rich white mica, respectively. White dashed rectangle refers to the P–T interval shown in (b) and (c). **(b)** Detail of (a) contoured for garnet composition. White dashed polygon constrains the P–T conditions for the growth of garnet (peak P–T conditions). **(c)** P–T trajectory inferred for the metapelite sample 14–52 (blue arrow). Dotted–line (melt–in) in (a) to (c) represents the H_2O-saturated solidus.

Retrograde evolution

The retrograde portion of the L-GHS P-T paths is generally less well constrained than the prograde one. A cooling and decompression retrograde path can be nevertheless inferred for most samples, based on the following observations:

- **Sample 14–03** – Occurrence of rare sillimanite at the rim of garnet and white mica qualitatively constrains the retrograde path at P–T conditions below the kyanite–sillimanite transition.
- **Samples 14–25b and 14–24** – Retrograde evolution is tightly constrained at 590-650 °C, < 8.0 kbar by the growth of staurolite replacing kyanite, and by the rare occurrence of fibrolitic sillimanite replacing garnet rim.
- **Sample 14–44a** – Cooling and decompression retrograde path is compatible with the observed zoning in plagioclase, that is enriched in anorthite component toward the rim, as predicted by the plagioclase compositional isopleths (not reported in the figures).

- **Sample 14–61b** – Any cooling and decompression retrograde path would imply the entrance in the kyanite (or sillimanite) stability field (Fig. 3.33c). Neither kyanite nor sillimanite are observed in metapelite 14–61b; however, the calculated isomodes predict that their modal amount is lower than 0.1 vol%.
- **Sample 14–71** – Occurrence of rare sillimanite indicates that the retrograde P–T path enters the sillimanite stability field (Fig. 3.34c).
- **Sample 14–52** – Garnet porphyroblasts are wrapped by the main foliation defined by oriented biotite and sillimanite, with additional plagioclase and quartz in equilibrium with them. This assemblage is modelled by the large esa-variant field biotite + plagioclase + garnet + sillimanite + quartz + H_2O at T>670 °C and P < 10.1 kbar (Fig. 3.35c). The observed slight zoning of plagioclase is further consistent with decompression associated with cooling.

3.4.3.3 Upper Greater Himalayan Sequence

Prograde and peak P–T conditions

- **Sample 14–08a** – Equilibrium assemblage, consisting of garnet, biotite, k-feldspar, plagioclase, sillimanite, quartz, ilmenite and melt, is modelled by a large quadri-variant field at 650<T<850 °C and P<9 kbar (Fig. 3.36a). Further constrains are given by the compositional isopleths of garnet and biotite. Garnet is quite homogeneous in composition, reflecting diffusional homogenization effects at high temperatures; a slight increase in calcium is observed toward the rim (XCa=0.035–0.045). This Ca increase can be interpreted as related to the crossing of the muscovite dehydration melting curve, along a nearly isobaric P–T trajectory at about 7–8 kbar (Fig. 3.36b). Maximum XMg of garnet (XMg=0.12) constrains the equilibration temperatures at ~760 °C; slightly higher temperatures (T=760–800 °C) are indicated by XMg isopleths of biotite included in garnet (XMg=0.38; Fig. 3.36b and Tab. 3.5a). Due to possible compositional reset during cooling, the obtained temperatures should be considered as “minimum” estimates.

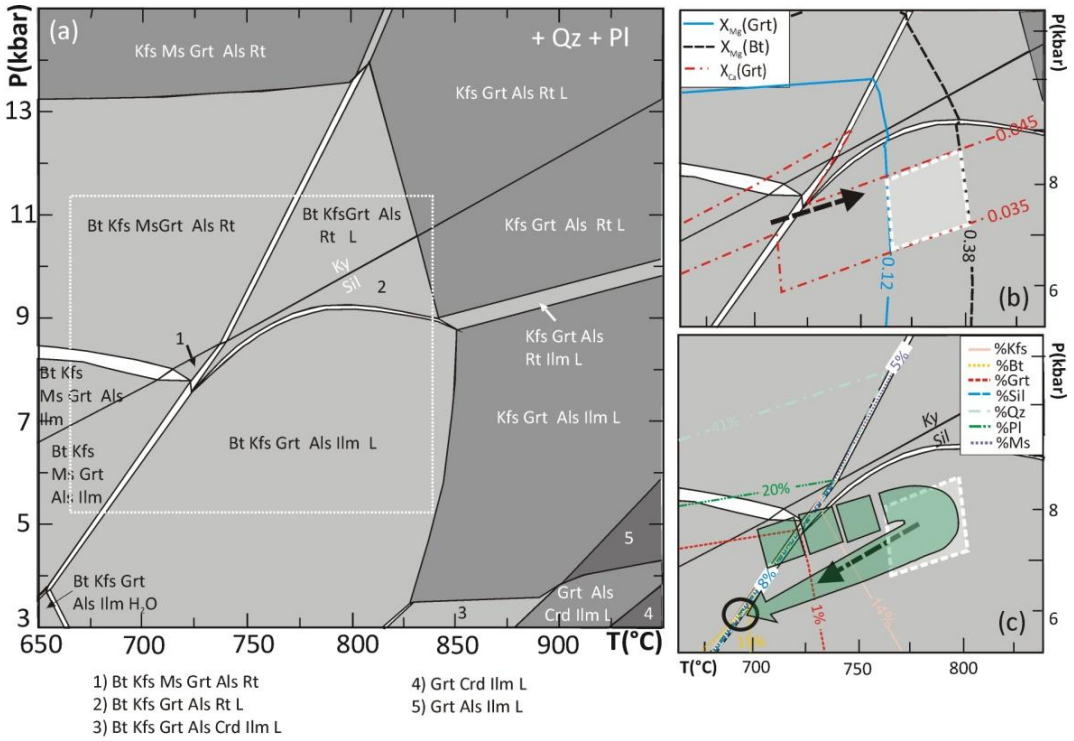

Fig. 3.36 - (a) P–T pseudosection for sample 14–08a (GHS, Langtang section) calculated in the MnNKCFMASTH system. Variance of the fields as in Fig. 3.27. White dotted rectangle refers to the P–T interval reported in (b–e). **(b)** Detail of (a) contoured for garnet composition (XCa and XMg) and biotite (XMg). Dashed arrow represents the possible trajectory to explain the weak grossular zoning observed in garnet (XCa = 0.035–0.045). White dashed polygon constrains the P–T conditions for the growth of garnet. **(c)** Detail of (a) with isomodes for mineral phases (vol%); the black ellipse constrains the P–T conditions for the final crystallization of the melt. Green arrow represents the P–T path inferred for sample 14–08a.

Retrograde evolution

- **Sample 14–08a** – Retrograde evolution of this sample is inferred using the calculated isomodes for all mineral phases. The intersection between the modelled isomodes and the solidus constrain the P–T conditions for the final melt crystallization at ~700 °C, 6 kbar (Fig. 3.36c). Back-reactions between solids and melt during melt crystallization are responsible for the formation of symplectitic intergrowths between: (i) biotite + sillimanite + plagioclase + quartz (according to the back-reaction: garnet + k-feldspar + L → biotite + alumo-silicate + plagioclase + quartz at higher T), and (ii) white mica + plagioclase + quartz (according to the back-reaction: k-feldspar + alumo-silicate + garnet + L → white mica + plagioclase + quartz at lower T, i.e. at the solidus).

3.4.4 Optimal thermobarometry

Average PT method has been applied to 14 samples (including 10 samples already investigated using the P-T pseudosection approach). Resulting pressures and temperatures (with uncertainties) are reported in Tab. 3.4 and plotted in the P-T diagram of Fig. 3.37; mineral chemical data used for the calculation are reported in Appendix 3. In this section, a synthesis of the results is discussed, from lower to upper structural levels.

T/depth ratio is calculated assuming an average lithostatic pressure gradient of 0.3 kbar/km, constant along the investigated transect. Results are the same as using the T/P ratio (removing the uncertainties of converting to depth), also concerning the error propagation. It is therefore used T/depth ratio, which is more commonly found in the geological literature.

(i) In the LHS phyllitic micaschists (samples 15-19, 14-27a, 15-28), both to the prograde and the peak equilibrium assemblages (defining the $S1_{LHS}$ and the S2LHS foliations, respectively) define enough equilibria to converge to an AvPT result. The obtained P-T results are similar for all the samples: the prograde $S1_{LHS}$ development is estimated at about 540 °C and 6.6-7.0 kbar, while peak P-T conditions occurred at about 590-600 °C and 7.1-8.2 kbar (Fig. 3.37a,b). Overall, the LHS samples recorded a prograde P-T evolution characterized by an increase in both P and T up to the peak metamorphic events, corresponding to a T gradient of 24 °C/km (Tab. 3.5b).

(ii) Sample 15-26b, exposed within the Ramgarh Thrust Sheet just below the MCT, gives higher P-T conditions for both the prograde and peak assemblage: specifically, prograde P-T conditions are estimated at about 585 °C, 7.8 kbar, while peak P-T conditions occurred at ~600 °C, 8.8 kbar, i.e. at higher P than the structurally lower samples (Fig. 3.37a,b). The geometry of the prograde P-T path is nevertheless similar to that of the other LHS samples, but the T/depth ratio is lower (21 °C/km, Tab. 3.5b).

(iii) L-GHS metapelitic samples (14-03, 14-25b, 14-24, 15-38, 14-44a, 14-61b, 14-71) recorded peak P-T conditions for the development of $S2_{GHS}$ in the range 660-710°C, 8.3-9.8 kbar, with a slight increase in both P and T proceeding structurally up in the section (Fig. 3.37c-f). The structurally lowermost samples (14-03, 14-25b and 15-38) preserve evidence of their prograde history, corresponding to the development of $S1_{GHS}$, at 585-640 °C, 6.4-7.8 kbar (Fig. 3.37c-f). Lowering the aH_2O to 0.9 to simulate the occurrence of incipient partial melting conditions, would result in a decrease of both T and P of about 10-15 °C, 0.1-0.5 kbar (Tab. 3.4). Estimated peak metamorphic conditions correspond to a T gradient of about 23 °C/km (Tab. 3.5b). Sample 14-52 records unusually high peak P-T conditions (850 ± 68 °C, 11.3 ± 2.6 kbar) but also shows the highest uncertainties.

(iv) U-GHS samples (14-08a and 14-12) do not preserve relics of their prograde history, and experienced various degrees of partial melting. These samples recorded peak P-T

conditions of 800-815 °C, ~6 kbar, well within the sillimanite-stability field, defining a T gradient of 40 °C/km (Tab. 3.5b, Fig. 3.37c,d).

Uncertainties (2σ values) associated with the AvPT results are generally greater than ± 20 °C and ± 1 kbar; these relatively large uncertainties might be due to several factors, including analytical uncertainties or uncertainties in the thermodynamic data and in the activity-composition relationships (e.g. Fraser et al., 2000). However, it is worth noting that P-T conditions independently constrained using the pseudosection approach plot very close to, or totally within the uncertainties of, the AvPT results (Fig. 3.39). The T gradients obtained with the Average PT method are quite similar to the ones obtained with the pseudosections as concerning the LHS and L-GHS samples (Tab. 3.5b); the AvPT results for U-GHS samples define a higher T gradient with respect to that constrained using pseudosections (40 ± 12 °C /km *vs*. 30 ± 4 °C /km), due to the large uncertainties in the P estimates, but the results are in any case in agreement with those of Fraser et al. (2000), who applied the same method in the Langtang transect.

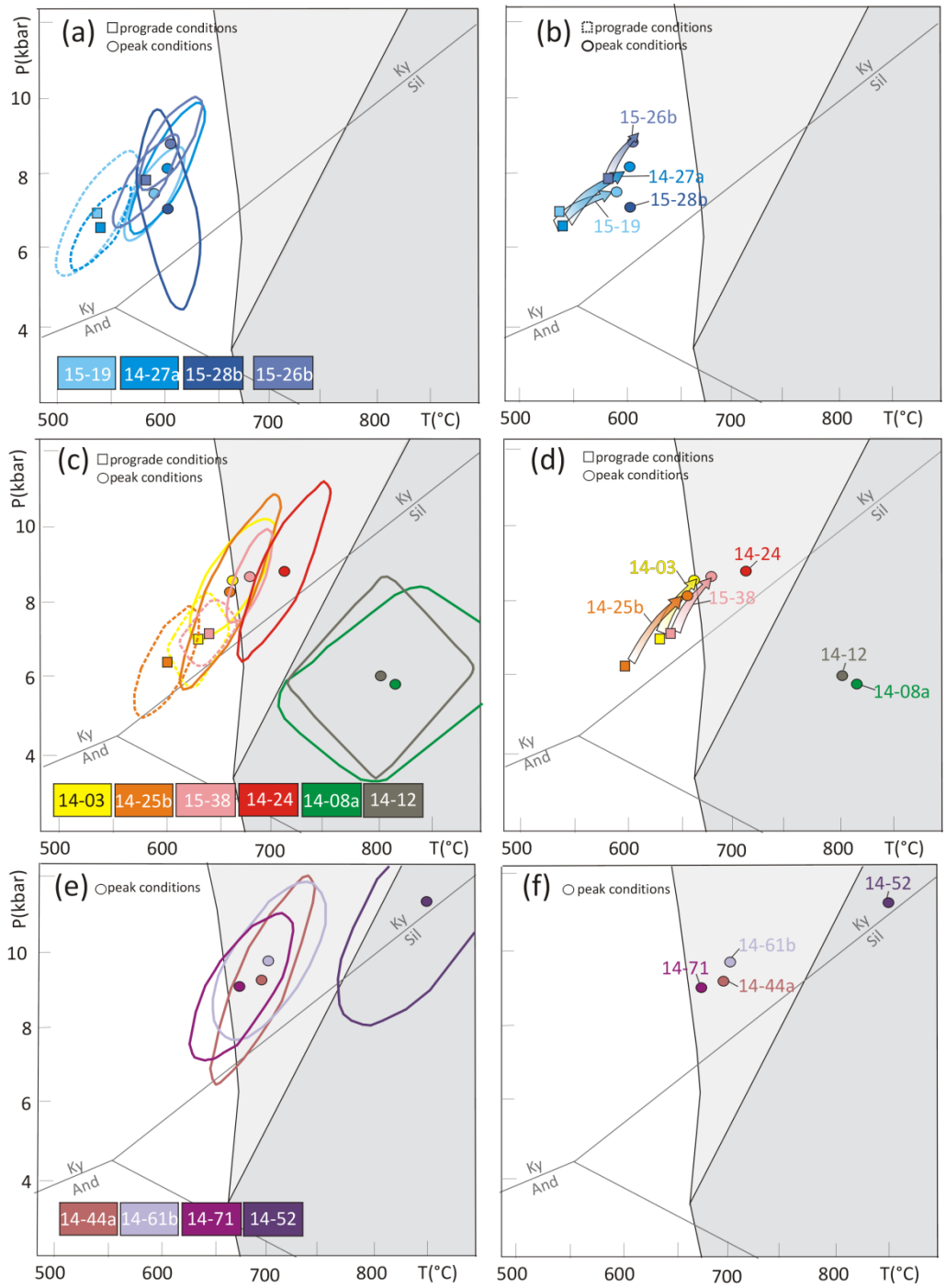

Fig. 3.37 - P-T conditions obtained through the "average PT"' method applied to LHS and GHS metapelite samples. LHS samples. **(a,b)** Prograde and peak P-T conditions with uncertainties (a) and (b) same as (a), with indication of the prograde P-T evolutions inferred based on AvPT results (arrows). L-GHS samples of Gatlang-Langtang transect. **(c,d)** Prograde and peak P-T conditions with uncertainties (c) and (d) same as (c), with indication of the prograde P-T evolutions inferred based on AvPT results (arrows). L-GHS samples of Gosainkund-Helambu transect. **(e,f)** Prograde and peak P-T conditions with uncertainties (e) and (f) same as (e), with indication of the prograde P-T evolutions inferred based on AvPT results (arrows). Light grey and dark grey fileds represent white mica dehydration melting field and from the biotite dehydration melting field, respectively, separated by the H_2O-saturated solidus and the white mica–out reaction (from White et al.,

2001).

Table 3.4 - Average pressure-temperatures estimates for the selected metapelites

	Sample	Assemblage	aH_2O	T (°C)	P (kbar)	N° of reactions
LHS	15-19*	Grt-Bt-Wm-Pl-Qz-H2O	1	538±31	7.0±1.3	5
	15-19	Grt-Bt-Wm-Pl-Qz-H2O	1	591±23	7.5±1.0	5
	14-27a*	Grt-Bt-Wm-Pl-Qz-H2O	1	541±23	6.6±0.9	4
	14-27a	Grt-Bt-Wm-Pl-Qz-H2O	1	603±28	8.2±1.4	5
	15-28b	Grt-Bt-Wm-St-Ky-Qz-H2O	1	604±23	7.1±2.1	5
LHS (RTS)	15-26b*	Grt-Bt-Wm-Pl-Qz-H2O	1	584±25	7.8±1.0	4
	15-26b	Grt-Bt-Wm-Pl-Qz-H2O	1	607±24	8.8±1.0	4
L-GHS	14-03*	Grt-Bt-Wm-Pl-Qz-H2O	1	632±22	7.0±1.0	5
	14-03	Grt-Bt-Wm-Pl-Qz-H2O	1	673±31	8.7±1.3	5
			0.9	663±32	8.6±1.3	5
	14-25b*	Grt-Bt-Wm-Pl-Qz-H2O	1	602±25	6.4±1.2	4
	14-25b	Grt-Bt-Wm-Pl-Ky-Qz-H2O	1	660±37	8.3±2.1	6
			0.9	648±36	8.2±2.1	6
	14-24	Grt-Bt-Wm-Pl-Ky-Qz-H2O	1	711±35	8.9±1.9	6
			0.9	699±34	8.8±1.9	6
	15-38*	Grt-Bt-Wm-Pl-Qz-H2O	1	640±20	7.2±0.7	7
	15-38	Grt-Bt-Wm-Pl-St-Ky-Qz-H2O	1	678±17	8.7±1.0	9
			0.9	666±17	8.5±1.1	9
	14-44a	Grt-Bt-Wm-Pl-Ky-Qz-H2O	1	696±39	9.3±2.2	6
			0.9	676±34	8.9±1.9	6
	14-61b	Grt-Bt-Wm-Pl-Qz-H2O	0.9	701±42	9.8±1.7	6
	14-71	Grt-Bt-Wm-Pl-Qz-H2O	1	676±39	9.1±1.6	5
			0.9	662±55	8.3±2.3	5
	14-52	Grt-Bt-Wm-Pl-Ky-Qz-H2O	1	850±68	11.3±2.6	7
			0.9	835±67	11.3±2.7	7
U-GHS	14-08a	Grt-Bt-Pl-Kfs-Sil-Qz-H2O	0.7	816±86	5.9±2.0	4
	14-12	Grt-Bt-Pl-Kfs-Sil-Qz-H2O	0.7	803±68	6.1±2.1	4

* refer to the prograde mineral assemblage

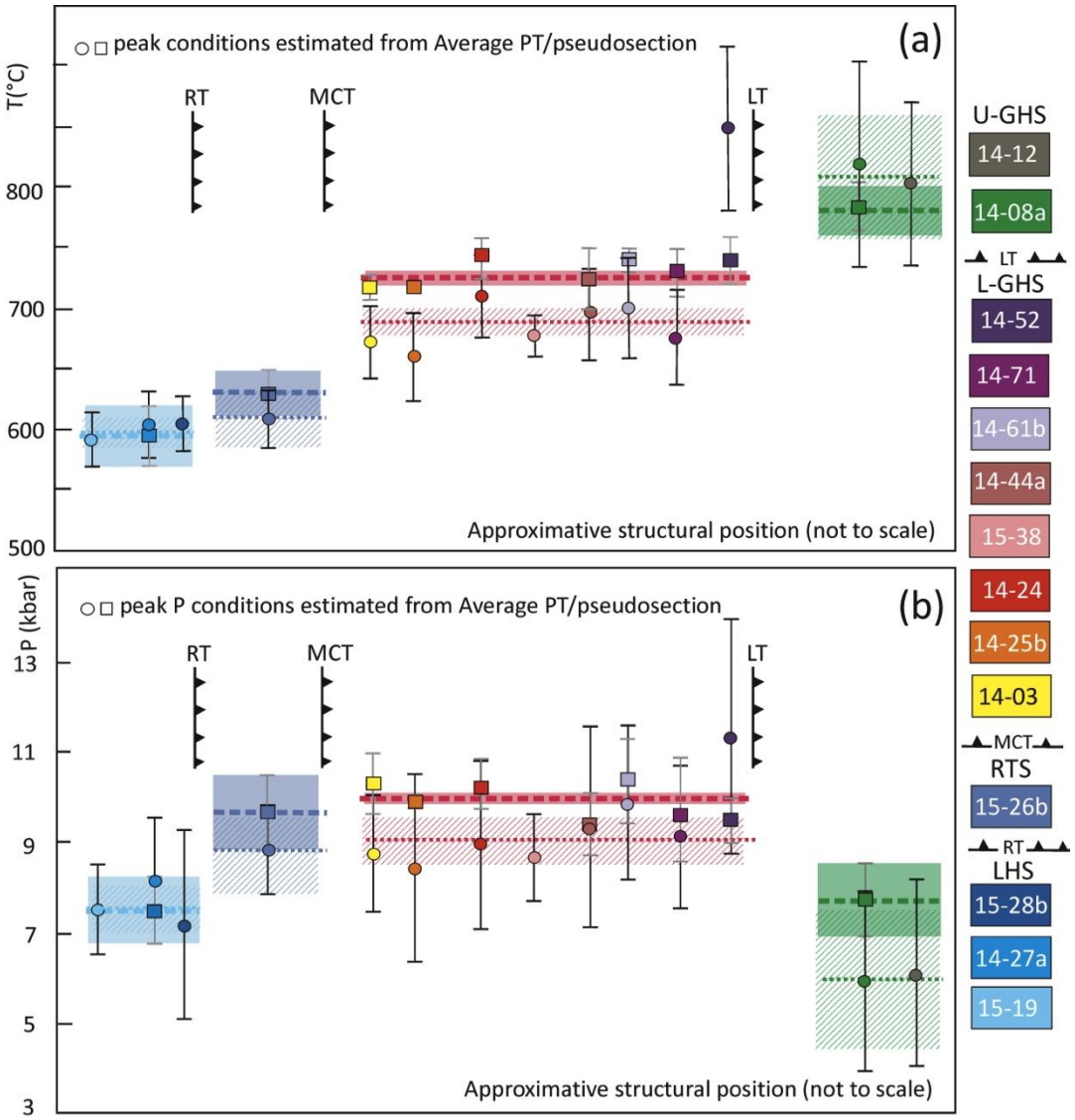

Fig. 3.38 – Peak temperatures (a) and pressures (b) conditions, reported from lower to upper structural levels. X-axis is not to scale. T and P results constrained using theAverage PT method (circles) are compared to results obtained using pseudosections (squares). Weighted average with errors are also reported (filled boxes: pseudosection approach, dashed boxes: AvPT). RT: Ramgarh Thrust; MCT: Main Central Thrust; LT: Langtang Thrust.

3.5 Discussion

3.5.1 Metamorphic evolution of the study area

Results of fieldwork activity combined to detailed petrological modelling of selected metapelite samples in the studied area indicate the occurrence of four distinct tectono-metamorphic units, characterized by different chemical zoning patterns in garnets, different P-T paths and T/depth ratios.

- Structurally lowest samples belong to the LHS. Metamorphic evolution inferred for these metapelites consists of a narrow hairpin P–T path characterized by a prograde increase in both T and P, followed by decompression associated with cooling (Fig. 3.39). Garnet porphyroblasts systematically show a preserved growth zoning. Estimated peak conditions define a T/depth ratio of 24 ± 3 °C/km using the phase diagram approach, and of 24 ± 3 °C/km using the AvPT approach (Tab. 3.5a,b),

- Structurally upper sample 15-26b is characterized by a P-T evolution at higher P-T conditions and defines a lower T/depth ratio of 20 ± 2 °C/km (21 ± 3 °C/km using AvPT). Based on the difference in peak metamorphic conditions and T/depth ratios, the occurrence of a tectono-metamorphic discontinuityis inferred, which separates an uppermost thin package of LHS rocks (LHS-Ramgarh Thrust Sheet, see discussion section 3.5.2) from the subjacent LHS.

- Structurally intermediate unit (Lower Greater Himalayan Sequence: L–GHS) mainly consists of medium-grade, garnet ± kyanite ± staurolite ± sillimanite –bearing two-mica schists, lacking evidence of partial melting at the outcrop scale. These lithologies are characterized by garnet zoning profiles from strongly zoned to slightly zoned, to homogeneous proceeding up in the section. In the **Gatlang-Langtang sections** the structurally lower samples (samples 14-03 and 14-25) preserve evidence of their prograde history, characterized by an increase in both P and T up to average peak metamorphic conditions of 720 ± 10 °C, 10.3 ± 0.7 kbar, in the kyanite stability field (Fig. 3.39a). Similar peak P–T conditions are inferred for the structurally higher sample (sample 14-24: 743 ± 18 °C, 10.3 ± 0.6 kbar), which does not preserve evidences of its prograde evolution and is characterized by garnet homogeneous in composition. These peak P–T conditions correspond to a T/depth ratio of 22 ± 0.5 °C/km (23 ± 2 °C/km using the AvPT approach) (Tab. 3.5). Furthermore, peak metamorphic conditions of these three samples lie just above the H_2O-saturated solidus; the predicted amount of melt at these P–T conditions is very low and is in agreement with the occurrence of nanogranites at the transition between garnet core and garnet rim. The retrograde evolution of these metapelites is characterized by cooling and decompression in the staurolite stability field Fig. 3.39a). All of the other samples from the **Gosainkund–Helambu section** are two-mica/biotite –bearing schists or gneisses

that do not show evidence of anatexis at the outcrop scale. They consist of chemically homogeneous minerals and do not preserve relicts of their prograde history. Estimated average peak metamorphic conditions (734 ± 19 °C, 10 ± 0.8 kbar) lie in the kyanite stability field (Fig. 3.39). These peak temperatures are compatible with the beginning of partial melting, in agreement with microstructural observations (i.e. occurrence of peritectic garnet, nanogranites etc.), which indicate that these metapelites experienced an incipient partial melting, at temperatures below the muscovite dehydration melting curve. The structurally highest sample (sample 14-52) does not show microstructural evidences of partial melting, probably due to the low amounts of white mica originally present in the rock. Estimated peak P–T conditions correspond to a T/depth ratio of 23 ± 1 °C/km (22 ± 3 with the AvPT approaches) (Tab. 3.5a,b). The retrograde path for all these samples is characterizedby cooling and decompression, still inside the kyanite stability field or in the sillimanite stability field.

- The structurally higher unit (Upper Greater Himalayan Sequence: U–GHS) mainly consists of high-grade migmatites with widespread evidence of partial melting at the outcrop scale. These metapelitic migmatites are characterized by chemically homogeneous minerals and equilibrated assemblages and do not preserve relics of their prograde history. Peak metamorphic conditions of 780 ± 20 °C, 7.8 ± 0.8 kbar (i.e. at T higher than the white mica dehydration-melting curve) have been inferred using the pseudosection approach (Fig. 3.39a), in agreement with field and microstructural observations which indicate a widespread anatexis. Melt crystallization along the retrograde path occurred well within the sillimanite stability field (Fig. 3.39a). Peak P–T conditions inferred for the U–GHS unit correspond to a T/depth ratio of 30 ± 4°C/km (40 ± 12 °C/km using the AvPT method; Tab. 3.5a,b).

Field data integrated with petrologic results help to **correlate** the samples from the **Gosainkund–Helambu transect to** those of the **Gatlang-Langtang section**, and allow the reconstruction of the tectono-metamorphic architecture of the GHS in the Gosainkund–Helambu region. The following observations can be made:

(i) Peak-P conditions recorded by the Gosainkund–Helambu samples are broadly homogeneous; no abrupt decreases in peak–P are observed along the transect, thus indicating that the studied samples all belong to a coherent tectono-metamorphic unit;

(ii) T/depth ratios recorded by the Gosainkund–Helambu metapelites is uniform (23 ± 1 °C/km) and consistent with that recorded by the L–GHS samples from the Langtang section (22 ± 0.5 °C/km) (Fig. 3.38 and Tab. 3.5a).

Overall, these observations indicate that the rocks in the Gosainkund–Helambu region belong entirely to the L-GHS unit.

Table 3.5a - Summary of the peak P-T constraints obtained from pseudosections (with errors) and T/depth ratios

		Sample	min T (°C)	max T (°C)	min P (kbar)	max P (kbar)	min depth (km)	max depth (km)	average T (°C)	error (σ) T (°C)	weight T	average P (kbar)	error (σ) P (kbar)	weight P	average depth (km)	error (σ) depth (km)	weight depth	average T/depth (°C/km)	error (σ) T/depth (°C/km)	weight T/depth
Gatlang-Langtang	**U-GHS**	14-08	760	800	7	8.5	23	28	***780***	***20***		***7.8***	***0.8***		26	3		***30***	***4***	
	L-GHS	14-24	725	760	9.7	10.8	32	36	743	18	0.003	10.3	0.6	3.31	34	2	0.298	22	2	0.36
		14-25b	715	725	9.7	10.0	32	33	720	5	0.040	9.9	0.2	44.44	33	1	4.000	22	0.5	4.23
		14-03	710	730	9.6	11.0	32	37	720	10	0.010	10.3	0.7	2.04	34	2	0.184	21	2	0.34
Gosainkund-Helambu	**L-GHS**	14-52	720	760	9.0	10.0	30	33	740	20	0.003	9.5	0.5	4.00	32	2	0.360	23	2	0.29
		14-71	710	750	8.5	10.8	28	36	730	20	0.003	9.7	1.2	0.76	32	4	0.068	23	3	0.09
		14-61b	730	750	9.4	11.3	31	38	740	10	0.010	10.4	1.0	1.11	35	3	0.100	21	2	0.20
		14-44a	700	750	8.6	10.0	29	33	725	25	0.002	9.3	0.7	2.04	31	2	0.184	23	3	0.15
		*weighted mean**							***725***	***4***		***9.9***	***0.1***					***22***	***0.4***	
	LHS-RTS	15-26b	620	650	8.7	10.4	29	35	***635***	***15***		***9.6***	***0.9***		32	3		***20***	***2***	
	LHS	14-27a	570	620	6.7	8.2	22	27	***595***	***25***		***7.5***	***0.8***		25	3		***24***	***3***	

Table 3.5b - Summary of the peak P-T constraints obtained from "Average PT" method (with errors) and T/depth ratios

Gatlang-Langtang	**U-GHS**	14-12	735	871	4	8.2	13	27	803	68	0.0002	6.1	2.1	0.23	20	7	0.020	39	17	0.00
		14-08a	730	904	4	8	13	27	816	86	0.0001	6.0	2.0	0.25	20	7	0.023	41	18	0.00
		*weighted mean**							***808***	***53***		***6.0***	***1.4***					***40***	***12***	
	L-GHS	14-24	676	746	7.0	10.8	23	36	711	35	0.0008	8.9	1.9	0.28	30	6	0.025	24	6	0.03
		14-25b	623	697	6.2	10.4	21	35	660	37	0.0007	8.3	2.1	0.23	28	7	0.020	24	7	0.02
		15-38	661	695	7.7	9.7	26	32	678	17	0.0035	8.7	1.0	1.00	29	3	0.090	23	3	0.09
		14-03	642	704	7.4	10.0	25	33	673	31	0.0010	8.7	1.3	0.59	29	4	0.053	23	5	0.05
Gosainkund-Helambu	**L-GHS**	14-52	782	918	8.7	13.9	29	46	850	68	0.0002	11.3	2.6	0.15	38	9	0.013	23	7	0.02
		14-71	637	715	7.5	10.7	25	36	676	39	0.0007	9.1	1.6	0.39	30	5	0.035	22	5	0.04
		14-61b	659	743	8.1	11.5	27	38	701	42	0.0006	9.8	1.7	0.35	33	6	0.031	21	5	0.04
		14-44a	657	735	7.1	11.5	24	38	696	39	0.0007	9.3	2.2	0.21	31	7	0.019	22	7	0.02
		*weighted mean**							***687***	***11***		***9.0***	***0.6***					***23***	***2***	
	LHS-RTS	15-26b	583	631	7.8	9.8	26	33	***607***	***24***		***8.8***	***1.0***		29	3		***21***	***3***	
	LHS	15-28b	581	627	5	9.2	17	31	604	23	0.0019	7.1	2.1	0.23	24	7	0.020	26	9	0.01
		14-27a	*572*	*620*	*6.6*	*8.4*	*22*	*28*	*596*	*24*	0.0017	*7.5*	*0.9*	1.23	25	3	0.111	24	4	0.07
		15-19	568	614	6.5	8.5	22	28	591	23	0.0019	7.5	1.0	1.00	25	3	0.090	24	4	0.06
		*weighted mean**							***597***	***13***		***7.5***	***0.6***					***24***	***3***	

*Where more than one sample are available, the weighted mean (with error) is calculated (i.e. values with smaller errors weight more than values with bigger errors).

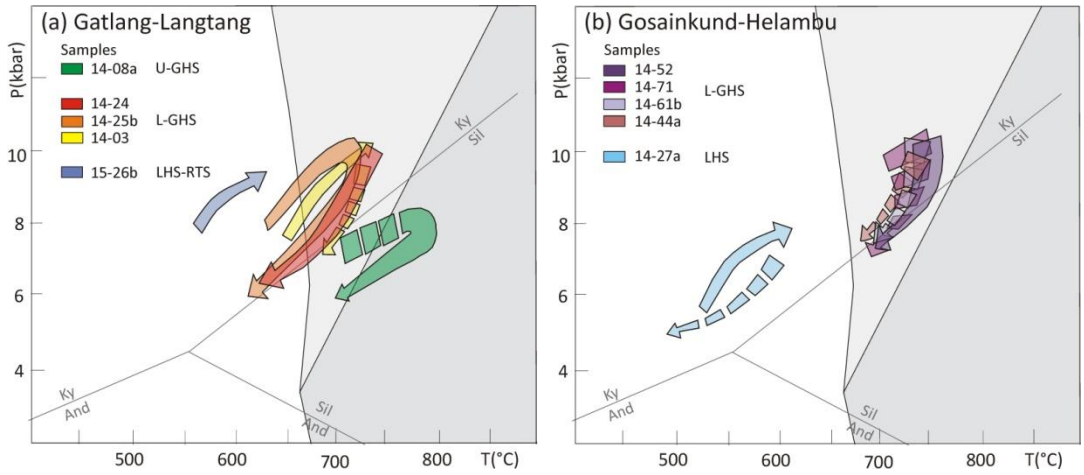

Fig. 3.39 - P–T diagrams with the P–T trajectories obtained for the modelled metapelites from the Gatlang-Langtang **(a)** and Gosainkund–Helambu **(b)** sections, with the pseudosection approach. Light grey and dark grey fileds represent white mica dehydration melting field and from the biotite dehydration melting field, respectively, separated by the H_2O-saturated solidus and the white mica–out reaction (modified from White et al., 2001).

3.5.2 Comparison with previous studies

Results obtained from the **Gatlang-Langtang section** are consistent with those published by previous authors, using different petrologic approaches. Inger and Harris (1992) first documented the increase in peak–T and the decrease in peak–P upsection in the GHS along the Langtang transect, using multi-equilibrium thermobarometry applied to a large number of metapelite samples. However, they attributed the two populations of peak–P to a diachronous metamorphism between the kyanite and the sillimanite zones, rather than to the presence of a cryptic metamorphic discontinuity. Reddy et al. (1993) also argued for the presence of a tectonic break between kyanite– and sillimanite–grade rocks in the GHS, combining geochemical, structural and textural arguments, but they did not provide P–T data. Fraser et al. (2000), using the Average–PT (ΔPT) approach, recognized the presence of two distinct, possibly duplicated units, based on different peak–P estimates. More recent estimates of peak P–T conditions from the Langtang section are those by Kohn et al. (2004, 2005) and Kohn (2004, 2008): conventional thermobarometry and trace element thermometry were to a significant number of metapelite samples and provided detailed P–T constraints for the metamorphic peak at different structural levels. Thermobarometric data mostly referred to the peak mineral assemblages and did not allow the reconstruction of the whole P–T evolution of the studied samples; however, geochronological data combined with P–T estimates were interpreted to indicate three main P–T–t discontinuity along the Langtang section. The lowermost discontinuity coincides with the Ramghar Thrust (RT) (Munsiari Thrust in Kohn, 2008) and separates a package of LHS rocks (LHS-Ramghar Thrust Sheet; LHS-RTS) which experienced earlier (20-10 Ma) peak metamorphism at higher P-T conditions (~608 °C, 11 kbar) from the other

LHS rocks which experienced later (< 5 Ma) peak metamorphism at lower P-T conditions (~550 °C, 8 kbar). The structurally intermediate discontinuity is the MCT, which separates the LHS from the GHS. MCT coincides with an abrupt increase in both P and T, with a strong gradient up to 725 °C, 10-12 kbar over a structural distance of less than 2 km. The uppermost discontinuity is defined as Langtang Thrust (LT: Kohn et al., 2005) and separates the GHS in two units, characterized by different peak P–T conditions and by different P–T–t histories: partial melting (and melt crystallization) occurred earlier in the U–GHS (20–18 Ma) than in the L–GHS (16–13 Ma), consistently with in-sequence thrusting of the U–GHS over the L–GHS.

Our peak P–T conditions (as well as garnet zoning patterns) obtained for samples 14-27a, 15-26b, 14–03, 14–25b, 14–24 and 14–08a using the pseudosection approach are in very good agreement with those obtained by Kohn et al. (2004, 2005) and Kohn (2004, 2008) on samples from the same structural levels (LT01-98, LT01-65a, LT01–74/75, LT01–29b, LT01–27b and LT01–6c, respectively) using the conventional thermobarometry approach (Tab. 3.6 and Fig. 3.40). The pseudosection approach has the advantage of allowing the reconstruction of the prograde and/or retrograde P–T evolution of the studied samples, which can outline the differences and similarities of P–T paths in a set of samples otherwise only grouped by coherent peak P–T conditions. T/depth ratios calculated for the Kohn (2008) original data are also consistent with those obtained from our samples, and highlight the existence of four different T/depth ratio populations of 24 ± 3 °C/km, 20 ± 2 °C/km, 22 ± 0.5 °C/km and 30 ± 4 °C/km in the LHS (ZL1-3 in Kohn, 2008: 21 ± 2 °C/km), LHS Ramghar Thrust Sheet (ZL4 in Kohn, 2008: 17 ± 1 °C/km), L–GHS (ZG1 and ZG2 in Kohn, 2008: 19 ± 1 °C/km) and U–GHS (ZG3 and ZG4 in Kohn, 2008: 28 ± 2 °C/km), respectively (Fig. 3.40 and Tab. 3.6). The upper metamorphic discontinuity coincides with the abrupt increase in the T/depth ratio upsection inferred from our own data and from those of Kohn (2008) roughly coincides with the geochronological discontinuity marked by the increase in ages upsection as reported in Kohn et al. (2005) and Kohn (2008). There may be minor mismatch between the metamorphic and the geochronologic discontinuities (see Fig. 3.1b), mainly related to the attribution of sample LT01–10 of Kohn (2008) to the upper *vs.* lower GHS unit. It is therefore indicated that T/depth ratio is a useful parameter, alternative and/or complementary to the geochronological constraints, for the identification of metamorphic discontinuities within the GHS (see also Groppo et al., 2009).

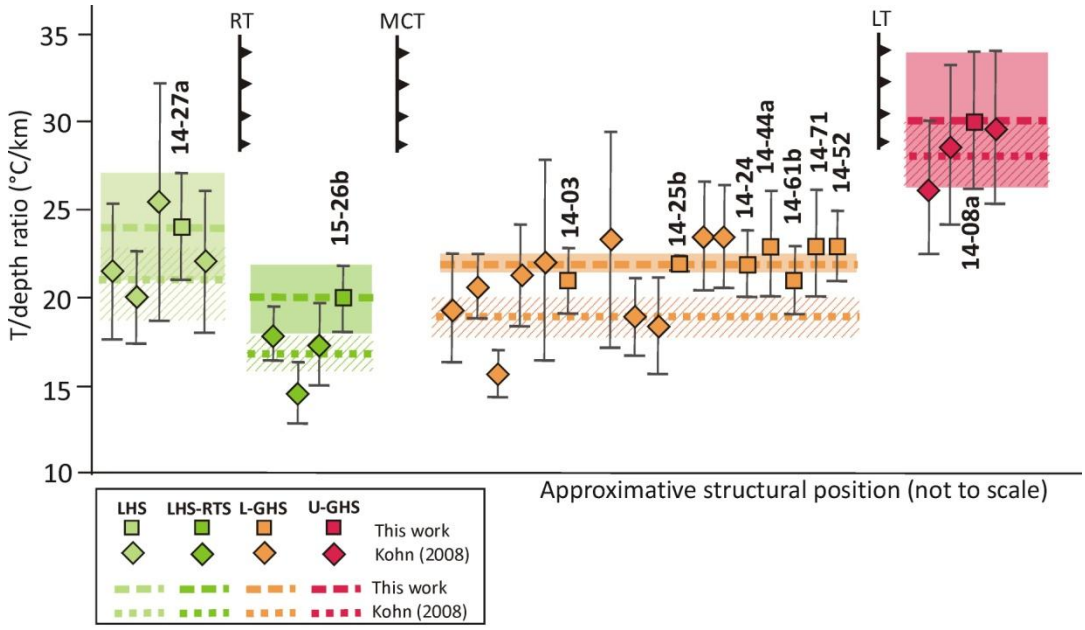

Fig. 3.40 - T/depth ratios (°C/km) (with errors) plotted as a function of the (approximate) structural position for the samples studied in this work (squares) using the pseudosection approach and those studied by Kohn (2008) (diamonds) using conventional thermobaromtry (his ZL1-3, ZL4 and ZG1 to ZG4 zones). Dashed and dotted lines are the weighted average T/depth values obtained from the studied samples and from those of Kohn (2008), respectively, with their errors (filled boxes and dashed boxes, respectively). It is evident that the LHS, LHS-RTS, L–GHS and U–GHS samples define four distinct clusters of T/depth ratios (light green, dark green, orange and red boxes).

Prior to this investigation, a limited number of P–T data on the **Gosainkund–Helambu section** were published. Apart from a couple of samples from the Gosainkund area investigated by Macfarlane (1995) and Fraser et al. (2000), giving P–T constraints of 640–680 °C, 7.8–8.2 kbar, the only comprehensive study of this area is that by Rai et al. (1998). These authors applied both conventional and multi-equilibrium thermobarometry on nine metapelites samples. Although their data are affected by large uncertainties (especially on pressures), they are consistent with our results with a great homogeneity in peak P–T conditions along the transect, with T and P broadly in the range 670–700 °C, 7.2–8.2 kbar (Rai et al., 1998). Langtang Thrust (LT), which divides the GHS into two tectono-metamorphic units, is structurally too high to be intersected in the Gosainkund–Helambu section.

Table 3.6 - Summary of the peak P-T constraints (with errors) and T/depth ratios for the Kohn (2008) samples

	Sample	min T (°C)	max T (°C)	min P (kbar)	max P (kbar)	min depth (km)	max depth (km)	avT (°C)	error T (°C)	weight T	avP (kbar)	error P (kbar)	weight P	average depth (km)	error (σ) depth (km)	weight depth	av T/depth (°C/km)	error T/depth (°C/km)	weight T/depth
U-GHS	LT01-14b	800	850	7.5	9.5	25	32	825	25	0.002	8.5	1.0	1	28	3	0.09	29	4	0.05
	LT01-6c	725	775	7.0	9.0	23	30	750	25	0.002	8.0	1.0	1	27	3	0.09	28	4	0.05
	LT01-4b	750	800	8.0	10.0	27	33	775	25	0.002	9.0	1.0	1	30	3	0.09	26	4	0.07
	U-GHS (average)							*783*	*14*		*8.5*	*1*		*28.3*	*2*		*28*	*2*	
L-GHS	LT01-27b	685	705	8.0	10.0	27	33	695	10	0.010	9.0	1.0	1	30	3	0.09	23	3	0.12
	LT01-29b	680	710	8.0	10.0	27	33	695	15	0.004	9.0	1.0	1	30	3	0.09	23	3	0.11
	LT01-71d	675	775	11.0	13.0	37	43	725	50	0.000	12.0	1.0	1	40	3	0.09	18	3	0.13
	LT01-73d	725	775	11.0	13.0	37	43	750	25	0.002	12.0	1.0	1	40	3	0.09	19	2	0.21
	LT01-31a	685	785	8.0	12.0	27	40	735	50	0.000	10.0	2.0	0.25	33	7	0.023	22	6	0.03
	LT01-67b	600	650	7.0	11.0	23	37	625	25	0.002	9.0	2.0	0.25	30	7	0.023	21	5	0.03
	LT01-75e	675	725	9.0	11.0	30	37	700	25	0.002	10.0	1.0	1	33	3	0.09	21	3	0.12
	LT01-102a	575	625	11.0	12.0	37	40	600	25	0.002	11.5	0.5	4	38	2	0.36	16	1	0.56
	LT01-66a	625	675	9.0	10.0	30	33	650	25	0.002	9.5	0.5	4	32	2	0.36	21	2	0.29
	LT01-66c	650	750	10.0	12.0	33	40	700	50	0.000	11.0	1.0	1	37	3	0.09	19	3	0.10
	L-GHS (average)							*686*	*7*		*10*	*0.3*		*35*	*0.9*		*19*	*1*	
LHS (RT)	LT01-65a	575	625	9.5	11.5	32	38	600	25	0.002	10.5	1.0	1	35	3	0.09	17	2	0.18
	LT01-77	575	625	11.5	13.5	38	45	600	25	0.002	12.5	1.0	1	42	3	0.09	14	2	0.33
	LT01-78b	600	650	10.0	11.0	33	37	625	25	0.002	10.5	0.5	4	35	2	0.36	18	2	0.41
	LHS-RT (average)							*608*	*14*		*10.8*	*0*		*36.1*	*1*		*17*	*1*	
LHS	LT01-50	540	610	7	9	23	30	575	35	0.001	8	1	1	27	3	0.09	22	4	0.06
	LT01-40d	530	590	5.5	8.5	18	28	560	30	0.001	7	1.5	0.4	23	5	0.04	24	6	0.02
	LT01-98	535	585	7.75	9.25	26	31	560	25	0.002	8.5	0.75	1.8	28	3	0.16	20	3	0.14
	LT01-42c	500	550	6.5	8.5	22	28	525	25	0.002	7.5	1	1	25	3	0.09	21	4	0.07
	LHS (average)							*551*	*14*		*8*	*0*		*27*	*2*		*21*	*2*	

3.5.3 Tectono-metamorphic architecture of the Gosainkund–Helambu area and implications for the Himalayan kinematic models

Obatined results have interesting implications for the interpretation of the Kathmandu Nappe (KN). Structural and metamorphic architecture of the KN has been recently reviewed by He et al. (2015) (refer to that paper and references therein for further details). Here are summarized the main points relevant to this discussion. KN is conventionally divided, from top to bottom, in the Phulchauki Group, Bhimpedi Group and Sheopuri Gneiss. Phulchauki Group is generally correlated to the TSS, whereas the interpretation of the Bhimpedi Group is debated. Bhimpedi–Phulchauki succession is characterized by a right–way–up thermal gradient (Fig. 3.41a), ranging from the kyanite zone (~650 °C) at its base to anchi-metamorphic or un-metamorphosed rocks at its top (Johnson et al., 2001; Webb et al., 2011). Bhimpedi–Phulchauki succession occurs in the hanging wall of the Galchi Shear Zone (Webb et al., 2011), which separates the Bhimpedi and Phulchauki Groups from the Sheopuri Gneiss in the footwall. Sheopuri Gneiss, thrusted over the LHS by the MCT, is interpreted as belonging to the GHS. However, the correlation of the Sheopuri Gneiss to the L-GHS *vs.* U-GHS remained ambiguous so far.

Four structural models have been proposed to explain the architecture of the KN (He et al., 2015 and references therein) (Fig. 3.41a): Model A (Rai et al., 1998; Upreti and Le Fort, 1999; Hodges, 2000) considers the KN as entirely belonging to the LHS. This model has been recently criticized (e.g. He et al., 2015; Khanal et al., 2015). According to model B (Johnson et al., 2001; Gehrels et al., 2003; Robinson et al., 2003), the KN is completely ascribed to the GHS (i.e. the STDS does not occur in the KN). Model C (Khanal et al., 2015; see also Yin, 2006, although less explicit) correlates the KN to both the GHS (lower Bhimpedi Group) and the TSS (upper Bhimpedi Group + Phulchauki Group), thus implying that: (i) the STDS is located within the KN, separating the lower Bhimpedi Group from the upper Bhimpedi Group, and (ii) that the Galchi Shear Zone is an intra–GHS thrust juxtaposing two different GHS units. Khanal et al. (2015) further indicate that the Galchi Shear Zone correlates with the Langtang Thrust, which merges with the MCT on the northern side of the KN. According to this model, the lower Bhimpedi Group and the Sheopuri Gneiss can be thus correlated to the U–GHS and L–GHS, respectively. Model D (Webb et al., 2011; see also He et al., 2015) correlates the KN to the TSS. This model implies that the Galchi Shear Zone coincides with the STDS, which merges with the MCT on the northern side of the KN. According to this model the Bhimpedi Group and the Sheopuri Gneiss can be thus correlated to the TSS and L–GHS, respectively.

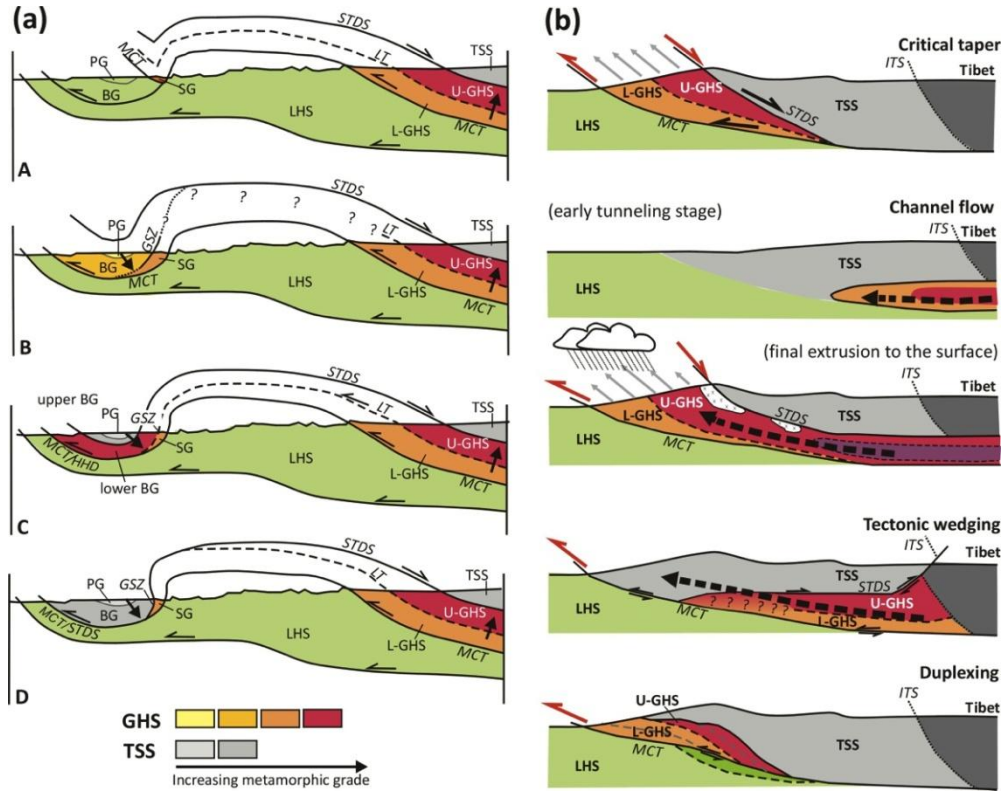

Fig. 3.41 - (a) Structural models of the Kathmandu Nappe (modified from He et al., 2015). Reference papers for each models are: (A) Rai et al. (1998), Upreti and Le Fort (1999), Hodges (2000); (B) Johnson et al. (2001), Gehrels et al. (2003), Robinson et al. (2003); (C) Khanal et al., 2015; Yin (2006); (D) Webb et al. (2011). Colours from yellow to red imply increasing metamorphic grade in the GHS; the colours from light grey to dark grey imply increasing metamorphic grade in the TSS (see also the black arrows). Units in the Kathmandu Nappe are: BG: Bhimpedi Group; PG: Phulchauki Group; SG: Sheopuri Gneiss. LHS: Lesser Himalayan Sequence (undifferentiated); L–GHS: Lower Greater Himalayan Sequence; U–GHS: Upper–Greater Himalayan Sequence; TSS: Tethyan Sedimentary Sequence. MCT: Main Central Thrust; LT: Langtang Thrust; STDS: South Tibetan Detachment System; GSZ: Galchi Shear Zone. **(b) Sketch of the main current Himalayan tectonic models for the exhumation of GHS** (modified from Montomoli et al., 2013, Cottle et al., 2015 and He et al., 2015). Colours and abbreviations as in (a) and in Fig. 3.1; ITS: Indus–Tsangpo suture.

Results of this study demonstrate that the Sheopuri Gneiss should be correlated to the lower portion of the GHS (i.e. L–GHS), being the Gosainkund–Helambu region entirely carved within the L–GHS (i.e. all the studied samples along the Gosainkund–Helambu section experienced the same P–T evolution and are characterized by the same T/depth gradients as the L–GHS samples from the Langtang section). In considering on these results, the following issues arise: (i) if ithe Sheopuri Gneiss is interpreted as the southern equivalent of the L–GHS, model B has serious geometrical problems to explain the right–way–up thermal gradient

observed in the KN, opposite to the inverted thermal gradient observed northward within the GHS. In other words, there are no simple geometrical features able to explain why the L–GHS is overlain by higher-grade rocks to the north and by lower-grade rocks to the south. (ii) Both models C and D are compatible with the correlation of the Sheopuri Gneiss to the L-GHS and are able to explain the right–way–up thermal gradient in the Bhimpedi–Phulchauki succession. He et al. (2015) and Khanal et al. (2015) also provide geochronological constraints on the movement of the Galchi Shear Zone. Although their results are very similar (i.e. 23.1–18.8 Ma: He et al., 2015; > 22.5 ± 2.3 Ma: Khanal et al., 2015), their final interpretations are significantly different. Being limited to the footwall of the Galchi Shear Zone, results of this study are not sufficient to definitively discriminate between model C and D. Thermobarometric data published by Johnson et al. (2001) (conventional thermobarometry) indicate that the base of the Bhimpedi Group experienced peak T ≤ 650 °C (see also He et al., 2015 for similar temperatures obtained using the quartz c–axis thermometry method); these temperatures are significantly lower than those estimated for the U–GHS rocks in the Langtang region, and are not compatible with the widespread evidence of anatexis that characterize the U–GHS (e.g. sample 14–08a and 14-12 in this study). This study therefore indicates that the results (i.e. Sheopuri Gneiss = L–GHS; T > 770 °C estimated for the U–GHS *vs.* T ≤ 650 °C reported for the Bhimpedi Group) better support model D rather than model C (Fig. 3.41a).

If it is assumed that the KN is correlated to the TSS (model D), further implications for the Himalayan kinematic models can be briefly discussed (for a more detailed and comprehensive discussion about the complexities of both the end-members and hybrid kinematic models see for example the reviews by Cottle et al., 2015 and He et al., 2015). Among the end-member kinematic models commonly used to explain the evolution of the Himalaya, the critical taper (e.g. Hodges et al., 1992, 2001; Vannay and Grasemann, 2001; Kohn, 2008) and the wedge extrusion/channel flow (e.g. Burchfieldand Royden, 1985; Burchfieldet al., 1992; Grujic et al., 1996; Beaumont et al., 2001, 2004;Godin et al., 2006) models all imply that the TSS overlies the high-grade, migmatitic, upper portion of the GHS (U–GHS) (Fig. 3.41b). This is not consistent with the results of this study, which demonstrate that the KN (equivalent to the TSS) directly overlies the L–GHS, not the U–GHS. Predictions of the tectonic wedge model (e.g. Webb et al., 2007) on the relative geometry of the TSS with respect to the L–GHS are more ambiguous (Fig. 3.41b). The only end-member model able to unambiguously predict the overlap of the TSS on the medium- to high-grade L–GHS is the duplexing model (e.g. Webb et al., 2013; Larson and Cottle, 2014; Cottle et al., 2015; Larson et al., 2015) (Fig. 3.41b). It is therefore possible to speculate that in this sector of the Himalayan chain, the most

appropriate kinematic model able to explain the observed tectono-metamorphic architecture of the GHS is the duplexing model or hybrid models which combine the duplexing model with another end-member model (e.g. duplexing + tectonic wedge model: Webb et al., 2013; He et al., 2015; duplexing + spatially and temporally evolving channel tunnelling/tectonic wedging model: Larson and Cottle, 2014; Cottle et al., 2015; Larson et al., 2015). This does not necessarily imply that the other kinematic models proposed were not relevant in different sectors of the Himalayan chain. As a provocative clue it is to notice that the L–GHS rocks in the studied area as well as in other sectors of western Nepal Himalaya (e.g. Carosi et al., 2010; Montomoli et al., 2013; Iaccarino et al., 2015) experienced clockwise P–T paths characterized by an increase in both P and T (i.e. peak P is reached at peak–T). This P–T evolution is significantly different from that experienced by L–GHS rocks in the central-eastern Nepal Himalaya (e.g. Goscombeand Hand, 2000; Goscombe et al., 2006; Groppo et al., 2009; Mosca et al. 2012, Larson et al., 2013; Rolfo et al. 2015a), where the clockwise P–T paths are characterized by heating during decompression (i.e. peak–P is reached prior to peak–T).

This may indicates different burial and exhumation mechanisms active in different sectors of the Himalayan chain (see also Cottle et al., 2015 for a discussion on this point).

Chapter 4

Metamorphic CO_2-source rocks in collisional orogens: types, occurrence, textures and protoliths of these not-(always) obvious CO_2-producing lithologies

4.1 Introduction

A number of studies suggest that metamorphic degassing from active collisional orogens may deliver to the atmosphere relatively high volumes of the global solid-Earth derived CO_2, representing a significant contributing factor in the long-term (>1 Ma) global carbon cycle (Kerrick and Caldeira 1993; Selverstone and Gutzler 1993; Bickle 1996; Berner 1999; Morner and Etiope, 2002; Gaillardet and Galy 2008; Evans 2011; Skelton, 2011, 2013). The Himalayan belt is the largest ''large-hot'' collisional orogen on Earth (Beaumont et al., 2010), where tectonic processes are still active nowadays (Ader et al., 2012), and where metamorphic CO_2-producing lithologies are widespread at different structural levels; it is therefore the ideal natural laboratory in which to study the metamorphic CO_2-producing processes. However, these CO_2-producing lithologies have been largely ignored in previous studies, being mainly mentioned as intercalations within the LHS and GHS metapelitic sequences (e.g. Goscombe et al., 2006).

In collisional contexts, decarbonation reactions mostly occurred during prograde regional metamorphism (at relatively high temperatures) within carbonate-bearing metasediments; CO_2-rich fluxes towards the Earth surface should have been promoted by crustal-scale discontinuities acting as conduits (Kerrick and Caldeira, 1993). Major uncertainties in the quantitative estimate of the contribution of collisional orogens to regional metamorphic CO_2-production are due to the so-far limited knowledge of the nature, magnitude and distribution of the CO_2-producing processes (Morner and Etiope, 2002; Evans, 2011), as well as on the types, distribution and volumes of the CO_2-source rocks (Rolfo et al., 2017).

This Chapter focuses on types, mineral assemblages and distribution of the CO_2-source rocks in the central-eastern sector of the Himalaya (central-eastern Nepal and Sikkim), as revealed by detailed fieldwork, petrographic observations and minero-chemical characterization of the different lithologies. Moreover, major and trace elements bulk-rock compositions allow to clarify the nature of the protolith(s) of the different CO_2-source rock types.

4.2 Methods

4.2.1 Fieldwork, petrography and mineral chemistry

Fieldwork was performed in central Nepal, in the Gatlang-Langtang and Gosainkund-Helambu regions (see §3.3.1). 35 CO_2-source rock samples were collected at different structural levels in different tectono-metamorphic units of the belt (LHS, L-GHS and U-GHS). In order to have a more robust database, field observations and samples were integrated with data already available from eastern Nepal and Sikkim (India), collected by the group of Torino (Dr. Chiara Groppo, Dr. Pietro Mosca and Prof. Franco Rolfo) over more than ten years (Fig. 4.1). A total of more than 120 CO_2-source rocks have been therefore studied. Microstructural features (and mineral chemical data) are discussed in detail for the 35 samples collected in the study area, whereas the petrographic features of all the samples are summarized in Appendix 2. Representative outcrop occurrences of the different lithologies are given in Fig. 4.2-4.3. The rock-forming minerals were analysed using the same equipment and analytical procedure described in §3.3.2. The most representative microstructures are reported in Figs 4.4–4.9; mineral chemical data are reported in Fig. 4.10 and Appendix 3.

4.2.2 Bulk-rock analysis

Whole-rock geochemical analysis of major, minor and trace elements were performed on 45 CO_2-source rocks belonging to different chemical groups and collected from different structural domains. Bulk-rock compositions were acquired by inductively coupled plasma mass spectrometry (ICP-MS) in the laboratories of ALS Geochemistry (Sevilla, Spain). Tab. 4.1 summarizes the obtained chemical data. Data were normalized to the average upper crust composition of Taylor and McLennan (1985). Eu and Ce anomalies were calculated according to Taylor and McLennan (1985): $Eu/Eu^* = Eu_N/(Sm_N \times Gd_N)^{0.5}$, $Ce/Ce^* = Ce_N/(La_N \times Pr_N)^{0.5}$. The subscript N indicates chondrite normalized values (McDonough and Sun, 1995 – for carbonaceous chondrite).

4.3 Results

4.3.1 Field occurrence of CO_2-source rocks

Although CO_2-source rocks are widespread in the metamorphic core of the Himalaya, both in the LHS and in the GHS, they are generally not differentiated from the host metapelites in most of the geological maps and tectonic schemes. Among the few notable exceptions is noteworthy the “Formation II” in the Annapurna and Manaslu regions of central Nepal, already distinguished by Le Fort (1975), which is a thousands of meters thick unit dominated by banded calc-silicate gneisses with minor marbles. At the outcrop scale, most (but not all) CO_2-source rocks are usually intensively folded and/or boudinated because of their relatively stiff rheological behaviour compared to the host rocks.

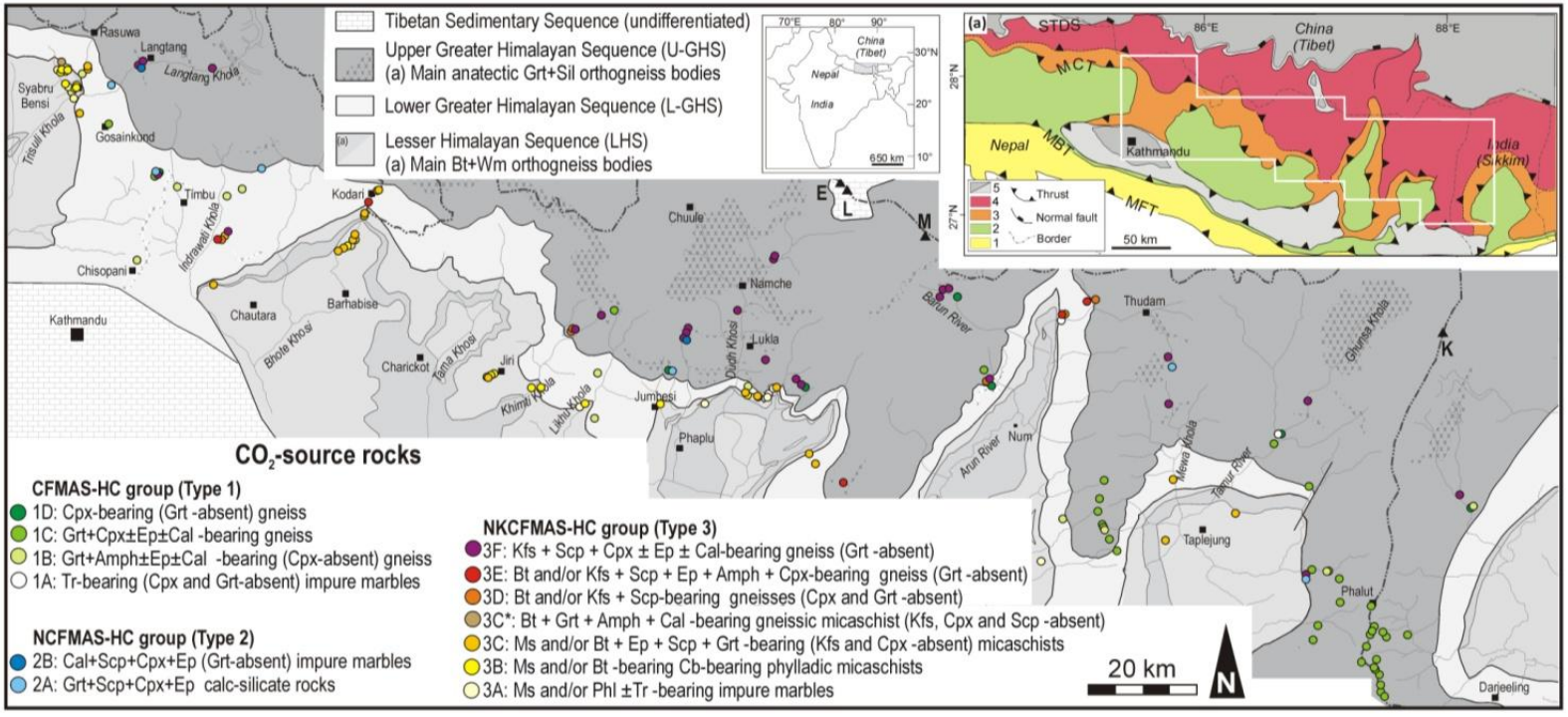

Fig. 4.1– Simplified geological map of central-eastern Nepal showing the occurrence of the different types of CO_2-source rocks discussed in the text (modified after Rolfo et al., 2017; Goscombe *et al.*, 2006; Dasgupta *et al.*, 2004; Mosca *et al.*, 2012; Mosca et al., 2013; He et al., 2015; Wang et al., 2016). CO_2-source rocks are grouped in three major chemical systems, based on data collected in this study and on data from Rolfo et al. (2017). MFT: Main Frontal Thrust; MBT: Main Boundary Thrust. MCT: Main Central Thrust; STDS: South Tibetan Detachment System; L: Lhotse; E: Everest; M: Makalu; K: Kangchenjunga; grey dotted line: political borders. The insets shows the location of the study area (white rectangle) in the framework of the Himalayan chain.

4.3.1.1 CO_2-source rocks in the LHS

In the **LHS**, CO_2-source rocks are represented by laminated impure marbles, calcareous phyllites and calcschists. **Marbles** occur as pluri-dm to pluri-m intercalations in the upper structural levels of the LHS (Fig. 4.2a), often associated to calcschists. Grain size and structure are variable, ranging between two end-members: (i) very fine-grained, dark grey/light grey marbles with a massive structure (Fig. 4.2b), and (ii) medium-grained, light beige/light green banded marbles with a more or less well-developed schistosity. The schistosity is defined by white mica ± bronze phlogopite ± dark biotite concentrated in sub-millimetric thick layers; in few samples, a dark green amphibole is associated to phlogopite along the main foliation (Fig. 4.2c). Ankerite-rich, mm-thick, brownish layers locally occur in the marbles, generally showing a corroded appearance.

Calcareous phyllites and **calcschists** constitute dm- to pluri-m thick layers intercalated in the upper portion of the LHS pelitic sequence; they show a well-developed schistosity characterized by mm- to pluri-mm thick yellowish carbonatic domains alternated with pluri-mm thick grey silicatic domains, with variable modal amounts of the main components (Fig. 4.2d-g). The grain size is too fine to recognize the mineral assemblages at the outcrop scale; the carbonatic domains are locally corroded and brownish, suggesting the occurrence of ankerite. Some lithologies are enriched in graphite, and dm-thick layers of graphitic phyllites with minor carbonate also occur (Fig. 4.2d), with the main schistosity defined by fine-grained white mica. Locally, the carbonatic component is quite abundant; the rock is pale-green, with pluri-cm thick carbonatic domains alternated to mm- to pluri-mm thick silicatic layers, in which the main schistosity is defined by bronze phlogopite.

A less frequent lithology observed in the upper structural levels of the LHS, is a **garnet + epidote + quartz + amphibole calc-silicate granofels,** occurring in pluri-cm thick layers alternating to quartzite (Fig. 4.2h). The peculiarity of this lithology is the occurrence of radiated aggregates of dark green amphibole statically overgrowing the other mineral phases, reaching several mm in size.

Fig. 4.2 – Representative field occurrences of CO_2-source rocks in the LHS. (a) pluri-m layers of marbles occurring along the path connecting Syabru Bensi to Gatlang. The marbles are easily recognizable for the light brownish colour on the surfaces exposed to weathering. **(b)** Fine-grained massive marble outcropping SW of Syabru Bensi. **(c)** Foliated and folded marble with a well-developed compositional layering and medium grain size; the white arrow indicates a dark green amphibole-rich layer. **(d)** Graphite-rich carbonate-bearing phyllite. Graphite is concentrated in dm-thick dark-grey layers. **(e)** Dm-thick nodules of reddish carbonate occur within calcschists. **(f,g)** Different varieties of calcschists and calcareous phyllites, characterized by different modal amounts of silicates (more abundant in f) and carbonates (more abundant in g). **(h)** Cm-thick layers of whitish garnet + epidote calc-silicate rock with radiated aggregates of dark green amphibole alternated with fine-grained grey quartzites.

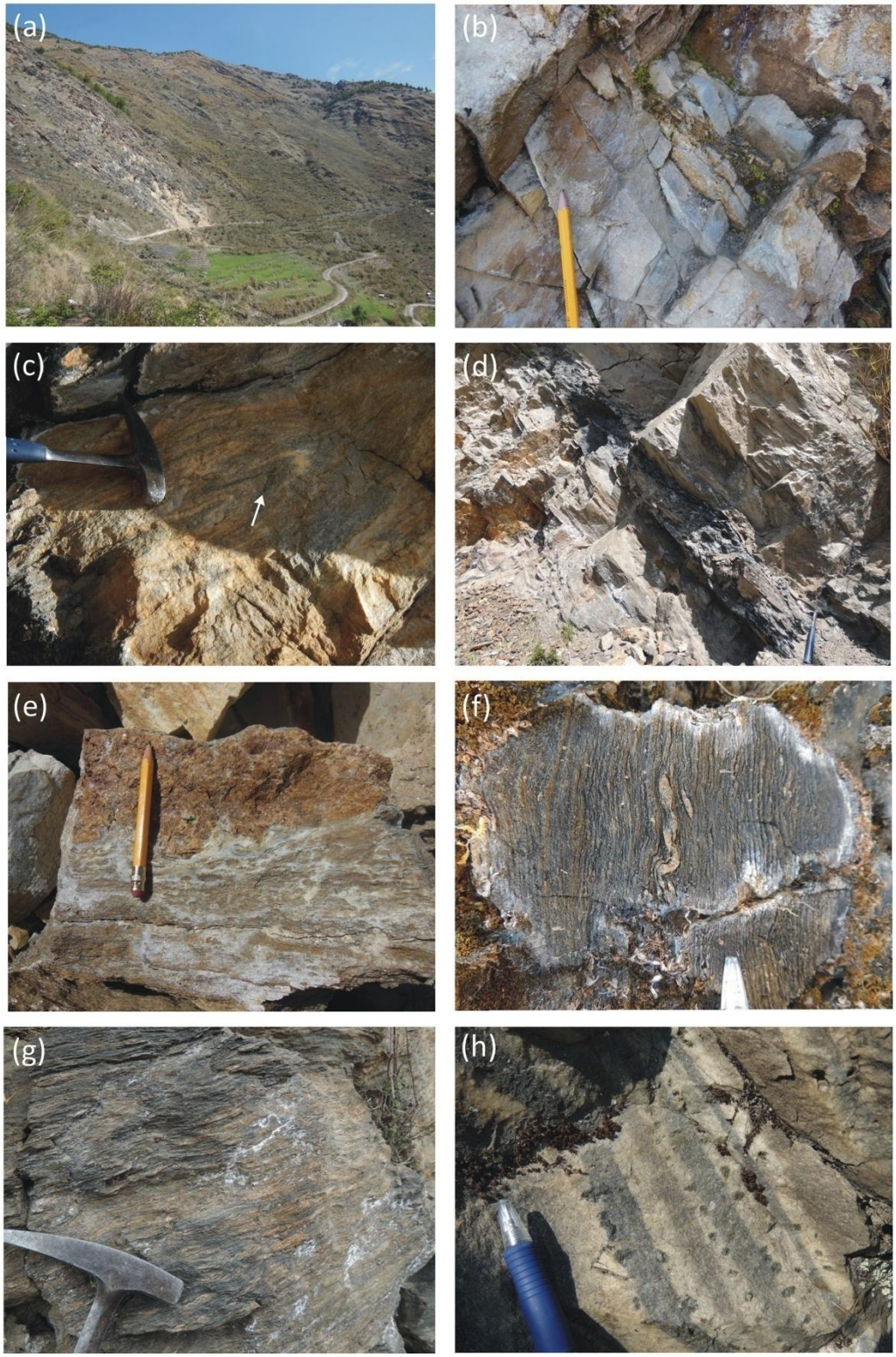

Fig. 4.2

4.3.1.2 CO_2-source rocks in the GHS

(i) As already pointed out by Rolfo et al. (2017) for eastern Nepal, CO_2-source rocks show two different ways of occurrence at different structural levels in the GHS: (i) in the L-GHS, CO_2-source rocks mostly occur as pluri-cm to dm- thick layers or massive boudins (Fig. 4.3e-g) enveloped by the main foliation of the host medium- to high-grade two-mica + garnet ± kyanite ± staurolite –bearing gneissic micaschist; (ii) in the structurally upward U-GHS, CO_2-source rocks mostly occur as tens to hundreds of meters thick layers intensively folded within the migmatitic gneiss (Fig. 4.3a,b). At the outcrop scale, the CO_2-source rocks more easy to be recognised are:

(ii) **Clinopyroxene + k-feldspar + plagioclase/scapolite/epidote ± quartz ± calcite ± amphibole calc-silicate granofels** (Fig. 4.3a,b,e,h). These rocks are commonly fine-grained and homogeneous, but banded structures locally occur at a pluri-mm to cm-scale, with domains rich in amphibole and/or clinopyroxene and domains depleted in these mineral phases. Calcite is sometimes present, locally constituting cm-thick horizons alternating to clinopyroxene-rich domains. This lithology is particularly abundant in the U-GHS, but it has also been observed in the upper structural levels of the L-GHS.

(iii) **Garnet + quartz + plagioclase + clinopyroxene/amphibole calc-silicate granofels** (Fig. 4.3f,g). The structure is granofelsic and the grain size is extremely variable, since some samples are fine-grained and homogeneous, with sub-mm porphyroblasts of red/pink garnet and green clinopyroxene/amphibole, while others are characterized by a coarse grain-size, with pluri-mm light red garnet porphyroblasts and cm- dark green amphibole set in a whitish quartz + plagioclase matrix. This lithology is typically banded at a centimetre to a decimetre scale, with bands consisting of the same mineral assemblage, but in different modal proportions. Carbonate is locally present, with the typical corroded aspect. Garnet and clinopyroxene are sometimes oxidized, assuming a brownish colour. This lithology is more common in the upper structural levels of the U-GHS, and generally form thin (dm-thick) layers.

Fig. 4.3 - Representative field occurrence of CO_2-source rocks in the GHS. (a,b) The upper Langtang valley (U-GHS) is characterized by a large volume of calc-silicate rocks, highly folded and deformed. In (b) the mountainside is several decametres high. **(c,d)** Biotite ± white mica –bearing gneisses and micaschists outcropping in the lower structural levels of the L-GHS in the Gosainkund and Langtang transects. These lithologies are CO_2-source rocks hardly recognizable on the field. **(e)** Massive boudin of calc-silicate rocks mainly consisting of green clinopyroxene, whitish quartz + plagioclase + scapolite ± carbonate and minor garnet (Gosainkund-Helambu transect). **(f)** Cm-thick layers of calc-silicate rocks consisting of green clinopyroxene, pink/red garnet and whitish quartz + plagioclase ± carbonate. (Gosainkund-Helambu transect). **(g)** Cm-thick layer of a calc-silicate rock in the Langtang region, with pink garnet, green clinopyroxene and white plagioclase + quartz. **(h)** Metre-thick layer of the CO_2-source rock type more common in the U-GHS and in the upper structural levels of L-GHS (Helambu region). The compositional banding is well-developed, with green clinopyroxene and white plagioclase concentrated in cm-thick bands.

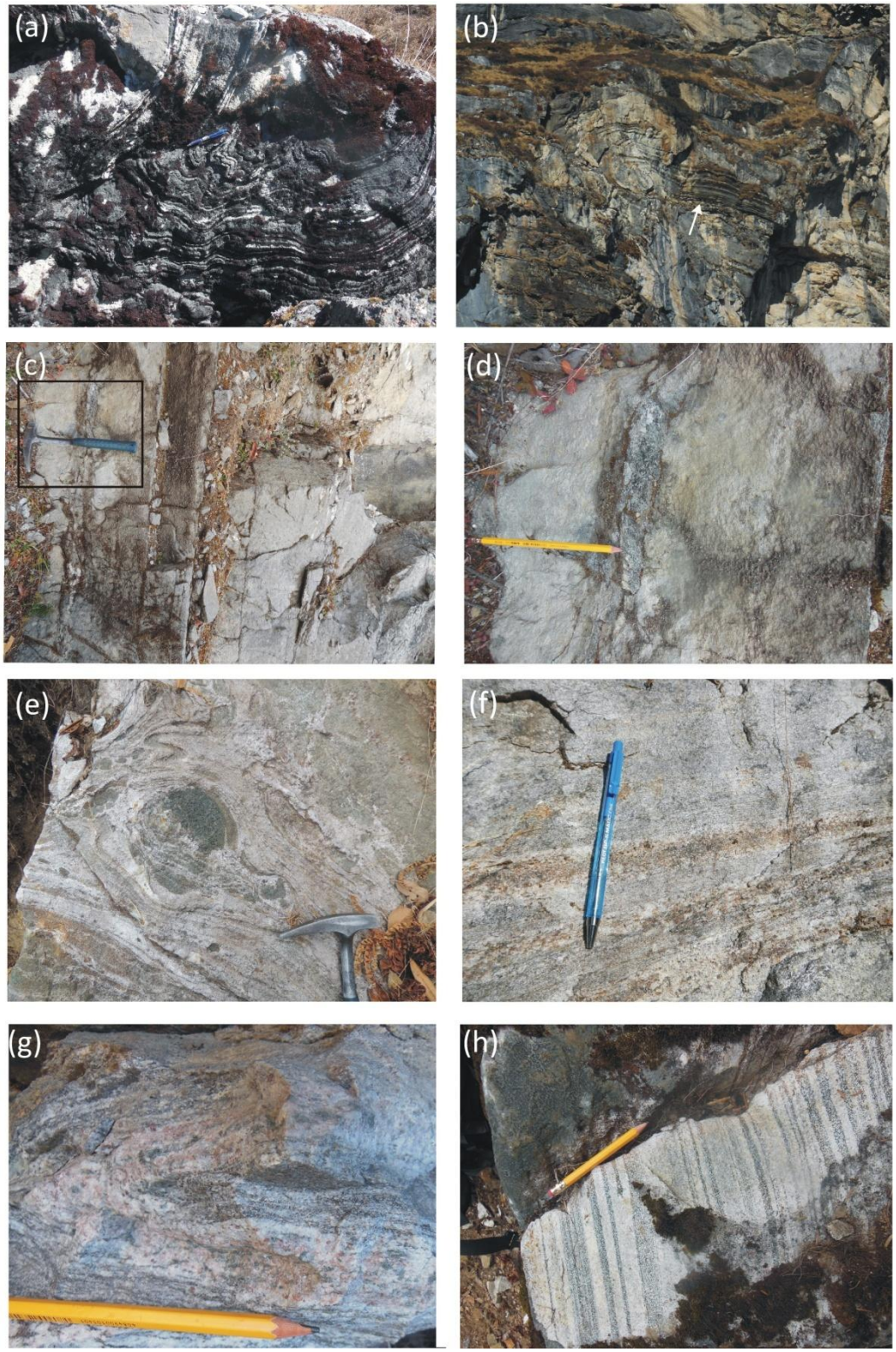

Fig. 4.3

Besides these easily identifiable lithologies, the GHS is also characterized by the occurrence of CO_2-source rocks which, at the outcrop scale, totally resemble common fine-grained two-mica gneisses or gneissic micaschists with porphyroblastic red garnet (Fig. 4.3c,d). In these lithologies (i.e. calcareous metapelites and their higher-grade equivalents), garnet can reach several mm in diameter, and pale green epidote is locally evident at the hand-sample scale. The recognition of these lithologies as CO_2-source rocks is possible only at the microscope, which allows the identification of various calc-silicate minerals (scapolite, green amphibole, ± clinopyroxene) ± calcite. It is therefore possible that these lithologies have been highly overlooked in the past studies.

The transition between the metapelite and the CO_2-source rocks is generally gradual, characterized by the progressive disappearance of biotite ± white mica and the gradual increase of calc-silicate minerals (clinopyroxene and garnet are the easiest ones to be identified in the outcrops).

4.3.2 Petrography of CO_2-source rocks

The different types of CO_2-source rocks are classified following Rolfo et al. (2017), with minor modifications according to the specific mineral assemblages observed in the study area. Three different groups have been recognized, and they can be described in terms of relatively complex chemical groups: (i) CFMAST-HC (CaO-FeO-MgO-Al_2O_3-SiO_2-TiO_2-H_2O-CO_2) group, (ii) NCFMAST-HC (Na_2O-CaO-FeO-MgO-Al_2O_3-SiO_2-TiO_2-H_2O-CO_2) group and (iii) NKCFMAST-HC (Na_2O-K_2O-CaO-FeO-MgO-Al_2O_3-SiO_2-TiO_2-H_2O-CO_2) group. The CFMAST-HC group is significantly more abundant in the U-GHS, while the NCFMAST-HC and NKCFMAST-HC groups occur in both the LHS and GHS (L-GHS and U-GHS); however, CO_2-source rocks belonging to these chemical groups occur as layers and/or boudins in the LHS and L-GHS, while they can reach a thickness of several hundred metres in the U-GHS.

In all the chemical groups, the main mineral assemblages vary from lower to upper structural levels, according to the increase in the metamorphic grade.

Among the CO_2-source rock types recognized by Rolfo et al. (2017), some of them have not been observed in the study area (i.e. CFMAST-HC: Type A; NKCFMAST-HC: Types D, E), while others have been added (i.e. the whole NCFMAST-HC group). In this section, the average petrographic features of each CO_2-source rock type are described; a more detailed microstructural description of the samples selected for the thermodynamic modelling is presented in Chapter 5.

4.3.2.1 CFMAST-HC group (group 1)

The different petrographic types are described from lower to upper structural levels.

(1A) Tremolite-bearing (clinopyroxene and garnet-absent) impure marbles

This lithology has not been observed in the study area, but has been recognized sporadically in eastern Nepal (Rolfo et al., 2017), as m-thick layers within the two-mica garnet ± staurolite ± kyanite -bearing schists of the L-GHS, and more rarely in the U-GHS. Beside calcite, these marbles are characterized by the presence of tremolite, often occurring as cm-long, slightly oriented, poikiloblasts locally replaced by aggregates of talc, and minor graphite.

(1B) Garnet + plagioclase ± amphibole ± epidote ± calcite –bearing (clinopyroxene -absent) calc-silicate rocks

In the study area this type of CO_2-source rocks occur as thin layers (cm- to dm-thick) intercalated in the micaschists of the L-GHS, and rarely in the quartzites of the upper structural levels of the LHS.

The main mineral assemblage consists of **quartz + garnet + plagioclase + epidote + titanite ± calcite ± amphibole**; mineral modes vary from sample to sample, but in general quartz and garnet are the most abundant phases. These rocks are generally fine-grained with porphyroblastic garnet, but in few cases quartz and plagioclase grain size also increases. The structure is generally granofelsic; a banded structure is locally observed, defined by alternating cm-thick layers consisting of plagioclase + quartz ± amphibole and minor garnet, and pluri-mm thick layers in which garnet becomes more abundant.

Garnet occurs as porphyroblasts (up to 3 mm in diameter) with a typical spongy appearance (Fig. 4.4a,b,d) due to numerous inclusions of quartz, plagioclase, calcite, ± epidote ± chlorite ± amphibole ± titanite. An exception is represented by sample 15-51c (from the LHS), in which garnet occurs as small idioblasts (up to 400 μm in diameter, Fig. 4.4e,f) including quartz, calcite, amphibole, graphite (± plagioclase?). Calcic **plagioclase** occurs as fine- to medium-grained crystals, varying from idioblastic to poikilitic/interstitial (in sample 15-51c); it includes rounded quartz and epidote (Fig. 4.4c). It is locally surrounded by a thin corona of albite (Fig. 4.4c) and replaced along fractures by clay minerals, white mica and/or calcite. Rare **K-feldspar** is locally included in garnet. **Epidote** modal amount is highly variable; it can be almost absent (i.e. in sample 14-58b it is only found included in plagioclase), or significantly abundant (i.e. in sample 14-74b and 15-51c). It is generally fine-grained, but it can locally reach ~1 mm in length. Epidote is included in garnet and plagioclase porphyroblasts; in the matrix, it is generally surrounded by a discontinuous plagioclase corona. Epidote may show a concentric

zonation, and it rarely has an allanitic core. **Amphibole** habit varies from relatively idioblastic to spongy/poikilitic to radiated (Fig. 4.4e,f); grain size is highly variable, from sub-mm to ~1 cm in length (in the radiated varieties). Amphibole is locally included in garnet porphyroblasts; in the matrix it is partly replaced by plagioclase. In sample 14-51c, cm-thick amphibole aggregates overgrow the other mineral phases; these aggregates consist of radiated amphibole and minor fine-grained garnet idioblasts, epidote and calcite. In all the samples, amphibole is strongly pleochroic (from almost colourless to pale green/jade green). **Chlorite** is locally found included in garnet (Fig. 4.4b,d); in the matrix it replaces amphibole and garnet. **Quartz** habit and grain size vary from granoblastic and fine-grained to anhedral and medium-grained with undulose extinction; in sample 14-74b, which is slightly deformed, quartz grains are elongated parallel to the shear planes. **Calcite** mainly occurs as inclusions within garnet porphyroblasts (Fig. 4.4b), with corroded and lobate margins; in the matrix, it occurs either in small granoblasts in equilibrium with the other mineral phases, or replacing epidote and plagioclase. **Titanite** is abundant and generally fine-grained, but it can locally reach ~800 μm (e.g. in sample 14-74b). It is included in all the phases and it locally includes quartz and opaques. **Graphite** is present in almost all the samples of this group, but in variable modal amounts (e.g. almost absent in samples 14-74b and 15-05, very abundant in sample 14-58b and 15-51c). Graphite forms randomly oriented flakes located at the grain-boundaries of the main mineral phases; it is locally included in garnet (Fig. 4.4d).

The transition from the calc-silicate rock to the host paragneiss is generally gradual; it is characterized by a decrease in the plagioclase, garnet and epidote content and a gradual increase in biotite and/or white mica modal amounts (Fig. 4.4d). Locally, graphite increases at the contact calc-silicate/gneiss.

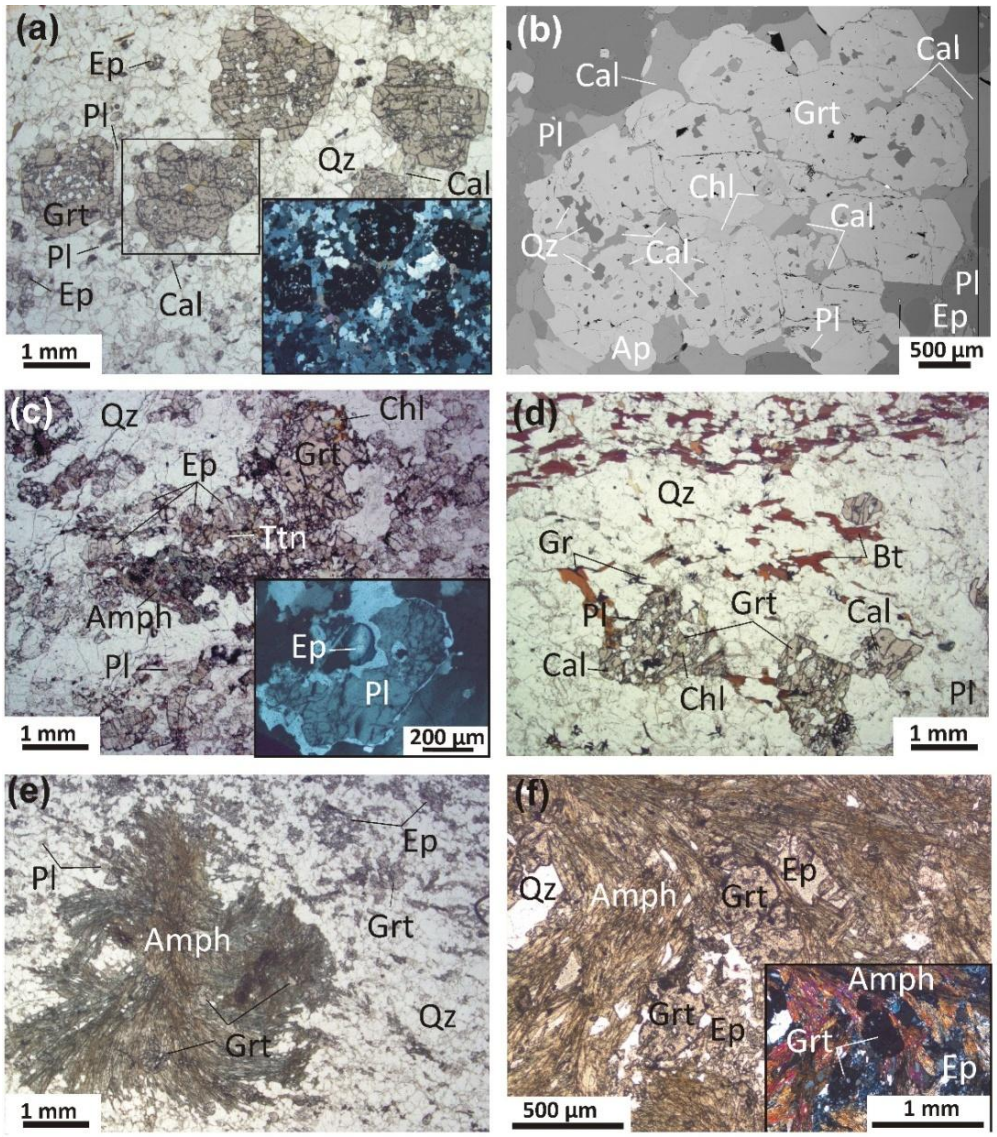

Fig. 4.4 – Representative microstructures of Type 1B CO_2-source rocks. Sample 15-05. **(a, b**) Garnet porphyroblasts with spongy appearance due to numerous inclusions of quartz, calcite, plagioclase and chlorite. Garnet is in equilibrium with calcite in the matrix (straight contacts in (b)) (a: PPL and XPL; b: BSE). Sample 14-74b. **(c)** Quartz + plagioclase + garnet + amphibole calc-silicate rock. Amphibole locally includes epidote (PPL). The inset shows Ca-rich plagioclase and epidote both rimmed by a Na-rich plagioclase (XPL). Sample 14-58b. **(d)** Gradual transition from biotite + garnet -bearing gneissic micaschist and quartz + plagioclase + garnet + calcite + amphibole calc-silicate rock; the transition is marked by a decrease in biotite and an increase in garnet, quartz, and plagioclase (PPL). Garnet porphyroblasts include calcite + chlorite + quartz. Sample 15-51b **(e, f)** Quartz + plagioclase + amphibole + epidote + garnet + calcite calc-silicate rock, in which radiated aggregates of amphibole (+ garnet + epidote) overgrow the matrix minerals (e: PPL; f: PPL and XPL).

(1C) Garnet + clinopyroxene + plagioclase ± epidote ± calcite –bearing calc-silicate rocks

This type of CO_2-source rocks occurs as dm-thick boudins in the GHS. The structure is typically banded, with dm-thick garnet-rich and clinopyroxene-poor discontinuous

domains, alternated to cm-thick clinopyroxene-rich and garnet-poor discontinuous domains (Fig. 4.5a,b,e). The main mineral assemblage consists of **garnet + clinopyroxene + plagioclase + quartz + titanite ± calcite ± epidote** in both layers. The grain size is fine to coarse; some samples are homogeneously fine-grained except for quartz, which has an extremely variable grain size and occurs as large poikilitic crystals (up to 6 mm) at the contact with the host metapelite. Other samples are more heterogeneous, with garnet and clinopyroxene porphyroblasts being coarse-grained and reaching 3 mm in size, while quartz, plagioclase and epidote vary from sub-mm to 1 mm. **Garnet** porphyroblasts include quartz + clinopyroxene + plagioclase ± epidote ± chlorite ± calcite and minor titanite ± amphibole; they have locally a spongy appearance, being intimately intergrown with quartz ± epidote ± calcite ± clinopyroxene ± plagioclase (Fig. 4.5c,d). **Clinopyroxene** granoblasts occurring in the matrix are locally slightly zoned and partially replaced by garnet. **Amphibole** is mostly a retrograde mineral, except for the rare inclusions in garnet and/or clinopyroxene, which are interpreted as relics of the prograde assemblage. The late green amphibole is generally associated with epidote and calcite and grows at the expenses of clinopyroxene. **Calcite** in the matrix is rare, and related to the retrograde evolution (Fig. 4.5c). **Epidote** is found either intimately intergrown with garnet (Fig. 4.5e) and locally included in plagioclase, or more frequently associated with amphibole and calcite as a retrograde phase replacing clinopyroxene and plagioclase. It locally includes chlorite. Among accessory minerals, titanite is ubiquitous and tourmaline is locally observed. **Titanite** is abundant both in the matrix and included in garnet and clinopyroxene. **Tourmaline** is strongly pleochroic (beige/brown). Sample 14-53b from the upper structural levels of the L-GHS (Fig. 4.5e) differs from the common CFMAST-HC Type C rocks being characterized by the presence of dark orange garnet, brilliant dark green clinopyroxene (oxidized along fractures) and abundant epidote, likely reflecting high content of Fe^{3+} in the bulk composition. The transition from the calc-silicate rock to the host biotite + garnet -bearing gneiss is characterized by a progressive decrease in garnet modal amount and size, a progressive disappearance of titanite, clinopyroxene and amphibole and a progressive appearance and modal increase of biotite.

Fig. 4.5 – (a-e) Representative microstructures of Type 1C CO_2-source rocks. Sample 14-44c. **(a, b)** Clinopyroxene-rich domains (a) alternate to clinopyroxene-poor domains (b) (PPL, XPL). **(c,d)** Garnet porphyroblasts replacing clinopyroxene showing lobate margins (c), and calcite, chlorite and plagioclase (d) (XPL). Amphibole + calcite + epidote in (c) are retrograde phases. Sample 14-53b. **(e)** Garnet-rich domain in which garnet porphyroblasts have a spongy appearance and are intimately intergrown with epidote (PPL). The inset shows a clinopyroxene-rich domain in the same sample (PPL). All the mineral phases are highly coloured due to high amounts of Fe^{3+}. **(f-h) Representative microstructures of Type 1D CO_2-source rocks.** Sample 14-53a. (f-h). Clinopyroxene-rich domains (f) alternates to clinopyroxene-poor domains (g) (PPL, XPL). In (h) clinopyroxene porphyroblasts show equilibrium contacts with plagioclase and quartz (PPL). Small dark green amphibole crystals grow at the clinopyroxene rim.

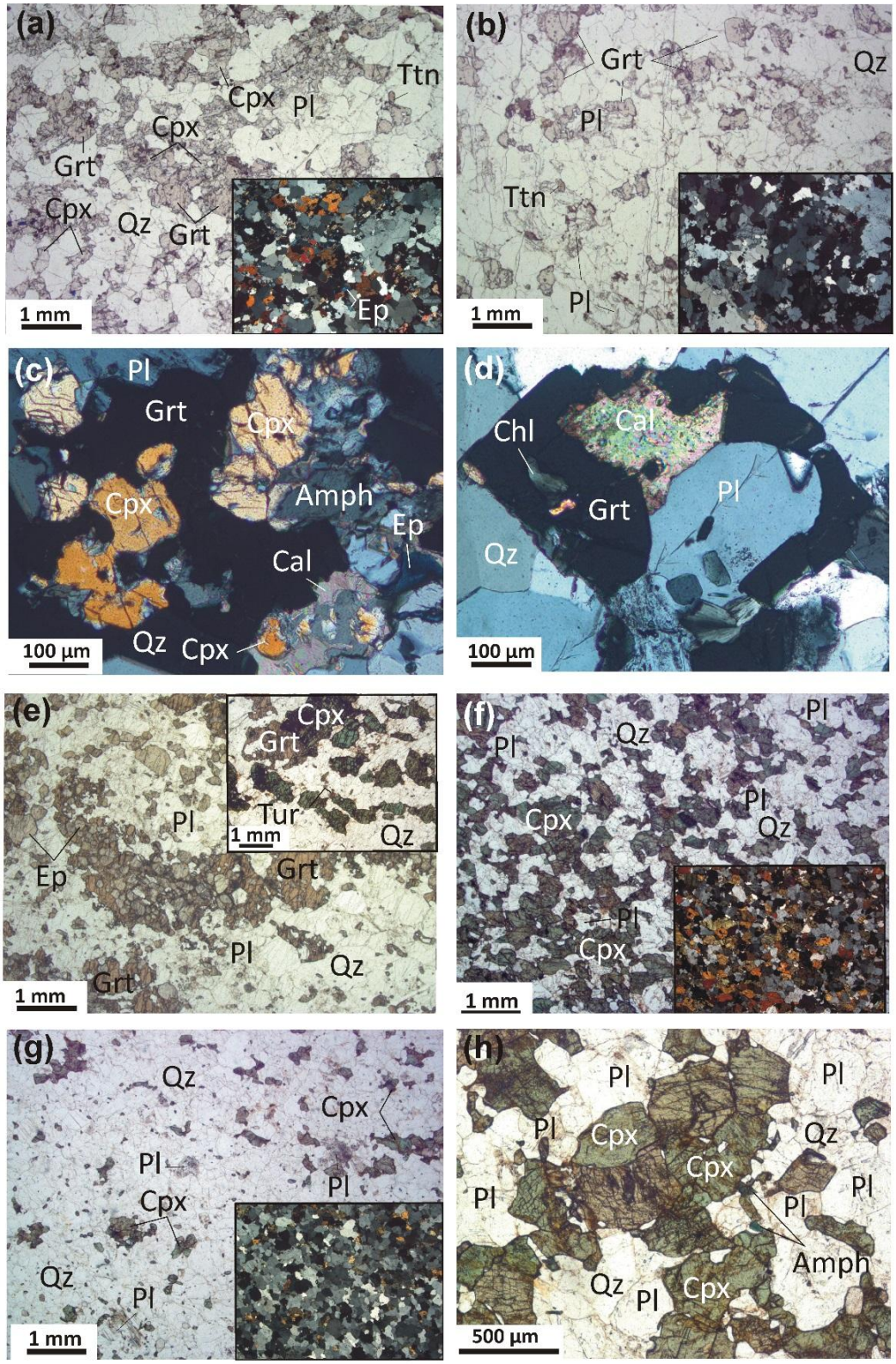
(a)
Ttn
Cpx
Pl
Cpx
Grt
Cpx
Qz
Grt
Ep
1 mm
(b)
Grt
Qz
Pl
Ttn
Pl
1 mm
(c)
Pl
Grt
Cpx
Cpx
Amph
Ep
Cal
Qz
Cpx
100 µm
(d)
Chl
Cal
Pl
Grt
Qz
100 µm
(e)
Cpx
Grt
Tur
1 mm
Qz
Pl
Ep
Grt
Pl
Qz
1 mm
Grt
(f)
Pl
Pl
Qz
Pl
Cpx
Qz
Pl
Cpx
1 mm
(g)
Qz
Cpx
Pl
Pl
Cpx
Qz
Pl
1 mm
(h)
Pl
Pl
Pl
Cpx
Qz
Cpx
Pl
Pl
Pl
Amph
Qz
Pl
Cpx
500 µm

Fig. 4.5

(1D) Clinopyroxene + plagioclase -bearing (garnet-absent) calc-silicate rocks

These calc-silicate rocks are locally observed in the GHS, as pluri-dm thick layers intercalated in the host biotite + garnet ± k-feldspar ± sillimanite ± kyanite metapelites, locally associated with Type 1C (CFMAST-HC group), Type 2A (NCFMAST-HC group) and Type 3F (NKCFMAST-HC group). The structure is homogeneously fine-grained and banded, with mm-to cm-thick alternated domains showing the same mineral assemblages but different mineral modes. Specifically, the different domains are alternatively clinopyroxene-rich and clinopyroxene-poor (Fig. 4.5f,g). The mineral assemblage consists of clinopyroxene, plagioclase and quartz, with accessory titanite.

Clinopyroxene locally includes quartz, titanite and plagioclase. Plagioclase core is often replaced by fine-grained white mica. Bluish-green very fine-grained amphibole locally develops at the expenses of clinopyroxene porphyroblasts, along cleavages and at the grain boundaries (Fig. 4.5h); a prograde generation of amphibole is also locally included in clinopyroxene porphyroblasts.

4.3.2.2. NCFMAST-HC group (group 2)

The different petrographic types are described from lower to upper structural levels.

(2A) Garnet + clinopyroxene + scapolite + calcite –bearing calc-silicate rocks

This lithology is not abundant, and occurs as pluricm-thick layers and boudins in the GHS, locally associated to Type 1C and 1D (CFMAST-HC group), and Type 3F (NKCFMAST-HC group).

The structure is typically banded, with pluri-mm thick clinopyroxene-rich, garnet-poor, scapolite-absent bands at the contact with the host metapelite (Fig. 4.6a), and cm-thick garnet + calcite-rich domains alternating with pluri-cm thick scapolite + plagioclase-rich, clinopyroxene-poor domains (Fig. 4.6f,g). Grain size is fine-to coarse proceeding from the host metapelite to the centre of calc-silicate layer/boudin. **Garnet** porphyroblasts (up to 3 mm in diameter) have a spongy appearance, being intergrown with calcite, plagioclase, quartz ± scapolite (Fig. 4.6c-e); garnet locally includes also titanite, chlorite, epidote and clinopyroxene. **Clinopyroxene** (up to 2 mm in length) is locally oxydized along fractures or replaced by amphibole + calcite + epidote. **Scapolite** can be either fine-grained and in equilibrium with the other mineral phases, or it constitutes large porphyroblasts (up to 5 mm in length) locally intergrown with garnet (Fig. 4.6c) and including epidote, clinopyroxene and quartz (± plagioclase?). Scapolite is locally replaced by a plagioclase corona at the rim. **Plagioclase** is fine- to coarse-grained, reaching 6 mm in length. When it develops large porphyroblasts, it has a poikiloblastic habit, including all the other mineral

phases (Fig. 4.6b,f,g). In these cases it is also extremely zoned, with a core richer in anorthite and an irregular sub-mm Na-richer rim. **Calcite** is generally intergrown with garnet (Fig. 4.6d,e); locally, it is concentrated in calcite-rich layers where it develops porphyroblasts with a granoblastic texture.

Some samples belonging to this petrographic type are Fe-rich, being both garnet and clinopyroxene strongly coloured (garnet: deep pink; clinopyroxene: deep green).

(2B) Calcite + clinopyroxene + scapolite + epidote (garnet –absent) impure marbles

This lithology is not abundant and occurs as pluri-dm layers in the GHS; it generally occurs as layers intercalated in the most-common Type 3F (NKCFMAST-HC group). The structure is granoblastic and relatively homogeneous (Fig. 4.6h,i), with the main minerals being sub-mm in size except for scapolite, which occurs as millimetric porphyroblasts. **Calcite** is the predominant mineral phase; it occurs either in the matrix in equilibrium with scapolite, clinopyroxene and quartz, or associated to epidote + amphibole and scapolite + epidote as a retrograde phase replacing clinopyroxene and plagioclase, respectively. Relict prograde calcite is locally included in scapolite. **Scapolite** porphyroblasts include clinopyroxene, titanite, quartz and minor calcite; it locally replaces plagioclase together with epidote and calcite (Fig. 4.6i). Scapolite is locally rimmed by an epidote corona. **Clinopyroxene** is partly replaced by amphibole + calcite. **Plagioclase** is not abundant, and always rimmed by epidote + calcite ± scapolite; it includes scapolite and quartz. **Epidote** occurs as plagues replacing scapolite, clinopyroxene and plagioclase. **Quartz** is rare.

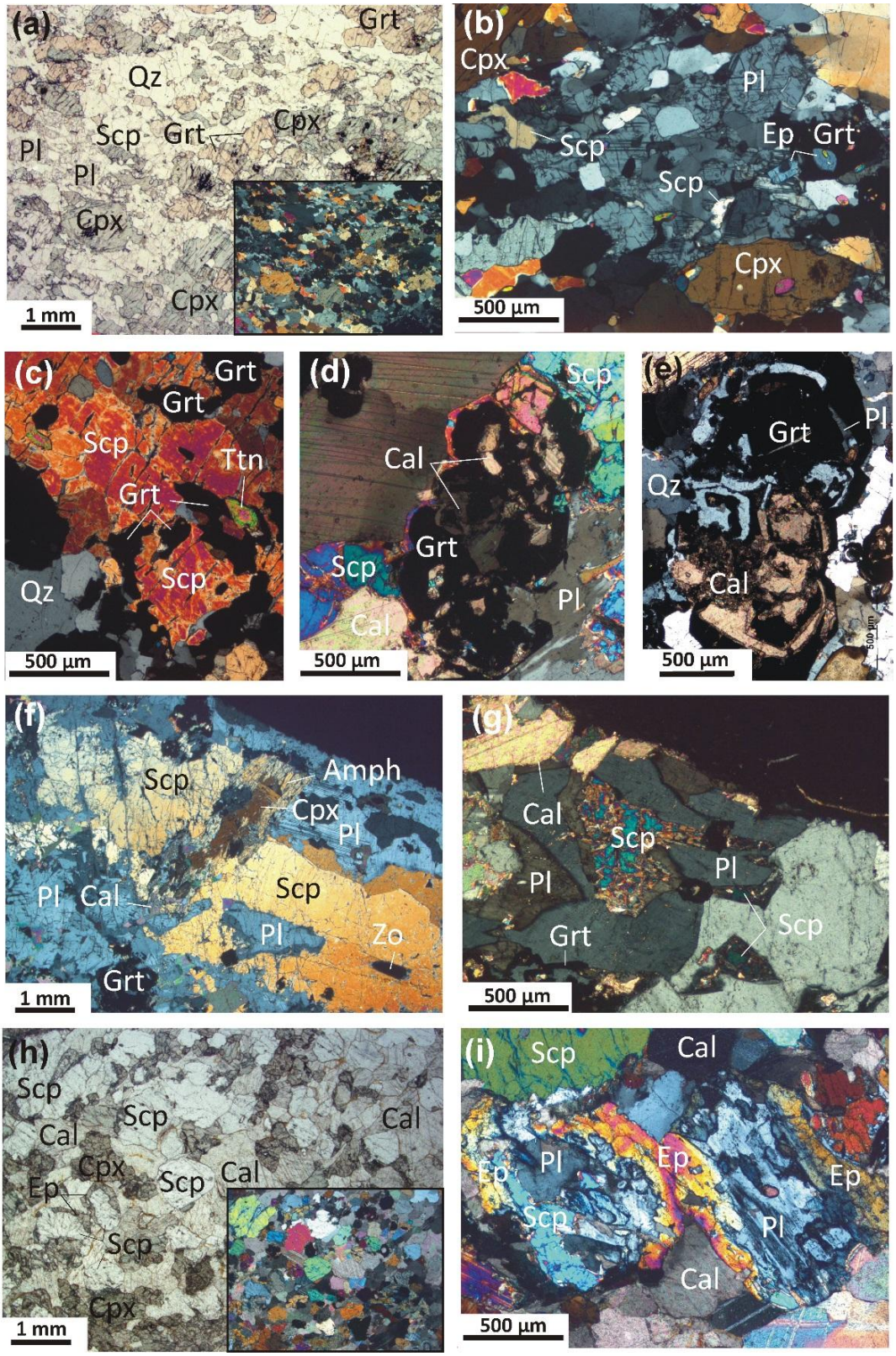
(a)
Grt
Qz
Scp
Grt
Cpx
Pl
Pl
Cpx
Cpx
1 mm
(b)
Cpx
Pl
Scp
Ep
Grt
Scp
Cpx
500 µm
(c)
Grt
Grt
Scp
Ttn
Grt
Qz
Scp
500 µm
(d)
Scp
Cal
Grt
Scp
Pl
Cal
500 µm
(e)
Pl
Grt
Qz
Cal
500 µm
(f)
Scp
Amph
Cpx
Pl
Pl
Cal
Scp
Pl
Zo
Grt
1 mm
(g)
Cal
Scp
Pl
Pl
Grt
Scp
500 µm
(h)
Scp
Scp
Cal
Cal
Cpx
Scp
Cal
Ep
Scp
Cpx
1 mm
(i)
Scp
Cal
Ep
Pl
Ep
Ep
Scp
Pl
Cal
500 µm

Fig. 4.6

Fig. 4.6 – (a-g) Representative microstructures of Type 2A CO_2-source rocks. Sample 15-53d. **(a)** Alternating garnet-rich, clinopyroxene-poor domains (top of the picture) and clinopyroxene-rich, garnet-poor domains (bottom) (PPL, XPL). **(b)** Plagioclase is poikiloblastic and zoned and it includes scapolite (XPL). **(c)** Garnet porphyroblasts are intimately intergrown with scapolite (XPL). Sample 14-21**. (d,e)** Garnet porphyroblasts are intimately intergrown with calcite, scapolite, quartz and plagioclase (XPL). **(f,g)** Detail of a scapolite and plagioclase-rich, clinopyroxene-poor domain. scapolite and plagioclase are coarse-grained; amphibole replaces clinopyroxene (XPL). Plagioclase is extremely zoned. **(h-i) Representative microstructures of Type 2B CO_2-source rocks.** Sample 14-20a. Impure marble (PPL, XPL). Plagioclase is not abundant and it is replaced by scapolite and a later epidote corona (i).

4.3.2.3 NKCFMAST-HC group (group 3)

The following petrographic types can be observed from lower to upper structural levels:

(3A) White mica/phlogopite ± tremolite –bearing impure marbles

These marbles occur as dm- to pluri-m thick layers in the upper structural levels of the LHS, locally associated to Type 3B of the same group.

They are generally homogeneously fine-grained, with sporadic calcite crystals larger in size. They always show an oriented structure, defined by the alignment of white mica and/or phlogopite concentrated in discontinuous sub- to mm-thick domains. A compositional layering (parallel to the main foliation) may occur, with alternated cm-thick calcite-rich and quartz-poor domains and calcite-poor, quartz-rich domains (Fig. 4.7a,b). Millimetric coarse-grained quartz + ankerite layers are present. Minor tremolite, graphite and plagioclase are also locally present in the mineral assemblage; tremolite is skeletal and oriented parallel to the main foliation (Fig. 4.7b). Accessory tourmaline and opaques are present.

(3B) White mica ± biotite/phlogopite + calcite ± epidote –bearing carbonatic phyllites and calcschists

These rocks crop out as dm-thick layers in the upper structural levels of the LHS. They are characterized by a mixture of silicates and carbonates in variable proportions, consisting of quartz, plagioclase, white mica, biotite/phlogopite and calcite (Fig. 4.7c-e). The structure is characterized by a well-developed schistosity, defined by white mica ± biotite/phlogopite lepidoblasts in sub-mm continuous domains, alternated to quartz ± plagioclase domains, with a variable amount of calcite. Relict ankerite may locally occur.

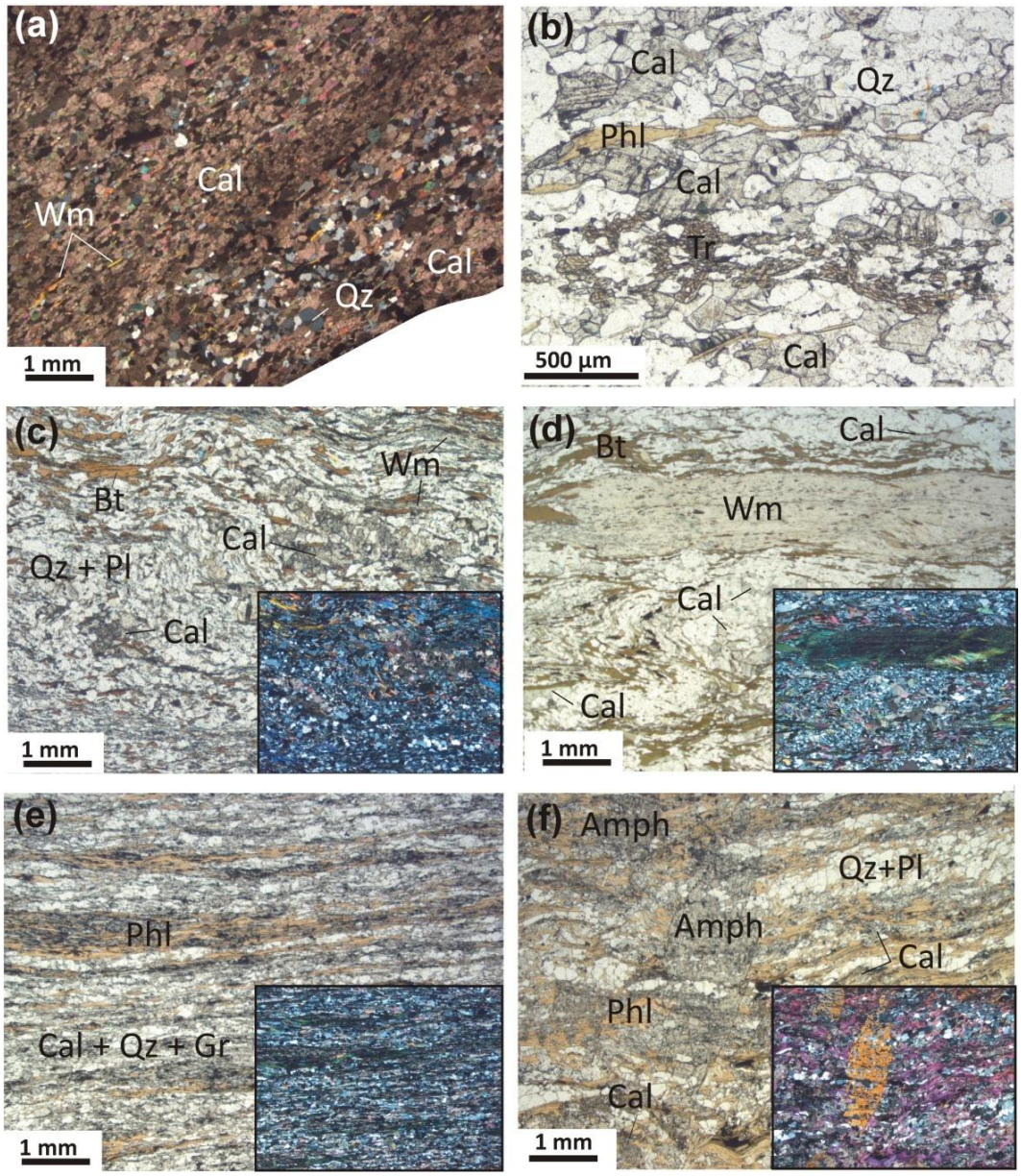

Fig. 4.7 – (a, b) Representative microstructures of Type 3A CO_2-source rocks. Sample 14-30. **(a)** White mica-bearing marble (XPL)**.** Sample 15-13. **(b)** Phlogopite + tremolite-bearing impure marble (PPL). In both (a) and (b), quartz-rich mm-thick domains define a compositional banding parallel to the main foliation defined by white mica ± phlogopite ± Tr. **(c-f) Representative microstructures of Type 3B CO_2-source rocks.** Sample 15-09:c; Sample 15-13b:d; Sample 15-11:e.(c-e) Carbonate-bearing biotite ± white mica –bearing phyllitic micaschists and calcschists with variable amounts of the main mineral phases (PPL, XPL). Biotite has different colours, from brownish orange (c), to greenish brown (d), to slightly coloured, beige phlogopite (e). Graphite is also present in different modal amounts. Sample 15-28. (f) Layer of phlogopite -bearing carbonatic phyllite with coarse-grained amphibole porphyroblasts statically overgrowing the main schistosity (PPL, XPL).

Slightly coloured **phlogopite** prevails over biotite; however, **biotite** with a peculiar greenish-brown pleochroism locally occur in the carbonatic phyllites (Fig. 4.7d). Tourmaline, graphite, opaques and minor rutile and epidote occur as accessory mineral phases. Epidote presents sometimes an allanitic core.

Rare phlogopite –bearing carbonatic phyllites with porphyroblastic amphibole are locally associated to this type of CO_2-souce rocks (Fig. 4.7f). Amphibole is colourless (tremolite) and occurs as large skeletal porphyroblasts (up to 4 mm in length) overgrowing the main foliation defined by phlogopite lepidoblasts.

(3C) White mica + biotite + garnet + epidote/scapolite/plagioclase ± calcite ± amphibole (k-feldspar and clinopyroxene –absent) gneissic micaschists and gneisses

This lithology is not commonly observed, probably because at the outcrop scale it resembles a common biotite ± white mica + garnet –bearing micaschist or gneiss. In the study area it occurs as dm- to m-thick layers intercalated in the lower structural levels of the L-GHS. These rocks are fine- to medium-grained, with a more or less well-developed schistosity defined by biotite ± white mica concentrated in discontinuous mm-thick domains together with quartz ± garnet, alternating with pluri-mm thick quartz + scapolite + plagioclase ± garnet domains (Fig. 4.8a-c). The modal amount of white mica is extremely variable: in two-mica gneissic micaschists its amount is comparable to that of biotite, but in the majority of the samples biotite is predominant over white mica (Fig. 4.8b,c).

The main mineral assemblage consists of biotite + white mica + garnet + quartz + plagioclase + scapolite + epidote/clinozoisite ± calcite ± amphibole + accessory titanite. **Garnet** porphyroblasts (up to 4 mm in diameter) have a skeletal habit (Fig. 4.8b-d) and include rounded quartz, calcite, zoizite, plagioclase and minor biotite, white mica and chlorite. **Scapolite** may include rounded epidote (Fig. 4.8e), quartz, biotite and plagioclase; it is often replaced by a plagioclase ± calcite corona (Fig. 4.8f). **Plagioclase** in the matrix may occur as fine-grained granoblasts (< 1 mm in size) with a multitude of rounded quartz inclusions, locally overgrowing the main foliation and including biotite flakes and minor epidote, or as zoned crystals that probably derive from the replacement of former scapolite (Fig. 4.8f). **Epidote** in the matrix is locally abundant, showing a concentric zoning. **Biotite** often shows a peculiar greenish-brown pleochroism. **Amphibole** is pale green; it occurs in cm-thick layers with a skeletal habit, locally including biotite and epidote. **Calcite** in the matrix is rare, and mostly associated to plagioclase replacing scapolite, or replacing garnet rims and amphibole where present. **Titanite** is common as accessory mineral.

(3C*) Biotite + garnet + carbonate + amphibole ± plagioclase (k-feldspar, scapolite and clinopyroxene –absent) gneissic micaschists

This lithology, occurring as dm- to m-thick layers intercalated in the upper structural levels of the LHS (LHS-RTS unit), is not commonly observed. It is considered as a different variety of the 3C CO_2-source rock type (3C*), because the mineral assemblage is similar but the modal proportions of mineral phases are very different from the more common 3C Type. Specifically, femic minerals (biotite, garnet and amphibole) are much more abundant, whereas Na-rich phases (plagioclase) are significantly less abundant, probably reflecting primary difference in the protolith composition. These rocks are fine- to medium-grained, with a schistosity defined by biotite ± amphibole concentrated in discontinuous mm-thick domains, alternated to quartz ± plagioclase domains (Fig. 4.8g,h). The main mineral assemblage consists of biotite + garnet + quartz + carbonate + amphibole + accessory ilmenite and rare plagioclase. Porphyroblastic **garnet** (up to several mm in diameter) is present in both the layers; it includes quartz, ilmenite, carbonate, biotite and minor plagioclase, apatite and chlorite. It is locally zoned, with a dark pink core and a lighter rim (Fig. 4.8h). **Biotite** is dark brown and occurs both as inclusion in garnet and in the matrix; it is generally fine-grained, but locally some lepidoblasts at garnet contact have larger size and may include amphibole. **Amphibole** is rarely included in garnet while it is abundant in the matrix, where it constitutes mm-thick discontinuous layers with calcite + biotite and minor quartz and plagioclase. Amphibole is dark green to colourless, and locally zoned. **Carbonate** is included in both garnet core and rims, with corroded margins; in the matrix it is more abundant in the amphibole-rich layers, and it is in equilibrium with both amphibole and biotite. **Plagioclase** is rare, both in garnet and in the matrix. **Ilmenite** is abundant, both as inclusion in garnet, where it occurs as fine-grained iso-oriented crystals or as larger crystals which include biotite, calcite and quartz, and in the matrix.

Fig. 4.8 – (a-f) Representative microstructures of Type 3C CO_2-source rocks. Sample 14-38a. **(a)** Biotite + white mica –bearing gneissic micaschist, with porphyroblastic garnet. scapolite occurs in pluri-cm thick domains (PPL, XPL). The inset shows location of (e). Sample 15-47:b; Sample 15-46:c. **(b,c)** The main gneissic schistosity is mainly defined by biotite lepidoblasts. garnet occurs as large skeletal porphyroblasts with numerous inclusions, mostly of quartz (PPL, XPL). Amphibole is locally present. **(d)** Detail of a garnet porphyroblast with rounded quartz + calcite + zoisite inclusions (XPL). Sample 14-38a:e; Sample 15-46:f. **(e,f)** Scapolite includes rounded quartz and epidote (e), and it is partly replaced by a zoned plagioclase + calcite corona (XPL). **(g-h) Representative microstructures of Type 3C* CO_2-source rocks.** Sample 15-26c. (g) The main schistosity is defined by biotite + amphibole. Garnet porphyroblasts are full of inclusions, mainly ilmenite, quartz, biotite and carbonate (PPL). (h) Detail of the alternation of biotite-rich domains and amphibole + calcite domains. Note the zoned garnet porphyroblast (bottom left) (PPL).

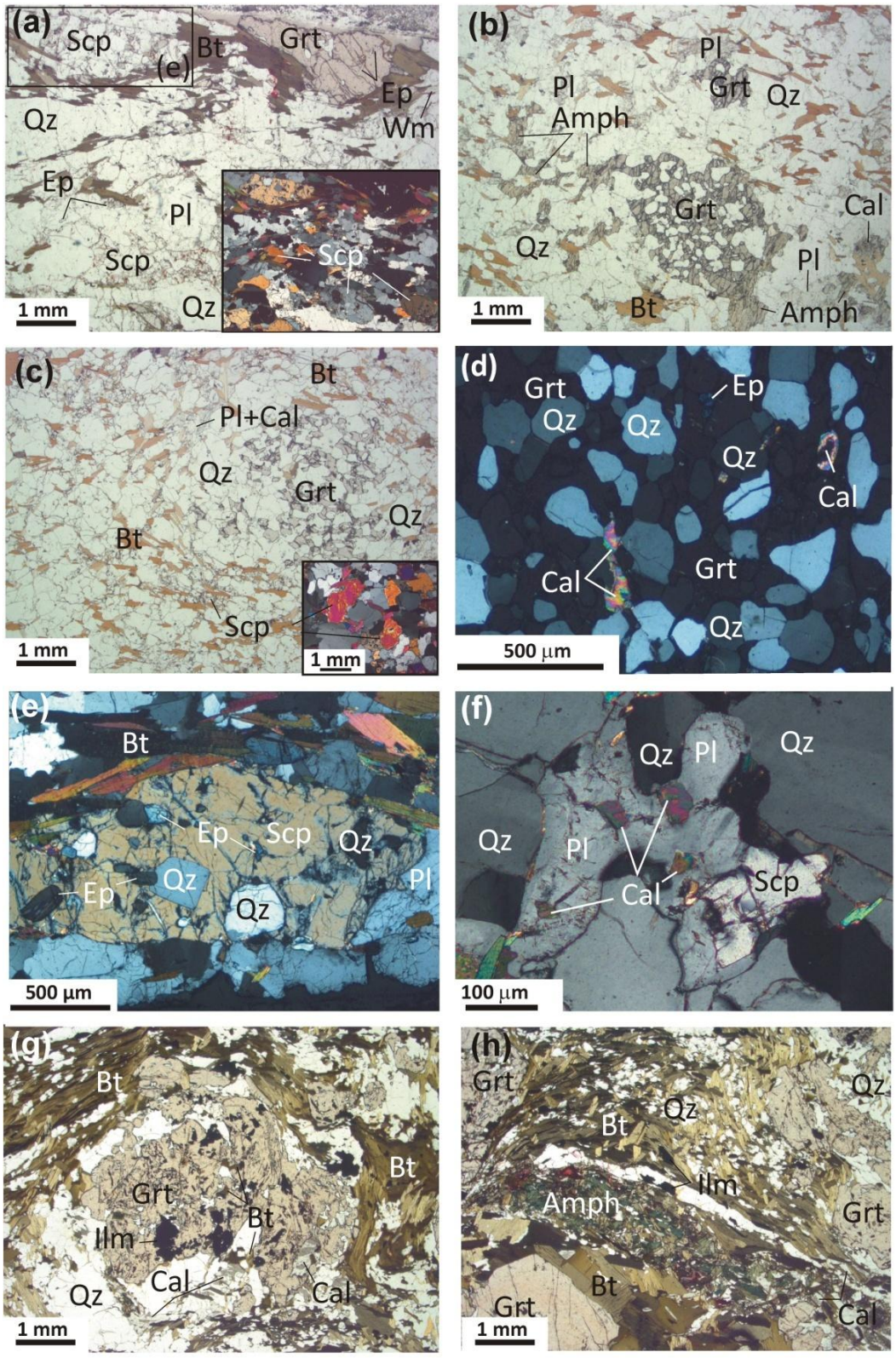
(a)
Scp
Bt
(e)
Grt
Ep
Wm
Qz
Ep
Pl
Scp
Scp
Qz
1 mm
(b)
Pl
Pl
Grt
Qz
Amph
Grt
Cal
Qz
Pl
Bt
Amph
1 mm
(c)
Bt
Pl+Cal
Qz
Grt
Qz
Bt
Scp
1 mm
1 mm
(d)
Grt
Ep
Qz
Qz
Qz
Cal
Cal
Grt
Qz
500 µm
(e)
Bt
Ep
Scp
Qz
Ep
Qz
Pl
Qz
500 µm
(f)
Qz
Pl
Qz
Qz
Pl
Cal
Scp
100 µm
(g)
Bt
Bt
Grt
Bt
Ilm
Qz
Cal
Cal
1 mm
(h)
Grt
Qz
Bt
Qz
Ilm
Amph
Grt
Bt
Grt
Cal
1 mm

Fig. 4.8

(3D) Biotite/k-feldspar + scapolite/plagioclase –bearing (garnet- and clinopyroxene - absent) calc-silicate gneisses

This lithology has not been observed in the study area, but has been recognized sporadically in eastern Nepal (Rolfo et al., 2017), as m-thick layers often associated with Type 3E (NKCFMAST-HC group).

(3E) Biotite/k-feldspar + scapolite/plagioclase/epidote + amphibole + clinopyroxene – bearing (garnet-absent) calc-silicate gneisses

This lithology has not been observed in the study area, but has been recognized sporadically in eastern Nepal (Rolfo et al., 2017), as m-thick layers often associated with Type 3D (NKCFMAST-HC group). The occurrence of amphibole in equilibrium with clinopyroxene and epidote/plagioclase is the most common feature of this calc-silicate rock type.

(3F) K-feldspar + scapolite/plagioclase/epidote + clinopyroxene ± calcite ± biotite – bearing (garnet-absent) calc-silicate gneisses and granofels

This lithology is the most abundant of the NKCFMAST-HC group; these calc-silicate rocks mostly occur as ten to hundred ms-thick layers intercalated in the migmatites of the U-GHS; however, the same lithology is also rarely observed in the upper structural levels of the L-GHS, as boudins enveloped by the host metapelites. In the study area they are locally associated to Types 2A and 2B (NCFMAS-HC group) and to Types 1C and 1D (CFMAS-HC group).

The structure is typically banded, with the repetition of pluri-cm calcite-rich domains (locally grading to impure marbles, Fig. 4.9b) with pluri-cm thick calcite-poor domains (Fig. 4.9a). The main mineral assemblage consists of k-feldspar + clinopyroxene + scapolite + plagioclase ± quartz ± calcite ± biotite, accessory titanite and retrograde epidote ± calcite ± amphibole replacing scapolite and clinopyroxene porphyroblasts. **Clinopyroxene** includes relict biotite and amphibole + calcite + quartz with corroded margins in the core (Fig. 4.9c,d), while inclusions of scapolite, k-feldspar, quartz and titanite mostly occur in the rims of the porphyroblasts. **Scapolite** is also found included in plagioclase and k-feldspar; in the matrix it is locally replaced by symplectitic epidote + calcite + quartz intergrowths (Fig. 4.9f), or by epidote coronas. **Plagioclase** is rarely preserved as inclusion in scapolite; in the matrix it is often replaced by a epidote ± calcite corona (Fig. 4.9e,g). **Biotite** is also locally present in the matrix, especially in the calcite-poor domains, as deformed lamellae. Allanitic **Epidote** is locally present. Among the accessory minerals, **titanite** is ubiquitous, while bluish tourmaline is rare.

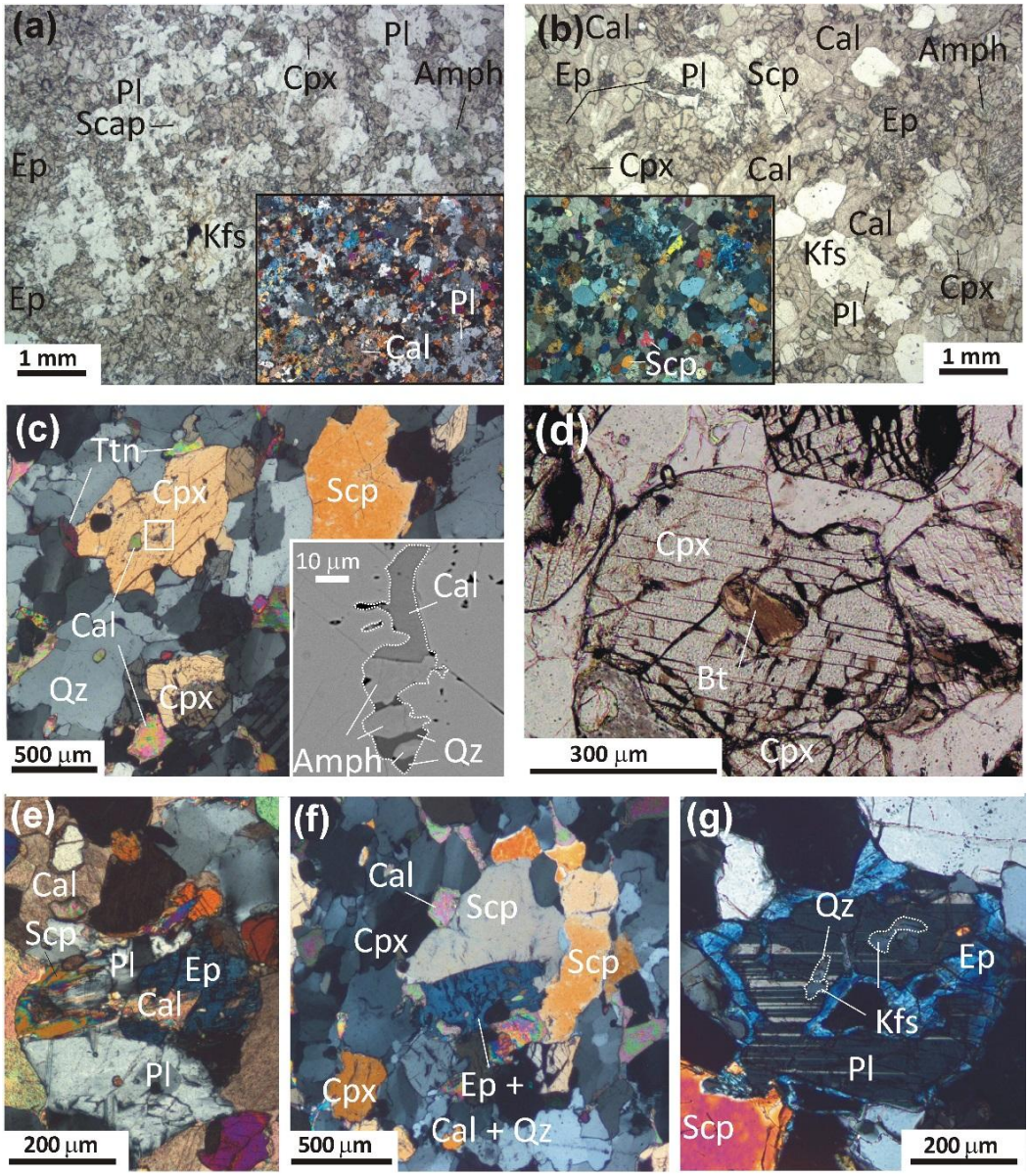

Fig. 4.9 – Representative microstructures of Type 3F CO_2-source rocks. Sample 14-20a. **(a)** K-feldspar + clinopyroxene + scapolite + plagioclase + quartz + titanite ± calcite ± biotite calc-silicate granofels, with abundant clinopyroxene and quartz and minor calcite (PPL, XPL). **(b)** The same mineral assemblage of (a) is present, but calcite is significantly more abundant (impure marble layer) (PPL, XPL). Sample 14-53c. **(c,d)** clinopyroxene porphyroblasts include relict amphibole + calcite + quartz (inset: BSE) and biotite (XPL, PPL). Sample 14-20a:e; Sample 14-53c:f,g. **(e-g)** Retrograde epidote ± calcite coronas and symplectitic microstructures developed on plagioclase and scapolite porphyroblasts (XPL).

4.3.3 Mineral chemistry

In this section, the average mineral chemical features of each CO_2-source rock type are described; more detailed mineral chemical data are provided in Chapter 5 for those samples that were selected for the thermodynamic modelling. Mineral chemical data are summarized in Fig. 4.10-Fig. 4.13 and Appendix 2.

4.3.3.1 Garnet

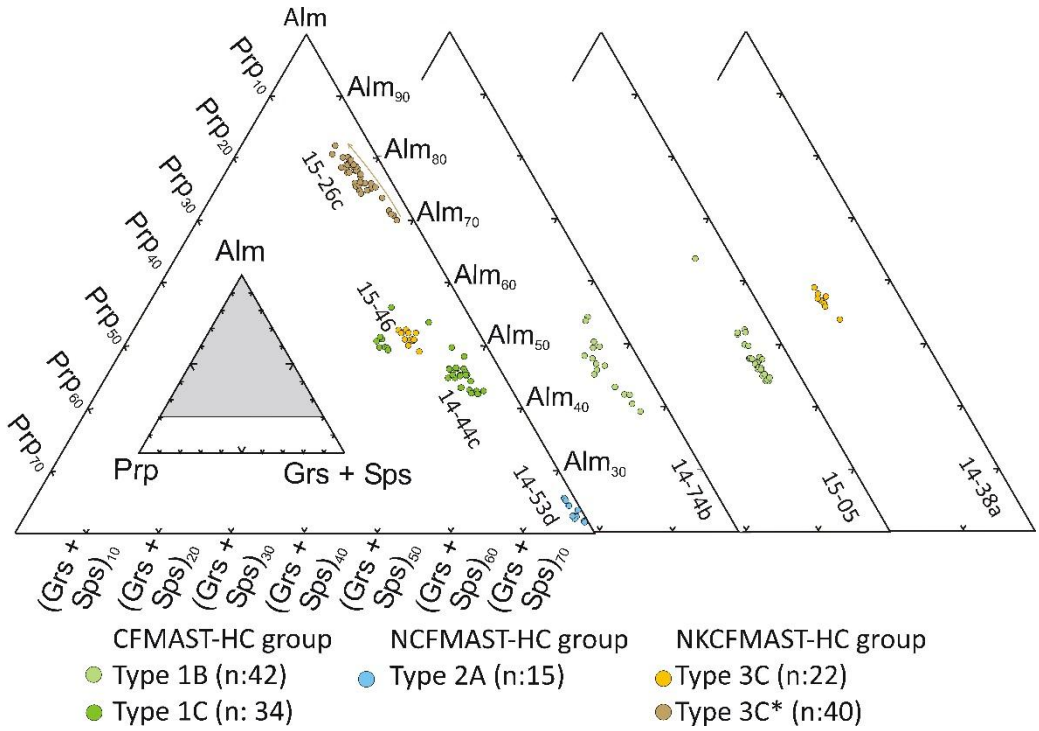

Fig. 4.10 – Compositional diagrams for garnet.

- *CFMAST-HC and NCFMAST-HC groups* - In Type 1B lithologies, garnet porphyroblasts are mostly almandine-grossular solid solutions, showing locally a weak zonation, with XCa increasing toward the rim, while XMn, XMg and XFe are more homogeneous (core: XCa=0.40-0.44, XFe=0.43-0.47, XMn=0.03-0.07, XMg=0.05-0.08; rim: XCa=0.36-0.50, XFe=0.43-0.52, XMn=0.03-0.07, XMg=0.04-0.08) [XCa=Ca/(Ca+Mg+Fe+Mn), and XFe, XMg and XMn defined accordingly]. Some porphyroblasts show an oscillatory zoning in the grossular and almandine content, with XCa=0.37-0.54, XFe=0.39-0.54 and XMg and XMn being constant, varying from 0.03 to 0.06. In Type 1C lithologies, garnet is locally weakly zoned, with XCa increasing and XFe and XMg decreasing from core to rim, while XMn remain constant (core: XCa=0.48-0.49, XFe=0.30-0.31, XMn=0.14-0.15, XMg=0.07-0.08; rim: XCa=0.50-0.53, XFe=0.27-0.29, XMn=0.14-0.15,

XMg=0.04-0.07). In Type 2A lithologies, garnet is almost a pure grossular (Fig. 4.10), with XCa=0.72-0.78, XFe=0.20-0.24, XMn=0.02 and XMg=0.00-0.02.

- *NKCFMAST-HC group* - garnet in Type 3C lithologies is mostly an almandine-grossular solid solution and it shows a weak zonation, with homogeneous XCa and XFe, XMn slightly decreasing and XMg slightly increasing toward the rim (core: XFe=0.48-0.59, XCa=0.24-0.32, XMg=0.08, XMn: 0.09; rim: XFe=0.46, XCa=0.37, XMg=0.11, XMn: 0.05). garnet of group 3C* has strong and continuous zonation (Fig. 4.10), with XFe and XMg increasing from core to rim, while both XCa and XMn decrease (XFe from 0.70 to 0.82, XMg from 0.03 to 0.06, XCa from 0.16 to 0.10 and XMn from 0.13 to almost 0).

4.3.3.2 Scapolite, plagioclase, epidote and K-feldspar

- *CFMAST-HC and NCFMAST-HC groups* - In Type 2A lithologies, **scapolite** has a homogeneous composition in the range eqAn=0.66-0.68 (eqAn=(Al-3)/3).

  In all the petrographic types of both the CFMAST-HC and NCFMAST-HC groups, **plagioclase** is almost a pure anorthite, ranging in composition from XAn=0.90 to XAn=0.97 (Fig. 4.11b), sometimes showing a Na-richer thin rim with XAn=0.23-0.44. Locally, plagioclase included in other mineral phases is more sodic, with XAn=0.28-0.46. An exception is represented by sample 15-05, which is at the contact with the host paragneiss: in this case plagioclase is richer in Na than the average, with XAn=0.63-0.68. **K-feldspar** is almost pure (XOr=0.95-1) in Type 1B samples, and is pure Or in Type 1C samples. Matrix **epidote** in the CFMAST-HC group has, on average, XZo=0.50-0.91 [XZo=Al/(Al+Fe^{+3})]; a lower XZo content is generally observed in epidote included in other minerals (XZo=0.31-0.64). Epidote is locally zoned, with XZo decreasing from core to rim. In the NCFMAST-HC group, epidote has XZo=0.33-0.44.

- *NKCFMAST-HC group* - **Scapolite** in Type 3C lithologies varies from eqAn=0.53-0.55 to eqAn=0.63-0.65 depending on the sample (Fig. 4.11a). In Type 3F, scapolite included in other minerals has, on average, a similar composition (eqAn=0.48-0.75) compared to scapolite in the matrix (eqAn=0.41-0.68) (Fig. 4.11a); a few inclusions show lower eqAn values (eqAn=0.39).

  In Type 3C lithologies, **plagioclase** is slightly zoned, with higher An contents toward the contact with scapolite (from XAn=0.46 to XAn=0.35). Most of the plagioclase in the matrix likely derives from the replacement of scapolite, because it shows the same zoning and composition (Fig. 4.11b); plagioclase crystals included in other minerals are strongly variable in composition (XAn=0.34-0.81). In Type 3C* lithologies, plagioclase is sodic (XAn=0.13-0.01).

  In Type 3F lithologies, plagioclase in the matrix is often anorthitic, with XAn=0.90-0.97, while some inclusions have a more sodic composition, with XAn=0.26-0.78. In

sample 14-17, which is the structurally highest, plagioclase in the matrix has a variable composition and it is locally zoned, with a more calcic core and a sodic rim (XAn=0.68 to 0.20).

In Type 3C lithologies, **epidote** is highly variable in composition, ranging from XZo=0.58-0.68 to XZo=0.32-0.36 depending on the sample. In Type 3F lithologies, epidote included in other minerals has XZo=0.56-0.68; epidote forming the symplectitic aggregates replacing scapolite is locally zoned, with either XZo decreasing from core to rim or XZo increasing toward the rim, depending on the sample (XZo varying between 0.55 and 0.91). Epidote replacing plagioclase and clinopyroxene has a similar composition.

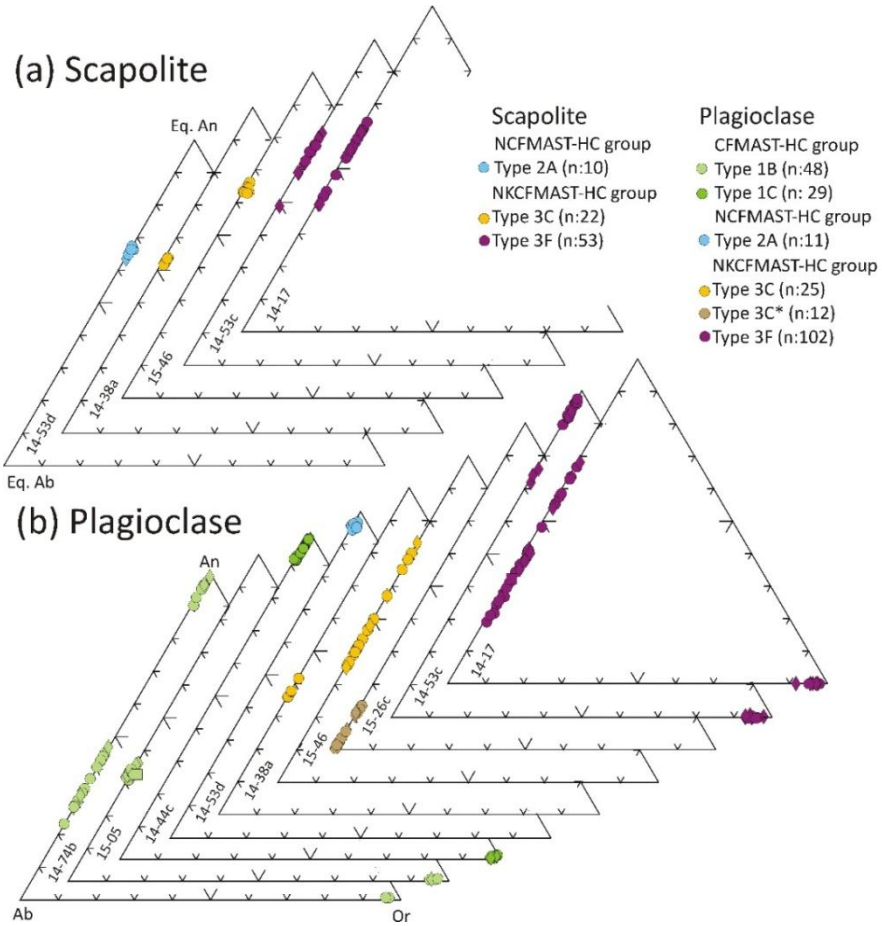

Fig. 4.11 – Compositional diagrams for (a) scapolite and (b) plagioclase and K-feldspar. Circles: matrix; diamonds: inclusions; squares: late.

4.3.3.3 Clinopyroxene and amphibole

❖ *CFMAST-HC and NCFMAST-HC groups* - In Type 1C lithologies, **clinopyroxene** is mostly a diopside (Fig. 4.12a) with relatively high XMg (XMg=0.68-0.75), both in the inclusions and in the matrix (and Mn=0-0.04 a.p.f.u.) [XMg=Mg/(Mg+Fe)]. In Type 2A lithologies, clinopyroxene has higher Fe^{2+} content (XMg=0.40-0.48) and lower Mn content (0-0.02 a.p.f.u.). **Amphibole** has a wide range of compositions, but it is always a Ca-rich amphibole (Fig. 4.12b). In the CFMAST-HC group, amphibole is mostly an actinolite, with the local occurrence of Mg-horneblende, tchermarkite and Fe-pargasite in Type 1B lithologies. XMg ranges from 0.36 to 0.98, but it is mostly comprised in the range 0.6-0.8 (with no significant differences between inclusions and matrix grains).

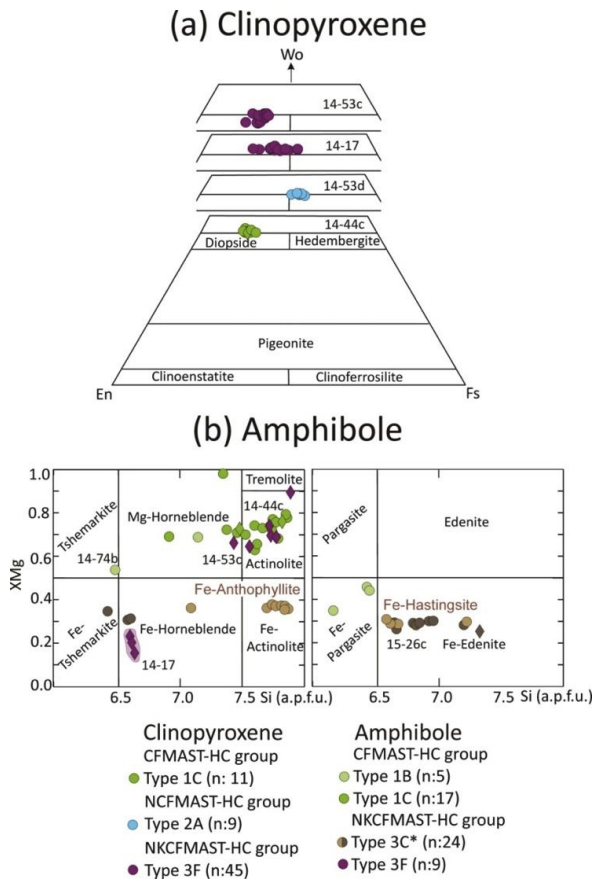

❖ *NKCFMAST-HC group* – In Type 3C* lithologies, **amphibole** is highly variable in composition and always Fe-rich: it is mostly a Fe-Horneblende/Fe-Tschermarkite/Fe-Edenite/Fe-Hastingite, with minor Fe-Anthophyllite, found either as individual crystals in the matrix and in the rims of Fe-edenites and hastingites. XMg ranges from 0.28 to 0.37 (Fe-anthophyllites are on average more Mg-rich, with XMg=0.36-0.38). In Type 3F lithologies, **clinopyroxene** is a diopside with a variable XMg, ranging from 0.44 to 0.67. XMg locally decreases toward the rims of the porphyroblasts. In the same lithologies, amphibole is found as inclusions in clinopyroxene and could be either an actinolite/tremolite with XMg=0.65-0.90 or a Fe-horneblende with XMg=0.15-0.23 depending on the sample.

Fig. 4. 12 – Compositional diagrams for (a) clinopyroxene (after Morimoto, 1988) and **(b) amphibole** (after Leake et al., 1997). Circles: matrix; diamonds: inclusions. In (b) amphibole plotted in the diagram on the left have $XCa_B>1.50$ and $(Na+K)_A<0.50$, whereas amphibole plotted in the diagram on the right have $XCa_B>1.50$ and $(Na+K)_A>0.50$; for Type 3C*, light brown colours refer to amphibole with $Al^{iv}<Fe^{3+}$ whereas dark brown colours refer to amphibole with $Al^{iv}>Fe^{3+}$.

4.3.3.4 Biotite, white mica and chlorite

Biotite and white mica only occur in the NKCFMAST-HC group. **Biotite** has different chemical compositions depending on the lithological type (Fig. 4.13a). In Type 3C* lithologies biotite is homogeneous in composition and Fe-rich, with XMg=0.22-0.47 and Ti=0.10-0.20 a.p.f.u.) [XMg=Mg/(Mg+Fe)]; in Type 3C lithologies, biotite has XMg=0.44-0.63 and Ti=0.03-0.18 a.p.f.u. (some inclusions have locally lower XMg and Ti content compared to crystals in the matrix). In Type 3F lithologies, biotite is Mg-rich, with XMg=0.57-0.71 and Ti=0.04-0.10 a.p.f.u.

White mica is a muscovite, and only occurs in Type 3C lithologies (Fig. 4.13b), having Si=3.00-3.13 a.p.f.u. and Na=0.03-0.06 a.p.f.u. Ca content varies from 0 to 0.12 a.p.f.u.

Chlorite has different chemical compositions in different chemical groups (Fig. 4.13c). In Type 1B lithologies, chlorite has high XMg compared to Type 1C lithologies of the same chemical group, while Si content is comparable; the late chlorite generation is generally Mg-richer than the prograde one. In this group, chlorite is locally zoned, with XMg increasing toward the rim; Mn content is generally high, varying between 0.09 and 0.35 a.p.f.u., with higher values in chlorite included in garnet. In Type 3C, chlorite has quite high Mn content, varies from 0.06 to 0.21 a.p.f.u. In Type 3C* chlorite is a daphnite, with XMg=0.04-0.10.

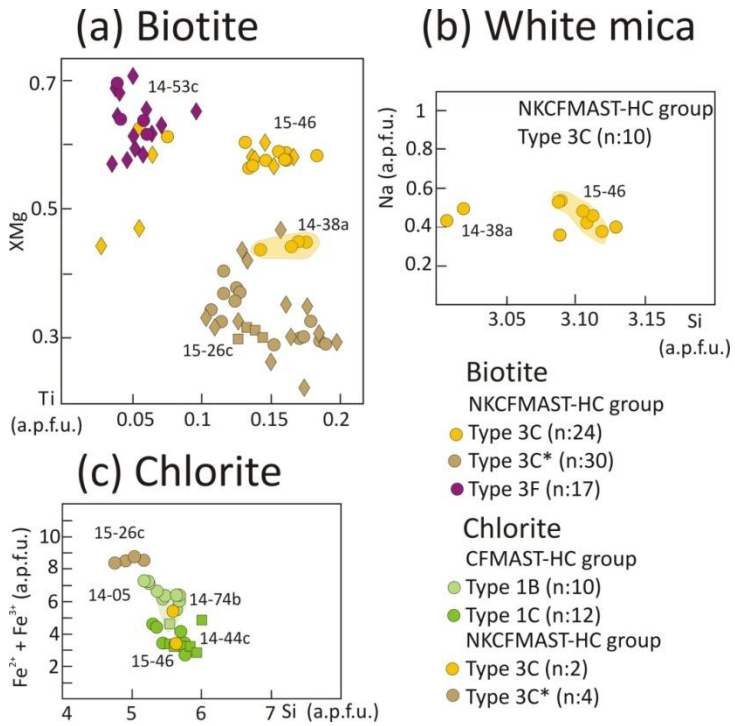

Fig. 4.13 – Compositional diagrams for (a) biotite, (b) white mica and (c) chlorite. Circles: matrix; diamonds: inclusions; squares: late.

4.3.3.5 Carbonates

- *CFMAST-HC group* - **Carbonate** in this group is almost a pure calcite, but locally it contains significant amounts of Mn and minor Fe (Mn=0.01-0.20 a.p.f.u., Fe=0-0.04 a.p.f.u.).
- *NKCFMAST-HC group* - In Type 3C lithologies, carbonate is calcite; calcite included in other minerals is characterized by higher XMn contents (up to 0.12 a.p.f.u.) with respect to calcite in the matrix (Mn=0.00-0.01 a.p.f.u.). In Type 3C* lithologies carbonate has a wide range of compositions, ranging from almost pure calcite to a siderite-rodochrosite solid solution (Fe=0.12-0.60 a.p.f.u, Mn=0.01-0.35 a.p.f.u., Mg=0.00-0.35 a.p.f.u.). In Type 3F lithologies, calcite is almost pure, with small amounts of Fe (0.01-0.02 a.p.f.u.) and Mg (0.01 a.p.f.u.).

4.3.4 Bulk rock compositions

4.3.4.1 Major and minor elements composition

The analysed CO_2-source rocks exhibit a wide range of bulk compositions, with major elements in the range: SiO_2 (3.4-79.9 wt%), Al_2O_3 (0.1-22.3 wt%), FeO (0.6-7.2 wt%), MgO (0.3-39.5 wt%), MnO (0-1.2 wt%), CaO (2.7-89.4 wt%), Na_2O (0-3.5 wt%), K_2O (0-6.1 wt%), TiO_2 (0-0.9 wt%), P_2O_5 (0-0.7 wt%). Samples belonging to the CFMAST-HC and NCFMAST-HC groups have a K_2O content <0.5 wt% and NaO content <1 wt% (Fig. 4.14), consistently with the observed low amounts of Na-rich minerals and the lack of K-bearing minerals. Moreover, samples belonging to these groups have lower Mg# [Mg#=MgO/(MgO+FeO_{tot}] compared to samples of the NKCFMAST-HC group (Mg#=0.1-0.5 with a mean of 0.36 compared to XMg= 0.5-0.9 with a mean of 0.61).

SiO_2, Al_2O_3, FeO, MgO and CaO are the most abundant rock-forming oxides and constitute $\geq$ 93 wt% in all the samples from different chemical groups. According to the SiO_2 amount, the studied samples can be divided in SiO_2-poor lithologies (SiO_2=0-50 wt%: mostly impure marbles and calcschists) and SiO_2-rich lithologies (SiO_2=50-100 wt%: calc-silicate rocks and carbonate-rich metapelites).

- *SiO_2-POOR LITHOLOGIES*

  In these samples, there is a positive correlation between SiO_2 and Al_2O_3, FeO, Na_2O, P_2O_5 and TiO_2 and a negative correlation between SiO_2 and CaO for all the different chemical groups (Fig. 4.14). MgO shows two different behaviours: it is inversely correlated to SiO_2 in the Mg-richer samples belonging to the NKCFMAST-HC group,

whereas it is positively correlated to SiO_2 in samples with MgO < 10 wt% in all the chemical groups.

One sample (13-72) from Type 1A and four samples (10-59, 14-30, 12-1b, 13-82a) belonging to Types 3A and 3B have high MgO content (in the range 16-40 wt%) and CaO content in the range 23-56 wt%. These samples additionally show low TiO_2 and Al_2O_3 contents (TiO_2=0-0.3 wt%; Al_2O_3=0.1-7 wt%). The other SiO_2-poor lithologies have higher CaO and lower MgO contents compared to samples previously described (CaO=28-90 wt%; MgO=0.4-5.1 mol%); Al_2O_3 and TiO_2 abundances are slightly higher (Al_2O_3=1-17.2 wt% and TiO_2=0.05-0.61 mol%). The other major oxides are present in similar amounts in all the SiO_2-poor lithologies (FeO=0.6-5.3 wt%; MnO=0.03-0.16 wt%, with the exception of the NCFMAST-HC sample 14-21b, which has a MnO content >1 wt%; Na_2O=0.02-1.9 wt%, K_2O=0.04-3.2 wt%, P_2O_5=0.05-0.14 wt%). K_2O is absent and Na_2O is low in the NCFMAST-HC group (Na_2O=0.95 wt%, K_2O=0.08-0.11 wt%), while in the NKCFMAST-HC group they both increase with increasing SiO_2 (Na_2O=0.02-1.9 wt % and K_2O=0.37-3.1 wt%).

❖ *SiO_2-RICH LITHOLOGIES*

In these samples, Al_2O_3, CaO, FeO, MnO, and Na_2O are inversely correlated to SiO_2 in all the chemical groups; MgO is inversely correlated to SiO_2 in the NKCFMAST-HC group, while it doesn't vary in the CFMAST-HC and NCFMAST-HC groups (Fig. 4.14). P_2O_5 and TiO_2 have the opposite behaviour, since they are inversely correlated to SiO_2 in the CFMAST-HC and NCFMAST-HC groups and they do not show systematic variations in the NKCFMAST-HC group. Variation in K_2O content does not appear significantly correlated to SiO_2 in all the groups.

The MnO content of the CFMAST-HC group is significantly higher (MnO=0.11-1 wt%, compared to the NKCFMAST-HC group, in which MnO varies between 0.04 and 0.18 wt%. More in detail, MnO is especially high in Types 1B and 1C (MnO=0.4-1 wt%). On the contrary, TiO_2 content is, on average, higher in the NKCFMAST-HC group (TiO_2=0.67 wt% in the NKCFMAST-HC group and TiO_2=0.50 wt% in the CFMAST-HC and NCFMAST-HC groups, Fig. 4.14). K_2O and Na_2O are almost absent in the CFMAST-HC group (K_2O=0.01-0.48 wt%; Na_2O=0.01-0.94 wt%); in the NCFMAST-HC group, Na_2O=0.58 mol% and K_2O is almost absent, while in the most complex NKCFMAST-HC group, Na_2O=0.1-2.7 wt% and K_2O=1.8-5.7 wt%. Al_2O_3 content does not vary systematically in the different chemical groups (Al_2O_3=8-22 wt%). CaO is 6.3-17.6 wt% in the CFMAST-HC and NCFMAST-HC groups, while MgO content is low (MgO=0.26-2.6 wt%). In the NKCFMAST-HC group, CaO and MgO contents vary according to the different lithological types: Type 3F has, on average, higher CaO and lower MgO compared to group 3C, 3D and 3E (3F: CaO=4-18.7 wt% and MgO=0.1-3.7 wt%; 3C, 3D, 3E: CaO=2.7-9.9 wt% and MgO=2.2-7.2 wt%). FeO is on average lower in the CFMAST-HC group and in Type 3F of the NKCFMAST-HC group, compared to the

NCFMAST-HC group and to Types 3C, 3D and 3E of the NKCFMAST-HC group (FeO=2.2-6.2 wt% compared to 4.2-7.2 wt%).

Major and minor elements bulk rock compositions normalized to the average composition of post-Archean upper continental crust (TM85: Taylor and McLennan, 1985) are reported in Fig. 4.15. The following points can be highlighted:

- *SiO_2-POOR LITHOLOGIES: Types 1A (CFMAST-HC) and 3A (NKCFMAST-HC)*

  Types 1A and 3A (i.e. impure marbles) are generally depleted in SiO_2, Al_2O_3, FeO, Na_2O, K_2O, P_2O_5 and TiO_2, while they are enriched in CaO. MgO is depleted or enriched depending on the samples (Fig. 4.15) and MnO is similar to TM85.

- *SiO_2-RICH LITHOLOGIES: CFMAST-HC and NCFMAST-HC groups*

  Types 1B, 1C and 1D and the whole NCFMAST-HC group exhibit SiO_2, Al_2O_3, FeO and TiO_2 contents similar to TM85, they are generally enriched in CaO and MnO and depleted in Na_2O and K_2O, while the MgO and P_2O_5 contents are variable (from similar to depleted in the CFMAST-HC group and more constant in the NCFMAST-HC group) (Fig. 4.15).

- *SiO_2-RICH LITHOLOGIES*: *NKCFMAST-HC group*

  Types 3B and 3F show a similar trend of major elements compared to TM85: they have similar amounts of SiO_2, Al_2O_3, FeO, MnO and TiO_2 compared to TM85, they are enriched in CaO, slightly depleted in Na_2O and P_2O_5, while MgO and K_2O are more variable (Fig. 4.15). Samples belonging to Types 3C, 3D and 3E have a similar and more constant trend, with a general depletion in Na_2O and P_2O_5 contents with respect to TM85 and a slight CaO and MgO enrichment in Type 3E (Fig. 4.15).

Table 4.1. Whole rock major and trace element compositions of CO_2-source rocks from central and eastern Himalaya

	(N)CFMAST-HC group														
Sample	**09-17a**	**13-72**	**12-37c**	**06-48**	**06-57**	**10-37a**	**12-24b**	**13-29b (I)**	**13-39 (I)**	**13-41b (I)**	**14-44c**	**13-60b**	**14-53d**	**14-21b**	**14-20b**
SiO_2	7.30	3.41	66.09	64.34	65.60	71.64	54.08	68.31	69.62	63.22	79.88	62.10	63.16	42.01	43.31
Al_2O_3	0.97	0.09	16.03	15.18	13.43	13.49	22.31	16.41	12.77	13.33	8.76	15.95	12.50	17.17	11.12
FeO*	1.02	0.58	5.97	3.89	5.56	3.69	4.56	2.27	3.77	4.19	2.29	6.15	5.47	4.02	5.26
CaO	89.37	56.15	8.35	13.81	13.07	8.21	16.53	11.21	11.95	17.62	6.33	11.32	16.11	32.55	34.98
MgO	0.71	39.54	0.95	0.71	0.80	0.56	0.78	0.37	0.44	0.26	1.39	2.58	1.28	1.34	3.48
Na_2O	0.02	0.05	0.49	0.18	0.10	0.94	0.41	0.17	0.03	0.01	0.21	0.39	0.58	0.95	0.95
K_2O	0.35	0.04	0.09	0.02	0.02	0.16	0.07	0.02	0.01	0.01	0.19	0.48	0.09	0.11	0.08
TiO_2	0.05	0.00	0.84	0.28	0.43	0.66	0.54	0.39	0.40	0.31	0.33	0.79	0.50	0.56	0.55
MnO	0.16	0.05	0.49	0.90	0.91	0.53	0.40	0.64	0.89	1.00	0.60	0.11	0.24	1.16	0.18
P_2O_5	0.05	0.07	0.69	0.69	0.09	0.12	0.31	0.20	0.11	0.05	0.02	0.13	0.07	0.13	0.09
Sum	100	100	100	100	100	100	100	100	100	100	100	100	100	100	100
LOI %	41.4	43.6	2.69	0.27	1.86	1.05	0.3	1.02	2.38	1.14	0.47	0.47	0.68	15.2	13.15
Li	10	<10	10	<10	<10	10	10	<10	<10	<10	<10	10	30	10	10
Sc	1	<1	9	4	8	8	5	5	7	5	5	14	7	5	8
V	<5	<5	92	45	61	35	119	43	50	60	32	76	43	60	53
Cr	<10	<10	50	30	50	20	40	40	40	30	30	80	30	20	30
Co	3	2	9	9	10	6	6	2	10	6	6	17	13	9	13
Ni	6	1	13	15	17	10	13	6	16	10	7	35	19	16	23
Cu	10	4	<1	12	<1	<1	15	7	2	6	4	15	16	2	18
Zn	53	8	53	36	54	39	31	16	53	30	17	81	45	55	143
Ga	0.7	<0.1	34.5	25.4	16.3	18.5	57.4	26.4	17.3	24.8	10.7	22.4	18.4	20.9	13.9
As	2.4	0.9	5.1	7.7	0.3	1.8	0.9	12.2	3.8	0.1	1	1.2	1.2	2	2.2
Se	1	0.4	0.5	0.4	0.3	0.3	0.3	0.5	0.2	0.2	<0.2	0.6	0.2	<0.2	0.3
Rb	7	0.3	6.1	1.8	0.6	6.5	5.4	1.2	1.1	0.7	9.8	25.3	4.9	5.3	2.8
Sr	304	60.6	205	203	292	258	613	386	110.5	10.7	90.3	448	242	572	348
Y	10.3	1.7	41	36	38.3	35.7	45.1	29.6	32.1	40.4	15.1	33.5	26.6	17.8	32.4
Zr	23	2	314	119	210	410	195	169	200	131	259	222	221	69	115
Nb	0.7	<0.2	16.5	11	9.3	15.6	14.7	16.6	9.7	6.8	10.5	17.8	13.7	13	13.7
Sn	1	<1	12	12	6	7	25	6	36	8	3	6	50	9	7
Sb	0.16	0.14	0.33	<0.05	<0.05	<0.05	<0.05	<0.05	<0.05	<0.05	<0.05	<0.05	0.06	0.06	0.14
Cs	0.24	0.06	3.24	0.14	0.06	0.18	5.26	0.11	0.32	0.05	0.23	0.79	0.33	2.29	2.33
Ba	39.2	2	32.3	4.9	32.2	14.2	11.3	19.6	70.5	59.1	5.9	204	48.1	23.9	12.2
La	9.7	1	51.5	25.6	33.5	43.5	37.4	28.4	32.1	23.6	23.5	51.5	13	14.4	29
Ce	18	1	99.2	51.2	67.1	84	73.3	52.4	60.5	40.7	46.8	99.8	30.6	28.4	59.5
Pr	2.02	0.17	11.1	5.55	7.36	9.43	7.6	5.56	6.86	4.89	5.27	10.9	3.97	3.27	6.97
Nd	7.8	0.8	43.2	23.1	29.2	36.9	32.4	22.2	27.1	19.8	21.5	42.5	15	13.2	24.9
Sm	1.49	0.14	8.63	4.74	5.7	6.94	6.17	4.27	5.32	4.44	4.78	8	3.66	3.26	5.34
Eu	0.3	0.04	2.12	1.08	1.46	1.08	1.44	0.97	1.25	1.47	1.22	1.56	0.78	1.32	0.93
Gd	1.45	0.16	7.36	4.65	5.59	6.04	6.17	3.93	4.69	4.42	3.88	6.5	3.35	3.27	4.59
Tb	0.23	0.02	1.19	0.81	1	0.99	0.91	0.64	0.75	0.84	0.55	1.03	0.66	0.52	0.8
Dy	1.39	0.16	6.77	4.76	5.78	5.95	5.7	4.15	4.86	5.3	3.02	5.99	5.37	3.15	5.04
Ho	0.31	0.04	1.31	0.98	1.25	1.22	1.36	0.85	1.01	1.18	0.54	1.21	1.17	0.55	1.04
Er	0.86	0.11	4.12	2.74	3.51	3.49	3.89	2.57	2.98	3.51	1.38	3.55	4.05	1.48	2.85
Tm	0.13	0.03	0.58	0.39	0.54	0.52	0.59	0.41	0.45	0.56	0.21	0.53	0.89	0.2	0.46
Yb	0.78	0.1	4.02	2.3	3.51	3.68	4.2	2.62	2.77	3.66	1.34	3.43	7.57	1.23	2.9
Lu	0.12	0.01	0.6	0.37	0.48	0.54	0.59	0.4	0.44	0.52	0.21	0.54	1.26	0.17	0.47
Hf	0.6	<0.2	8.1	3	5.9	10.5	6	4.3	5.2	3.7	6.8	6.1	6.4	1.9	3.2
Ta	0.1	0.1	1.3	0.5	0.7	1	1	0.7	0.6	0.3	1.1	1.3	4.6	0.7	1.2
W	<1	<1	1	3	2	<1	156	1	10	1	1	2	27	3	2
Tl	<0.02	<0.02	0.02	<0.02	0.02	<0.02	<0.02	<0.02	0.05	<0.02	<0.02	0.1	0.03	<0.02	<0.02
Pb	35	3	21	<2	6	19	15	15	2	<2	13	14	<2	22	10
Bi	0.16	0.02	6.25	0.36	1.14	0.72	1.19	1.14	0.23	0.1	0.96	0.25	2.68	1.44	0.6
Th	2.01	0.1	19	7.28	10.85	20.5	10.9	9.11	10.75	6.71	7.82	22.8	9.05	4.23	8.03
U	1.97	0.21	4.82	1.48	1.78	2.87	2.12	1.68	2	1.12	2.7	3.92	4.16	2.01	9.61
La_N/Yb_N	8	7	9	7	6	8	6	7	8	4	12	10	1	8	7
Eu/Eu*	0.59	0.77	0.77	0.66	0.75	0.48	0.67	0.68	0.72	0.96	0.82	0.62	0.64	1.17	0.54
Ce/Ce*	0.98	0.58	1.00	1.03	1.03	1.00	1.05	1.00	0.98	0.91	1.01	1.01	1.03	1.00	1.01

Major elements are normalyzed to 100% anhydrous basis. Major oxides are in wt%, trace elements are in ppm.

Table 4.1. ***Continued***

NKCFMAST-HC group

Sample	10-47b	10-59	14-30	10-49c	12-1b	13-82a	10-38a	13-38a	14-38a	07-40	12-11b	13-31	05-41 (I)	08-31	08-36
SiO_2	13.18	47.59	24.68	47.98	44.48	41.81	64.33	63.77	63.91	65.54	66.68	63.91	63.96	61.91	54.16
Al_2O_3	2.33	7.13	0.82	9.97	6.44	6.20	16.69	17.41	16.78	17.42	15.27	16.28	13.65	15.86	15.08
FeO*	1.74	3.12	1.26	4.08	2.53	4.48	7.10	6.22	7.23	5.76	5.28	5.79	6.25	4.16	6.35
CaO	76.20	22.56	42.83	27.50	24.19	27.51	3.11	6.21	2.73	4.42	3.02	3.94	5.89	4.65	9.93
MgO	5.06	16.23	29.70	4.80	19.38	17.33	3.37	2.34	2.67	2.30	2.24	2.56	5.95	5.50	7.22
Na_2O	0.03	0.72	0.02	1.93	0.20	0.59	0.46	0.46	0.96	1.63	2.69	2.30	0.11	1.14	0.70
K_2O	1.25	2.17	0.37	3.19	2.40	1.53	4.11	2.53	4.76	1.92	3.81	4.14	3.33	6.09	5.70
TiO_2	0.10	0.30	0.03	0.30	0.21	0.24	0.58	0.81	0.68	0.75	0.81	0.90	0.58	0.49	0.61
MnO	0.03	0.11	0.22	0.11	0.11	0.18	0.14	0.12	0.11	0.08	0.07	0.07	0.17	0.05	0.13
P_2O_5	0.08	0.08	0.07	0.14	0.07	0.12	0.10	0.12	0.18	0.17	0.13	0.12	0.10	0.14	0.12
Sum	100	100	100	100	100	100	100	100	100	100	100	100	100	100	100
LOI %	39	25	39	18.75	26.9	15.3	2.05	1.41	2.2	3.46	0.85	0.9	1.4	2.21	1.16
Li	<10	<10	<10	<10	10	<10	10	60	20	40	20	30	20	10	10
Sc	2	4	<1	6	4	6	15	16	16	12	12	14	13	10	14
V	5	29	<5	42	20	29	74	82	126	72	79	87	67	66	82
Cr	10	20	<10	30	20	20	80	90	110	80	90	90	60	60	80
Co	4	6	4	8	11	7	39	20	19	17	16	20	14	8	26
Ni	4	13	5	18	12	10	27	45	50	36	32	40	27	24	31
Cu	4	1	5	1	<1	<1	248	19	38	<1	3	43	<1	17	347
Zn	10	10	17	6	2	30	54	153	55	86	83	97	55	21	17
Ga	1.7	6.7	0.5	11.7	6.7	8.3	23.4	24	23.2	22.6	21.7	23	17.7	21	19.8
As	1.1	2.1	2.9	15.2	3.7	0.8	15.1	7.6	8.9	0.1	0.4	1.4	4.3	2.4	1.3
Se	0.6	0.4	<0.2	0.6	<0.2	1.1	<0.2	0.5	0.3	0.4	<0.2	0.3	0.2	<0.2	0.4
Rb	18.3	72.6	7.8	116.5	79.6	50.6	261	182.5	210	119	265	228	197.5	263	236
Sr	88	49.3	50.1	50.3	44	51.7	27.9	328	46.2	207	307	355	75.4	54.1	48.7
Y	3.3	9.7	1.6	17.2	8.2	19.8	43.1	41.1	44	31.3	36	37	31.8	23.6	20.3
Zr	22	54	4	111	44	62	169	219	198	187	284	265	199	131	171
Nb	1	4.7	0.2	6.5	3.3	4.2	13.4	17.1	15.2	15.9	16.9	18.9	11.7	10.3	13.5
Sn	1	2	2	27	6	3	13	25	22	4	4	5	10	8	5
Sb	<0.05	0.34	0.1	0.71	0.14	0.08	0.25	0.26	0.16	<0.05	<0.05	<0.05	0.13	0.25	0.11
Cs	0.8	2.17	0.3	3.58	3.79	1.18	18.75	22.9	5.94	5.08	12.55	9.19	18.5	4.58	6.07
Ba	360	1755	40.7	694	276	58.7	273	649	848	410	690	792	300	447	363
La	6.2	19.5	2.8	43.7	18.6	17.8	73.4	67.8	73.1	47.1	56	63.8	41.1	51.8	53.9
Ce	11.7	36.4	5.5	79.1	34.5	35.7	125	127.5	138.5	88.9	107.5	119	78.1	94.1	100
Pr	1.31	3.94	0.62	7.38	3.86	4.38	13.65	14.25	14.45	9.79	12.05	13.45	8.56	10.55	11.05
Nd	5.4	14.5	2.3	28.3	14.3	17.7	52.3	55.3	58.3	38.4	47.6	52.1	32.5	38.1	41.2
Sm	0.93	2.48	0.45	4.62	2.46	4.18	10.05	10.4	10.5	7.24	8.83	9.86	6.27	5.82	6.72
Eu	0.12	0.44	0.09	0.75	0.39	0.82	2.06	1.73	1.82	1.52	1.59	1.69	1.11	0.91	1.36
Gd	0.66	1.83	0.32	3.45	1.9	3.6	8.86	8.12	8.5	6.43	6.94	8.06	5.4	4.43	5.26
Tb	0.09	0.29	0.05	0.49	0.28	0.58	1.47	1.3	1.27	1.05	1.1	1.21	0.93	0.72	0.72
Dy	0.62	1.68	0.27	2.86	1.43	3.37	8.1	7.67	7.18	5.82	6.41	6.94	5.85	3.99	3.89
Ho	0.13	0.33	0.05	0.61	0.3	0.66	1.54	1.45	1.52	1.08	1.33	1.42	1.12	0.83	0.75
Er	0.36	0.96	0.14	1.68	0.81	1.85	4.19	4.33	4.25	2.91	3.93	3.9	3.39	2.43	2.21
Tm	0.06	0.15	0.03	0.23	0.13	0.27	0.58	0.62	0.57	0.41	0.57	0.55	0.52	0.39	0.35
Yb	0.33	0.92	0.14	1.57	0.84	1.83	3.96	4.08	4.1	2.38	3.61	3.44	3.63	2.65	2.26
Lu	0.04	0.13	0.02	0.24	0.11	0.25	0.59	0.62	0.62	0.32	0.55	0.53	0.57	0.36	0.35
Hf	0.6	1.5	<0.2	2.9	1.1	1.5	4.7	6	5.6	5	8.1	7.4	5.4	3.5	4.6
Ta	0.1	0.5	0.1	0.6	0.4	0.4	1.3	1.4	1.3	1.6	1.5	1.4	1.1	1	1.3
W	<1	1	5	13	4	<1	8	6	13	1	<1	1	3	4	1
Tl	0.06	0.11	0.05	0.25	0.18	0.17	1.39	1.02	0.75	0.62	1.17	0.97	0.99	0.27	0.53
Pb	9	4	5	2	2	<2	9	29	16	16	13	23	2	4	10
Bi	0.03	0.04	0.08	0.48	0.12	0.02	0.91	0.39	0.48	0.22	0.04	0.1	0.19	0.25	0.2
Th	1.47	7.34	0.56	10.95	6.63	6.61	23.5	28.5	32.8	19.95	23.6	27.1	19.85	19	21.3
U	0.18	1.35	0.39	2.22	2.54	5.68	5.67	4.33	3.88	5.02	3.97	4.22	3.24	4.25	5.13
La_N/Yb_N	13	14	13	19	15	6	12	11	12	13	10	12	8	13	16
Eu/Eu*	0.44	0.60	0.68	0.54	0.52	0.61	0.63	0.54	0.56	0.64	0.59	0.55	0.55	0.52	0.66
Ce/Ce*	0.99	1.00	1.01	1.06	0.98	0.97	0.95	0.99	1.03	1.00	1.00	0.98	1.00	0.97	0.99

Table 4.1. ***Continued***

NKCFMAST-HC group

Sample	04-28 (I)	05-55	07-20	07-22	07-41	08-57	08-67	09-25	10-4	12-12a	12-64b	12-65	13-64	14-20a	14-53c
SiO_2	58.42	31.62	57.60	42.12	30.83	56.54	61.68	54.63	68.37	65.56	67.51	62.64	52.15	44.83	71.27
Al_2O_3	12.88	6.84	16.11	10.89	8.89	14.36	14.25	15.86	12.56	12.86	12.72	13.25	14.45	11.96	9.39
FeO*	4.05	2.45	5.30	3.91	3.42	5.10	2.49	5.47	3.60	2.15	3.66	4.31	5.05	4.01	2.97
CaO	16.75	51.99	14.73	34.40	50.30	14.31	13.31	16.16	8.37	3.96	7.91	11.97	18.71	30.89	10.65
MgO	2.05	3.70	2.86	4.03	4.00	3.18	1.78	3.66	2.09	0.07	1.70	2.72	3.50	4.44	2.90
Na_2O	1.52	1.52	0.53	0.89	0.63	1.01	3.47	1.22	1.04	0.80	1.22	1.32	1.83	1.24	0.43
K_2O	3.46	1.19	1.82	3.09	1.34	4.62	2.57	2.08	3.07	8.04	4.40	2.78	3.45	1.82	1.83
TiO_2	0.65	0.45	0.81	0.53	0.46	0.69	0.33	0.74	0.72	1.17	0.70	0.79	0.70	0.61	0.42
MnO	0.09	0.16	0.08	0.07	0.06	0.08	0.04	0.10	0.05	5.24	0.06	0.08	0.06	0.09	0.04
P_2O_5	0.13	0.07	0.15	0.08	0.05	0.10	0.07	0.09	0.13	0.16	0.13	0.13	0.10	0.11	0.10
Sum	100	100	100	100	100	100	100	100	100	100	100	100	100	100	100
LOI %	6.42	25	0.59	15.25	23.6	2.68	5.15	1.15	0.77	0.58	0.91	1.59	5.61	11.95	0.82
Li	10	<10	<10	20	10	20	10	<10	<10	<10	<10	10	10	10	30
Sc	9	5	13	8	6	12	7	13	10	11	10	11	12	9	6
V	65	30	79	52	36	75	22	73	64	73	55	66	67	63	33
Cr	70	30	80	40	20	70	10	70	60	70	40	50	60	50	20
Co	13	8	18	12	10	16	6	14	11	13	12	14	16	12	7
Ni	23	13	37	27	18	35	10	31	26	29	26	30	35	27	11
Cu	8	11	14	19	6	18	<1	1	38	3	1	2	39	1	<1
Zn	32	38	93	64	57	94	44	107	54	70	58	68	86	100	22
Ga	17.1	8	23.6	14.6	9.7	21.9	20.3	23.1	18.5	18.5	17.4	18.8	18.4	16.6	12.2
As	1.4	0.8	2	2.8	0.8	2.4	0.2	3.8	1.7	2.8	0.6	0.7	2.4	1.8	0.3
Se	0.2	0.3	0.2	0.3	0.6	0.2	0.4	0.4	0.5	0.2	0.4	0.2	0.3	0.3	<0.2
Rb	124	76.8	106.5	141.5	64.4	257	112.5	95.8	172	260	206	172.5	171.5	107	108.5
Sr	258	648	398	859	781	445	609	633	540	483	434	622	795	1005	311
Y	21.7	17.6	32.7	23	14.6	29.5	11.6	32.1	34.4	35.5	32.5	36.3	29.2	20	23.4
Zr	214	90	207	158	73	246	78	162	360	333	353	293	159	131	275
Nb	14.4	8	17.6	9.2	7.9	14.3	13.7	16.8	15.4	18.2	13.2	15.9	13.8	11.5	8.6
Sn	4	2	6	4	2	5	2	15	4	5	3	4	3	4	3
Sb	<0.05	<0.05	0.06	1.97	0.12	0.61	0.06	<0.05	<0.05	0.08	0.13	0.06	0.16	0.05	<0.05
Cs	3.68	31.8	3.68	8.53	4.23	11.15	4.69	2.63	2.66	4.42	7.6	7.46	5.8	3.69	9.47
Ba	414	178.5	425	410	221	697	311	576	819	1100	832	836	544	493	346
La	38.8	24.1	56.4	43.3	19.4	52.1	12.7	55.5	49	54.1	47.1	53	46.6	26.6	32.8
Ce	71.2	45.7	105.5	80.3	38.1	99.6	29.9	104.5	100	104.5	93	108.5	90	53.6	65.4
Pr	7.74	5.24	11.75	8.92	4.59	11.45	4.12	12	11.8	11.6	10.9	12.75	10.35	6.48	7.79
Nd	29.6	18.7	44.4	30.3	16.2	40.3	16.4	41.1	42.1	45.5	38.1	44.4	35.9	22.4	26.1
Sm	5.44	3.59	8.11	5.38	3.28	7.71	4.38	7.85	8.27	8.4	7.96	8.92	6.95	4.7	4.78
Eu	1	0.68	1.42	0.96	0.56	1.24	0.71	1.51	1.45	1.52	1.26	1.58	1.1	0.95	0.98
Gd	4.53	3.33	6.25	4.58	2.76	5.92	3.82	6.92	7.06	6.66	6.48	7.4	5.73	4	4.26
Tb	0.67	0.5	1.02	0.67	0.43	0.86	0.53	0.99	1.09	1.04	0.99	1.11	0.9	0.57	0.65
Dy	3.98	2.71	5.73	3.87	2.61	4.93	2.75	6.07	6.24	5.99	5.87	6.5	5.04	3.63	3.72
Ho	0.8	0.55	1.15	0.84	0.49	1.06	0.46	1.22	1.21	1.22	1.14	1.31	1.03	0.73	0.79
Er	2.21	1.5	3.11	2.28	1.37	2.81	1.14	3.06	3.29	3.51	3.17	3.42	2.79	2.04	2.13
Tm	0.34	0.25	0.51	0.36	0.21	0.45	0.17	0.51	0.52	0.51	0.47	0.57	0.43	0.33	0.36
Yb	2.18	1.45	3.1	2.16	1.26	2.71	0.91	2.89	3.06	3.46	2.9	3.41	2.56	1.86	2.36
Lu	0.33	0.23	0.46	0.32	0.21	0.41	0.13	0.45	0.45	0.53	0.45	0.51	0.39	0.28	0.36
Hf	5.7	2.4	5.6	3.9	1.8	6.4	2.6	4.7	9.5	8.3	9.5	7.9	4.5	3.7	7.1
Ta	1.3	0.7	1.4	0.8	0.7	1.2	2.5	1.3	1.3	1.3	1.2	1.3	1.2	1	0.8
W	1	1	2	1	1	2	1	2	1	2	1	2	1	3	1
Tl	0.03	0.04	0.11	0.12	0.13	<0.02	0.02	<0.02	0.06	0.02	0.04	0.04	0.02	<0.02	0.2
Pb	13	27	13	22	16	26	17	14	25	29	30	19	18	20	3
Bi	0.15	1.7	0.12	0.24	0.11	0.57	0.1	4.5	0.23	0.11	0.17	0.13	0.06	0.62	0.12
Th	13.95	7.12	24.8	13.15	8.1	25.1	9.3	22.7	25.2	21	22.1	24.5	19.3	11.75	12.85
U	3.11	1.39	3.9	3.31	1.5	2.01	4.1	4.23	4.09	3.91	4.14	3.92	3.12	2.98	2.06
La_N/Yb_N	12	11	12	13	10	13	9	13	11	10	11	10	12	10	9
Eu/Eu*	0.58	0.57	0.58	0.56	0.54	0.53	0.50	0.59	0.55	0.59	0.51	0.56	0.50	0.63	0.63
Ce/Ce*	0.99	0.98	0.99	0.98	0.97	0.98	1.00	0.98	1.00	1.01	0.99	1.01	0.99	0.98	0.99

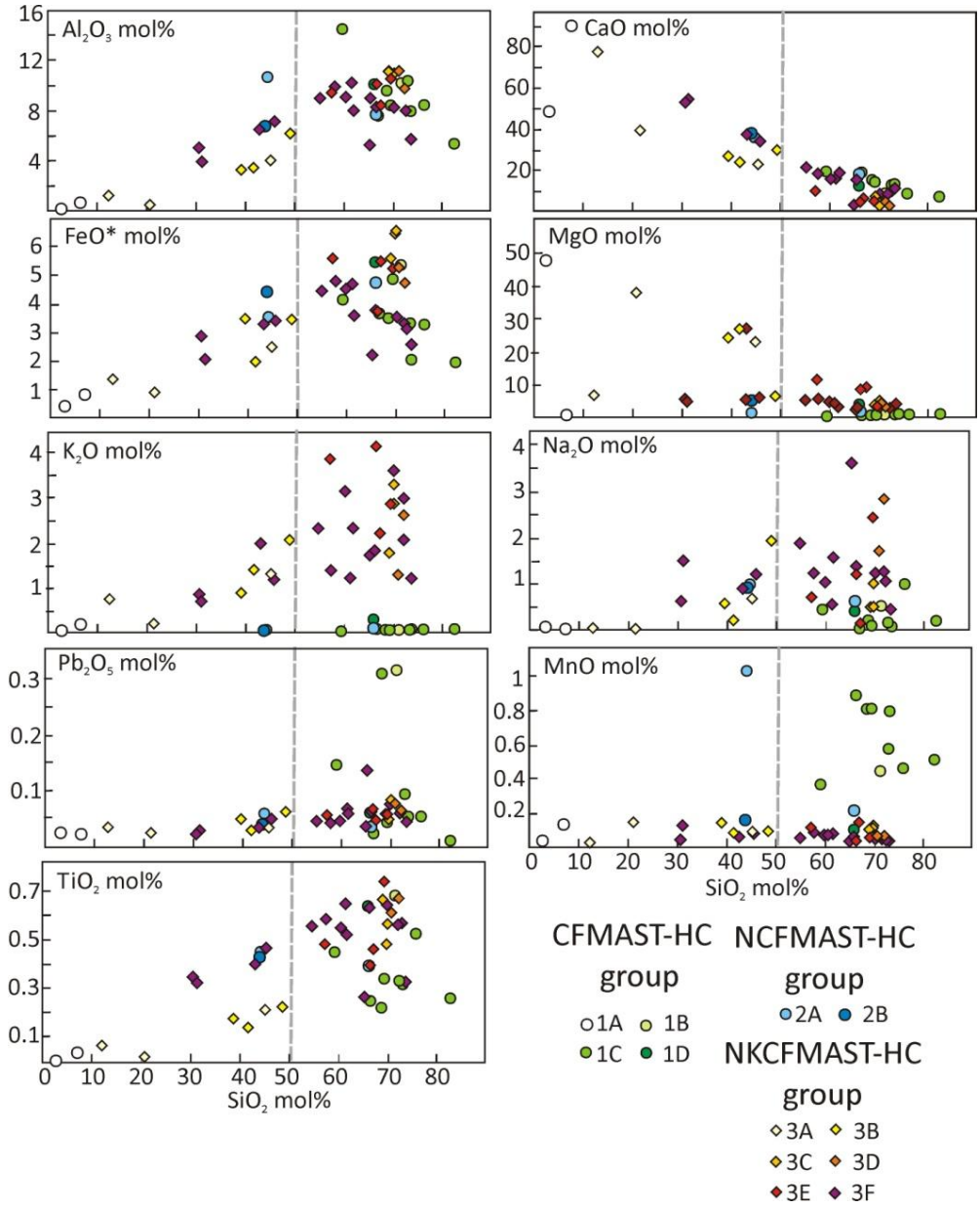

Fig. 4.14 – Whole-rock concentrations of major and selected minor elements versus SiO_2 (mol% oxides) for CO_2-source rocks of different chemical groups. *All iron is reported as FeO. The light grey dashed line divides marbles, impure marbles and calcschists (left) from calc-silicate rocks (right).

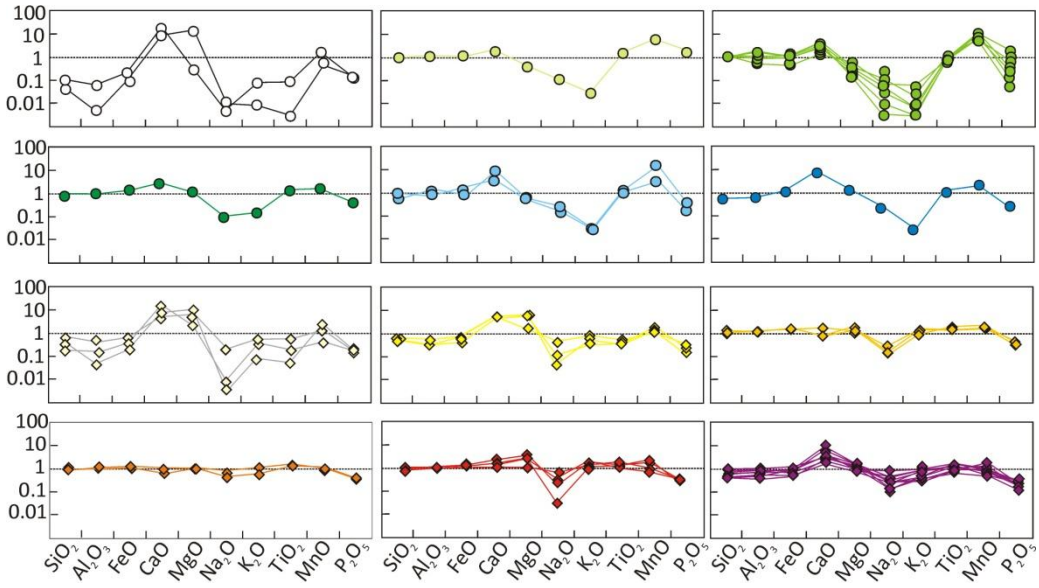

Fig. 4.15 - Whole-rock major and minor elements concentrations normalized to the average composition of upper continental crust (TM85: Taylor and McLennan, 1985). Colour code as in Fig. 4.14.

4.3.4.2 Trace elements composition

❖ *SiO_2-POOR LITHOLOGIES: Types 1A (CFMAST-HC) and 3A (NKCFMAST-HC)*

Impure marbles of Types 1A and 3A are generally depleted in all trace elements compared to TM85 reference (Fig. 4.16, Fig. 4.17a,c). Type 3A marbles are less depleted compared to the others, especially in Rb and Ba, which is particularly high (Ba=2-1755 ppm). The Se content is quite high (up to ~20 times that of TM85; Se=0.4-1 ppm). As concerning REE (La-Lu), these samples show a slight enrichment in light rare earth elements (LREE: La-Eu) and depletion in heavy rare earth elements (HREE: Gd-Lu), given by a La_N/Yb_N ratio in the ranges 7-8 and 13-14 for Types 1A and 3A, respectively. All the Type A samples show a slight enrichment in Tm (Tm=0.03-0.15 ppm) and a moderate to high Eu anomaly (Eu/Eu*=0.44-0.77). No Ce anomalies occur, except for one sample of the CFMAST-HC group (Ce/Ce*=0.58).

❖ *SiO_2-RICH LITHOLOGIES: CFMAST-HC and NCFMAST-HC groups*

Types 1B, 1C and 1D and Types 2A and 2B exhibit a similar pattern of trace elements and REE, with minor differences (Fig. 4.16, Fig. 4.17a,b). Type 1B has higher Bi and Sb compared to the other types (Bi=6.3 ppm, Sb=0.3 ppm *vs*. Bi=0.1-2.7 ppm, Sb=0-0.14 ppm); Type 1D shows slightly higher amounts of Cr, Co and Ni compared to the other types (Cr=80 ppm, Co=17 ppm, Ni=35 ppm compared to Cr=20-50 ppm, Co=2-10 ppm and Ni=6-23 ppm), as well as higher amounts of Ba and Tl (Ba=204 ppm, Tl=0.1 ppm compared to Ba=4.9-70.5 ppm, Tl<0.05 ppm). W locally reaches quite high values in both the CFMAST-HC and NCFMAST-HC groups, up to 156 ppm (Fig. 4.16). Cs content is relatively low (Cs=0.06-5.26 ppm).

Relative to TM85, Rb and Ba are significantly depleted in these groups, as well as Cs (with few exceptions); Cu and Pb are also depleted (Pb positively correlates with CaO, suggesting that its abundance/scarcity is related to CaO content), but less compared to the previous elements. Ta is always depleted with the exception of sample 14-53d (Type A of the NCFMAST-HC group). Y, Sn, Lu, and Se are locally enriched compared to TM85 (Se is enriched in all the samples). Almost all the samples of these groups show a moderate to high Eu anomaly and a slight enrichment in LREE compared to HREE (Eu/Eu*=0.48-0.8, La_N/Yb_N =4-9), with the exception of Type 2A which may have a positive Eu anomaly (Eu/Eu*=1.2) and be enriched in HREE (La_N/Yb_N=1); only one sample 13-41b(I) (Type 1B) does not show Eu anomaly. No Ce anomaly occur (Ce/Ce*=0.98-1.05).

❖ *SiO_2-RICH LITHOLOGIES*: *NKCFMAST-HC group*

CO_2-source rocks belonging to Types 3B, 3C, 3D, 3E and 3F have a similar trace element pattern compared to each other and to TM85 (Fig. 4.16, Fig. 4.17c). Rb and Ba are in general enriched or slightly depleted with respect to TM85, with higher absolute concentrations compared to the CFMAST-HC group (Rb=51-263 ppm vs. 0.6-25 ppm; Ba=179-1100 *vs.* 5-204 ppm). Nb and Tb are lower in Type 3B (Nb=3.3-6.5 ppm, Tb=8-18.2 ppm, while in the other Types Nb=0.28-0.58 ppm, Tb=0.5-1.3 ppm). Y, Tm and Yb are, on average, higher and enriched in Types 3C, 3D and 3E compared to Types 3B and 3F, in which they are generally depleted (3C, 3D, 3E: Tm=0.35-0.62 ppm, Y=20.3-43.1 ppm, Yb=2.4-4.1 ppm; 3B, 3F: Tm=0.13-0.57 ppm, Y=8.2-36.3 ppm, Yb=0.84-3.5 ppm). Sr is highly variable from depleted to enriched compared to TM85, depending on the CaO content of the sample (Sr=28-1005 ppm). Nb and Ta are almost always depleted compared to TM85 in all the samples of this group (Ta is depleted in all samples except in 08-67); Sn, W, As, Sb and Cu vary from depleted to moderately enriched in some samples (Sn=2-25 ppm, with higher values in groups 3B and 3C; W=1-13 ppm and As=0.3-15.1 ppm, with higher values in groups 3B and 3C; Sb=<0.05-1.97 ppm; Cu=<1-347 ppm). Se and Tl are enriched compared to TM85 in all the analysed samples of this group. All the samples present a moderate to high Eu anomaly (Eu/Eu*=0.50-0.64) and are enriched in LREE (La_N/Yb_N=6-16). No Ce anomaly occur (Ce/Ce*=0.95-1.03).

Overall, both the (N)CFMAST-HC and NKCFMAST-HC groups have trace element patterns quite similar to the composition of the upper continental crust; the more significant differences are bound to specific elements like Rb, Cs, Ba, and Tl, which are higher in the NKCFMAST-HC group with respect to the (N)CFMAST-HC group, and W, that on the opposite is higher in the (N)CFMAST-HC group; minor differences are bound in Co, Ni, and REEs (Fig. 4.17d).

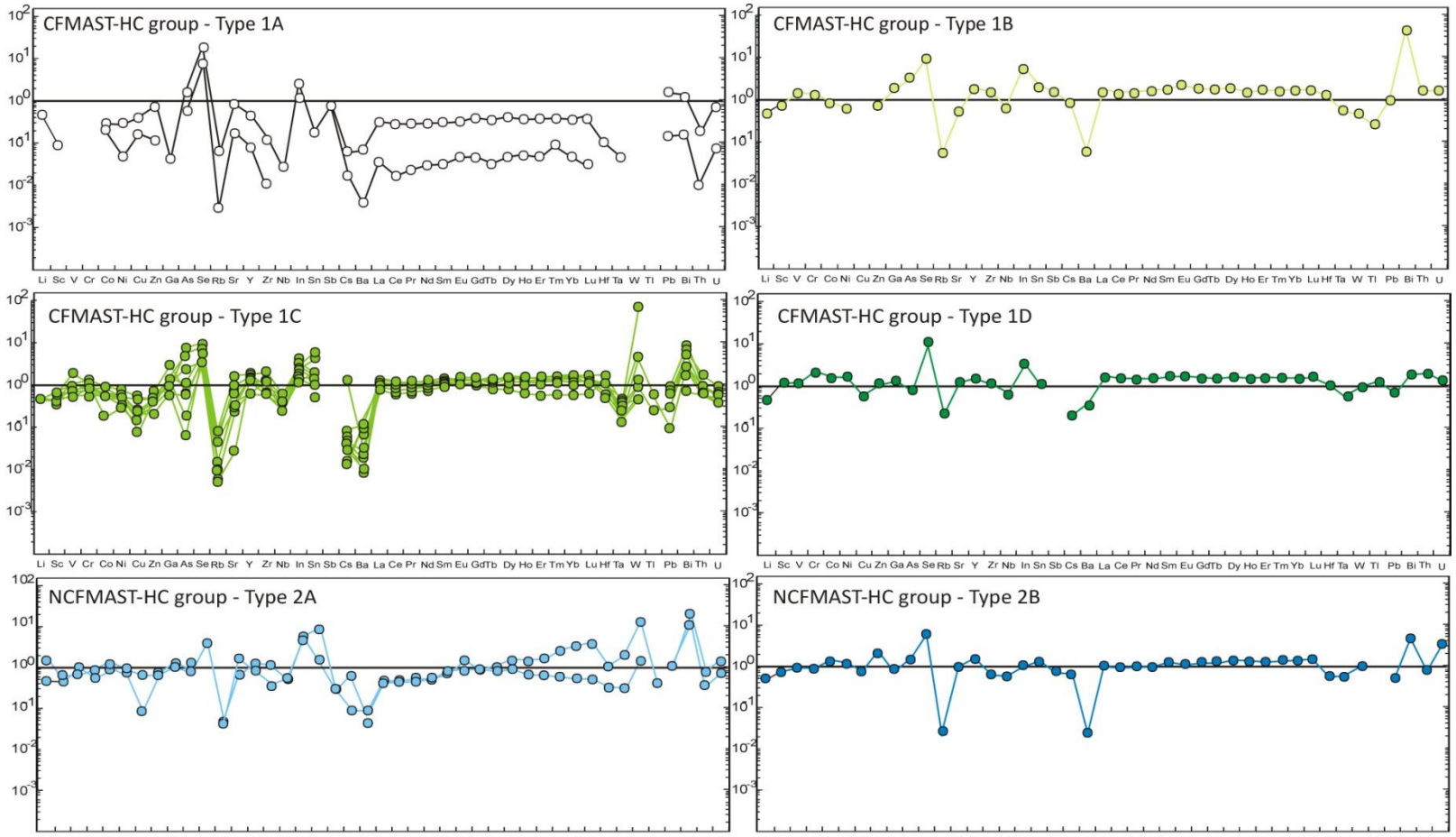

Fig. 4.16 - Trace elements patterns of CO_2-source rocks normalized to TM85 for all the chemical groups.

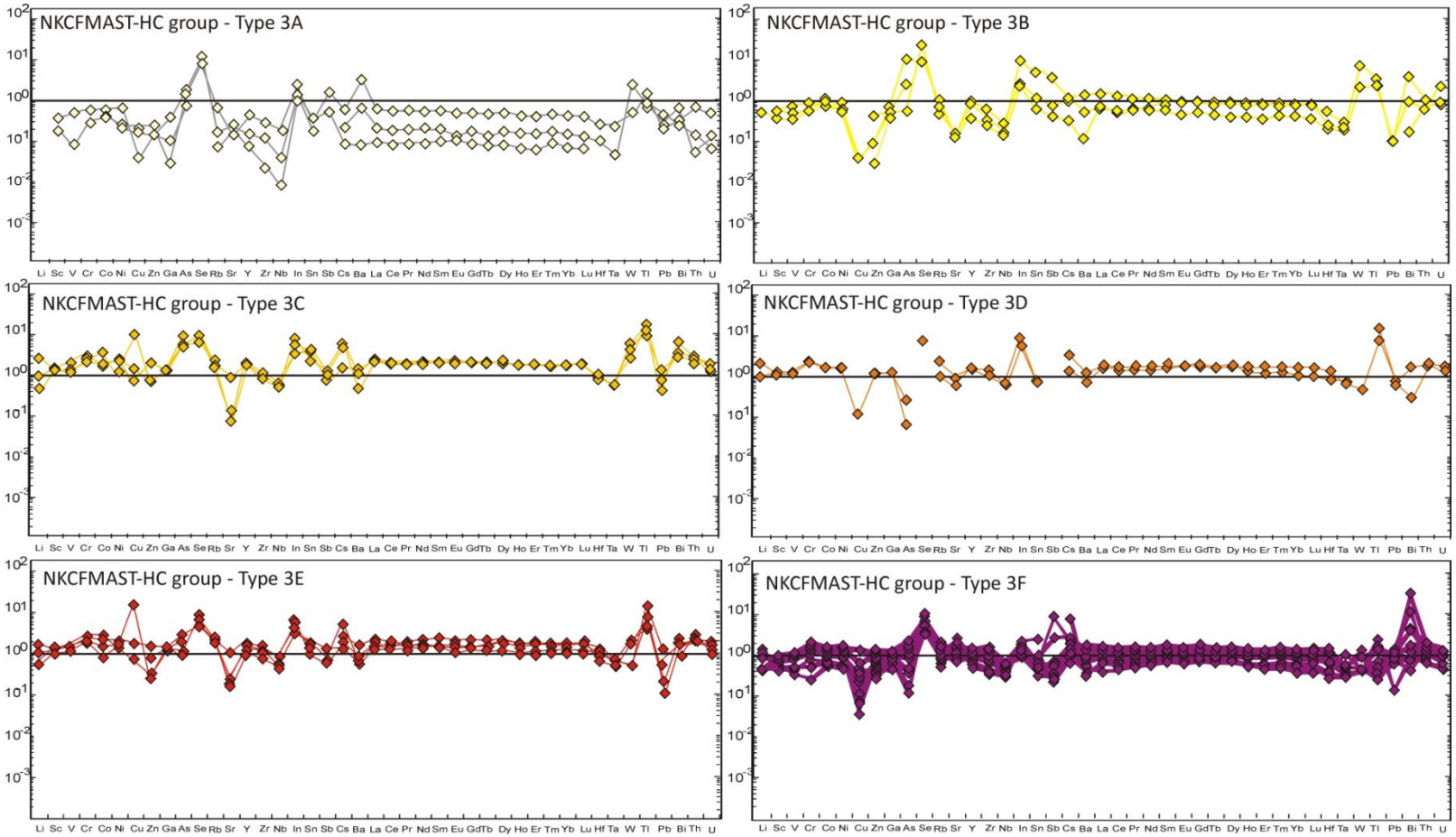

Fig. 4.16 – Continued.

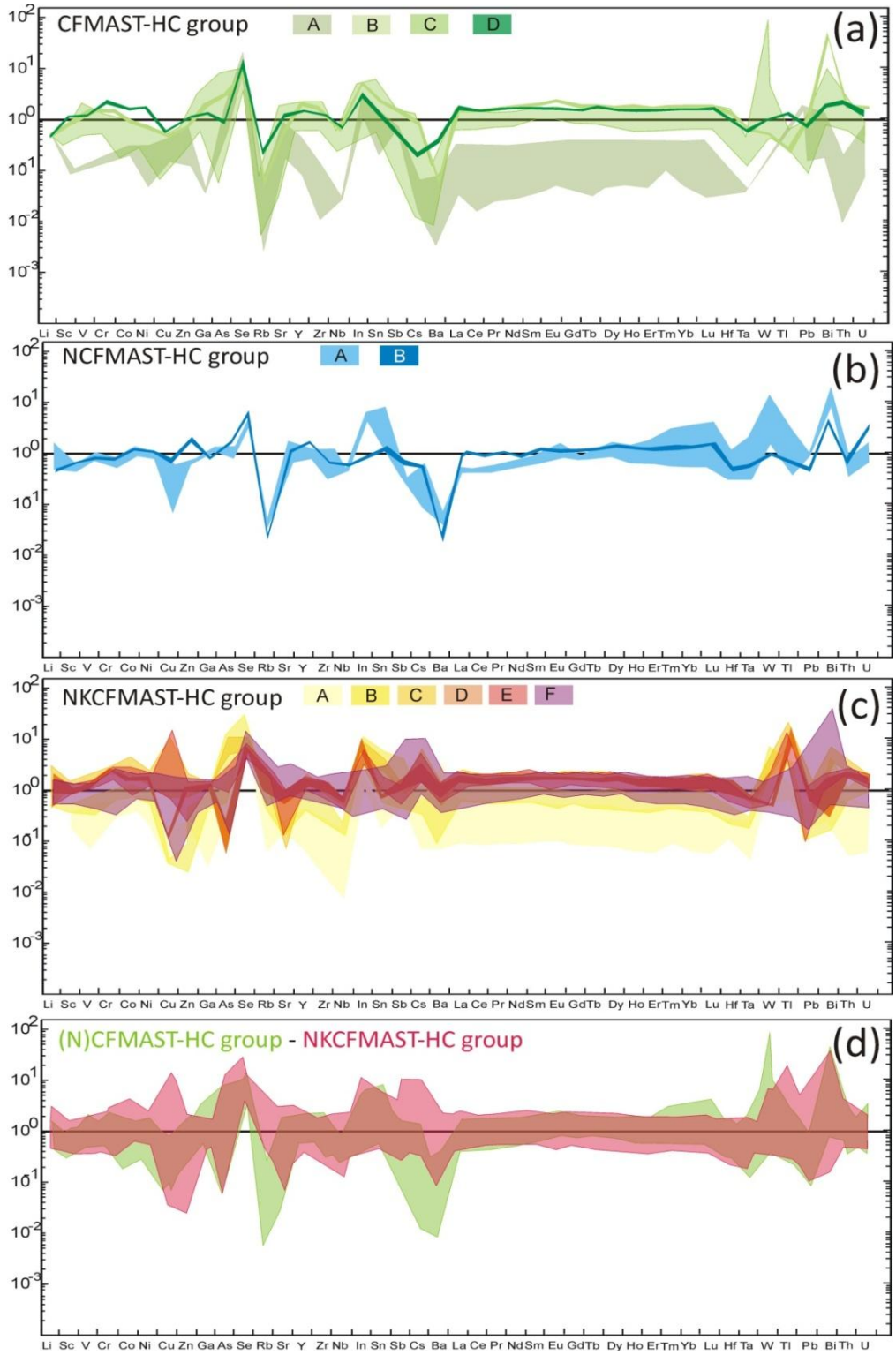

Fig. 4.17 – Trace elements patterns of CO_2-source rocks normalized to TM85 for **(a)** CFMAST-HC group, **(b)** NCFMAST-HC group, **(c)** NKCFMAST-HC group and **(d)** comparison between the (N)CFMAST-HC (green) and NKCFMAST-HC (red) groups excluding impure marbles (Types 1A and 3A).

4.4 Discussion

4.4.1 Protoliths of CO_2-source rocks

Several end-member sources contribute to the total bulk of a sediment, including continental and volcanic detritus, biogenic phases like opal and carbonate, authigenic phases like Mn-Fe hydroxides and others, each of them with its characteristic chemical composition. Moreover, weathering of the source as well as sedimentary and/or metamorphic processes can cause element mobility, fractionation and differentiation, resulting in a more or less heightened modification of the original detrital mineralogical composition (Cullers et al., 1987; Crichton and Condie, 1993; Condie et al., 1995; Cox and Lowe, 1995; Nesbitt et al., 1996). For all these reasons, converting geochemical data of metamorphic rocks to lithological data is not an easy task, even if chemical signature of the source can resist medium grade metamorphism (Shaw, 1954; Roser and Korsch, 1986; Gieré et al., 2011).

A first order interpretation of the protoliths of CO_2-source rocks is possible through the analysis of the major elements components, and successive refinements can be done through trace elements chemistry analysis. Useful markers of the sedimentological cycle are alkali elements (K, Rb, Cs), alkaline earth elements (Sr, Ba), rare earth elements, high field strength elements (HFSTEs: Hf, Zr, Nb, Ta, Ti, Th), U and Th (Plank and Langmuir, 1998; McLennan, 2001), and they are largely used to interpret protoliths and tectonic environments of metasediments, including calc-silicate rocks (Buriànek and Pertoldova, 2009; Gieré et al., 2011; Nutman et al., 2010; Tanner et al., 2013; Roser and Korsch, 1988), due to their low sensibility to post-depositional mobilization and metamorphism (Bathia and Crook, 1986; McLennan et al., 1993).

4.4.1.1 Protoliths deduced from major elements composition

Samples belonging to the CFMAST-HC and NCFMAST-HC groups have a significantly different trend in their major and minor components with respect to those of the NKCFMAST-HC group (Fig. 4.18a,c): they are strongly depleted in K_2O (± Na_2O), they have on average lower TiO_2 content and Mg#, while MnO content is higher with respect to the NKCFMAST-HC samples. These features, combined with field and petrographic observations, suggest that the (N)CFMAST-HC and NKCFMAST-HC groups derive from different protoliths. The same conclusion is suggested by the ternary diagram reported in Fig. 4.18a,b, in which bulk rock compositions are plotted as a function of: biogenic components (simplified by CaO: calcite, Mg-calcite and dolomite), detritic components (simplified by K_2O: illite, micas and feldspars) and authigenic components (simplified by FeO + MnO: Fe-Mn oxyhydroxides). It appears that samples of the (N)CFMAST-HC and

NKCFMAST-HC groups plot in two totally different fields, thus reflecting original difference in their protoliths.

❖ *NKCFMAST-HC group*

Most of the samples from the NKCFMAST-HC group plot in a relatively narrow area connecting the CaO apex with the average pelite composition, suggesting that they derive from a marly protolith, i.e. from a sediment consisting of a mixture of pelitic and carbonatic components, in different amounts (Fig. 4.18b).

More specifically, two different chemical subgroups can be distinguished (Fig. 4.18c,d):

- most of the NKCFMAST-HC samples (i.e. Types 3C, 3D, 3F and part of Types 3A and 3B) plot in a narrow area connecting the Mg-calcite component with the average pelite field, thus suggesting that they derive either from impure limestones (impure marbles of Type 3A and 3F) or from marly protoliths consisting of a mixture of Mg-calcite and pelitic sediments (Types 3C, 3D, 3F);
- few NKCFMAST-HC samples (i.e. Type 3E and part of Types 3A and 3B) plot in a narrow area connecting the dolomite component with the average pelite field, thus suggesting that they derive either from impure dolostones (Type 3A) or from marly protoliths consisting of a mixture of dolomite and pelitic sediments (Type 3B and 3E).

❖ *CFMAST-HC and NCFMAST-HC groups*

Fig. 4.18a suggests that the protolith of the samples from the CFMAST-HC and NCFMAST-HC groups should have been consisted of a mixture of smectite and carbonates, thus resembling smectite-rich bentonites, deriving from altered ash layers in marine basins.

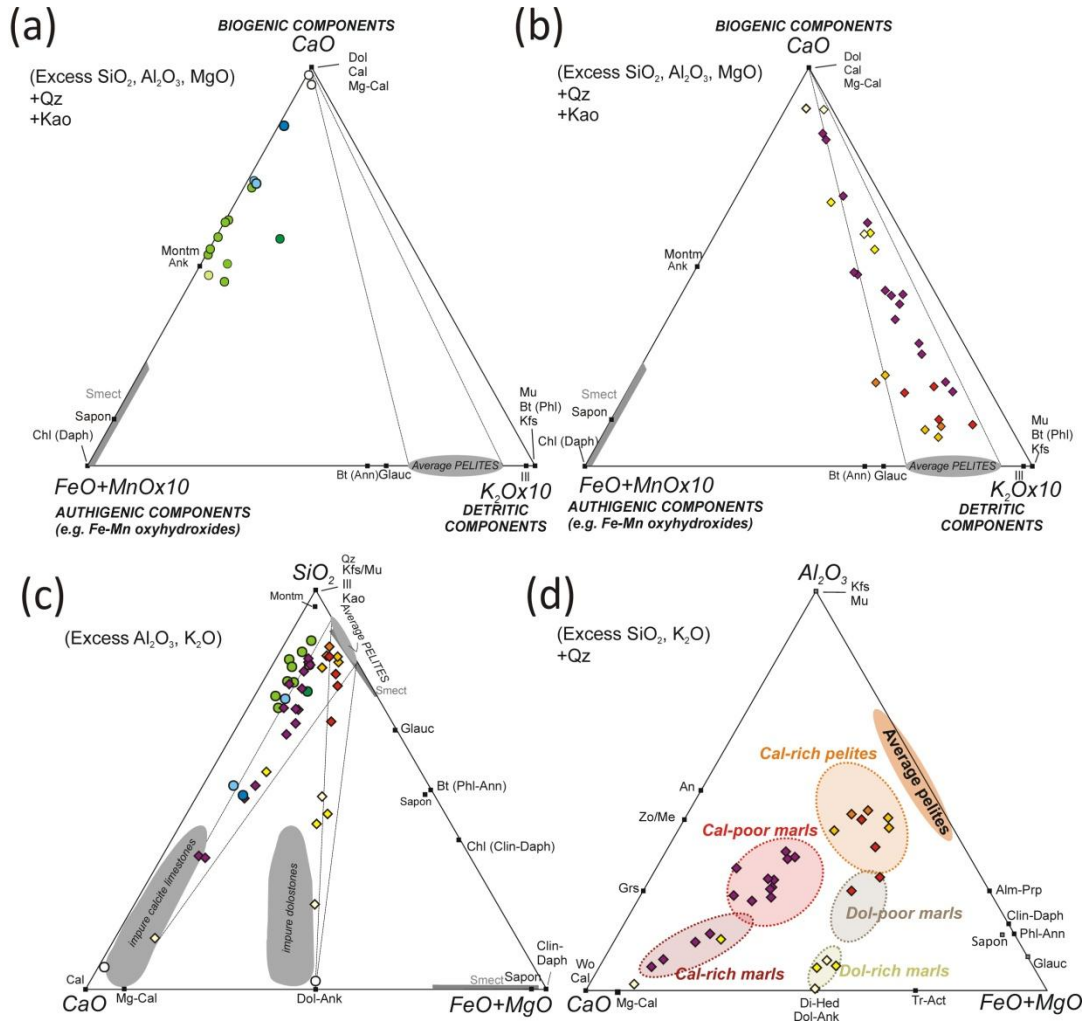

Fig. 4.18 – Diagrams of bulk-rock compositions for the analysed CO_2-source rock samples. (a,b) CaO-K_2Ox10-(FeO+MnO x10) diagrams for the (N)CFMAST-HC (a) and NKCFMAST-HC (b) groups, highlighting the different mineralogical components of the protoliths. The "Average pelite composition" field derives from bulk rock compositions of metapelites from this study (see also Rapa et al., 2016) and from Groppo et al. (2009). **(c)** CaO-SiO_2-(FeO+MgO) diagram for both the (N)CFMAST-HC and NKCFMAST-HC groups Compositional fields of impure calcitic limestones and dolomites are from Tracey and Frost (1991), compiled after Ehlers and Blatt (1982). **(d)** Al_2O_3-CaO-(FeO+MgO) diagram for Type 3 of CO_2-source rocks, highlighting Mg-calcite and dolomite -derived sediments.

4.4.1.2 Protoliths deduced from trace elements composition

Trace elements pattern in the different chemical groups show a trend comparable to values of the upper continental crust; however, significant differences occur among the (N)CFMAST-HC and NKCFMAST-HC groups, which support the hypothesis of a different protolith's nature for the three groups. Specifically:

- **Alkalis (K, Rb, Cs)** are largely contained in the detrital components of marine sediments; in the CFMAST-HC and NCFMAST-HC groups they are strongly depleted,

while in the NKCFMAST-HC group they are present in high concentrations, from similar to enriched compared to TM85 (Fig. 4.19). Other factors controlling K abundance could be clay mineralogy, volcanoclastic input and diagenetic uptake of K (Plank and Langmuir, 1998). The incorporation of volcanoclastic detritus generally results in a low K_2O/Al_2O_3 ratio (Ben Hothman et al., 1989), while diagenetic uptake of K has the opposite effect (Karl et al., 1992); in our case, the first hypothesis seems more consistent with the data, showing lower K_2O/Al_2O_3 ratio in the (N)CFMAST-HC groups compared to the NKCFMAST-HC group. Rb and Cs have a similar behaviour to that of K (Fig. 4.19).

- **Strontium** has a positive correlation with CaO (Fig. 4.19), and its abundance is mainly controlled by the relative proportion of calcium carbonate, clays and quartz in the protolith, being more concentrated in CaO-rich samples in each chemical group.

- **Barium** is always depleted in the (N)CFMAST-HC groups, while it is similar to TM85 in the NKCFMAST-HC group (Fig. 4.19); Ba is positively correlated with Al_2O_3, and, to a lesser extent, to SiO_2, suggesting that it was present in the clay fraction of the protoliths. Ba contents minor than 200 ppm have been reported for volcanic sediments (Peate et al., 1997), further supporting a volcanoclastic origin for the (N)CFMAST-HC samples.

- **Rare Earth Elements** patterns of marine sediments reflect those of the continents, which are quite uniform (Taylor and McLennan, 1985). All the samples from different groups have a REE pattern comparable to TM85, with no positive or negative Ce anomalies typical of slow rate accumulating sediments or hydrothermal ones (Plank and Langmuir, 1998). REE show a linear positive correlation to Al_2O_3 in almost all the samples, suggesting that they were hosted in the clay fraction of the sediment. Samples belonging to the (N)CFMAST-HC groups have, on average, lower REE total amounts compared to the NKCFMAST-HC group, reflecting lower abundance of clays in the protolith and/or weathering. Marbles (Types 1A and 3A) have low concentrations of REE (as commonly observed in sedimentary carbonatic rocks: Haskin et al., 1966; Jarvis et al., 1975), and in each group the MgO-rich samples have lower REE amounts compared to CaO-rich samples. Another factor controlling REE pattern could be the incorporation of volcanic detritus, leading to flat REE trends (depending on the source), small Eu anomalies and lower concentrations of REE (McLennan et al., 1990). La_N/Yb_N ratio in the NKCFMAST-HC samples is comparable to continental detritus (LREE-enriched, up to 19), while contributions of volcanic sources in the (N)CFMAST-HC samples could have been responsible for the observed flat patterns (La_N/Yb_N up to 10). Furthermore, negative Eu anomalies are observed in the NKCFMAST-HC samples, while they are less developed in the (N)CFMAST-HC samples (positive only in one sample, probably related to the high plagioclase content), consistently with the hypothesis of a calc-alkaline volcanic input in the source for the (N)CFMAST-HC groups.

- **High field strength elements** (Y, Nb, Ta, Ti, Zr, Hf and Th) generally show a positive correlation with Al_2O_3 in a variety of sediments (Plank and Langmuir, 1998), suggesting a detrital origin. For the studied samples, this is true for Th, Y and Nb for all the chemical groups, while Zr and Hf show less systematic variations; in the NKCFMAST-HC samples Ta and TiO_2 are positively correlated to Al_2O_3, while in the (N)CFMAST-HC samples these trace elements are present in low amounts. A low Th/Al_2O_3 ratio such as that in the (N)CFMAST-HC groups is consistent with volcanic input (Plank and Langmuir, 1998). Detrital zircons can easily accumulate with quartz in the sandy fraction of the sediments (Taylor and McLennan, 1985; McLennan et al., 2001), resulting in Zr enrichment in SiO_2-rich samples. Here, Zr positively correlates with SiO_2 in Types 3B and 3F, while in Types 3C, 3D and 3E and in the (N)CFMAST-HC samples this correlation is less developed (and Zr amount is lower). Sedimentary sorting can also affect the bulk Ti, Th, La, Ce and Nd due to Ti-oxides, monazite, apatite and other heavy minerals accumulation (Fletcher et al., 1992). Here, whole-rock composition of these elements is similar to, or slightly enriched (max 3 times in groups 3C, 3D, 3E and 3F) with respect to TM85. The slight enrichment in La and Th compared to TM85 in some samples can be due to sedimentary sorting, but overall the other trace elements reveal that fractionation did not alter the total bulk composition (McLennan and Taylor., 1981; Taylor and McLennan, 1985, Garcia et al., 1984).

- **Niobium and Tantalum** are considered pair elements with a limited range in their ratio (Nb/Ta=11-17 in most rocks on Earth: Munker et al., 2003); here, (N)CFMAST-HC samples have higher Nb contents compared to the NKCFMAST-HC samples, leading to a higher Nb/Ta ratio (14 *vs.* 11.5). Higher Nb/Ta ratios are typical of volcanic input, while lower values indicate a continental source (Plank, 2014; Fig. 4.20b).

- **Scandium** shows a well-developed linear positive correlation with Al_2O_3 in the NKCFMAST-HC group, suggesting a detrital origin, while it is depleted and varies unsystematically in the (N)CFMAST-HC groups (Fig. 4.19).

- **Nichel and Chromium** positively correlate with Al_2O_3 in the NKCFMAST-HC group, suggesting again a detrital origin, while they are present in lower concentrations in the (N)CFMAST-HC groups, without a clear systematicity (Fig. 4.19).

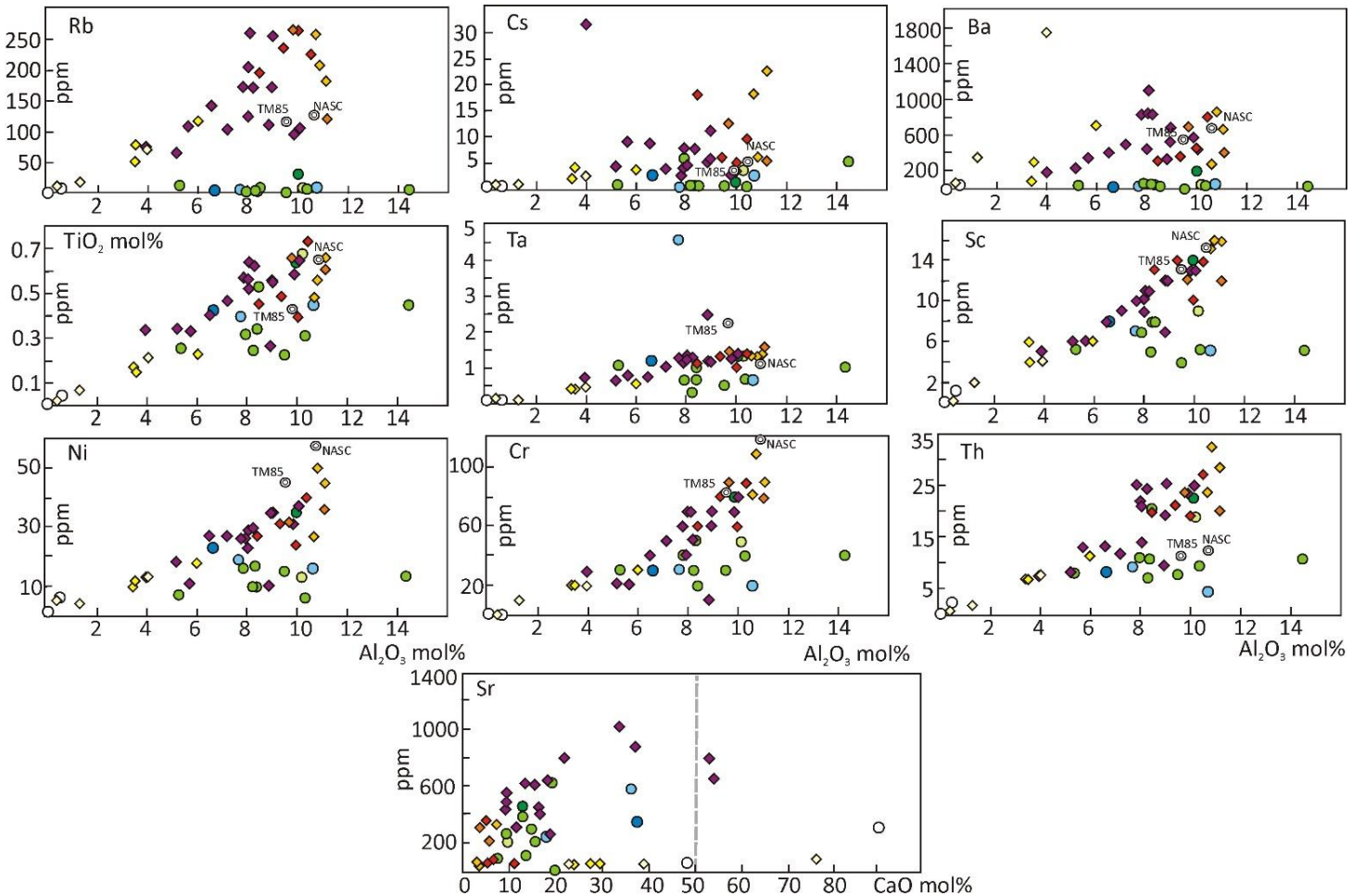

Fig. 4.19 - Trace elements of CO_2-source rocks plotted against Al_2O_3 mol% (and CaO mol%). Colours and symbols as in Fig. 4.14. NASC: North American Shale Composite (Haskin et al., 1966).

– A further evidence supporting the hypothesis of a volcanic input in the protolith of the (N)CFMAST-HC groups is provided by the **incompatible trace elements (e.g. Th, U, Cs, Rb and REE)**. All the incompatible trace elements positively correlate with Al_2O_3 in the NKCFMAST-HC samples, consistently with incorporation in the detrital phase, whereas in the (N)CFMAST-HC samples they are present in lower concentrations (Fig. 4.19), without a clear correlation with Al_2O_3. This trend is typical of sediments with andesitic volcanic input (Taylor and McLennan, 1985; Plank and Langmuir, 1998).

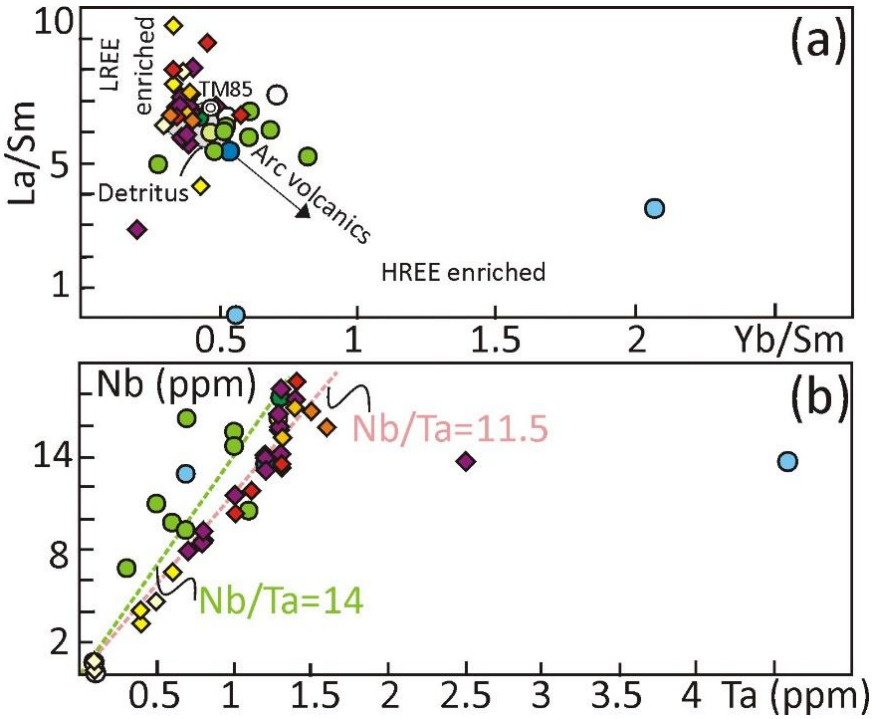

Fig. 4.20 - Diagrams of REE and HFSEs for the analysed CO_2-source rocks. (a) La/Sm ratio reflect LREE enrichment, while Yb/Sm reflects HREE enrichment. Continental detritus (grey area) is typically enriched in LREE, while sediments with volcanic input have a more flat pattern. Continental detritus is from Taylor and McLennan (1985), Gromet et al. (1984), and Ben Othman et al. (1989). (b) Nb –Ta define two slightly different trend in the different chemical groups.

4.4.2 Conclusions

CO_2-source rocks are widespread in the central and eastern sector of the Himalayan chain, at different structural levels of both LHS and GHS. Petrographic observations, together with bulk-rock major and trace elements geochemical analysis, allow to distinguish three main CO_2-source rock chemical groups, which reflect primary differences in the protolith compositions.

Field data suggest that: (i) (N)CFMAST-HC samples occur as thin (dm to m-thick) layers in the host metapelitic sequence, locally cropping out at structural levels that can be traced over hundreds of kilometres, features typical of bentonite occurrence (Elzea and Murray, 1994); (ii) NKCFMAST-HC samples constitute thick layers (metre to hundreds of m -thick) in the host metapelites, resembling a typical basin pelitic sequence with marly intercalations. Specific trace elements show different patterns in the different chemical groups, supporting again the hypothesis of a different protolith's nature for the three groups.

Chapter 5

Timing, duration and magnitude of CO_2-degassing in the Himalayas

5.1 Introduction

Being the most prominent recent and still active "large-hot" orogen on Earth, the Himalayan belt is the best candidate for the generation of a significant amount of metamorphic CO_2 during the Cenozoic. Previous studies aimed at quantifying metamorphic CO_2 degassing in the Himalayas yield conflicting results and argue either in favour of a significant contribution to periods of greenhouse global warming in the past (Becker et al., 2008; Kerrick and Caldeira, 1993), or against it (Kerrick and Caldeira, 1998, 1999; Selverstone and Gutzler, 1993). The nature and magnitude of the metamorphic CO_2 cycle in the Himalaya, however, is still poorly known because, as pointed out by Kohn and Corrie (2011), Himalayan calc-silicate rocks have been largely ignored in previous metamorphic studies. Major uncertainties are: **(1)** the volumes of CO_2-source rocks and their relevant mineral assemblages; **(2)** the nature of the metamorphic CO_2-producing reactions; **(3)** the P-T conditions at which the decarbonation reactions took place; **(4)** the timing and duration of CO_2-producing events, which is essential for understanding whether the Himalayan orogeny was responsible for ancient periods of global warmth and for estimating the annual mass flux of CO_2 released during these periods.

Concerning **point (1)**, although calc-silicate rocks in the metamorphic core of the Himalaya (i.e. in the Greater Himalayan Sequence: GHS) have been reported since the pioneering works of Bordet (1961), Gansser (1964) and Le Fort (1975), a systematic study of the different types of calc-silicate rocks and of their distribution within the GHS has been undertaken only recently (Rolfo et al., 2015b, 2017 and this study, see Chapter 4). **Point (2)** has also been a major focus of recent studies (Groppo et al., 2013b, 2017): devolatilization reactions in two different types of Himalayan calc-silicate rocks (i.e. Types 1C and 3F) have been investigated using a novel approach which combines phase diagram modelling with a detailed interpretation of microstructures. New CO_2-producing reactions have been recognised, involving Ca-Mg-Fe- (garnet, clinopyroxene) and Ca-Na- (plagioclase, scapolite) solid solutions, as well as K-bearing phases (biotite, muscovite, K-feldspar). Groppo et al. (2017) also provided preliminary insights on point (4) by demonstrating that, in internally buffered systems, CO_2 is mainly produced at isobaric invariant points, thus suggesting that the duration of the CO_2-producing events is significantly shorter than the duration of prograde metamorphism.

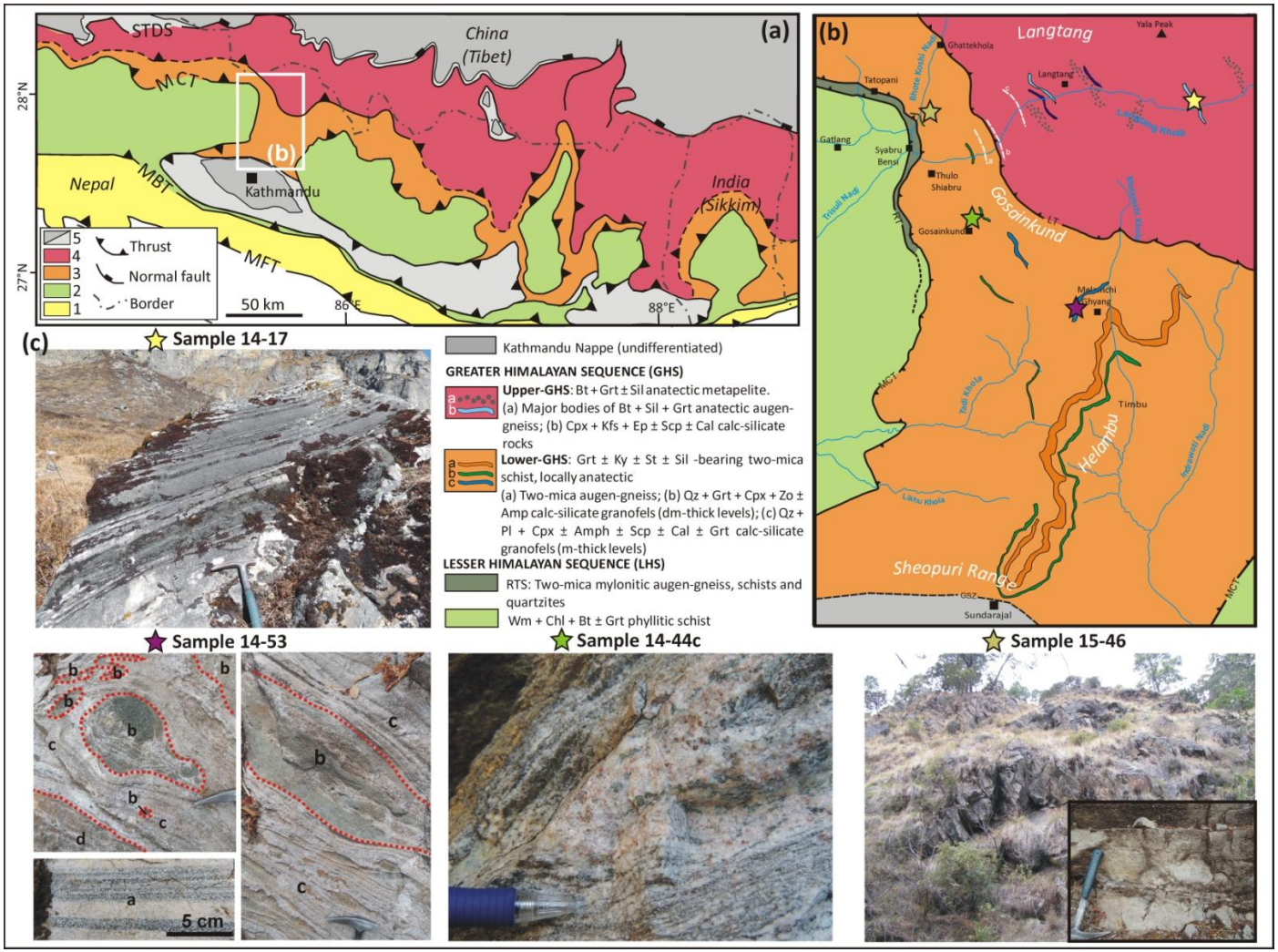
(a)
STDS
China
(Tibet)
MCT
(b)
Kathmandu
Nepal
MBT
India
(Sikkim)
MFT
28°N
27°N
86°E
88°E
50 km
5
4
3
2
1
Thrust
Normal fault
Border
(b)
Langtang
Yala Peak
Ghattekhola
Tatopani
Langtang
Gatlang
Syabru Bensi
Thulo Shiabru
Gosainkund
Melamchi Ghyang
Timbu
Helambu
Sheopuri Range
Sundarajal
GSZ
MCT
(c)
Sample 14-17
Kathmandu Nappe (undifferentiated)
GREATER HIMALAYAN SEQUENCE (GHS)
Upper-GHS: Bt + Grt ± Sil anatectic metapelite.
(a) Major bodies of Bt + Sil + Grt anatectic augen-gneiss; (b) Cpx + Kfs + Ep ± Scp ± Cal calc-silicate rocks
Lower-GHS: Grt ± Ky ± St ± Sil -bearing two-mica schist, locally anatectic
(a) Two-mica augen-gneiss; (b) Qz + Grt + Cpx + Zo ± Amp calc-silicate granofels (dm-thick levels); (c) Qz + Pl + Cpx ± Amph ± Scp ± Cal ± Grt calc-silicate granofels (m-thick levels)
LESSER HIMALAYAN SEQUENCE (LHS)
RTS: Two-mica mylonitic augen-gneiss, schists and quartzites
Wm + Chl + Bt ± Grt phyllitic schist
Sample 14-53
5 cm
Sample 14-44c
Sample 15-46

Fig. 5.1 - (a) Geological sketch map of the central–eastern Nepal Himalaya, showing major tectono-metamorphic units (modified from Goscombe & Hand, 2000; He et al., 2015; Wang et al., 2016 and based on our own data). The white rectangle indicates the location of (b). 1: Siwalik deposits; 2: Lesser Himalayan Sequence; 3: Lower Greater Himalayan Sequence; 4: Upper Greater Himalayan Sequence; 5: Tethyan Sedimentary Sequence (dark: Ordovician-Mesozoic; light: Precambrian-Cambrian). MFT, Main Frontal Thrust; MBT, Main Boundary Thrust; MCT: Main Central Thrust; STDS: South Tibetan Detachment System. **(b)** Geological map of study area in central Nepal Himalaya (modified from Rapa et al., 2016 and Chapter 3) and location of the studied samples (stars). RT: Ramgarh Thrust; GSZ, Galchi Shear Zone (from He et al., 2015); MCT, Main Central Thrust; LT, Langtang Thrust. **(c)** Representative field occurrence of the studied samples. Mineral assemblages for different portion of sample 14-53: (a) quartz + clinopyroxene + Ca-plagioclase; (b) garnet + Ca-plagioclase + clinopyroxene + zoisite; (c) quartz + clinopyroxene + Ca-plagioclase + k-feldspar + scapolite ± calcite; (d) quartz + garnet + scapolite + clinopyroxene + Ca-plagioclase.

Points (3) and (4), i.e. the estimate of both the P-T conditions and the timing of CO_2-producing events which occurred during the Himalayan prograde metamorphism, are addressed in this Chapter. The direct estimate of the P-T evolution experienced by calc-silicate rocks is not straightforward because the composition of the fluid is a non-negligible variable (i.e. this is a three-variables issue). The P-T conditions experienced by these rocks can be indirectly estimated using the associated metapelites (e.g. Groppo et al., 2013b, 2017). As a drawback, indirect P-T estimations only provide qualitative knowledge about the timing of the events.

Alternatively, the relatively recent trace element thermometer based on the zirconium content in titanite (Zr-in-titanite: Hayden et al., 2008) is a promising method to directly constrain the thermal history of calc-silicate rocks, because titanite is a common accessory mineral in these lithologies and the Zr-in-titanite thermometer is independent from $X(CO_2)$ in the fluid. Titanite's Zr diffusivity is sufficiently slow allowing to retain the Zr-temperature up to at least 750-775 °C (Cherniak, 2006; Kohn and Corrie, 2011; see also Kohn, 2016, 2017 for a review). The Zr-in-titanite thermometer is, therefore, applicable to calc-silicate rocks from the GHS, which experienced peak temperatures $\leq$ 800 °C (e.g. Groppo et al., 2013b, 2017; Kohn and Corrie, 2011). A further advantage of titanite is that it can also be used as a chronometer (e.g. Frost et al., 2000; Kohn, 2017; Walters & Kohn, 2017), thus linking U-Pb ages with temperatures through simultaneous geochronology and trace element thermometry in single microanalytical spots. Recent petrochronological studies have demonstrated that Pb diffusivity in titanite is very slow (e.g. Kohn and Corrie, 2011; Gao et al., 2012; Spencer et al., 2013; Stearns et al., 2015). As a consequence, titanite crystals act as recorders of their prograde growth at high temperature. Few studies have successfully obtained titanite U-Pb ages from Himalayan calc-silicate rocks and other Himalayan lithologies (e.g. Cottle et al., 2011; Kohn and Corrie, 2011; Warren et al., 2012; Walters and Kohn, 2017). However, although well constrained in term of T and P, the titanite ages obtained so far are still not related to specific CO_2-producing events.

The aim of this Chapter is to constrain the P-T-t conditions at which CO_2 was produced during the Himalayan orogeny, focusing on different types of CO_2-source rocks, in order to point out similarities and/or differences in the CO_2-producing processes. In detail, type C of the CFMAST-HC group (Type 1C) and Types C and F of the NKCFMAST-HC group (Types 3C and 3F) are discussed. Types 1C and 3F are the most representative and abundant among their chemical groups (Rolfo et al., 2017) and derive from bentonitic and marly protoliths, respectively (see Chapter 4); Type 3C is representative of a carbonate-rich pelitic protolith, hardly recognizable in the field because carbonate has been often totally consumed during prograde metamorphism. This latter lithology (named "pelite" in Kerrick and Caldeira, 1999) has never been studied in terms of CO_2-productivity, so far. For all the studied samples, the different metamorphic CO_2-producing reactions are petrologically investigated and the amounts of CO_2 produced per volume unit of reacting rock are estimated. Furthermore, for one sample (Type 3F), metamorphic reactions that led to the simultaneous growth of titanite and production of CO_2 are identified and fully characterized for the first time.

The correlation of T-t data from different titanite generations with specific CO_2-producing reactions, allows constraining the timing, duration and P-T conditions of the main CO_2-producing events, as well as the amounts of CO_2 produced.

5.2 Methods

5.2.1 Whole-rock microstructural and mineral chemical characterization

Qualitative major element X–ray maps of the whole thin sections were acquired using the same technique and procedure of §3.3.3. Quantitative modal amounts of each mineral phase were obtained by processing the μ-XRF maps with the software program Petromod (Cossio et al., 2002).

The rock-forming minerals were analysed using the same technique and procedure of §3.3.2. For samples 15-46, 14-53 and 14-17, the bulk rock compositions (Tab. 5.1, Fig. 5.2) were calculated by combining the mineral proportions obtained from the modal estimate of the μ-XRF maps with mineral chemistry acquired with the SEM–EDS. The fine-grained nature of epidote in sample 14-53c hampered its discrimination in the μ-XRF map; therefore, its modal amount was estimated visually. For sample 14-17, the homogeneous domain was chosen. For sample 14-44c, the bulk rock composition was obtained through ICP-MS technique at ALS-geochemistry laboratory of Sevilla, Spain.

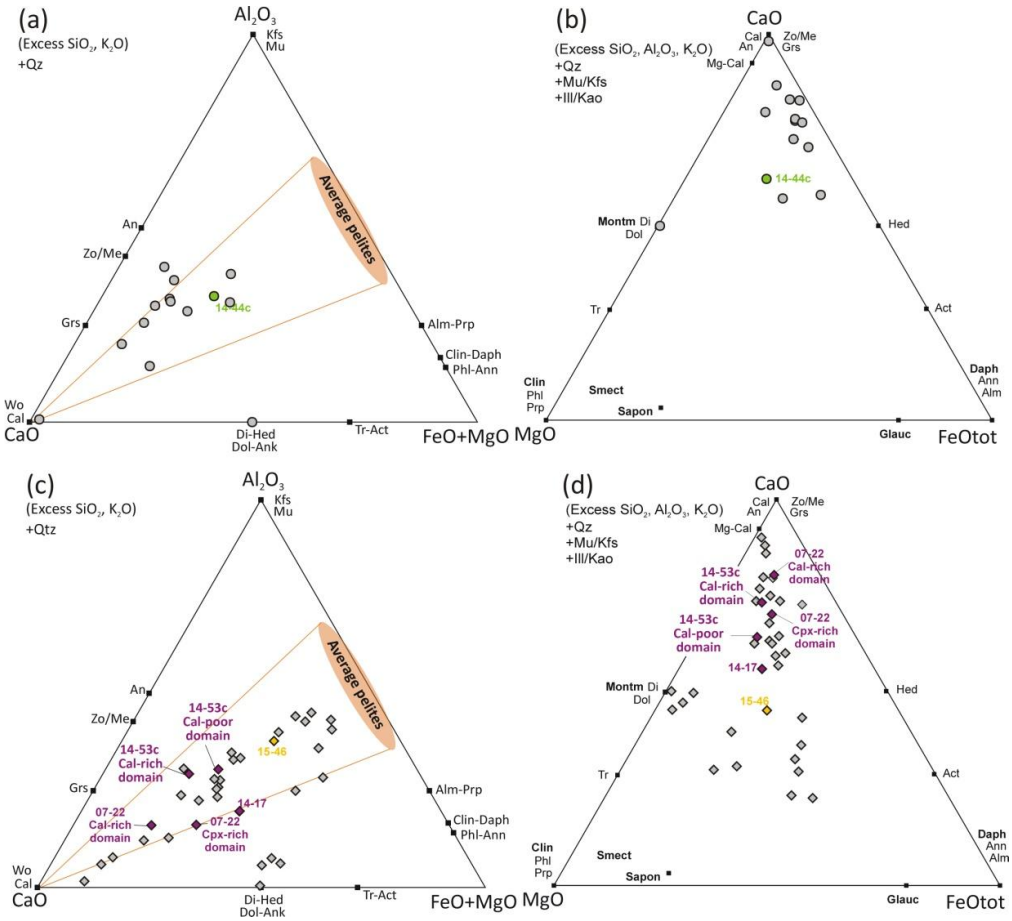

Fig. 5.2 – (a,b) Bulk compositions of Types 1 and 2 CO_2-source rocks (sample 14-44c is reported in green) collected in central-eastern Nepal (along cross-sections 5 to 14 reported in §Fig. 6.2) projected onto the ACF (Al_2O_3–CaO–MgO+FeO) and CMF (CaO–MgO–FeO) diagrams. **(c,d)** Bulk compositions of Type 3 CO_2-source rocks from both the L-GHS and U-GHS of central and eastern Nepal projected onto the ACF (Al_2O_3–CaO–MgO+FeO) and CMF (CaO–MgO–FeO) diagrams. Bulk compositions of the studied sample 14-53c (calcite-rich and calcite-poor domains) and those of sample 07-22 studied by Groppo et al. (2017) are reported purple (Type 3F). Bulk composition of sample 15-46 is reported in yellow (Type 3C). Average pelite composition in (a) and (c) is calculated from Rapa et al. (2016).

Table 5.1 Bulk compositions of the modelled samples (mol%)

Sample	14-44c	15-46	14-53c		14-17
			Cal-poor domain	Cal-rich domain	
SiO_2	80.00	79.12	74.81	67.91	60.13
TiO_2	0.29	0.46	0.92	0.62	0.78
Al_2O_3	6.59	6.86	6.76	8.65	7.22
MgO	0.98	3.42	3.56	3.74	6.75
FeO	1.03	2.74	1.93	2.00	4.89
MnO	0.69	0.07	0.00	0.00	0.00
CaO	9.44	5.12	9.77	15.29	15.28
Na_2O	0.88	1.12	0.32	0.65	1.02
K_2O	0.10	1.09	1.93	1.15	3.93
Total	100.00	100.00	100.00	100.00	100.00

5.2.2 Detailed description of the studied samples

5.2.2.1 Sample 14-44c (Type 1C)

Sample 14-44c was collected from a calc-silicate boudin outcropping in the Gosainkund region of central Nepal (N28°05'13.0'' E85°23'33.9''; ~ 4625 m a.s.l.; Fig. 5.1a,b); the boudin is embedded in the host metapelites of the L-GHS. The metapelitic gneisses hosting the studied sample experienced peak P-T conditions of 700-750 °C, 8.6-10 kbar (sample 14-44a: Rapa et al., 2016 and Chapter 3). The sample texture is granoblastic and fine-grained, being characterized by a mineral assemblage consisting of quartz + plagioclase + garnet + clinopyroxene + epidote + amphibole + calcite + titanite. Representative microstructures and mineral chemical data are reported in Fig. 5.3 and Fig. 5.4.

Garnet is mostly a grossular-almandine solid solution, showing locally a weak zonation, with XMg and XFe decreasing from core to rim, while XCa increases and XMn is constant

(core: XMg=0.07-0.08, XCa=0.48-0.49, XFe=0.30-0.31, XMn=0.14-0.15; rim: XMg=0.04-0.05, XCa=0.50-0.53, XFe=0.27-0.29 and XMn=0.14-0.15). This compositional zoning is locally patchy (Fig. 5.3e,g). Garnet porphyroblasts include chlorite (XMg=0.48-0.72, with Mn content up to 0.35 a.p.f.u.), calcite (pure, with Mn=0.06 a.p.f.u., Mg=0.04 a.p.f.u. and Fe^{2+}=0.04 a.p.f.u.) and quartz, showing lobate and corroded margins against it (Fig. 5.3a-h), plagioclase and rare clinopyroxene, amphibole and k-feldspar. Equilibrium relationships between garnet, clinopyroxene, plagioclase and quartz are observed. **Clinopyroxene** porphyroblasts are diopsidic in composition, with XMg=0.71-0.75 (and Mn up to 0.04 a.p.f.u.); clinopyroxene inclusions in garnet have a similar composition. Clinopyroxene may include quartz, amphibole (mostly actinolite with XMg=0.72-0.46) and titanite.

Plagioclase is almost a pure anorthite (XAn=0.90-0.97). Plagioclase included in garnet is often replaced by an unknown Ca+Al+Si hydrated phase, probably zeolite-like. **K-feldspar** rarely included in garnet is pure orthoclase. **Epidote** is locally zoned, with XZo decreasing from core to rim (XZo from 0.89 to 0.61). **Calcite** in the matrix is almost pure, with Mn=0-0.06 a.p.f.u., Mg=0-0.02 a.p.f.u. and Fe^{2+}=0-0.03 a.p.f.u.

Retrograde microstructures are widespread, with the development of amphibole (mostly actinolite and minor Mg-hornblende, with XMg=0.63-1.00) + epidote + calcite ± chlorite (XMg=0.47-0.71, with Mn up to 0.19 a.p.f.u.) aggregates at the expenses of clinopyroxene and plagioclase (Fig. 5.3i-n).

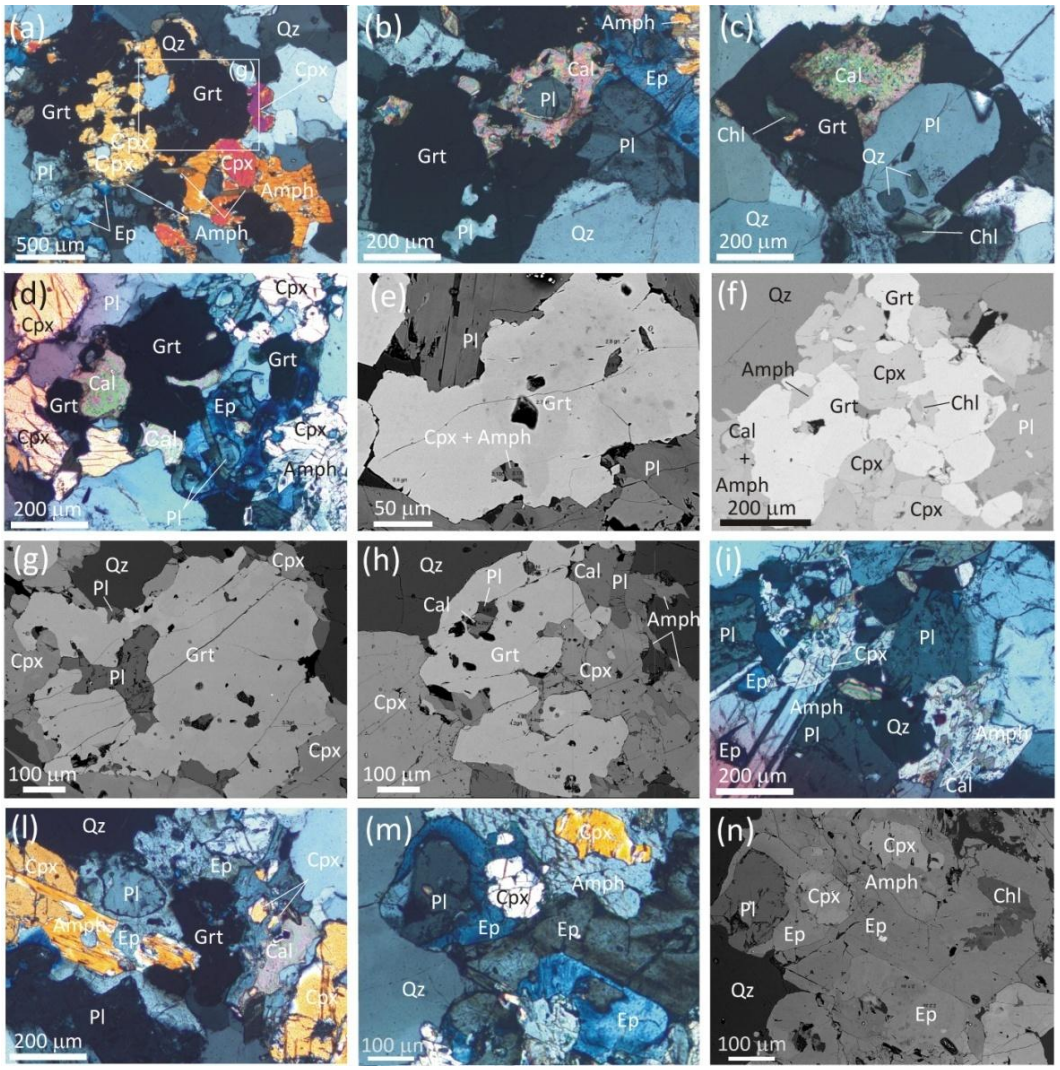

Fig. 5.3 – Representative microstructures of sample 14-44c. (a) Garnet porphyroblast growing at the expenses of clinopyroxene, which shows lobate margins against it. Late amphibole develops on clinopyroxene (XPL). **(b-d)** Garnet porphyroblasts include calcite ± plagioclase ± chlorite with lobate and corroded margins (PPL). In (d) late epidote (anomalous blue interference colours) develops at the expenses of plagioclase and garnet. **(e)** Inclusions of amphibole + clinopyroxene in garnet, which shows a patchy zoning (different brightness in BSE colours). **(f)** Garnet, clinopyroxene and plagioclase grow in equilibrium, with sharp contacts between each other. Late calcite + amphibole develop on garnet (BSE). **(g)** Plagioclase included in garnet, showing lobate margins (BSE). **(h)** Garnet porphyroblast growing at the expenses of calcite + plagioclase ± clinopyroxene (BSE). **(i-n)** Retrograde microstructures, with development of amphibole + epidote + calcite aggregates at the expenses of clinopyroxene (i,m,n), garnet (l) and plagioclase (i,m,n). In (m,n) epidote is zoned: the prograde vs. late epidotes are characterized by grey vs. blue anomalous interference colours. The prograde epidote includes chlorite (XPL, BSE).

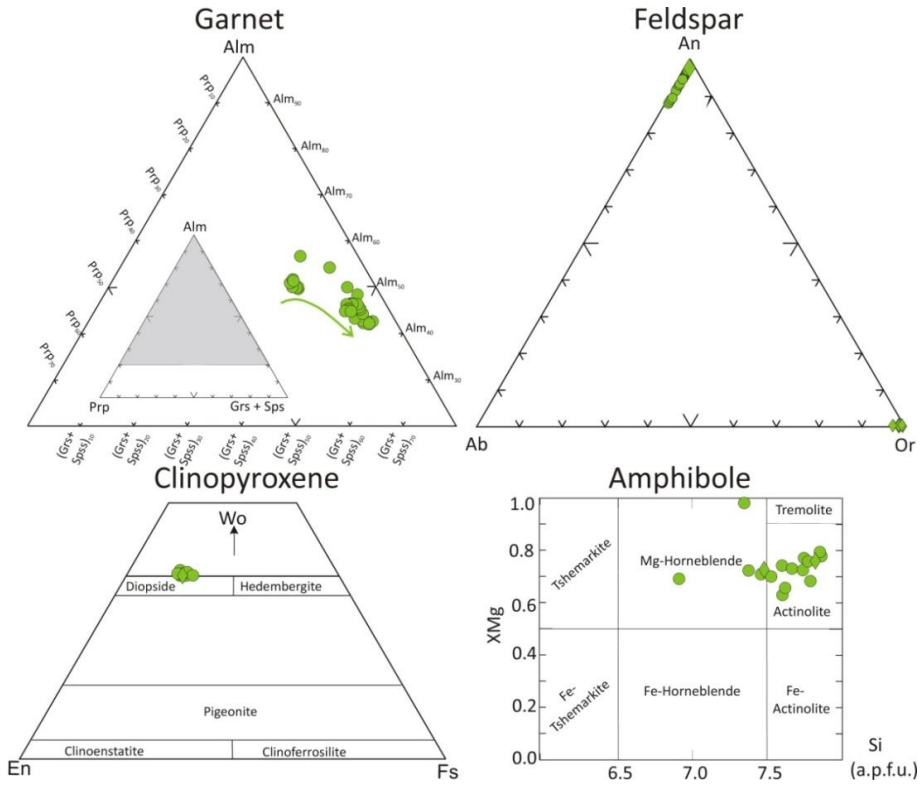

Fig. 5.4 - Compositional diagrams for garnet, plagioclase, clinopyroxene and amphibole in sample 14-44c. Circles: matrix; diamonds: inclusions.

5.2.2.2 Sample 15-46 (Type 3C)

Sample 15-46 was collected in the Gatlang-Langtang region, from the lower structural levels of the L-GHS (N28°12'39.1'', E85°21'43.8'' - 1905 m a.s.l.; Fig. 5.1); the outcrop mainly consists of a fine-grained two-mica + garnet –bearing gneiss with metric intercalations of fine-grained, garnet-bearing biotitic gneiss with calc-silicate minerals. The metapelitic gneiss hosting the studied sample experienced peak P-T conditions of 710-730 °C and 9.6-11 kbar (sample 14-03, Chapter 3).

Sample 15-46 is a fine-grained gneiss consisting of (in vol%) quartz (56%), scapolite (16%), biotite (15%), plagioclase (10%), minor garnet (1.5%), calcite (<1%) and epidote, and accessory titanite (Fig. 5.5a). Representative microstructures and mineral chemical data are reported in Fig. 5.5, Fig. 5.6 and Fig. 5.7. The main foliation is defined by biotite alignment in discontinuous mm-thick domains, alternating with pluri-mm thick quartz + scapolite + plagioclase domains (Fig. 5.5b,c).

Garnet porphyroblasts (up to 0.4 cm across) have a skeletal habit and include rounded quartz, calcite and epidote (Fig. 5.6a-e), and minor biotite, white mica and chlorite flakes. Rounded plagioclase is often included in garnet and in quartz in turn included in garnet.

Calcite relics included in garnet are characterized by higher XMn contents (up to XMn=0.12) with respect to calcite in the matrix (XMn=0.00-0.01). Garnet is mostly an almandine-grossular solid solution and it shows a weak zonation, with XCa slightly increasing and XFe and XMn slightly decreasing toward the rim (core: XFe=0.48, XCa=0.32, XMg=0.10, XMn: 0.09; rim: XFe=0.46, XCa=0.37, XMg=0.11, XMn: 0.06). **Scapolite** includes rounded epidote, quartz and plagioclase (XAn=0.47-0.56) and minor biotite flakes (Fig. 5.6f-h); it is homogeneous in composition, with eqAn=0.63-0.65. scapolite is often replaced by a plagioclase ± calcite corona (Fig. 5.6i-m). **Plagioclase** in the corona is slightly zoned, with higher An contents toward the contact with scapolite (from XAn=0.46 to XAn=0.38). Most of the plagioclase in the matrix likely derives from the replacement of scapolite, because it shows the same zoning and compositions as the plagioclase in the corona surrounding scapolite. Plagioclase included in garnet is XAn=0.34-0.81. **Biotite** included in garnet has lower XMg (XMg=0.44-0.47) and Ti content (Ti=0.03-0.06 a.p.f.u.) compared to biotite included in plagioclase, scapolite and in the matrix (XMg=0.57-0.63, Ti=0.06-0.18 a.p.f.u.). **Epidote** has XZo=0.56-0.66. **White mica** is rare; it is found either as inclusions in garnet or in the matrix (Fig. 5.6m). It is a muscovite, with Si=3.04-3.16 a.p.f.u. and Na=0-0.05 a.p.f.u. Ca content varies from 0 to 0.1 a.p.f.u. **Chlorite** is included in garnet and has high Mn content, varying from 0.06 to 0.20 a.p.f.u. Titanite is ubiquitous.

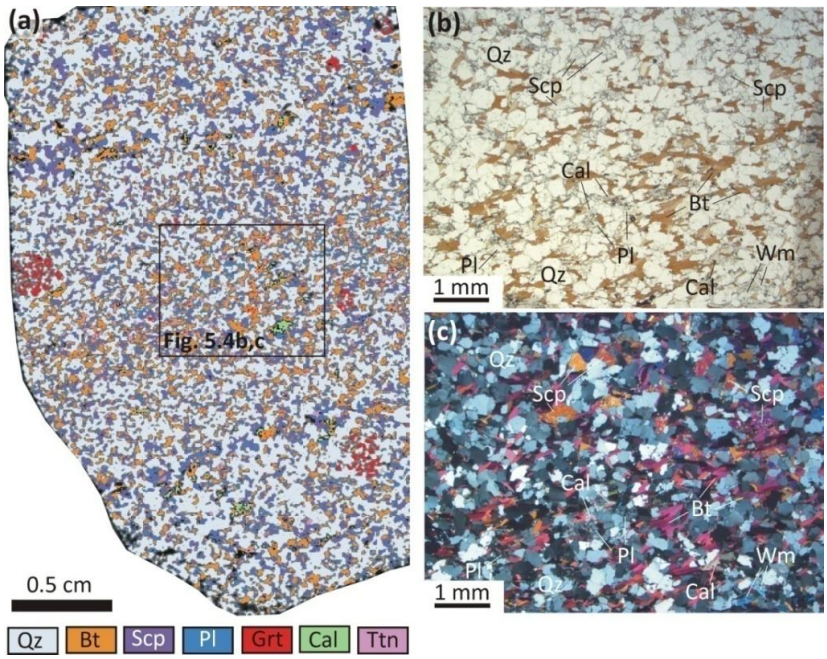

Fig. 5.5 - Representative microstructures of sample 15-46. (a) Processed µ-XRF map of sample 15-46. **(b,c)** Detail showing the gneissic foliation defined by biotite; white mica and calcite (often associated with plagioclase) are rare (b: PPL; c: XPL).

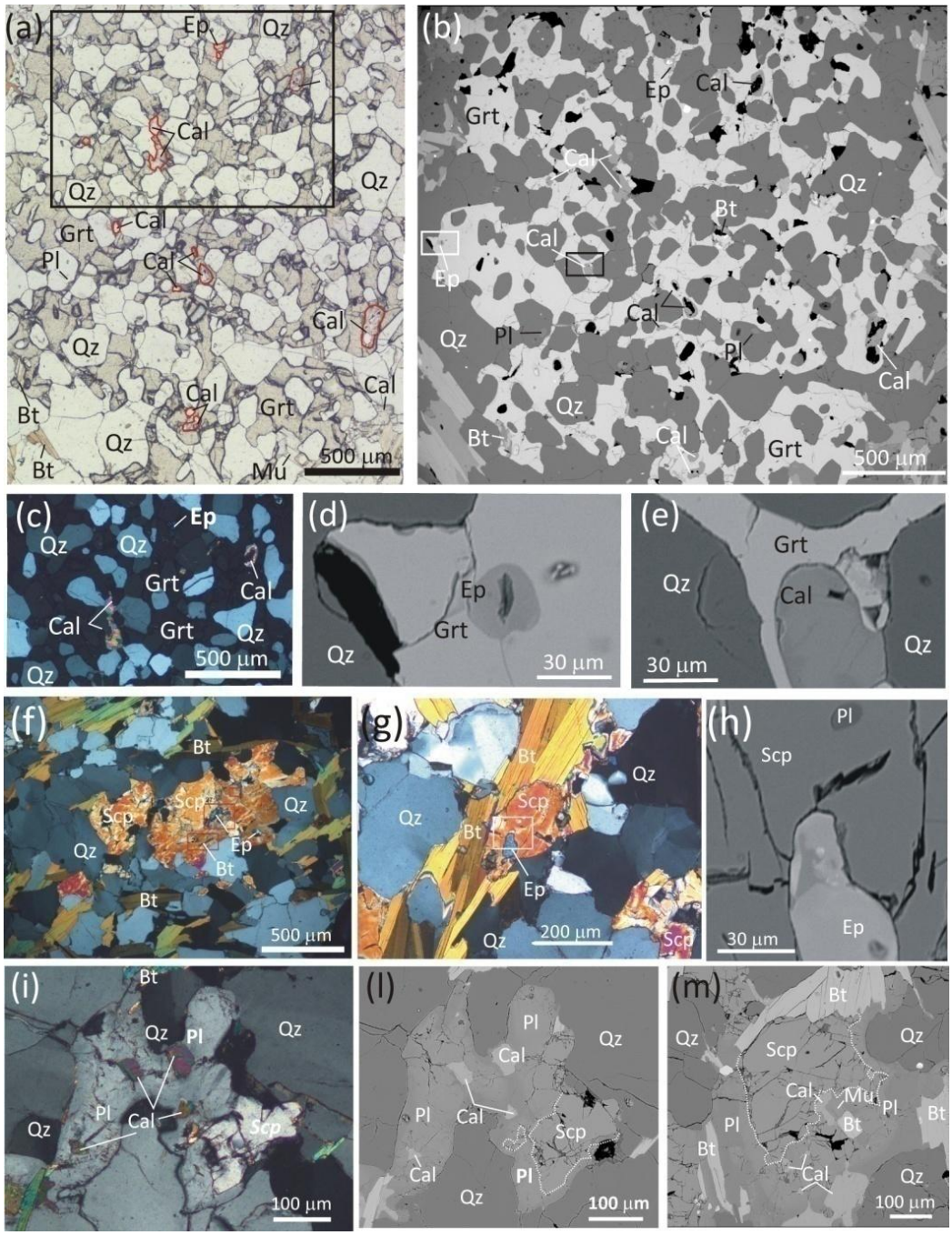

Fig. 5.6 - Representative microstructures of sample 15-46. (a-e) Garnet microstructures. (a,b) Garnet porphyroblast with a skeletal habit, including rounded quartz, calcite and epidote, and minor biotite. (a: PPL, b: BSE). The inset in (a) refers to (c); the insets in (b) refer to (d) and (e). **(c)** Detail of (a), showing calcite relics included in garnet (XPL). **(d,e)** Details of (b), showing rounded inclusions of epidote (d) and calcite (e) in garnet (BSE). **(f-m) Scapolite microstructures. (f,g)** Scapolite grains including rounded epidote crystals and minor biotite (XPL). The white inset in (g) refers to (h). (h) Detail of (g) showing rounded inclusions of epidote and plagioclase within scapolite (BSE). **(i-m)** Scapolite relicts replaced by plagioclase + calcite corona. Plagioclase is more calcic toward the contact with scapolite (brighter in the BSE images) (i: XPL; l,m: BSE).

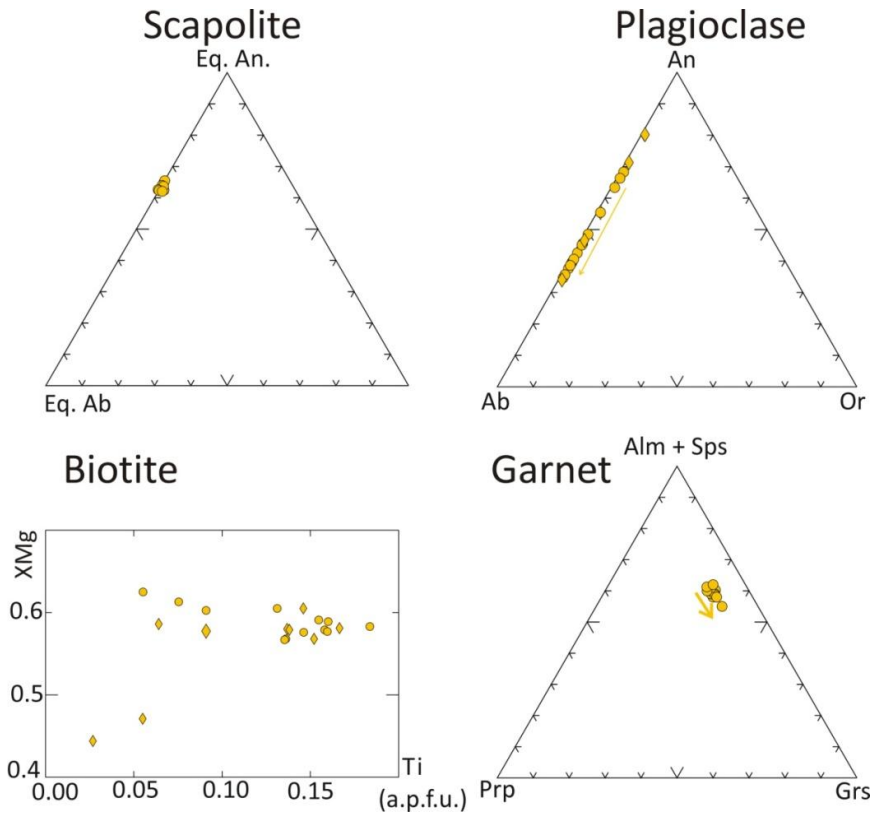

Fig. 5.7 - Compositional diagrams for scapolite, plagioclase, biotite and garnet in sample 15-46c. The arrow in the plagioclase diagram indicates a decrease in XAn from core to rim. The arrow in the garnet triangle indicates a grossular enrichment from core to rim. Circles: matrix; diamonds: inclusions.

5.2.2.3 Sample 14-53c (Type 3F)

Sample 14-53c was collected from a calc-silicate layer (~2 m -thick) embedded within metapelitic gneisses of the L-GHS, in the Gosainkund-Helambu region of central Nepal (N28°00'37.3'' E85°29'50.9''; 3365 m a.s.l.; Fig. 5.1b). The metapelitic gneisses hosting the studied sample experienced peak P-T conditions of 720-760 °C, 9-10 kbar (sample 14-52: Rapa et al., 2016). The calc-silicate layer from which the studied sample was collected shows a banded structure, being characterized by dm-thick layers with different mineral assemblages (Fig. 5.1c). These layers consist of: quartz + clinopyroxene + Ca-plagioclase (sample 14-53a); garnet + Ca-plagioclase + clinopyroxene + epidote (14-53b); quartz + clinopyroxene + Ca-plagioclase + k-feldspar + scapolite ± calcite (14-53c); quartz + garnet + scapolite + clinopyroxene + Ca-plagioclase (14-53d).

The studied sample 14-53c is a fine-grained calc-silicate rock with a granoblastic banded structure in which calcite -rich domains alternate to calcite -poor domains, defining a cm-thick layering (Fig. 5.8a). The main mineral assemblage in both domains consists of quartz + clinopyroxene + Ca-plagioclase + k-feldspar + scapolite ± calcite, minor epidote, biotite and titanite (Fig. 5.8b-e), and accessory bluish tourmaline and zircon. The modal proportion of the mineral phases is different in the two domains (in vol%): calcite-poor

domain: quartz (45%), clinopyroxene (11%), Ca-plagioclase (10%), k-feldspar (15%), scapolite (9%), epidote (4%), biotite (4%), titanite (2%); calcite-rich domain: quartz (34%), clinopyroxene (14%), Ca-plagioclase (14%), k-feldspar (9%), scapolite (17%), calcite (1%), epidote (6%), biotite (3%), titanite (2%). Representative microstructures and mineral chemical data are reported in Fig. 5.8-5.10.

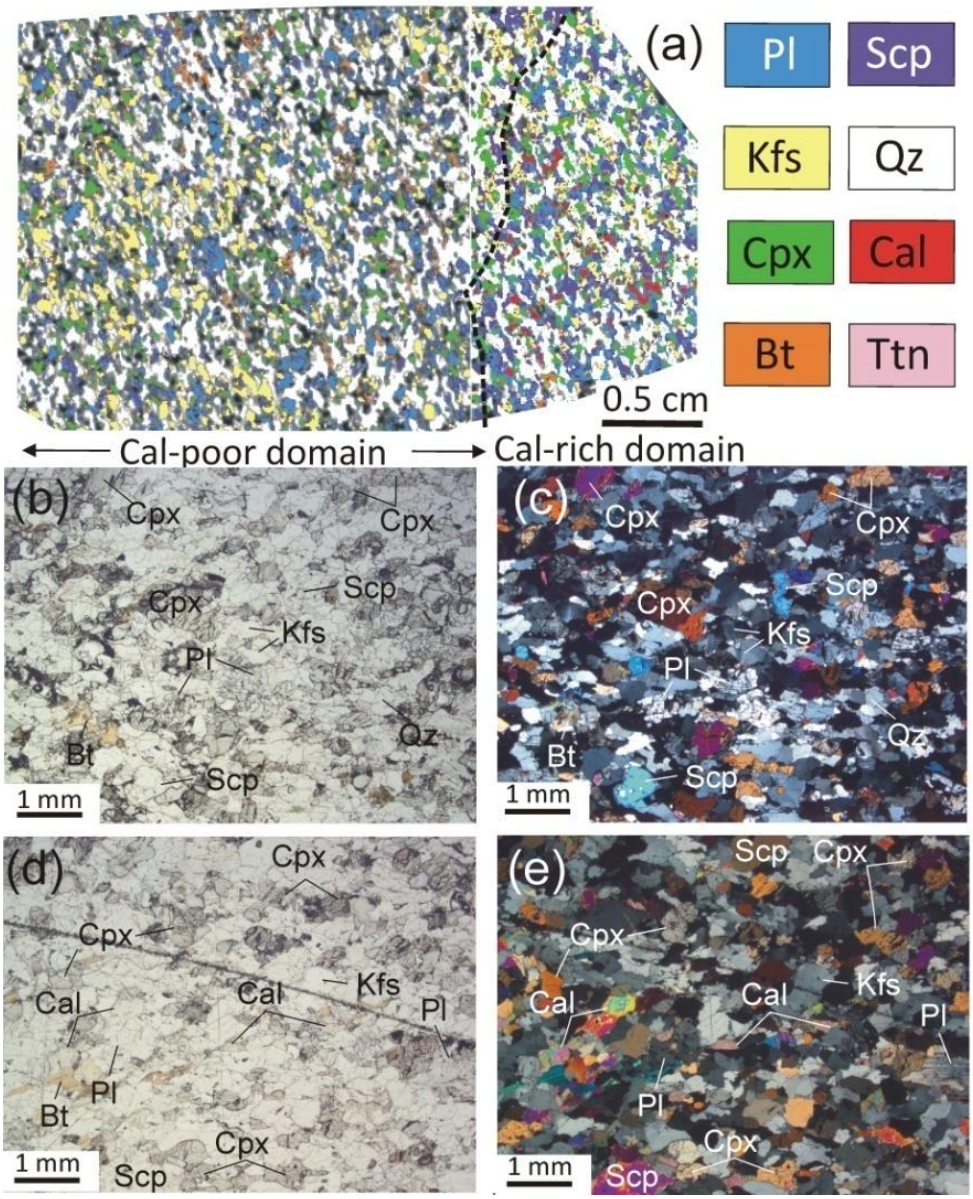

Fig. 5.8 – (a) Processed µ-XRF map of the whole thin section 14-53c, with distinction of calcite-rich and calcite-poor domains. Note that the small size of epidote hampered its discrimination in the µ-XRF map. Calcite-rich domains are characterized by higher modal amounts of calcite, scapolite and plagioclase and lower amounts of k-feldspar, quartz and biotite. **(b,c)** Details of the calcite-poor domain (b: PPL; c: XPL). **(d,e)** Details of the calcite-rich domain (d:PPL; e:XPL).

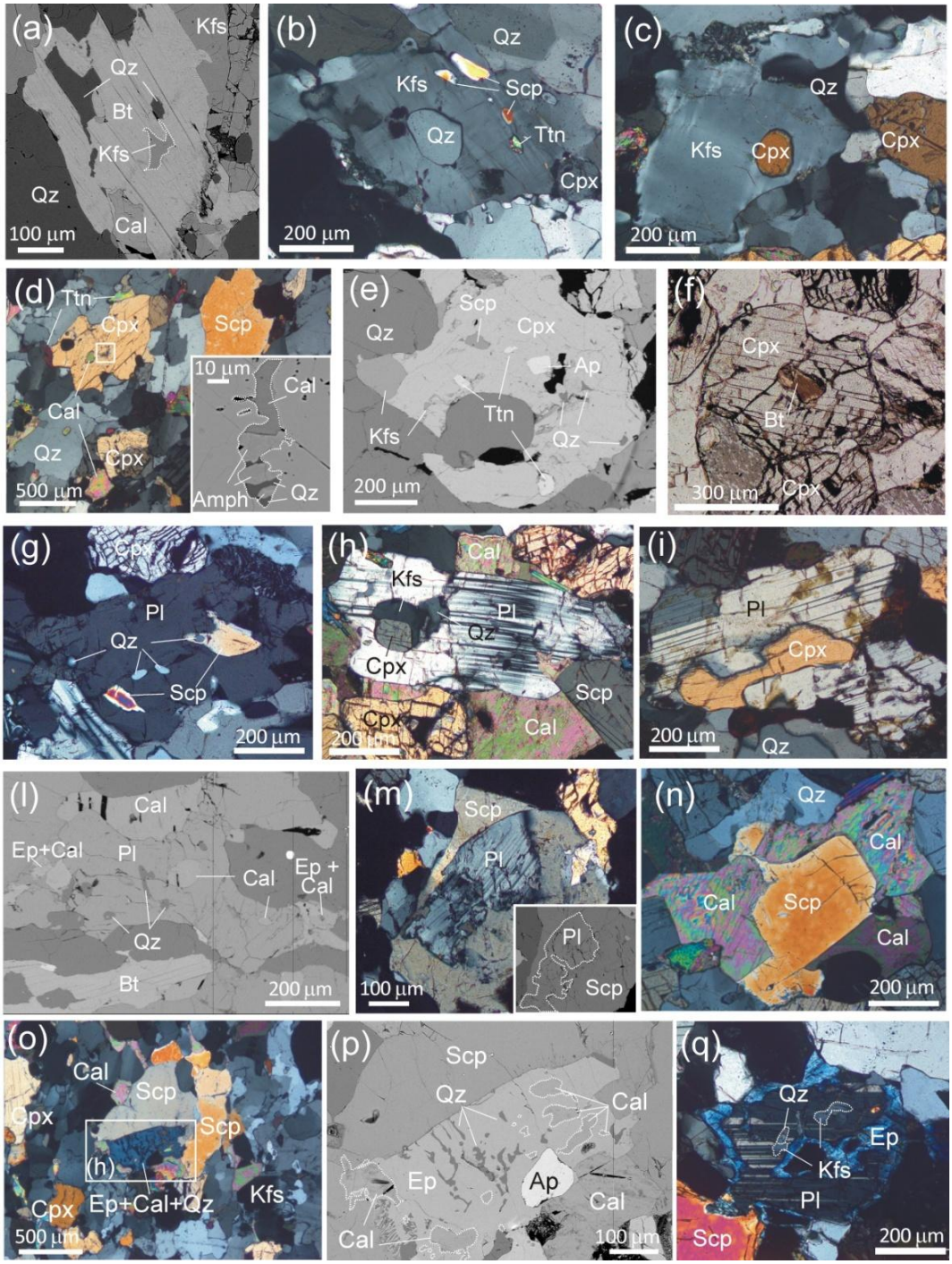
(a)
Kfs
Qz
Bt
Kfs
Qz
Cal
100 µm
(b)
Qz
Kfs
Scp
Qz
Ttn
Cpx
200 µm
(c)
Qz
Kfs
Cpx
Cpx
200 µm
(d)
Ttn
Cpx
Scp
10 µm
Cal
Cal
Qz
Cpx
500 µm
Amph
Qz
(e)
Scp
Qz
Cpx
Ap
Ttn
Kfs
Qz
200 µm
(f)
Cpx
Bt
300 µm
Cpx
(g)
Cpx
Pl
Qz
Scp
200 µm
(h)
Cal
Kfs
Pl
Qz
Cpx
Scp
Cpx
200 µm
Cal
(i)
Pl
Cpx
200 µm
Qz
(l)
Cal
Ep+Cal
Pl
Cal
Ep +
Cal
Qz
Bt
200 µm
(m)
Scp
Pl
Pl
Scp
100 µm
(n)
Qz
Cal
Cal
Scp
Cal
200 µm
(o)
Cal
Scp
Cpx
Scp
(h)
Cpx
Ep+Cal+Qz
Kfs
500 µm
(p)
Scp
Qz
Cal
Ep
Ap
Cal
Cal
100 µm
(q)
Qz
Ep
Kfs
Pl
Scp
200 µm

Fig. 5.9

Fig. 5.9 - (a-f) Representative microstructures of sample 14-53c involving k-feldspar and clinopyroxene. (a) K-feldspar and quartz inclusions in a biotite flake (BSE). **(b)** K-feldspar includes rounded quartz and scapolite crystals (XPL). **(c)** Rounded inclusion of clinopyroxene in k-feldspar (XPL). **(d)** Clinopyroxene granoblast in a calcite-rich domain (XPL). The inset shows a detail of the amphibole + calcite + quartz polymineralic inclusion hosted in the clinopyroxene core, with corroded and lobated margins against clinopyroxene (BSE). **(e)** Clinopyroxene granoblast in a calcite-poor domain, with scapolite, titanite and quartz inclusions in the rims. K-feldspar in the matrix exhibits straight contacts with the clynopiroxene (BSE). **(f)** Rounded biotite included in the clinopyroxene core in a calcite-rich domain (PPL). **(g-q) Representative microstructures of sample 14-53c involving plagioclase and scapolite. (g)** Scapolite and quartz inclusions in plagioclase, showing lobated and rounded margins against it (XPL). **(h)** Plagioclase granoblast in a calcite-rich domain, including clinopyroxene, k-feldspar and quartz (XPL). **(i)** Plagioclase in a calcite-poor domain, growing at the expenses of clinopyroxene (XPL). **(l)** Plagioclase from a calcite-rich domain includes rounded quartz and calcite. It is replaced by an aggregate of epidote + calcite at its margins (BSE). **(m)** Relict of plagioclase (bytownite) replaced by scapolite (XPL). The inset highlights the corroded margins of plagioclase (BSE). **(n)** Calcite growing on scapolite in a calcite-rich domain. (XPL). **(o)** Epidote + quartz + calcite symplectitic aggregate growing at the expense of scapolite (retrograde microstructure) (XPL). **(p)** Detail of (g) (BSE). **(q)** Plagioclase including k-feldspar and quartz, replaced by a epidote rim (retrograde microstructure) in a calcite-poor domain (XPL).

K-feldspar (XOr=0.95-1) in both domains includes quartz, rare scapolite and clinopyroxene (Fig. 5.9c,d), and is locally included in plagioclase; myrmekitic microstructures are observed at the interface with plagioclase. In the calcite -rich layers, k-feldspar is locally included in biotite, showing corroded and lobate margins against it (Fig. 5.9a). Triple joints between k-feldspar and scapolite are observed in the matrix. **Clinopyroxene** (XMg=0.64-0.67) is pale green and occurs as mm-sized granoblasts. The clinopyroxene core contains rare small mono- and polymineralic inclusions of amphibole (mostly actinolite with XMg=0.65-0.90) + calcite + quartz + titanite + biotite with corroded margins (Fig. 5.9d,f), while the rim includes mono-mineralic inclusions of quartz, scapolite, titanite and k-feldspar (Fig. 5.9e). Clinopyroxene is rarely included in plagioclase in both domains. **Plagioclase** (XAn=0.90-0.97) mainly occurs as medium-grained granoblasts in the matrix. In the calcite-poor domains, plagioclase often includes vermicular quartz and mono-mineralic inclusions of scapolite (Fig. 5.9g), k-feldspar, and rare epidote. In the calcite-rich layers it includes rounded calcite, scapolite, clinopyroxene, k-feldspar, and quartz (Fig. 5.9h,i,l). A less calcic plagioclase (XAn=0.73-0.78) is rarely preserved as relict inclusions in scapolite (Fig. 5.9d) and titanite. Plagioclase is locally surrounded by a rim of epidote in the calcite-poor domains (Fig. 5.9h), and of epidote + calcite in the calcite-rich domains. **Scapolite** in the matrix ranges from eqAn=0.61-0.68 in the calcite-poor domains, to eqAn=0.45-0.68 in the calcite-rich domains and contains some Cl (0.31-1.55 wt%). Matrix scapolite includes quartz, rare relict plagioclase (XAn=0.73-0.78) and titanite, and is locally partially replaced by symplectitic aggregates of epidote + quartz ± calcite (Fig. 5.9f,g). Scapolite, included in k-feldspar, plagioclase, and clinopyroxene, has a composition in the range eqAn=0.64-0.75; a few inclusions in titanite show lower eqAn values (eqAn=0.48).

Biotite (XMg=0.57-0.66; Ti=0.04-0.06 a.p.f.u.) in the matrix occurs as deformed lamellae with corroded margins; it is sometimes included in clinopyroxene and titanite, with lobate

and rounded margins against the host mineral. **Epidote** included in plagioclase has XZo=0.65. Czo forming the symplectitic aggregates replacing scapolite is locally zoned, with XZo=0.57-0.63 in the core and XZo=0.81 in the rim. Epidote replacing plagioclase and clinopyroxene has XZo=0.61-0.79. **Calcite** is almost pure, with small amounts of Fe (0.01-0.02 a.p.f.u.) and Mg (0.01 a.p.f.u.). In both calcite-poor and calcite-rich domains, calcite is preserved as inclusion within clinopyroxene (in association with amphibole and quartz) and titanite; in the calcite-rich domains, it is also included in plagioclase. Calcite granoblasts in the matrix only occur in the calcite-rich domains, where locally overgrow scapolite (Fig. 5.9e).

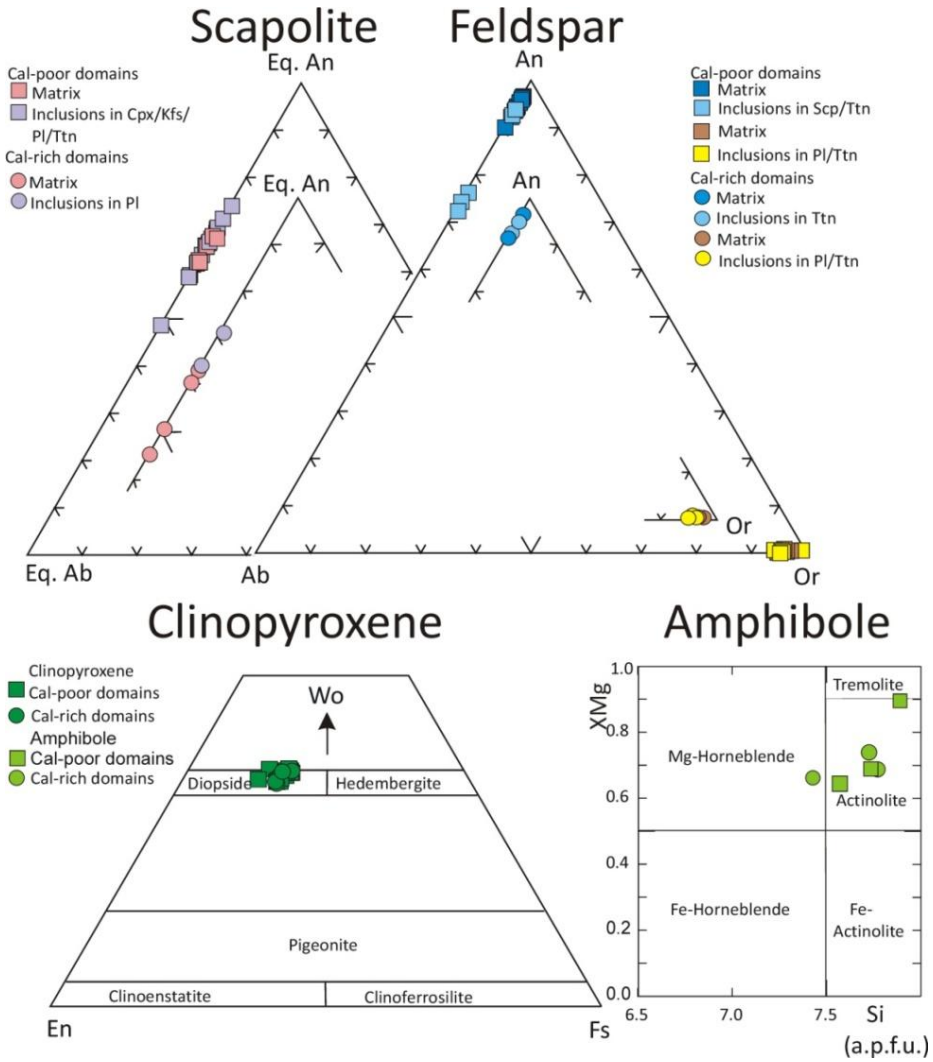

Fig. 5.10 - Compositional diagrams for scapolite, plagioclase, clinopyroxene and amphibole in sample 14-53c.

5.2.2.4 Sample 14-17 (Type 3F)

Sample 14-17 was collected from a boulder fallen down from the northern cliff of the upper Langtang Valley (N28°11'47.4'' E85°37'02.8'', 3940 m a.s.l.; Fig. 5.1b), and belongs

to the U-GHS. The host migmatitic metapelites experienced peak P-T metamorphic conditions of 760-800 °C and 7-8.6 kbar (sample 14-08a, Rapa et al., 2016). The sample shows a well-developed banded structure, defined by alternating cm-thick layers with the same mineral assemblage, but in different modal proportions (Fig. 5.11): specifically, scapolite-rich/k-feldspar-poor, scapolite-poor/k-feldspar-rich, and more homogeneous domains can be distinguished. The main mineral assemblage consists of k-feldspar + scapolite + clinopyroxene + plagioclase + minor quartz, titanite and epidote. Representative microstructures and mineral chemical data are reported in Fig. 5.11-Fig. 5.13. The structure is granoblastic (Fig. 5.12a-d) and medium to fine-grained. **Clinopyroxene** granoblasts are diopsidic in composition and locally zoned, with XMg decreasing from core to rim (XMg from 0.61 to 0.44). Clinopyroxene may include amphibole (mainly Fe-horneblende with XMg from 0.15 to 0.23), calcite, k-feldspar, Na-rich plagioclase (XAn=0.28-0.55), scapolite (eqAn=0.39-0.60) and minor apatite and epidote. **K-feldspar** (XOr=0.94-0.97) includes scapolite (eqAn=0.61) and rare plagioclase (XAn=0.39) (Fig. 5.12e); myrmekites grow at the contact with plagioclase, as well as pertithic exsolutions (XAn=0.08). **Scapolite** (eqAn=0.41-0.64) in the matrix includes rare k-feldspar and quartz; it is always replaced by a plagioclase ± calcite corona (Fig. 5.12f,g), or by symplectitic aggregates of epidote + calcite + quartz (Fig. 5.12h,i). **Plagioclase** in the corona is strongly zoned, with XAn increasing at the contact with scapolite (XAn from 0.68 to 0.20). Most of the plagioclase in the matrix likely derives from the replacement of scapolite, because it shows the same zoning and compositions as the plagioclase in the corona surrounding scapolite. Calcite is almost pure and only occurs as inclusions in other minerals and/or as a retrograde phase. **Epidote** in the matrix is locally zoned, with XZo decreasing toward the rim from 0.87 to 0.57. **Titanite** includes scapolite, plagioclase, k-feldspar, epidote, calcite and quartz.

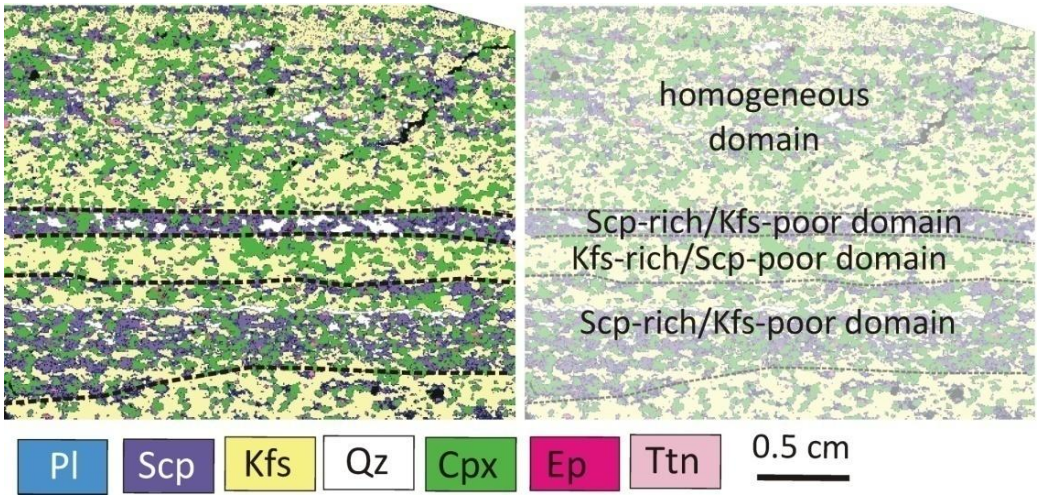

Fig. 5.11 - Processed µ-XRF map of the whole thin section 14-17, with distinction of scapolite-rich/k-feldspar-poor, scapolite-poor/k-feldspar-rich and homogeneous domains.

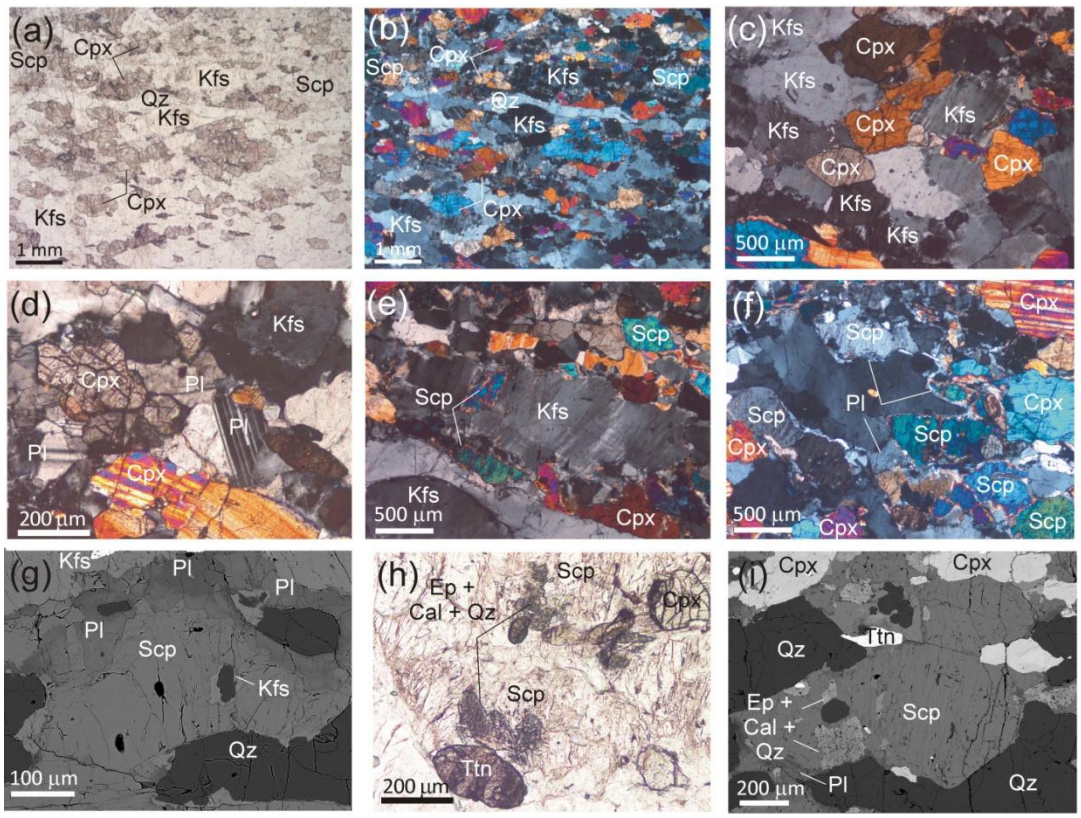

Fig. 5.12 – Representative microstructures of sample 14-17. (a,b) Detail of a homogeneous domain (PPL, XPL). **(c)** Clinopyroxene and k-feldspar granoblasts showing equilibrium relationships (XPL). **(d)** Plagioclase, k-feldspar and clinopyroxene at equilibrium (XPL). **(e)** K-feldspar includes scapolite (XPL). **(f,g)** Scapolite granoblasts are replaced by a plagioclase ± calcite corona; plagioclase is zoned, with higher An content (brighter colours in the BSE image) at the contact with scapolite (e:XPL; f:BSE). **(h,i)** Symplectitic aggregates of epidote + calcite + quartz replace scapolite crystals (g:PPL; h:BSE).

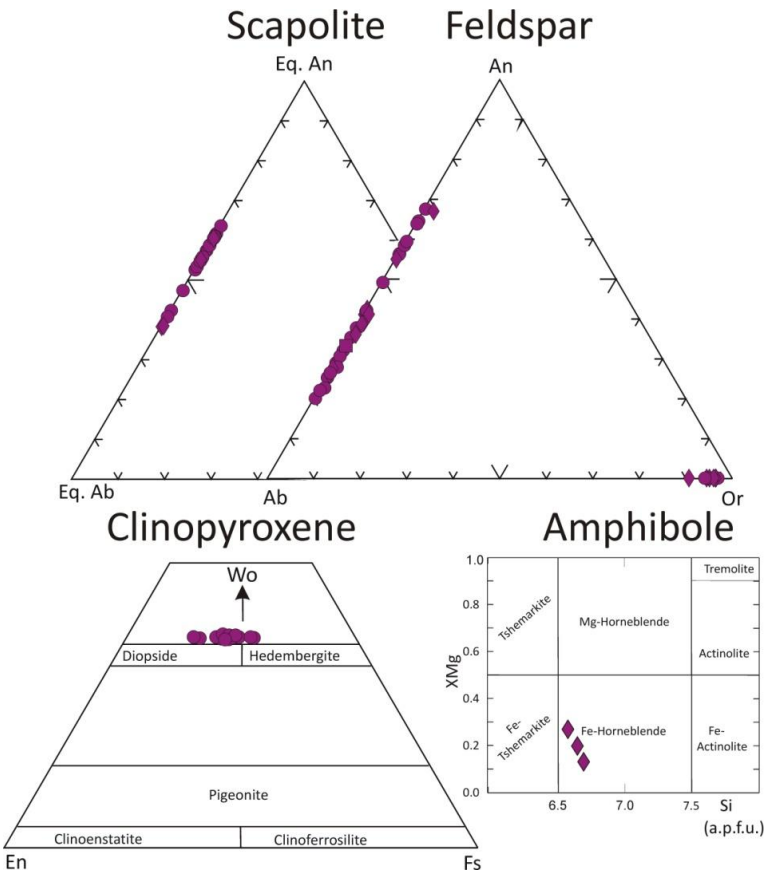

Fig. 5.13 - Compositional diagrams for scapolite, feldspar, clinopyroxene and amphibole in sample 14-17.

5.2.3 Textural, chemical and isotopic characterization of titanite in sample 14-53c

The textural relationships between titanite and the other minerals, as well as the major element composition of titanite, were investigated by SEM (same equipment used for analysing the main rock-forming minerals; see §5.2.1). Titanite is abundant in both calcite-poor and calcite-rich layers; it often includes scapolite, quartz and biotite, and less frequently plagioclase (An=0.73-0.94), k-feldspar, calcite, zoisite and apatite (Fig. 5.14a-f). Size of crystals is 100 to 250 µm in length and 20 to 100 µm in width. Most of the analyzed titanite grains are dispersed in the rock matrix; a few analyses have been performed on titanite grains included in clinopyroxene and scapolite. titanite shows a patchy zoning, as already observed by other authors (e.g. Franz and Spear, 1985; Hayden et al., 2008; Kohn and Corrie, 2011; Kohn, 2017).

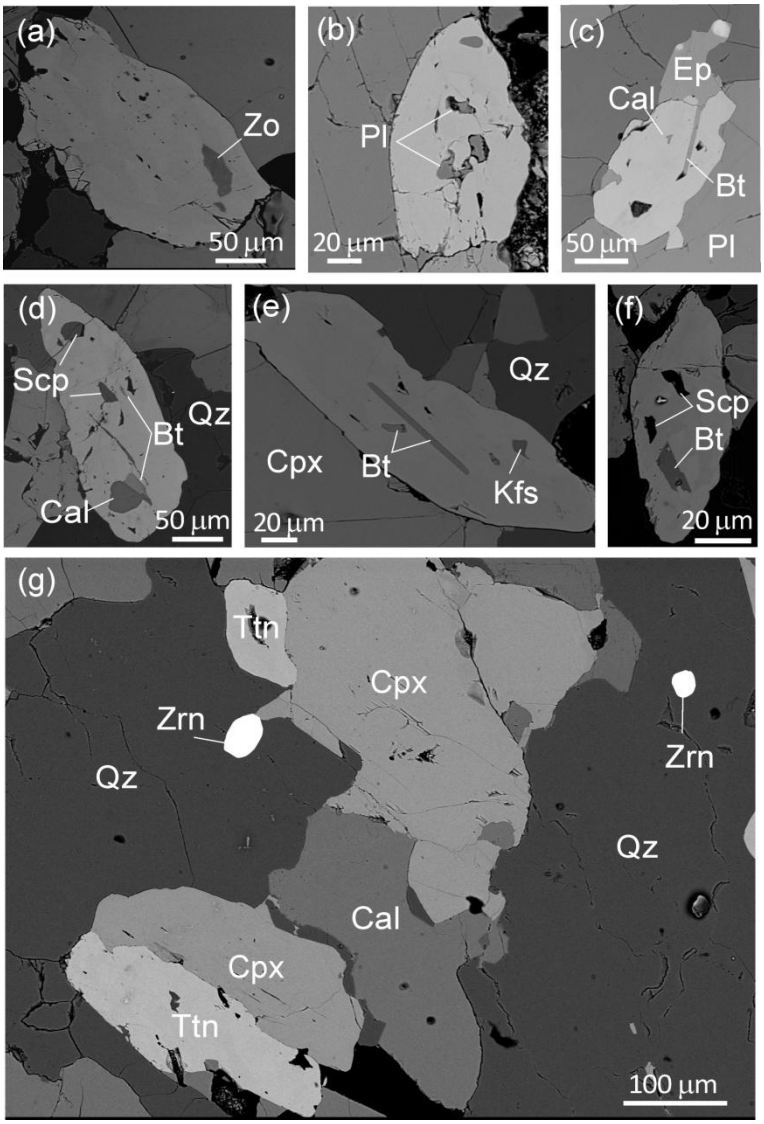

Fig. 5.14 - Representative microstructural relationships between titanite and the other rock-forming minerals in sample 14-53c (BSE). a,e,f,g: calcite-poor domain; b,c,d: calcite-rich domain. (g) BSE image showing the coexistence of zircon and titanite (i.e. the sample is saturated in quartz and zircon).

In situ trace element analyses and U/Pb age determinations of titanite samples were performed by Laser Ablation Inductively Coupled plasma Mass Spectrometry (LA-ICP-MS) at the Department of Physics and Geology, University of Perugia (Petrelli et al., 2016). The LA-ICP-MS system was a G2 Teledyne Photon Machine ArF excimer (193 nm) LA system coupled with an iCAPQ Thermo Fisher Scientific ICP-MS. LA-ICP-MS operating conditions were tuned before each analytical session to provide maximum signal intensity and stability for the ions of interest. Oxides formation (ThO/Th <0.5) and Th/U sensitivity ratio (Th/U ~1) were also monitored to maintain robust plasma conditions (e.g. Petrelli et al., 2016). Because of the reduced dimensions of the analysed titanite samples, a laser beam diameter ranging between 30 and 40 μm was utilized. The laser energy on the sample

surface and the repetition rate were fixed to 3.5 J/cm^2 and 8 Hz, respectively. In detail, trace elements determinations, performed on the isotopes ^{90}Zr, ^{232}Th and ^{238}U, were calibrated using the NIST SRM 612 glass reference material (Pearce et al., 1997). The OLT1 (Kennedy et al., 2010) and MKED1 (Spandler et al., 2016) titanite reference materials were employed as quality controls for trace element determinations. Data reduction was performed using the IOLITE 3 (Paton et al., 2011) software utilizing the protocol described by Longerich et al. (1996). U/Pb age determinations were performed using the same protocol reported by Chew et al. (2016). The OLT1 (Kennedy et al., 2010) and MKED1 (Spandler et al., 2016) titanite reference materials were employed as calibrator and quality control, respectively. These titanite standards are significantly older than the analysed sample (i.e. ca. 1.0-1.5 Ga); however, titanite standards of significantly younger age and/or homogeneous Zr content are not available (see also Kohn and Corrie, 2011 for discussion). Absolute ages obtained here can be in any case validated against existing monazite chronologic data for the region (e.g. Kohn et al., 2004, 2005; see the Discussion section §5.4.2.2). Both U/Pb age determinations and trace element analyses were performed preferably in the most homogeneous portions of each titanite grain. Results on unknown samples are reported in Tab. 5.2; results from the quality controls are reported in Tab. 5.4-5.5.

5.2.4 Phase diagram computation

Phase diagrams were calculated using Perple_X (version 6.7.4, November 2016) (Connolly 1990, 2009). References for the solution models are given in Tab. 5.2. The P/T gradients adopted are consistent with P-T constraints obtained from the associated metapelites (Rapa et al., 2016 and Chapter 3).

Table 5.2 Solution models used for the calculation of the phase diagrams

Sample 14-44c	Perple_X abbreviation	Ref.	Type of phase diagram in which the model was used		
			P/T-X(CO$_2$) grids	***P/T-X(CO$_2$) pseudosections***	***P-T mixed volatile projection***
Amphibole	Tr	1, 2	x	x	x
Chlorite	Chl(HP)	10	x	x	x
Clinopyroxene	Cpx(HP)	4	x	x	x
Dolomite	Do(HP)	4		x	
Garnet	Gt(HP)	4	x	x	x
Carbonate	Carb	9		x	

Sample 15-46	Perple_X abbreviation	Ref.	***P/T-X(CO$_2$) pseudosections***
Amphibole	cAmph(DP2)	1, 2	x
Biotite	Bio(TCC)	3	x
Chlorite	Chl(HP)	10	x
Clinopyroxene	Cpx(HP)	4	x
Dolomite	Do(HP)	4	x
Garnet	Gt(HP)	4	x
Plagioclase	Pl(h)	5	x
Scapolite	Scap	6	x
White mica	Mica(CHA)	8	x
Carbonate	Carb	9	x

Sample 14-53c and 14-17	Perple_X abbreviation	Ref.	Type of phase diagram in which the model was used		
			P/T-X(CO$_2$) grids	***P/T-X(CO$_2$) pseudosections***	***P-T mixed volatile projection***
Amphibole	cAmph(DP2)	1, 2		x	
Biotite	Bio(TCC)	3	x	x	x
Chlorite	Chl(HP)	10		x	
Clinopyroxene	Cpx(HP)	4		x	
Dolomite	Do(HP)	4		x	
Garnet	Gt(HP)	4		x	
Plagioclase	Pl(h)	5	x	x	x
Scapolite	Scap	6	x	x	x
Fluid	F	7			x

(1) Diener et al., 2007; (2) Diener & Powell, 2012; (3) Tajcmanova et al., 2009; (4) Holland & Powell, 1998; (5) Newton et al., 1980; (6) Kuhn et al., 2005; (7) Connolly & Trommsdorff, 1991 (8) Coggon & Holland 2002; Auzanneau et al., 2010 (9) ideal model; (10) Holland et al., 1998.

5.2.4.1 Sample 14-44c (Type 1C)

The P/T-X(CO_2) pseudosection has been calculated in the MnO-CaO-FeO-MgO-Al_2O_3-SiO_2-TiO_2-H_2O-CO_2 (MnCFMAST-HC) system along a P/T gradient reflecting the P-T path recorded by the host metapelites (Rapa et al., 2016). For the calculation of the P/T-X(CO_2) pseudosections, solid solution models were used for garnet, chlorite, dolomite, amphibole, clinopyroxene and Mn-Fe-Mg carbonate (see Tab. 5.2). Plagioclase (pure An), margarite, titanite, rutile, ilmenite, zoisite, aluminosilicate and quartz were considered as pure end-members. The binary H_2O-CO_2 fluid is considered as a saturated fluid phase.

The P/T-X(CO_2) grids were calculated in the simplified (i.e. no MnO and TiO_2) CFMAS-HC system considering garnet, clinopyroxene, amphibole and chlorite as solid solutions; plagioclase (pure An), zoisite, calcite, quartz, titanite, aluminosilicate, corundum were considered as pure end-members. Following the method illustrated in Groppo et al. (2017), wollastonite and dolomite were excluded from the calculation of the P/T-X(CO_2) grids because they are not relevant for the studied sample. Quartz and calcite are not considered in excess.

5.2.4.2 Sample 15-46 (Type 3C)

The P/T-X(CO_2) pseudosection has been calculated in the MnO-Na_2O-K_2O-CaO-FeO-MgO-Al_2O_3-SiO_2-TiO_2-H_2O-CO_2 (MnNKCFMAST-HC) system along a composite P/T gradient (Fig. 5.17c). Solution models were used for dolomite, chlorite, garnet, clinopyroxene, amphibole, biotite, white mica, plagioclase, scapolite, Mn-Fe-Mg carbonate (see Tab. 5.2). K-feldspar, titanite, rutile, ilmenite, quartz, zoisite and aluminosilicate were considered as pure end-members. The binary H_2O-CO_2 fluid is considered as a saturated fluid phase. It was not possible to calculate P/T-X(CO_2) grids due to the complexity of the system, in particular to the occurrence of Mn-bearing solid solutions actively involved in the main prograde reactions.

5.2.4.3 Samples 14-53c and 14-17 (Type 3F)

The P/T-X(CO_2) pseudosections have been calculated in the Na_2O-K_2O-CaO-FeO-MgO-Al_2O_3-SiO_2-TiO_2-H_2O-CO_2 (NKCFMAST-HC) system. Solution models were used for dolomite, chlorite, garnet, clinopyroxene, amphibole, biotite, plagioclase and scapolite (see Tab. 5.2). Calcite, k-feldspar, muscovite, paragonite, margarite, aluminosilicate, quartz, titanite, rutile, ilmenite, and zoisite were considered as pure end-members. In the pseudosection modelling, the binary H_2O-CO_2 fluid is considered as a saturated fluid phase.

For sample 14-53c, P/T-X(CO_2) grids and P-T mixed-volatile projection were calculated in

the simplified (i.e. no FeO) NKCMAST-HC system considering the following mineral phases: plagioclase, scapolite and biotite (phlogopite-Ti-biotite) solid solutions; activity modified end-members for chlorite, amphibole, clinopyroxene and zoisite, matching the measured compositions (i.e. aClc=0.7; aTr=0.7; aDi=0.7; aZo=0.75); calcite, aluminosilicate, k-feldspar, muscovite, quartz, titanite, rutile and geikielite pure end-members. A binary solution model for H_2O-CO_2 fluid was additionally used for the P-T mixed-volatile projection (see Tab. 5.2). Following the method illustrated in Groppo et al. (2017), dolomite, margarite, garnet, and wollastonite were excluded from the calculations of the P/T-X(CO_2) grids and P-T mixed-volatile projection, because they do not occur in the studied sample and their stability fields are confined either to low pressure or to very low or very high X(CO_2) conditions. Corundum was included in the calculation, but the corundum-bearing equilibria are not shown. Calcite and quartz are not considered in excess.

5.2.5 Zr-in-titanite thermometry

Zr-in-titanite temperatures were estimated using the calibration of Hayden et al. (2008). Pressure was set to 10.0-10.5 kbar, based on the results of the pseudosection modelling (see section 5.4.1.3 and Tab. 5.3); these values are in good agreement with peak-P conditions constrained from the host metapelites (Rapa et al., 2016 and Chapter 3). We assumed $a$$SiO_2$=1 because quartz is abundant in both the calcite-poor and calcite-rich domains (> 30 vol%); rutile is absent, therefore TiO_2 is undersaturated. $a$$TiO_2$=0.60 and $a$$TiO_2$=0.55 were estimated for the calcite-poor and calcite-rich domains respectively, following Ashley and Law (2015) (i.e. the chemical potential of the TiO_2 component, μTiO_2, was calculated with Perple_X at the P-T conditions of interest and for the specific bulk composition of each domain, and converted to $a$$TiO_2$ according to the expression proposed by Ashley and Law, 2015). It is worth noting that, although these $a$$TiO_2$ values are lower than that suggested by Corrie and Kohn (2011) and Kohn and Corrie (2011) for similar rutile-absent assemblages (i.e. $a$$TiO_2$=0.85), they give Zr-in-titanite temperatures which are consistent with the temperatures constrained independently for both the studied sample and the host metapelites, using the phase equilibria approach. Zircon is distributed throughout the sample (Fig. 5.14g). Measurement precision for Zr in titanite propagates to temperature uncertainties < 1 °C; uncertainties of ± 0.05 in $a$$TiO_2$ and ± 0.5 kbar propagate to additional systematic errors of ± 5 °C and ± 6 °C, respectively.

5.3 Results

5.3.1 Phase diagram modelling

5.3.1.1 Sample 14-44c (Type 1C)

Compared to other Type 1C samples, sample 14-44c is significantly richer in Mg (Fig. 5.2a,b). MgO is mostly partitioned in clinopyroxene, amphibole and chlorite, characterized by high values of XMg, but not in garnet, which is Fe-rich. This does not allow to model sample 14-44c in the simpler CMAST-HC or CFAST-HC systems, as was done for example by Groppo et al. (2013).

P/T-X(CO_2) grid in the system CFMAS-HC

The P/T-X(CO_2) grid modelled in the CFMAS-HC system and reported in Fig. 5.15b shows only the equilibria relevant for the studied sample. The following description is focused on those equilibria, which are relevant for the interpretation of the observed microstructures, therefore the equilibria involving phases not observed in the studied sample 14-44c (e.g. kyanite) are neglected. The relevant equilibria are one univariant equilibrium (reaction 1) in the CAS-HC subsystem, and two isobaric/isothermal invariant and 9 univariant equilibria in the CFMAS-HC subsystem (invariant points I1 and I2, and univariant reactions 2 to 10). Reaction 7 is divided into two portions by a singular point at which the stoichiometric coefficient of zoisite becomes zero (7a: Calcite + amphibole + garnet = zoisite + chlorite + clinopyroxene; 7b: Calcite + amphibole + garnet + zoisite = chlorite + clinopyroxene). The composition of all the Fe-Mg solid solutions (chlorite, clinopyroxene, garnet and amphibole) change continuously along the univariant curves, with either increasing (reactions 2, 10) or decreasing (reactions 4, 5, 6) values of XMg at increasing T in both reactants and products, or a combination of these two behaviours (reactions 7, 9).

P/T-X(CO_2) pseudosection in the system MnCFMAST-HC

The P/T-X(CO_2) pseudosection calculated in the MnCFMAST-HC system is dominated by quadri-, tri- and divariant fields (Fig. 5.15a). Predicted mode variations are given in Fig. 5.16. Quartz is stable in the entire P/T-X(CO_2) range of interest; Dol is stable at low to medium T (T<700 °C) in a wide range of X(CO_2) (>0.1), while Cal is predicted to be stable also at higher T (up to 800 °C) and high X(CO_2) values (0.6-1). Amphibole stability field is quite wide, since it is predicted to be stable up to 670°C and X(CO_2)= 0.6; clinopyroxene is stable at moderate to high T (from T=610 °C up to 800 °C) in almost the entire range of X(CO_2) (up to 0.9). Garnet is stable in almost the entire P/T-X(CO_2) range of interest,

except at low T and moderate to high X(CO_2) values. Plagioclase (pure anorthite) stability field is confined to high T and high X(CO_2) values (T>550 °C and X(CO_2)>0.4). On the opposite, zoisite is stable at low X(CO_2) values in a wide range of T. Trivariant fields in the pseudosection correspond to divariant fields in the corresponding P/T-X(CO_2) grid calculated in the simplified CFMAS-HC system, while divariant fields in the pseudosection correspond to univariant reactions in the grid (Fig. 5.14c). The narrow divariant fields in the pseudosection mark discontinuous reactions (i.e. the abrupt appearance or disappearance of one or more phases; Fig. 5.15b and Fig. 5.16); on the opposite, trivariant fields in the pseudosection represent continuous reactions (i.e. mainly Fe-Mg exchange) between Fe-Mg solid solutions (e.g. chlorite-amphibole, amphibole-clinopyroxene, chlorite-garnet, amphibole-garnet, garnet-clinopyroxene etc.). In fact, at least two Fe-Mg solid solutions are stable in each trivariant field (Fig. 5.16).

Fig. 5.15 - (a) P/T-X(CO_2) pseudosection calculated for sample 14-44c, in the system MnCMFAST-HC along a P/T gradient reflecting the P-T path followed by the host metapelites (Rapa et al., 2016; P (bar) = 20.5 T(K) – 10294). White, light- and dark-grey fields are di-, tri- and quadrivariant fields, respectively; the narrow divariant fields correspond to the univariant reactions in the corresponding P/T-X(CO_2) grid reported in (c). Dashed fields are dolomite- and/or margarite-bearing fields, not relevant for this study (because these phases are not observed in the studied sample). **(b)** Same isobaric P/T–X(CO_2) pseudosection as in (a): the univariant and invariant equilibria relevant to the sample are outlined. Note that the univariant curves and invariant points overlap the (narrow) divariant fields and (short) univariant lines of the pseudosection. **(c)** P/T–X(CO_2) phase diagram section calculated in the system CFMAS-HC along the same P/T gradient as in (a). Isobaric/isothermal univariant reactions and invariant points are represented separately and with different colours for each subsystem. The small white circle along equilibrium 7 is a singular point.

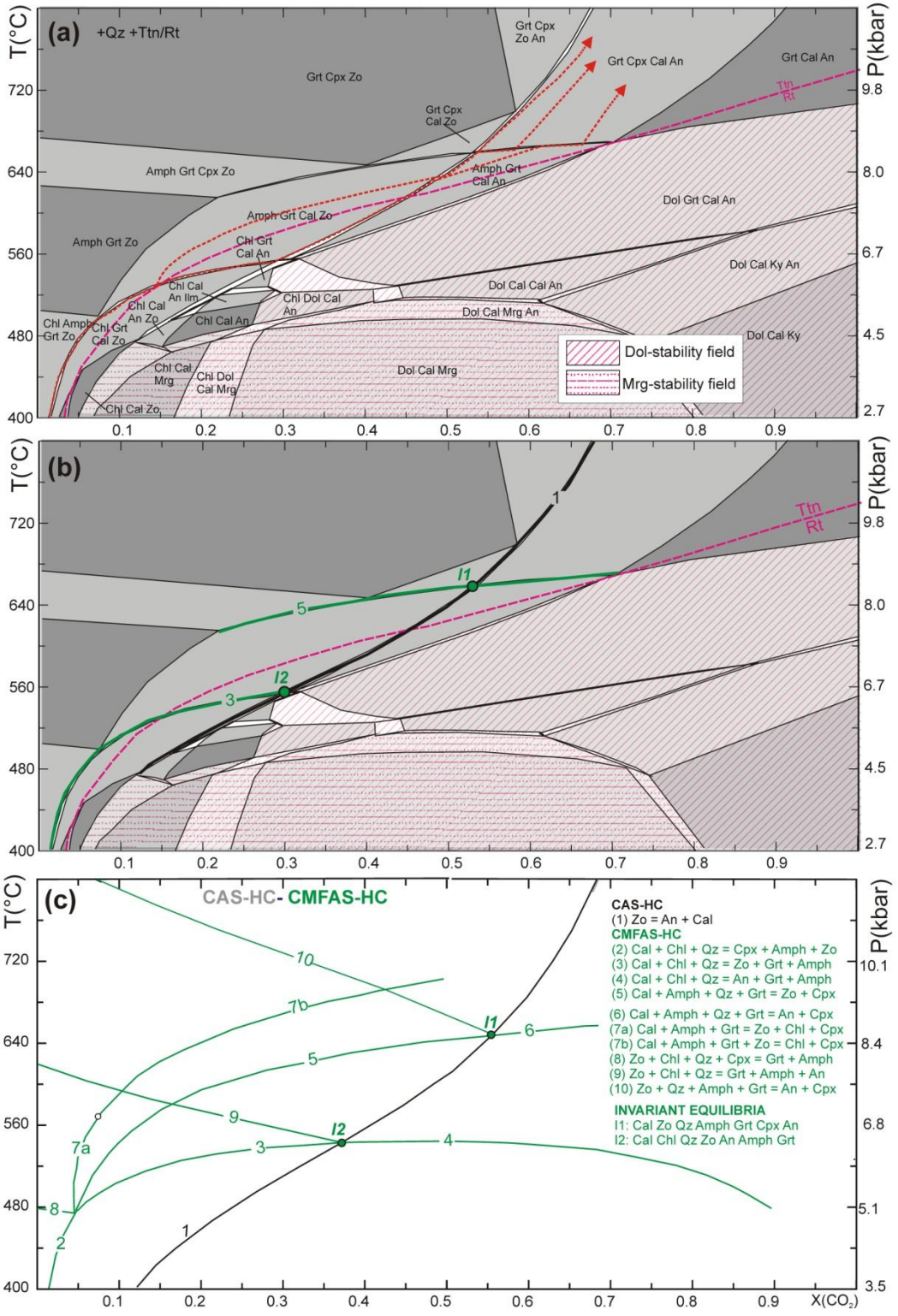
(a)
+Qz +Ttn/Rt
Grt Cpx Zo
Grt Cpx Zo An
Grt Cpx Cal An
Grt Cal An
Grt Cpx Cal Zo
Amph Grt Cpx Zo
Amph Grt Cal An
Amph Grt Cal Zo
Amph Grt Zo
Chl Grt Cal An
Dol Grt Cal An
Dol Cal Ky An
Chl Cal An Ilm
Chl Cal An Zo
Chl Dol Cal An
Dol Cal Cal An
Dol Cal Mrg An
Chl Amph Grt Zo
Chl Grt Cal Zo
Chl Cal An
Dol Cal Ky
Chl Cal Mrg
Chl Dol Cal Mrg
Dol Cal Mrg
Chl Cal Zo
Dol-stability field
Mrg-stability field
Ttn
Rt
T(°C)
P(kbar)
(b)
1
I1
5
I2
3
(c)
CAS-HC- CMFAS-HC
CAS-HC
(1) Zo = An + Cal
CMFAS-HC
(2) Cal + Chl + Qz = Cpx + Amph + Zo
(3) Cal + Chl + Qz = Zo + Grt + Amph
(4) Cal + Chl + Qz = An + Grt + Amph
(5) Cal + Amph + Qz + Grt = Zo + Cpx
(6) Cal + Amph + Qz + Grt = An + Cpx
(7a) Cal + Amph + Grt = Zo + Chl + Cpx
(7b) Cal + Amph + Grt + Zo = Chl + Cpx
(8) Zo + Chl + Qz + Cpx = Grt + Amph
(9) Zo + Chl + Qz = Grt + Amph + An
(10) Zo + Qz + Amph + Grt = An + Cpx
INVARIANT EQUILIBRIA
I1: Cal Zo Qz Amph Grt Cpx An
I2: Cal Chl Qz Zo An Amph Grt
10
7b
I1
6
5
9
I2
7a
3
4
8
2
1
X(CO2)

Fig. 5.15

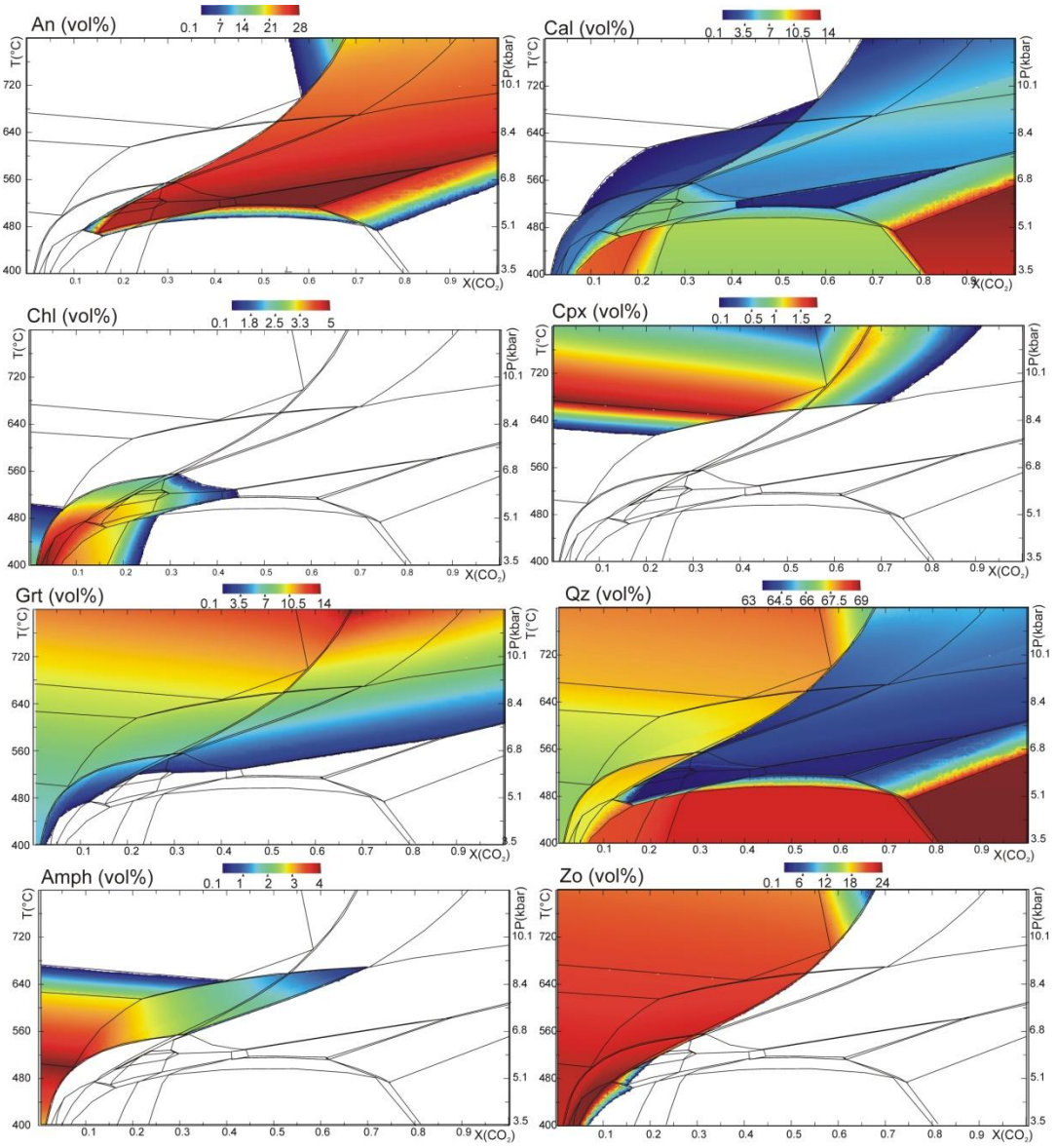

Fig. 5.16 - Predicted modes of mineral phases (vol%) and CO_2 amounts (wt%) for sample 14-44c, based on the P/T-X(CO_2) pseudosection of Fig. 5.15a.

5.3.1.2 Sample 15-46 (Type 3C)

P/T-X(CO_2) pseudosection in the system MnNKCFMAST-HC

The P/T-X(CO_2) pseudosection is characterized by quadri-, quini- and esavariant fields at T>560 °C, while at lower temperatures trivariant fields become predominant (Fig. 5.17a,b). Predicted mode variations are given in Fig. 5.19. At T<550 °C one or two carbonates (calcite and/or ankerite) and white micas (muscovite and/or paragonite) are predicted to be stable. Moreover, Ca-rich white mica (margarite), is stable in a narrow P-T-X(CO_2) field (X(CO_2)=0.1-0.5, T=510-550 °C, P=6.2-6.7 kbar). Biotite and garnet are the only relevant femic minerals predicted to be stable for the bulk composition of interest (Fig. 5.19). In fact, amphibole and clinopyroxene are present only for low values of X(CO_2) and in very low amounts (Fig. 5.19, amphibole=0-0.5 vol%; clinopyroxene=0-3.5 vol%). The scapolite-stability field is wide (T>510°C and X(CO_2)>0.11); it is the only mineral phase that incorporates CO_2 at high P/T conditions. K-feldspar is stable at high T or at high values of X(CO_2).

The peak mineral assemblage defined by biotite + garnet + plagioclase + scapolite + titanite is stable in a quite wide range of P-T-X(CO_2) conditions (T=600-750 °C, P=7.0-10.7 kbar, X(CO_2)=0.2-0.6). Further constraints are given by garnet compositional isopleths (XMg=0.10-0.11; XCa=0.32-0.37; XMn=0.06-0.09; XFe=0.46-0.48: Fig. 5.17a), that suggest an increase in both P and T up to peak metamorphic conditions of T=690-720 °C, P=9.1-9.8 kbar, X(CO_2)=0.38-0.47 (Fig. 5.17a), in agreement with data obtained from the host metapelites (Rapa et al., 2016 and Chapter 3, sample 14-03: T=710-730 °C and P=9.6-11 kbar).

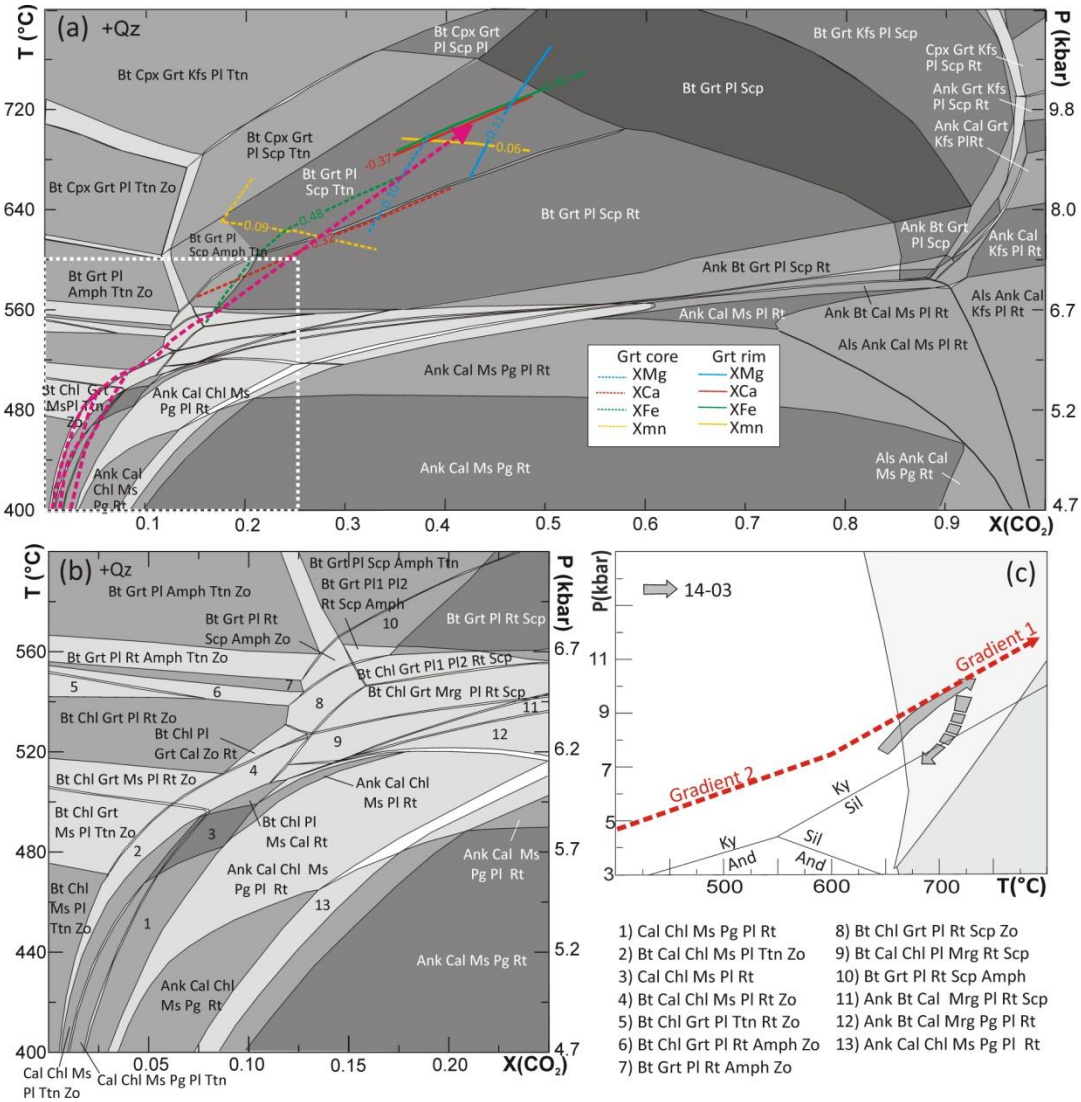

Fig. 5.17 - (a) P/T-X(CO_2) pseudosection calculated for sample 15-46, in the system MnNKCFMAST-HC along the composite P/T gradient represented in (c) and reflecting the P-T path followed by the host metapelites. The coloured lines are the modelled garnet compositional isopleths corresponding to the measured composition of garnet core (dashed) and garnet rim (continuous). The purple arrow approximates the P/T-X(CO_2) fluid evolution as constrained by the relevant microstructures (see §5.4.1.2). **(b)** Detail of (a). **(c)** P/T gradient used for the P/T-X(CO_2) pseudosection calculation and comparison with the P-T paths constrained for the surrounding metapelite (sample 14-03) (gradient 2: P (bar) = 12.02 T(K) – 3331; gradient 1 from Rapa et al., 2016; P (bar) = 20.5 T(K) – 10294).

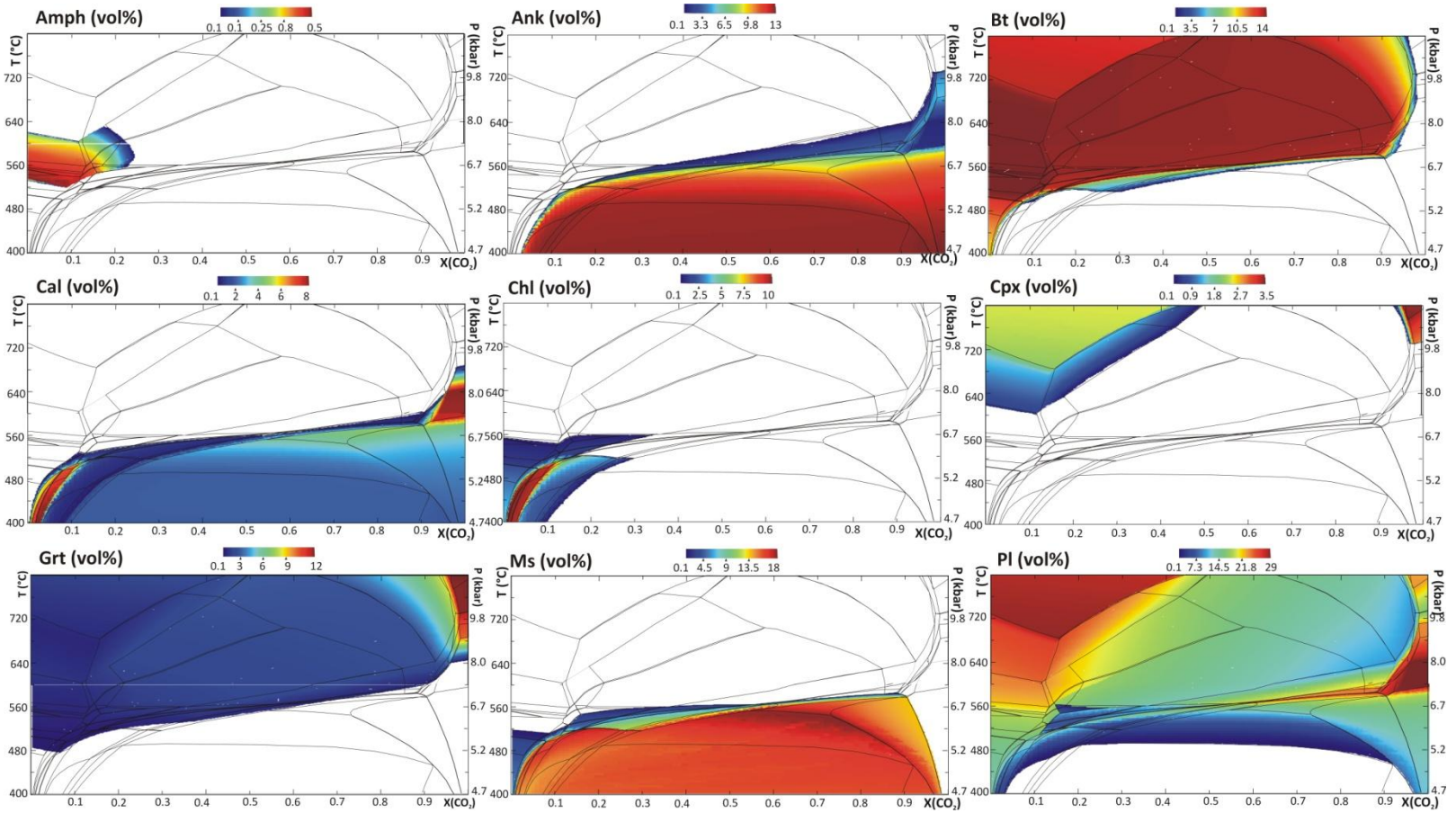

Fig. 5.18 - Predicted modes of mineral phases (vol%) for sample 15-46, based on the composite P/T-X(CO_2) pseudosection of Fig. 5.17a.

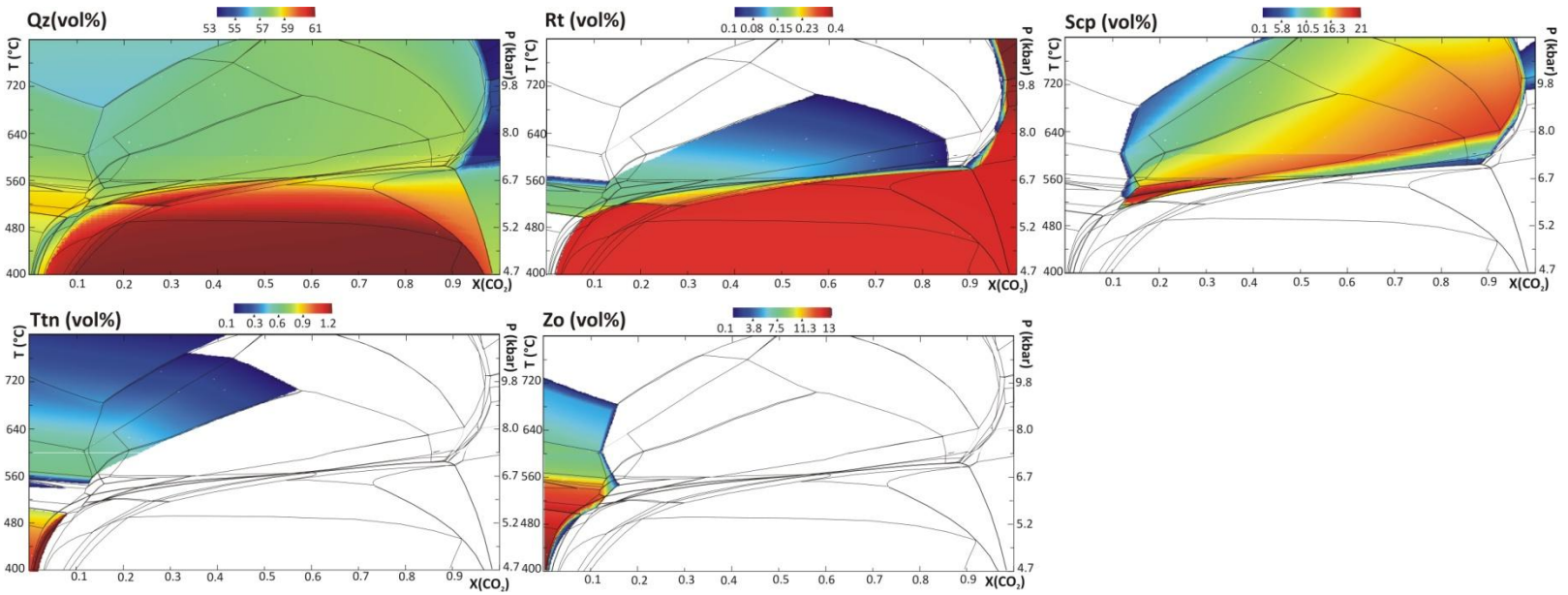

Fig. 5.19 – (continued).

5.3.1.3 Sample 14-53c (Type 3F)

P/T-X(CO_2) grids in the system NKCMAST–HC

The P/T-X(CO_2) grids were calculated in the Na_2O-K_2O-CaO-MgO-Al_2O_3-SiO_2-TiO_2-H_2O-CO_2 (NKCMAST-HC) system. This nine-component system may be described in terms of several subsystems: one five-component subsystem (CAS-HC), five six-component subsystems (CAST-HC, KMAS-HC, KCAS-HC, NCAS-HC, CMAS-HC), seven seven-component subsystems (KMAST-HC KCAST-HC, NCAST-HC, CMAST-HC, NKCAS-HC, KCMAS-HC, NCMAS- HC) and four eight-component subsystems (NKCMAS-HC, NKCAST-HC, KCMAST-HC, NCMAST-HC). Reaction equilibria in the Ti-absent subsystems have been widely discussed in the paper by Groppo et al. (2017) and are therefore only briefly summarized here, whereas major emphasis is given in the following to the Ti-bearing equilibria (note that the T-X(CO_2) grid discussed in Groppo et al. (2017) is an isobaric grid, whereas in this case the grid is calculated along a P/T gradient). The following description is focused on those equilibria which are relevant for the interpretation of the observed microstructures, therefore the equilibria involving phases not observed in the studied sample 14-53c (e.g. pure anorthite and phologopite end-members, kyanite, chlorite) are neglected. Furthermore, quartz- and calcite-absent equilibria are explicitly indicated: quartz-absent equilibria are not relevant for the studied sample because quartz is very abundant in both calcite-poor and calcite-rich domains (45 and 30 vol%, respectively); calcite-absent equilibria might be relevant at high temperature and/or low X(CO_2) values if calcite is completely consumed.

CAS-HC, CAST-HC, KCAS-HC and KCAST-HC subsystems

These subsystems do not involve neither Na-Ca solid solutions (plagioclase, scapolite) nor mafic phases (diopside, tremolite, clinochlore). Five isobaric/isothermal invariant points occur in these subsystems (I1: CAS-HC; I2: CAST-HC, I3, I4: KCAS-HC, I5: KCAST-HC; Fig. 5.21a), among which only I5 is relevant for the discussion. I5 involves the exchange of Ti between rutile and titanite. Nine isobaric/isothermal univariant equilibria are modelled in the Ti-absent CAS-HC (1 to 4) and KCAS-HC (7 to 11) subsystems, among which only reaction 7 (calcite + muscovite + quartz → k-feldspar + zoizite) is relevant for the studied sample. Four univariant equilibria are modelled in the Ti-bearing CAST-HC and KCAST-HC subsystems (Fig. 5.21a), but one of them (6) involves pure anorthite and it can be therefore neglected. The decarbonation reaction 5 (rutile + calcite + quartz → titanite) is particularly important for the studied sample; the presence of titanite, in fact, limits the univariant equilibria (and invariant points) relevant to this study to those lying above the titanite-in reaction curve. Equilibria 12 and 13 emanate from the invariant point I5 and are, respectively, calcite- and quartz-absent; they both involve the exchange of Ti between rutile and titanite.

NCAS-HC and NCAST-HC subsystems

Seven univariant equilibria describe the relationship between plagioclase, zoisite and scapolite in the Ti-absent NCAS-HC subsystem (Fig. 5.19a). The degenerate equilibria 14a and 14b involve calcite, scapolite, plagioclase and zoisite, with plagioclase and scapolite changing their compositions along each curve. In reaction 14a a Na-rich plagioclase (XAn=0.33) reacts with calcite and zoisite to form scapolite (XMe=0.62-0.66) (calcite + plagioclase + zoisite → scapolite), while in reaction 14b scapolite (XMe=0.66-0.88) reacts with zoisite to form a Ca-rich plagioclase (XAn=0.90-0.93) and calcite (scapolite + zoisite → calcite + plagioclase). All the other equilibria (except 18) can be neglected because they involve kyanite; equilibrium 18 is calcite- and quartz- absent, and involve two plagioclase (Na-rich and Ca-rich, respectively).

The addition of Ti to the NCAS-HC subsystem leads to the stabilization of two duplicated invariant points (I8 and I8'in Fig. 5.19a) and of one univariant equilibrium (21) emanating from these invariant points. Reaction 21 is divided into two portions by a singular point at which the stoichiometric coefficient of zoisite becomes zero (21a: quartz + rutile + scapolite → plagioclase + titanite + zoisite; 21b: quartz + rutile + scapolite + zoisite → plagioclase + titanite). The plagioclase composition changes continuously along this equilibrium curve, with the Ca-richer compositions toward higher-T (i.e. from XAn=0.33 at I8 to XAn=0.83 at I8').

CMAS-HC and CMAST-HC subsystems

The CMAS-HC and CMAST-HC subsystems describe the phase relationships between calcite, quartz, zoisite, anorthite, kyanite and the mafic phases tremolite, diopside and clinochlore, ± titanite and rutile. Nine invariant points occur in the CMAS-HC and CMAST-HC subsystems (CMAS-HC: I9 to I14, CMAST-HC: I15 to I17) (Fig. 5.19b). Most of them involve phases not observed in the studied sample and can be therefore neglected; only the invariant point I16 is relevant for the discussion. Only one out of the fifteen univariant equilibria (24 to 38) modelled in the Ti-absent CMAS-HC subsystem is relevant for the studied sample: this is equilibrium 25 (calcite + quartz + tremolite → diopside). Six univariant equilibria are modelled in the Ti-bearing CMAST-HC subsystem (Fig. 5.19b), among which only equilibria 39 and 42 are relevant for the studied sample. Both of them emanate from the invariant point I16; equilibrium 39 is quartz-absent, whereas equilibrium 42 (tremolite + titanite → diopside + quartz + rutile) is calcite-absent.

KCMAS-HC and KCMAST-HC subsystems

The Ti-absent KCMAS-HC subsystem involves the K-bearing phases muscovite, biotite (pure phlogopite) and k-feldspar in addition to the phases described by the CMAS-HC subsystem. Twelve invariant points are modelled in this subsystem (I18 to I30; Fig. 5.21c):

among them, only I22 is relevant for the discussion, the others involving phases not observed in the studied sample. Most of the univariant equilibria modelled in the KCMAS-HC subsystem can be neglected; the only exception are the quartz-absent equilibrium 54 (calcite + k-feldspar + tremolite + zoisite → diopside + muscovite) and the calcite-absent equilibrium 59 (diopside + muscovite + quartz → k-feldspar + tremolite + zoisite), emanating from I22. The Ti-bearing KCMAST-HC subsystem involves biotite solid solution (Phl-Ti-biotite), titanite and rutile in addition to the phases described by the KCMAS-HC subsystem. Thirteen invariant points are modelled in the KCMAST-HC subsystem (I31 to I43; Fig. 5.21d), among which only I34, I35, I37 and I40 are relevant for the discussion. Ten univariant equilibria (78, 79, 85, 89, 90, 91, 94, 98, 99, 100) emanate from the invariant points I34, I35, I37 and I40 (Fig. 5.19b); four of them are calcite-absent (89, 90, 91, 98) and three are quartz-absent (78, 79, 99). The other three equilibria imply the exchange of Ti between biotite and titanite (equilibria 85, 94) or rutile (equilibrium 100). These three reactions all involve biotite, calcite and quartz as reactants, and k-feldspar, tremolite/diopside and titanite/rutile as products (85: biotite + calcite + quartz → k-feldspar + tremolite + titanite; 94: biotite + calcite + quartz → diopside + k-feldspar + titanite; 100: biotite + calcite + quartz → diopside + k-feldspar + rutile), and are therefore particularly relevant for the studied sample.

NKCAS-HC and NKCAST-HC subsystems

The Ti-absent NKCAS-HC subsystem involves plagioclase and scapolite solid solutions, zoisite, calcite, quartz and the K-bearing phases muscovite, biotite (pure phlogopite) and k-feldspar. Two invariant points (I44 and I45; both are duplicated) are modelled in the Ti-absent NKCAS-HC subsystem, with three reactions originating from them (Fig. 5.19e). Equilibrium 106 is calcite-absent; it is divided in two portions (106a and 106b) by a singular point at which the stoichiometric coefficient of zoisite becomes zero. Equilibria 107a and 107b involve muscovite, quartz, calcite, k-feldspar, scapolite and plagioclase, with both scapolite and plagioclase changing compositions along the reaction curves. More in detail, Na-rich plagioclase (XAn=0.31-0.34) reacts to form scapolite (XMe=0.66) along reaction 107a (calcite + muscovite + plagioclase + quartz → k-feldspar + scapolite), while at slightly higher temperatures scapolite (XMe=0.66) reacts to form Ca-rich plagioclase (XAn=0.90-0.93) along reaction 83b (calcite + muscovite + quartz + scapolite → k-feldspar + plagioclase). Reaction 108 can be neglected because it involves kyanite.

The Ti-bearing NKCAST-HC subsystem involves biotite solid solution (phlogopite - Ti-biotite), titanite and rutile in addition to the phases described by the NKCAS-HC subsystem. Two invariant points (I46 and I47) are modelled in the NKCAST-HC subsystem, and three univariant equilibria emanate from them (Fig. 5.19e). Reaction 109 is calcite-absent; it is divided in two portions (109a and 109b) by a singular point at which the

stoichiometric coefficient of quartz becomes zero. Plagioclase changes its composition along these equilibria, becoming more calcic at increasing temperatures (XAn=0.34 to 0.60 from I46 to I47). Equilibria 110 and 111 are quartz-absent. All the three univariant equilibria involve the exchange of Ti between rutile and titanite.

NCMAS-HC and NCMAST-HC subsystems

The Ti-absent NCMAS-HC subsystem involves plagioclase and scapolite solid solutions, zoisite, calcite, quartz, kyanite and the mafic phases clinochlore, tremolite and diopside. Six invariant points (I48 to I53) are modelled in this subsystem (four of them are duplicated: I48, I49, I51 and I53; Fig. 5.19e); I49 (and the duplicated I49') are the only invariant points relevant for the studied sample. Among the nine univariant equilibria modelled in the NCMAS-HC subsystem, the only relevant to this study is equilibrium 114. This is a calcite-absent equilibrium, that is divided in two portions (114a and 114b) by a singular point at which the stoichiometric coefficient of zoisite becomes zero. Along this curve, plagioclase becomes more calcic in composition at increasing $X(CO_2)$. The Ti-bearing NCMAST-HC subsystem involves titanite and rutile in addition to the phases described by the NCMAS-HC subsystem. Two invariant points (I54, I55) are modelled, and one univariant equilibrium emanates from them (Fig. 5.19e). Reaction 121 is calcite-absent and involves the exchange of Ti between rutile and titanite (121: scapolite + tremolite + titanite → diopside + plagioclase + rutile + zoisite).

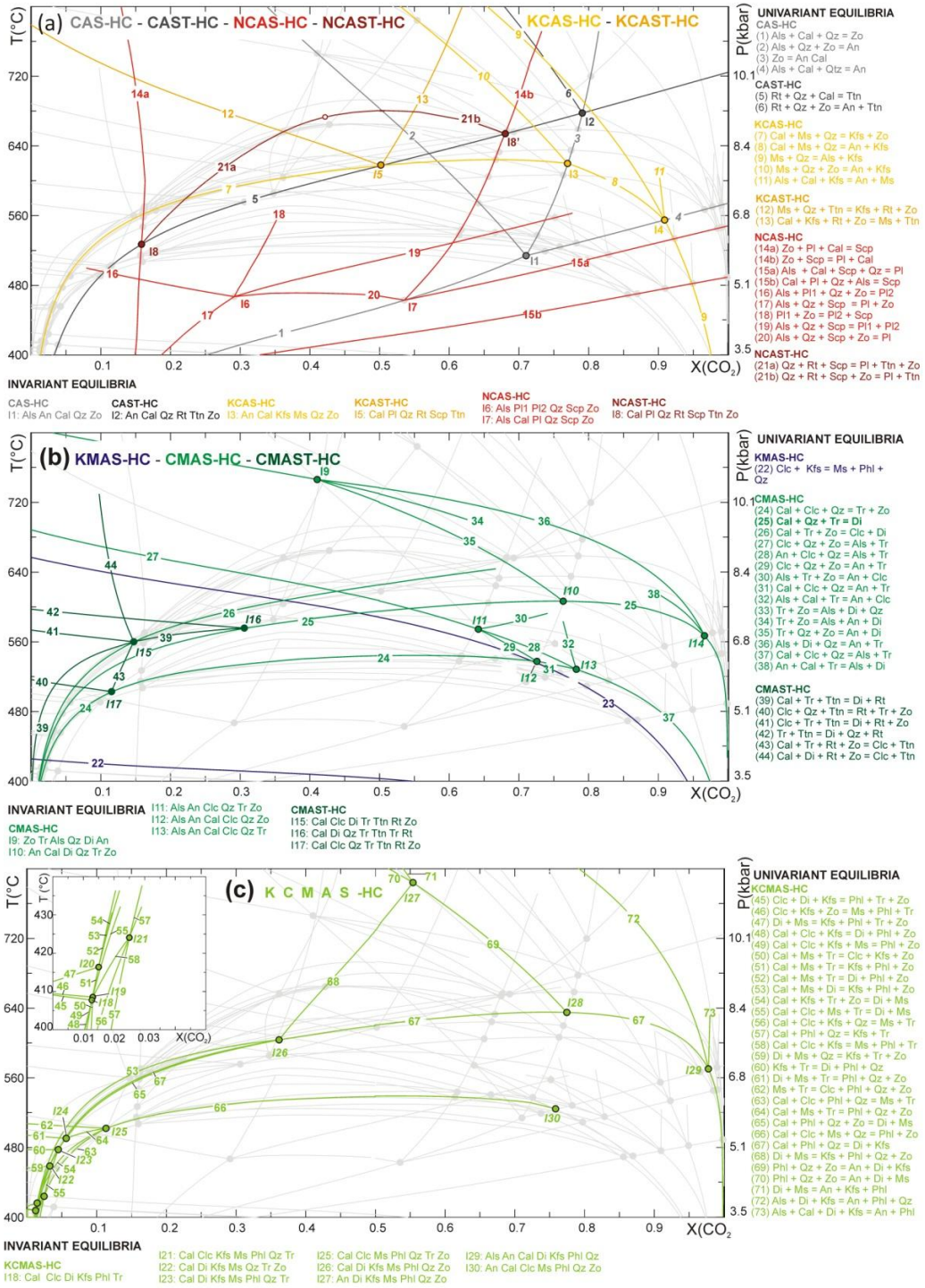

Fig. 5.20 – (a-f) P/T–X(CO_2) phase diagram sections calculated in the system NKCMAST-HC along the P/T gradient reflecting the P-T path followed by the host metapelites (Rapa et al., 2016 and for *a*Clc=0.7, *a*Tr=0.7, *a*Di=0.7, *a*Zo=0.75. Isobaric/isothermal univariant reactions and invariant points are represented separately and with different colours for each subsystem. Small empty points are singular points.

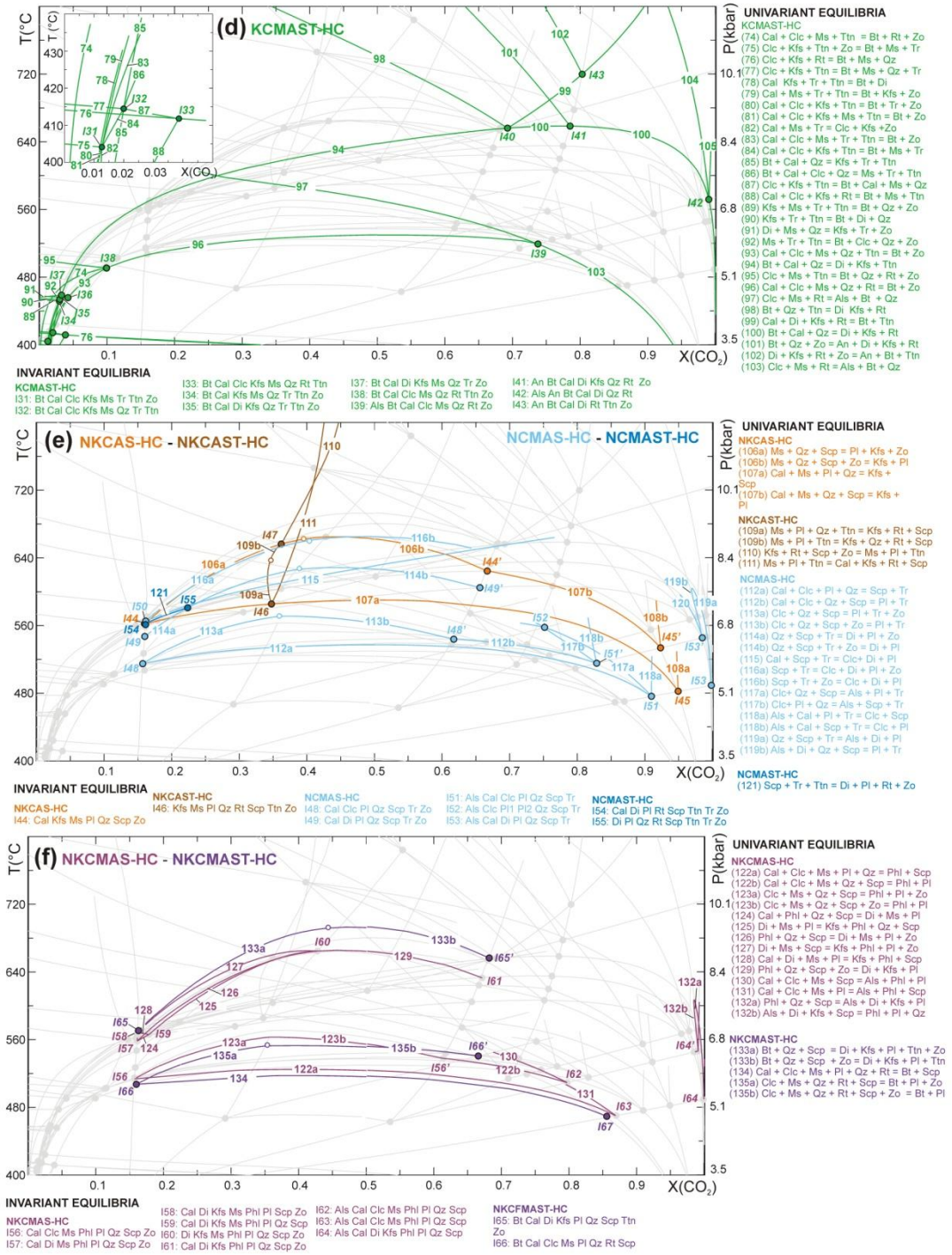

Fig. 5.21 – (continued).

NKCMAS-HC subsystem and NKCMAST-HC full system

In the Ti-absent NKCMAS-HC subsystems nine invariant points (I56 to I64) and eleven univariant equilibria (122 to 132) are modelled (Fig. 5.21f). All these invariant points and univariant reactions are not relevant for the discussion because they involve phases that have not been observed in the studied sample (e.g. pure phlogopite end-member, clinochlore, kyanite). The Ti-bearing NKCMAST-HC system represents the total system of interest. Three invariant points (I65 to I67) are modelled in this system, and two of them are duplicated (I65 and I66) (Fig. 5.19f). Only the duplicated invariant points I65 and I65' are relevant for this study. Among the three univariant equilibria modelled in this system (133 to 135), only the equilibrium 133 is relevant to the discussion. The calcite-absent equilibrium 133 connects the duplicated invariant points I65 and I65' and is divided in two portions (133a and 133b) by a singular point at which the stoichiometric coefficient of zoisite becomes zero. Equilibria 133a and 133b involve biotite, quartz, zoisite, diopside, k-feldspar, titanite, scapolite and plagioclase. A Na-rich plagioclase (XAn=0.34) and zoisite are produced from reacting scapolite (XMe=0.66) along equilibrium 133a (biotite + quartz + scapolite → diopside + k-feldspar + plagioclase + titanite + zoisite), while zoisite and scapolite (XMe=0.66) react to form a Ca-rich plagioclase (XAn=0.90) along equilibrium 133b (biotite + quartz + scapolite + zoisite → diopside + k-feldspar + plagioclase + titanite). Reaction 133 also implies the exchange of Ti between biotite and titanite.

P/T-X(CO_2) pseudosections in the system NKCFMAST-HC

Two P/T-X(CO_2) pseudosections were calculated in the NKCFMAST-HC system, using the bulk compositions representative of the calcite-poor and calcite-rich domains, respectively (Tab. 5.1). The two pseudosections are topologically very similar (Fig. 5.22 and Fig. 5.24). Predicted modes variation are given in Fig. 5.23 and Fig. 5.25. Both the pseudosections are dominated by large trivariant fields separated by narrow divariant fields. Quadrivariant fields only appear at high temperatures or for high values of X(CO_2). Quartz is stable in the whole P/T-X(CO_2) range of interest. On the contrary, carbonates stability fields are limited to specific P/T-X(CO_2) conditions: calcite is stable at X(CO_2)>0.01 for T=400 °C, and at X(CO_2)>0.5 for T=720 °C; in the calcite-poor domains its stability field is limited at T<750 °C, whereas in the calcite-rich domains it is predicted to be stable at T>800 °C. Dolomite is limited to low-T conditions (T<600 °C) or to high X(CO_2) values (X(CO_2)>0.6). Plagioclase (with variable composition) is stable over most of the P/T-X(CO_2) range of interest, except for a relatively large field at 0.05<X(CO_2)<0.55 and T<730 °C. scapolite is stable in a wide range of P/T-X(CO_2) conditions at X(CO_2)>0.05 and T>470 °C, with few differences between the calcite-rich and calcite-poor domains. Zoisite is limited to X(CO_2)<0.55 in both domains. The chlorite stability field is limited to T<480 °C,

$X(CO_2)<0.15$; amphibole is confined to an even smaller field at T<450 °C, $X(CO_2)<0.02$. Clinopyroxene is predicted to be stable at $X(CO_2)<0.02$ for T=400 °C, and at $X(CO_2)<0.45$ for T=700°C. An almandine-rich garnet is predicted to be stable in both the pseudosections at T>730 °C and $X(CO_2)>0.5$; in the calcite-rich domains a grossular-rich garnet is also modelled at T>650 °C, $X(CO_2)<0.15$.

At low T, muscovite is stable over a wide range of $X(CO_2)$ (i.e. $X(CO_2)=0.03$-0.97); its stability field extends up to ~630 °C. The breakdown of muscovite coincides with the appearance of k-feldspar. Biotite is predicted to be stable in a wide range of P/T-$X(CO_2)$ conditions, but in the calcite-rich domains its stability field is limited at T<730 °C, whereas in the calcite-poor domains it is predicted to be stable at T>800 °C. Finally, the rutile stability field is limited at $X(CO_2)>0.05$ for T=400 °C and at $X(CO_2)>0.9$ for T=700 °C; titanite is stable at lower $X(CO_2)$ conditions for the same T conditions.

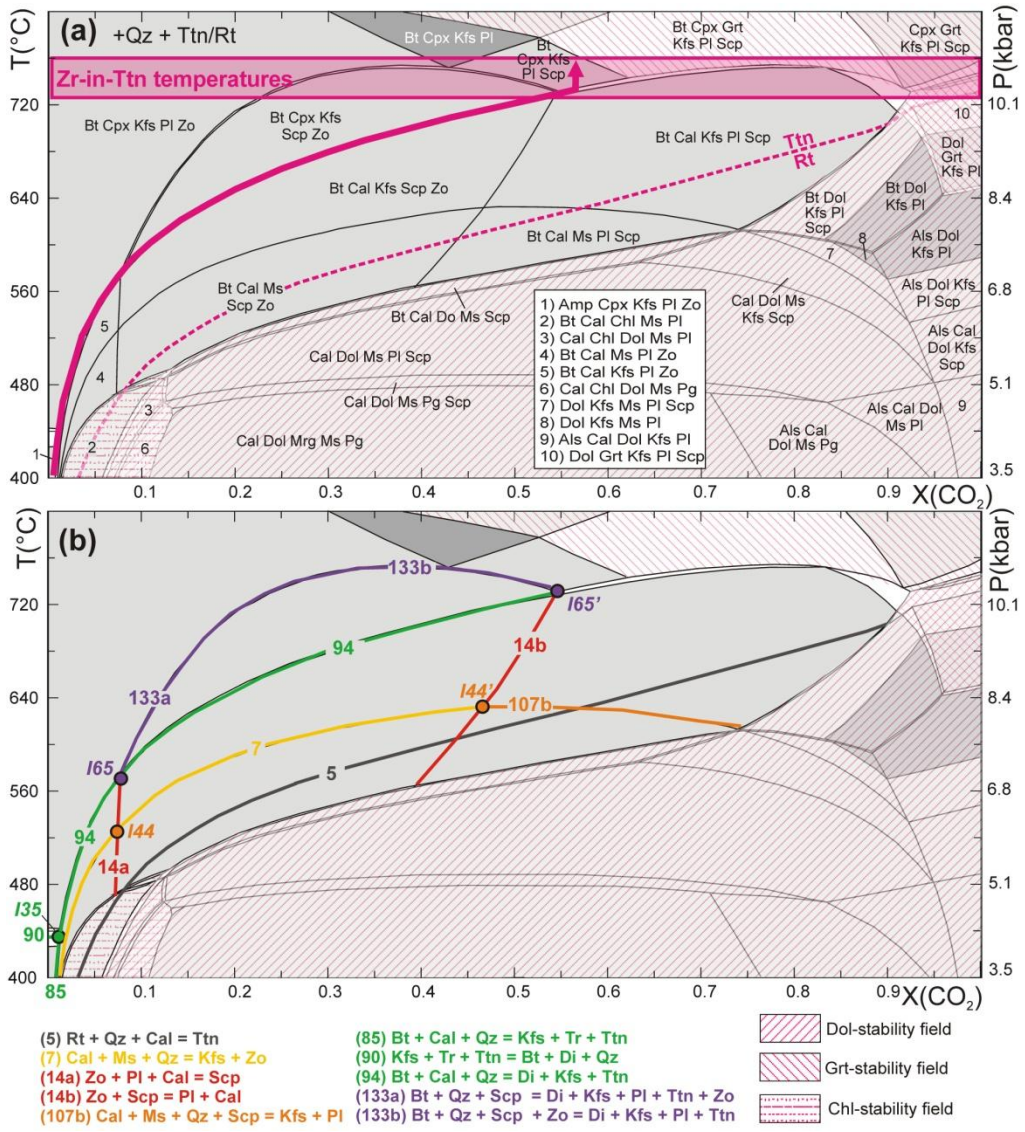

Fig. 5.22 - (a) P/T-X(CO_2) pseudosection calculated for the calcite-poor domain, in the system NKCFMAST-HC along a P/T gradient reflecting the P-T path followed by the host metapelites (Rapa et al., 2016; P (bar) = 20.5 T(K) – 10294). White, light- and dark-grey fields are di-, tri- and quadrivariant fields, respectively; the narrow divariant fields correspond to the univariant reactions in the corresponding P/T-X(CO_2) sections (see Fig. 5.19). Dashed fields are dolomite-, garnet-, and/or chlorite-bearing fields, not relevant for this study (because these phases are not observed in the studied sample). The purple arrow approximates the P/T-X(CO_2) internally buffered fluid evolution as constrained by the relevant microstructures (see §5.4.1.3). The purple box constrains the Zr-in-titanite temperatures obtained from the analysed titanite grains (see §5.3.2). **(b)** Same isobaric P/T–X(CO_2) pseudosection as in (a): the univariant and invariant equilibria relevant to the calcite-poor domain are outlined (reactions labels and colors as in Fig. 5.19). Note that the univariant curves and invariant points overlap the (narrow) divariant fields and (short) univariant lines of the pseudosection.

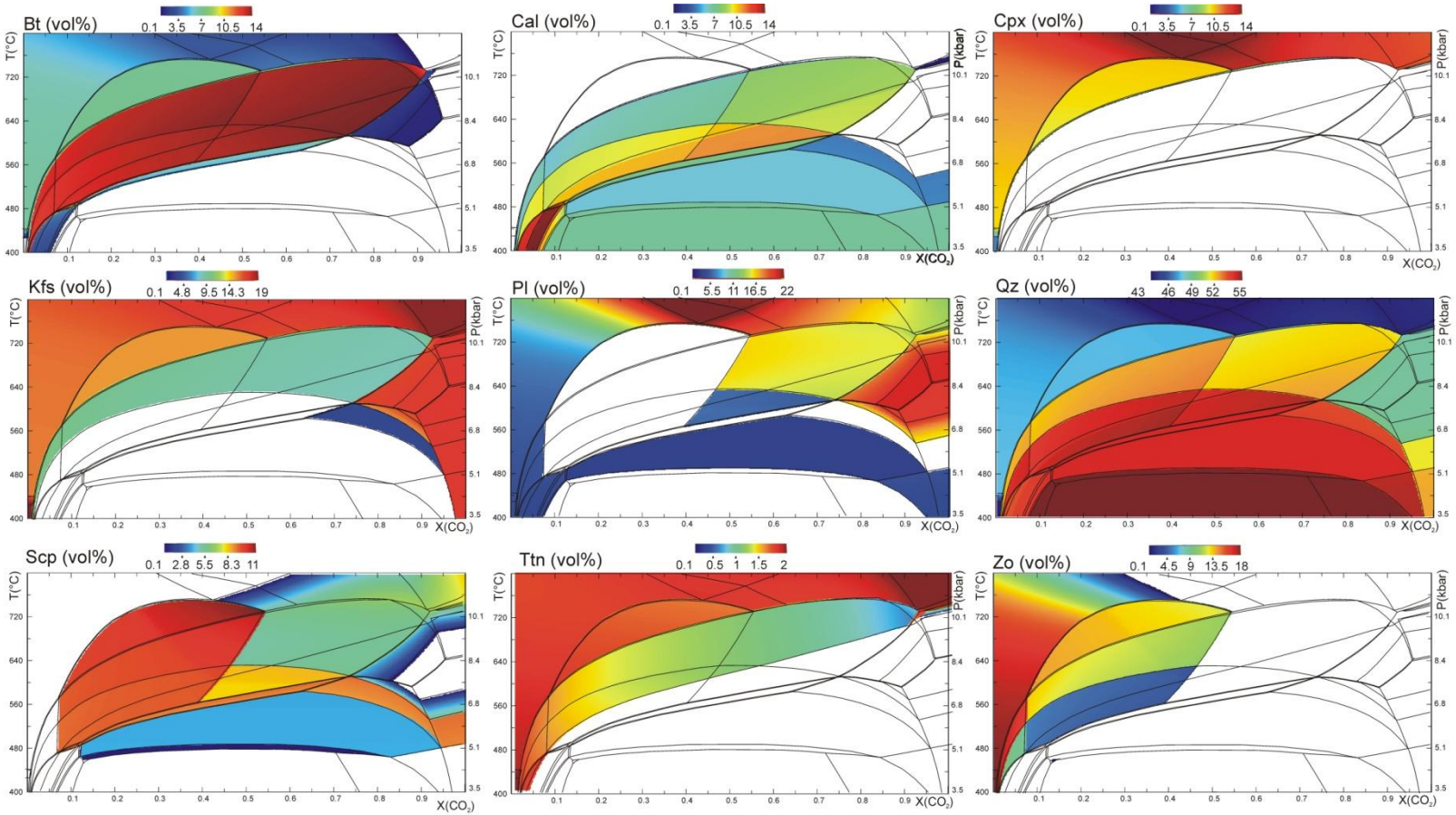

Fig. 5.23 – Predicted modes of mineral phases (vol%) for the calcite-poor domains of sample 14-53c, based on the P/T-X(CO_2) pseudosection of Fig. 5.22.

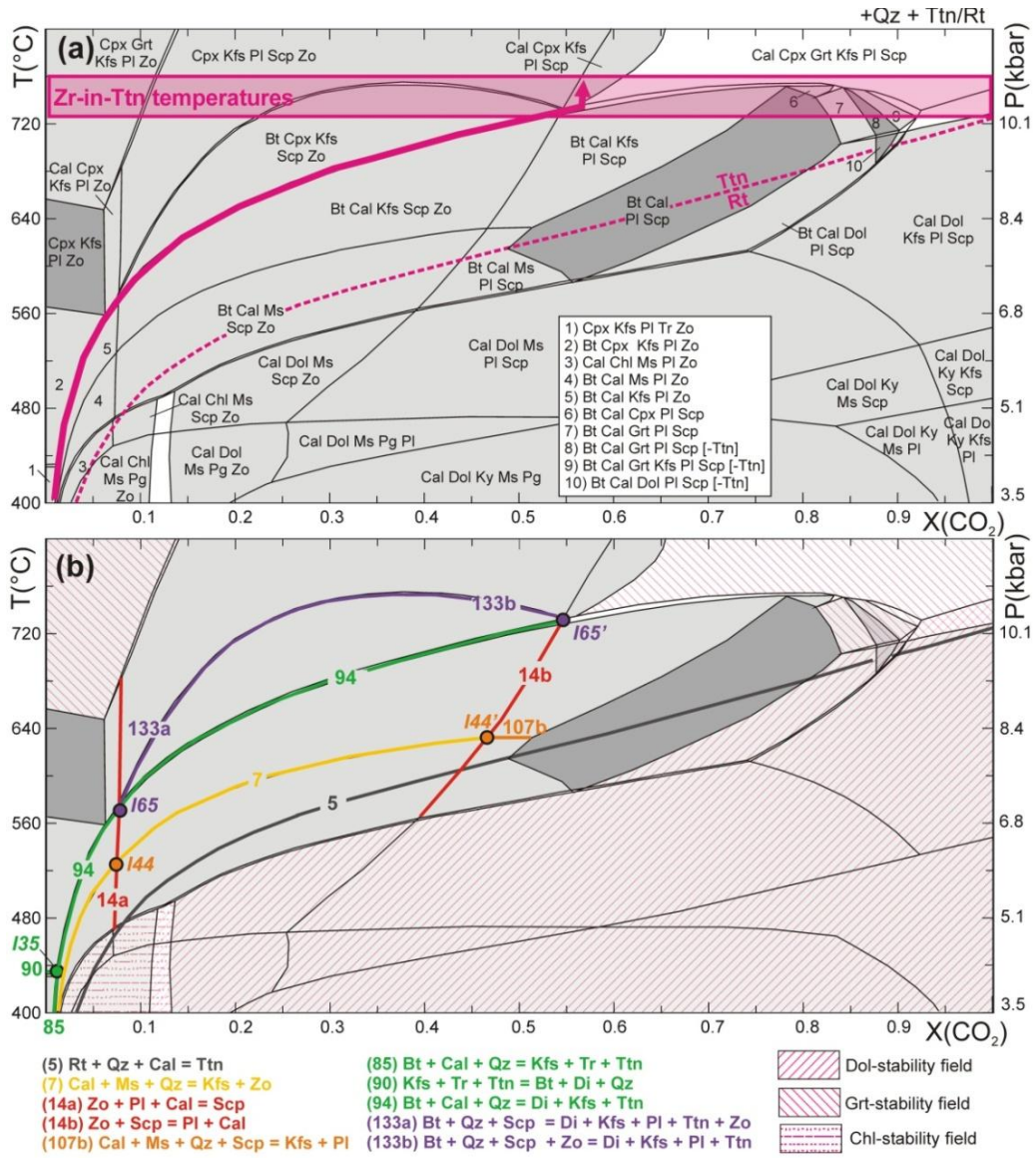

Fig. 5.24 - (a) P/T-X(CO_2) pseudosection calculated for the calcite-rich domain of sample 14-53c, in the system NKCFMAST-HC along a P/T gradient reflecting the P-T path followed by the host metapelites (Rapa et al., 2016; P (bar) = 20.5 T(K) – 10294). White, light- and dark-grey fields are di-, tri- and quadrivariant fields, respectively; the narrow divariant fields correspond to the univariant reactions in the corresponding P/T-X(CO_2) sections (see Fig. 5.19). Dashed fields are dolomite-, garnet-, and/or chlorite-bearing fields, not relevant for this study (because these phases are not observed in the studied sample). The purple arrow approximates the P/T-X(CO_2) internally buffered fluid evolution as constrained by the relevant microstructures in each domain (see §5.4.1.3). The purple box constrains the Zr-in-titanite temperatures obtained from the analysed titanite grains. **(b)** Same isobaric P/T–X(CO_2) pseudosection as in (a): the univariant and invariant equilibria relevant to the calcite-rich domain are outlined (reactions labels and colors as in Fig. 5.19). Note that the univariant curves and invariant points overlap the (narrow) divariant fields and (short) univariant lines of the pseudosection.

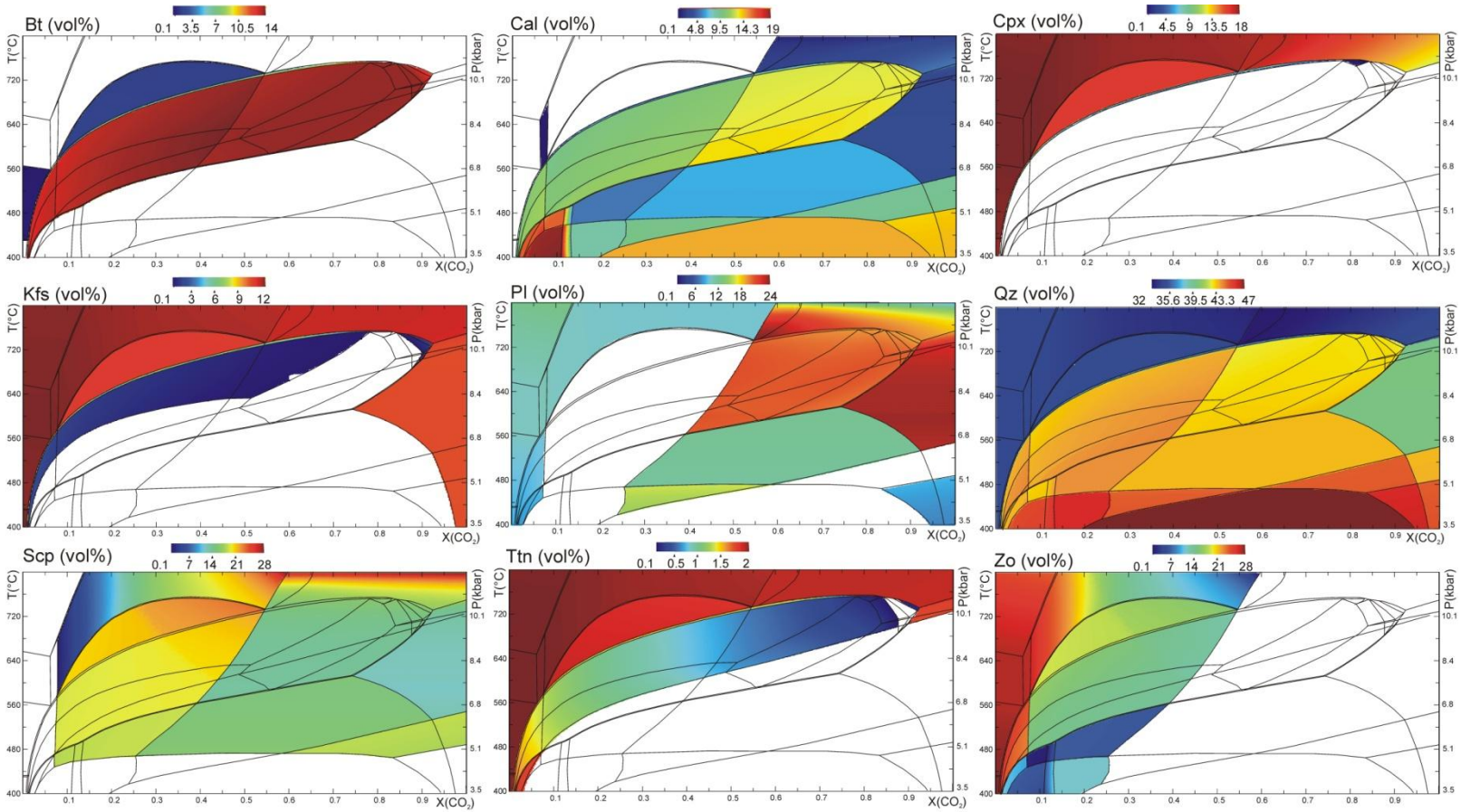

Fig. 5.25 – Predicted modes of mineral phases (vol%) for the calcite-rich domains of sample 14-53c, based on the P/T-X(CO_2) pseudosection of Fig. 5.22.

Mixed volatile P-T projection in the system NKC(F)MAST-HC

The mixed-volatile P-T projection of Fig. 5.26 shows the "truly" univariant curves corresponding to the invariant points I35, I65 and I65' previously discussed for the P/T-X(CO_2) grid and identified as relevant for the studied sample (see Groppo et al., 2017 for further details on the relationships between P/T-X(CO_2) grids and mixed-volatile P-T projections).

The "truly" univariant curve corresponding to the invariant point I35 (in the following referred to as U35) has a negative slope in the P-T space and is located at T<500 °C, P<6 kbar. U35 is a titanite-consuming, CO_2-producing reaction (U35: calcite + k-feldspar + tremolite + titanite → biotite + diopside + quartz + Fluid), therefore it is not relevant for this study and it will not be further discussed.

The "truly" univariant curves corresponding to the duplicated invariant points I65 and I65' (in the following referred to as U65a and U65b/c, respectively) have a positive slope. Plagioclase, scapolite, biotite and fluid change their compositions along these curves; in particular, the fluid becomes enriched in CO_2 at increasing pressure. One of these univariant curves is characterized by a singular point, at which the stoichiometric coefficient of calcite becomes zero. This singular point thus divides the univariant curve in two portions (U65b and U65c). Fig. 5.26 shows the relative position of the mixed-volatile truly univariant curves U65a, U65b and U65c with respect to the prograde P-T evolution inferred from the host metapelites associated to the studied calc-silicate rock (i.e. same P/T gradient used for the calculation of the P/T-X(CO_2) grids and pseudosections). The first truly univariant curve crossed during the prograde evolution is U65a (biotite + calcite + plagioclase + quartz + zoisite → diopside + k-feldspar + scapolite + titanite + Fluid); this reaction is crossed at relatively low temperature and releases a fluid moderately enriched in CO_2 (X(CO_2)=0.15). At higher P and T, the truly univariant reaction U65c is crossed (biotite + calcite + quartz + scapolite + zoisite → diopside + k-feldspar + plagioclase + titanite + Fluid), which releases a CO_2-rich fluid (X(CO_2)=0.68). Both reactions U65a and U65c are responsible for the growth of titanite at the expense of biotite and produce a fluid variably enriched in CO_2.

The slight difference in the P/T-X(CO_2) location of the "truly" univariant curves in the mixed-volatile P-T projection (Fig. 5.26) compared to the pseudosection (Fig. 5.22 and Fig. 5.24) is due to the inevitable simplification of the model system (i.e. FeO is no considered), and consequently of the solution models, required to calculate the mixed-volatile P-T projection.

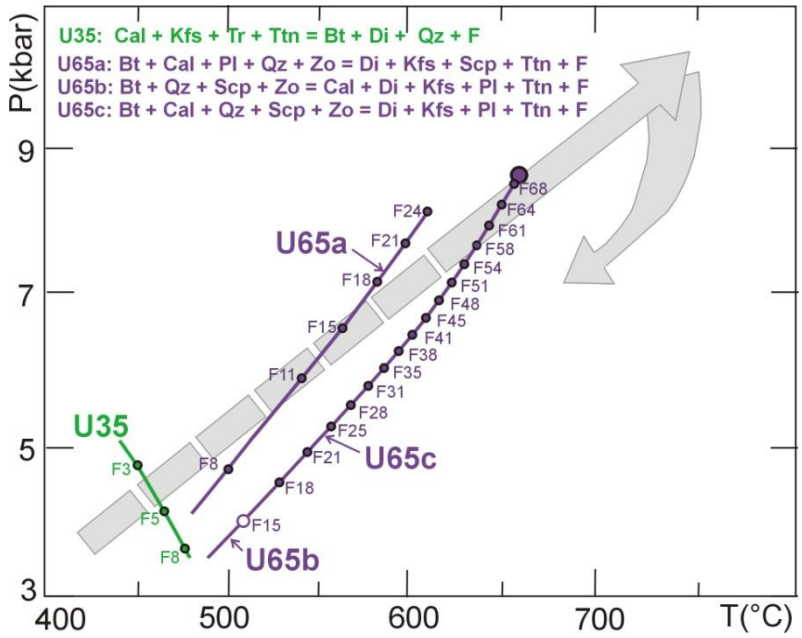

Fig. 5.26 - Mixed-volatile P–T projection in the system NKCMAST-HC calculated for *a*Tr=0.7, *a*Di=0.7, *a*Zo=0.75, showing a selection of the truly univariant curves relevant for the studied sample (i.e. U35, corresponding to the isobaric/isothermal invariant point I35; U65, corresponding to the duplicated isobaric/isothermal invariant points I65 and I65'). Colour code is the same as in Fig. 5.19. Solid large points are truly-invariant points; empty small points are singular points. The variation of fluid composition ($X(CO_2)$) along each univariant curve is reported (e.g. F54 means a H_2O-CO_2 fluid with $X(CO_2)$ = 0.54). The P–T evolution inferred from the host metapelites (Rapa et al., 2016) is reported with grey arrows.

The results of P/T-$X(CO_2)$ grids and pseudosections suggest that the calcite-poor and calcite-rich domains are sensitive to the same univariant and invariant equilibria (Fig. 5.22 and Fig. 5.24):

(i) CAST-HC reaction 5 (calcite + quartz + rutile → titanite + CO_2), that controls the relative stability of rutile vs. titanite;

(ii) KCAS-HC reaction 7 (calcite + muscovite + quartz → k-feldspar + zoisite + H_2O + CO_2), that marks the appearance of k-feldspar at $X(CO_2)$<0.45 and the breakdown of muscovite;

(iii) NCAS-HC reactions 14a (calcite + plagioclase + zoisite + CO_2 → scapolite + H_2O) and 14b (scapolite + zoisite + CO_2 → calcite + plagioclase + H_2O), that control the relative stability of plagioclase, scapolite, zoisite and calcite;

(iv) KCMAST-HC univariant reactions 85, 90 and 94 and invariant point I35. Reactions 90 (k-feldspar + tremolite + titanite → biotite + diopside + quartz + H_2O + CO_2) and 85 (biotite + calcite + quartz → k-feldspar + tremolite + titanite + H_2O + CO_2) limit the stability field of amphibole at T<450 °C, whereas reaction 94 (biotite + calcite + quartz → diopside + k-feldspar + titanite + H_2O + CO_2) marks the appearance of clinopyroxene at T > 450 °C;

(v) NKCAS-HC univariant reaction 107b and invariant points I44 and I44'. Reaction 107b (calcite + muscovite + quartz + scapolite → k-feldspar + plagioclase + H_2O + CO_2) marks the appearance of k-feldspar (and the breakdown of muscovite) at $X(CO_2)$ > 0.45;

(vi) NKCMAST-HC univariant reactions 133a and 133b and invariant points I65 and I65'. The calcite-absent reactions 133a (biotite + quartz + scapolite → diopside + k-feldspar + plagioclase + titanite + zoisite + H_2O + CO_2) and 133b (biotite + quartz + scapolite + zoisite → diopside + k-feldspar + plagioclase + titanite + H_2O + CO_2) represent plagioclase-forming reactions at relatively low values of $X(CO_2)$.

Among these univariant equilibria, reactions 5, 85, 94 and 133 are titanite-forming and CO_2-producing and, except for reaction 5, they involve mineral phases observed in the studied sample (reaction 5 involves rutile as a reactant, which is not observed in the sample). Reactions 85, 94 and 133 are therefore particularly relevant for this study; they emanate from the titanite-bearing invariant points I35, I65 and I65', which correspond to the following "truly" univariant reactions in the P-T mixed-volatile projection (Fig. 5.26):

U35: calcite + k-feldspar + tremolite + titanite → biotite + diopside + quartz + Fluid,

U65a: biotite + calcite + plagioclase + quartz + zoisite → diopside + k-feldspar + scapolite + titanite + Fluid, U65c: biotite + calcite + quartz + scapolite + zoisite → diopside + k-feldspar + plagioclase + titanite + Fluid, where Fluid indicates an H_2O-CO_2 fluid, whose composition changes as a function of P and T [$X(CO_2)$ values are reported in Fig. 5.26; e.g. F54 means a H_2O-CO_2 fluid with $X(CO_2)$ = 0.54].

5.3.1.4 Sample 14-17 (Type 3F)

Sample 14-17 is characterized by a mineral assemblage very similar to that of sample 14-53c, although its P-T evolution is different (Fig. 5.25). Therefore, as a first approximation, the same isobaric/isothermal univariant and invariant equilibria discussed in §5.3.1.3 also apply to sample 14-17 and are not further discussed in the following.

P/T-X(CO_2) pseudosection in the system NKCFMAST-HC

The P/T-$X(CO_2)$ pseudosection is dominated by large trivariant fields separated by narrow divariant fields (Fig. 5.25a). Predicted mode variations are given in Fig. 5.28. Quadrivariant fields occur at T>560 °C for different values of $X(CO_2)$. Quartz and plagioclase with variable composition are stable in the whole T-$X(CO_2)$ range of interest. On the contrary, calcite is stable at T<680 °C, while dolomite is limited to T<580 °C or to high $X(CO_2)$ values ($X(CO_2)$>0.65). Scapolite is stable in a wide range of T-$X(CO_2)$ conditions at $X(CO_2)$>0.05 and T>560 °C; zoisite is limited to $X(CO_2)$<0.09. Amphibole is confined to a small field at

T<460 °C, X(CO_2)<0.02. Clinopyroxene is predicted to be stable at X(CO_2)<0.02 for T=400 °C, and at X(CO_2)<0.45 for T=680 °C. An almandine-rich garnet is predicted to be stable at T>490 °C and X(CO_2)<0.1. Muscovite is stable at T<580 °C in a wide range of X(CO_2); muscovite breakdown coincides with the appearance of k-feldspar. Biotite is predicted to be stable at 580<T<720 °C for X(CO_2)=0.6, and at 470<T<620 °C for X(CO_2)=0.1. Finally, the rutile stability field is limited to X(CO_2)>0.02 for T=400 °C and to X(CO_2)>0.9 for T=670 °C; titanite is stable at lower X(CO_2) for the same T conditions.

The results of the T-X(CO_2) pseudosection combined with the equilibria discussed in §5.3.1.3 for the same system, suggest that the sample is sensitive to the following univariant and invariant equilibria (Fig. 5.25a), CAST-HC reaction 5 (calcite + quartz + rutile → titanite + CO_2), that controls the relative stability of rutile vs. titanite;

(i) KCAS-HC reaction 7 (calcite + muscovite + quartz → k-feldspar + zoisite + H_2O + CO_2), that marks the appearance of K-feldspar at X(CO_2)<0.45 and the breakdown of muscovite;

(ii) NCAS-HC reaction 14a (calcite + plagioclase + zoisite + CO_2 → scapolite + H_2O) that controls the relative stability of plagioclase, scapolite, zoisite and calcite;

(iii) KCMAST-HC univariant reactions 85, 90 and 94 and invariant point I35. Reactions 90 (k-feldspar + tremolite + titanite → biotite + diopside + quartz + H_2O + CO_2) and 85 (biotite + calcite + quartz → k-feldspar + tremolite + titanite + H_2O + CO_2) limit the stability field of amphibole at T<460 °C, whereas reaction 94 (biotite + calcite + quartz → diopside + k-feldspar + titanite + H_2O + CO_2) marks the appearance of clinopyroxene at T > 460 °C;

(iv) NKCAS-HC univariant reaction 107a and invariant point I44. Reaction 107a (calcite + muscovite + quartz + plagioclase → k-feldspar + scapolite + H_2O + CO_2) marks the appearances of k-feldspar and scapolite (and the breakdown of muscovite) at X(CO_2) > 0.1;

(v) NKCMAST-HC univariant reactions 133a and invariant point I65. The calcite-absent reaction 133a (biotite + quartz + scapolite → diopside + k-feldspar + plagioclase + titanite + zoisite + H_2O + CO_2) represents the plagioclase-forming reaction at relatively low values of X(CO_2).

Among these univariant equilibria, reactions 5, 85, 94 and 133 are CO_2-producing reactions and, except for reaction 5, they involve mineral phases observed in the studied sample (reaction 5 involves rutile as a reactant, which is not observed in the sample).

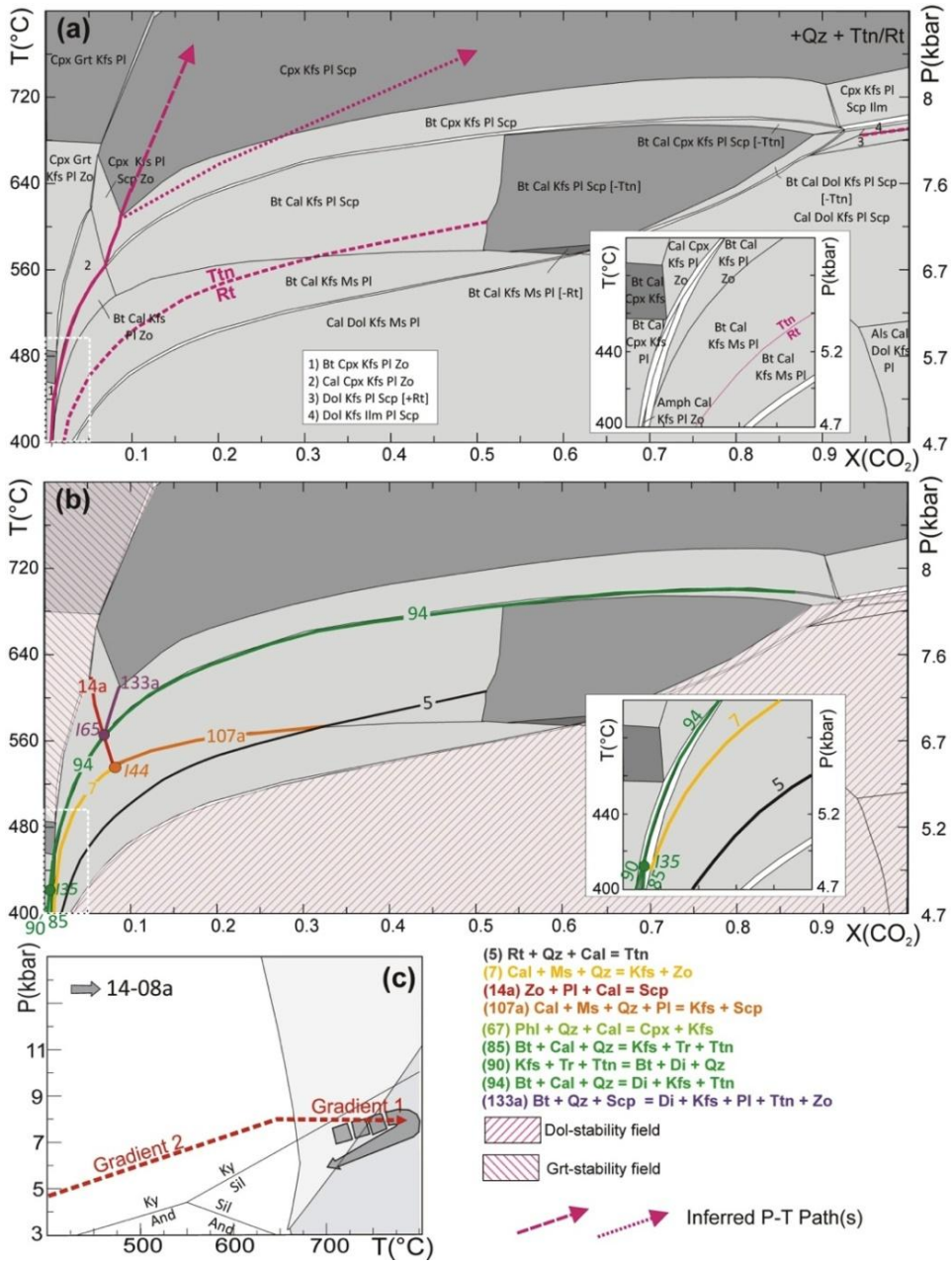

Fig. 5.27 – (**a**) **P/T-X(CO_2) pseudosection calculated for sample 14-17**, in the system NKCFMAST-HC along the composite P/T gradient represented in (c) and reflecting the P-T path followed by the host metapelites. White, light- and dark-grey fields are di-, tri- and quadrivariant fields, respectively; the narrow divariant fields correspond to the univariant reactions in the corresponding T-X(CO_2) sections (see Fig. 5.19). Dashed fields are dolomite- and garnet- bearing fields, not relevant for this study (because these phases are not observed in the studied sample). The purple arrows approximates the P/T-X(CO_2) internally buffered fluid evolution as constrained by the relevant microstructures (see §5.4.1.3). **(b)** Same P–T–X(CO_2) pseudosection as in (a): the relevant univariant and invariant equilibria are outlined (reactions labels and colors as in Fig. 5.19). Note that the univariant curves and invariant points overlap the (narrow) divariant fields and (short) univariant lines of the pseudosection. **(c)** P/T gradient used for the P/T-X(CO_2) pseudosection calculation and comparison with the P-T paths constrained for the surrounding metapelite (sample 14-08a) (gradient 2: P (bar) = 12.02 T(K) – 3331; gradient 1: P=8 kbar).

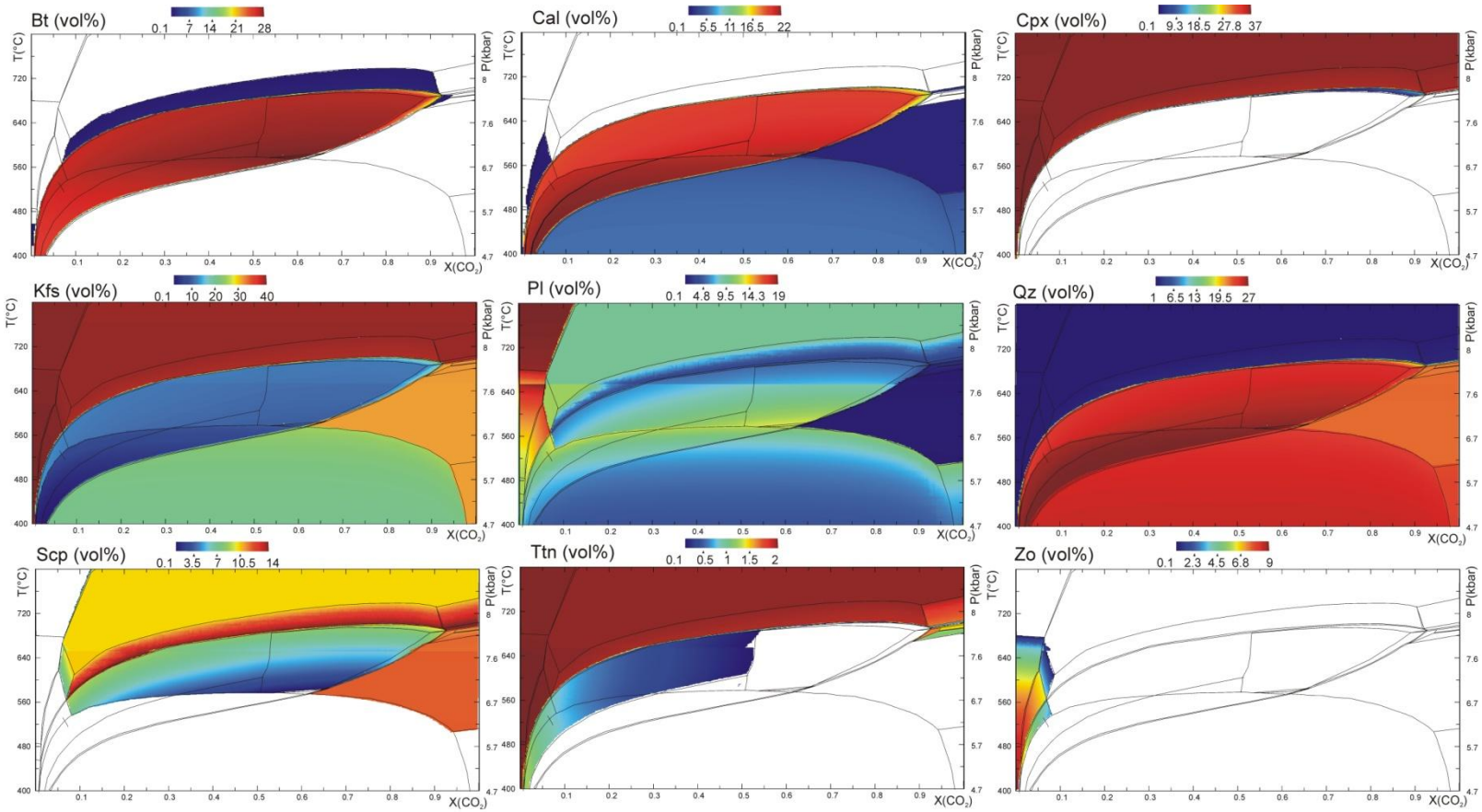

Fig. 5.28 - Predicted modes of mineral phases (vol%) for sample 14-17, based on the P/T-X(CO_2) pseudosection of Fig. 5.25.

5.3.2 Zr-in-titanite thermometry and U-Pb data in sample 14-53c

Al and Ti in the titanite show an inverse correlation and have a bimodal distribution (Al = 0.23-0.28 a.p.f.u., Ti = 0.70-0.76 a.p.f.u. *vs*. Al = 0.31-0.35 a.p.f.u., Ti = 0.63-0.69 a.p.f.u.); Zr shows a positive correlation with Al, in agreement with the commonly observed substitution of Al and Zr for Ti (e.g. Kohn, 2017). Overall, the Zr content in the analysed titanite grains is relatively high, spanning between 114 and 237 ppm, corresponding to Zr-in-titanite temperatures of 729-764 °C (± 15 °C) (Tab. 5.3). The frequency distribution of Zr-in-titanite temperatures shows two main peaks at 731-735 °C and 741-750 °C, suggesting the existence of two different titanite populations crystallized at T<740 °C and at T>740 °C, respectively (Fig. 5.29b). The mean values of Zr-in-titanite temperatures calculated for the two titanite populations have been compared by the Student *t*-test, which confirmed that they are statistically significant (the results of the statistical analysis are reported in Tab. 5.6).

U ranges between 19 and 207 ppm and shows a linear correlation with Zr, except for two titanite grains which are enriched in U compared to the other grains with similar Zr content. A slight correlation between chemical variations (i.e. Zr content) and ages is observed for most of the analysed titanite. Specifically, titanite grains recording higher temperature of crystallisation are, on average, younger than titanite grains crystallized at lower temperatures (Fig. 5.29a and Tab. 5.3). This feature was also observed by Kohn & Corrie (2011) in similar calc-silicate rocks from the U-GHS, but here it is less pronounced. Overall, the thermometric and geochronological data suggest that the studied calc-silicate rock experienced protracted heating from 730-740 °C at 30-26 Ma to peak-T of 750-760 °C at 25-20 Ma (Tab. 5.3, Fig. 5.29 and Fig. 5.30). Two U-enriched titanite grains record younger ages (~15 Ma) and are therefore interpreted as related to a retrograde re-crystallization/re-equilibration event. Zr-temperatures for this retrograde event are poorly constrained, due to the uncertainty in the estimation of pressure; temperatures of ~720 °C have been estimated for P = 9 kbar (Tab. 5.3).

It is worth noting that the relative distribution of titanite ages is independent from the assumed common Pb composition ($^{207}Pb/^{206}Pb$ = 0.84, following Stacey and Kramers, 1975); however, higher values of common lead such as those used by Kohn and Corrie (2011) for similar calc-silicate rocks (i.e. common Pb $^{207}Pb/^{206}Pb$ = 0.87) would imply slightly older and more spread absolute ages (Fig. 5.29c), whereas lower values of common lead would imply younger and more overlapped absolute ages.

Table 5.3 Zirconium temperature and isotopic data for sample 14-53c

Analysis	$a(TiO_2)$	P (GPa)	Zr (ppm)	U (ppm)	T (°C)[§]	$^{238}U/^{206}Pb$	± 2σ	$^{207}Pb/^{206}Pb$	± 2σ	Age (Ma)	± 95%
"Near peak" Ttn generation											
A.1 ttn2	0.55	1	133	19	729	120.34	8.69	0.428	0.064	28	5
4.g ttn16	0.6	1	130	32	732	85.25	6.54	0.551	0.061	28	6
B.2 ttn	0.6	1	139	34	735	151.52	9.41	0.333	0.058	27	4
8.d ttn28	0.55	1	140	42	735	162.34	15.81	0.325	0.080	26	5
N.1 ttn	0.6	1	145	28	737	154.80	8.39	0.378	0.040	24	2
L.1 ttn2	0.6	1	149	29	739	143.06	14.74	0.342	0.065	28	5
"Peak" Ttn generation											
8.m ttn34	0.6	1.05	140	31	741	168.63	19.05	0.423	0.078	20	4
G.1 ttn1	0.6	1.05	142	37	742	152.91	12.63	0.471	0.061	20	4
D.1 ttn1	0.6	1.05	145	28	743	132.63	9.15	0.447	0.065	24	4
3.c ttn10	0.6	1	164	67	744	133.33	10.13	0.383	0.054	28	4
8.c ttn27	0.6	1	169	73	745	180.18	17.53	0.305	0.073	24	4
H.2 ttn	0.6	1.05	157	41	747	177.62	11.99	0.354	0.042	22	2
N.2 ttn 1	0.6	1.05	157	57	747	196.08	12.30	0.270	0.033	24	2
6.a ttn21	0.6	1	177	62	747	106.04	10.57	0.444	0.053	30	5
7.a ttn24	0.6	1	183	116	749	209.64	11.87	0.213	0.033	24	2
3.a ttn9	0.6	1.05	167	57	750	227.27	25.83	0.259	0.063	21	3
H.1 ttn2	0.6	1.05	169	63	751	136.43	8.38	0.441	0.043	24	3
F.1 ttn1	0.6	1	193	96	752	65.45	3.94	0.610	0.024	29	3
I.1 ttn2	0.6	1.05	181	82	754	173.91	12.40	0.349	0.050	23	3
4.a ttn12	0.6	1.05	183	89	755	236.97	14.04	0.167	0.030	23	2
H.1 ttn1	0.6	1.05	195	112	758	238.66	14.81	0.135	0.028	24	2
A.1 ttn	0.55	1	237	207	758	147.93	5.47	0.367	0.018	26	1
L.1 ttn1	0.6	1.05	201	104	760	227.79	15.05	0.165	0.031	24	2
E.2 ttn	0.6	1.05	211	130	762	239.81	17.25	0.247	0.028	20	2
G.1 ttn3	0.6	1.05	216	140	764	291.55	21.25	0.142	0.024	19	2
Late Ttn generation											
C.1.l ttn3	0.6	0.9	130	73	720	238.10	23.81	0.414	0.069	15	3
I.1 ttn1	0.6	0.9	133	91	721	366.30	32.20	0.155	0.037	15	2

[§]Uncertanties in T is assumed to be ± 10°C.

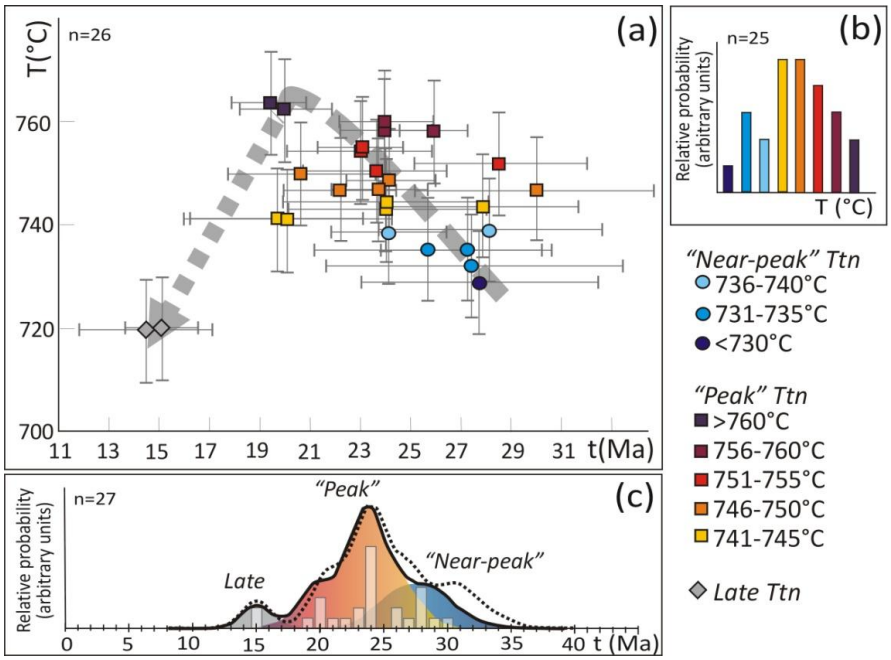

Fig. 5.29 - (a) Temperature-time diagram for sample 14-53c, showing gradually increasing temperatures between 28 and 19 Ma and a retrograde cooling at ~15 Ma (grey symbols refer to the retrograde titanite generation). Errors on temperatures are ± 10 °C (see Section 5.2.5 for Discussion). **(b) Frequency distribution of Zr-in-titanite temperatures**; the two titanite grains interpreted as retrograde are not considered, due to the uncertainties in the estimate of their temperature of crystallization. **(c) Probability density plot for U-Pb ages** (common Pb $^{207}Pb/^{206}Pb$ = 0.84); although partially overlapped, the "near peak" and "peak" titanite generations are clearly distinguishable. The dotted line refers to titanite ages obtained for a higher common Pb value ($^{207}Pb/^{206}Pb$ = 0.9).

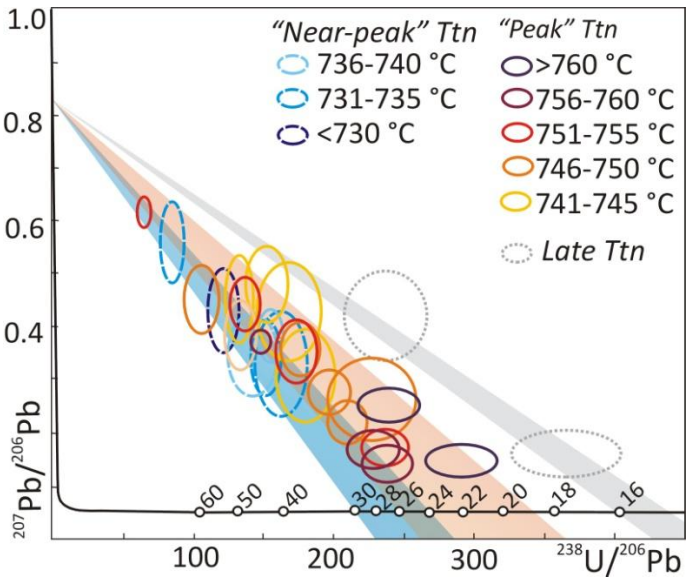

Fig. 5.30 Inverse isochrone plot of the titanite U–Pb data, plotted using ISOPLOT (Ludwig, 2001). The numbers marked along the concordia line are ages in Ma. Color coded according to Zr-in-titanite temperatures (as in Fig. 5.29).

Table 5.4 - Trace elements for MKED1 - Quality control

Spot	Zr (ppm)	± 2σ	Th (ppm)	± 2σ	U (ppm)	± 2σ
T_MKED1_1	223	4	341	7	117	2
T_MKED1_2	226	4	347	7	120	3
T_MKED1_3	220	4	332	6	116	2
T_MKED1_4	216	4	324	5	114	2
T_MKED1_5	223	4	326	6	116	2
T_MKED1_6	225	4	328	7	118	3
T_MKED1_1	218	3	336	6	127	2
T_MKED1_2	218	3	335	5	116	2
T_MKED1_3	211	3	323	7	111	2
T_MKED1_4	223	5	342	9	126	5
T_MKED1_5	228	3	349	5	126	2
T_MKED1_1	211	3	344	5	118	2
T_MKED1_2	207	3	326	4	115	2
T_MKED1_3	212	3	340	5	115	1
T_MKED1_4	218	4	345	6	118	2
Average	219	6	336	9	118	4
MKED1 (from Spandler et al., 2016)	236	13	369	24	131	7

Table 5.5 - Isotopic data for MKED1 - Quality control

Spot	$^{207}Pb/^{235}U$	± 2σ	$^{206}Pb/^{238}U$	± 2σ	Age $^{206}Pb/^{238}U$	± 2σ	Age $^{207}Pb/^{235}U$	± 2σ
T_MKED1_1	3.51	0.12	0.265	0.005	1512	26	1526	26
T_MKED1_2	3.48	0.11	0.267	0.005	1524	26	1519	24
T_MKED1_3	3.52	0.17	0.265	0.004	1513	22	1524	37
T_MKED1_4	3.48	0.11	0.264	0.004	1512	18	1518	24
T_MKED1_5	3.47	0.12	0.265	0.005	1513	24	1518	27
T_MKED1_6	3.47	0.10	0.265	0.005	1512	25	1518	23
T_MKED1_1	3.54	0.10	0.266	0.005	1520	25	1534	24
T_MKED1_2	3.52	0.09	0.268	0.003	1531	17	1528	20
T_MKED1_3	3.49	0.09	0.266	0.003	1520	15	1523	20
T_MKED1_4	3.58	0.17	0.264	0.007	1511	35	1541	37
T_MKED1_5	3.50	0.08	0.264	0.004	1509	23	1525	19
T_MKED1_1	3.51	0.26	0.266	0.005	1519	26	1524	59
T_MKED1_2	3.44	0.09	0.264	0.006	1510	33	1512	21
T_MKED1_3	3.48	0.09	0.267	0.004	1524	18	1519	21
T_MKED1_4	3.50	0.08	0.266	0.004	1520	19	1526	18
Average	3.50	0.03	0.265	0.001	1517	6	1524	7
ID-TIMS Ref. from Spandler et al., 2016	3.46	0.04	0.265	0.024	LA-ICP-MS 1519	3	LA-ICP-MS 1517	2

Table 5.6 - Student t-test (unpaired values) of mean values of Zr-in-Ttn T in the two Ttn generations

"Near peak" Ttn generation			*"Peak" Ttn generation*				
χ	σ	n	χ	σ	n	t	p
735	3.3	7	751	7	19	5.93	0.00001

χ = mean T value; σ = standard deviation; n = number of Ttn; t = value of Student t-test for unpaired values; p = probability (null hypothesis). Values of p lower than 0.01 are considered strongly indicative of a difference between two mean values.

5.4 Discussion

5.4.1 P-T-X(CO_2) prograde evolution and CO_2-producing processes in different types of CO_2-source rocks

5.4.1.1 Sample 14-44c (Type 1C)

❖ **P-T-X(CO_2) prograde evolution**

The following microstructural evidences allow constraining the prograde P-T-X(CO_2) evolution of the sample:

(i) Mg-chlorite is preserved in zoisite and garnet porphyroblasts (Fig. 5.3c,f,m,n). Garnet also includes calcite + quartz (Fig. 5.3b,c,h). This suggests that the prograde mineral assemblage was characterized at least by chlorite + calcite + quartz. The univariant CFMAS-HC reaction calcite + chlorite + quartz → zoisite + garnet + amphibole (reaction 3 in Fig. 5.15b,c) is compatible with these microstructures. This univariant reaction corresponds to a narrow divariant field in the MnCFMAST-HC pseudosection of Fig. 5.15a.

(ii) The peak mineral assemblage is represented by garnet + clinopyroxene + anorthite + calcite. Garnet porphyroblasts include calcite, quartz, plagioclase and minor amphibole and clinopyroxene. Moreover, equilibrium microstructures between garnet, clinopyroxene and plagioclase are also observed, suggesting that garnet partly grew in the plagioclase + clinopyroxene stability fields.

(iii) Microstructural evidences of the retrograde evolution are ubiquitous, and are mainly represented by the development of amphibole + calcite + zoisite aggregates at the expense of clinopyroxene and plagioclase (Fig. 5.3l-n).

Many possible paths connecting the prograde and peak mineral assemblages fields can be proposed (Fig. 5.15a), and because the two fields are stable at significantly different $X(CO_2)$ values, the system likely remained, at least partially, internally buffered. The CFMAS-HC reaction calcite + chlorite + quartz → zoisite + garnet + amphibole (reaction 3 in Fig. 5.15b,c) was responsible for the disappearance of chlorite and the appearance of garnet and prograde amphibole. If the system remained internally buffered, this reaction proceeded until the invariant point I2 (Fig. 5.15b,c) is reached. Alternatively, if one of the reactants (e.g. chlorite) was exhausted before reaching I2, the system entered in the trivariant amphibole + garnet + calcite + zoisite field.

Whatever the P-T-$X(CO_2)$ path followed within this field, the system should have left the amphibole-stability field, because prograde amphibole is not preserved (except for rare inclusions within garnet). This implies crossing either the trivariant amphibole + garnet + calcite + zoisite field, or the amphibole + garnet + calcite + anorthite field (or evolving within the divariant amphibole + garnet + calcite + zoisite + anorthite field). In all these cases, amphibole was consumed and garnet was produced at increasing P-T conditions. Amphibole was totally exhausted when CMFAS-HC reactions 5 (calcite + amphibole + quartz + garnet → zoisite + clinopyroxene) or 6 (calcite + amphibole + quartz + garnet → anorthite + clinopyroxene) (Fig. 5.15b,c) were reached, which correspond to the narrow divariant garnet + clinopyroxene + calcite + anorthite/zoisite + amphibole fields in the P/T-$X(CO_2)$ pseudosection of Fig. 5.15a. Once crossed these reactions, the system entered the trivariant garnet + clinopyroxene + calcite + anorthite field. With increasing P and T within this field, garnet was continuously produced through calcite consumption, and became progressively enriched in the grossular component, in agreement with the measured compositional zoning (see §5.2.2.1).

❖ **CO_2-producing processes**

Along the inferred P-T-$X(CO_2)$ trajectories, the fluid was progressively enriched in CO_2, reaching values of $X(CO_2)$ >0.6 at peak P-T conditions (T=700-750 °C, §3.4.3.1). As long as the system remained internally buffered, the amount of CO_2 released was very low, because modal changes are only minor along univariant curves (e.g. Greenwood, 1975; Groppo et al., 2017). This implies that, for the studied sample, CO_2 production mostly occurred when the buffering ability of the system ceased due to the complete consumption of amphibole, i.e. when the system entered the trivariant field garnet + clinopyroxene + calcite + anorthite. In this field, calcite was progressively consumed (and garnet simultaneously grew), leading to CO_2 release. Therefore, the CO_2-producing

process was a continuous process, and mostly occurred at relatively high T conditions. The final CO_2 production was of ~1.5 wt% of CO_2 (Fig. 5.31).

It is worth noting that most of the observed retrograde microstructures (e.g. replacement of clinopyroxene and plagioclase by amphibole + calcite + zoisite aggregates) involve the formation of retrograde calcite. This suggests that at least some of the CO_2-rich fluid internally produced during the prograde evolution of this sample remained confined within the system, allowing carbonation reactions to proceed at decreasing P-T conditions. This implies that the overall CO_2 productivity of this sample was significantly lower than 1 wt% of CO_2, and more likely almost negligible.

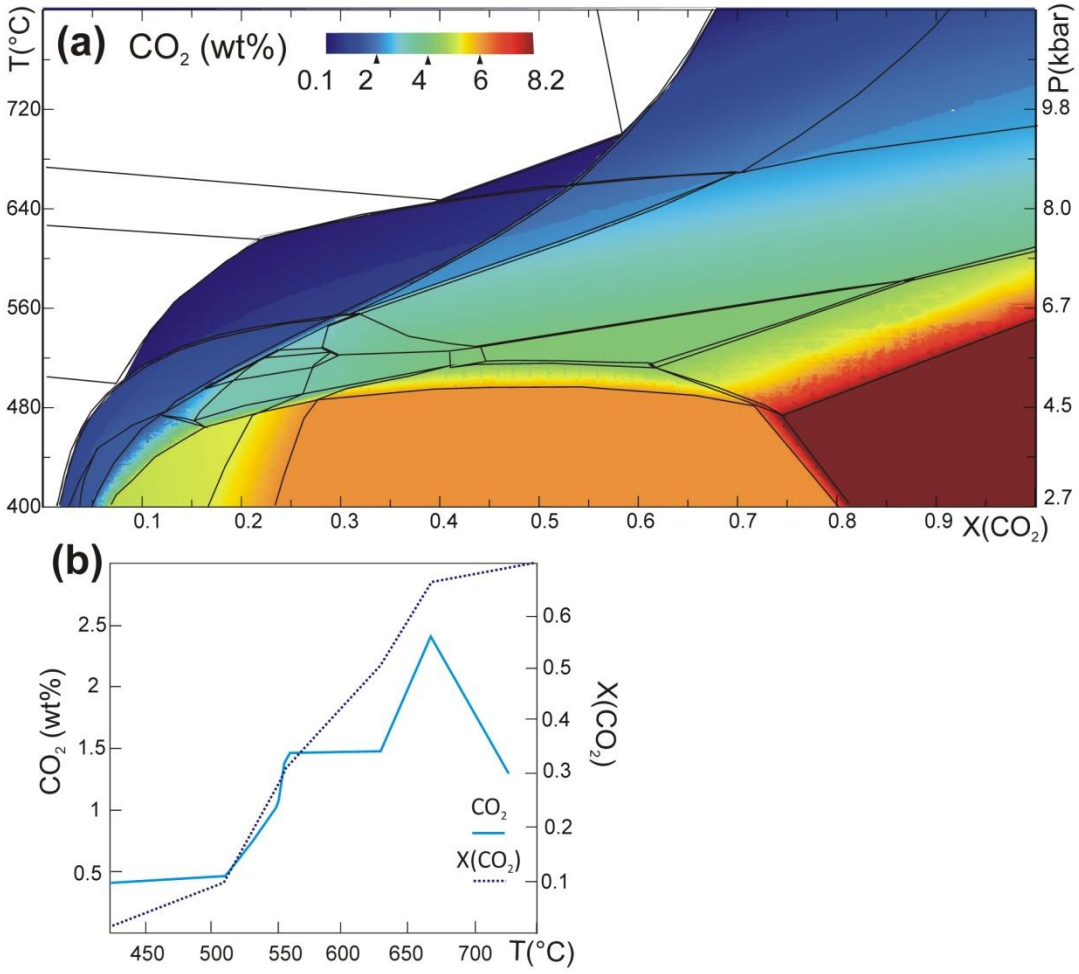

Fig. 5.31 – **(a)** Same P/T-X(CO_2) pseudosection of Fig. 5.15a, with the P-T-X(CO_2) evolution inferred for sample 14-44c and the modelled CO_2 (wt%) amounts. **(b)** Modelled CO_2 amount (wt%) and fluid composition along the P-T-X(CO_2) path which the maximun CO_2 production.

5.4.1.2 Sample 15-46 (Type 3C)

❖ **P-T-X(CO_2) prograde evolution**

The following microstructural relationships allow constraining the prograde P-T-X(CO_2) evolution of the sample:

(i) garnet grew at the expense of calcite + quartz + zoisite (Fig. 5.6c-e), in the biotite-stability field (Fig. 5.32a,b);

(ii) scapolite grew at the expense of zoisite + quartz + plagioclase (XAn=0.47-0.56) (Fig. 5.6f-h), in the biotite-stability field (Fig. 5.32a,c);

(iii) amphibole and margarite have not been observed in the sample (Fig. 5.32a,d).

All together these observations constraint part of the prograde P-T-X(CO_2) trajectory as indicated in Fig. 5.32e; this P-T-X(CO_2) path is especially well constrained by the conditions inferred for garnet and scapolite growth (Fig. 5.32b,c) and points to a gradual increase of X(CO_2) at increasing T and P. Mode variations along the P-T-X(CO_2) trajectory are given in Fig. 5.35.

Trying to constrain the P-T-X(CO_2) path followed by the sample before the first appearance of garnet is difficult and highly speculative; however, the systematic absence of ankerite relics in garnet porphyroblasts suggests that the prograde P-T-X(CO_2) path remained confined in the fields with only calcite as stable carbonate (Fig. 5.32a,e). It is plausible that the system remained internally buffered until the total consumption of calcite, which is indeed practically absent in the sample. The successive growth of scapolite at the expense of zoisite + plagioclase constraints the prograde path to enter the trivariant quartz + biotite + chlorite + scapolite + plagioclase + garnet + zoisite + rutile field (Fig. 5.32e). The increase in the P-T conditions led to the total consumption of chlorite and to the entrance in the quinivariant quartz + biotite + scapolite + plagioclase + garnet + titanite field, producing the observed peak mineral assemblage.

❖ **CO_2-producing processes**

The main calcite-out reaction curve relevant for the studied sample coincides with the garnet-in reaction curve; this is the discontinuous reaction $calcite_{ss}$ + quartz + $chlorite_{ss}$ → $garnet_{ss}$ (with $calcite_{ss}$, $chlorite_{ss}$, and $garnet_{ss}$ being Mn-bearing solid solutions), corresponding to a narrow divariant field in the pseudosection of Fig. 5.17a and Fig. 5.32a. It is worth noting that, in the Mn-free system, this reaction is not modelled, and garnet appearance is predicted at higher P-T conditions (T>560 °C, P>6.7 kbar), well outside the calcite and zoisite stability fields (Fig. 5.33). However, the observed microstructures clearly demonstrate that garnet grew at the expenses of both calcite (which is relatively rich in Mn) and zoisite, thus confirming the validity of the pseudosection modelled in the Mn-bearing system. These results imply that Mn-bearing

solid solutions, and especially Mn-rich calcite, play a key-role in the modelling of CO_2-producing processes in such systems (i.e. derived from calcite-rich pelites), as already pointed out by Nabelek and Chen (2014). Specifically, these authors suggest that Mn-rich calcite crystals served as nucleation sites into which other necessary components for garnet growth readily migrate over short distances from surrounding reactants minerals.

This discontinuous calcite-consuming and garnet-forming reaction, however, is responsible for the production of relatively low amounts of CO_2 (CO_2 < 0.5 wt%; Fig. 5.34a,b). The majority of CO_2 (~2.5 wt%) is released through continuous reactions (calcite + chlorite + quartz + muscovite ± paragonite ± rutile ± titanite = Na-plagioclase ± biotite ± garnet ± zoisite) occurring in tri- and quadrivariant fields at relatively low P-T conditions (T< 500 °C; P< 6 kbar), during the early prograde evolution of the studied sample (Fig. 5.32e: paths 1 to 3; Fig. 5.34b,c). Overall, the CO_2 productivity of this sample is therefore < 3.5 wt%.

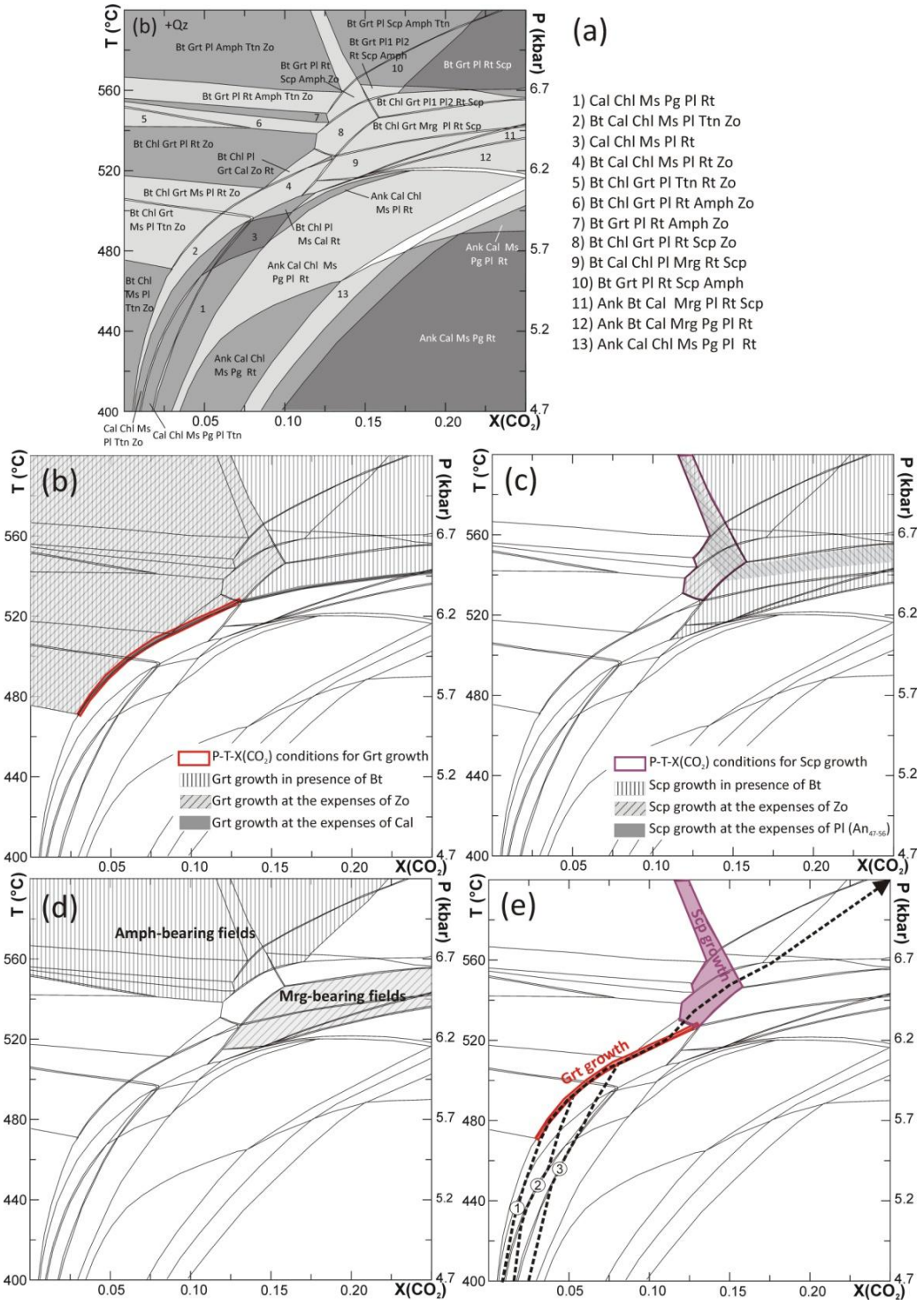

Fig. 5.32 – **(a)** Same P/T-X(CO_2) pseudosection as in Fig. 5.17b. The main constraints used to infer the P-T-X(CO_2) path are reported in (a) to (d). **(b)** Garnet growth. **(c)** Scapolite growth. **(d)** Amphibole- and margarite-bearing fields. **(e)** Inferred early prograde P-T-X(CO_2) evolution (dashed black arrows). Numbers 1-3 refer to possible prograde P-T-X(CO_2) paths followed by the sample.

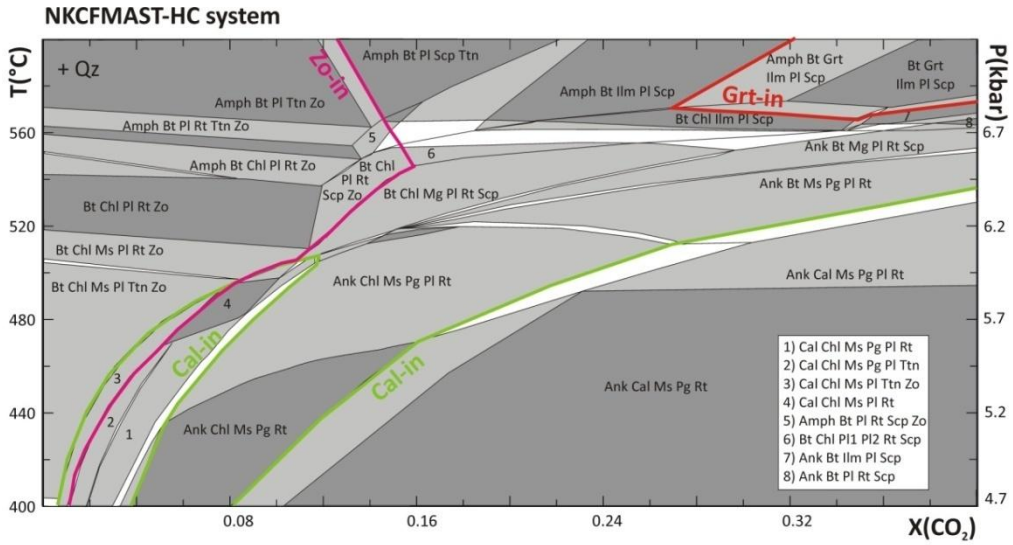

Fig. 5.33 - Same P/T-X(CO_2) pseudosection of Fig. 5.17a, calculated for sample 15-46 in the system NKCFMAST-HC (Mn-free system). Calcite- garnet- and zoisite-stability fields are highlighted.

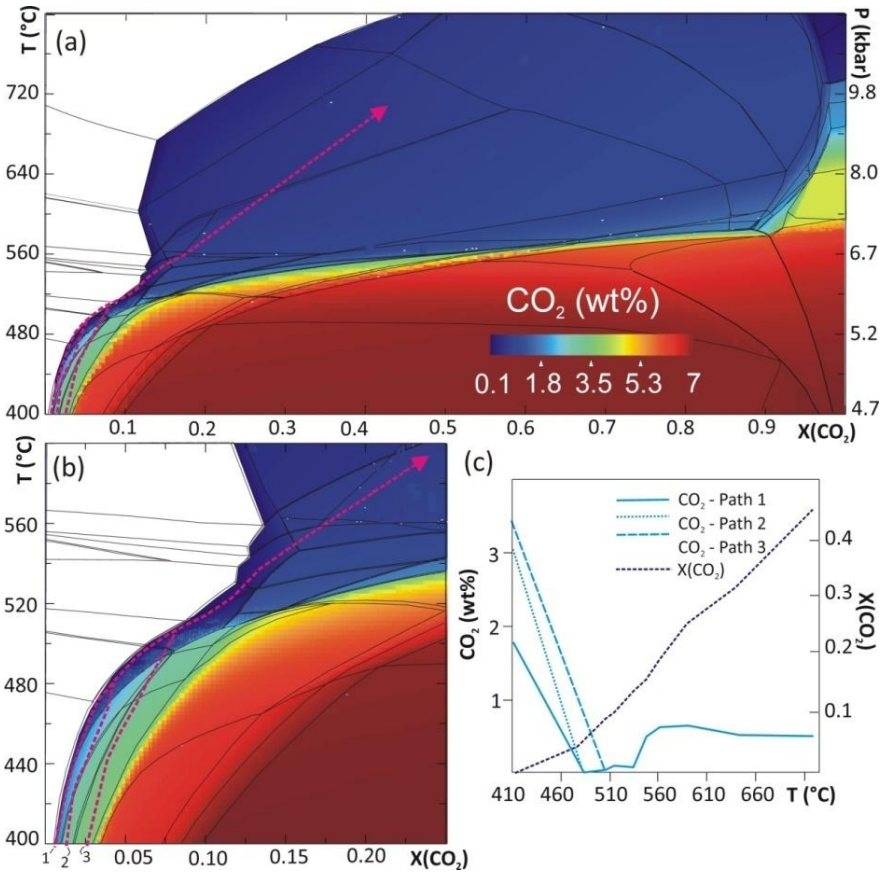

Fig. 5.34 – (a,b) P/T-X(CO_2) evolution inferred for the studied sample and modelled CO_2 amounts (wt%). The low-P/T-XCO_2 portion of the pseudosection is enlarged in (b). **(c)** Modelled CO_2 amounts (wt%) and fluid composition along the three P-T- X(CO_2) paths.

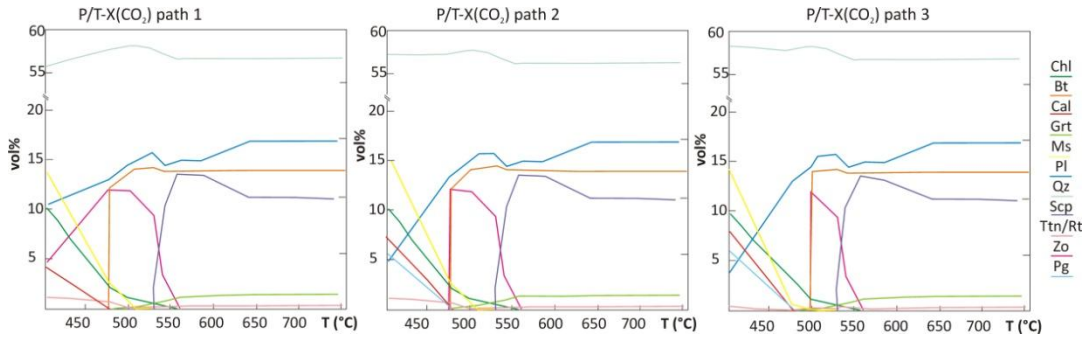

Fig. 5.35 -Modal evolution (vol%) along the same inferred P/T-X(CO_2) paths of Fig. 5.32e**.**

5.4.1.3 Samples 14-53c and 14-17 (Type 3F)

❖ P-T-X(CO_2) prograde evolution

In both samples 14-53c and 14-17 most of the observed microstructures reflect either isobaric/isothermal univariant or invariant assemblages, thus suggesting that the system remained internally buffered for most of its metamorphic evolution. Moreover, the close similarity between the modal amounts of minerals observed in both the samples and those predicted by the pseudosections (Tab. 5.7), suggests that little or no externally-derived fluid interacted with the rock.

Table 5.7 Mineral modes of Type 3F samples

Predicted *vs*. observed modal amount (vol%) of minerals

	14-53c				14-17 (*)		
	Cal-poor domain		Cal-rich domain				
	Predicted at 750°C, 10.7 kbar X(CO_2)=0.57	Observed	Predicted at 750°C, 10.7 kbar X(CO_2)=0.57	Observed	Predicted at 760°C, 8 kbar, X(CO_2)=0.16	Predicted at 760°C, 8 kbar, X(CO_2)=0.5	Observed
Bt	3.0	4	-	3	-	-	-
Cal	-	-	1.8	1	-	-	-
Cpx	12.8	11	17.0	14	36.1	36.1	36
Kfs	16.1	15	10.9	9	39	39	40
Pl	19.1	10	22.7	14	11.4	11.4	6
Qz	43.5	45	31.5	34	2	2	2
Scp	3.5	9	14.6	17	9.5	9.5	13
Ttn	2.0	2	1.5	2	2	2	2
Zo	-	4	-	6	-	-	0.5

(*) For sample 14-17, mineral modes have been calculated following the two inferred P-T-X(CO_2) paths of Fig. 5.19a.

In both the samples, the occurrence of rare amphibole relics preserved in the core of clinopyroxene, tightly constrains the first portion of the P-T-X(CO_2) evolution in the narrow amphibole stability field, which is limited by the univariant equilibria 85 and 90 (Fig. 5.22, Fig. 5.24 and Fig. 5.25). Moreover, microstructural evidence suggests that clinopyroxene cores grew at the expenses of amphibole + calcite ± quartz (Fig. 5.9e). This microstructure can be explained by the truly univariant reaction U35, calcite + k-feldspar + tremolite + titanite → biotite + diopside + quartz + Fluid (corresponding to the isobaric/isothermal invariant point I35; Fig. 5.22, Fig. 5.24, Fig. 5.26 and Fig. 5.25); the same reaction could also explain the rare occurrence of corroded inclusions of K-feldspar in biotite in sample 14-53c (Fig. 5.9b).

Once that at least one of the reactants of reaction U35 (i.e. amphibole) was completely consumed, the system evolved along the univariant reaction 94 (biotite + calcite + quartz → diopside + k-feldspar + titanite + H_2O + CO_2) until it reached the invariant point I65 (i.e. truly univariant reaction U65a: biotite + calcite + plagioclase + quartz + zoisite →diopside + k-feldspar + scapolite + titanite + Fluid) (Fig. 5.22, Fig. 5.24, Fig. 5.26 and Fig. 5.25). Reaction U65a could explain the rare occurrence of Na-rich plagioclase preserved as corroded inclusions within scapolite and titanite in both the samples (Fig. 5.9n and Fig. 5.14b). The system departed from the invariant point I65 once that one of the reactants was totally consumed. Two possibilities can be discussed: (a) calcite was completely consumed, and the system evolved along the univariant reactions 133a and 133b; (b) Na-rich plagioclase was completely consumed, and the system evolved along the univariant reaction 94.

For sample 14-53c, the first possibility (total consumption of calcite) is unlikely, because reactions 133a (biotite + quartz + scapolite → diopside + k-feldspar + plagioclase + titanite + zoisite + H_2O + CO_2) and 133b (biotite + quartz + scapolite + zoisite → diopside + k-feldspar + plagioclase + titanite + H_2O + CO_2) would have implied the growth of Na-rich plagioclase, which is instead not observed in the studied sample. Rather, the second possibility (i.e. total consumption of Na-rich plagioclase) is more likely. The system thus evolved along equilibrium 94 (biotite + calcite + quartz → diopside + k-feldspar + titanite + H_2O + CO_2) until it reached the truly univariant reaction U65c, corresponding to the isobaric/isothermal invariant point I65' (Fig. 5.22, Fig. 5.24 and Fig. 5.26). Reaction U65c (calcite + biotite + scapolite + zoisite + quartz → clinopyroxene + k-feldspar + plagioclase + titanite + Fluid) was responsible for the growth of most of the Ca-rich plagioclase observed in sample 14-53c and is consistent with the occurrence of: (i) inclusions of scapolite, zoisite and quartz in Ca-rich plagioclase (Fig. 5.9h); (ii) inclusions of scapolite, biotite, calcite, quartz and zoisite in titanite (Fig. 5.14a,c,d,e,f); (iii) inclusions of biotite, quartz, calcite and scapolite in the clinopyroxene rims (Fig. 5.9e,f); (iv) inclusions of scapolite in K-feldspar (Fig. 5.9c). Once that zoisite was exhausted, the system further evolved along the univariant reaction 94. In calcite-poor domains it is likely that reaction

94 (and its buffering ability) ceased due to the complete consumption of calcite, thus implying that the system entered the biotite + clinopyroxene + k-feldspar + plagioclase + quartz + scapolite + titanite stability field that represents the observed peak assemblage (Fig. 5.22a). In calcite-rich domains, biotite is probably completely consumed, and the system entered the calcite + clinopyroxene + k-feldspar + plagioclase + quartz + scapolite + titanite stability field, in agreement with the observed peak assemblage (Fig. 5.24).

For sample 14-17, once that the system departed from the invariant point I65, an evolution along the univariant reaction 133a (biotite + quartz + scapolite → diopside + k-feldspar + plagioclase + titanite + zoisite + H_2O + CO_2) is more consistent with the observed occurrence of Na-rich plagioclase in equilibrium with clinopyroxene and k-feldspar (Fig. 5.11c) and the absence of calcite. The lack of biotite in the main mineral assemblage further suggests that the system entered the clinopyroxene + k-feldspar + plagioclase + scapolite +quartz + titanite field (Fig. 5.27a), which corresponds to the observed mineral assemblage. This field could have been reached in different ways, involving either (i) the simultaneous consumption of zoisite and biotite (dashed arrow in Fig. 5.27a), or (ii) the entrance in the trivariant field biotite + clinopyroxene + k-feldspar + plagioclase + scapolite + quartz + titanite through the exhaustion of zoisite, followed by the complete consumption of biotite (dotted arrow in Fig. 5.25a). The stability field of the observed peak mineral assemblage is quite large (T>630 °C, $X(CO_2)$>0.1); peak T are known from the associated metapelites (T≈780 °C; see §3.5.1), whereas it is not possible to constrain in further detail the $X(CO_2)$ fluid composition. Mineral modes (and their compositions) are nevertheless constant in this four variant field (Tab. 5.7, Fig. 5.23, Fig. 5.25, Fig. 5.28 and Fig. 5.37c).

Overall, the thermodynamic modelling results demonstrate that sample 14-53c and 14-17 followed a similar P-T-$X(CO_2)$ evolution during the early stages of prograde metamorphism, but then evolved along different P-T-$X(CO_2)$ paths, depending on the order in which the various rectants (calcite, Na-rich plagioclase) were progressively exhausted (which is ultimately controlled by the bulk composition, e.g. by the original abundance of calcite in the protolith). These results highlight the importance of modelling each sample separately from the others, even if they are characterized by similar peak mineral assemblages (as in this case). A careful microstructural study combined with detailed themodynamic modelling is essential for the definition of the P-T-$X(CO_2)$ evolution of these calc-silicate rocks (see also Groppo et al., 2017).

❖ **CO_2-producing processes**

It has been demonstrated that, as long as a system remains internally buffered, sudden and volumetrically-significant appearance of new phases and the simultaneous disappearance of previously abundant phases occur at the isobaric/isothermal invariant points, whereas modal changes are only minor along the univariant curves (e.g.

Greenwood, 1975; Groppo et al., 2017; see Fig. 5.37). On the opposite, univariant reactions lead to volumetrically-significant appearance of new phases when the buffering ability of the system ceases due to the complete consumption of one or more reactants.

According to the P-T-X(CO_2) evolution previously discussed, both the calcite-poor and calcite-rich domains of sample 14-53c remained internally buffered up to ~740 °C, i.e. up to temperatures slightly higher than I65', whereas sample 14-17 remained internally buffered up to ~620 °C, i.e. up to temperatures slightly higher than I65. In both the samples, the buffering ability of the system ceased due to the complete consumption of one or more reactants (calcite/biotite in the calcite-poor/calcite-rich domains of sample 14-53c; zoisite, biotite and calcite in sample 14-17), respectively. It follows that the most important episodes of mineral growth/consumption and of CO_2 production occurred:

- for sample 14-53c, at the invariant points I35, I65, and I65', and at T > 740 °C once that calcite/biotite were completely consumed in the calcite-poor/calcite-rich domains, respectively. In the following, these events will be called early prograde (I35), prograde (I65), near peak (I65') and peak (total consumption of calcite/biotite) events, respectively;
- for sample 14-17, at the invariant points I35, I65, and at T > 620°C once that zoisite, biotite and calcite were completely consumed. In the following, these events will be called early prograde (I35), prograde (I65) and peak (total consumption of zoisite and biotite) events, respectively.

The amounts of CO_2 produced for each of these episodes of CO_2 production, as predicted by the P/T-X(CO_2) pseudosections (Fig. 5.34a-c), are summarized in Tab. 5.8. More in detail:

- for sample 14-53c, most of CO_2 was produced during the early prograde event, at ~430°C, 4 kbar (0.5/0.8 wt% of CO_2 in the calcite-poor/calcite-rich domains, respectively) and at peak event, at >740 °C, 10.5 kbar (1.2/1.4 wt% of CO_2 in the calcite-poor/calcite-rich domains, respectively; Tab. 5.8). On average, 2.0/3.0 wt% of CO_2 were produced by the calcite-poor/calcite-rich domains, respectively, during the whole prograde evolution.
- For sample 14-17, most of CO_2 was produced during the early prograde event, at ~412 °C, 4.5 kbar (3.3 wt% of CO_2) and at prograde event, at ~ 565 °C, 6.8 kbar (5 wt%) of CO_2. A total production of 8.4 wt% of CO_2 during the whole prograde evolution can be constrained for this sample (Tab. 5.8).

It has been therefore demonstrated that, for this type of CO_2–source rocks (Type 3F), CO_2 was produced through distinct, short-lived events, which occurred at specific P-T conditions along the whole prograde metamorphic evolution, and especially at relatively high temperature (Fig. 5.34a-c; see also Groppo et al., 2017). The predicted amounts of

produced CO_2 are quite high (from a minimum of 2 wt% to > 8 wt% of CO_2) and vary as a function of the bulk composition. Intermediate values of 4-5 wt% of CO_2 were calculated by Groppo et al. (2017) for similar calc-silicate rocks, thus confirming the high CO_2 productivity of this lithology (Type 3F).

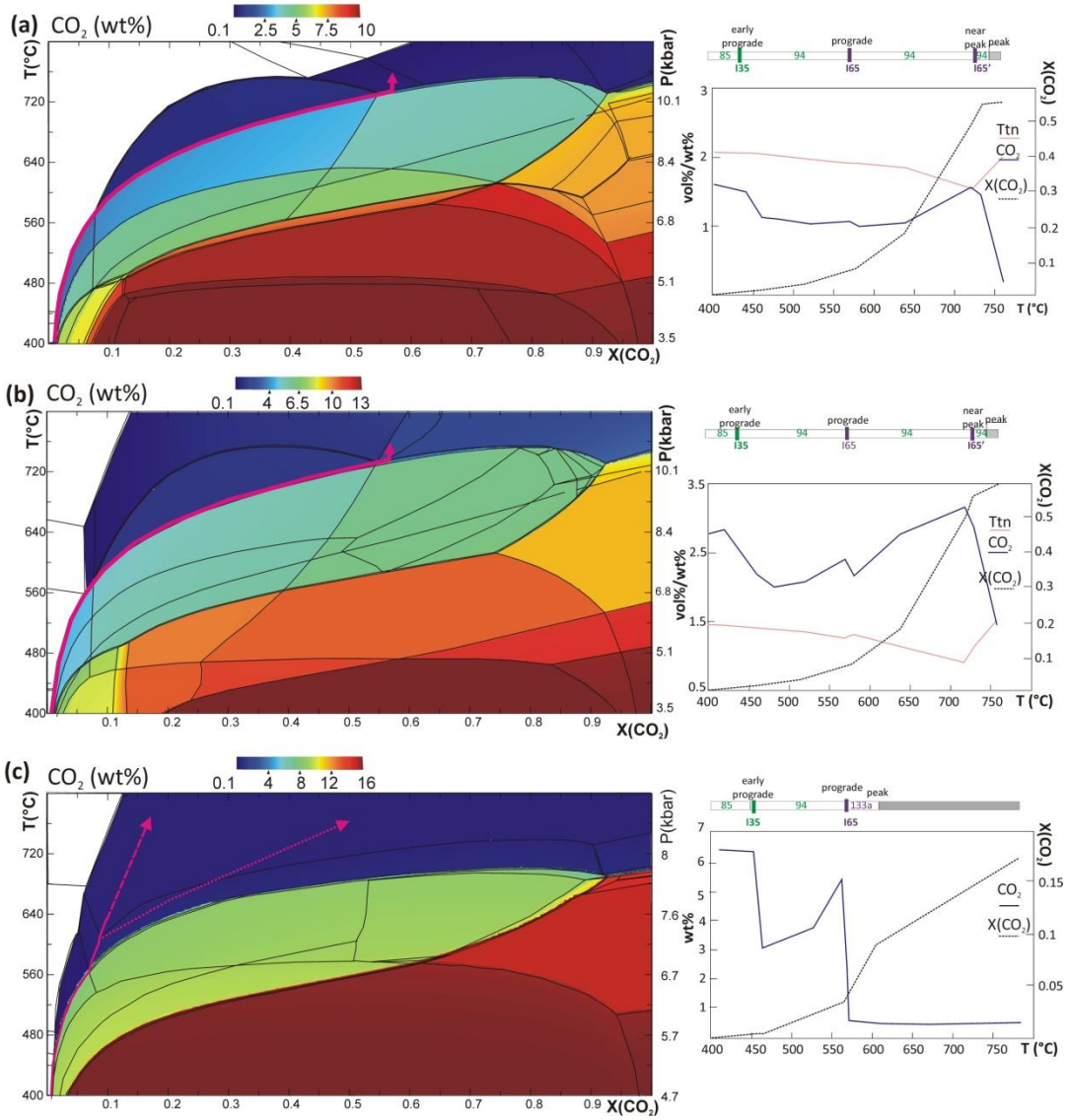

Fig. 5.36 - P/T-X(CO_2) evolution inferred for the studied samples (Type 3F) with CO_2 (wt%) and titanite (vol%) amounts, and fluid composition (X(CO_2)) modelled along the inferred P/T-X(CO_2) paths (purple arrows)**.** (a,b) Sample 14-53c (a: calcite-poor domain; b: calcite-rich domain); (c) sample 14-17 (c) and CO_2 amount (wt%), titanite amounts (vol%). The main episodes of CO_2 production are reported at the top.

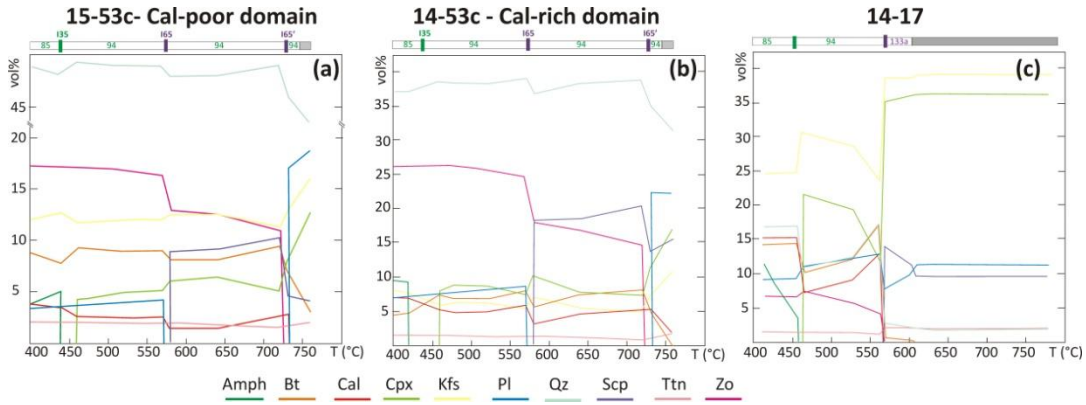

Fig. 5.37 - Modal evolution (vol%) along the P/T-X(CO_2) path inferred for sample 14-53c (purple arrow in Fig. 5.22a) and Fig. 5.24a) calculated for the calcite-poor **(a)** calcite-rich domain **(b)** of sample 14-53c, and for sample 14-17 **(c)**. The isobaric univariant curves and invariant points are reports at the top.

Table 5.8 - Type 3F. Predicted amounts of titanite and CO_2 produced during different events

	14-53c				**14-17**
	Cal-poor domain		Cal-rich domain		
	Ttn (vol%)	CO_2 (wt%)	Ttn (vol%)	CO_2 (wt%)	CO_2 (wt%)
early prograde	-0.1	0.50	-0.1	0.85	3.3
prograde	0.02	0.10	0.05	0.30	4.9
near-peak	0.1	0.15	0.2	0.25	
peak	0.4	1.25	0.4	1.45	0.2
Total	0.4	**2.0**	0.6	**2.9**	**8.4**

5.4.2 Dating the CO_2-producing processes: the case study of sample 14-53c

Most of the CO_2-producing reactions modelled in the Type 3F CO_2-source rocks (e.g. samples 14-53c and 14-17) also produced titanite. Taking advantage of the possibility of simultaneously applying U-Pb geochronology (e.g. Frost et al., 2000; Kohn, 2017) and trace element thermometry (Zr-in-titanite: Hayden et al., 2008) on titanite, sample 14-53 was selected as a case study for constraining the timing of CO_2 production in the most abundant type of CO_2-source rocks within the GHS. The obtained results, extrapolated to the scale of the whole orogen, allowed estimating – for the first time – the CO_2 metamorphic flux from the Himalaya (§6.1). Moreover, the P-T-t constraints on Himalayan prograde metamorphism obtained for the studied sample have been compared with those already published for the same region.

5.4.2.1 P-T-t conditions of titanite growth and CO_2 production

The results of thermodynamic modelling of sample 14-53c predict the following three main episodes of titanite growth and CO_2 production (Fig. 5.22, Fig. 5.24 and Tab. 5.3): (i) a prograde event occurred at ~570 °C, 7 kbar (i.e. at I65 through reaction U65a: biotite + calcite + plagioclase + quartz + zoisite → diopside + k-feldspar + scapolite + titanite + Fluid), producing a small amount of titanite and ~0.1/0.3 wt% of CO_2 in the calcite-poor/calcite-rich domains, respectively; (ii) a near-peak event occurred at ~730 °C, 10 kbar (i.e. at I65' through reaction U65c: biotite + calcite + quartz + scapolite + zoisite → diopside + k-feldspar + plagioclase + titanite + Fluid) and produced ~0.1/0.2 vol% of titanite and ~0.2/0.3 wt% of CO_2 in the calcite-poor/calcite-rich domains, respectively; (iii) a peak event occurred at conditions of 740-765 °C, 10.5 kbar through reaction 94 (biotite + calcite + quartz → diopside + k-feldspar + titanite + H_2O + CO_2), leading to a titanite production of ~0.4 vol% in both domains and to the release of ~1.2/1.4 wt% of CO_2 in the calcite-poor/calcite-rich domains, respectively.

The prediction of thermodynamic modelling is in very good agreement with the Zr-in-titanite thermometric results, which suggest the existence of two different titanite populations, crystallized at 730-740 °C (near-peak event) and 740-765 °C (peak event), respectively (Fig. 5.29b). Moreover, the frequency distribution of the measured Zr-temperatures (i.e. peak titanite grains are more frequent than near-peak titanites) reflects the volume amounts of the two titanite generations as predicted by the thermodynamic modelling (Tab. 5.8). The lack of titanite grains preserving Zr-temperatures of ~570 °C suggests a complete re-equilibration/re-crystallization of the early generation of prograde titanite during the near-peak and/or peak events.

Although the absolute ages of the two titanite generations are partially overlapped, the peak titanite grains are, on average, younger than the near-peak titanite grains (Fig. 5.29a,c & Fig. 5.30), pointing to ages of 30-26 Ma for the near-peak event and of 25-20 Ma for the peak event, respectively. These two episodes of titanite growth are also documented by the probability density plot (Fig. 5.30 c). Moreover, because it has been demonstrated that the titanite-forming events correspond to the main CO_2-producing events (see §5.4.1.3), these geochronological data provide tight constraints on the ages of the main CO_2-producing processes which occurred in this type of CO_2-source rocks.

5.4.2.2 P-T-t constraints on Himalayan prograde metamorphism compared with previous data

Results suggest that the studied calc-silicate sample 14-53c from the L-GHS experienced a high-T evolution at T > 730 °C for at least 10 Ma (from ~30 to ~20 Ma), followed by a retrograde event at ~15 Ma. The good match between the Zr-temperatures obtained from the analysed titanite grains and the P-T conditions independently estimated for the associated metapelites (Rapa et al., 2016 and Chapter 3), further confirm the validity of

our new P-T data. It is to be noted that peak P-T conditions estimated for the associated metapelites suggest incipient partial melting conditions, i.e. most of the associated metapelites still contain abundant white mica, but show microstructural features (e.g. nanogranites included in garnet) indicative of incipient anatexis (Rapa et al., 2016, Chapter 3).

Absolute ages obtained for sample 14-53c can be validated against existing monazite chronologic data for the region (Fig. 5.39). Specifically, the prograde evolution of the L-GHS in the Langtang region has been constrained at 35-17 Ma by Kohn et al. (2004, 2005) (early prograde: 37-24 Ma; late prograde: 24-17 Ma), whereas monazite ages younger than ~17 Ma were interpreted as related to final cooling (i.e. melt crystallization). Titanite ages fit well with these data (Fig. 5.38), although Kohn et al. (2004, 2005) interpreted both the early prograde and late prograde monazite as sub-solidus phases, thus implicitly assuming that they grew at T < ~760 °C. However, the same authors (Kohn, 2014) noticed that their interpretation is in contrast with the high Zr-temperatures registered by titanites (Kohn and Corrie, 2011) and discussed the possibility that monazite petrogenesis of core compositions was misinterpreted (e.g., the compositions of monazite cores reflect dissolution-reprecipitation in the presence of melt, not prograde sub-solidus growth).

Compared to the geochronological results obtained by Kohn and Corrie (2011) on titanite from U-GHS calc-silicate rocks from the Annapurna region (some tens of km westward of our studied area), titanites are few million years younger (peak titanite: ~24 Ma *vs.* ~20 Ma). This is in agreement with the monazite data discussed by Kohn et al. (2004, 2005) and Corrie and Kohn (2011) (summarized in Kohn, 2014), which show that peak metamorphism in the L-GHS was systematically younger than in the U-GHS.

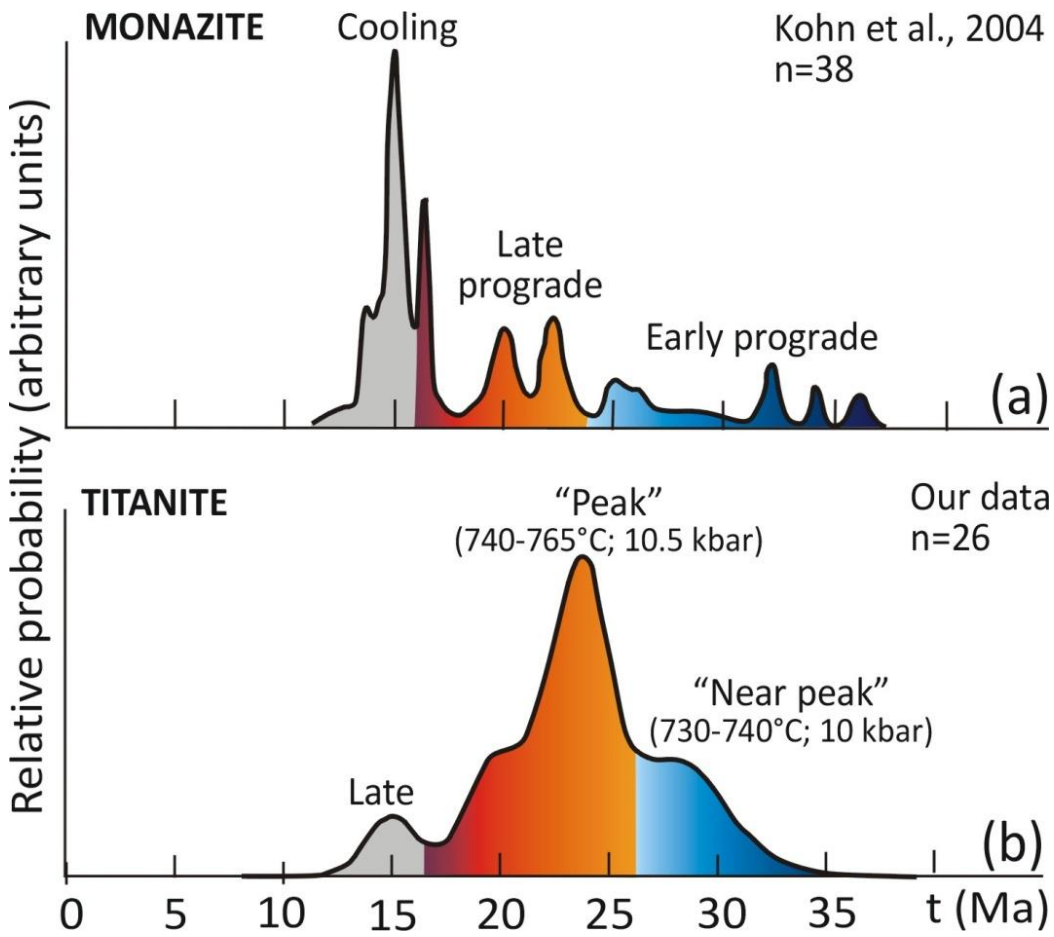

Fig. 5.38 - Comparison between monazite and titanite ages from the L-GHS unit in the Langtang-Gosainkund region of central Nepal (see Fig. 5.39 for the location of the analysed samples). **(a)** Probability distribution of monazite ages from Kohn et al. (2004, 2005). **(b)** Probability distribution of titanite ages (this study). Note the good match between the two sets of data, which reinforces the validity of our results. Color coded as in Fig. 5.29.

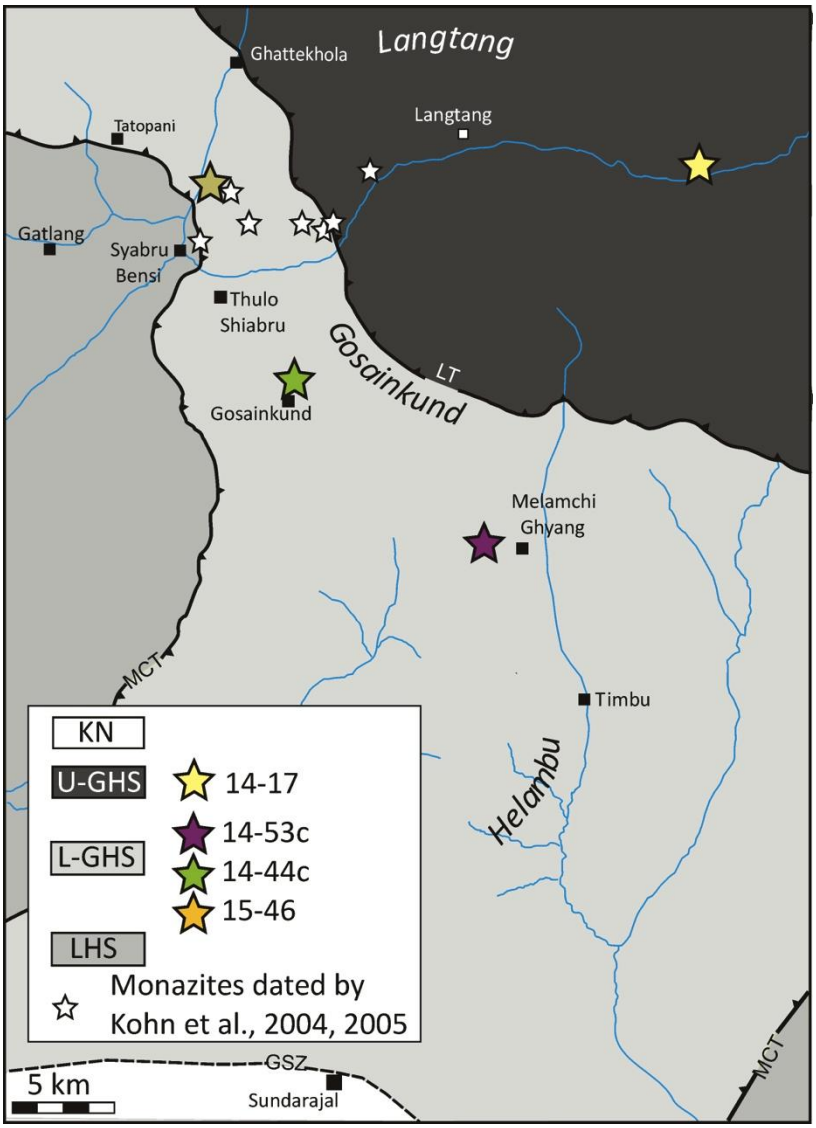

Fig. 5.39 – Location of the CO_2-source rocks studied in Chapter 5 and of monazites dated by Kohn et al., 2004.

5.4.3 Fluid inclusion analysis to reveal fluid composition and carbon speciation

In contrast to the thermodynamic approach, which provide indirect information about the fluid composition and the amount of CO_2 produced through decarbonation reactions, direct evidence can be obtained from the study of fluid inclusions (FI), which represent "fossil" fluids entrapped in specific mineral phases. In principle, FI analysis from different types of CO_2-source rocks belonging to different structural levels could provide information about fluid composition, salinity and density, as well as carbon source, mobility and speciation during the prograde and/or retrograde evolution of the samples. However, to my knowledge, a systematic study of FI in Himalayan calc-silicate rocks has

never been performed so far. Therefore, it is not possible to know if these lithologies are suitable for FI analysis (i.e. if FI are easily entrapped and preserved in calc-silicate minerals).

To test the feasibility of FI analysis on CO_2-source rocks, a preliminary study on FI has been done on a well-characterized sample from eastern Nepal: sample 07-22, Type 3F (for details refer to Groppo et al., 2017). Both microthermometric analysis and micro-Raman technique have been used, and will be quickly described in the following.

5.4.3.1 Fluid inclusions petrography

Fluid inclusions petrography has been performed at the University of Torino on bipolished thin sections (~100 µm thick). Clinopyroxene was chosen as host mineral since the P-T-X(CO_2) conditions of its growth have been constrained in detail and referred to specific decarbonation reactions by Groppo et al. (2017). Petrographic observations led to the identification of two main groups of FI: (i) primary FI, hosted in both clinopyroxene cores and rims, and (ii) pseudosecondary FI, hosted along fractures which do not cross the entire crystals. Both types of FI are not very common, and they often show decrepitation features, as commonly observed in the metamorphic environment. Secondary FI (crossing the crystals borders) have been neglected during the preliminary observations, in order to focus on the characterization of the prograde fluid.

Primary FI range from ~1 µm to ~30 µm in length; more commonly, FI are clustered, and less frequently isolated. In both cases primary FI can be: (i) multiphase (Type I - Fig. 5.40a), with different kinds of solids and L(H_2O) + V(H_2O). In this case the vapour phase is visible, while the liquid observation is hindered by the presence of the solids; (ii) biphase (Type II - Fig. 5.40b), with L(H_2O) + V(H_2O), typically in a proportion of 70:30.

Pseudosecondary FI usually are smaller (1-10 µm in length) and show the same characteristics of Type I FI, being multiphase inclusions with L(H_2O) + V(H_2O) + solids (Fig. 5.40c,d).

Beside clinopyroxene, FI have also been observed in other mineral phases such as titanite (Fig. 5.38d); pseudosecondary FI are more common compared to primary FI, and seem to have the same characteristics of Type I FI observed in clinopyroxene.

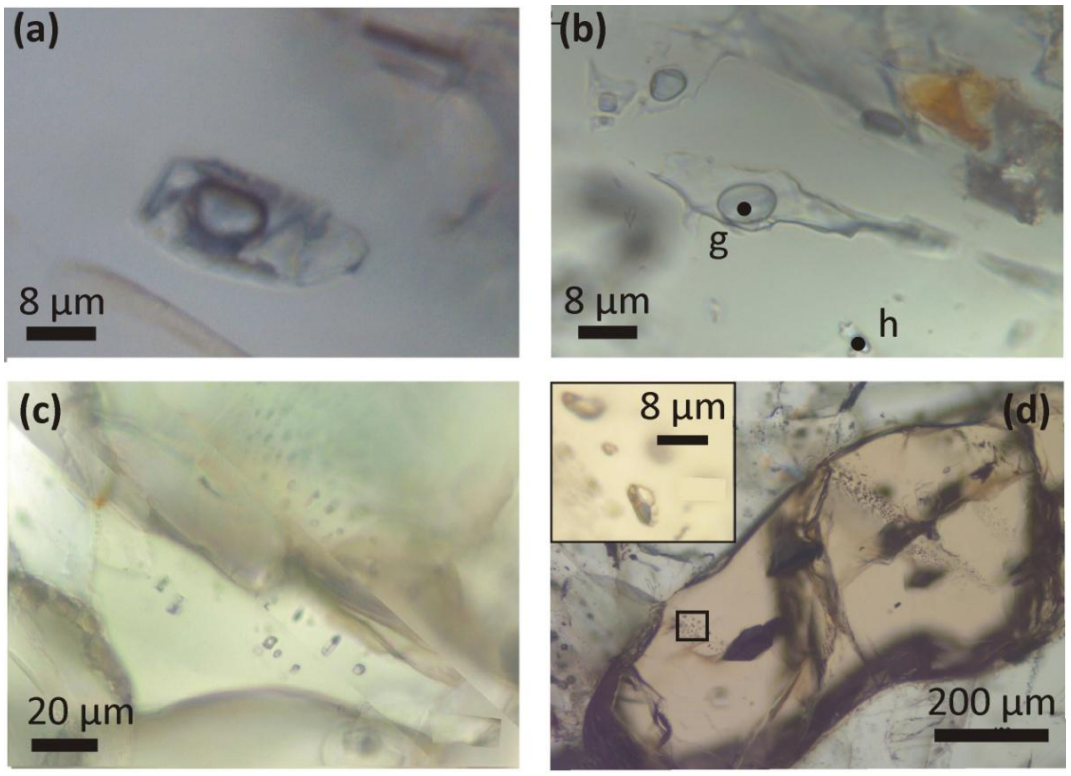

Fig. 5.40 – Photomicrographs of FI. (a) Isolated primary Type I FI in Cpx core. It is a multiphase inclusion, with different kinds of solids + V(H_2O) + undetectable L(H_2O). Raman analysis are presented in Fig. 5.41 and Fig. 5.42. **(b)** Cluster of primary Type II FI hosted in Cpx core. FI are biphase, with L(H_2O) + V(H_2O) and show decrepitation features. Raman analysis (spectra g and h reported in Fig. 40) in the bubble reveal the presence of N_2 and CH_4. **(c)** Pseudosecondary FI trail in Cpx rim. Raman analysis reveal the same phases of primary Type I FI. **(d)** Pseudosecondary FI trail in Ttn. Further analysis on these FI have not been performed yet, but petrographic observations suggest that these FI are similar to Type I FI (see inset).

5.4.3.2 Microthermometry

Microthermometry of primary fluid inclusions assemblages hosted within clinopyroxene was performed using a Linkam THMSG600 heating-freezing stage coupled with an Olympus polarizing microscope (100X objective) at the University of Torino, Italy. In this preliminary study, only 8 Type II inclusions have been measured; consequently, the results must be considered as purely indicative and not statistically relevant. The accuracy, estimated using synthetic fluid inclusion standards, is about 0.4 °C at the triple point of CO_2. Although Type II FI show phase transitions during microthermometry, these are very difficult to be observed due to the low salinity of the system. During cooling down to -140 °C, the freezing temperature (Tf) was measured. During the subsequent heating, final melting temperature of ice (Tm_{ice}) and homogenisation temperature in the liquid (Th_L) were measured.

In Type II FI, Tf occurs at ~ -30 °C, Tm_{ice} varies from -2.3 °C to -1.2 °C, and the Th_L varies from 298.1 °C to 309.1 °C. The Tf values are typical for a H_2O-NaCl system, and the high Tm_{ice} indicates a very low salinity. The bulk composition of the Type I FI were calculated using the software package FLUIDS, Program 1: BULK, version 01/03 (Bakker, 2003). For the aqueous solution, the purely empirical thermodynamic model of Bodnar (1993) (for NaCl) was chosen. Giving Tm_{ice} =-2.3 °C, a salinity of 3.87% was obtained, with a density of 1.03 g/cc. Isochores for Type II FI were determined using the software package FLUIDS, Program 2: ISOC, version 01/03 was used (Bakker, 2003). The equation of state of Bodnar and Vityk (1994) and Knight and Bodnar (1989) (for H_2O-NaCl mixtures) was chosen. Both the lower (298.1 °C) and the higher (309.1 °C) Th_L were used to calculate the isochores. Assuming a trapping temperature of 600-700 °C (Groppo et al., 2017), the calculated highest trapping pressure preserved by the FI is 3.2-4.2 kbar (Th_L as minimum value), while the lowest is 3.0-3.9 kbar (Th_L as maximum value). These results are quite different from the inferred peak P=9 kbar estimated by Groppo et al. (2017), thus suggesting that peak pressures are not preserved, because all the analyzed inclusions experienced post-trapping decrepitation.

Similarly to what done with Type II FI, also Type I FI have been cooled down to -140 °C, but phase transitions have not been observed. This could be attributed to the presence of many solids combined with the optical properties of the host mineral (high relief and colour), which hinder the observation of phase transition within FI.

5.4.3.3 Micro-Raman spectroscopy

Micro-Raman spectra and maps were acquired using the integrated micro/macro- Raman LABRAM HRVIS (Horiba Jobin Yvon Instruments) of the Interdepartmental Center "G. Scansetti" (Department of Earth Sciences, University of Torino, Italy), equipped with a computer-controlled, automated X–Y mapping stage. Operating conditions for single analysis were: laser: green (λ: 532 nm); grating: 600 grooves/mm; hole: 200 µm; slit: 300 µm; objective: 100X (laser spot of 1 µm). The spectra of clinopyroxene were collected by 2 accumulations of 5 s, those of Mg-calcite and amphibole by 2 accumulations of 10 s, those of N_2, CH_4 and H_2O by 2-3 accumulations of 30-60 s. The 27 × 12 µm map (with steps of 3 µm and a laser spot of 1 × 1 µm) was acquired by one accumulation of 3 s, each step.

The Raman spectral image of a primary Type I fluid inclusion (Fig. 39) allows to visualize the distribution of the phases within the inclusion and to qualitatively estimate their proportions. The host clinopyroxene shows typical peaks at 1013, 665, 387, 321, 355 and 558 cm^{-1} (Fig. 5.42a). Solid phases are Mg-calcite (peaks at 1088, 283 and 715 cm^{-1}; Fig. 5.41a and Fig. 5.40b), amphibole (peaks at 222 and OH stretching vibration at 3660, 3644, 3673 and 3625 cm^{-1}; Fig. 5.41b and Fig. 5.42c,d) and a non-Raman active cubic crystal (asterisk in Fig. 5.41f), probably a salt. In the bubble are present N_2 (peak at 2326 cm^{-1};

Fig. 5.41c and Fig. 5.42e) and CH_4 (peak at 2914 cm^{-1}; Fig. 5.41d and Fig. 5.42e); interstitial liquid H_2O is also present (broad band between 3100 and 3700 cm^{-1}; Fig. 5.41e and Fig. 5.42f). Raman spectra of primary Type II fluid inclusions reveal the presence of N_2 and CH_4 in the vapour bubble (Fig. 5.42g,h).

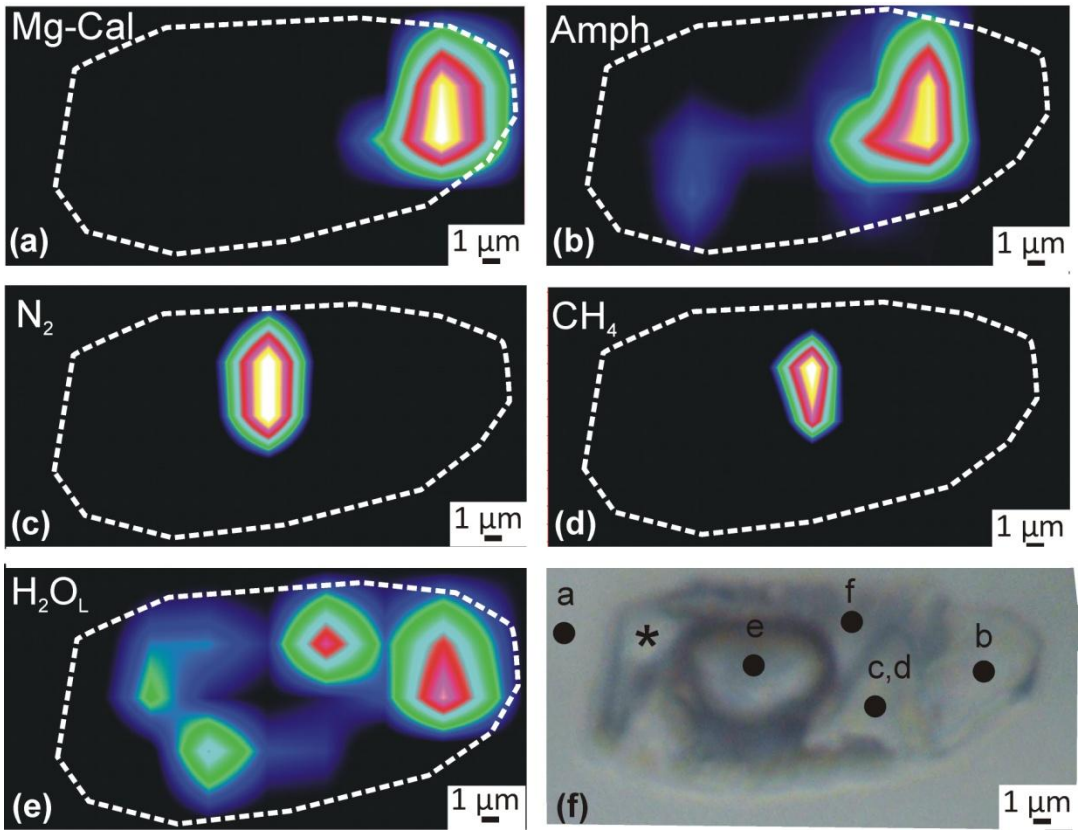

Fig. 5.41 - Raman spectral images of daughter minerals distribution and gaseous phases in a Type I fluid inclusion. (a-e) Spectral images of Mg-Cal, Amph, N_2, CH_4 and H_2O_L distribution in the fluid inclusion. The colour intensity of the mineral phases (from black to white) reflects the increase in the intensity of the Raman band. **(f)** Optical microphotograph of the mapped fluid inclusion hosted within clinopyroxene. The Raman spectra of each analysis (a-f) are reported in Fig. 5.42. The asterisk (*) indicates a non-Raman active phase.

Considering the information achieved with the different techniques, the FI study have led to the following preliminary, but interesting considerations: (i) type I FI are remnants of a C-O-H-N_2 brine; (ii) in type I FI, salt and Mg-calcite probably are daughter minerals, whereas amphibole is a step-daughter mineral derived from a chemical interaction between the aqueous part of the fluid and the host clinopyroxene; (iii) Type II FI are remnants of a C-O-H-N_2 low-salinity low-density aqueous fluid; (iv) peak pressures are not recorded/preserved by Type II FI because they experienced an important event of re-equilibration/decrepitation at ~3-4 kbar; (v) because Type I and Type II FI have similar distribution but relatively different composition, Type II could probably represent

decrepitated Type I FI; (vi) although FI are not very common in the studied Type 3F calc-silicate rock, the combined use of micro-thermometry and micro-Raman spectroscopy could represent a promising approach to obtain direct information on the nature of the fluids.

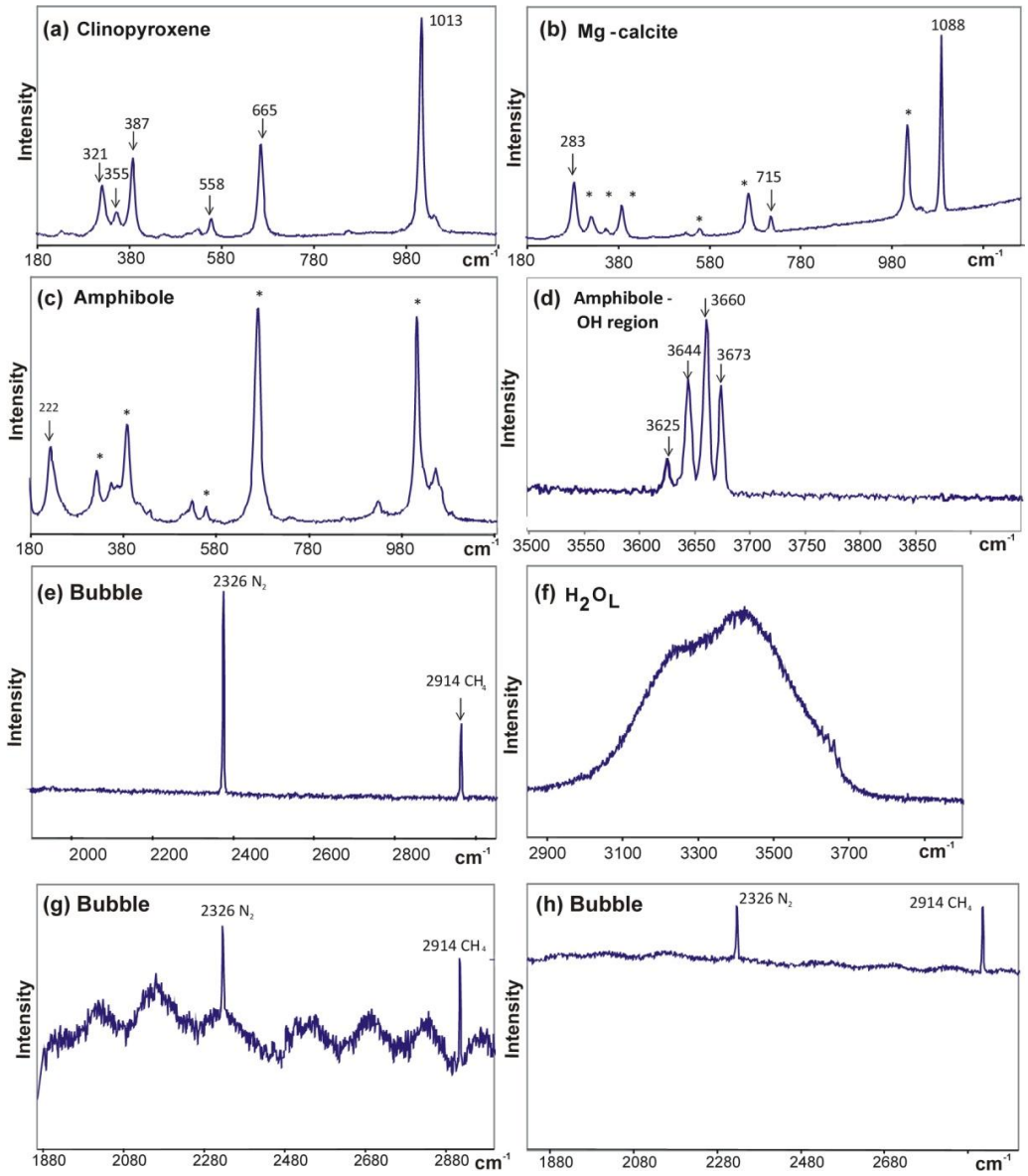

Fig. 5.42 – (a-f) Raman spectra and relative wavenumbers for minerals, gaseous phases and liquid H_2O in the Type I FI of Fig. 5.41. **(g,h)** Raman spectra and relative wavenumbers for gaseous phases in the Type II FI of Fig. 5.41.

Chapter 6

Metamorphic CO_2-production: discussion

6.1 Estimating the CO_2 metamorphic flux from the Himalaya

In order to extrapolate the amount of produced CO_2 estimated for the studied CO_2-source rocks to the orogen scale, an estimate of the total volume of all types of CO_2-source rocks in the whole Himalayan belt is needed. This is not an easy task, because in most of Himalaya's geological maps CO_2-source rocks are not differentiated from the host metapelites; moreover, many CO_2-source rocks are not easy to be recognised in the field (see §4.3.1). Type 3F CO_2-source rocks (derived from a marly protolith) are by far the easiest to be recognised in the field, therefore they have been used as starting point for our calculations. A preliminary estimate of their volume was proposed by Groppo et al. (2017) based on original field data from eastern Nepal Himalaya. Here those preliminary estimates are refined by considering additional field data from central-eastern Nepal and literature data from central-western Nepal (Fig. 6.2). According to these data, Type 3F CO_2-source rocks are more abundant in the central and western Nepal Himalaya, where they represent up to ~40 vol% of the whole GHS sequence, than in the eastern Nepal Himalaya, where they represent less than 10 vol% of the whole GHS (~5 vol% on average) (Fig. 6.2). We therefore consider a conservative (minimum) value of 10 vol% as representative of the total volume of this type of CO_2-source rocks with respect to the whole GHS. The entire volume of GHS rocks that experienced Himalayan metamorphism is approximately ~5 x 10^6 km^3 (considering a strike length of 2500 km, an average thickness of 10 km and an average width of 200 km; e.g. Long et al., 2011); consequently, the total volume of the CO_2-source rocks was ~5 x 10^5 km^3.

Considering the results obtained for sample 14-53c as concerning the CO_2 (minimum) productivity of such lithologies, this estimate would result in a total CO_2 production of ~4 x 10^6 Mt and ~2 x 10^7 Mt of CO_2 during the near peak and peak events (see §5.4.1.3), respectively. Although we have demonstrated that CO_2 production occurred in pulses for specific volumes of calc-silicate rocks, extrapolation of the CO_2 flux at the orogen scale should integrate these amounts over the time needed for the entire GHS to reach the P-T conditions required for CO_2 production, which can be approximated to ~20 Ma (e.g. Kohn, 2014). This would result in metamorphic CO_2 flux for the near-peak and peak events of 0.2 and 1 Mt/yr, respectively. The lack of field evidence for pervasive carbonation and/or massive graphite precipitation in the lithologies structurally overlying the main calc-silicate layers in the GHS (according to our own observations along transects 5-14 in Fig. 6.2), suggests that most of the CO_2 produced through the investigated metamorphic reactions reached Earth's surface without interacting with the host rocks.

This calculated metamorphic CO_2 flux is a minimum estimate. Sensitivity analysis applied to our estimates (Table 6.1) shows that:

(1) CO_2 productivity – Sample 14-53c experienced at least two additional CO_2-producing events: an early prograde one at ~430 °C, 4 kbar (i.e. at I35 through reaction U35), which released ~0.8 wt% CO_2, and a prograde one at ~575 °C, 7 kbar (i.e. at I35 through reaction U35), which released ~0.3 wt% CO_2 (see §Table 5.8). Summed to the amounts produced at near peak and peak events, a total production of ~3 wt% CO_2 would result (Table 5.8). Furthermore, compared to other samples of Type 3F CO_2-source rocks, sample 14-53c is derived from a marly protolith relatively poor in calcite (Fig. 6.1). It has been demonstrated that the CO_2 productivity of similar Type 3F CO_2-source rocks derived from marls with a slightly different bulk composition (e.g. sample 14-17 of this study; sample 07-22 studied by Groppo et al., 2017; Fig. 6.1) is higher, up to ~8 wt% CO_2 (Table 6.1). On average, a maximum CO_2 productivity of ~4 wt% CO_2 could be therefore considered for this calc-silicate type.

(2) GHS total volume - Other authors proposed larger estimates for the total volume of GHS rocks (e.g. Kerrick and Caldeira, 1999 considered a value of 9×10^5 km^3).

(3) Volume of Type 3F CO_2-source rocks - The estimate of the volume of Type 3F CO_2-source rocks is a minimum estimate; a value of 25 vol% could be realistically considered as a maximum estimate.

(4) Duration of the CO_2-producing process in the whole GHS - The time needed for the entire GHS to reach the P-T conditions required for CO_2 production is poorly constrained. In the sensitivity analysis, it have been considered durations of 20 and 30 Ma as minimum and maximum values, respectively.

(5) Contribution of other CO_2-source rocks - Beside Type 3F CO_2-source rocks, which is the most abundant in the Himalaya and derived from a marly protolith (Fig. 6.1), other CO_2-source rocks occur in the GHS (see §4.3.1.2 and Rolfo et al., 2017 for a review). The contribution of Types 1 (1B, 1C and 1D) and 2 lithologies (i.e. likely derived from original bentonitic layers: see §4.4.1.1) is probably negligible, because it has been demonstrated that: (i) their volume is minimal, and (ii) most of the CO_2 produced during prograde metamorphism was likely consumed during exhumation, either through retrograde carbonation reactions (see sample 14-44c; §5.4.1.1) or through graphite precipitation (e.g. Groppo et al., 2013b). Rather, the contribution of the other Type 3 (3B, 3C, 3D, 3E) lithologies could be potentially significative. So far, there are some data for Type 3C, whereas the CO_2-productivity of the other Type 3 lithologies is still unknown. A total CO_2-production of < 3 wt% (i.e. lower than that of Type 3F lithologies) has been estimated for Type 3C lithologies (see sample 15-46; §5.4.1.2); similar CO_2 amounts could be predicted for the other Types 3 CO_2-source rocks. The abundance of Types 3B, 3C, 3D and 3E lithologies within the GHS is difficult to be constrained, because these rocks are not easy to be recognised in the field,

resembling common metapelites (see §4.3.1.2 and Rolfo et al., 2017). However, according to our experience, their vol% cannot exceed that of Type 3F CO_2-source rocks. Overall, the contribution of the other Types 3 lithologies to the total orogenic CO_2 flux should be therefore minor than the CO_2 flux estimated for Type 3F CO_2-source rocks.

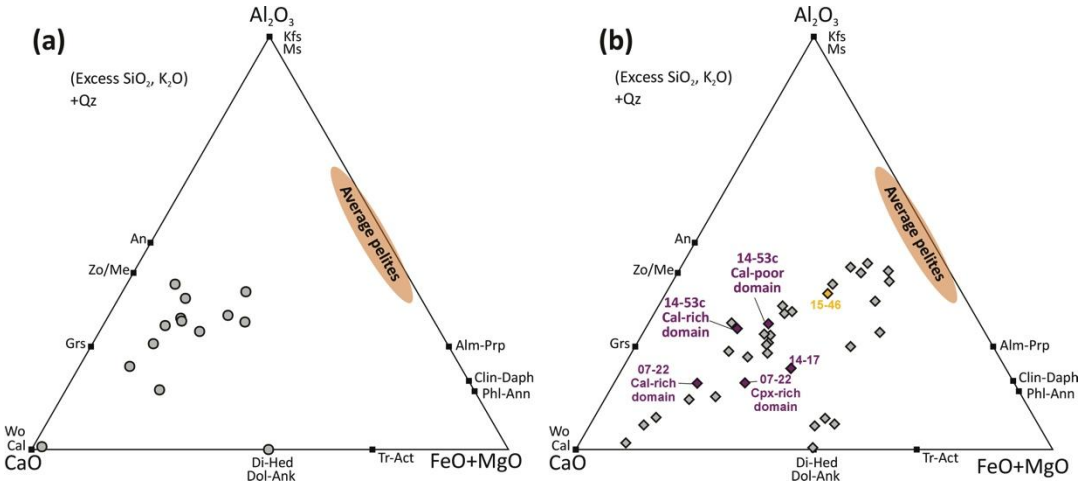

Fig. 6.1 – (a) Bulk compositions of Types 1 and 2 CO_2-source rocks collected in central-eastern Nepal (along cross-sections 5 to 14 reported in **Fig. 6.2**) projected onto the ACF (Al_2O_3–CaO–MgO+FeO) diagram. **(b)** Bulk compositions of Type 3 CO_2-source rocks from both the L-GHS and U-GHS of central and eastern Nepal projected onto the ACF diagram. Bulk compositions of the studied samples 14-53c (Cal-rich and Cal-poor domains), 14-17 and those of sample 07-22 studied by Groppo et al. (2017) are reported in purple (Type 3F). Bulk composition of sample 15-46 is reported in yellow (Type 3C). Average pelite composition is calculated from Rapa et al. (2016).

Considering the uncertainties associated with the input values (1) to (4), the metamorphic CO_2 flux resulting from Type 3F CO_2-source rocks ranges between a minimum value of 1.4 Mt/yr and a maximum value of 9.7 Mt/yr (Table 6.1). Adding the contribution of the other Types 3 CO_2-source rocks (input value 5), the resulting total metamorphic CO_2 flux from the GHS ranges between 1.4 and 19.4 Mt/yr. Further studies on the CO_2-source rocks derived from carbonate-rich pelitic protoliths (Types 3B, 3D, 3E CO_2-source rocks) would provide more precise constraints on the CO_2 productivity of such lithologies, and consequently on the total orogenic CO_2 flux.

Table 6.1 - Sensitivity analysis for the metamorphic CO_2 flux from the GHS Sequence of Himalaya

Variables	Values used in this work	Max duration of CO_2-producing process	Max V GHS	Max Vol% calc-silicate rocks	Max CO_2 productivity	Max CO_2 flux
V GHS (km^3)	5.0×10^6	5.0×10^6	9.0×10^6	5.0×10^6	5.0×10^6	9.0×10^6
Vol% calc-silicate rocks (%)	10	10	10	20	10	20
CO_2 productivity (Wt% CO_2)	3	3	3	3	4	4
Duration of the CO_2-producing process (Ma)	20	30	20	20	20	20
CO_2 flux* (Mt/yr)	**2.0**	**1.4**	**3.6**	**4.1**	**2.7**	**9.7**
Total CO_2 flux[§] (Mt/yr)	**< 4**	**< 3**	**< 7**	**< 8**	**< 5**	**< 19**

*CO_2 flux from the studied calc-silicate rock type (i.e. derived from marly protoliths, Type 3F); [§]Total CO_2 flux, including the contribution of other CO_2 source rocks (i.e. derived from Cal-rich pelitic protoliths; Types 3B, 3C, 3D, 3E). Grey cells correspond to the variable parameters.

6.2 Implications for the deep carbon cycle

Compared to the literature data, the estimated CO_2 flux (1.4 Mt/yr < CO_2 flux < 19.4 Mt/yr) is slightly lower than the past CO_2 flux estimated by Kerrick and Caldeira (1999) (9 Mt/yr < CO_2 flux < 24 Mt/yr) using the mass loss method. The discrepancy between the two values is probably due to the Kerrick and Caldeira (1999) slight over-estimation of the amount of CO_2 released from the CO_2-source rocks. Specifically, they assumed that: (i) the whole GHS contributed to the production of CO_2 (i.e. CO_2-source rocks = 100 vol%), and that (ii) the GHS protolith was a pelite with 5 wt% carbonate (i.e. ~2 wt% CO_2) and all carbonate was consumed during metamorphism.

Compared to the present-day CO_2 flux estimated on the basis of CO_2 degassed from spring waters located along the MCT, the estimated flux of CO_2 (1.4 Mt/yr < CO_2 flux < 19.4 Mt/yr) is lower than the estimate of Becker et al. (2008) (40 Mt/yr), but similar to that of Evans et al. (2008) (8.8 Mt/yr). Becker et al. (2008) based their estimates on data from the Marsyandi basin of central Nepal, which cover about ~4800 km^2, whereas the data used by Evans et al. (2008) refer to the larger Narayani basin, covering ~40000 km^2 and comprising the Marsyandi basin itself. According to the Evans et al. (2008) data, the contribution of the Marsyandi spring system to the total flux of CO_2 is nearly one order of magnitude higher than the contributions of the other spring systems of the Narayani basin. It therefore appears that the Becker et al. (2008) extrapolation to the whole orogen is biased by the exceptional high CO_2 flux from the Marsyandi basin, whereas the estimate by Evans et al. (2008) probably approximates better the contribution of the majority of the spring systems of the Himalaya. The similarity between the estimated flux of CO_2 and that actually measured from spring waters thus suggests that CO_2-producing processes similar to those described in the present work still occur along the active Himalayan orogen (e.g. Girault et al., 2014a,b).

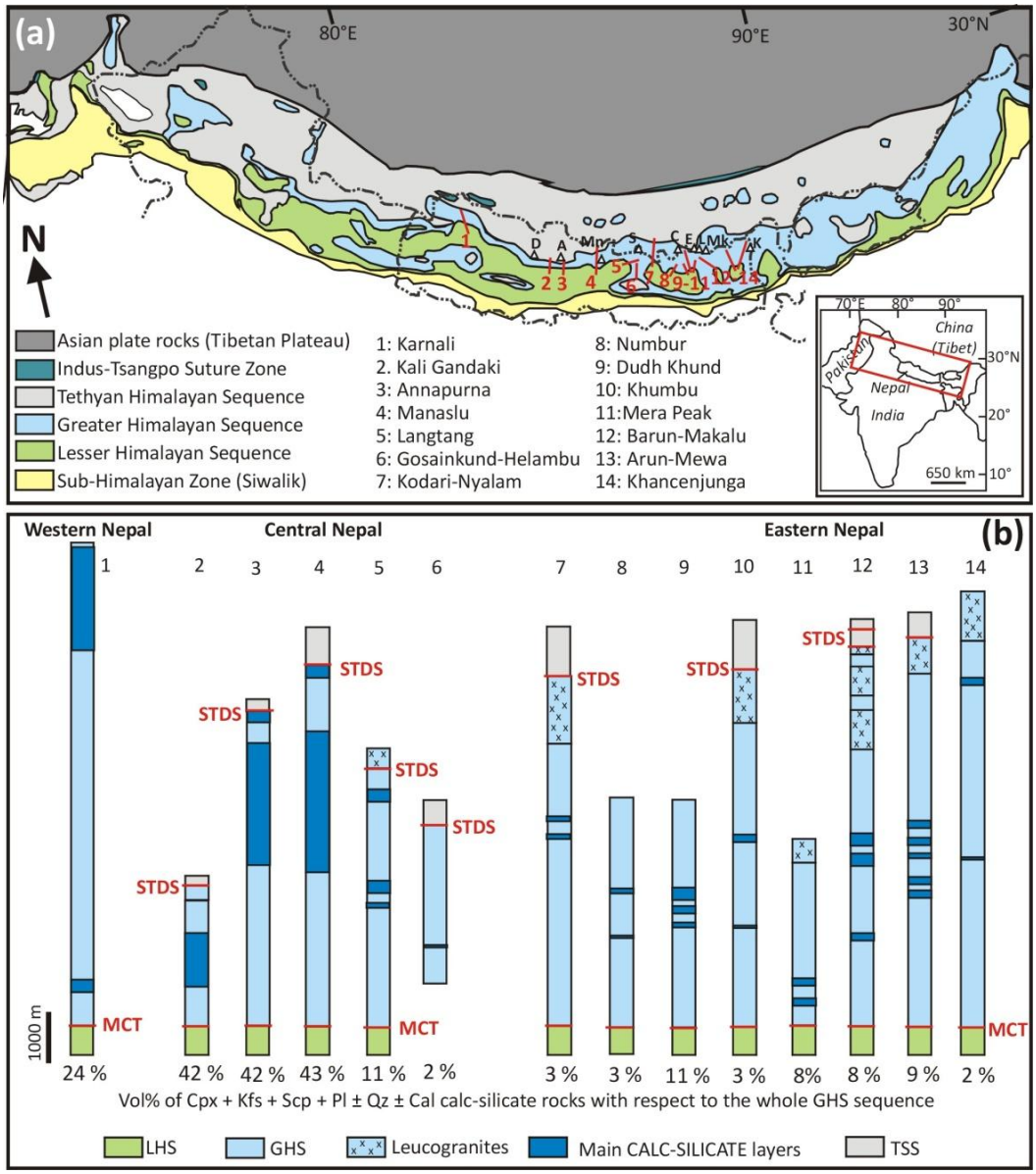

Fig. 6.2 – (a) Simplified tectonic map of the Himalayan-Tibetan orogen, with location of the cross-sections reported in (b). Modified from He et al. (2015) and Wang et al. (2016). **(b)** Fourteen schematic profiles across the Himalayan metamorphic core in Nepal, representing the main tectono-metamorphic units, major structures, and abundance of Type 3F CO_2-source rocks (vol%, below each profile). The profiles are constructed from detailed mapping along each sections by our group (cross-sections 5 to 14; see also Goscombe et al., 2006 for cross-sections 10, 12, 13, 14, and Leloup et al., 2015 for cross-section 7) and by other authors: 1: Yakymchuk & Godin, 2012; 2: Iaccarino et al., 2015; 3: Martin et al., 2010; Corrie and Kohn, 2011; 4: Colchen et al., 1980.

Table 6.2 - Earth CO_2 global emission estimates (Mt/yr)

	Volcanic					Non Volcanic	Estimated global CO_2 fluxes
	Volcanic plume passive degassing	Diffuse emissions from historically active volcanoes	Emissions from tectonic, hydrotermal or inactive volcanic areas	Volcanic lakes	MOR		
Mörner and Etiope, 2002	250	50				300	**600**
Burton et al., 2013	271	117	>66	94 [a]	97 [b]	300 [c]	**937**
Foley and Fischer, 2017	158	44	70*		154		**425**

[a] Perez et al., 2011; [b] Marty and Tolstikhin (1998); [c] Mörner and Etiope, 2002 *continental rifting

Recent global estimates for Earth CO_2 global geologic fluxes are given by Mörner and Etiope (2002), Burton et al. (2013) and Foley and Fischer (2017) (Table 6.2). Most of the data refer to volcanic emissions, including both active and inactive sources (and not considering the effective origin of CO_2 that is degassed). Burton et al. (2013) extensively reviewed volcanic CO_2 emissions data (Table 6.2) and extrapolated those measurements to the whole Earth scale to quantify the global volcanic CO_2 flux, which is reported as 637 Mt/yr. The previous comprehensive study made by Mörner and Etiope (2002) attested the global volcanic input at 300 Mt/yr; the discrepancy is mainly due to an underestimation of the role played by diffuse degassing and the exclusion of volcanic lakes and MOR in the computation made by Mörner and Etiope (2002). Foley and Fischer (2017) reported lower values for plume and diffuse degassing degassing (Table 6.2), but significantly investigated the role exerted by continental rifting and continental lithosphere in the deep carbon cycle and storage, including the mechanisms which led to the accumulation of carbonate-rich magmatic activity below rifts.

Non-volcanic CO_2 emissions include all the geological emissions occurring in the absence of present-day volcanism (Mörner and Etiope, 2002), predominantly through faults and fractures in the crust and geothermal systems. The only comprehensive review about the non-volcanic contribution to the global CO_2 emissions is from Mörner and Etiope (2002), who attested at 300 Mt/yr the non-volcanic CO_2 flux in the atmosphere, suggesting that volcanic and non-volcanic inputs are comparable. Summing up the volcanic and non-volcanic inputs, a global value of 937 Mt/yr of CO_2 has been proposed by Burton et al. (2013); this value is three times higher than the 367 Mt/yr reported in the International Panel of Climate Change 2013 (IPCC2013), used for the prediction of future climate scenarios.

In a recent paper, Flesia and Frezzotti (2015) analyzed results published in literature since the '80s, and showed inconsistencies between estimates, global extrapolations and measurements, thus concluding that the Earth's CO_2 natural emission budget, independently from its absolute value, is virtually unknown, as well as the geological processes controlling it. In this framework, the results obtained from this PhD project represent a valuable contribution toward a better understanding of the CO_2-producing processes in collisional settings. To my knowledge, this is the first time that CO_2-

producing metamorphic processes occurring during an orogenic event have been fully characterized in term of P-T conditions, time, duration and amounts of CO_2 produced. Although the volumes of the CO_2-source rocks involved in such processes could be potentially better constrained in the future, it is suggested that these metamorphic CO_2 fluxes should be considered in any future attempts of estimating the global budget of non-volcanic carbon fluxes from the lithosphere.

References

Ader, T., Avouac, J.-P., Liu-Zeng, J., Lyon-Caen, H., Bollinger, L., Galetzka, J., Genrich, J., Thomas, M., Chanard, K., Sapkota, S.N., Rajaure, S., Shrestha, P., Ding, L. & Flouzat, M., 2012. Convergence rate across the Nepal Himalaya and interseismic coupling in the Main Himlayan Thrust: implications for seismic hazard. Journal of Geophysical Research, 117, B04403.

Ague, J.J., 2000. Release of CO_2 from carbonate rocks during regional metamorphism of lithologically heterogeneous crust. *Geology*, **28**, 1123-1126.

Allégre, C.J., Courtillot, V., Tapponnier, P., Hirn, A., Mattauer, M., Coulon, C., Jaeger, J.J., Achache, J., Scharer, U., Marcoux, J., Burg, J.P., Girardeau, J., Armijo, R., Gariepy, C., Gopel, C., Li, T.D., Xiao, X.C., Chang, C.F., Li, G.Q., Lin, B.Y., Teng, J.W., Wang, N.W., Chen, G.M., Han, T.L., Wang, X.B., Den, W.M., Sheng, H.B., Cao, Y.G., Zhou, J., Qiu, H.R., Bao, P.S., Wang, S.C., Wang, B.X., Zhou, Y.X. & Ronghua, X., 1984. Structure and evolution of the Himalaya–Tibet orogenic belt. *Nature*, **307**, 17–22.

Ambrose, T.K., Larson, K.P., Guilmette, C., Cottle, J.M., Buckingham, H. & Rai, S., 2015. Lateral extrusion, underplating, and out-of-sequence thrusting within the Himalayan metamorphic core, Kanchenjunga, Nepal. *Lithosphere*, **7,** 441–464.

Ao, A. & Bhowmik, S.K., 2014. Cold subduction of the Neotethys: the metamorphic record from finely banded lawsonite and epidote blueschists and associated metabasalts of the Nagaland ophiolite complex, India. *Journal of Metamorphic Geology*, **32**, 829–860.

Arita, K., 1983. Origin of the inverted metamorphism of the Lower Himalayas Central Nepal. *Tectonophysics***, 95,** 43–60.

Arita, K., Ohta, Y., Akiba, C., & Maruo, Y., 1973. Kathmandu Region. In: Hashimoto, S., Ohta, Y. & Akiba, C. (eds.), Geology of the Nepal Himalayas. Himalayan Committee of Hokkaido University, Japan, 99–145.

Arita, K., Dallmeyer, R.D. & Takasu, A., 1997. Tectonothermal evolution of the Lesser Himalaya, Nepal: constraints from $^{40}Ar/^{39}Ar$ ages from the Kathmandu Nappe. *The Island Arc*, **6**, 372–385.

Ashley, K.T. & Law, R.D., 2015. Modeling prograde TiO_2 activity and its significance for Ti-in-quartz thermobarometry of pelitic metamorphic rocks. *Contribution of Mineralogy and Petrology*, **169**, 23.

Auzanneau, E., Schmidt, M.W., Vielzeuf, D. & Connolly, J.A.D., 2010. Titanium in phengite: a geobarometer for high temperature eclogites. *Contributions to Mineralogy and Petrology*, **159,** 1–24.

Bakker, R.J., 2003. Package FLUIDS 1. Computer programs for analysis of fluid inclusion

data and for modelling bulk fluid properties. *Chemical Geology*, **194**, 3–23.

Bathia, M.R. & Crook, K.A.W., 1986. Trace element characteristics of greywackes and tectonic setting discrimination of sedimentary basins. *Contributions to Mineralogy and Petrology*, **92**, 181-193.

Beaumont, C., Jamieson, R.A., Nguyen, M.H. & Lee, B., 2001. Himalayan tectonics explained by extrusion of a low viscosity crustal channel coupled to focused surface denudation. *Nature*, **414,** 738–742.

Beaumont, C., Jamieson, R.A., Nguyen, M.H. & Medvedev, S., 2004. Crustal channel flows: 1. Numerical models with applications to the tectonics of the Himalayan-Tibetan orogeny. *Journal of Geophysical Research*, **109,** B06406.

Beaumont, C., Jamieson, R. & Nguyen, M., 2010. Models of large, hot orogens containing a collage of reworked and accreted terranes. *Canadian Journal of Earth Sciences*, **47**, 485-515.

Becker, J.A., Bickle, M.J., Galy, A. & Holland, T.J.B., 2008. Himalayan metamorphic CO_2 fluxes: Quantitative constraints from hydrothermal springs. *Earth and Planetary Science Letters*, **265**, 616–629.

Ben Othman, D., White, W.M. & Patchett, J., 1989. The geochemistry of marine sediments, island arc magma genesis and crust-mantle recycling. *Earth and Planetary Science Letters*, **94**, 1-21.

Berner, R.A., 1999. A new look at the long-term carbon cycle. *GSA Today,* **9**, 1–6.

Bhattarai, D.R., 1980. Some geothermal springs of Nepal. *Tectonophysics*, **62**, 7–11.

Bhowmik, S. & Ao, A., 2016. Subduction initiation in the Neo-Tethys: constraints from counterclockwise P–T paths in amphibolite rocks of the Nagaland Ophiolite Complex, India. *Journal of Metamorphic Geology*, **34**, 17-44.

Bickle, M.J., 1996. Metamorphic decarbonation, silicate weathering and the long-term carbon cycle. *Terra Nova,* **8**, 270–276.

Bilham, R., Larson, K. & Freymuller, J., 1997. Indo-Asian convergence rates in the Nepal Himalaya. *Nature*, **386**, 61 – 64.

Bodnar, R.J., 1993. Revised equation and table for determining the freezing point depression of H_2O-NaCl solutions. Geochimica et Cosmochimica Acta, 57, 683-684.

Bodnar, R.J. & Vityk, M.O., 1994. Interpretation of microthermometric data for H_2O-NaCl fluid inclusions. In: De Vivo, B. & Frezzotti, M.L. (eds.), Fluid inclusions in minerals, Methods and Applications. Virginia Tech, 117-130.

Bogacz, W., & Kotarba, M., 1981. Structural mesoscopic studies in the Kali Gandaki thermal springs area (Nepal Himalayas). *Bulletin of the Polish Academy of Sciences. Earth Sciences*, **29**, 293–301.

Bollinger, L., Henry, P. & Avouac, J.P., 2006. Mountain building in the Nepal Himalaya: thermal and kinematic model. *Earth and Planetary Science Letters*, **244**, 58–71.

Bordet, P., 1961. Recherches geologiques dans l'Himalaya du Nepal, region du Makalu. Paris: Centre National de la Recherche Scientifique.

Burbank, D. W., Beck, R. A. & Mulder, T., 1997. The Himalayan foreland basin. In: Yin, A. & Harrison, M., (eds.), The tectonic evolution of Asia. Cambridge University Press, 149–188.

Burchfield, B.C. & Royden, L.H., 1985. North-south extension within the convergent Himalayan region. *Geology*, **13,** 679–682.

Burchfiel, B. C., Chen, Z., Hodges, K. V., Liu, Y., Royden, L. H., Deng, C. & Xu, J., 1992. The South Tibetan Detachment System, Himalayan orogen: extension contemporaneous with and parallel to shortening in a collisional mountain belt. Geological Society of America Special Paper, **269**, 41 pp.

Burg, J.P. & Chen, G.M., 1984. Tectonics and structural zonation of southern Tibet, China. *Nature*, **311**, 219–223.

Burianek, D. & Pertoldova, J., 2009, Garnet-forming reactions in calc-silicate rocks from the Policka Unit, Svratka Unit and SE part of the Moldanubian Zone. *Journal of Geosciences*, **5**4, 245-268.

Burton, M.R., Sawyer, G.M. & Granieri, D., 2013. Deep Carbon Emissions from Volcanoes. *Reviews in mineralogy & Geochemistry*, **75**, 323-354.

Carapezza, M.L., Barberi, F., Ranaldi, M., Ricci, T., Tarchini, L., Barrancos, J., Fischer, C., Perez, N., Weber, K., Di Piazza, A. & Gattuso, A., 2011. Diffuse CO_2 soil degassing and CO_2 and H_2S concentrations in air and related hazards at Vulcano Island (Aeolian arc, Italy). *Journal of Volcanology and Geothermermal Research*, **207**, 130–144.

Carosi, R., Lombardo, B., Molli, G., Musumeci, G. & Pertusati, P.C., 1998. The South Tibetan Detachment System in the Rongbuk valley, Everest region. Deformation features and geological implications. *Journal of Asian Earth Sciences,* **16,** 299–311.

Carosi, R., Montomoli, C., Rubatto, D. & Visonà, D., 2010. Late oligocene high-temperature shear zones in the core of the Higher Himalayan Crystallines (Lower Dolpo, western Nepal). *Tectonics*, **29,** TC4029.

Carosi, R., Montomoli, C., Langone, A., Turina, A., Cesare, B., Iaccarino, S., Fascioli, L., Visonà, D., Ronchi, A. & Rai, S.M., 2015. Eocene partial melting recorded in peritectic

garnets from kyanite-gneiss, Greater Himalayan Sequence, central Nepal. In: Mukherjee, S., Carosi, R., van der Beek, P.A., Mukherjee, B.K. & Robinson, D.M. (eds), Tectonics of the Himalaya. *Geological Society of London, Special Publication*, **412,** 111-129.

Cattin, R. & Avouac, J.P., 2000. Modeling mountain building and the seismic cycle in the Himalaya of Nepal. *Journal of Geophysical Research: Solid Earth*, **105**, 13389–13407.

Cenki, B., Kriegsman, L.M. & Braun, I., 2002. Melt-producing and melt-consuming reactions in the Achankovil cordierite gneisses, South India. *Journal of Metamorphic Geology*, **20,** 543–561.

Cesare, B., Ferrero, S., Salvioli-Mariani, E., Pedron, D. & Cavallo, A., 2009. ''Nanogranite'' and glassy inclusions: the anatectic melt in migmatites and granulites. *Geology*, **37,** 627–630.

Chamberlain, C.P., Koons, P.O., Meltzer, A.S., Park, S.K., Craw, D., Zeitler, P. & Poage, M.A., 2002. Overview of hydrothermal activity associated with active orogenesis and metamorphism: Nanga Parbat, Pakistan Himalaya. *American Journal of Science*, **302**, 726–748.

Chatterjee, N. & Ghose, N.C., 2010. Metamorphic evolution of the Naga Hills eclogite and blueschist, Northeast India: implications for early subduction of the Indian plate under the Burma microplate. *Journal of Metamorphic Geology*, **28**, 209–225.

Cherniak, D.J., 2006. Zr diffusion in titanite. *Contribution of Mineralogy and Petrology,* **152**, 639–647.

Chew, D.M., Petrus, J.A. & Kamber, B.S., 2016. U–Pb LA–ICPMS dating using accessory mineral standards with variable common Pb. *Chemical Geology,* **363**, 185–199.

Clarke, G.L., White, R.W., Lui, S., Fitzherbert, J.A. & Pearson, N.J., 2007. Contrasting behaviour of rare earth and major elements during partial melting in granulite facies migmatites, Wuluma Hills, Arunta Block, central Australia. *Journal of Metamorphic Geology*, **25,** 1–18.

Coggon, R. & Holland, T.J.B., 2002. Mixing properties of phengitic micas and revised garnet–phengite thermobarometers. *Journal of Metamorphic Geology*, **20,** 683–696.

Colchen, M., Le Fort, P. & Pêcher, A., 1980. Notice explicative de la carte géologique Annapurna–Manaslu–Ganesh (Himalaya du Népal) au 1:200 000e (bilingual: French–English), CNRS, Paris, 1986.

Colchen, M., LeFort, P. & Pecher, A., 1986. Notice explicative de la carte geologique Annapurna-Manaslu-Ganesh (Himalaya du Nepal) au 1:200.000e. Cent. National de la Recherche Scientifique, Paris, 137 pp.

Condie, K.C., Dengate, J. & Cullers, R.L., 1995. Behavior of rare earth elements in a paleoweathering profile on granodiorites in the Front Range, Colorado, USA. *Geochimica et Cosmochimica Acta,* **59**, 279-294.

Connolly, J.A.D., 1990. Multivariable phase diagrams: an algorithm based on generalized thermodynamics. *American Journal of Science*, **290,** 666–718.

Connolly, J.A.D., 2009. The geodynamic equation of state: what and how. *Geochemistry, Geophysics, Geosystems*, **10,** Q10014.

Connolly, J.A.D. & Trommsdorff, V., 1991. Petrogenetic grids for metacarbonate rocks: pressure–temperature phase-diagrams for mixed-volatile systems. *Contribution to Mineralogy and Petrology*, **108**, 93-105.

Corfield, R.I., Searle, M. P. & Green, O.R., 1999. Photang thrust sheet: an accretionary complex structurally below the Spontang ophiolite constraining timing and tectonic environment of ophiolite obduction, Ladakh Himalaya, NW India. *Journal of the Geological Society*, **156**, 1031–1044.

Corrie, S.L. & Kohn, M.J., 2011. Metamorphic history of the central Himalaya, Annapurna region, Nepal, and implications for tectonic models. *Geological Society of America Bulletin*, **123,** 1863–1879.

Cossio, R., Borghi, A. & Ruffini, R., 2002. Quantitative modal determination of geological samples based on X-ray multielemental map acquisition. *Microscopy and Microanalysis*, **8,** 139–149.

Cottle, J.M., Waters, D.J., Riley, D., Beyssac, O. & Jessup, M.J., 2011. Metamorphic history of the South Tibetan Detachment System, Mt. Everest region, revealed by RSCM thermometry and phase equilibria modelling. *Journal of Metamorphic Geology,* **29**, 561–582.

Cottle, J.M., Larson, K.P. & Kellett, D.A., 2015. How does the mid-crust accommodate deformation in large, hot collisional orogens? A review of recent research in the Himalayan orogen. *Journal of Structural Geology*, **78**, 119–133.

Cox, C. & Lowe, D.R., 1995. A conceptual review of the regional-scale controls on the composition of clastic sediment and the co-evolution of continental blocks and their sedimentary cover. *Journal of Sedimentary Research,* **A65**, 1-12.

Crichton, J.G. & Condie, K.C., 1993. Trace elements as source indicators in cratonic sediments: a case study from the early Proterozoic Libby Creek Group, southwestern Wyoming. *Journal of Geology*, **101**, 319-332.

Critelli, S., & Garzanti, E., 1994. Provenance of the lower Tertiary Murree redbeds (Hazara-Kashmir syntaxis, Pakistan) and initial rising of the Himalayas. *Sedimentary Geology*, **89**, 265–284.

Cullers, R.L., Barrett, T., Carlson, R. & Robinson, B., 1987. Rare-earth element and mineralogic changes in Holocene soil and stream sediment: a case study in the Wet Mountains, Colorado, USA. *Chemical Geology*, **63**, 275-297.

Dasgupta, S., Ganguly, J. & Neogi, S., 2004. Inverted metamorphic sequence in the Sikkim Himalayas: crystallization history, P–T gradient and implication. *Journal of Metamorphic Geology*, **22,** 395–412.

DeCelles, P.G., Gehrels, G.E., Quade, J., Ojha, T.P., Kapp, P.A. & Upreti, B.N., 1998a. Neogene foreland basin deposits erosional unroofing and the kinematic history of the Himalayan fold-thrust belt, western Nepal. *Geological Society of America Bulletin*, **110**, 2-21.

DeCelles, P.G., Gehrels, G.E., Quade, J. & Ojha, T.P, 1998b. Eocene-early Miocene foreland basin development and the history of Himalayan thrusting, western and central Nepal. *Tectonics,* **17**, 741 – 765.

DeCelles, P.G., Gehrels, G.E., Quade, J., LaReau, B. & Spurlin, M., 2000. Tectonic implications of U–PL zircon ages of the Himalayan orogenic belt in Nepal. *Science*, **288**, 497–499.

DeCelles, P.G., Robinson, D.M., Quade, J., Ojha, T.P., Garzione, C.N., Copeland, P. & Upreti, B.N., 2001. Stratigraphy, structure and tectonic evolution of the Himalayan fold–thrust belt in western Nepal. *Tectonics*, **20**, 487–509.

DeCelles, P.G., Gehrels, G.E., Najman, Y., Martin, A.J., Carter, A. & Garzanti, E., 2004. Detrital geochronology and geochemistry of Cretaceous–Early Miocene strata of Nepal: implications for timing and diachroneity of initial Himalayan orogenesis. *Earth and Planetary Science Letters*, **227**, 313–330.

Dewey, J.F., Cande, S. & Pitman III, W.C., 1989. Tectonic evolution of the India/ Eurasia collision zone. *Eclogae Geologicae Helvetiae*, **82**, 717–734.

Diener, J.F.A. & Powell, R., 2012. Revised activity-composition models for clinopyroxene and amphibole. *Journal of Metamorphic Geology*, **30**, 131-142.

Diener, J.F.A., Powell, R., White, R.W. & Holland, T.J.B., 2007. A new thermodynamic model for clino- and orthoamphiboles in the system Na_2O–CaO–FeO–MgO–Al_2O_3–SiO_2–H_2O–O. *Journal of Metamorphic Geology*, **25**, 631-656.

Dithal, M.R., 2015. Geology of Nepal Himalaya. Regional perspective of the classic collided orogen. Regional geology Review, Springer.

Ehlers, E.G. & Blatt, H., 1982. Petrology: Igneous, Sedimentary and Metamorphic. San Francisco, W.H. Freeman and Company., 732 p.

Elzea, J. & Murray, H.H., 1994. Clays: Bentonite. In: Carr, D.D. (eds.), Industrial Minerals & Rocks, 6th edition. SME Littleton Co., pp 233-246.

Evans, K.A., 2011. Metamorphic carbon fluxes: how much and how fast? *Geology*, **39**, 95–96.

Evans, M.J., Derry, L.A. & France-Lanord, C., 2004. Geothermal fluxes of alkalinity in the Narayani river system of central Nepal, *Geochemistry Geophysics Geosystems*, **5**, Q08011.

Evans, M.J., Derry, L.A. & France-Lanord, C., 2008. Degassing of metamorphic carbon dioxide from the Nepal Himalaya. *Geochemistry, Geophysics, Geosystems,* **9**, Q04021.

Ferrero, S., Bartoli, O., Cesare, B., Salvioli-Mariani, E., Acosta-Vigil, A., Cavallo, A., Groppo C. & Battiston, S., 2012. Microstructures of melt inclusions in anatectic metasedimentary rocks. *Journal of Metamorphic Geology*, **30,** 303-322.

Fettes, D. & Desmons, J., 2007. Metamorphic Rocks: A Classification and Glossary of Terms. Cambridge University Press, 256 p.

Flesia, C. & Frezzotti, M.L., 2015. The dilemma of the dwarf Earth's CO2 degassing: Irrelevant or crucial? *Journal of Geochemical Exploration*, **152**, 118-122.

Fletcher, I.R., Paul, D.K. & Trendall, A.F., 1992. Sm-Nd and geochemical characteristics of metasedimentary rocks at Mt. Narryer, Western-Australia. *Australian Journal of Earth Sciences*, **39**, 67-78.

Frank, W., Gansser, A. & Trommsdorff, V., 1977. Geological observations in the Ladakh area (Himalayas) - A preliminary report. *Schweizerische Mineralogische und Petrographische Mitteilungen*, **57**, 89–133.

Frank, W., Miller, C. & Grasemann, B., 1995. Ar/Ar ages of detrital micas and paleogeographic provenance of Proterozoic clastic sediments in the Himalayas. In: Spencer, D. A., Burg, J.-P. & Spencer-Cervato, C. (eds.), 10th Himalaya-Karakoram-Tibet Workshop Abstract Volume, Zürich, Mitteilungen aus dem Geologischen Institut der ETH und der Universität Zürich, **298**.

Fraser, G.,Worley, B. & Sandiford, M., 2000. High-precision geothermobarometry across the High Himalayan metamorphic sequence, Langtang Valley, Nepal. *Journal of Metamorphic Geology*, **18,** 665–681.

Franz, G., Spear, F.S., 1985. Aluminous titanite from the Eclogite Zone, south central Tauern Window, Austria. *Chemical Geology,* **50**, 33–46.

Frost, B.R., Chamberlain, K.R. & Schumacher, J.C., 2000. Sphene (titanite): phase relations and role as a geochronometer. *Chemical Geology,* **172**, 131–148.

Gaetani, M. & Garzanti, E., 1991. Multicyclic history of the northern India continental margin (north- western Himalaya). *AAPG Bulletin*, **75**, 1427–1446.

Gaillardet J.. & Galy, A., 2008. Himalaya-carbon sink or source? *Science,* **320**, 1727–1728.

Galy, A. & France-Lanord, C., 1999**.** Weathering processes in the Ganges-Brahmaputra basin and the riverine alkalinity budget. *Chemical Geology***, 159,** 31-60.

Gansser, A., 1964. Geology of the Himalayas. London, Wiley Interscience.

Gao, X.Y., Zheng Y.Z., Chen, Y.X. & Guo J., 2012. Geochemical and U-Pb age constraints on the occurrence of polygenetic titanites in UHP metagranite in the Dabie orogen, *Lithos,* **136**, 93-108.

Garcia, D., Fonteilles, M., & Moutte, J., 1994. Sedimentary fractionations between Al, Ti, and Zr and the genesis of strongly peraluminous granites. *Journal of Geology*, **102**, 411-422.

Garzanti, E., 1999. Stratigraphy and sedimentary history of the Nepal Tethys Himalaya passive margin. *Journal of Asian Earth Sciences*, **17**, 805–827.

Gehrels, G.E., DeCelles, P.G., Martin, A., Ojha, T.P., Pinhassi, G. & Upreti, B.N., 2003. Initiation of the Himalayan orogen as an early Paleozoic thin-skinned thrust belt. *GSA Today*, **13,** 4–9.

Gehrels, G.E., DeCelles, P.G., Ojha, T.P. & Upreti, B.N., 2006. Geologic and U-Th-Pb geochronologic evidence for early Paleozoic tectonism in the Kathmandu thrust sheet, central Nepal Himalaya. *Geological Society of America Bulletin*, **118**, 185–198.

Ghose, N.C. & Singh, R.N., 1980. Occurrence of blueschist facies in the ophiolite belt of Naga Hills, east of Kiphire, N.E., India. *Geologische Rundschau*, **69**, 41–43.

Giere, R., Rumble, D., Gunther, D., Connolly, J., & Caddick, M.J., 2011. Correlation of growth and breakdown of major and accessory minerals in metapelites from Campolungo, Central Alps. *Journal of Petrology*, **52**, 2293-2334.

Giggenbach, W.F., Gonfiantini, R., Jangi, B.L. & Truesdell, A.H., 1983. Isotopic andchemical composition of Parbati valley geothermal discharges, north-westHimalaya, India. *Geothermic,s* **12**, 199–222.

Girault, F., Bollinger, L., Bhattarai, M., Koirala, B.P., France-Lanord, C., Rajaure, S., Gaillardet, J., Fort, M., Sapkota, S.N. & Perrier, F., 2014. Large-scale organization of carbon dioxide discharge in the Nepal Himalayas. *Geophysical Research Letters,* **41**, 6358–6366.

Girault, F., Perrier, F., Crockett, R., Bhattarai, M., Koirala, B.P., France-Lanord, C., Agrinier, P., Ader, M., Fluteau, F., Gréau, C. & Moreira, M., 2014b. The Syabru-Bensi hydrothermal system in central Nepal: 1. Characterization of carbon dioxide and radon fluxes. *Journal of Geophysical Research: Solid Earth,* **119**, doi:10.1002/2013JB010301.

Godin, L., Grujic, D., Law, R. & Searle, M.P., 2006. Crustal flow, extrusion, and exhumation in continental collision zones: an introduction. In: Law, R., Searle, M.P. & Godin, L., (eds.), Channel flow, ductile extrusion, and exhumation in continental collision zones. *Geological Society, London, Special Publication*, **268,** 1–23.

Goscombe, B. & Hand, M., 2000. Contrasting P-T paths in the Eastern Himalaya, Nepal: inverted isograds in a paired metamorphic mountain belt. *Journal of Petrology*, **41,** 1673–1719.

Goscombe, B., Gray, D. & Hand, M., 2006. Crustal architecture of the Himalayan metamorphic front in eastern Nepal. *Gondwana Research*, **10**, 232–255.

Granieri, D., Avino, R., & Chiodini G., 2010. Carbon dioxide diffuse emission from the soil: Ten years of observations at Vesuvio and Campi Flegrei (Pozzuoli), and linkages with volcanic activity. *Bulletin of Volcanology*, **72**, 103–118.

Greenwood, H.J., 1975. Buffering of pore fluids by metamorphic reactions. *American Journal of Science***, 275**, 573–593.

Gromet, L.P., Dymek, R., Haskin, L.A. & Korotev, R.L., 1984. The ''North American Shale Composite'': Its compilation, major and trace element characteristics. *Geochimica et Cosmochimica Acta*, **48**, 2469-2482.

Groppo, C., Rolfo, F. & Lombardo, B., 2009. P-T evolution across the Main Central Thrust Zone (Eastern Nepal): hidden discontinuities revealed by petrology. *Journal of Petrology*, **50**, 1149–1180.

Groppo, C., Rolfo, F. & Indares, A., 2012. Partial melting in the Higher Himalayan Crystallines of Eastern Nepal: the effect of decompression and implications for the ''channel flow'' model. *Journal of Petrology*, **53,** 1057–1088.

Groppo, C., Rolfo, F. & Mosca, P., 2013a. The cordierite-bearing anatectic rocks of the Higher Himalayan Crystallines (eastern Nepal): low-pressure anatexis, melt-productivity, melt loss and the preservation of cordierite. *Journal of metamorphic Geology,* **31,** 187–204.

Groppo, C., Rolfo, F., Castelli, D. & Connolly, J.A.D., 2013b. Metamorphic CO_2 production from calc-silicate rocks via garnet-forming reactions in the CFAS–H_2O–CO_2 system. *Contribution to Mineralogy and Petrology*, **166**, 1655–1675.

Groppo, C., Rubatto, D., Rolfo, F. & Lombardo, B., 2010. Early Oligocene partial melting in

the Main Central Thrust Zone (Arun Valley, eastern Nepal Himalaya). *Lithos*, **118**, 287–301.

Groppo C., Rolfo F., Sachan H.K. & Rai S. K., 2016. Petrology of blueschist from the western Himalaya (Ladakh, NW India): exploring the complex behaviour of a lawsonite-bearing system in a palaeo-accretionary setting. *Lithos*, **252-253**, 41-56.

Groppo, C., Rolfo, F., Castelli, D. & Mosca, P., 2017. Metamorphic CO_2 production in collisional orogens: petrologic constraints from phase diagram modeling of Himalayan, scapolite-bearing, calc-silicate rocks in the NKC(F)MAS(T)-HC system. *Journal of Petrology*, **58**, 53-83.

Grujic, D., Casey, M., Davidson, C., Hollister, S. L., Kundig, R., Pavlis, T. & Schmid, S., 1996. Ductile extrusion of the Higher Himalayan Crystalline in Bhutan: evidence from quartz microfabrics. *Tectonophysics*, **260,** 21–43.

Guillot, S., Mahéo, G., de Sigoyer, J., Hattori, K.H. & Pecher, A., 2008. Tethyan and Indian subduction viewed from the Himalayan high- to ultrahigh-pressure metamorphic rocks. *Tectonophysics*, **451**, 225–241.

Hagen, T., 1969. Report on the geological survey of Nepal. Volume 1: Preliminary reconnaissance. *Zurich, Social Helvétique Sciences Natural Mémoir*, **86,** 185.

Harris, N.B.W. & Massey, J., 1994. Decompression and anatexis of Himalayan metapelites. *Tectonics*, **13,** 1537–1546.

Haskin, L.A., Wildeman, T.R., Frey, F.A., Collins, K.A., Keedy, C.R. and Haskin, M.A., 1966. Rare earths in sediments. *Journal of Geophysical Research: Solid Earth*, **71**, 6091-6105.

Hayden, L.A., Watson, E.B. & Wark, D.A., 2008. A thermobarometer for sphene (titanite). *Contribution to Mineralogy and Petrology,* **155**, 529–540.

He, D., Webb, A.A.G., Larson, K.P., Martin, A.J. & Schmitt, A.K., 2015. Extrusion *vs.* duplexing models of Himalayan mountain building. 3: duplexing dominates from the Oligocene to Present. *International Geology Review*, **57**, 1–27.

Heim, A. & Gansser, A., 1939. Central Himalaya: geological observations of the Swiss expedition 1936. *Denkschriften der Schweizerischen Naturforschenden Gesellschaft, Band LXXIII*, **1**, 245 pp.

Herman, F., Copeland, P., Avouac, J-P., Bollinger, L., Mahéo , G., Le Fort, P., Rai, S., Foster, D., Pêcher, A., Stüwe, K. & Henry, P., 2010. Exhumation, crustal deformation, and thermal structure of the Nepal Himalaya derived from the inversion of thermochronological and thermobarometric data and modeling of the topography. *Journal of Geophysical Research*, **115**, B06407, doi:10.1029/2008JB006126.

Hey, M.H., 1954. A new review of the chlorites. Mineralogical Magazine, 30, 277–292.

Hodges, K., 2000. Tectonics of Himalaya and southern Tibet from two perspectives. *Geological Society of American Bullettin*, **112**, 324–350.

Hodges, K.V., Parrish, R.R., Housh, T.B., Lux, D.R., Burchfiel, B. C., Royden, L.H. & Chen, Z., 1992. Simultaneous Miocene extension and shortening in the Himalayan orogeny. *Science*, **258,** 1466–1470.

Hodges, K.V., Hurtado, J.M. & Whipple, K.X., 2001. Southward extrusion of Tibetan crust and its effect on Himalayan tectonics. *Tectonics*, **20,** 799–809.

Hodges, K.V., Wobus, C., Ruhl, K., Schildgen, T. & Whipple, K., 2004. Quaternary deformation, river steepening, and heavy precipitation at the front of the higher Himalayan ranges. *Earth Planetary Science Letters*, **220**, 379–389.

Holland, T.J.B. & Powell, R., 1998. An internally consistent thermodynamic data set for phases of petrologic interest. *Journal of Metamorphic Geology*, **16,** 309–343.

Holland, T.J.B. & Powell, R., 2001. Calculation of phase relations involving haplogranitic melts using an internally consistent thermodynamic dataset. *Journal of Petrology*, **42,** 673–683.

Holland, T.J.B. & Powell, R., 2011. An improved and extended internally consistent thermodynamic dataset for phases of petrological interest, involving a new equation of state for solids. *Journal of Metamorphic Geology*, **29**, 333– 383.

Holland, T., Baker, J. & Powell, R., 1998. Mixing properties and activity-composition relationships of chlorites in the system MgO-FeO-Al2O3-SiO2-H2O. *European Journal of Mineralogy*, **10,** 395–406.

Holness, M.B. & Clemens, J. D., 1999. Partial melting of the Appin Quartzite driven by fracture controlled H_2O infiltration in the aureole of the Ballachulish Igneous Complex, Scottish Highlands. *Contributions to Mineralogy and Petrology*, **136,** 154–168.

Holness, M.B. & Sawyer, E.W., 2008. On the pseudomorphing of melt-filled pores during the crystallization of migmatites. *Journal of Petrology*, **49,** 1343–1363.

Honegger, K., Le Fort, P., Mascle, G. & Zimmerman, J.L., 1989. The blueschists along the Indus Suture zone in Ladakh, NWHimalaya. *Journal of Metamorphic Geology*, **7**, 57–72.

Hu, X., Garzanti, E., Wang, J., Huang, W., An, W. & Webb, A., 2016. The timing of India-Asia collision onset – Facts, theories, controversies. *Earth-Science Reviews*, **160**, 264-299.

Iaccarino, S., Montomoli, C., Carosi, R., Massonne, H.J., Langone, A. & Visonà, D., 2015. Pressure-temperature-time-deformation path of kyanite-bearing migmatitic paragneiss in the Kali Gandaki valley (Central Nepal): investigation of Late Eocene-Early Oligocene melting processes. *Lithos*, **231,** 103–121.

Imayama, T., Takeshita, T. & Arita, K., 2010. Metamorphic P–T profile and P–T path discontinuity across the far-eastern Nepal Himalaya: investigation of channel flow models. *Journal of Metamorphic Geology*, **28,** 527–549.

Imayama, T., Takeshita, T., Yi, K., Cho, D.-L., Kitajima, K., Tsutsumi, Y., Kayama, M., Nishido, H., Okumura, T., Yagi, K., Itaya, T. & Sano, Y., 2012. Two-stage partial melting and contrasting cooling history within the Higher Himalayan Crystalline Sequence in the far-eastern Nepal Himalaya. *Lithos*, **134-135**, 1–22.

Indares, A., White, R.W. & Powell, R., 2008. Phase equilibria modelling of kyanite-bearing anatectic paragneiss from the central Grenville Province. *Journal of Metamorphic Geology*, **26,** 815–836.

Inger, S. & Harris, N.B.W., 1992. Tectonothermal evolution of the High Himalayan crystalline sequence, Langtang Valley, northern Nepal. Journal of Metamorphic Geology, **10**, 439–452.

IPCC, 2013. Climate change 2013: the physical science basis. In: Stocker, T.F., Qin, D., Plattner, G.K., Tignor, M., Allen, S.K., Boschung, J., Nauels, A., Xia, Y., Bex, V. & Midgley, P.M. (eds.), Contribution of Working Group I to the Fifth Assessment Report of the Intergovernmental Panel on Climate Change. Cambridge University Press, Cambridge and New York, 1535 pp.

Jamieson, R.A., Beaumont, C., Medvedev, S. & Nguyen, M. H., 2004. Crustal channel flows: 2. Numerical models with implications for metamorphism in the Himalayan-Tibetan orogeny. *Journal of Geophysical Research*, **109,** B6.

Jarvis, J.C., Wildeman, T.R. & Banks, N.G., 1975. Rare earth elements in the Leadville Limestone and its marble derivates. *Chemical Geology*, **16**, 27-37.

Johnson, M.R.W. & Rogers, G., 1997. Rb-Sr ages of micas from the Kathmandu Complex, Central Nepalese Himalaya: implications for the evolution of the Main Central Thrust. *Journal of the Geological Society, London*, **154**, 863– 869.

Johnson, M.R.W., Oliver, G.J.H., Parrish, R.R. & Johnson, S.P., 2001. Synthrusting metamorphism, cooling, and erosion of the Himalayan Kathmandu complex, Nepal. *Tectonics*, **20,** 394–415.

Joshi, P.R., Khan, H.R., Singh, S., Khadka, D.R. & Napt, D.K., 2003. Map N° E-2. Geothhermal hot springs resources in Nepal. DMG Mineral Resources Division.

Karl, S.M., Wandless, G.A. & Karpoff, A.M., 1992. Sedimentological and geochemical characteristics of ODP Leg 129 siliceous deposits. In: Larson, R., Lancelot, Y., et al. (eds.), Proc. Ocean Drilling Program, Scientific Results, 129. Ocean Drilling Program, College Station, TX, pp. 31–80.

Kellett, D.A., Grujic, D., Warren, C., Cottle, J., Jamieson, R. & Tenzin, T., 2010.

Metamorphic history of a syn-convergent orogen-parallel detachment: the south Tibetan detachment system, eastern Himalaya. *Journal of Metamorphic Geology*, **28**, 785–808.

Kennedy, A.K., Kamo, S.L., Nasdala, L. & Timms, N.E., 2010. Grenville skarn titanite: potential reference material for SIMS U-Th-Pb analysis. *Canadian Mineralogist,* **48,** 1423–1443.

Kerrick D.M. & Caldeira, K., 1993. Paleoatmospheric consequences of CO2 released during early Cenozoic regional metamorphism in the Tethyan orogen. *Chemical Geology*, **108**, 201–230.

Kerrick, D.M. & Caldeira, K., 1998. Metamorphic CO_2 degassing from orogenic belts. *Chemical Geology*, **145**, 213–232.

Kerrick, D.M. & Caldeira, K., 1999. Was the Himalayan orogen a climatically significant coupled source and sink for atmospheric CO_2 during the Cenozoic*? Earth and Planetary Science Letters,* **173**, 195–203.

Khanal, S., Robinson, D.M., Kohn, M.J. & Mandal, S., 2015. Evidence for a far-traveled thrust sheet in the Greater Himalayan thrust system, and an alternative model to building the Himalaya. *Tectonics*, **34**, 31–52.

Knight, C.L. & Bodnar, R.J., 1989. Synthetic fluid inclusions: IX. Critical PVTX properties of NaCl-H_2O solutions. *Geochimica et Cosmochimica Acta*, **53**, 3-8.

Kohn M.J., 2004. Oscillatory- and sector-zoned garnets record cyclic (?) rapid thrusting in central Nepal. *Geochemistry Geophysics Geosysems*, **5,** Q12014.

Kohn, M.J., 2008. PTt data from central Nepal support critical taper and repudiate large-scale channel flow of the Greater Himalayan Sequence. *Geological Society of America Bulletin*, **120**, 259–273.

Kohn, M.J., 2014. Himalayan metamorphism and its tectonic implications. Annual Review of *Earth and Planetary Science Letters*, **42**, 381–419.

Kohn, M.J., 2016. Metamorphic chronology - a tool for all ages: Past achievements and future prospects. American Mineralogist 101, 25–42.

Kohn, M.J., 2017. Titanite petrochronology, in: Kohn, M.J., Engi, M. and Lanari, P. (eds.), Petrochronology: Methods and Applications. *Reviews in Mineralogy and Geochemistry*, **83**, 419-417.

Kohn, M.J. & Corrie, S.L., 2011. Preserved Zr-temperatures and U–Pb ages in high-grade metamorphic titanite: Evidence for a static hot channel in the Himalayan orogen. *Earth and Planetary Science Letters,* **311**, 136–143.

Kohn, M. J., Wieland, M. S., Parkinson, C. D. & Upreti, B. N., 2004. Miocene faulting at plate tectonic velocity in the central Himalaya, Nepal. *Earth and Planetary Science Letters,* **228**, 299–310.

Kohn, M.J., Wielnand, M., Parkinson, C. D. & Upreti, B.N., 2005. Five generation of monazite in Langtang gneisses: implication for chronology of the Himalayan metamorphic core. *Journal of Metamorphic Geology*, **23,** 399–406.

Kohn, M.J., Paul, S.K., & Corrie, S.L., 2010. The lower Lesser Himalayan Sequence: A Paleoproterozoic arc on the northern margin of the Indian plate. *Geological Society of America Bulletin*, **122**, 323-335.

Kotarba, M., 1986. Hydrogeological investigations in Seti Khola and Trisuli thermal springs areas (Nepal Himalayas), *Geologia*, **12**, 37–51.

Kotarba, M., Sokolowski, A. & Bogacz, W., 1981. Hydrogeological investigations in the Kali Gandaki thermal springs area (Nepal Himalayas), *Bulletin of the Polish Academy of Sciences. Earth Sciences*, **29**, 283–291.

Kriegsman, L.M. & lvarez-Valero, A.M., 2010. Melt-producing versus melt-consuming reactions in pelitic xenoliths and migmatites. *Lithos*, **116,** 310–320.

Kuhn, B.K., Reusser, E. & Powell, R., 2005. Metamorphic evolution of calc-schists in the Central Alps, Switzerland. *Schweizerische Mineralogische und Petrographische Mitteilungen*, **85**, 175-190.

Larson, K.P. & Cottle, J.M., 2014. Midcrustal discontinuities and the assembly of the Himalayan mid-crust. *Tectonics*, **33,** 718–740.

Larson, K. M., Burgmann, R., Bilham, R., & Freymueller, J.T., 1999. Kinematics of the India-Eurasia collision zone from GPS measurements, *Journal of Geophysical Research*, **104**, 1077 – 1093.

Larson, K.P., Godin, L. & Price, R.A., 2010. Relationships between displacement and distortion in orogens: linking the Himalayan foreland and hinterland in central Nepal. *Geological Society of America Bulletin*, **122**, 1116–1134.

Larson, K.P., Gervais, F. & Kellett, D.A., 2013. A P–T–t–D discontinuity in east-central Nepal: Implications for the evolution of the Himalayan mid-crust. *Lithos*, **179**, 275–292.

Larson, K.P., Ambrose, T.K., Webb, A.G., Cottle, J.M. & Shrestha, S., 2015. Reconciling Himalayan midcrustal discontinuities: the Main Central thrust system. *Earth and Planetary Science Letters*, **429**, 139–146.

Lavé, J., & Avouac, J.-P., 2000. Active folding of fluvial terraces across the Siwaliks Hills, Himalayas of central Nepal. *Journal of Geophysical Research*, **105**, 5735–5770.

Le Fort, P., 1975, Himalayas: The collided range: Present knowledge of the continental

arc. *American Journal of Science*, **275-A**, 1–44.

Le Fort, P. & Rai, S.M., 1999. Pre-Tertiary felsic magmatism of the Nepal Himalaya. Recycling of continental crust. *Journal of Asian Earth Sciences,* **17**, 607 628.

Leake et al., 1997. Nomenclature of amphiboles: report of the subcommittee of amphiboles of the international mineralogical association, commission of new minerals and mineral manes. *Canadian Mineralogist*, **35**, 219-246.

Leech, M.L., Singh, S., Jain, A.K., Klemperer, S.L. & Manickavasagam, R.M., 2005. The onset of India–Asia continental collision: early, steep subduction required by the timing of UHP metamorphism in the western Himalaya. *Earth and Planetary Science Letters*, **234**, 83–97.

Leloup, P.H., Liu, X., Mahéo, G., Paquette, J.-L., Arnaud, N., Aubray, A. & Liu, X., 2015. New constraints on the timing of partial melting and deformation along the Nyalam section (central Himalaya): implications for extrusion models, in: Mukherjee, S., Carosi, R., van der Beek, B.K., and Robinson, D.M. (eds.), Tectonics of the Himalaya, *Geological Society of London, Special Publication*, **412**, 131-175.

LePichon, X., Fournier, M. & Jolivet, L., 1992. Kinematics, topography, shortening, and extrusion in the India–Eurasia collision. *Tectonics*, **11**, 1085–1098.

Lombardo, B., Pertusati, P. & Borghi, A., 1993. Geology and tectono-magmatic evolution of the eastern OHimalaya along the Chomolungma–Makalu transect. In: Treloar, P. J. & Searle, M. P. (eds.), Himalayan Tectonics. *Geological Society of London, Special Publication,* **74,** 341–355.

Long, S.L., McQuarrie, N., Tobgay, T. & Grujic, D., 2011. Geometry and crustal shortening of the Himalayan fold-thrust belt, eastern and central Bhutan. *GSA Bulletin,* **123**, 1427–1447.

Longerich, H.P., Jackson, S.E. & Günther, D., 1996. Laser ablation inductively coupled plasma mass spectrometric transient signal data acquisition and analyte concentration calculation. *Journal of Analytical Atomic Spectrometry*, **11**, 899–904.

Ludwig, K.K., 2001. Isoplot ⁄ Ex Version 2.49. A Geochronological Toolkit for Microsoft Excel. Berkeley Geochronology Centre, Special Publication, Berkeley.

Macfarlane, A.M., 1993. Chronology of tectonic events in the crystalline core of the Himalaya, Langtang National Park, central Nepal. *Tectonics*, **12,** 1004–1025.

Macfarlane, A.M., 1995. An evaluation of the inverted metamorphic gradient at Langtang National Park, Central Nepal, Himalaya. *Journal of Metamorphic Geology*, **13,** 595–612.

Macfarlane, A.M., Hodges, K.V. & Lux, D., 1992. A structural analysis of the Main Central Thrust zone, Langtang National Park, central Nepal Himalaya. *Geological Society of America Bulletin*, **104,** 1389–1402.

Mahéo, G., Fayoux, C., Guillot, S., Garzanti, E., Capiez, P. & Mascle, G., 2006. Geochemistry of ophiolitic rocks and blueschists from the Sapi-Shergol mélange (Ladakh, NW Himalaya, India): implication for the timing of the closure of the Neo-Tethys Ocean. *Journal of Asian Earth Sciences*, **26**, 695–707.

Martin, A.J., 2017. A review of definitions of the Himalayan Main Central Thrust. *International Journal of Earth Sciences*, **106**, 2131-2145.

Martin, A.J., Ganguly, J. & De Celles, P.G., 2010. Metamorphism of Greater and Lesser Himalayan rocks exposed in the Modi Khola valley, central Nepal. *Contribution to Mineralogy and Petrology*, **159**, 203–223.

Marty, B. & Tolstikhin, I.N., 1998. CO_2 fluxes from mid-ocean ridges, arcs and plumes. *Chemical Geology*, **145**, 233-248.

McDonough, W. F. & Sun, S., 1995. The composition of the Earth. *Chemical Geology,* **120**, 223–253.

McLennan, S.M., 2001. Relationship between the trace element composition of sedimentary rocks and upper continental crust. *Geochemistry, Geophysics, Geosystems*, 2000GC000109.

McLennan , S.M. & Taylor, S.R., 1981. Role of subducted sediments in island-arc magmatism: constraints from REE patterns. *Earth and Planetary Science Letters*, **54**, 423-430.

McLennan, S.M., Hemming, S., McDaniel, D.K. & Hanson, G.N., 1993. Geochemical approaches to sedimentation, provenance, and tectonics. In: Johnsson, M. J. & Basu, A., (eds.), Processes Controlling the Composition of Clastic Sediments: Boulder, Colorado. *Geological Society of America Special Paper,* **284**, 21-40.

Menzies, C.D., Wright, S.L., Craw, D., James, R.H., Alt, J.C., Cox, S.C., Pitcairn, I.K. & Teagle, D.A.H., 2018. Carbon dioxide generation and drawdown during active orogenesis of siliciclastic rocks in the Southern Alps, New Zealand. *Earth and Planetary Science Letters*, **481**, 305–315.

Miller, C., Klötzli, U., Frank, W., Thöni, M., Grasemann, B., 2000. Proterozoic crustal evolution in the NW Himalaya (India) as recorded by circa 1.80 Ga mafic and 1.84 Ga granitic magmatism. *Precambrian Research*, **103**, 191–206.

Montomoli, C., Iaccarino, S., Carosi, R., Langone, A. & Visonà, D., 2013. Tectonometamorphic discontinuities within the Greater Himalayan Sequence in Western Nepal (Central Himalaya): Insights on the exhumation of crystalline rocks.

*Tectonophysic*s, **608**, 1349–1370.

Montomoli, C., Carosi, R. & Iaccarino, S., 2015. Tectonometamorphic discontinuities in the Greater Himalayan Sequence: a local or a regional feature? *Geological Society London, Special Publications*, **412**, 25–41.

Morimoto, N., 1988. Nomenclatures of pyroxenes. *Mineralogical magazine*, **52**, 535-550.

Mörner N.A. & Etiope G., 2002. Carbon degassing from the lithosphere. *Global and Planetary Change*, **33**, 185-203.

Mosca, P., Groppo, C. & Rolfo, F., 2012. Structural and metamorphic features of the Main Central Thrust Zone and its contiguous domains in the eastern Nepalese Himalaya. *Journal of Virtual Explorer, Electronic Edition*, **41,** paper 2.

Mosca, P., Groppo, C. & Rolfo, F., 2013. Main geological features of the Rolwaling-Khumbu Himal between the Khimti Khola and Dudh Khosi valleys (eastern-central Nepal Himalaya). *Rendiconti Online della Società Geologica Italiana*, **29,** 112-115.

Munker, C., Pfander, J.A., Weyer, S., Buchl, A., Kleine, T. & Mezger, K., 2003. Evolution of planetary cores and the Earth-Moon system from Nb/Ta systematic. *Science*, **301**, 84-87.

Nabelek, P.I. & Chen, Y., 2014. The initial garnet-in reaction involving siderite-rhodocrosite, garnet re-equilibration and P-T-t paths of graphitic schists in the Black Hills orogen, South Dakota, USA. *Journal of Metamorphic Geology,* **32**, 133-150.

Nelson, K.D., Zhao, W., Brown, L.D., Kuo, J., Che, J., Liu, X., Kemperer, S.L., Makovsky, Y., Meissner, R., Mechie, J., Kind, R., Wenzel, F., Nabelek, J., Leshou, C., Tan, H., Wei, W., Jones, A.G., Booker, J., Unsworth, M., Kidd, W.S.F., Hauck, M., Alsdorf, D., Ross, A., Cogan, M., Wu, C., Sandvol, E. & Edwards, M. , 1996. Partially molten middle crust beneath Southern Tibet: synthesis of project INDEPTH results. *Science,* **274**, 1684–1696.

Nesbitt, H.W., Young, G.M., McLennan, S.M. & Keays, R.R., 1996. Effect of chemical weathering and sorting on the petrogenesis of siliciclastic sediments, with implications for provenance studies. *Journal of Geology*, **104**, 525-542.

Newton, R.C., Charlu, T.V. & Kleppa, O.J., 1980. Thermochemistry of the high structural state plagioclases. *Geochimica et Cosmochimica Acta*, **44,** 933–941.

Nutman, A.P., Friend, C.R.L., Bennett, V.C., Wright, D. & Norman, M.D., 2010. ≥3700 Ma pre-metamorphic dolomite formed by microbial mediation in the Isua supracrustal belt (W. Greenland): Simple evidence for early life? *Precambrian Research*, **183**, 725-737.

Parrish, R.R. & Hodges, K.V., 1996. Isotopic constraints on the age and provenance of the

Lesser and Greater Himalayan sequences, Nepalese Himalaya. *Geological Society of America Bulletin*, **108**, 904–911.

Paton, C., Hellstrom, J., Paul, B., Woodhead, J., Hergt, J., Kosler, J., Fonneland, H., Sylvester, P., Tubrett, M., Pedersen, R., Jackson, S.E., Pearson, N.J., Griffin, W.L., Belousova, E.A., Jackson, S.E., Longerich, H.P., Dunning, G.R., Freyer, B.J., Ulrich, T., Kamber, B.S., Jugo, P.J., Tinkham, D.K., Woodhead, J.D., Hellstrom, J., Hergt, J.M., Greig, A., Maas, R., Paton, C., Woodhead, J., Hergt, J., Phillips, D., Shee, S., Bizzarro, M., Paton, C., Larsen, K., Schiller, M., Trinquier, A., Ulfbeck, D., Paton, C., Woodhead, J.D., Hellstrom, J.C., Hergt, J.M., Greig, A., Maas, R., Hampel, F.R., Rousseeuw, P.J., Croux, C., Reinsch, C., Craven, P. & Wahba, G., 2011. Iolite: Freeware for the visualisation and processing of mass spectrometric data. *Journal of Analytical Atomic Spectrometry,* **26**, 2508-2518.

Patriat, P. & Achache, J., 1984. The chronology of the India–Eurasia collision. Implications for crustal shortening and the driving mechanism of plates. *Nature*, **311**, 615–621.

Pearce, N.J.G.G., Perkins, W.T., Westgate, J.A., Gorton, M.P., Jackson, S.E., Neal, C.R. & Chenery, S.P., 1997. A compilation of new and published major and trace element data for NIST SRM 610 and NIST SRM 612 Glass Reference Materials. *Geostandards and Geoanalytical Research,* **21**, 115–144.

Pearson, O.N., 2002. Structural evolution of the central Nepal fold-thrust belt and regional tectonic and structural significance of the Ramgarh thrust. Ph.D., University of Arizona.

Pearson, O.N. & DeCelles, P.G., 2005. Structural geology and regional tectonic significance of the Ramgarh Thrust, Himalayan fold-thrust belt of Nepal. *Tectonics*, **24,** TC4008.

Peate, D.W., Pearce, J.A., Hawkesworth, C.J., Colley, H., Edwards, C.M.H. & Hirose, K., 1997. Geochemical variations in Vanuatu arc lavas: the role of subducted material and a variable mantle wedge composition. *Journal of Petrology*, **38**, 1331–1358.

Pêcher, A., 1989. The metamorphism in Central Himalaya. *Journal of Metamorphic Geology*, **7,** 31–41.

Pérez, N.M., Hernandez, P.A., Padilla, G., Nolasco, D., Barrancos, J., Melian, G., Padron, E., Dionis, S., Calvo, D., Rodriguez, F., Notsu, K., Mori, T., Kusakabe, M., Arpa, M.C., Reniva, P. & Ibarra, M., 2011. Global CO_2 emission from volcanic lakes. *Geology*, **39**, 235-238.

Perrier, F., Richon, P., Byrdina, S., France-Lanord, C., Rajaure, S., Koirala, B.P., Shrestha, P.L., Gautam, U.P., Tiwari, D.R., Revil, A., Bollinger, L., Contraires, S., Bureau, S. & Sapkota, S.N., 2009. A direct evidence for high carbon dioxide and radon-222 discharge in Central Nepal. *Earth and Planetary Science Letters*, **278**, 198–207.

Petrelli, M., Morgavi, D., Vetere, F. & Perugini, D., 2016. Elemental imaging and petro-volcanological applications of an improved Laser Ablation Inductively Coupled Quadrupole Plasma Mass Spectrometry. *Periodico di Mineralogia,* **85**, 25-39.

Plank, T., 2014. The chemical composition of subducting sediments. Treatise on geochemistry (2 ed.).

Plank, T. & Langmuir, C.H., 1998. The chemical composition of subducting sediment and its consequences for the crust and mantle. *Chemical Geology, **145**,* 325-394.

Pognante, U. & Benna, P., 1993. Metamorphic zonation, migmatization and leucogranites along the Everest transect (eastern Nepal and Tibet): record of an exhumation history. In: Treloar, P.J. & Searle, M.P. Himalayan Tectonics. *Geological Society of London, Special Publication*, **74**, 323–340.

Pouchou, J.L. & Pichoir, F., 1988. Determination of mass absorption coefficients for soft X-rays by use of the electron microprobe. In: Newbury, D.E. (eds.), Microbeam Analysis. San Francisco, CA: San Francisco Press, 319-324.

Powell, R. and Holland, T. J. B., 1994. Optimal geothermometry and geobarometry. American Mineralogist 79, 120-133.

Powers, P.M., Lillie, R.J. & Yeates, R.S., 1998. Structure and shortening of the Kangra and Dehra Dun reentrants, Sub-Himalaya, India. *Geological Society of America Bulletin*, **110**, 1010 – 1027.

Pradhan BM, Kumar R., Shasa N, Binghadm K., 1978. Geological setting and tectonics of Central Nepal,areview.Proc.Internat.Geodyn. **Conf.** (Alpine- HimalayanRegion), Kathmandu, Tectonophysics.

Rai, S.M., Guillot, S., Le Fort, P. & Upreti, B.N., 1998. Pressure-temperature evolution in the Kathmandu and Gosainkund regions, Central Nepal. *Journal of Asian Earth Sciences*, **16,** 283–298.

Rapa, G., Groppo, C., Mosca, P. & Rolfo, F., 2016. Petrological constraints on the tectonic setting of the Kathmandu Nappe in the Langtang–Gosainkund–Helambu regions, central Nepal Himalaya. *Journal of metamorphic Geology*, **34**, 999-1023.

Rapa, G. Groppo, C., Rolfo, F., Petrelli, M., Mosca, P. & Perugini, D., 2017. Titanite-bearing calc-silicate rocks constrain timing, duration and magnitude of metamorphic CO_2 degassing in the Himalayan belt. *Lithos*, **292–293**, 364–378.

Rapa, G., Mosca, P., Groppo, C. & Rolfo, F., in press. Tectono-metamorphic discontinuities within the Himalayan orogen: structural and petrological constraints from Rasuwa District, Central Nepal Himalaya. *Journal of Asian Earth Sciences.*

Reddy, S.M., Searle, M.P. & Massey, J.A., 1993. Structural evolution of the High Himalayan

gneiss sequence, Langtang Valley, Nepal. In: Treloar, P.J. & Searle, M.P. (eds.), Himalayan Tectonics. *Geological Society of London, Special Publication*, **74**, 375–389.

Robert, X., van der Beek, P., Braun, J., Perry, C., Dubille, M. & Mugnier, J-L., 2009. Assessing Quaternary reactivation of the Main Central thrust zone (central Nepal Himalaya): New thermochronologic data and numerical modeling. *Geology*, **37**, 731-734.

Robertson, A., 2000. Formation of mélanges in the Indus Suture Zone, Ladakh Himalaya by successive subduction-related, collisional and post-collisional processes during Late Mesozoic–Late Tertiary time. In: Khan, M.A., Treolar, P.J., Searle, M.P., Jan, Q. (eds.), Tectonics of the Nanga Parbat Syntaxis and the Western Himalaya. *Geological Society of London, Special Publication*, **170**, 333–374.

Robertson, A. & Degnan, P., 1994. The Dras arc complex: Lithofacies and reconstruction of a Late Cretaceous oceanic volcanic arc in the Indus suture zone. *Sedimentary Geology*, **92**, 117–145.

Robinson, D.M., DeCelles, P.G., Garzione, C.N., Pearson, O.N., Harrison, T.M. & Catlos, E.J., 2001. The kinematic evolution of the Nepalese Himalaya interpreted from Nd isotopes. *Earth and Planetary Science Letters*, **192**, 507–521.

Robinson, D.M., DeCelles, P.G., Garzione, C.N., Pearson, O.N., Harrison, T.M. & Catlos, E.J., 2003. Kinematic model for the Main Central Thrust in Nepal. *Geology*, **31,** 359–362.

Rolfo, F., Lombardo B., Compagnoni, R., Le Fort, P., Lemennicier, Y. & Pecher, A., 1997. Geology and Metamorphism of the Ladakh Terrain and Shyok Suture Zone in the Chogo Lungma - Turmik area (northern Pakistan). *Geodinamica Acta*, **10**, 251-270.

Rolfo, F., Groppo, C. & Mosca, P., 2015a. Petrological constraints of the "Channel Flow" model in eastern Nepal. In: Mukherjee, S., Carosi, R., van der Beek, P.A., Mukherjee, B.K. & Robinson, D.M. (eds.), Tectonics of the Himalaya. *Geological Society of London, Special Publication*, **412,** 177–197.

Rolfo, F., Groppo, C., Mosca, P., Ferrando, S., Costa, E. & Kaphle, K.P., 2015b. Metamorphic CO_2 degassing in the active Himalayan orogen: exploring the influence of orogenic activity on the long-term global climate changes. In: Lollino et al. (eds.), Engineering Geology for Society and Territory, 1, 21-25. Springer International. Publishing Switzerland.

Rolfo, F., Groppo, C. & Mosca, P., 2017. Metamorphic CO_2 production in calc-silicate rocks from the eastern Himalaya. *Italian Journal of Geosciences*, **136**, 28-38.

Rosen, O., Desmons, J. & Fettes, D., 2005. Regional metamorphism of carbonate deposits: statistical study of mineral composition variety and a proposed classification of metacarbonate rocks. *Russian Geology and Geophysics*, **46**, 351-360.

Roser, B.P. & Korsch, R.J., 1986. Determination of tectonic setting of sandstone-mudstone suites using SiO_2 content and K_2O/Na_2O ratio. *Journal of Geology*, **94**, 635-650.

Schelling, D., 1992. The tectonostratigraphy and structure of the eastern Nepal Himalaya. *Tectonics*, **11**, 925–943.

Schelling, D. & Arita, K., 1991. Thrust tectonics, crustal shortening, and the structure of the far-eastern Nepal, Himalaya. *Tectonics,* **10**, 851–862.

Searle, M.P., Law, R.D., Godin, L., Larson, K.P., Streule, M.J., Cottle, J.M. & Jessup, M.J., 2008. Defining the Himalayan Main Central Thrust in Nepal. *Journal of the Geological Society of London*, **165**, 523–534.

Selverstone, J. & Gutzler, D.S., 1993. Post-125 Ma carbon storage associated with continent–continent collision. *Geology,* **21**, 885–888.

Sengör, A.M.C., 1987. Tectonics of the tethysides: orogenic collage development in a collisional setting. *Annual Review of Earth and Planetary Sciences*, **15**, 213–244.

Shaw, D.M., 1954. Trace elements in pelitic rocks. Part I: variations during metamorphism. *Geological Society of American Bulletin*, **65**, 1151-1166.

Singh, R., et al., 2004. Geochemistry of thermal springs from Bhutan Himalaya. *Journal of the Geological Society of India*, **64**, 191–198.

Skelton, A., 2011. Flux rates for water and carbon during greenschist facies metamorphism. *Geology*, **39**, 43–46.

Skelton, A., 2013. Is orogenesis a net sink or source of atmospheric CO2? *Geology Today,* **29**, 102–107.

Spandler, C., Hammerli, J., Sha, P., Hilbert-Wolf, H., Hu, Y., Roberts, E. & Schmitz, M., 2016. MKED1: A new titanite standard for in situ analysis of Sm–Nd isotopes and U–Pb geochronology. *Chemical Geology,* **425**, 110–126.

Spencer, K.J., Hacker, B.R., Kylander-Clark, A.R.C., Andersen, T.B., Cottle, J.M., Stearns, M.A., Poletti, J.E. & Seward, G.G.E., 2013. Campaign-style titanite U–Pb dating by laser-ablation ICP: Implications for crustal flow, phase transformations and titanite closure. *Chemical Geology*, **341**, 84–101.

Stearns, M.A., Hacker, B.R., Ratschbacher, L., Rutte, D. & Kylander-Clark, A.R.C., 2015. Titanite petrochronology of the Pamir gneiss domes: Implications for middle to deep crust exhumation and titanite closure to Pb and Zr diffusion. *Tectonics*, **34**, 784–802.

Stacey J.S. & Kramers, J.D., 1975. Approximation of terrestrial lead isotope evolution by a two-stage model. *Earth and Planetary Science Letters,* **26**, 207-221.

Stöcklin, J., 1980. Geology of Nepal and its regional frame. *Journal of the Geological*

Society of London, **137**, 1-34.

Stöcklin, J., & Bhattarai, K. D., 1977. *Geology of Kathmandu area and central Mahabharat Range, Nepal Himalaya. HMG/UNDP mineral exploration project*. Technical Report, New York, 64 (Unpublished).

Tajcmanova, L., Connolly, J.A.D., Cesare, B., 2009. A thermodynamic model for titanium and ferric iron solution in biotite. *Journal of Metamorphic Geology*, **27**, 153-165.

Takagi, H., Arita, K., Sawaguchi, T., Kobayashi, K. & Awaji, D., 2003. Kinematic history of the Main Central Thrust zone in the Langtang area, Nepal. *Tectonophysics*, **366**, 151–163.

Tanner, P.W.G., Armstrong, H.A. & Owen, A.W., 2013. Rare earth element and La–Th–Sc analysis of cherts from the Highland Border Complex, Scotland: Geochemical determination of the sedimentary environment in greenschist facies rocks. *Scottish Journal of Geology*, **49**, 15-31.

Tapponier, P., Peltzer, G. & Armijo, R., 1986. On the mechanics of the collision between India and Asia. *Geological Society of London, Special Publication*, **19**, 115–157.

Taylor, S.R. & McLennan, S.M., 1985. The Continental Crust: its Composition and Evolution. Blackwell., Oxford. 312 p.

Thompson, J.B. & Hovis, G.L., 1979. Entropy of mixing in sanidine. *American Mineralogist,* **64**, 57–65.

Tiwari, S.K., Rai, S.K., Bartarya, S.K., Gupta, A.K. & Negi, M., 2016. Stable isotopes (13CDIC, _D, _18O) and geochemical characteristics of geothermal springs of Ladakh and Himachal (India): Evidence for CO_2 discharge in northwest Himalaya. *Geothermics*, **64**, 314-330.

Tracy, R.J. & Frost, B.R., 1991. Phase-Equilibria and Thermobarometry of Calcareous, Ultramafic and Mafic Rocks, and Iron Formations. *Reviews in Mineralogy*, **26**, 207-289.

Upreti, B. N., 1999. An overview of the stratigraphy and tectonics of the Nepal Himalaya. *Journal of Asian Earth Sciences*, **17**, 577–606.

Treolar, P.J., Petterson, M.G., Jan, M.Q. & Sullivan, M.A., 1996. A re-evaluation of the stratigraphy and evolution of the Kohistan arc sequence, Pakistan Himalaya : implications for magmatic and tectonic arc-building processes. *Journal of the Geological Society of London*, **153**, 681-693.

Upreti B.N. & Yoshida M., 2005. Giudebook for Himalayan trekkers. Geology and natural hazard along the Kaligandaki Valley, Nepal. Tribhuvan University Press, Lalipur, Nepal. 165 pp.

Upreti, B.N. & Le Fort, P., 1999. Lesser Himalayan crystalline nappes of Nepal: problem of

their origin. In: Macfarlane, A., Quade, J. & Sorkhabi, R. (eds.), Himalaya and Tibet: mountain roots to mountain tops. *Geological Society of America Special Paper*, **328**, 225–238.

Valdiya, K.S., 1998. Dynamic Himalaya. Universities Press (India) Limited, Hyderabad, 178 pp.

Vannay, J.C. & Grasemann, B., 2001. Himalayan inverted metamorphism and syn-convergence extension as a consequence of a general shear extrusion. *Geological Magazine*, **138,** 253–276.

Visonà, D. & Lombardo, B., 2002. Two mica- and tourmaline leucogranites from the Everest–Makalu region (Nepal-Tibet): Himalayan leucogranite genesis by isobaric heating? *Lithos*, **62,** 125-150.

Wadia, D.N., 1933. Note on the Geology of Nanga Parbat (Mt. Diamir), and adjoining portions of Chilas, Gilgit District, Kashmir. *Records of the Geological Survey of India*, **66-2**, Calcutta.

Walters, J.B. & Kohn, M.J, 2017. Protracted thrusting followed by late rapid cooling of the Greather Himalyan Sequence, Annapurna Himlaya, central Nepal: Insights from titanite petrochronology. *Journal of Metamorphic Geology*, **35**, 897-917.

Wang, J.-M., Zhang, J.-J., Liu, K., Wang, X.-X., Rai, S. & Scheltens, M., 2016. Spatial and temporal evolution of tectonometamorphic discontinuities in the Central Himalaya: constraints from P-T paths and geochronology. *Tectonophysics*, **679**, 41–60.

Warren, C.J., Grujic, D., Cottle J.M. & Rogers, N.W., 2012. Constraining cooling histories: rutile and titanite chronology and diffusion modelling in NW Bhutan. *Journal of Metamorphic Geology*, **30**, 113-130.

Waters, D.J., 2001. The significance of prograde and retrograde quartz-bearing intergrowth microstructures in partially melted granulite-facies rocks. *Lithos,* **56,** 97–110.

Webb, A.A.G., Yin, A., Harrison, T.M., Célérier, J. & Burgess, W.P., 2007. The leading edge of the Greater Himalayan Crystalline complex revealed in the NW Indian Himalaya: Implications for the evolution of the Himalayan Orogen. *Geology*, **35,** 955–958.

Webb, A.A.G., Schmitt, A.K., He, D. & Weigand, E.L., 2011. Structural and geochronological evidence for the leading edge of the Greater Himalayan Crystalline complex in the central Nepal Himalaya. *Earth and Planetary Science Letters*, **304,** 483–495.

Webb, A.A.G., Yin, A. & Dubey, C.S., 2013. U-Pb zircon geochronology of major lithologic units in the eastern Himalaya: implications for the origin and assembly of Himalayan rocks. *Geological Society of America Bulletin*, **125,** 499–522.

White, R.W., Powell, R. & Holland, T.J.B., 2001. Calculation of partial melting equilibria in the system Na_2O-CaO-K_2O-FeO-MgO-Al_2O_3-SiO_2-H_2O (NCKFMASH). *Journal of Metamorphic Geology* , **19,** 139–153.

White, R.W., Powell, R. & Holland, T.J.B., 2007. Progress relating to calculation of partial melting equilibria for metapelites. *Journal of Metamorphic Geology,* **25,** 511–527.

Whitney, D.L. & Evans, B.W., 2010. Abbreviations for names of rock-forming minerals. *American Mineralogist*, **95**, 185–187.

Yakymchuk, C. & Godin, L., 2012. Coupled role of deformation and metamorphism in the construction of inverted metamorphic sequences: an example from far-northwest Nepal. *Journal of Metamorphic Geology*, **30**, 513–535.

Yin, A., & Harrison, T.M., 2000. Geologic evolution of the Himalayan-Tibetan orogen. *Annual Review of Earth and Planetary Sciences*, **28**, 211–280.

Yin, A., 2006. Cenozoic tectonic evolution of the Himalayan orogen as constrained by along-strike variation of structural geometry, exhumation history, and foreland sedimentation. *Earth Science Reviews*, **76**, 11–131.

Zhao, W., Nelson, K.D. & the Project INDEPTH Team, 1993. Deep seismic reflection evidence for continental underthrusting beneath southern Tibet. *Nature*, **366**, 557–559.

Zhu, B., Kidd, W.S.F., Rowley, D.B., Currie, B.S. & Shafique, N., 2005. Age of initiation of the India–Asia collision in the east-central Himalaya. *Journal of Geology*, **113**, 265–285.

Zhu, D.C., Zhao, Z.D., Niu, Y., Dilek, Y., Hou, Z.Q. & Mo, X.X., 2013. The origin and pre-Cenozoic evolution of the Tibetan Plateau. *Gondwana Research*, **23**, 1429–1454.

Ringraziamenti

Eccomi giunta alla fine di questi tre anni di dottorato. Anni splendidi ed intensi, in cui ho avuto la possibilità di arricchirmi sia dal punto di vista professionale, che umano. Le esperienze che ho vissuto, l'opportunità di visitare e ''conoscere'' (anche se sicuramente solo in piccola parte) il Nepal, un paese meraviglioso con delle persone gentili e sempre sorridenti, mi hanno resa sicuramente una persona più ricca.

Il mio primo pensiero ed immenso ringraziamento è quindi per Chiara Groppo e Franco Rolfo, che mi hanno coinvolta in questo progetto ''himalayano''. A loro, e a Pietro Mosca, va tutta la mia gratitudine per il costante supporto, la passione che hanno saputo trasmettermi e la costante rapidità e prontezza con cui hanno affrontato tutte le questioni che si sono presentate nel corso degli anni, dalle noie burocratiche alle discussioni scientifiche, fino alla lettura e correzione di ogni singola parola presente in questa lunga e (spero) bella tesi.

Un ringraziamento speciale va a Chiara, che mi ha introdotta al magico regno delle rocce a silicati di calcio già durante la mia laurea triennale (nell'ormai lontano 2011!) e che è sempre stata il mio punto di riferimento negli anni a venire .

Ringrazio le guide Bakhta e Nendu, che hanno reso sicuro e agevole il nostro girovagare sui sentieri del Nepal, e i portatori Dorje e Pasang, che hanno portato i campioni per chilometri e chilometri.

A Maurizio Petrelli vanno i ringraziamenti per aver reso possibile la datazione della titanite presso il Dipartimento di Fisica e Geologia dell'Università di Perugia.

Ringrazio Simona Ferrando per l'aiuto nelle analisi delle inclusioni fluide, sia in microtermometria che per l'acquisizione degli spettri Raman, e per la loro interpretazione.

Un grazie di cuore è per i miei genitori, che mi hanno sempre sostenuta ed incoraggiata nel fare quello che desideravo.

Ai colleghi ed amici che hanno condiviso con me questo percorso di dottorato (tutto o in parte) va un pensiero speciale. Vi ringrazio per tutte le chiacchierate, le pause-caffè, i giovedì-birra, le risate, le uscite e le gite che hanno reso leggeri e divertenti questi anni.

I colleghi di ufficio che più di tutti hanno condiviso le (talvolta) interminabili ore di ufficio, la musica dei più svariati generi, le incursioni dei tutor, le armi batteriologiche (tazze e tazzine!): Serena, Stephan e Francesca, è stato bello trascorrere tutto questo tempo con voi!

Ai miei amici geologi vanno tutta la mia gratitudine e il mio affetto per gli anni universitari più belli che avessi mai potuto desiderare. Vi elencherei tutti, ma siete tantissimi!

Infine, un grazie speciale va ai miei amici nonché coinquilini (ed ex-) di Casa Barriera: Anna, Sandy, Rasha, Eleonora, Elisabetta, Martina, Karam, Fabio ed Ernesto. Sono stati due anni intensi e meravigliosi di condivisione, ed è soprattutto merito vostro.
Perché l'unione fa la forza, sempre.

APPENDIX 1.

List of the collected samples with mineral assemblage and location

Sample	Rock type	Main Assemblage	Accessory minerals	Location
14-01	Two-mica mylonitic augen gneiss	Qz, Kfs, Pl, Wm, Bt	Ap, Tur	Upward Syabru old [N28°09'45.1'' E85°20'46.8''] - 1470 m
14-02	Two-mica aplitic gneiss	Qz, Pl, Kfs Wm, Bt	Ap, Tur, Op	Upward Syabru old [N28°09'35.4'' E85°20'55.7''] - 1512 m
14-03	Wm + Bt + Grt gneissic micaschist	Qz, Pl, Wm, Bt, Grt	Rt, Ilm, Tur	[N28°09'03.7'' E85°21'56.2''] - 1620 m
14-04	Wm + Bt + Grt micaschist	Qz, Pl, Wm, Bt, Grt	Rt, Ilm	Before Bamboo [N28°09'10.2'' E85°22'45.3''] - 1750 m
14-05	Two-mica + Grt gneissic micaschist	Qz, Pl, Wm, Bt, Grt	Ap, Gr, Tur	[N28°09'18.0'' E85°24'07.0''] - 2060 m
14-06a	Two-mica + Grt gneiss	Qz, Pl, Wm, Bt, Grt	Ilm, Rt, Gr	Beyond Remche [N28°09'32.5'' E85°25'23.6''] - 2475 m
14-06b	Fine-grained Bt + Grt gneiss with rare late Wm	Qz, Pl, Bt, <<Wm, Grt	Ap, Gr, Tur	Suparata Remche [N28°09'32.5'' E85°25'23.6''] - 2475 m
14-07	Fine-grained Bt-gneiss with minor Grt, rare Sil and late-Wm	Qz, Pl, Kfs, Bt, Wm , Grt, <<<Sil	Gr, Ilm, Tur	After Lama Hotel [N28°10'06.2'' E85°26'05.9''] - 2560 m
14-08a	Bt + Sil + Grt migmatite with late Wm	Qz, Pl, Bt, Wm, Kfs, Grt, Sil	Ilm	Before Ghodatabela [N28°11'37.5'' E85°26'56.9''] - 2850 m
14-08b	Bt + Sil + Grt gneiss with late Wm	Qz, Pl, Bt, Wm, Kfs, Grt, Sil	Ilm, Gr	Before Ghodatabela [N28°11'37.5'' E85°26'56.9''] - 2850 m
14-09	Banded Bt + Sil + Grt migmatite	Qz, Pl, Bt, <Wm, Kfs, Grt, Sil	Ilm	[N28°12'12.6'' E85°27'56.1''] - 3080 m
14-10a	Fine-grained Bt + Grt gneiss	Qz, Pl, Bt, <<Wm, Kfs, Grt	Op	Tangsyap [N28°12'30.9'' E85°28'33.9''] - 3210 m
14-10b	Fine-grained Bt-gneiss with Sil+Qz nodules	Qz, Pl, Bt, <<Wm, Kfs, Grt, Sil		Tangsyap [N28°12'30.9'' E85°28'33.9''] - 3210 m
14-10c	Bt-bearing anatectic orthogneiss with rare Sil and late Wm	Qz, Pl, Bt, <<Wm, Kfs, <<Sil		Tangsyap [N28°12'30.9'' E85°28'33.9''] - 3210 m
14-10d	Amph + Cpx + Kfs + Pl + Qz calc-silicate gneiss	Amph, Cpx, Kfs, Pl, Qz, <<Bt	Aln, Op, Ttn	Tangsyap [N28°12'30.9'' E85°28'33.9''] - 3210 m

14-11a	Fine-grained Bt-gneiss with Sil+Qz nodules	Qz, Pl, Bt, <Wm, Kfs, Grt, Sil	Op	N of Langtang [N28°13'06.1'' E85°30'26.6''] - 3450 m
14-11b	Migmatitic Bt + Sil orthogneiss	Qz, Pl, Bt, <Wm, Kfs, Sil	Op	N ofLangtang [N28°13'06.1'' E85°30'26.6''] - 3450 m
14-11c	Wm + Bt + Grt leucogranite	Qz, Pl, Kfs, Wm, Bt, Grt		N of Langtang [N28°13'06.1'' E85°30'26.6''] - 3450 m
14-12	Bt + Sil + Grt migmatite with late Wm	Qz, Pl, Bt, Wm, Kfs, Grt, Sil	Ilm	Sindum [N28°13'04.5'' E85°31'11.7''] - 3540 m
14-13	Bt + Sil + Grt migmatitic orthogneiss	Qz, Pl, Bt, Wm, Kfs, <Grt, Sil	Op	[N28°12'39.1'' E85°32'19.6''] - 3635 m
14-13b	Banded fine-grained Bt-bearing gneiss	Qz, Pl, Kfs?, Bt, <Wm	Op	Before Kyanjin Gumba [N28°12'39.1'' E85°32'19.6''] - 3635 m
14-14	Fine-grained Bt-bearing gniess	Qz, Pl, Kfs, Bt	<<Op	
14-15	Bt + Sil + Grt migmatitic orthogneiss with late Wm	Qz, Pl, Bt, Wm, Kfs, <Grt, Sil	Op	Path towards Langshisa Kharka [N28°12'13.3'' E85°34'53.8''] - 3825 m
14-16	Fine-grained Bt-bearing gniess	Qz, Pl, Kfs, Bt, Chl	Ilm, Ttn, Ep	Path towards Langshisa Kharka [N28°11'48.8'' E85°36'38.7''] - 3935 m
14-17	Cpx + Ep + Kfs + Pl + Scp + <Qz calc-silicate rock	Cpx, Ep, Kfs, Pl, <Qz, Scp	Ttn	Path towards Kharka [N28°11'47.4'' E85°37'02.8''] - 3940 m
14-18	Fine-grained Bt-bearing gniess	Qz, Pl, Kfs, Bt, Chl	Op	[N28°12'24.9'' E85°39'02.6''] - 4030 m
14-19	Bt + Sil + Grt migmatitic orthogneiss	Qz, Pl, Bt, Wm, Kfs, <Grt, Sil	Op	Path towards Ganja La [N28°11'22.5'' E85°34'17.4''] - 4230 m
14-20a	Cal + Cpx + Ep + Kfs + Pl + Qz + Scp calc-silicate rock	Cal, Cpx, Ep, Kfs, Pl, Qz, Scp, <<Bt	Aln, Op, Ttn	Chechpoint [N28°12'37.2'' E85°28'55.9''] - 3260 m
14-20b	Cal + Cpx + Ep + Pl + Qz + Scp calc-silicate rock	Cal, Cpx, Ep, Pl, Qz, Scp	Op, Ttn	Checkpoint [N28°12'37.2'' E85°28'55.9''] - 3260 m
14-21	Bt + Wm + Grt gneissic micaschist	Qz, Pl, Kfs, Wm, Bt, Grt	Ilm	Path W of Remche [N28°09'36.3'' E85°24'54.1''] - 2560 m
14-21b	Cal + Cpx + Ep + Grt + Pl + Qz + Scp calc-silicate rock	Cal, Cpx, Ep, Pl, Qz, Scp, Amph (late)	Op, Ttn	Path W of Remche [N28°09'36.3'' E85°24'54.1''] - 2560 m
14-21c	Cal + Cpx + Ep + Grt + Pl + Qz + Scp calc-silicate rock	Cal, Cpx, Ep, Pl, Qz, Scp, Amph (late), <<<Wm	Ttn	Path W of Remche [N28°09'36.3'' E85°24'54.1''] - 2560 m

14-22	Bt + Wm + Grt gneissic micaschist	Qz, Pl, Wm, Bt, Grt, Kfs?	Ap, Ilm	Before Sherpagaon [N28°09'39.4'' E85°24'31.5''] - 2560 m
14-23	Bt + Wm + Grt gneissic micaschist	Qz, Pl, Wm, Bt, Grt, Kfs?	Gr, Op	
14-24	Wm + Bt + Grt + Ky gneissic micaschist	Qz, Pl, Wm, Bt, Grt, Ky, St	Rt, Ilm, Tur	[N28°09'50.4'' E85°23'42.6''] - 2575 m
14-25a	Bt-gneiss with rare Grt and late Wm	Qz, Pl, Kfs, Wm, Bt, Grt	Rt, Op	[N28°09'46.8'' E85°23'16.0''] - 2625 m
14-25b	Wm + Bt + Grt + Ky + St micaschist	Qz, Pl, Wm, Bt, Grt, Ky, St	Rt, Ilm, Tur	[N28°09'46.8'' E85°23'16.0''] - 2625 m
14-26	Wm + Bt + Grt micaschist	Qz, Pl, Wm, Bt, Grt	Rt, Ilm, Gr, Tur	[N28°09'41.7'' E85°22'44.2''] - 2750 m
14-27a	Two-mica graphitic phyllite, with porphyroblastic garnet	Qz, Pl, Wm, Bt, Chl, Grt	Ep, Gr, Tur, Op	Thulo Bharkhu [N28°07'49.3'' E85°18'58.7''] - m
14-27b	Two-mica foliated quartzite (metasandstone)	Qz, Pl, Wm, Bt	Gr, Tur	Thulo Bharkhu [N28°07'49.3'' E85°18'58.7''] - m
14-28a	Two-mica phyllite, with porphyroblastic garnet	Qz, Pl, Wm, Bt, Chl, Grt	Tur, Op	[N28°07'59.7'' E85°18'59.4''] - 1950 m
14-28b	Two-mica phyllitic Qz-rich micaschist with porphyroblastic garnet	Qz, Pl, Wm, Bt, Chl, Grt	Tur, Op	[N28°07'59.7'' E85°18'59.4''] - 1950 m
14-28c	Fine-grained quarzitic Bt-gneiss with levels with porphyroblastic Grt + Bt + Chl	Q, Pl, Bt, Grt, Chl	Op, Tur	[N28°07'59.7'' E85°18'59.4''] - 1950 m
14-29	Two-mica Grt-bearing phyllite	Qz, Pl, Wm, Bt, Grt	Gr, Op, Tur	Block in the woods [N28°08'27.9'' E85°19'26.6''] - 2180 m
14-29b	Bt + Wm quarzite	Qz, Wm, Bt	Op, Tur	[N28°08'27.9'' E85°19'26.6''] - 1950 m
14-30	Wm-bearing impure marble	Cal, Wm, Qz		[N28°08'26.6'' E85°20'00.0''] - 2370 m
14-31	Two-mica foliated quarzite	Qz, Wm, Bt	Op, Tur	Before Brabal [N28°08'23.9'' E85°20'57.5''] - 2370
14-32	Two-mica micaschist with rare Grt	Qz, Pl, Wm, Bt, Grt	Op	[N28°08'48.8'' E85°20'33.5''] - 2405 m
14-33	Wm + Bt gneiss	Qz, Pl, Wm, Bt	Op, Ttn?	[N28°08'45.2'' E85°20'48.9''] - 2305 m
14-33b	Wm + Bt + Grt micaschist	Qz, Pl, Wm, Bt, Grt	Rt, Ilm, Ap, Tur	[N28°08'45.2'' E85°20'48.9''] - 2305 m
14-34	Fine-grained Bt + Wm + Grt gneiss with rare late Wm	Qz, Pl, Bt, <<Wm, Grt	Rt, Ilm	Just before Thulo Shiabru [N28°08'36.2'' E85°21'23.3''] - 2240 m
14-35	Bt-gneiss with rare Grt and late Wm	Qz, Pl, Bt, Wm, Grt	Gr, Ap, Tur	Beyond Thulo Siabru [N28°07'54.2'' E85°21'13.1''] - 2795 m

14-36	Bt + Wm + Grt gneissic micaschist	Qz, Pl, Bt, Wm, Grt	Gr	Beyond Thulo Siabru [N28°07'40.5'' E85°20'49.4''] - 3200 m
14-37	Bt + Wm + Grt micaschist	Qz, Pl, Bt, Wm, Grt	Ep, Tur, Ilm, Gr	Beyond Phoprang Danda [N28°07'12.5'' E85°20'25.0''] - 3260 m
14-38a	Bt + Wm + Ep + Grt + Scp gneissic micaschist	Bt, Ep, Grt, Pl, Qz, Scp	Op	Path at Sin Gompa [N28°06'40.3'' E85°20'28.2''] - 3335 m
14-38b	Fine-grained Bt-gneiss and level of Bt + Wm + Grt micaschist	Qz, Pl, Bt, Wm, Grt	Ep, Tur*, Ilm, Gr	Path at Sin Gompa [N28°06'40.3'' E85°20'28.2''] - 3335 m
14-39	Bt + Wm + Grt gneissic micaschist	Qz, Pl, Bt, Wm, Grt	Ep, Tur, Ilm, Gr	Woods [N28°06'14.9'' E85°21'40.3''] - 3510 m
14-40	Bt + Wm + Grt + Ky micaschist (Bt>>Wm)	Qz, Pl, Bt, Wm, Grt, Ky	Rt, Ilm, Tur	Going up beyond Cholangpaty [N28°05'46.4'' E85°22'28.8''] - 3775 m
14-41	Bt + Wm + Grt + Ky micaschist	Qz, Pl, Bt, Wm, Grt, Ky	Ilm, Gr, Ap	Beyond Laurebina [N28°05'13.3'' E85°23'33.6''] - 4275 m
14-42	Fine-grained Bt + Grt gneiss with late Wm	Qz, Pl, Bt, Wm, Grt	Ilm, Gr	Beginning of path towards Gosainkund [N28°05'07.7'' E85°26'46.4''] - 4345 m
14-43	Two-mica + Grt + Ky gneissic micaschist	Qz, Pl, Bt, Wm, Grt, Ky	Rt, Ilm, Tur	Path towards Gosainkund [N28°05'05.5'' E86°24'13.8''] - 4390 m
14-44a	Wm + Bt + Grt + Ky micaschist	Qz, Pl, Bt, Wm, Grt, Ky	Rt, Ilm, Gr	Crest N of Gosainkund [N28°05'13.0'' E85°23'33.9''] - 4625 m
14-44b	Bt-gneiss with porphyroblastic Grt and rare late Wm	Qz, Pl, Bt, <<<Wm, Grt	Rt, Ilm, Gr	Crest N of Gosainkund [N28°05'13.0'' E85°23'33.9''] - 4625 m
14-44c	Cal + Cpx + Ep + Grt + Pl + Qz calc-silicate rock	Cal, Cpx, Ep, Grt, Pl, Qz, Amph (late)	Ttn	Crest [N28°05'13.0'' E85°23'33.9'']- 4625m
14-45	Fine-grained Bt + Grt gneiss with late Wm	Qz, Pl, Bt, <<Wm, Grt	Rt, Ilm	Lake, S shore [N28°04'50.8'' E85°24'56.5''] - 4400 m
14-46	Bt + Wm + Grt gneissic micaschist	Qz, Pl, Bt, Wm, Grt	Rt, Ilm, Gr	Just before Laurebina La [N28°04'26.2'' E85°25'41.2''] - 4650 m
14-47	Qz-rich Wm + Bt fine-grained gneiss with rare Grt	>Qz, Pl, <Kfs <Bt, Wm, Grt	Gr	Path at tea house of Bera Goth [N28°03'57.4'' E85°26'52.0''] - 4235 m

14-48	Banded Bt + Grt gneiss with rare Grt	Qz, Pl, Bt, Wm, Grt	Gr, Ilm, Tur	beyond Phedi [N28°03'26.8'' E85°27'35.1''] - 3700 m
14-48b	Bt + Wm + Grt gneiss with rare Sil	Qz, Pl, Bt, Wm, Grt, Sil, Chl	Rt, Ilm, Gr	Beyond Phedi [N28°03'26.8'' E85°27'35.1''] - 3700 m
14-49	Bt + Grt + Sil gneissic micaschist with late Wm	Qz, Pl, Kfs, Bt, Wm, Grt, Sil	Gr, Ilm	[N28°03'02.3'' E85°28'10.7''] - 3590 m
14-50	Qz-rich Bt + Grt gneiss with late Wm	Qz, Pl, Bt, <<Wm, Grt	Op	Woods before Gopte [N28°02'30.9'' E85°28'27.5''] - 3750 m
14-51	Bt-bearing gneiss with late Wm (Bt>>Wm) and rare Sil	Qz, Pl, Kfs, Bt, Wm (<<Kfs), Sil	Op	Path at Tharepati [N28°00'57.1'' E85°29'41.2''] - 3665 m
14-52	Banded fine-grained Bt + Sil gneiss with rare Grt and relict Ky	Qz, Pl, Bt, <<Wm, Grt, Sil, <Ky	Op	Woods beyond Tharepati [N28°00'42.5'' E85°29'42.6''] - 3550 m
14-53a	Banded Cpx + Pl + Qz calc-silicate gneiss	Cpx, Pl, Qz, Amph (late)	Ttn	Woods towards Melamchigaon [N28°00'37.3'' E85°29'50.9''] - 3365 m
14-53b	Cpx + Ep + Grt + Pl + Qz calc-silicate rock	Cpx, Ep, Grt, Pl, Qz	Ttn	Woods towards Melamchigaon [N28°00'37.3'' E85°29'50.9''] - 3365 m
14-53c	Banded Cpx + Ep + Kfs + Pl + Qz + Scp ± Cal calc-silicate gneiss	Cal, Cpx, Ep, Kfs, Pl, Qz, Scp, <<Bt	Ttn	Woods towards Melamchigaon [N28°00'37.3'' E85°29'50.9''] - 3365 m
14-53d	Cpx + Ep + Grt + Pl + Qz + Scp calc-silicate rock	Cpx, Ep, Grt, Pl, Qz, Scp, Amph (late)	Ttn	Woods [N28°00'37.3'' E85°29'50.9''] - 3365 m
14-54	Bt + Sil gneiss with rare Grt and late Wm	Qz, Pl, Bt, Wm, Grt, Sil	Ilm, Tur	Impluvium before Melamchigaon [N28°00'53.5'' E85°30'52.5''] - 2710 m
14-55a	Bt + Wm orthogneiss	Qz, Pl, Kfs, Bt, Wm, Chl (late)	Op	[N28°00'40.4'' E85°31'54.3''] - 2050 m
14-55b	Fine-grained Bt gneiss with late Wm	Qz, Pl, Kfs, Bt, <Wm	Ilm, Tur	Road beyond Melamchigaon [N28°00'40.4'' E85°31'54.3''] - 2050 m
14-56	Banded Bt + Sil gneiss with minor Grt	Qz, Pl, Kfs, Bt, Wm, Grt, Sil,	Gr, Ilm	Impluvium beyond Tharke Ghyang [N27°58'42.4'' E85°33'41.8''] -
14-57	Bt + Wm + Sil gneiss, with minor Grt and late Wm (Bt>Wm)	Qz, Pl, Kfs, Bt, Wm, Grt, Sil	Ilm	Beyond Tharke Ghyang [N27°58'28.1'' E85°33'29.4''] - 2295 m
14-58	Bt-gneiss with rare Sil and late Wm	Qz, Pl, Bt, Wm, <<Sil	Ilm, Rt	[N27°58'03.7'' E85°32'45.6''] - 2010 m
14-58b	Amph + Cal + Ep + Grt + Pl + Qz calc-silicate rock	Amph, Cal, Ep, Grt, Pl, Qz	Ttn	[N27°58'03.7'' E85°32'45.6''] - 2010 m

14-59	Bt-gneiss with rare Grt and late Wm	Qz, Pl, Bt, Wm, Grt, Cb	Ilm	Woods towards Timbu [N27°57'11.9'' E85°32'54.7''] - 1452 m
14-60	Two-mica + Grt + Sil micaschist	Qz, Pl, Bt, Wm, Grt, Sil	Ilm, <Rt, Gr	Timbu bridge [N27°56'59.4'' E86°32'39.1''] - 1280 m
14-61	Fine-grained Bt + Wm gneiss with minor Grt with rare Sil	Qz, Pl, Kfs, Bt, <Wm, Grt	Ilm, Gr	Up beyond Timbu [N27°56'54.4'' E85°32'36.6''] - 1385 m
14-61b	Bt + Wm + Grt micaschist with late Wm	Qz, Pl, Kfs, Bt, Wm, Grt	Rt, Ilm	Up beyond Timbu [N27°56'54.4'' E85°32'36.6''] - 1385 m
14-62	Banded Bt + Wm gneiss with rare Grt	Qz, Pl, Kfs, Bt, Wm, Grt	Ilm	Up beyond Timbu [N27°56'55.8'' E85°32'25.8''] - 1645 m
14-63	Bt + Wm foliated gneiss, with rare Grt	Qz, Pl, Kfs, Bt, Wm, Grt	Rt, Ilm	[N27°56'46.1'' E85°32'14.8''] - 1795 m
14-64	Bt + Wm augen gneiss	Qz, Pl, Kfs, Bt, Wm	Ap	[N27°56'52.2'' E85°31'17.9''] - 2445 m
14-65	Bt + Sil gneissic micaschist, with late Wm	Qz, Pl, Bt, Wm, <Sil	Ilm	Impluvium along the path [N27°57'28.1'' E85°29'50.7''] - 2580 m
14-66	Bt + Wm + Sil micaschist, with late Wm and Bt	Qz, Pl, Bt, Wm, Sil	>Ap, Gr, Ilm, blue Turm	Small waterfall [N27°57'04.7'' E85°29'33.9''] - 2540 m
14-67	Bt + Wm augen gneiss	Qz, Pl, Kfs, Bt, Wm	Ap	[N27°55'56.9'' E85°29'13.5''] - 2510 m
14-68	Foliated Bt + Wm orthogneiss	Qz, Pl, Kfs, Bt, Wm	Ap	[N27°54'18.4'' E85°28'47.1''] - 2190 m
14-69	Bt + Wm augen gneiss	Qz, Pl, Kfs, Bt, Wm		[N27°53'51.1'' E85°28'38.5''] - 2200 m
14-70	Bt + Sil + Grt + Ky micaschist	Qz, Pl, Bt, Grt, Sil, Ky	Rt, Ilm	[N27°53'00.4'' E85°28'09.3''] - 2385 m
14-71	Bt + Wm + Grt gneissic micaschist with rare Sil	Qz, Pl, Bt, Wm, Grt, <<Sil	Ilm	Beyond tea house of Lapcho Danda [N27°52'35.7'' E85°27'28.9''] - 2420 m
14-72	Qz-rich fine-grained Bt-gneiss with late Wm	Qz, Pl, Bt, Wm	Ilm, Tur	[N27°52'12.1'' E85°27'20.8''] - 2210 m
14-73	Qz-rich aplitic gneiss with minor Grt	Qz, Pl, Kfs, <<Bt, Wm, Grt	Gr, Tur	Beyond Chipling [N27°51'53.6'' E85°27'27.5''] - 2060 m
14-73b	Fine-grained banded Bt + Wm + Grt gneiss	Qz, Pl, Kfs, Bt, Wm, Grt	<<Op	Beyond Chipling [N27°51'53.6'' E85°27'27.5''] - 2060 m
14-74a	Fine-grained Bt + Grt gneiss, with Wm in layers	Qz, Pl, Bt, Wm (all late?), Grt		Before Pati Banjang [N27°50'56.6'' E85°27'33.3''] - 1810 m
14-74b	Amph + Ep + Grt + Pl + Qz calc-silicate rock	Amph, Ep, Grt, Pl, Qz	Tur, Ttn	Before Pati Banjang [N27°50'56.6'' E85°27'33.3''] - 1810 m

14-75	Bt + Wm augen gneiss	Qz, Pl, Kfs, Bt, Wm	Ap, >Op	Path beyond Chisopani [N27°49'24.2'' E85°26'50.2''] - 2140 m
14-76	Aplitic Wm-bearing gneiss with Wm-bearing granitic dike	Qz, Pl, Kfs, Wm	Ap	[N27°47'52.7'' E85°26'02.7''] - 2225 m
14-77	Banded Bt + Sil gneiss	Qz, Pl, Bt, Wm, Sil	Ilm	[N27°46'39.9'' E85°25'51.8'] - 2130 m
15-01	Two-mica mylonitic orthogneiss	Qz, Kfs, Pl, Wm, Bt	Ap, Ep, Op	Beyond checkpoint [N28°10'04.7'' E85°20'31.1'] - 1455 m
15-02	Two-mica augen gneiss	Qz, Kfs, Pl, Wm, Bt	Ap, Rt	Beyond checkpoint [N28°10'33.1'' E85°20'32.2'] - 1460 m
15-03	Two-mica augen gneiss	Qz, Kfs, Pl, Wm, Bt	Ap	Beyond the bridge along the riverpath [N28°10'56.7'' E85°20'29.8'] - 1490 m
15-04a	Two-mica + Grt micaschist	Qz, Pl, Bt, Wm, Grt	Ilm	Over the bridge [N28°11'08.9'' E85°20'44.0'] - 1490 m
15-04b	Banded Wm + Bt gneiss with rare Grt	Qz, Pl, Bt, Wm, Grt	Ilm	Over the bridge [N28°11'08.9'' E85°20'44.0'] - 1490 m
15-04c	Bt + Wm micaschist	Qz, Pl, Bt, Wm	Ilm, Tur	Over the bridge [N28°11'08.9'' E85°20'44.0'] - 1490 m
15-05	Qz-rich fine-grained Bt + Grt gneiss	Qz, Pl, Bt, Grt	Op	Road before Medambou [N28°11'23.3'' E85°20'52.7'] - 1510 m
15-05	Cal + Ep + Grt + Pl + Qz calc-silicate rock	Cal, Ep, Grt, Pl, Qz	Op, Ttn	Road before Medambou [N28°11'23.3'' E85°20'52.7'] - 1510 m
15-06a	Qz-rich Bt + Wm + Grt gneiss	Qz, Pl, Bt, Wm, Grt	Ilm, Tur	Beyond Medambou [N28°11'47.7'' E85°21'62.8'] - 1530 m
15-06b	Foliated two-mica quartzite with Grt	Qz,< Bt, Wm, Grt	Tur	Beyond Medambou [N28°11'47.7'' E85°21'62.8'] - 1530 m
15-06c	Qz-rich Wm + Bt gneissic micaschist with rare Grt	Qz, Pl, < Bt, Wm, Grt	Op	Just beyond Medambou [N28°11'47.7'' E85°21'62.8'] - 1530 m
15-07	Bt + Wm gneissic micaschist with rare Grt	Qz, Pl, Bt, Wm, Grt	Op, Tur	[N28°12'12.9'' E85°21'13.3'] - 1555 m
15-08	Graphitic two-mica phyllite	Qz, Pl, Wm, Bt	Gr, Op, Tur	Second bend going up from Syabru Bensi [N28°09'44.2'' E85°20'03.3'] - 1535 m

15-09	Cb-bearing Bt + Wm phyllitic micaschist	Bt, Cb, Wm, Pl, Qz	Gr, Op, Tur	Forth bend going up from Syabru Bensi [N28°09'47.0'' E85°19'58.4'] - 1610 m
15-10	Phl-bearing impure marble	Cb, <<Pl, Phl, Qz		Before the sixth bend going up from Syabru Bensi [N28°09'48.3'' E85°19'54.2'] - 1670 m
15-11	Phl-bearing graphitic calc-schist	Cb, Pl?, Phl, Qz	Gr, Op	Before the bend along the path [N28°09'57.0'' E85°20'52.0'] - 1710 m
15-12	Phyllitic two-mica garnet micaschist	Qz, Pl, Wm, Bt, Grt	Gr, Op, Tur	Before the bend along the path [N28°10'01.4'' E85°20'06.6'] - 1760 m
15-12b	Impure marble with minor Wm	Cb, Qz, Wm		Before the bend along the path [N28°10'01.4'' E85°20'06.6'] - 1760 m
15-12c	Wm-bearing graphitic phyllite with minor Cb	<Cb, Qz, Wm	Gr	Before the bend along the path [N28°10'01.4'' E85°20'06.6'] - 1760 m
15-12d	Phl-bearing impure marble with rare Wm	Cb, <<Pl, Phl, Qz, <Wm	Tur	Before the bend along the path [N28°10'01.4'' E85°20'06.6'] - 1760 m
15-13	Phl + Tr -bearing impure marble	Cb, <<Pl, Phl, Qz, Tr	Rt	Beyond the bend along the path [N28°10'05.9'' E85°20'17.4'] - 1760 m
15-13b	Cb-bearing Bt + Wm phyllitic micaschist	Bt, Cb, Wm, Pl, Qz	Ilm, <<Rt	Beyond the bend along the path [N28°10'05.9'' E85°20'17.4'] - 1760 m
15-14	Phl-bearing impure marble	Cb, Phl, Qz		Beyond the steep bends [N28°10'09.4'' E85°20'09.6'] - 1960 m
15-15a	Bt + Wm micaschist	Qz, Pl, Bt, <<Wm	Op, Tur	Along the path [N28°10'10.1'' E85°20'00.0'] - 1980 m
15-15b	Two-mica graphitic phyllite, with porphyroblastic Grt and St	Qz, Pl?, Wm, Bt, Chl, Grt, St	Gr, Op, Tur	Block along the path [N28°10'10.1'' E85°20'00.0'] - 1980 m
15-16a	Phl-bearing impure marble	Cb, Phl, Qz		Beyond the tea-house at the pass [N28°09'59.7'' E85°19'17.7'] - 2250 m
15-16b	Cb-bearing Phl + Wm + <Chl phyllitic micaschist	Cb, <Chl, Pl?, Qz, Wm	Gr, Tur	Beyond the tea-house at the pass [N28°09'59.7'' E85°19'17.7'] - 2250 m
15-17	Bt + Wm + Chl phyllitic micaschist, with porphyroblastic garnet	Qz, Pl, Wm, Bt, Chl, Grt	Gr, Aln, Tur	[N28°10'03.5'' E85°18'30.1'] - 2290 m

15-18	Two-mica phyllite, with porphyroblastic Grt and Bt	Qz, Pl, Wm, Bt, Chl, Grt	Gr, Op	[N28°10'13.5'' E85°18'02.5'] - 2350 m
15-19	Two-mica Grt micaschist with late Chl	Qz, Pl, Wm, Bt, Chl, Grt	Op, Tur	[N28°10'08.2'' E85°17'48.5'] - 2390 m
15-19b	Fine-grained Bt-gneiss with porphyroblastic Grt and Amph + Chl aggregates	Qz, Pl, Bt, rare Wm, Grt, Amph, Chl	Op, Tur	[N28°10'08.2'' E85°17'48.5'] - 2390 m
15-20	Wm + Bt + Chl phyllite, with late porphyroblastic Bt	Qz, Pl, Wm, Bt, Chl, Grt	Op, Tur	[N28°09'36.2'' E85°17'01.0'] - 2355 m
15-21	Two-mica phyllite	Qz, Pl, Wm, Bt	Op, Tur	Going down from Gotlang, second big impluvium [N28°09'52.2'' E85°16'59.5'] - 2140 m
15-22	Two-mica phyllite	Qz, Pl, Bt, Wm	Gr, Op, Tur	[N28°11'06.6'' E85°17'57.3'] - 1770 m
15-23	Two-mica phyllite with rare Grt	Qz, Pl, Wm, Bt, Grt	Op	before the bridge at Chilime [N28°11'06.6'' E85°17'57.3'] - 1770 m
15-24	Cb-bearing Phl + Wm phyllitic schist	Cb, Pl, Phl, Qz, Wm	Op, Tur	Crossed the bridge, going up [N28°11'41.5'' E85°17'48.4'] - 1950 m
15-25a	Phl-bearing impure marble	Cb, Phl, Qz		Before The road to Tatopani [N28°12'00.7'' E85°17'47.7'] - 2290 m
15-25b	Graphitic phyllitic schist	Qz, Pl?, Wm	Gr	Before the path at Tatopani [N28°12'00.7'' E85°17'47.7'] - 2290 m
15-26a	Foliated Wm + Bt + Chl + St quartzite	Qz, Wm, Bt, Chl, St (phl??)	Tur	Beyond Tatopani [N28°13'11.4'' E85°18'03.7'] - 2655 m
15-26b	Bt + Wm micaschist with porphyroblastic Grt	Qz, Pl, Bt, Wm, Grt, <<<Sil	Rt, Ilm	Beyond Tatopani [N28°13'11.4'' E85°18'03.7'] - 2655 m
15-26c	Amph + Bt + Cb + Grt + Pl micaschist	Amph, Bt, Cb, <Pl, Qz	Ap, Ilm	Beyond Tatopani [N28°13'11.4'' E85°18'03.7'] - 2655 m
15-26d	Wm graphitic phyllite, with porphyroblastic Grt and St	Qz, Pl?, Wm, Grt, St	Gt, Rt, Ilm	Beyond Tatopani [N28°13'11.4'' E85°18'03.7'] - 2655 m
15-27	Phl + Wm graphitic calc-schist	Cb, Phl, Pl, Qz, Wm	Gr, Rt, Ilm	Beyond a small ridge [N28°12'04.8'' E85°18'24.2'] - 2670 m
15-28	Phl-bearing carbonatic phyllite with porphyroblastic Amph	Amph, Cb, Phl, Qz	Gr, Op	[N28°11'51.1'' E85°18'30.6'] - 2615 m

15-28b	Two-mica Grt + St + Ky phyllitic micaschist	Qz, Wm, Bt, Grt, St, Ky	Ilm	[N28°11'51.1'' E85°18'30.6'] - 2615 m
15-29	Two-mica mylonitic augen gneiss	Qz, Kfs, Pl, Wm, Bt	Ap	Just before the hillcrossing [N28°11'45.8'' E85°19'08.9'] - 2690 m
15-30	Fine-grained two-mica orthogneiss	Qz, Kfs, Pl, Wm, Bt	Ap	downward in the woods [N28°11'59.6'' E85°19'31.1'] - 2700 m
15-31	Wm + Bt + Grt gneissic micaschist	Qz, Pl, Bt, Wm, Grt	Rt, Ilm	Going down in the woods [N28°12'11.8'' E85°19'37.8'] - 2650 m
15-32	Wm + Bt gneiss with Qz vein	Qz, Pl, Bt, Wm	Ilm	In the woods towards Tuman [N28°12'17.3'' E85°19'58.3'] - 2505 m
15-33	Wm + Bt gneissic micaschist with porphyroblastic Ky	Qz, Pl, Bt, Wm, Grt, Ky	Rt, Ilm, Tur	[N28°13'10.4'' E85°20'26.3'] - 2295 m
15-34	Two-micaschist with rare Grt	Qz, Pl, Bt, Wm, Grt	Ilm, Tur	Just before the crest beyond Tuman [N28°13'14.4'' E85°20'39.8'] - 2275 m
15-34b	Bt + Wm + Grt gneissic micaschist with Qz vein	Qz, Pl, Bt, Wm, Grt	Rt, Ilm, Tur, Gr?	Just before the crest beyond Tuman [N28°13'14.4'' E85°20'39.8'] - 2275 m
15-35	Two-mica + Grt micaschist	Qz, Pl, Bt, Wm, Grt	Rt, Ilm	Viewpoint before Dalphedi [N28°13'30.9'' E85°21'06.8'] - 2300 m
15-36a	Fine-grained Qz-rich Bt + Wm + Chl gneiss with minor Grt	Qz, Pl, Bt, Wm, Grt, <<Chl		Riverside [N28°14'17.0'' E85°21'28.0'] - 1660 m
15-36b	Wm + Bt micaschist	Qz, Pl, Bt, Wm	Tur	Riverside [N28°14'17.0'' E85°21'28.0'] - 1660 m
15-37	Wm + Bt micaschist with rare Grt	Qz, Pl, Bt, Wm, Grt	Ilm, Gr, Aln?	Crossed the bridge [N28°14'27.0'' E85°21'30.9'] - 1645 m
15-38	Bt + Wm + Grt + Ky + St gneissic micaschist	Qz, Pl, Bt, Wm, Grt, ky, St	Rt, Ilm	Road towards Timure [N28°14'47.9'' E85°21'45.5'] -
15-39	Bt + Wm + Grt gneissic micaschist	Qz, Pl, Bt, Wm, Grt	Rt, Ilm, Ap	Beyond the check-point [N28°15'30.5'' E85°22'06.9'] - 1720 m
15-39b	Bt + Wm + Grt + Sil gneissic micaschist	Qz, Pl, Bt, Wm, Grt, Sil	Rt, Ilm, Gr	Beyond the check-point, 100 m after [N28°15'30.5'' E85°22'06.9'] - 1720 m
15-40a	Bt-gneissic micaschist with rare Grt and late Wm	Qz, Pl, Kfs, Bt, Wm, Grt, Sil	Ilm, Gr	Along the road [N28°15'42.2'' E85°22'22.9'] - 1780 m

15-40b	Bt + Wm fine-grained gneiss (<<Wm), with late Wm	Qz, Pl, Bt, Wm, Kfs	Ilm	Along the road [N28°15'42.2'' E85°22'22.9'] - 1780 m
15-41	Migmatitic Bt + Sil banded gneiss with minor Grt and late Wm	Qz, Pl, Bt, Wm, Kfs, Grt, Sil	Gr, Ilm	[N28°16'10.1'' E85°22'40.0'] - 1795 m
15-42	Wm + Bt + Grt micaschist	Qz, Pl, Bt, Wm, Grt, Chl	Rt, Ilm, Tur	Crossed the bridge [N28°14'11.3'' E85°21'34.8'] - 1690 m
15-42b	Bt + Wm gneiss with porphyroblastic Ky	Qz, Pl, Bt, <<Wm, Grt, Ky, <<Sil	Rt, Ilm	[N28°14'11.3'' E85°21'34.8'] - 1690 m
15-43	Bt + Wm + Grt + Ky gneissic micaschist	Qz, Pl, Bt, Wm, Grt, Ky	Rt, Ilm, Tur	Along the path [N28°13'50.0'' E85°21'39.5'] - 1650 m
15-44	Wm + Bt micaschist with porphyroblastic Grt	Qz, Pl, Bt, Wm, Grt	Rt, Ilm, Tur	Along the path [N28°13'28.1'' E85°21'42.3'] - 1610 m
15-44b	Wm + Bt gneiss with Grt	Qz, Pl, Bt, Wm, Grt	Ilm, Tur	Along the path [N28°13'28.1'' E85°21'42.3'] - 1610 m
15-45	Bt + Grt gneissic micaschist	Qz, Pl, Bt, <<<Wm, Grt, < Chl	Rt, Ilm	Along the path [N28°13'05.8'' E85°21'04.7'] - 1570 m
15-46	Fine-grained Bt + Ep + Grt + Pl + Scp gneiss, with minor Cb and rare Wm	Bt, Cb, Ep, Grt, Pl, Scp, Wm, <<Chl	Ttn	Going up beyond Lingling [N28°12'39.1'' E85°21'43.8'] - 1905 m
15-47a	Bt + Wm micaschist with minor Grt	Qz, Pl, Bt, Wm, Grt	Ilm, Tur	Impluvium before Briddim [N28°12'13.2'' E85°21'44.1'] - 2025 m
15-47b	Amph + Bt + Ep + Grt + Pl + Scp gneissic micaschist	Amph, Bt, Cb, Pl, Scp, Qz	Op, Ttn	Impluvium before Briddim [N28°12'13.2'' E85°21'44.1'] - 2025 m
15-48	Bt + Wm + Ky gneissic micaschist	Qz, Pl, Bt, Wm, Ky	Ilm, Tur, Ap	Going down along the path [N28°11'14.5'' E85°21'17.1'] - 2110 m
15-49	Fine-grained Bt-gneiss with rare Grt; cm-thick level with Ap + Pl + Qz + Wm + Bt and Qz-vein	Qz, Pl, Bt, Wm, Grt	Op	[N28°10'58.7'' E85°20'57.9'] - 1880 m
15-50	Two mica + Grt fine-grained gneiss	Qz, Pl, Wm, Bt, Grt	Op, Tur	Beyond Wangel [N28°10'35.0'' E85°20'47.9'] - 1670 m
15-51a	Two-mica phyllitic micaschist with minor Grt and late Chl	Qz, Pl, Wm, Bt, Grt, Chl	Ilm, Tur, Rt, Aln	Before Syabru Bensi [N28°09'33.0'' E85°20'04.0'] - 1430 m

15-51b	Wm + Bt phyllite with porphyroblastic Grt and late Chl	Qz, Pl, Wm, Bt, Grt, Chl	Ilm, Tur	Before Syabru Bensi [N28°09'33.0'' E85°20'04.0'] - 1430 m
15-51c	Qz-rich Cb + Grt + Ep + Pl calc-silicate rock, with radiate Amph aggregates	Amph, <Cb, Ep, Grt, Pl, Qz	Aln, Op, Gr?	Road before Syabru Bensi [N28°09'33.0'' E85°20'04.0'] - 1430 m
15-52	Two-mica phyllitic micaschist	Qz, Pl, Wm, Bt	Tur	Before the bridge [N28°09'28.5'' E85°19'56.4'] - 1410 m

APPENDIX 2.

List of CO_2-source rock samples from central and eastern Nepal (and Sikkim) with mineral assemblage

Type 1 (CFMAST-HC group) CO_2-source rocks with mineral assemblage and location

	Sample	Cal	Qz	Pl	Ep/Zo	Scp	Wm	Bt	Kfs	Amph	Cpx	Grt
A	13-76c	x								x		
	13-72	x								x		
	09-17a	x	x	x								
B	04-4 (I)		x	x						x		x
	06-26		x	x	<			<<		>		x
	06-61		x	x						x		x
	12-37c		x	x	x					x		x
	12-44c		x	x			<	<<		<		x
	14-58b	x	x	x	x					x		x
	14-74b		x	x	x					x		x
	15-05	x	x	x	x							x
	15-51c	x	x	x	x					x		x
C	06-40		x	x						x	x	x
	06-48		x	x	x						x	x
	06-57		x	x	x						x	x
	06-59		x	x							x	x
	06-60		x	x							x	x
	06-62		x	x	x						x	x
	06-65		x	x							x	x
	07-15		x	x							x	x
	09-16b		x	x	<						x	x
	09-63b		x	x	<						x	x
	10-37a		x	x	>>					x	x	x
	10-37b		x	x	>>					x	x	x
	12-24b		x	x	x						x	x
	13-15 (I)		x	x	x						x	x
	13-16b (I)		x	x							x	x
	13-18a (I)		x	x							x	x
	13-21b (I)		x	x							x	x
	13-22b (I)		x	x							x	x
	13-23b (I)		x	x						x	x	x
	13-26 (I)		x	x							x	x
	13-28b (I)		x	x							x	x
	13-29b (I)		x	x							x	x
	13-30b (I)		x	x						x	x	x
	13-32b (I)		x	x						x	x	x
	13-38b (I)		x	x	x					x	x	x
	13-39 (I)		x	x	x						x	x
	13-40b (I)		x	x							x	x
	13-41b (I)		x	x	x						x	x

	Sample	Cal	Qz	Pl	Ep/Zo	Scp	Wm	Bt	Kfs	Amph	Cpx	Grt
	13-42b (I)		x	x							x	x
	13-45b (I)		x	x							x	x
	14-53b		x	x	x						x	x
	14-44c	x	x	x	x					late	x	x
D	04-4* (I)		x	x							x	
	07-45		x	x	x					x	x	
	09-17b		x	x							x	
	12-57b		x	x	x					x		
	13-60b		x	x						x	x	
	14-53a		x	x						late	x	

Type 2 (NCFMAST-HC group) CO_2-source rocks with mineral assemblage and location

	Sample	Cal	Qz	Pl	Ep/Zo	Scp	Wm	Bt	Kfs	Amph	Cpx	Grt
A	08-58		x	x	x	x					x	x
	12-58a		x	x	x	x					x	x
	12-58b		x	x	x	x					x	x
	10-37a		x	x	>>					x	x	x
	13-41b(I)		x	x	>>						x	x
	14-21b	x	x	x	x	x				late	x	x
	14-21c	x	x	x	x	x	<			late	x	x
	14-53d		x	x	x	x				late	x	x
B	12-66a	>>	x	x	x	x					x	
	14-20b	>>	x	x	x	x				late	x	

Type 3 (NKCFMAST-HC group) CO_2-source rocks with mineral assemblage and location

	Sample	Cal	Qz	Pl	Ep/Zo	Scp	Wm	Bt	Kfs	Amph	Cpx	Grt
A	06-12	>>	x					x				
	10-59	x	x	x			x	x				
	10-47b	x	x				x	x				
	13-76b	x	x				x			x		
	14-30	x	x				x					
	15-10	x	x	<<				Phl				
	15-12b	x	x				x					
	15-12d	x	x	<<			<<	Phl				
	15-13	x	x	<<				Phl		x		
	15-14	x	x					Phl				
	15-16a	x	x					Phl				
	15-25a	x	x					Phl				

	Sample	Cal	Qz	Pl	Ep/Zo	Scp	Wm	Bt	Kfs	Amph	Cpx	Grt
B	**13-82a**	x	x	x				Phl		x		
	13-82b	x	x	x			x	red				
	12-1a	x	x	x			x	green				
	12-1b	x	x	x			x	Phl				
	12-1c	x	x	>>				green				
	10-39	x	x	x			x	green				
	10-49c	x	x	x			x	green				
	10-58b	x	x	x			x	green				
	10-64	x	x	x			x	green				
	15-09	x	x	x			x	x				
	15-11	x	x	?				Phl				
	15-12c	x	x	x			x					
	15-13b	x	x	x	?		x	green				
	15-16b	x	x	?			x	Phl				
	15-27	x	x	x			x	Phl				
	15-28	x	x					Phl		x		
	15-24	x	x	x	<<		x	Phl				
C	**10-38a**		x	x	>		x	x				x
	13-38		x	x	x	<	x	x				x
	14-38a		x	x	x	<	x	green				x
	15-46	<<	x	x	x	x	<<	x				x
	15-47b	<<	x	x		<		x		x		x
C*	15-26c	x	x	<<				green		>>		x
D	**07-40**		x	x		>	x	>	x			
	12-11a		x	x		<<		>	x			
	12-11b		x	x	<	<		>	x			
	12-12b		x	x	>	x	x	>	x			
	08-42		x	<	>	x		x	>	<<		
E	**05-41 (I)**		x	x	>			>			<	
	08-31		x	x	>			>	<	x	<	
	08-36		x	x	<	<<*		>	x	x	x	
	12-21b	<<	x	x	>	<*			<<	x	<	
	13-31		x	x	x	x		>	x	x		
F	**04-28 (I)**	x	x	x	x	x			x	late	x	
	05-55	x	x	x				rel	x	x	x	
	05-56	>>	<	x				Phl		late	x	
	07-20	<<	x	x						late	x	
	07-22	x	<<	x	<	x	rel	rel	x	<	x	
	07-41	>>	x	x	x	x		Phl	x	late	x	
	07-60		x	x	x	x			x	late	x	
	08-67	x	x	x				rel	x	late	x	
	08-57	x	x	x	x	ex?			x	late	x	

Sample	Cal	Qz	Pl	Ep/Zo	Scp	Wm	Bt	Kfs	Amph	Cpx	Grt
09-25	<	x	x	x	ex?			x	late	x	
10-4		x	x	x	x		rel	x	late	x	
12-12a		x	x	>	<			>	x	<	
12-64a	x	x	x	x	x			x	x	x	
12-64b	x	x	x	x	x			x	x	x	
12-65	x	x	x	x	x			x	x	x	
12-66a	>>	x		x	x				x	x	
12-66b	x	x	x	x	x			x	x	x	
13-62c		x	x	x	x			x	x	x	
13-64	x	x	x	x	x			x	x	x	
14-17		x	x		x			x		x	
14-20a	x	x	x	x	x		rel	x		x	
14-53c	x	x	x	x	x		x	x		x	
14-10d		x	x				x	x	x	x	

(I) refer to samples from Sikkim (India)

APPENDIX 3.

SEM-EDS analysis of metapelites (Chapter 3) and CO_2-source rocks (Chapter 4 and 5)

Chapter 3. Representative SEM-EDS analysis of Biotite

	15-19	15-19	14-27a	14-27a	15-28b	15-26b	15-26b	14-03	14-03	14-25b	14-25b	15-38	15-38	14-24	14-44a	14-61b	14-71	14-52	14-08a	14-12
	2.50 Bt	1.24 Bt	1.1 Bt	2.31 bt	1.37 Bt	0.8 Bt	6.15 Bt	2.18 Bt	1.21 Bt	3.7 Bt	2.22 Bt	6.17 Bt	2.23 Bt	1.30 Bt	3.22 Bt	3.24 Bt	5.5 Bt	2.11 bt	1.19 Bt	1.21 Bt
SiO_2	34.64	34.96	34.57	34.23	37.17	37.43	36.53	36.17	35.48	34.38	34.37	36.10	37.04	34.25	34.23	34.78	33.73	35.26	34.53	33.99
TiO_2	0.52	1.64	1.86	1.33	1.47	1.81	1.92	2.01	2.87	2.16	2.94	1.93	2.10	3.39	2.74	2.59	3.58	3.14	2.80	0.59
Al_2O_3	19.04	17.87	17.53	17.29	18.34	18.45	17.82	18.28	16.94	17.36	17.54	18.78	18.51	16.96	17.78	17.83	18.37	17.74	19.37	20.41
FeO	21.44	21.75	22.40	23.67	16.41	15.67	18.21	14.44	19.80	20.91	21.20	17.90	18.30	20.79	19.84	24.52	22.14	19.28	22.10	21.41
MgO	7.58	8.10	8.43	8.75	11.51	12.22	10.40	12.79	10.29	9.26	8.22	10.40	10.27	8.50	9.26	6.67	5.96	9.84	7.61	7.44
Na_2O	0.00	0.36	0.00	0.00	0.00	0.00	0.00	0.50	0.30	0.37	0.30	0.00	0.00	0.00	0.37	0.00	0.30	0.00	0.00	0.00
K_2O	8.90	8.94	9.65	9.55	8.98	9.34	9.64	7.88	8.40	8.74	9.05	8.72	8.74	8.87	9.23	9.81	9.51	9.84	10.06	8.95
Total	92.13	93.62	94.44	94.82	93.88	94.91	94.52	92.07	94.08	93.16	93.62	93.83	94.96	92.76	93.45	96.20	93.59	95.10	96.47	92.79
Si	2.80	2.80	2.75	2.71	2.87	2.85	2.85	2.80	2.78	2.74	2.76	2.80	2.84	2.76	2.73	2.76	2.76	2.76	2.71	2.72
Ti	0.03	0.10	0.11	0.08	0.09	0.10	0.11	0.12	0.17	0.13	0.17	0.11	0.12	0.21	0.16	0.15	0.22	0.19	0.17	0.04
Al	1.81	1.68	1.64	1.61	1.67	1.66	1.64	1.67	1.56	1.63	1.66	1.72	1.68	1.61	1.67	1.67	1.77	1.64	1.79	1.92
Fe^{3+}	0.00	0.00	0.00	0.00	0.00	0.00	0.00	0.00	0.00	0.00	0.00	0.00	0.00	0.00	0.00	0.00	0.00	0.00	0.00	0.00
Fe^{2+}	1.45	1.45	1.49	1.57	1.06	1.00	1.19	0.94	1.30	1.40	1.42	1.16	1.18	1.40	1.33	1.63	1.52	1.26	1.45	1.43
Mg	0.91	0.97	1.00	1.03	1.32	1.39	1.21	1.48	1.20	1.10	0.98	1.20	1.18	1.02	1.10	0.78	0.73	1.15	0.89	0.89
Na	0.00	0.06	0.00	0.00	0.00	0.00	0.00	0.08	0.05	0.05	0.05	0.00	0.00	0.00	0.06	0.00	0.05	0.00	0.00	0.00
K	0.92	0.91	0.98	0.96	0.88	0.91	0.96	0.78	0.84	0.89	0.93	0.86	0.86	0.91	0.94	0.99	0.99	0.98	1.00	0.91
Tot cat	7.92	7.97	7.98	7.96	7.88	7.91	7.96	7.85	7.88	7.94	7.97	7.85	7.86	7.91	7.99	7.98	8.04	7.98	8.01	7.91
XMg	0.39	0.40	0.40	0.40	0.56	0.58	0.50	0.61	0.48	0.44	0.41	0.51	0.50	0.41	0.45	0.33	0.32	0.48	0.38	0.38

Chapter 3. Representative SEM-EDS analysis of White mica

	15-19	15-19	14-27a	14-27a	15-28b	15-26b	15-26b	14-03	14-03	14-25b	14-25b	15-38	15-38	14-24	14-44a	14-61b	14-71	14.52
	3.3 Wm	2.19 Wm	1.5 Wm	1.19 Wm	3.3 Wm	0.11 Wm	6.12 Wm	2.26 Wm	3.4 Wm	2.25 Wm	1.4 Wm	1.2 Wm	6.18 Wm	3.3 Wm	2.30 Wm	3.23 Wm	1.24 Wm	1.45 Wm
SiO_2	46.57	46.62	45.06	44.50	44.96	45.63	45.10	45.00	46.24	44.53	44.61	45.41	48.02	45.66	44.21	44.64	44.88	44.39
TiO_2	0.34	0.00	0.49	0.42	0.57	0.74	0.84	1.08	1.19	0.88	0.67	0.95	0.70	1.07	0.93	1.97	0.88	0.00
Al_2O_3	34.72	34.33	33.36	32.92	33.39	32.72	32.66	32.88	32.67	32.51	32.49	35.34	35.34	34.41	32.62	32.76	33.26	33.16
FeO	1.63	1.22	1.26	1.46	1.41	1.54	1.40	1.36	1.31	2.84	2.45	1.76	1.05	1.20	1.50	1.97	1.43	2.90
MgO	0.56	0.66	0.75	0.71	0.71	0.92	0.79	1.04	1.16	0.76	0.68	0.57	0.63	0.74	0.77	0.73	0.62	0.48
Na_2O	1.54	1.22	0.90	0.68	1.03	1.30	1.26	1.03	0.97	1.21	1.12	1.59	1.73	0.99	0.82	0.46	0.89	0.34
K_2O	9.18	9.76	10.28	10.61	9.76	9.41	9.33	9.60	9.95	9.79	9.66	8.58	8.86	10.45	10.26	11.17	10.30	11.48
Total	94.54	93.81	92.10	91.30	91.83	92.26	91.38	92.00	93.49	92.53	91.68	94.20	96.33	94.52	91.11	93.70	92.26	92.74
Si	3.11	3.14	3.11	3.11	3.10	3.13	3.13	3.09	3.14	3.07	3.10	3.03	3.09	3.08	3.09	3.09	3.10	3.08
Ti	0.02	0.00	0.03	0.02	0.03	0.04	0.04	0.06	0.06	0.05	0.04	0.05	0.03	0.05	0.05	0.05	0.05	0.00
Al	2.73	2.73	2.71	2.71	2.71	2.65	2.67	2.66	2.61	2.64	2.66	2.78	2.76	2.73	2.69	2.67	2.71	2.71
Fe^{3+}	0.04	0.00	0.00	0.00	0.03	0.02	0.00	0.06	0.01	0.10	0.08	0.00	0.01	0.00	0.00	0.00	0.00	0.08
Fe^{2+}	0.05	0.07	0.07	0.09	0.05	0.07	0.08	0.02	0.07	0.06	0.07	0.09	0.05	0.07	0.09	0.11	0.08	0.09
Mg	0.06	0.07	0.08	0.07	0.07	0.09	0.08	0.11	0.12	0.08	0.07	0.06	0.06	0.07	0.09	0.08	0.06	0.05
Na	0.20	0.16	0.12	0.09	0.14	0.17	0.17	0.14	0.13	0.16	0.15	0.21	0.22	0.13	0.11	0.06	0.12	0.05
K	0.78	0.84	0.91	0.95	0.86	0.82	0.83	0.84	0.86	0.86	0.86	0.73	0.73	0.90	0.92	0.99	0.91	1.01
Tot cat	6.98	7.00	7.03	7.04	7.00	7.00	6.99	6.98	6.99	7.02	7.01	6.95	6.95	7.03	7.04	7.05	7.03	7.06

Chapter 3. Representative SEM-EDS analysis of Plagioclase

	15-19	15-19	14-27a	14-27a	15-26b	15-26b	14-03	14-03	14-25b	14-25b	15-38	15-38	14-24	14-44a	14-61b	14-71	14-52	14-08a	14-12
	2.40 Pl	2.22 Pl	3.4 Pl	3.3 Pl	1.11 Pl	1.9 Pl	3.9 Pl	3.8 Pl	2.6 Pl	4.1 Pl	1.6 Pl	2.17 Pl	1.36 Pl	4.21 Pl	2.8 Pl	2.28 Pl	1.28 Pl	1.20 Pl	4.4 Pl
SiO_2	63.60	63.98	61.01	61.06	62.49	64.15	64.93	63.85	65.58	65.34	60.63	62.58	65.57	64.28	66.65	64.89	65.98	60.57	64.08
TiO_2	0.00	0.00	0.00	0.00	0.00	0.00	0.00	0.00	0.00	0.00	0.00	0.00	0.00	0.00	0.00	0.00	0.00	0.00	0.00
Al_2O_3	22.55	22.85	24.48	24.86	23.39	22.67	22.49	22.12	20.71	22.12	24.10	22.23	21.55	22.45	21.26	22.33	21.23	24.31	22.88
FeO	0.00	0.00	0.00	0.00	0.00	0.00	0.00	0.00	0.92	0.00	0.95	0.00	0.00	0.00	0.00	0.00	0.00	0.00	0.00
CaO	0.37	4.42	6.51	6.99	6.02	4.69	3.77	3.71	2.43	3.23	6.28	3.96	3.37	4.02	2.28	3.94	2.52	6.74	4.18
Na_2O	4.48	8.99	7.74	7.39	7.73	8.47	9.13	8.98	9.91	9.57	7.90	9.31	9.53	9.12	9.95	8.90	9.71	7.46	9.30
K_2O	8.87	0.00	0.00	0.00	0.00	0.00	0.00	0.00	0.00	0.00	0.00	0.00	0.00	0.00	0.00	0.00	0.00	0.23	0.16
Total	99.88	100.23	99.74	100.30	99.63	99.98	100.32	98.66	99.55	100.27	99.86	98.08	100.03	99.87	100.14	100.06	99.44	99.30	100.61
Si	2.83	2.83	2.73	2.72	2.80	2.86	2.87	2.88	2.91	2.88	2.71	2.82	2.90	2.85	2.94	2.88	2.93	2.72	2.82
Ti	0.00	0.00	0.00	0.00	0.00	0.00	0.00	0.00	0.00	0.00	0.00	0.00	0.00	0.00	0.00	0.00	0.00	0.00	0.00
Al	1.18	1.19	1.29	1.31	1.24	1.19	1.17	1.15	1.08	1.15	1.27	1.18	1.12	1.17	1.10	1.17	1.11	1.29	1.19
Fe^{3+}	0.00	0.00	0.00	0.00	0.00	0.00	0.00	0.00	0.00	0.00	0.00	0.00	0.00	0.00	0.00	0.00	0.00	0.00	0.00
Fe^{2+}	0.01	0.00	0.00	0.00	0.00	0.00	0.00	0.00	0.03	0.00	0.04	0.00	0.00	0.00	0.00	0.00	0.00	0.00	0.00
Ca	0.21	0.21	0.31	0.33	0.29	0.22	0.18	0.17	0.12	0.15	0.30	0.19	0.16	0.19	0.11	0.19	0.12	0.32	0.20
Na	0.76	0.77	0.67	0.64	0.67	0.73	0.78	0.80	0.85	0.82	0.68	0.81	0.82	0.78	0.85	0.77	0.84	0.65	0.79
K	0.00	0.00	0.00	0.00	0.00	0.00	0.00	0.00	0.00	0.00	0.00	0.00	0.00	0.00	0.00	0.00	0.00	0.01	0.01
Tot cat	5.00	5.00	5.00	5.00	5.00	5.00	5.00	5.00	5.00	5.00	5.00	5.00	5.00	5.00	5.00	5.00	5.00	4.99	5.01
XCa	0.22	0.21	0.32	0.34	0.30	0.24	0.19	0.17	0.12	0.16	0.31	0.19	0.16	0.20	0.11	0.20	0.13	0.33	0.21

Chapter 3. Representative SEM-EDS analysis of Garnet

	15-19		14-27a		15-28b	15-26b		14-03		14-25b		15-38		14-24	14-44a	14-61b	14-71	14-52	14-08a	14-12
	core	rim	core	rim	rim	core	rim	core	rim	core	rim	core	rim							
	2.41 Grt	2.32 Grt	4.15 Grt	2.1 Grt	1.19 Grt	5.6 Grt	6.3 Grt	1.9 Grt	2.41 grt	3.8 Grt	2.14 Grt	1.8 Grt	1.1 Grt	4.8 Grt	3.11 Grt	1.8 Grt	1.7 Grt	1.4 Grt	2.10 Grt	1.4 Grt
SiO_2	36.83	36.91	36.72	36.85	37.78	36.70	37.18	36.38	36.70	36.51	35.73	36.75	37.21	37.11	36.03	36.68	36.41	37.31	37.30	36.48
Al_2O_3	20.32	20.19	19.94	20.49	21.03	19.90	20.11	20.19	19.97	20.40	19.96	20.54	20.77	20.45	20.31	19.89	19.91	20.55	20.51	20.39
FeO	28.86	35.76	29.37	32.95	33.67	30.07	31.39	33.60	34.78	36.49	35.93	32.26	35.46	37.12	34.68	39.22	39.15	32.14	36.04	37.47
MnO	7.21	0.93	5.74	2.71	0.00	4.14	2.38	2.97	1.14	1.95	1.81	5.17	1.26	1.98	2.01	1.44	1.50	5.21	3.09	2.04
MgO	0.88	1.85	0.91	1.31	3.26	2.55	3.44	3.79	4.42	3.21	3.49	2.19	3.39	3.94	4.29	3.04	2.51	5.18	2.51	2.75
CaO	6.13	3.74	8.01	6.83	5.64	6.42	5.76	2.48	2.08	1.19	1.19	2.93	1.89	1.56	1.48	0.69	1.01	0.82	1.24	0.89
Total	100.23	99.38	100.69	101.14	101.38	99.78	100.26	99.41	99.09	99.75	98.11	99.85	99.98	102.16	98.80	100.96	100.49	101.20	100.69	100.02
Si	2.98	3.01	2.95	2.95	2.97	2.95	2.96	2.94	2.96	2.96	2.94	2.98	2.99	2.95	2.94	2.95	2.95	2.94	2.99	2.96
Al	1.94	1.94	1.89	1.93	1.95	1.89	1.89	1.92	1.90	1.95	1.93	1.96	1.97	1.91	1.94	1.88	1.90	1.91	1.94	1.95
Fe^{3+}	0.10	0.04	0.21	0.18	0.10	0.21	0.19	0.21	0.18	0.14	0.19	0.08	0.05	0.18	0.19	0.21	0.20	0.20	0.15	0.13
Fe^{2+}	1.85	2.39	1.76	2.02	2.12	1.81	1.90	2.06	2.17	2.33	2.28	2.10	2.33	2.24	2.16	2.43	2.46	1.92	2.27	2.41
Mn	0.49	0.06	0.39	0.18	0.00	0.28	0.16	0.20	0.08	0.13	0.13	0.36	0.09	0.11	0.16	0.10	0.10	0.35	0.22	0.14
Mg	0.11	0.22	0.11	0.16	0.38	0.31	0.41	0.46	0.53	0.39	0.43	0.26	0.40	0.47	0.49	0.36	0.30	0.61	0.30	0.33
Ca	0.53	0.33	0.69	0.58	0.48	0.55	0.49	0.21	0.18	0.10	0.10	0.25	0.16	0.13	0.13	0.06	0.09	0.07	0.12	0.08
Tot cat	8.00	8.00	8.00	8.00	8.00	8.00	8.00	8.00	8.00	8.00	7.99	7.99	7.99	8.00	8.00	7.99	8.00	8.00	7.99	8.00
XCa	0.16	0.10	0.23	0.20	0.15	0.17	0.15	0.07	0.06	0.04	0.03	0.08	0.05	0.04	0.04	0.02	0.03	0.03	0.04	0.02
XFe	0.64	0.80	0.61	0.69	0.73	0.64	0.67	0.71	0.74	0.79	0.78	0.72	0.79	0.76	0.74	0.83	0.85	0.65	0.80	0.82
XMg	0.03	0.07	0.04	0.05	0.12	0.10	0.13	0.15	0.18	0.13	0.14	0.09	0.13	0.16	0.17	0.12	0.10	0.21	0.10	0.11
XMn	0.17	0.02	0.13	0.06	0.00	0.09	0.05	0.07	0.03	0.05	0.04	0.11	0.03	0.04	0.05	0.03	0.03	0.12	0.07	0.04

Chapter 3. Representative SEM-EDS analysis of Staurolite

	15-28b	14-25b	15-38	14-24
Analysys	3.4 St	1.6 St	1.25 St	3.7 St
SiO_2	29.09	26.61	25.58	25.41
TiO_2	0.72	0.65	0.61	0.00
Al_2O_3	53.56	51.27	52.81	51.43
FeO	13.67	13.30	13.13	12.27
MgO	1.16	1.39	1.81	1.17
Total	98.20	95.24	93.94	90.29
Si	8.24	7.93	7.75	7.78
Ti	0.15	0.15	0.13	0.00
Al	17.88	18.00	18.14	18.55
Fe^{3+}	0.00	0.00	0.00	0.00
Fe^{2+}	3.24	3.31	3.20	3.14
Mg	0.49	0.62	0.79	0.53
Tot cat	30.00	30.00	30.00	30.00
XMg(Fe^{2+})	0.13	0.16	0.20	0.15

Chapter 4. Representative SEM-EDS analysis of Garnet

	15-05	14-74	14-44c	14-53d	14-38a	15-46	15-26c
Analysis	a.7 Grt	4.2 Grt	3.3 Grt	0.10 Grt	2.9 Grt	9.1 Grt	0.1 Grt
SiO_2	37.17	37.98	37.40	37.22	38.82	37.87	36.60
Al_2O_3	19.91	21.03	20.51	17.61	21.05	21.13	19.60
FeO	22.26	21.50	13.04	13.65	29.26	20.91	35.86
MnO	2.46	1.41	6.95	1.18	3.77	2.70	1.96
MgO	1.63	1.69	1.46	0.44	2.88	2.82	1.35
CaO	16.04	15.67	18.51	27.95	9.18	13.16	5.18
Total	99.47	99.28	97.87	98.05	101.20	98.59	100.55
Si	2.95	3.00	2.98	2.95	2.95	3.00	2.96
Al	1.86	1.96	1.93	1.64	1.88	1.97	1.87
Fe^{3+}	0.25	0.04	0.11	0.46	0.23	0.02	0.21
Fe^{2+}	1.22	1.38	0.76	0.44	1.63	1.37	2.21
Mn	0.17	0.09	0.47	0.08	0.24	0.18	0.13
Mg	0.19	0.20	0.17	0.05	0.33	0.33	0.16
Ca	1.36	1.33	1.58	2.37	0.75	1.12	0.45
Tot cat	8.00	8.00	8.00	7.99	8.00	7.99	7.99
XCa	0.41	0.44	0.52	0.72	0.25	0.36	0.15
XFe	0.47	0.46	0.27	0.24	0.57	0.48	0.75
XMg	0.06	0.07	0.06	0.02	0.11	0.10	0.05
XMn	0.06	0.03	0.15	0.02	0.08	0.06	0.04

Chapter 4. Representative SEM-EDS analysis of Feldspar

	15-05	15-05	14-74b	14-74b	14-44c	14-44c	14-53d	14-38a	15-46	15-26c	14-53c	14-53c	14-17	14-17
Analysis	a.9 Pl i	0.29 Kfs	1.5 Pl	0.2 Kfs	5.4 Pl	4.11 Kfs	4.3 Pl	0.34 Pl	0.5 Pl	1.18 Pl i	8.24 Pl	8.16 Kfs	3.10 Pl	6.1 Kfs
SiO_2	61.55	64.58	43.89	65.37	44.69	64.89	44.18	59.87	51.01	67.54	44.59	65.24	63.53	64.44
Al_2O_3	23.45	17.63	35.29	17.43	35.13	17.95	34.87	24.29	31.53	19.72	35.57	18.31	23.12	18.17
FeO	0.00	0.51	0.00	0.00	0.00	0.00	0.00	0.00	0.00	0.64	0.00	0.00	0.00	0.00
CaO	7.32	7.38	19.32	0.00	20.20	0.00	20.16	7.05	14.53	1.15	19.56	0.00	4.70	0.00
Na_2O	6.45	0.47	0.53	0.37	0.55	0.00	0.49	7.13	3.56	10.31	0.65	0.57	8.73	0.65
K_2O	0.22	16.59	0.00	16.85	0.00	16.58	0.00	0.00	0.00	0.00	0.00	16.04	0.14	16.02
Total	98.99	99.77	99.03	100.02	100.57	99.42	99.70	98.34	100.63	99.36	100.37	100.16	100.22	99.28
Si	2.78	3.00	2.05	3.02	2.05	3.02	2.05	2.72	2.31	3.00	2.05	3.01	2.81	3.00
Al	1.25	0.96	1.94	0.95	1.90	0.99	1.91	1.30	1.68	1.03	1.93	1.00	1.21	1.00
Fe^{3+}	0.00	0.02	0.00	0.00	0.00	0.00	0.00	0.00	0.00	0.00	0.00	0.00	0.00	0.00
Fe^{2+}	0.00	0.00	0.00	0.00	0.00	0.00	0.00	0.00	0.00	0.02	0.00	0.00	0.00	0.00
Ca	0.64	0.00	0.97	0.00	0.99	0.00	1.00	0.34	0.70	0.05	0.96	0.00	0.22	0.00
Na	0.31	0.04	0.05	0.03	0.05	0.00	0.04	0.63	0.31	0.89	0.06	0.05	0.75	0.06
K	0.01	0.98	0.00	0.99	0.00	0.99	0.00	0.00	0.00	0.00	0.00	0.94	0.01	0.95
Tot cat	4.99	5.00	5.01	4.99	4.99	5.00	5.00	4.99	5.00	4.99	5.00	5.00	5.00	5.01
XCa	0.66	0.96	0.95	0.97	0.95	1.00	0.96	0.35	0.69	0.06	0.94	0.95	0.23	0.94

Chapter 4. Representative analysis of Epidote and Scapolite

Epidote									Scapolite					
	15-05	14-74b	14-44c	14-53d	14-38a	15-46	14-53c	14-17		14-53d	14-38a	15-46	14-53c	14-17
Analysis	1.4 Ep	0.3 Ep in Grt	2.1 Ep	4.4 Ep	0.2 Ep	9.2 Ep	8.5 Ep	0.18 Ep	Analysis	4.2 Scp	0.1 Scp	8.3 Scp	8.19A Scp	1.2 Scp i
SiO_2	37.44	38.09	39.37	37.48	37.94	38.17	38.99	37.44	SiO_2	44.77	46.8	46.54	45.88	47.33
Al_2O_3	27.42	29.67	32.33	24.73	25.43	28.26	29.03	27.34	Al_2O_3	27.36	24.48	27.01	27.93	26.85
FeO	5.51	2.72	1.51	10.76	10.60	5.20	5.71	6.87	CaO	19.85	17.03	18.20	18.61	17.76
CaO	24.97	25.33	25.11	24.28	24.30	22.43	24.84	24.63	Na_2O	2.32	3.85	3.41	3.68	3.94
Total	95.34	95.81	98.32	97.25	98.27	94.06	98.57	96.28	K_2O	0.5	0.00	0.00	0.45	0.14
									Cl	0.00	0.00	0.02	0.48	0.53
Si	2.99	3.00	2.99	2.98	2.99	3.05	3.00	2.97	Total	94.8	92.16	95.18	97.03	96.55
Al	2.58	2.75	2.90	2.32	2.36	2.67	2.63	2.56	Si	6.98	7.42	7.13	6.99	7.19
Fe^{3+}	0.33	0.16	0.09	0.65	0.63	0.31	0.33	0.41	Al	5.02	4.58	4.87	5.01	4.81
Fe^{2+}	0.00	0.00	0.00	0.00	0.00	0.00	0.00	0	Ca	3.31	2.89	2.99	3.04	2.89
Ca	2.14	2.14	2.04	2.07	2.05	1.92	2.05	2.09	Na	0.7	1.18	1.01	1.09	1.16
									K	0.1	0	0.00	0.09	0.03
									Cl	0.00	0.00	0.01	0.12	0.14
XZo	0.64	0.82	0.91	0.33	0.35	0.68	0.66	0.56	CO_2	1	1	0.99	0.88	0.86
									Eq.An	0.68	0.53	0.63	0.67	0.60

Chapter 4. Representative analysis of Clinopyroxene and Amphibole

Clinopyroxene

	14-44c	14-53d	14-53c	14-17
Analysis	1.1 Cpx	0.8 Cpx	8.25 Cpx	2.1 Cpx
SiO_2	52.24	49.17	52.77	51.63
Al_2O_3	0.00	1.87	1.02	0.00
FeO	7.93	18.19	10.67	14.34
MnO	0.83	0.00	0.00	0.00
MgO	12.89	6.91	11.71	9.4
CaO	25.24	24.32	24.5	25.24
Total	99.13	100.46	100.67	100.61
Si	1.98	1.93	1.98	1.98
Al	0.00	0.09	0.05	0.00
Fe^{3+}	0.00	0.06	0.00	0.00
Fe^{2+}	0.25	0.53	0.33	0.46
Mn	0.03	0.00	0.00	0.00
Mg	0.73	0.40	0.65	0.54
Ca	1.03	1.02	0.98	1.04
Tot cat	4.02	4.03	3.99	4.02
XMg	0.74	0.43	0.66	0.54

Amphibole

Sample	14-74b	14-44c	15-26c	15-26c	14-53c	14-17
Analysis	5.8 Amph	2.10 Amph in Grt	3.19 Amph	1.26 Amph	1.5 Amph	3.1 Amph
SiO_2	49.05	53.56	41.73	50.26	55.50	43.28
TiO_2	0.00	0.00	0.51	0.00	0.00	0.00
Al_2O_3	7.34	1.21	9.43	0.00	2.42	18.36
FeO	14.04	9.98	27.44	35.05	4.73	9.76
MgO	13.29	16.85	6.18	10.82	19.49	0.94
MnO	0.00	0.66	0.00	0.00	0.00	0.86
CaO	12.02	13.09	8.89	0.56	11.47	21.27
Na_2O	0.70	0.00	1.16	0.00	1.09	0.00
K_2O	0.45	0.00	0.51	0.00	0.00	0.00
Total	96.89	95.35	95.85	96.69	94.70	94.47
Si	7.14	7.82	6.60	7.83	7.88	6.63
Ti	0.00	0.00	0.06	0.00	0.00	0.00
Al	1.26	0.21	1.76	0.00	0.41	3.31
Fe^{3+}	0.42	0.05	0.47	0.34	0.08	0.00
Fe^{2+}	1.29	1.17	3.15	4.22	0.49	1.25
Mg	2.89	3.67	1.46	2.51	4.13	0.21
MnO	0.00	0.08	0.00	0.00	0.00	0.11
Ca	1.88	2.05	1.51	0.09	1.75	3.49
Na	0.2	0.00	0.36	0.00	0.30	0.00
K	0.08	0.00	0.10	0.00	0.00	0.00
Tot cat	15.16	15.05	15.47	14.99	15.04	15.00
XMg	0.69	0.76	0.32	0.37	0.90	0.15

Chapter 4. Representative analysis of White mica, Biotite and Chlorite

White mica			Biotite					Chlorite				
	14-38a	15-46	Sample	14-38a	15-46	15-26c	14-53c	Sample	14-74b	14-44c	15-46	15-26c
Analysis	2.11 Wm	8.6 Wm	Analysis	0.8 Bt	9.8 Bt i	3.7 Bt	5.d Bt i	Analysis	5.3 Chl	4.9 Chl i	0.10 Chl	1.17 Chl
SiO_2	45.57	46.75	SiO_2	36.30	36.40	35.47	39.12	SiO_2	25.49	27.58	24.42	20.96
TiO_2	0.73	0.82	TiO_2	2.42	0.46	3.00	0.89	Al_2O_3	20.28	20.33	20.91	21.22
Al_2O_3	30.08	32.94	Al_2O_3	17.47	20.38	14.16	15.33	FeO	25.33	19.76	29.83	43.89
FeO	4.41	1.67	FeO	20.95	19.23	26.85	12.22	MgO	14.07	18.16	9.96	0.96
MgO	1.21	1.46	MgO	9.21	8.63	7.32	16.61	MnO	0.49	0.87	1.11	1.44
CaO	0.00	0.00	Na_2O	0.00	0.00	0.00	0.00	Total	85.66	86.70	86.23	88.47
Na_2O	0.36	0.29	K_2O	10.13	9.51	9.00	9.23					
K_2O	11.52	10.25	Total	96.48	94.61	95.80	93.40					
Total	93.88	94.18										
Si	3.14	3.12	Si	2.82	2.82	2.83	2.93	Si	5.54	5.75	5.44	4.91
Ti	0.04	0.04	Ti	0.14	0.03	0.18	0.04	Ti	0.00			
Al	2.44	2.60	Al	1.60	1.86	1.33	1.48	Al	5.20	5.00	5.49	5.86
Fe^{3+}	0.14	0.09	Fe^{3+}	0.00	0.00	0.00	0.00	Fe^{3+}	0.00	0.00		
Fe^{2+}	0.11	0.00	Fe^{2+}	1.36	1.25	1.79	0.89	Fe^{2+}	4.61	3.45	5.56	8.60
Mg	0.12	0.15	Mg	1.07	1.00	0.87	1.64	Mg	4.56	5.65	3.31	0.34
Ca	0.00	0.00	Na	0.00	0.00	0.00	0.00	Mn	0.09	0.15	0.21	0.29
Na	0.05	0.04	K	1.01	0.94	0.92	0.89					
K	1.01	0.87	Tot cat	8.00	7.90	7.92	7.87	Tot cat	20.00	20.00	20.01	20.00
Tot cat	7.05	6.91	XMg(Fe^{2+})	0.44	0.44	0.33	0.65	XMg(Fe^{2+})	0.50	0.62	0.37	0.04

Chapter 5. Representative SEM-EDS analysis of Feldpsar

	14-44c	14-44c	15-46	15-46	15-46	15-46	14-53c	14-53c	14-53c	14-53c	14-53c	15-53c	14-53c	14-17	14-17	14-17	14-17	14-17	14-17
Analysis	5.4 Pl	4.11 Kfs in Grt	2.5 Pl	8.2 Pl	9.11 Pl in Grt	9.13 Pl in Scp	8.24A Pl matrix	5.1B Pl matrix	6.2A Pl in Scp	L.2.bA Pl in Ttn	8.16A Kfs matrix	8.12B Kfs in Pl	F.1.hA Kfs in ttn	9.8 Pl matrix	9.9 Pl matrix	9.10 Pl in Cpx	8.1 Pl in Scp	6.1 Kfs	2.2 Kfs in Cpx
SiO_2	44.69	62.63	58.04	57.06	47.86	55.28	44.59	42.89	48.43	44.34	65.24	64.89	64.91	61.06	51.39	54.63	59.62	64.44	64.98
Al_2O_3	35.13	17.32	25.71	27.17	33.07	26.55	35.57	34.36	30.50	34.49	18.31	18.22	18.02	23.77	30.27	28.15	25.41	18.17	18.41
FeO	0.00	0.00	0.00	0.00	0.00	0.00	0.00	0.00	0.00	0.00	0.00	0.00	0.00	0.00	0.00	0.00	0.00	0.00	0.00
CaO	20.20	0.00	8.01	9.68	16.64	9.63	19.56	20.24	15.17	19.26	0.00	0.00	0.00	5.74	14.03	11.24	7.49	0.00	0.00
Na_2O	0.55	0.00	7.31	6.41	2.22	6.03	0.65	0.36	2.90	0.69	0.57	0.52	0.62	8.09	3.72	5.08	7.23	0.65	1.07
K_2O	0.00	16.00	0.00	0.00	0.00	0.00	0.00	0.00	0.00	0.00	16.04	16.12	16.39	0.15	0.00	0.00	0.14	16.02	15.64
Total	100.57	95.95	99.07	100.32	99.79	97.49	100.37	97.85	97.00	98.78	100.16	99.75	99.94	98.81	99.41	99.10	99.89	99.28	100.10
Si	2.05	3.02	2.61	2.55	2.19	2.55	2.05	2.03	2.28	2.07	3.01	3.00	3.00	2.75	2.35	2.49	2.67	3.00	2.99
Al	1.90	0.99	1.36	1.43	1.79	1.44	1.93	1.91	1.69	1.90	1.00	0.99	0.98	1.26	1.63	1.51	1.34	1.00	1.00
Fe^{3+}	0.00	0.00	0.00	0.00	0.00	0.00	0.00	0.00	0.00	0.00	0.00	0.00	0.00	0.00	0.00	0.00	0.00	0.00	0.00
Fe^{2+}	0.00	0.00	0.00	0.00	0.00	0.00	0.00	0.00	0.00	0.00	0.00	0.00	0.00	0.00	0.00	0.00	0.00	0.00	0.00
Ca	0.99	0.00	0.39	0.46	0.82	0.48	0.96	1.03	0.76	0.96	0.00	0.00	0.00	0.28	0.69	0.55	0.36	0.00	0.00
Na	0.05	0.00	0.64	0.56	0.20	0.54	0.06	0.03	0.26	0.06	0.05	0.05	0.06	0.71	0.33	0.45	0.63	0.06	0.10
K	0.00	0.99	0.00	0.00	0.00	0.00	0.00	0.00	0.00	0.00	0.94	0.95	0.97	0.01	0.00	0.00	0.01	0.95	0.92
Tot cat	4.99	5.00	5.00	5.00	5.00	5.01	5.00	5.00	4.99	4.99	5.00	4.99	5.01	5.00	5.00	5.00	5.00	5.01	5.01
XCa	0.95	1.00	0.38	0.46	0.81	0.47	0.94	0.97	0.74	0.94	0.95	0.95	0.95	0.28	0.68	0.55	0.36	0.94	0.91

A: Cal-poor domain; B: Cal-rich domain in sample 14-53c

Chapter 5. Representative SEM-EDS analysis of White mica, Biotite and Chlorite

White mica			Biotite					Chlorite			
	15-46	15-46		15-46	15-46	15-46	14-53c	14-53c		14-44c	14-44c	15-46
Analysis	8.6 Wm matrix	9.7 Wm in Grt	Analysis	9.8 Bt in Grt	3.5 Bt in Pl	2.3 Bt matrix	5.dB Bt in Ttn	3.8A Bt in matrix	Analysis	4.9 Chl	5.3 Chl in Grt	0.10 Chl in Grt
SiO_2	46.75	44.78	SiO_2	36.40	36.81	37.17	39.12	38.26	SiO_2	27.58	24.94	24.42
TiO_2	0.82	0	TiO_2	0.46	2.58	3.17	0.89	0.72	Al_2O_3	20.33	22.26	20.91
Al_2O_3	32.94	33.29	Al_2O_3	20.38	17.03	17.03	15.33	14.46	FeO	19.76	25.75	29.83
FeO	1.67	3.76	FeO	19.23	15.74	15.55	12.22	15.31	MgO	18.16	13.2	9.96
MgO	1.46	0.95	MgO	8.63	11.6	12.22	16.61	15.21	MnO	0.87	1.97	1.11
CaO	0.00	0.17	Na_2O	0.00	0.00	0.00	0.00	0.00	Total	86.70	86.70	86.23
Na_2O	0.29	0.33	K_2O	9.51	9.04	9.27	9.23	10.38				
K_2O	10.25	10.28	Total	94.61	92.80	94.41	93.40	94.34				
Total	94.18	93.56										
Si	3.12	3.04	Si	2.82	2.89	2.87	2.93	2.93	Si	5.75	5.3	5.44
Ti	0.04	0	Ti	0.03	0.15	0.18	0.04	0.04	Ti		0	
Al	2.60	2.67	Al	1.86	1.57	1.55	1.48	1.31	Al	5.00	5.58	5.49
Fe^{3+}	0.09	0.19	Fe^{3+}	0.00	0.00	0.00	0.00	0.00	Fe^{3+}	0.00	0	
Fe^{2+}	0.00	0	Fe^{2+}	1.25	1.03	1.00	0.89	0.98	Fe^{2+}	3.45	4.58	5.56
Mg	0.15	0.1	Mg	1.00	1.36	1.4	1.64	1.74	Mg	5.65	4.18	3.31
Ca	0.00	0.01	Na	0.00	0.00	0.00	0.00	0.00	Mn	0.15	0.35	0.21
Na	0.04	0.04	K	0.94	0.9	0.91	0.89	1.01				
K	0.87	0.89	Tot cat	7.90	7.90	7.91	7.87	8.01	Tot cat	20.00		20.01
Tot cat	6.91	6.94	XMg(Fe^{2+})	0.44	0.57	0.58	0.65	0.64	XMg(Fe^{2+})	0.62	0.48	0.37

Chapter 5. Representative SEM-EDS analysis of Epidote and Scapolite

Epidote										Scapolite							
	14-44c	14-44c	15-46	14-53c	14-53c	14-53c	14-53c	14-17	14-17		15-46	14-53c	14-53c	14-53c	14-53c	14-17	14-17
Analysis	2.1 Ep c	2.2 Ep r	9.2 Ep	8.5B Ep sympl.	8.6B Ep sympl.	0.3A Ep in Pl	8.13B Ep matrix	0.18 Ep matrix	6.10 Ep matrix	Analysis	8.3 Scp	8.19A Scp	5.12B Scp matrix	1.1B Scp in Cpx	S.2.bB Scp in Ttn	1.2 Scp i	0.29 Scp matrix
SiO_2	39.37	38.86	38.17	38.99	38.92	37.84	39.52	37.44	39.65	SiO_2	46.54	45.88	48.71	44.47	49.12	47.33	46.71
Al_2O_3	32.33	28.78	28.26	29.03	30.85	28.58	30.35	27.34	32.16	Al_2O_3	27.01	27.93	23.57	28.56	24.66	26.85	25.77
FeO	1.51	6.19	5.20	5.71	2.53	5.27	4.30	6.87	1.41	CaO	18.20	18.61	13.91	18.26	14.79	17.76	16.75
CaO	25.11	24.94	22.43	24.84	24.79	24.36	25.20	24.63	25.70	Na_2O	3.41	3.68	4.96	2.83	5.44	3.94	4.17
Total	98.32	98.77	94.06	98.57	97.09	96.05	99.37	96.28	98.92	K_2O	0.00	0.45	0.91	0.51	0.58	0.14	0.37
										Cl	0.02	0.48	1.55	0.42	0.95	0.53	0.77
Si	2.99	2.99	3.05	3.00	3.00	2.99	3.00	2.97	3.00	Total	95.18	97.03	93.61	95.05	95.54	96.55	94.54
Al	2.90	2.61	2.67	2.63	2.81	2.66	2.72	2.56	2.87								
Fe^{3+}	0.09	0.36	0.31	0.33	0.15	0.31	0.25	0.41	0.08	Si	7.13	6.99	7.64	6.83	7.54	7.19	7.27
Fe^{2+}	0.00	0.00	0.00	0.00	0.00	0.00	0.00	0.00	0.00	Al	4.87	5.01	4.36	5.17	4.46	4.81	4.73
Ca	2.04	2.06	1.92	2.05	2.05	2.06	2.05	2.09	2.08	Ca	2.99	3.04	2.34	3.00	2.43	2.89	2.79
										Na	1.01	1.09	1.51	0.84	1.62	1.16	1.26
XZo	0.91	0.63	0.68	0.66	0.81	0.65	0.72	0.57	0.91	K	0.00	0.09	0.18	0.10	0.11	0.03	0.07
										Cl	0.01	0.12	0.41	0.11	0.25	0.14	0.20
										CO_2	0.99	0.88	0.59	0.89	0.75	0.86	0.80
										Eq.An	0.63	0.67	0.45	0.72	0.49	0.60	0.58

Chapter 5. Representative SEM-EDS analysis of Clinopyroxene and Amphibole

Clinopyroxene							
	14-44c	14-44c	14-53c	14-53c	14-53c	14-17	14-17
Analysis	1.1 Cpx	2.12 Cpx in Grt	8.25A Cpx matrix	8.8B Cpx matrix	1.5 Cpx in Pl	9.12 Cpx matrix	5.3 Cpx matrix
SiO_2	52.24	51.4	52.77	52.54	52.05	52.3	50.81
Al_2O_3	0.00	0.00	1.02	1.02	0.8	0.00	0.48
FeO	7.93	8.69	10.67	10.67	10.11	12.17	16.93
MnO	0.83	0.62	0.00	0.00	0.00	0.00	0.00
MgO	12.89	12.82	11.71	11.67	11.9	10.56	7.57
CaO	25.24	24.27	24.5	24.81	23.55	25.8	24.94
Total	99.13	97.8	100.67	100.71	98.41	100.83	100.73
Si	1.98	1.98	1.98	1.97	1.99	1.98	1.97
Al	0.00	0.00	0.05	0.04	0.04	0.00	0.02
Fe^{3+}	0.00	0.00	0.00	0.01	0	0.00	0.02
Fe^{2+}	0.25	0.25	0.33	0.33	0.32	0.39	0.53
Mn	0.03	0.03	0.00	0	0	0.00	0.00
Mg	0.73	0.75	0.65	0.65	0.68	0.60	0.44
Ca	1.03	1	0.98	1	0.96	1.05	1.04
Tot cat	4.02	4.01	3.99	4	3.99	4.02	4.02
XMg	0.74	0.72	0.66	0.66	0.67	0.61	0.44

Amphibole					
	14-44c	14-44c	14-53c	14-53c	14-17
Analysis	2.10 Amph in Grt	1.1 Amph	1.5A Amph in Cpx	8.9B Amph in Cpx	3.1 Amph in Cpx
SiO_2	53.56	50.49	55.50	54.35	43.28
TiO_2	0.00	0.00	0.00	0.00	0.00
Al_2O_3	1.21	5.13	2.42	1.51	18.36
FeO	9.98	12.46	4.73	13.74	9.76
MgO	16.85	14.47	19.49	15.46	0.94
MnO	0.66	0.49	0.00	0.00	0.86
CaO	13.09	12.72	11.47	13.29	21.27
Na_2O	0.00	0.29	1.09	0.00	0.00
K_2O	0.00	0.00	0.00	0.00	0.00
Total	95.35	96.05	94.70	98.35	94.47
Si	7.82	7.38	7.88	7.78	6.63
Ti	0.00	0.00	0.00	0.00	0.00
Al	0.21	0.88	0.41	0.26	3.31
Fe^{3+}	0.05	0.29	0.08	0.14	0.00
Fe^{2+}	1.17	1.23	0.49	1.51	1.25
Mg	3.67	3.15	4.13	3.30	0.21
MnO	0.08	0.06	0.00	0.00	0.11
Ca	2.05	1.99	1.75	2.04	3.49
Na	0.00	0.08	0.30	0.00	0.00
K	0.00	0.00	0.00	0.00	0.00
Tot cat	15.05	15.06	15.04	15.03	15.00
XMg	0.76	0.72	0.90	0.68	0.15

Chapter 5. Representative SEM-EDS analysis of Garnet

	14-44c	14-44c	15-46	15-46
Analysis	3.3 Grt	3.7 Grt	0.12 Grt	9.1 Grt
SiO_2	37.40	37.93	38.67	37.87
Al_2O_3	20.51	20.16	21.49	21.13
FeO	13.04	15.15	21.78	20.91
MnO	6.95	6.45	4.13	2.70
MgO	1.46	1.98	2.85	2.82
CaO	18.51	17.15	11.64	13.16
Total	97.87	98.82	100.56	98.59
Si	2.98	2.95	3.02	3.00
Al	1.93	1.90	1.98	1.97
Fe^{3+}	0.11	0.20	0	0.02
Fe^{2+}	0.76	0.81	1.42	1.37
Mn	0.47	0.44	0.27	0.18
Mg	0.17	0.24	0.33	0.33
Ca	1.58	1.47	0.97	1.12
Tot cat	8.00	8.01	7.99	7.99
XCa	0.52	0.48	0.32	0.36
XFe	0.27	0.31	0.47	0.47
XMg	0.06	0.08	0.11	0.11
XMn	0.15	0.14	0.09	0.06